DE GRUYTER

GRADUATE

ADVANCED MATERIALS

Edited by Theo van de Ven and Armand Soldera

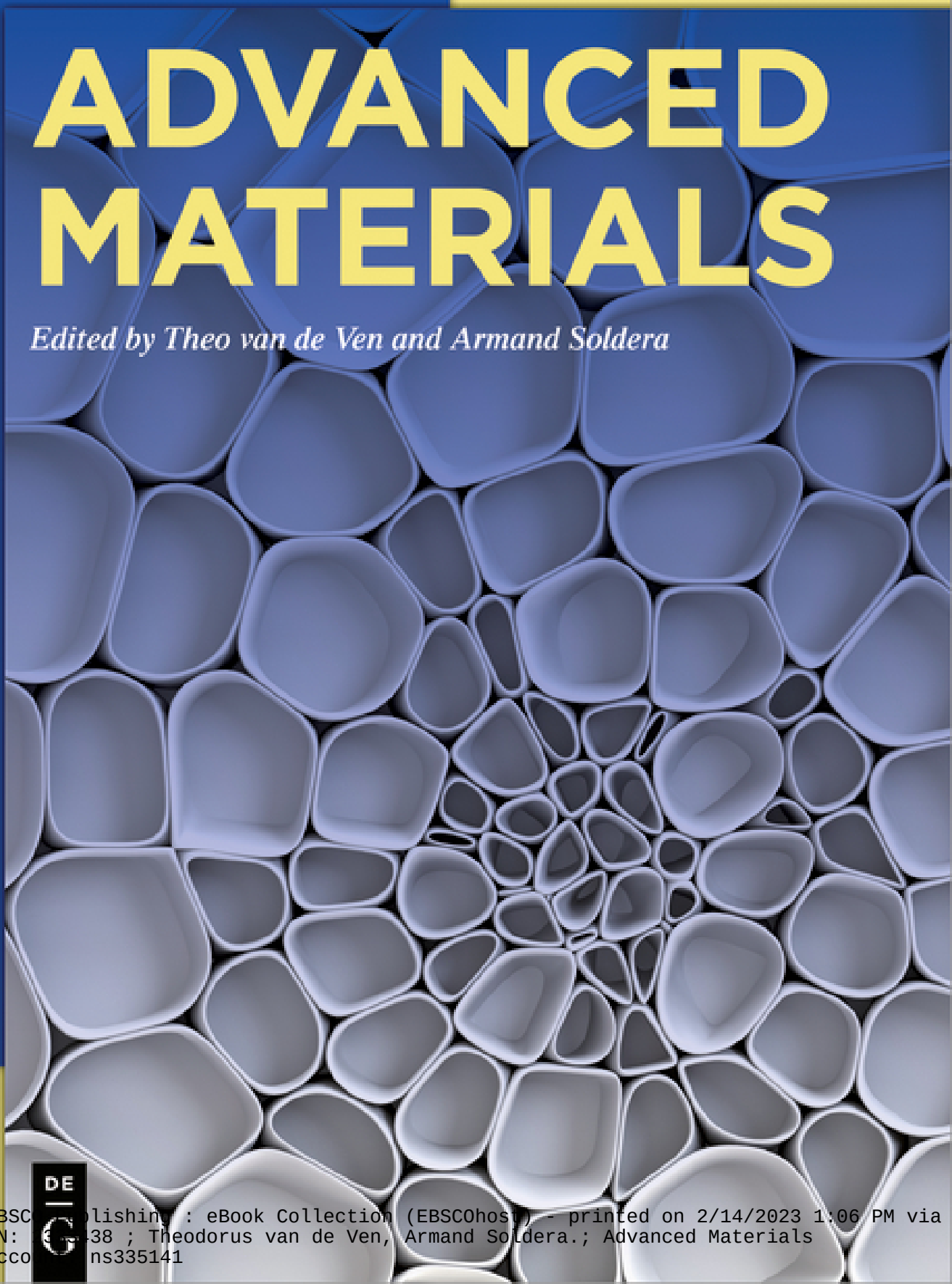

Copyright 2020. De Gruyter. All rights reserved. May not be reproduced in any form without permission from the publisher, except fair uses permitted under U.S. or applicable copyright law.

EBSCO Publishing : eBook Collection (EBSCOhost) - printed on 2/14/2023 1:06 PM via
AN: [illegible]38 ; Theodorus van de Ven, Armand Soldera.; Advanced Materials
Acco[illegible]ns335141

Theo van de Ven and Armand Soldera (Eds.)

Advanced Materials

EBSCOhost - printed on 2/14/2023 1:06 PM via . All use subject to https://www.ebsco.com/terms-of-use

Also of interest

Electrochemical Storage Materials
From Crystallography to Manufacturing Technology
Meyer, Leisegang, Zschornak, Stöcker, 2019
ISBN 978-3-11-049137-1, e-ISBN 978-3-11-049398-6

Carbon-based Smart Materials
Charitidis, Koumoulos, Dragatogiannis, 2019
ISBN 978-3-11-047774-0, e-ISBN 978-3-11-047913-3

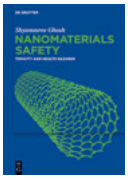

Nanomaterials Safety
Toxicity And Health Hazards
Ghosh, 2018
ISBN 978-3-11-057808-9, e-ISBN 978-3-11-057909-3

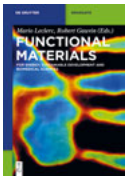

Functional Materials
For Energy, Sustainable Development and Biomedical Sciences
Lerclerc, Gauvin (Eds.), 2014
ISBN 978-3-11-030781-8, e-ISBN 978-3-11-030782-5

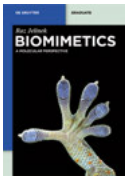

Biomimetics
A Molecular Perspective
Jelinek, 2013
ISBN 978-3-11-028117-0, e-ISBN 978-3-11-028119-4

EBSCOhost - printed on 2/14/2023 1:06 PM via . All use subject to https://www.ebsco.com/terms-of-use

Advanced Materials

Edited by
Theo van de Ven and Armand Soldera

DE GRUYTER

EBSCOhost - printed on 2/14/2023 1:06 PM via . All use subject to https://www.ebsco.com/terms-of-use

Editors
Prof. Theodorus van de Ven
Dept. of Chemistry
McGill University
Pulp & Paper Research Centre
3420 Rue University
Montreal, Québec H3A 2A7
Canada
Theo.Vandeven@mcgill.ca

Prof. Armand Soldera
Dept. of Chemistry
Faculty of Sciences
Université de Sherbrooke
2500 bld de l'université
Sherbrooke, Quebec, J1K 2R1
Canada
Armand.Soldera@USherbrooke.ca

ISBN 978-3-11-053765-9
e-ISBN (PDF) 978-3-11-053773-4
e-ISBN (EPUB) 978-3-11-053779-6

Library of Congress Control Number: 2019949952

Bibliographic information published by the Deutsche Nationalbibliothek
The Deutsche Nationalbibliothek lists this publication in the Deutsche Nationalbibliografie; detailed bibliographic data are available on the Internet at http://dnb.dnb.de.

© 2020 Walter de Gruyter GmbH, Berlin/Boston
Cover image: wacomka / iStock / Getty Images Plus
Typesetting: Integra Software Services Pvt. Ltd.
Printing and binding: CPI books GmbH, Leck

www.degruyter.com

EBSCOhost - printed on 2/14/2023 1:06 PM via . All use subject to https://www.ebsco.com/terms-of-use

Preface

In 2006, RAND published a report on the Global Technology Revolution 2020 (https://www.rand.org/pubs/technical_reports/TR303.html). Among the 56 technologies identified as having profound impacts by 2020, 16 are at the top of the list for their better chance of becoming established and for their social relevance. Among them, nine are directly related to advanced materials. A year before the reference year of this report, we show that research carried out in our Center is perfectly aligned with the expected trends. This Centre, Quebec Centre for Advanced Materials/Centre Québécois sur les Matériaux Fonctionnels (QCAM/CQMF), funded in 2017, arises from a merge between two recognized centers: Center for Self-Assembled Chemical Structure (CSACS), whose director was Prof. Theo van de Ven, and CQMF, whose director was Prof. Armand Soldera. Conceptually, it is divided into three fundamental themes devoted to advanced materials: self-assembly, polymer science, and nanoscience; and three applied themes dedicated to functional materials: energy, sustainable development, and biomedical applications. This book highlights the importance of research in materials in Quebec.

An advanced material can be defined as a material for which some properties have been greatly improved, comparatively to more conventional materials. This book contains the main trends regarding this topic from basic research to industrial applications. The topics of this book fall mainly under TRL (Technology Readiness Level) 1 to 5. It is also aimed at exposing research in advanced materials developed by members of CQMF/QCAM. Moreover, it represents a follow-up of our previous book entitled *Functional Materials* published by de Gruyter, which mainly represents a pedagogical treatment of these materials.

The guiding principle underlying the large development of advanced materials is certainly the way their design is performed. This rational design is at the heart of all the chapters of this book. All the aspects related to the design of advanced materials going from fundamental to applied research, or touching biomaterials to electronic structures, are thus inspected.

A very original design strategy has been envisioned by Rahbani and Sleiman (Chapter 7): the origami approach. It provides an ideal tool to specifically position functional objects and study their interactions at the nanoscale level. This way to fashion DNA leads to the development of nanomechanical devices for applications ranging from biomedicine to material sciences. The approach in designing biomaterials advocated by Hoesli et al. (Chapter 10) follows a different strategy. They propose to develop tailored functional materials in differentiating pancreatic cells for cellular therapy of diabetes. For this, an interdisciplinary approach is required to (1) design platforms to mimic pancreas development and (2) study developmental biology in vitro. From a different perspective, Odette and Mauzeroll (Chapter 4) propose to use redox-sensitive lipid-based materials for applications in biological

https://doi.org/10.1515/9783110537734-202

EBSCOhost - printed on 2/14/2023 1:06 PM via . All use subject to https://www.ebsco.com/terms-of-use

systems. They find there a very new source for the development of clinically therapeutic systems.

Thanks to a fine-tuning of their constituting molecules, new and optimal properties emerge. Rondeau-Gagné (Chapter 3) proposes the development of self-healing materials. This ability to regenerate spontaneously and autonomously has a strong potential to revolutionize many areas such as advanced technologies or consumer goods. The propensity of small molecules to form glass instead of the expected crystals also leads to a great variety of applications, including pharmaceutical, photonic, and optoelectronic. Molecular glasses are also noteworthy materials that can play an important role in such applications. However, their very understanding remains a challenge. An overview of the progress made in the last 25 years, from their design, synthesis, their characterization, and the simulation of their properties, is described by Lebel and Soldera (Chapter 9).

To design new materials that will ultimately lead to interesting applications, self-assembly remains a very stimulating avenue. van de Ven and Whitehead (Chapter 8) propose alternate copolymers, where specific self-assembly driving monomers are introduced to generate hollow nanotubes. Morphology transformation was triggered differently by Yu and Zhao (Chapter 2). It is CO_2 that plays this role, thanks to an appropriate introduction of functional groups into polymers. Different CO_2-responsive functional groups are thus proposed. Control of solid-state assembly is exploited by Schneider and Perepichka (Chapter 1) to regulate charge mobility in organic semiconductors. Structure–property relationships are thus elaborated to better tackle charge mobility. Achieving semiconducting properties from organic materials is actually very challenging. To address this issue, Morin et al. (Chapter 13) review some of the most important aspects regarding the synthesis, purification, and applications of two highly praised carbon nanomaterials, namely carbon nanotubes and graphene nanoribbons. Nanoparticles are advanced materials where self-assembly can leverage technological applications. Bayram and Blum (Chapter 12) present an overview of the internal and external methods for directing this self-assembly of nanoparticles. Stability of such nanosystems, actually for nanoparticles as large as 100 nm, was shown to greatly depend on the interface. The phase diagram of Au–Pt solid core–liquid shells was thus revisited by Braidy (Chapter 11).

Designing is also uncovered in the way materials are prepared. The centrifugal spinning is a novel efficient technique to prepare nanofiber. It consists in extruding fibers through high speed, rotating polymer solution jets. The setup and the mathematical model are discussed by Taghavi and Noroozi (Chapter 5).

Advanced materials have also a strong impact in designing fuel cells. Two studies reported in this book are concerned by improvement in this kind of application. Sun et al. (Chapter 6) explore the chemistry of Fe/N/C electrocatalysts to replace the rare and expensive platinum for the oxygen reduction reaction in polymer electrolyte fuel cells. Outstanding nonprecious metal catalyst emerges from their lab. Schougaard et al. (Chapter 14) survey researches on Li-ion batteries, revealing the

EBSCOhost - printed on 2/14/2023 1:06 PM via . All use subject to https://www.ebsco.com/terms-of-use

importance in their modeling to incorporate such devices in numerous applications like storage of renewable energy, electric vehicles, and energy recovery.

To foster the use of performing materials, chemists, physicists, biologists, engineers, and numerical experimentalists must combine their skills to rationalize the design of materials. This book reveals the powerful energy stemming from the research in Quebec in the domain of materials in 2019. Great strides in this domain are expected. This book, a follow-up of "Functional Materials" (de Gruyter), is certainly a concrete example.

EBSCOhost - printed on 2/14/2023 1:06 PM via . All use subject to https://www.ebsco.com/terms-of-use

EBSCOhost - printed on 2/14/2023 1:06 PM via . All use subject to https://www.ebsco.com/terms-of-use

Contents

EBSCOhost - printed on 2/14/2023 1:06 PM via . All use subject to https://www.ebsco.com/terms-of-use

EBSCOhost - printed on 2/14/2023 1:06 PM via . All use subject to https://www.ebsco.com/terms-of-use

List of Contributors

Cyril Aumaitre
Département de chimie and Centre de Recherche sur les Matériaux Avancés (CERMA)
Université Laval
1045 Ave de la Médecine
Québec
Canada G1V 0A6

Serene S. Bayram
Department of Chemistry
McGill University
Montreal, QC Canada

Amy Szuchmacher Blum
Department of Chemistry
McGill University
Montreal, QC, Canada
amy.blum@mcgill.ca

Nadi Braidy
Chemical and Biotechnological Engineering
Canada Research Chair in Synthesis and Charaterization in Multifunctional Nanomaterials
Université de Sherbrooke
2500, boul. Université
Sherbrooke, Québec J1K 2R1
Canada
Nadi.Braidy@USherbrooke.ca

Danny Chhin
Université du Québec à Montréal
Case postale 8888, succursale Centre-ville
Montréal, Québec H3C 3P8
Canada
chhin.danny@gmail.com

Corinne A. Hoesli
Department of Chemical Engineering
McGill University
Montreal, QC, Canada
corinne.hoesli@mcgill.ca

Anthony Jolly
Département de chimie and Centre de Recherche sur les Matériaux Avancés (CERMA)
Université Laval
1045 Ave de la Médecine
Québec
Canada G1V 0A6

Olivier Lebel
Department of Chemistry and Chemical Engineering
Royal Military College of Canada
Kingston, ON, Canada
Olivier.Lebel@rmc.ca

Janine Mauzeroll
Department of Chemistry
McGill University
801 Sherbrooke Street West, Room 21
Montreal, Québec
Canada H3A 0B8
janine.mauzeroll@mcgill.ca

Christopher Moraes
Department of Chemical Engineering
McGill University
Montreal, QC, Canada
chris.moraes@mcgill.ca

Jean-François Morin
Département de chimie and Centre de Recherchesur les Matériaux Avancés (CERMA)
Université Laval
1045 Ave de la Médecine
Québec
Canada G1V 0A6
jean-francois.morin@chm.ulaval.ca

Sooran Noroozi
Laboratory of Complex Fluids Research
Department of Chemical Engineering
Université Laval, Québec
QC G1V 0A6, Canada
sooran.noroozi.1@ulaval.ca

https://doi.org/10.1515/9783110537734-204

EBSCOhost - printed on 2/14/2023 1:06 PM via . All use subject to https://www.ebsco.com/terms-of-use

Michael U. Ocheje
Department of Chemistry and Biochemistry
University of Windsor
Windsor, ON
Canada
pocheje@uwindsor.ca

William L. Odette
Department of Chemistry
McGill University
801 Sherbrooke Street West, Room 21
Montreal, Québec
Canada H3A 0B8
william.odette@mail.mcgill.ca

Dmitrii F. Perepichka
McGill University
Department of Chemistry
801 Sherbrooke St.
West Montréal, Québec H3A 0B8
Canada
dmitrii.perepichka@mcgill.ca

Janane F. Rahbani
Quebec Centre for Advanced Materials
Department of Chemistry
McGill University
Montreal, QC, Canada
janane.rahbani@mail.mcgill.ca

Simon Rondeau-Gagné
Department of Chemistry and Biochemistry
University of Windsor
Windsor, ON, Canada
Simon.Rondeau-Gagne@uwindsor.ca

Md Sazzad Hossain
Université du Québec à Montréal
Case postale 8888, succursale Centre-ville
Montréal, Québec H3C 3P8
Canada
md.hossain3@mail.mcgill.ca

Julia A. Schneider
Fordham University
Department of Chemistry
441 E Fordham Rd,
Bronx NY 10458
jschneider43@fordham.edu

Steen B. Schougaard
Université du Québec à Montréal
Case postale 8888, succursale Centre-ville
Montréal, Québec H3C 3P8
Canada
schougaard.steen@uqam.ca

Hanadi F. Sleiman
Quebec Centre for Advanced Materials
Department of Chemistry
McGill University
Montreal QC Canada
hanadi.sleiman@mcgill.ca

Armand Soldera
Département de Chimie
Université de Sherbrooke
Sherbrooke, QC, Canada
Armand.Soldera@USherbrooke.ca

Shuhui Sun
Institut National de la Recherche
Scientifique-Energie Matériaux et
Télécommunications
Varennes
QC J3X 1S2, Canada
shuhui@emt.inrs.ca

Seyed Mohamad Taghavi
Laboratory of Complex Fluids Research
Department of Chemical Engineering
Université Laval, Québec
QC G1V 0A6, Canada
seyed-mohammad.taghavi@gch.ulaval.ca

M. Nazir Tahir
Department of Chemistry and Biochemistry
University of Windsor
Windsor, ON
Canada

Raymond Tran
Department of Chemical Engineering
McGill University
Montreal, QC, Canada
raymond.tran@mail.mcgill.ca

EBSCOhost - printed on 2/14/2023 1:06 PM via . All use subject to https://www.ebsco.com/terms-of-use

Theo G.M. van de Ven
Pulp and Paper Research Centre and
Quebec Centre for Advanced Materials
Department of Chemistry
McGill University
Montreal QC Canada
theo.vandeven@mcgill.ca

M.A. (Tony) Whitehead
Pulp & Paper Research Centre and
Quebec Centre for Advanced Materials
Department of Chemistry
McGill University
Montreal QC Canada
tony.whitehead@mcgill.ca

Qiliang Wie
Institut National de la Recherche
Scientifique-Energie Matériaux et
Télécommunications
Varennes
QC J3X 1S2, Canada

Kacper Wojtkiewicz
Department of Chemistry and Biochemistry
University of Windsor
Windsor, ON
Canada
wojtkie@uwindsor.ca

Bing Yu
Département de chimie
Université de Sherbrooke
Sherbrooke, Québec
Canada J1K 2R1
yu_bing0205@163.com

Gaixia Zhang
Institut National de la Recherche
Scientifique-Energie Matériaux et
Télécommunications
Varennes
QC J3X 1S2, Canada

Yue Zhao
Département de chimie
Université de Sherbrooke
Sherbrooke, Québec
Canada J1K 2R1

EBSCOhost - printed on 2/14/2023 1:06 PM via . All use subject to https://www.ebsco.com/terms-of-use

EBSCOhost - printed on 2/14/2023 1:06 PM via . All use subject to https://www.ebsco.com/terms-of-use

Julia A. Schneider, Dmitrii F. Perepichka

1 Design Principles for Organic Semiconductors

Designing organic semiconductors--whether polymers or small molecules--involves a myriad of synthetic choices. Every choice, from incorporating heteroatoms to substituents, effects the optoelectronic properties of the material, its morphology, and its ultimate device performance. This chapter presents the reader with current design strategies and known structure-property relationships. For context, this chapter also briefly discusses the history of the field, theories of charge transport, device applications, and concludes with a selection of reported organic semiconductors.

Keywords: organic electronics, organic semiconductor, photovoltaics, conjugated polymer, donor-acceptor, morphology, charge transport

1.1 Introduction

Organic electronics encompass devices in which molecules or polymers serve as the electrically active material. Notably, the properties of these organic materials can be endlessly tuned through structural modifications. The ability to tailor a semiconductor for a specific application is one of the most attractive aspects of organic electronics. Additionally, solution-processable materials offer the possibility of inexpensive, large area devices, via, for example, roll-to-roll or inkjet printing. Solar cells produced in this way could potentially satisfy the world's increasing energy demands in a sustainable manner. Organic electronics made entirely from biodegradable materials would help stem the accumulation of e-waste in landfills. For organic electronics to become widely adopted and compete with the existing inorganic materials, however, they need to demonstrate sufficiently long lifetimes and competitive optoelectronic properties. Since the 1970s, this has fueled a continuing quest for new high-performance, stable materials, as well as extensive research into what factors dictate charge transport and how to control them. The goal of this chapter is to contribute new design strategies for the synthesis of organic semiconductors (OSCs) and to better our understanding of structure–property relationships.

While some design strategies yield predictable results, many structure–property relationships are still not well understood, especially as they relate to

Julia A. Schneider, Department of Chemistry, Fordham University, NY
Dmitrii F. Perepichka, Department of Chemistry, McGill University, Québec

https://doi.org/10.1515/9783110537734-001

EBSCOhost - printed on 2/14/2023 1:06 PM via . All use subject to https://www.ebsco.com/terms-of-use

supramolecular ordering. In the last three decades, a multitude of OSCs have been synthesized, primarily by trial and error, with a material's solid-state packing and associated device performance only discussed after the fact. This chapter will introduce the reader to a number of electronically active molecules and polymers and will discuss the design strategies used to achieve certain characteristics. These design strategies will then be discussed in terms supramolecular ordering.

This chapter will cover four main topics: (1) the history of organic electronics, discussing the theories of charge transport, and devices that employ OSCs; (2) design principles for the synthesis of OSCs, along with an exemplifying case study; (3) design strategies specifically geared to supramolecular ordering; and (4) a review of representative reported OSCs that illustrate the current state of the field.

1.2 History of OSCs

Semiconductors are ubiquitous in modern technology: they can be found in the transistors and diodes that all our electronic devices use. The first transistor device was invented in 1947 while Bardeen, Brattain, and Shockley were studying surface states in a germanium crystal. Ever since, inorganic materials like silicon or gallium arsenide have been predominantly used in our electronic components. Conductive organic materials, however, had already been discovered, although perhaps unbeknownst to the discoverer. In 1862, Letheby observed conductive and electrochromic behavior in a unidentified "dirty blueish-black powder," now thought to be polyaniline [1]. Many small organic molecules were also known to be conductive, such as tetrathiafulvalene (TTF) chloride salts, as shown by Wudl in 1972 [2]. An enormous body of work then evolved around TTF complexes that gave rise to the first organic metal and organic superconductor [3, 4]. Using dopants to modulate the conductivity of an organic material was perhaps first described in iodine-doped polypyrroles (PPy) by Bolto et al. in 1963 [5]. Their results led them to conclude that the "orbital overlap between adjacent pyrrole rings in PPy suffices to impart a relatively high level of conductivity." The work that popularized conjugated polymers for organic electronics, however, was the famous discovery in 1977 by MacD iarmid and Heeger that thin films of polyacetylene (synthesized by Shirakawa) show unprecedented (for organic materials) high electrical conductivities when doped with halogens [6]. This discovery earned the trio the 2000 Nobel Prize in chemistry [7]. Suddenly conductive materials could be synthesized according to chemists' designs. Synthetic strategies from organic chemistry were married to charge transport theories from physics and the field of organic electronics was born.

EBSCOhost - printed on 2/14/2023 1:06 PM via . All use subject to https://www.ebsco.com/terms-of-use

Initially the impetus for organic electronics was to recreate the conducting properties of inorganic materials, which led to extensive studies on the conductivity of molecular crystals and conjugated polymers. The current prominence of the field, however, came about due to breakthroughs in device fabrication. While working for Eastman Kodak in the early 1980s, Tang filed patents for the first heterogeneous organic solar cell and the first electroluminescent device, making him one of the founders of organic electronics. His organic light-emitting diode (OLED) demonstrated not only that organic material could produce light in response to an electrical current, but also that organic materials could be used in commercially viable electronic devices [8]. A few years later, the Friend group, working at the Cavendish Laboratory, reported the first OLED based on a conjugated polymer, poly(phenylene vinylene), paving the way for solution-processable devices [9].

In the late 1980s, Friend and others were also making breakthroughs in organic field-effect transistors (OFET). An important contribution was the demonstration that charge carriers could be introduced into conjugated polymers, such as polyacetylene, by using an electric field [10]. Also paramount in the advancement of the field was Garnier's work with oligothiophene-based OFETs [11]. Early measurements of evaporated films of sexithiophene only displayed mobilities on the order of $10^{-4}\,cm^2/Vs$, but the possibility of using OSCs in conventional electronics was established.

Since these early discoveries, many OSCs – polymers and small molecules – have been synthesized and tested in devices. Organic electronics exhibit four key beneficial properties: flexibility, transparency, expendability, and the potential to be processed at low-cost over large surfaces through solution printing techniques [12]. Because of these properties, organic electronics can be advantageous for certain applications where inorganic materials would not be appropriate, though they do often suffer from low conductivities and poor operational stability. The incorporation of thin-film-printed OSCs in radio frequency identification tags, for example, would lower the tag's cost and improve their mechanical properties, making them viable for tracking large inventories, such as in supermarkets [13]. OSCs have also been heavily studied as sensors, where cost, flexibility, and disposability can be important factors, but fast switching speeds may not be necessary, for example, because the sensing process is limited by biochemical reactions and adsorption rates [14]. The first commercial use of OSCs was in OLED displays, which are thinner and use less energy than their inorganic analogues. The emission color of an OLED can also be tuned by modifying the organic chromophore. Organic photovoltaics (OPVs) are an example of devices that greatly benefit from the large-scale printing processes available to OSCs. Solution-processable OPVs can be light, flexible, and transparent, something that would be impossible in silicon-based solar cells [15]. Complimentary circuits, which rely on a combination of p- and n-type transistors, have also been made from OSCs, although their

EBSCOhost - printed on 2/14/2023 1:06 PM via . All use subject to https://www.ebsco.com/terms-of-use

development has been slow due in part to the relative scarcity of n-type semiconductors [16]. All these applications have made organic electronics one of the most rapidly growing fields over the last several decades. Ongoing research focuses on selectively tuning a material's electronic properties, on increasing solubility and stability, and on understanding and controlling supramolecular assemblies.

1.3 Band Gap

OSCs are π-conjugated molecules or polymers, meaning they contain alternating single and double bonds such that their π-orbitals overlap and form a network of delocalized electrons (Figure 1.1). These overlapping molecular orbitals and the energy levels of the electrons within are referred to as bands. The bonding molecular orbitals below the Fermi level form the valence band and the higher energy antibonding orbitals above the Fermi level form the conductance band. The energy difference between these bands is called the band gap and, at the molecular level, corresponds to the difference between the highest energy occupied molecular orbital (HOMO) and the lowest energy unoccupied molecular orbital (LUMO).

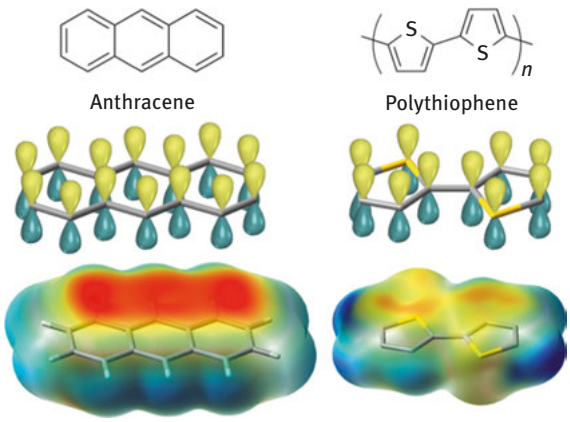

Figure 1.1: Conjugated molecules have alternating double and single bonds. Overlap between π-orbitals causes electrons to be delocalized throughout the structure, giving rise to electron density above and below the aromatic cores, as seen in the calculated electrostatic potential surfaces.

In a material with no band gap, termed "metallic," electrons can easily move into the empty states of the conductance band, creating "free" charge carriers that

EBSCOhost - printed on 2/14/2023 1:06 PM via . All use subject to https://www.ebsco.com/terms-of-use

provide high conductivities. Conversely, insulators exhibit low conductivities because their large band gap inhibits the movement of electrons into the conductance band (or holes into the valence band).

Electrons need an open path to move through a material, that is, the bands must be only partially filled. This is achieved when an electron moves from the full valence band into the empty conductance band (or is removed from the material), leaving a "hole" behind. A neighboring electron can then move over to the new hole, leaving its own hole behind. In effect, the hole is acting as a positive charge carrier moving through the valence band, while electrons move through the conductance band. OSCs are ambipolar and can be used in p- or n-type transistors, in which holes or electrons, respectively, are the charge carriers. All OSCs are "extrinsic semiconductors," meaning that they must be doped to be conductive. Dopants supply holes or electrons to the material and contract the band gap by creating intermediate states (Figure 1.2). A material can be chemically doped through oxidation or reduction, photochemically doped by promoting an electron from the valence band into the conductance band, or it can be doped via the injection of charge carriers by an electric field.

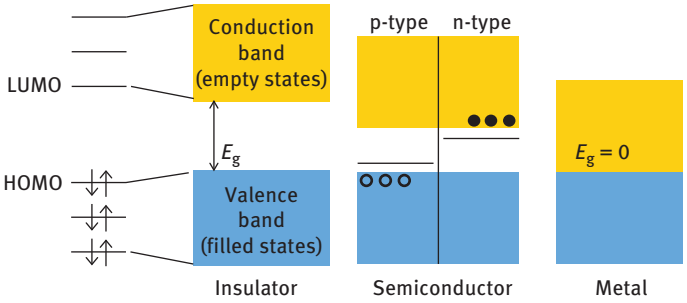

Figure 1.2: Molecular orbitals make up the energy bands and the size of the band gap determines the conductivity. p- and n-type doping of the band gap with respective charge accumulation is shown in the semiconductor. (Electrons are filled and holes are unfilled circles).

1.4 Theoretical Models for Charge Transport

Before looking at the design strategies for synthesizing OSCs, it is useful to understand, at least qualitatively, the theoretical models describing charge transport in small molecules and polymers. Charge transport in OSCs is characterized by measuring the charge mobility, or the time it takes for an electron or a hole to move through the material under an electric field. OSCs encompass materials with a large range of mobilities, making it hard for a single theoretical model to accurately

EBSCOhost - printed on 2/14/2023 1:06 PM via . All use subject to https://www.ebsco.com/terms-of-use

describe charge transport in all OSCs. Charge transport in an ultrapure crystal is different than that in an amorphous film, which will also be different from transport in semicrystalline polymer films. Several theories were developed and expanded upon to explain the observed characteristics of OSC devices, namely, temperature-dependent, field-dependent, and film-thickness-dependent charge-carrier mobility. Unfortunately, it is still hard to predict the effects of microstructures in inhomogeneous OSC films, such as crystalline domains in polymer films [17, 18]. The existing theories are generally characterized as band theory, hopping theory, and hybrid theories of the two.

Band theory is based on a model where charges are fully delocalized over several molecular units and exist in bands (equivalent to the conductance and valence bands introduced in Section 1.3). For band transport to occur, the interaction energy between nearest neighbors, called the electronic coupling (t), must be greater than disorder-induced energy barriers. Band transport is characterized by a decrease in charge carrier mobility with increasing temperatures, a property common to crystalline inorganic semiconductors, but rarely seen in OSCs. Karl and coworkers measured the hole and electron transport in assiduously purified naphthalene crystals at temperatures from 4 to 300 K, and proved that band transport can take place in ultrapure OSC crystals below 300 K [19]. When measuring electron transport along the three crystallographic directions of naphthalene crystals, a strong anisotropy was observed that coincided with the electronic couplings acquired from DFT calculations – a fact that emphasizes the dependence of band transport on crystallinity [20].

In amorphous OSCs, however, disorder effects become large and transport through a single delocalized band is no longer feasible. Disorder effects can be dynamic, such as vibrational changes when a molecule (or "site") becomes charged (seen in crystalline OSCs as well) or static, such as pre-existing variations in site energies and intersite distances [21]. In such an environment, a charge is localized on a single site and must "hop" to another localized site for conductivity to be observed. This process had been previously described by Marcus in the electron transfer between identical molecules in solutions – a theory for which he was awarded the 1992 Nobel Prize in chemistry [22, 23]. Hopping theory in OSCs was spearheaded by, among others, Mott and Holstein, who developed small polaron-hopping theory [24]. A polaron is the combination of a charge carrier and the lattice deformations associated with that carrier's movement. The distortions to the molecules and their environment lead to an energetic cost to charge transfer called the reorganization energy (λ). As a result, charge transfer is thermally activated and we observe an increase in mobility as temperature increases. Holstein's model for the rate of electron transfer is a function of the electronic coupling (t), the polaron binding energy (E_{pol}), and thermal energy ($k_B T$) shown in eq. (1.1).

EBSCOhost - printed on 2/14/2023 1:06 PM via . All use subject to https://www.ebsco.com/terms-of-use

$$k_{ET} = \frac{t^2}{\hbar}\sqrt{\frac{\pi}{2E_{pol}k_B T}}\exp\left[-\frac{E_{pol}}{2k_B T}\right] \tag{1.1}$$

The polaron-binding energy is defined as the relaxation energy of an ionized molecule, while reorganization energy is the sum of the relaxation energies of the initial neutral molecule and the resulting ionized molecule. Recognizing that the polaron-binding energy is essentially equal to half the reorganization energy ($E_{pol} = \lambda/2$), eq. (1.1) is identical to the semiclassical Marcus equation. The simplicity of this model, which relates transfer rates directly to electronic coupling (t) and reorganization energy (λ), has made it popular among chemists as a reasonable approximation for charge transport in OSCs.

Neither band theory nor two-state hopping theories, however, address the defects and static disorder present in the majority of OSC thin films, which are poly/semicrystalline. Variations in site energies and intersite distances at these disorder sites leads to asymmetric rates and therefore time-dependent mobilities. The Gaussian disorder model assumes a Gaussian energy distribution of these variations and takes into account the life-time of the charge carrier [25].

As device preparation techniques improved, OSCs started to show higher measured mobilities. Current theories therefore reconciled band-like and hopping transport into trap-limited transport [26]. The multiple-trap-and-release model (MTR) was first proposed by Shur and Hack to describe hydrogenated amorphous silicon [27]. The model assumes band-like charge transport occurs through delocalized states, but that trap states capture injected charge carriers, where they may be further excited into the conduction band (Figure 1.3). This model describes materials with a large range of mobilities, since the mobility is affected by the ratio of free to trapped charges. Horowitz successfully applied the MTR model to OSCs when explaining the changing temperature and field dependence of mobilities observed in polycrystalline films of sexithiophene [28].

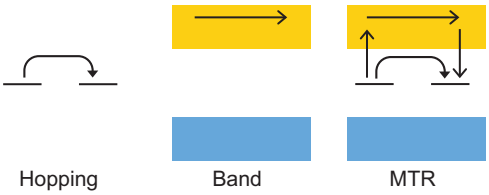

Figure 1.3: Theoretical charge transport models. On the left is the hopping method where only localized states exist. In the middle is band theory where all charges travel through the conductance band. On the right is the MTR model in which trapped charges can still move into the conductance band. (Note that these figures depict n-type transport).

EBSCOhost - printed on 2/14/2023 1:06 PM via . All use subject to https://www.ebsco.com/terms-of-use

In the context of molecular design for OSCs, maximizing nearest neighbor interactions and minimizing reorganization energy are crucial to increased charge mobilities. In the end, though, charge transport is often limited by the number of trap states. The efficacy of a trap depends on its energy level relative to the HOMO or LUMO, for hole or electron trapping, respectively [29]. Trapping sites can either be structural faults or chemical impurities. A commonly seen trap is oxygen or oxidation products, but not all such impurities need to act as traps. If the energy level of the potential trap lies above or below the material's band gap, the trap remains ineffective. The nature of the traps present, especially oxidation products, depend on the OSC and can sometimes be predicted and avoided.

1.5 OSC Devices

OSCs have been used in a wide range of electronics. While OSCs exhibit lower mobilities than their inorganic counterparts, their tunability and processing versatility give them a strong advantage for light-weight or one-time-use applications. OSCs can be printed from solution onto practically any surface, including flexible plastics [30] and paper [31]. This is advantageous for medical applications, such as electronic skin or biocompatible sensors [32]. This section will give a brief overview of three types of OSC devices.

1.5.1 Organic Light-Emitting Diodes

In terms of the commercialization of OSCs, OLEDs are undoubtedly leading the way. OLED-based displays can be found in a myriad of smartphone screens, including Samsung's Galaxy series, Google's Pixel, and Apple's iPhoneX, as well as in some tablets, television displays, and solid-state lighting panels [33].

An OLED device consists of an emissive layer and a transport layer, made of organic molecules or polymers. These layers are sandwiched between two electrodes and when a voltage is applied across the electrodes, electrons are injected into the emissive layer. The electrons drift to the interface with the transporting layer where the recombination with holes found there causes radiative emission. Since OLED devices directly generate light, there is no need for a backlight as in LCD displays, and creating true black is easily achieved by switching off the emitting pixel. OLED displays are therefore thinner and more energy efficient than LCD displays. OLEDs can be patterned into pixel-sized devices (much smaller than inorganic LED devices; Figure 1.4) or printed into large sheets for solid-state lighting [34]. Historically, blue OLEDs have trailed behind red and green emitting devices in terms of efficiency and life-times, but recent research is closing this gap [35].

EBSCOhost - printed on 2/14/2023 1:06 PM via . All use subject to https://www.ebsco.com/terms-of-use

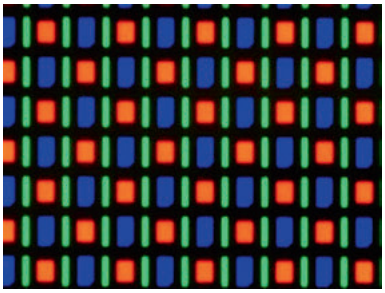

Figure 1.4: A 200× magnification of Google's Nexus One AMOLED screen shows the Red-Green-Blue arrangement of OLED pixels. Photograph by Matthew Rollings, distributed under a CC-BY 3.0 license.

1.5.2 Solar Cells

OPVs, though still tailing silicon-based solar panels in terms of efficiency, can be printed into lightweight, flexible, and transparent solar cells. These qualities are important mechanistic and aesthetic features when incorporating solar windows into urban architecture [36]. The solution processability of materials for roll-to-roll printing is especially important for OPVs due to the large-scale nature of this application.

OPVs produce electricity through the photoelectric effect illustrated in Figure 1.5 for a simple p–n junction. A p–n junction describes the interface between a p-type (donor) and n- type (acceptor) semiconductor. Incident light excites an electron into the conductance band of the donor or acceptor material, leaving a hole behind, thus creating an "electron–hole pair" or "exciton." This exciton must diffuse to the p–n junction where the charges can be separated: the hole into the p-type donor material and the electron into the n-type acceptor material. The charges are then channeled to their respective electrodes and produce an electric current.

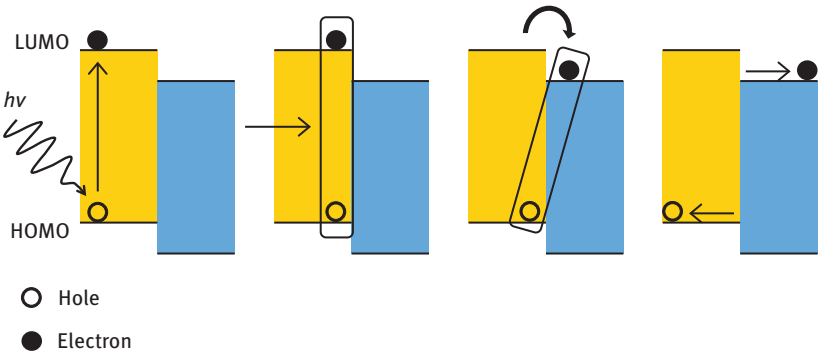

Figure 1.5: Once an exciton is generated (left) it must diffuse to the p–n junction before undergoing charge separation (right).

EBSCOhost - printed on 2/14/2023 1:06 PM via . All use subject to https://www.ebsco.com/terms-of-use

Efficient solar cells are constructed with a few key factors in mind.

- First, the active layer should have a broad absorbance spectrum that captures a majority of the sun's energy. This calls for a semiconductor with a small band gap ($\approx$ 1.5 eV). The band gap cannot be too small, however, to avoid large energy loss from exciton thermalization and the HOMO–LUMO offset of the cell [37].
- The lifetime of an exciton is on the order of nanoseconds and its diffusion length only $\approx$ 10 nm, necessitating small, regularly spaced domains of donor and acceptor phases to minimize exciton recombination.
- The driving force for charge separation at the p–n junction (the electropotential drop from the LUMO of the donor to the LUMO of the acceptor) needs to be greater than the exciton binding energy to drive exciton dissociation.
- The charge mobilities of the donor and acceptor materials should be reasonably high ($>10^{-4}\,cm^2/Vs$). They should also be balanced to avoid a build-up of electrons or holes, which leads to accelerated charge recombination.

Controlling the morphology of the donor and acceptor domains is an integral part of fabricating efficient devices. The most common practice is to dissolve the two materials in a common solvent and to create a blended active layer called a bulk heterojunction (BHJ) (Figure 1.6). Annealing and adding solvent additives can alter how each material crystallizes and thus affect the resulting domain sizes.

The power efficiency of a solar cell is defined by three parameters: the short-circuit current (I_{SC}), the open-circuit voltage (V_{OC}), and the fill factor (FF). These parameters are calculated from the current–voltage relationship of the device plotted in an I–V curve (Figure 1.7). The short-circuit current is the largest current that may be drawn from the solar cell and occurs when the bias across the cell is zero. While in the open-circuit state, charge carriers generated under illumination accumulate at the anode and cathode. When this growing potential difference cancels out the built-in potential, the current is zero and the measured open-circuit voltage is the maximum voltage the solar cell can provide to an external circuit [38]. In OPVs the V_{OC} is limited by the "band gap" of the cell, or $\left|LUMO_{\text{Acceptor}} - HOMO_{\text{Donor}}\right|$ (Figure 1.6), but empirically, large voltage losses are always observed due to the recombination of charges [39].

Power is the product of the current and voltage ($P = I \times V$), with the maximum power of the cell (P_{Max}) representing the point of peak efficiency. The fill factor (FF) is the ratio of the area bound by the I_{SC} and V_{OC} to the area bound by the current and voltage at P_{Max} as seen in eq. (1.2) and Figure 1.7. FF is often described as the "squareness" of the I–V curve, with an ideal value of 1.

$$\mathrm{FF} = \frac{I_{\mathrm{Max}} V_{\mathrm{Max}}}{I_{\mathrm{SC}} V_{\mathrm{OC}}} \tag{1.2}$$

EBSCOhost - printed on 2/14/2023 1:06 PM via . All use subject to https://www.ebsco.com/terms-of-use

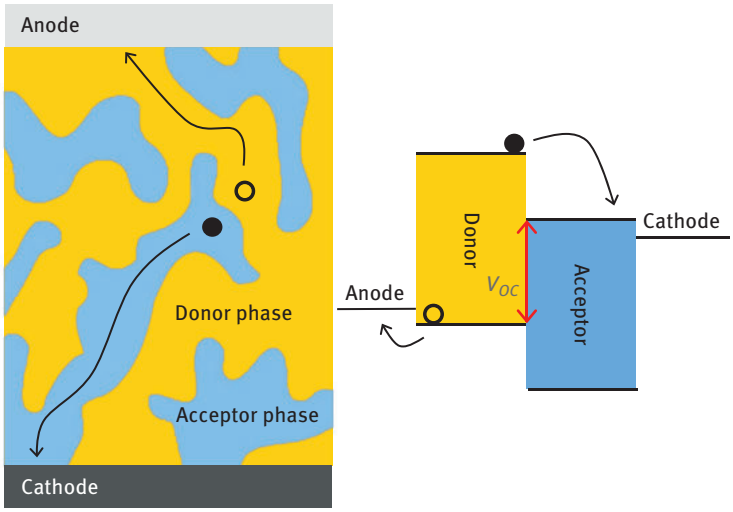

Figure 1.6: On the left is a simplified depiction of a bulk heterojunction showing the blended donor and acceptor domains. On the right is shown the V_{OC} as it relates to the HOMO of the donor and the LUMO of the acceptor, that is, the band gap of the cell.

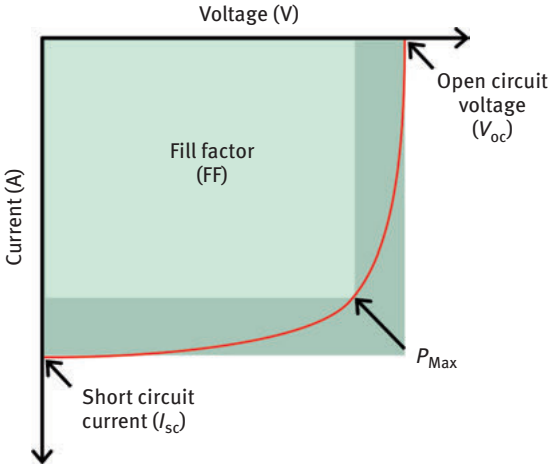

Figure 1.7: A characteristic *I*–*V* curve for an irradiated solar cell showing the V_{OC}, I_{SC}, and P_{Max}. The FF is the ratio between the two shaded areas.

The overall power efficiency of the cell is then defined as

$$\mathrm{PCE} = \frac{P_{\mathrm{Max}}}{P_{\mathrm{In}}} = \frac{\mathrm{FF}(I_{\mathrm{SC}} V_{\mathrm{OC}})}{P_{\mathrm{In}}} \tag{1.3}$$

EBSCOhost - printed on 2/14/2023 1:06 PM via . All use subject to https://www.ebsco.com/terms-of-use

How do these parameters relate to the design of OSCs? Lowering the band gap of the donor material means more light is harvested, which has a direct beneficial impact on the I_{SC}. Unfortunately, if shrinking the band gap increases the HOMO level of the donor material, this will limit the V_{OC}; therefore, simultaneously lowering the band gap and the HOMO level of the material is extremely desirable. Chen et al. observed that for each 0.1 eV drop in the HOMO level of differently substituted poly(benzodithiophene-thieno[3, 4-*b*]thiophene), they increased the V_{OC} by 0.07 V [40].

Both the I_{SC} and V_{OC} are limited by charge recombination as well. Exciton dissociation and charge recombination both occur at the donor–acceptor interface. It is therefore important to augment charge mobility with ordered films while maintaining adequate domain sizes for exciton dissociation. Efficient charge extraction at the electrodes will also help reduce recombination loss.

Polymers have been extensively tested as donor materials for BHJ solar cells, and a key property that influences the morphology of the films is molecular weight [41]. Larger molecular weight polymers show a propensity to form nanofibrillar morphologies and exhibit higher charge mobilities. For example, batches of poly(dioctylfluorene-dithienylbenzothiadiazole) displayed higher I_{SC}s with increasing MWs, though the V_{OC}s stayed constant [42]. Too large an MW, however, may decrease the mobility due to entanglement, which hinders intrachain transport [43].

To ensure the solution processability of high MW-conjugated polymers, solubilizing side chains are required, which will affect film morphology as well. The position, length, and bulkiness of alkyl side chains affects the π–π interactions between polymer chains. Increased π–π interactions lead to higher mobilities and I_{SC}s, but may have a detrimental effect on the film blends [44]. More examples of side chain engineering is discussed in Section 1.6.4

1.5.3 Field-Effect Transistors

A field-effect transistor (FET) is an electronic switch that uses an electric field to control the conductivity of a semiconductor. In our group, OFETs are routinely used to test the electrical properties of novel polymers and small molecules. Owing to the flexible nature of many OSCs, OFETs can be fabricated on a variety of substrates, including poly(ethylene terephthalate) films [45] or paper [46, 47]. Devices can also be made in several different architectures, but the most common and reproducible device is the “bottom-gate, top-contact” silicon wafer device described here.

OFETs consist of an active semiconductor layer, an insulating layer, and three contacts: the source, the drain, and the gate (Figure 1.8). The substrate for the device typically doubles as the gate electrode, as is the case with silicon wafers.

EBSCOhost - printed on 2/14/2023 1:06 PM via . All use subject to https://www.ebsco.com/terms-of-use

Above the gate is an insulating layer, called the gate dielectric layer, for example, SiO_2. When an electric field is applied to the gate charges accumulate in the dielectric layer. This causes an accumulation of complementary charges in the semiconductor at the semiconductor-dielectric interface. Once turned "on" by the electric field, the semiconductor becomes conductive and charges can migrate along the narrow transistor channel. Since charge migration occurs only at the semiconductor–dielectric interface, any defects can easily limit charge mobilities. "Smoothing" the dielectric layer, with polystyrene, for example, has been shown to greatly improve mobilities [48].

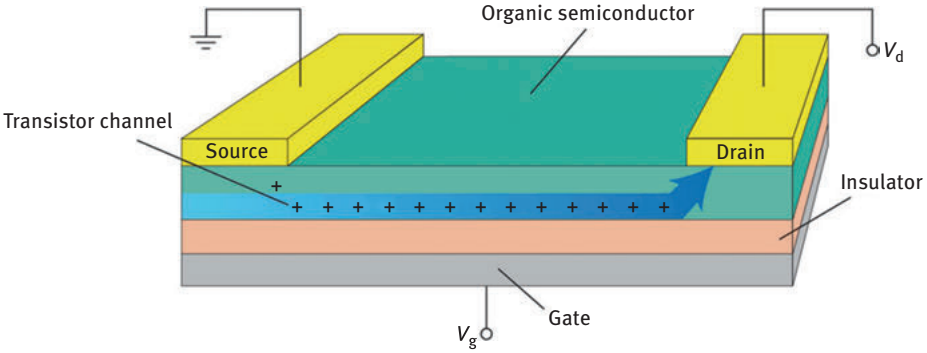

Figure 1.8: Schematic diagram of a bottom-gate, top-contact OFET showing the gate-induced charge transport channel. Reprinted by permission from Macmillan Publishers Ltd: Nature Materials [49], copyright 2010.

In the case of poorly soluble small molecules, films are deposited using vacuum vapor deposition, but for polymers or soluble small molecules, solution-processing techniques, such as spin-coating, are used. A single crystal can also be used as the active layer, enabling the measurement of mobilities specific to that packing architecture. The physical morphology of the OSC plays an important part in device performance, and so the method used to deposit the material can vastly affect charge mobility. This is starkly evident in the case of pentacene thin films, which are practically insulating ($\mu_h \approx 10^{-9}\,cm^2/Vs$) as amorphous films deposited at low temperatures, but display high mobilities in ordered films deposited at room temperature ($\mu_h \approx 1\,cm^2/Vs$) [50].

The charge mobility of an OFET is determined by recording the drain-source current (I_{DS}) as a function of drain-source bias (V_{DS}) at different gate voltages (V_G). When a small drain-source voltage V_{DS} is applied (smaller than the gate voltage minus the threshold voltage, $<(V_G - V_T)$) the device operates in the linear regime. As drain-source voltage increases and surpasses $(V_G - V_T)$ the device operates in a

EBSCOhost - printed on 2/14/2023 1:06 PM via . All use subject to https://www.ebsco.com/terms-of-use

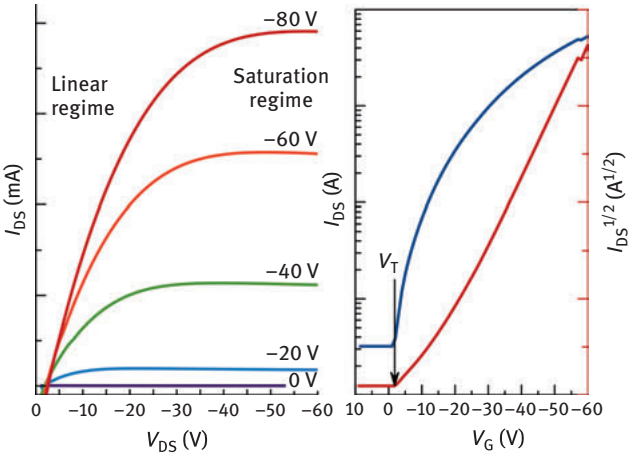

Figure 1.9: Typical electrical characteristics of a p-channel OFET device: (left) output curve and (right) transfer curve.

saturation regime (Figure 1.9). Charge mobilities can be calculated from either regime. In the saturation regime, drain current is independent of drain-source voltage, but rather varies as the square of the gate voltage as given in eq. (1.4):

$$I_{DS} = -\frac{W}{2L} C_i \mu (V_G - V_T)^2 \tag{1.4}$$

where W and L are the channel width and length and C_i is the capacitance of the dielectric. The threshold voltage, V_T, is the minimum gate voltage that is needed to generate the transistor channel. The field-effect carrier mobility, μ, can thus be determined from the slope of the curve plotting the square root of the saturation current as a function of gate voltage according to eq. (1.5):

$$\mu = \frac{2L}{W} \frac{1}{C_i} \left(\frac{\delta \sqrt{I_{DS}}}{\delta V_G} \right)^2 \tag{1.5}$$

It must be pointed out, however, that these equations are approximations. Equation (1.5) assumes that the mobility is independent of the gate voltage, which is not the case for several reasons. For example, at low gate voltages charges will be trapped by localized traps, limiting mobility [51, 52]. The charge mobility in eq. (1.5) is also not corrected for contact resistance at the metal/organic interface, which is a common issues in OFETs. Contact resistance can occur due to an energy level mismatch between the electrode metal and the OSC or disorder in the OSC film at the interface.

EBSCOhost - printed on 2/14/2023 1:06 PM via . All use subject to https://www.ebsco.com/terms-of-use

1.6 Molecular Design Strategies

The most attractive aspect of OSCs from a chemist's point of view is the opportunity to rationally design and synthesize a desired material. By altering the molecular structure of a material and testing its electronic properties, structure–property relationships can be defined and the factors affecting charge transport in OSCs illuminated. Charge transport in OSCs is highly dependent on the solid-phase morphology of the material and not solely on the molecule's electronic properties and since structure–property relationships encompass both the individual molecules' characteristics and the characteristics of the bulk material, it can be very difficult to ascertain if a modification is responsible for an observed property. In this chapter we try to divorce molecular structure from morphological aspects and study both separately, so as to better delineate structure–property relationships in OSCs.

Depending on its final application, an OSC can be designed to have vastly different properties. Will it be used for p- or n-type transport? Does it need to be soluble? Should it form amorphous films or be highly crystalline? Is broad absorption important or is strong emission at a specific wavelength required? The molecular design of an OSC will naturally reflect these sought-after properties, though the toolbox of design strategies available to realize them remains the same.

The first requirement for an OSC is a finite band gap. Since the 1980s, many strategies for controlling the band gap have been established. In an OSC the energy bands are made of overlapping π-orbitals, so that manipulating these energy levels is all about maintaining conjugation and expanding electron delocalization. There are four main factors (depicted in Figure 1.10) that influence band gap: (1) planarity, (2) bond-length alternation (BLA), (3) aromaticity, and (4) the electronic effect of substituents. A single design choice can easily affect all of these factors, so it is easier to consider specific strategies and discuss the affects on these factors as they apply.

1.6.1 Extending Conjugation with Spacer Groups

The most basic and prevalent unit in conjugated molecules is the benzene ring. The benzene ring contains six electrons in delocalized π-orbitals, but its ring structure gives it more resonance stabilization than linear hexatriene. Benzene is a very small conjugated system, so its HOMO–LUMO gap is large (ca. 5.5 eV).

To shrink the band gap, there are two ways of expanding the conjugation. The first is to connect multiple benzene or aromatic rings together with C–C single bonds, forming an oligomer or a polymer. This method preserves the aromatic stability of each ring, but planarity is lost due to steric hindrance between the benzene rings. The short distance between benzene rings will not accommodate the C–H

EBSCOhost - printed on 2/14/2023 1:06 PM via . All use subject to https://www.ebsco.com/terms-of-use

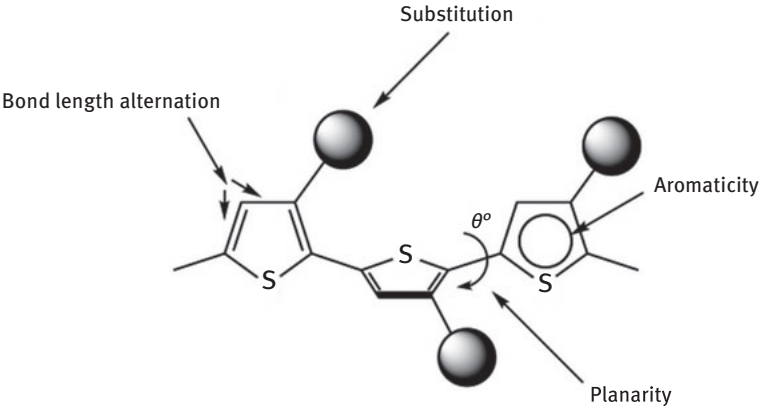

Figure 1.10: Factors that influence band gap labeled on polythiophene (PT). Reprinted with permission from Roncali [53]. Copyright 2007 John Wiley & Sons, Inc.

bonds on each ring, requiring the backbone of the polymer to twist (Figure 1.11a). When larger substituents need to be added, steric hindrances can cause serious torsional twists, interrupting the orbital overlaps between rings. A simple solution to planarize the polymer is to introduce a spacer group between each ring. The spacer group must also be conjugated and, in effect, it will "dilute" the aromaticity of the benzene rings. This promotes delocalization of electrons along the entire polymer, not just within nodes of the aromatic rings. Examples of such conjugated spacers are vinylene (Figure 1.11b) and ethynylene. The ethynylene spacer has no hydrogen atoms to contribute to sterics and therefore produces rod-like, planar polymers [54]. The disadvantage comes in the form of increased BLA, caused by the large difference in lengths between the C–C single bond and the much shorter C ≡ C triple bond.

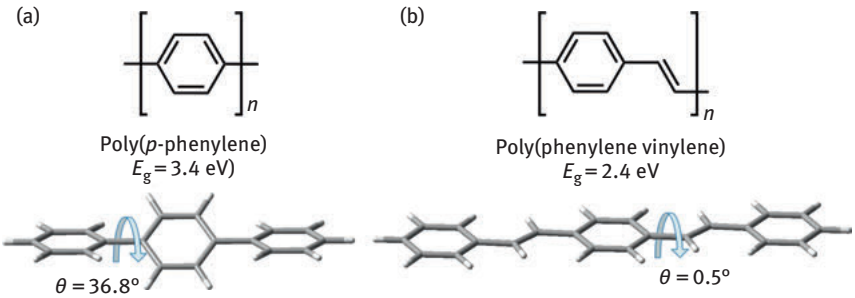

Figure 1.11: Simple polyphenylene has a twisted backbone (a) leading to a large band gap, which can be lowered by introducing a vinylene spacer, such as in poly(phenylene vinylene) (b). DFT calculations of the dihedral angles performed using B3LYP, 6-31G(d).

EBSCOhost - printed on 2/14/2023 1:06 PM via . All use subject to https://www.ebsco.com/terms-of-use

BLA is defined as the averaged differences in length of adjacent carbon–carbon bonds. Conjugated molecules can be thought to contain two competing resonance structures: the aromatic and the quinoidal (Figure 1.12), both containing alternating single and double (or triple) bonds. In a structure with a nondegenerate ground state, like polyphenylene or polythiophene (PT), where the aromatic form is preferred, the BLA is proportional to the band gap and decreases with increasing quinoidal character [55]. Even polyacetylene, a polymer with a degenerate ground state, has a BLA of 0.08 Å as a consequence of Peierls' distortion. In a 1D crystal lattice a net energy gain is brought about by distorting the periodicity of the lattice into "dimers," or if the 1D lattice is a carbon chain, into double and single bonds [56, 57].

Figure 1.12: Two resonance structures of polyphenylene.

An early approach to minimize BLA is to design a monomer unit that contains an aromatic cycle when the polymer backbone is in its quinoidal form. This counterbalances the aromaticity of the polymer core and favors delocalization, lowering the band gap and BLA. This approach was pioneered by Wudl in the synthesis of poly(isothianaphthene), which exhibits a very low band gap of 1.0 eV (Figure 1.13) [58]. A more recent example can be seen in polymer **1** (also known as PTB7), well known for achieving 9% efficiencies in OPVs [59]. In the thieno[3,4-*b*]thiophene unit, the fused thiophene ring is in its aromatic form when the backbone thiophene ring is its quinoidal form and vice versa (Figure 1.13) [60].

Besides acting as a measure for electron delocalization through the balance of aromatic and quinoidal character, BLA is extremely important as it relates to the polarizability of the molecule. Polarizability is the measure of electron cloud displacement (or induced dipole moment) in the presence of an electric field and it is inversely related to the polaron binding energy. As was described in Section 1.4, the polaron-binding energy is one of the key parameters affecting the rate of charge transfer in OSCs. The relationship between BLA and polarizability was experimentally proven by measuring the polarizability and non-linear hyperpolarizability of a series of donor–acceptor polyenes with end groups of increasing acceptor strength, thus having a range of BLAs from 0.11 Å for decatetraene to ≈ 0 Å for cyanine (Me_2N^+=CH(CH=CH)$_3$–NMe_2). The results indicated that molecular polarizability (α) is maximized as BLA approaches zero [61–63].

EBSCOhost - printed on 2/14/2023 1:06 PM via . All use subject to https://www.ebsco.com/terms-of-use

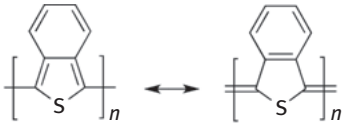

Poly(isothianaphthene)

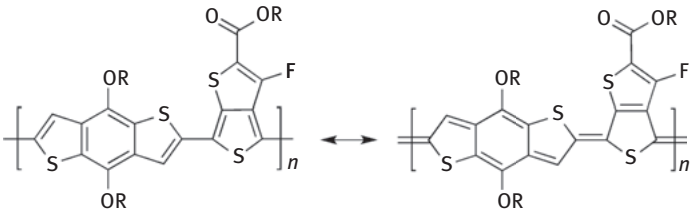

1 (PTB7)

Figure 1.13: Both isothianaphthene and thieno[3,4-*b*]thiophene contain a fused aromatic ring when the polymer is in quinoidal form.

A method to planarize aromatic rings and reduce BLA is to use a spacer group that impedes torsional twisting. The most well-known example of this is fluorene, which is essentially two benzene rings fused by a C–C single bond and an sp^2 carbon. Fusing the rings not only ensures better π-orbital interactions, but also shortens the C–C linking bond and elongates the C–C bonds within the five-membered rings, thus reducing the BLA (Figure 1.14). Polyfluorenes, therefore, are extremely popular OSCs, exhibiting good stability, interesting liquid–crystalline properties, as well as being excellent blue-light emitters [64]. In many other π-conjugated systems, such as PTs, the rigidification of molecules has proved to be a useful approach toward low-band gap materials [65, 66].

Biphenyl

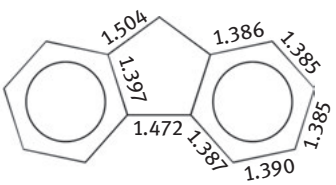

Fluorene

Figure 1.14: The fused spacer group in fluorene lowers BLA as compared to biphenyl. Averaged bond lengths (Å) reported in [67] for biphenyl and reported in [68] for fluorene.

EBSCOhost - printed on 2/14/2023 1:06 PM via . All use subject to https://www.ebsco.com/terms-of-use

1.6.2 Fusing Rings: Polycyclic Arenes

A different approach toward molecular rigidification, which does not require a spacer group, is fusing aromatic rings together. Multiple fused rings will share π-orbitals so that electrons are delocalized throughout the molecule, lowering the band gap of the molecule and raising the HOMO levels. In acenes, however, extending the conjugation linearly leads to increased biradical or "open-shell" character, making it vulnerable to oxidation (Figure 1.15). Hexacene is the longest acene that is stable under ambient conditions [69]. Higher order acenes form biradicaloids that are prone to intermolecular dimerization and oxidation [70].

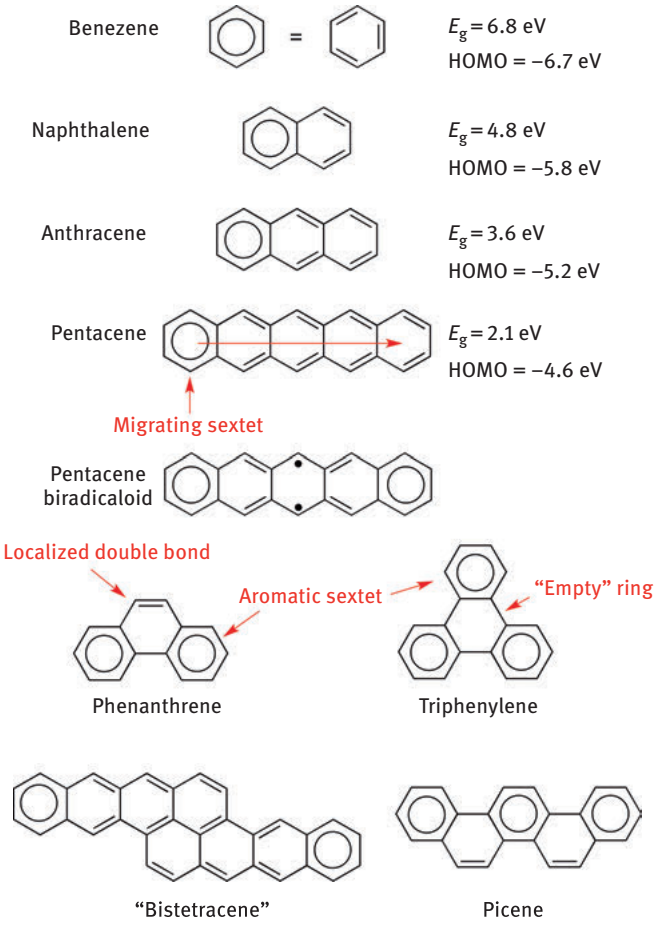

Figure 1.15: A drop in band gap and a raising of HOMO levels can be observed with the expansion of linear acenes. Below are nonlinear PAHs illustrating Clar's classification of six-membered rings.

EBSCOhost - printed on 2/14/2023 1:06 PM via . All use subject to https://www.ebsco.com/terms-of-use

Nonlinear polycyclic aromatic hydrocarbons (PAHs) exhibit higher band gaps and lower HOMO levels than their linear counterparts. Phenanthrene, for example, has a HOMO–LUMO gap ≈ 0.3 eV larger than its linear analogue anthracene. This lowering in HOMO levels (and thus increased oxidative stability) is explained by Clar's rule: the more aromatic sextets present in a molecule, the more stable that molecule will be. This is also the rationalization behind the formation of open-shell species. Clar's rule classifies six-membered rings in PAHs into four types: aromatic sextets, migrating sextets, empty rings, and rings with localized double bonds (Figure 1.15). Fusing linear acenes can yield molecules with two aromatic sextets, such as "bistetracene" (Figure 1.15). "Bistetracene" (substituted with triisopropylsilyl acetylene groups) contains eight fused rings, but its HOMO level is only −5.1 eV, allowing for air-stable FET devices and high mobilities ($\mu_h = 6.1\,cm^2/Vs$) [71]. Picene, the "zigzag" analogue of pentacene, contains three aromatic sextets and shows better environmental stability in p-channel FETs than pentacene [72]. Thermally deposited thin films of alkylated-picene have, like pentacene, shown extremely high mobilities (up to $\mu_h = 20\,cm^2/Vs$), but are stable under atmospheric conditions [73].

Extending the conjugation does more than affect energy levels: it also lowers the BLA (as discussed previously) and lowers the reorganization energy. As was discussed in Section 1.4 when a neutral molecule becomes charged it undergoes geometry modifications at an energy cost called the reorganization energy, an important factor in charge transport. Figure 1.16 shows how reorganization energy decreases as the number of rings increase in a series of molecules with different fused geometries. Reorganization energy is also affected by heteroatoms, which are discussed next.

1.6.3 Heteroatoms

Another design strategy in organic electronics is the use of heteroaromatics. Inserting heteroatoms into a polycyclic system will have a large impact on the structure and the electronic properties of the molecule or polymer. The work presented in this chapter focuses on two heteroatoms: sulfur and nitrogen. Sulfur and nitrogen both have lone electron pairs that can contribute to the aromaticity of a cycle, thus making aromatic five-membered rings possible (Figure 1.17). These five-membered rings, thiophene and pyrrole, are smaller and exhibit less torsional twisting in polymers than benzene rings Thiophene and pyrrole are less aromatic than benzene (according to thermodynamic stabilization), and thus PTs and polypyrroles (PPy) have stable quinoidal forms, leading to more delocalized electrons and smaller band gaps than poly(*p*-phenylene) (PPP) (theoretical E_g PT = 2.0 eV, PPy = 2.9 eV, PPP = 3.8 eV) [75].

Although PPy were among the first conductive organic materials studied [76, 77], it is PT and other thiophene-containing molecules that predominate the field of

EBSCOhost - printed on 2/14/2023 1:06 PM via . All use subject to https://www.ebsco.com/terms-of-use

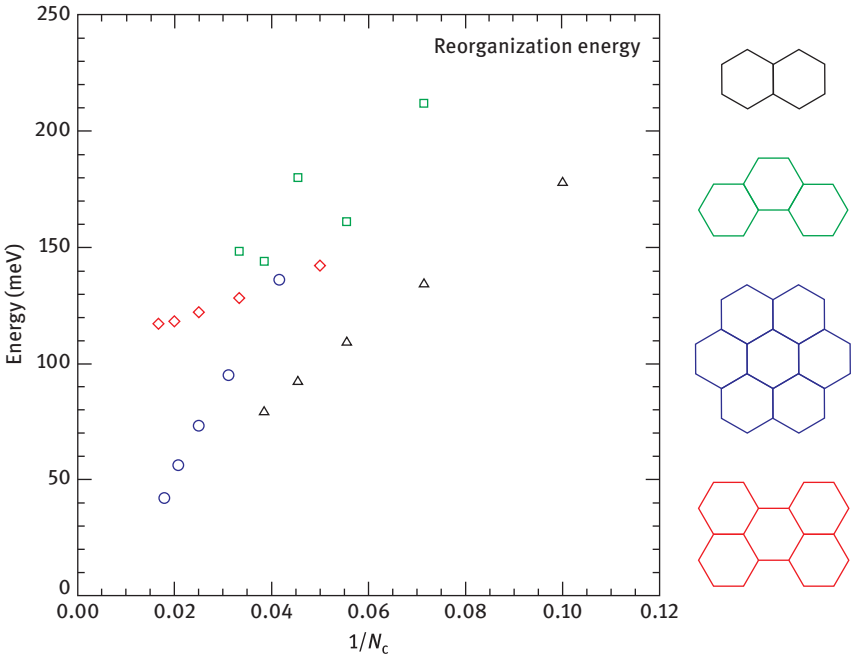

Figure 1.16: Molecular reorganization energies computed for (oligo)acenes (black triangles), phenacenes (green squares), circum(oligo)acenes (blue circles), and (oligo)perylenes (red diamonds), as a function of the inverse of the total number of carbon atoms N_C. Reprinted from Malloci et al. [74], Copyright 2014 with permission from Elsevier.

Figure 1.17: Pictured are several heteroaromatic structures. Electrons participating in the aromaticity are labeled in red.

organic electronics. Poly(3-hexylthiophene) (P3HT) for example, has become the benchmark donor material for bulk heterojunction solar cells, though its efficiency is limited by a relatively large band gap (E_g = 1.9 eV) and high HOMO level (–5.1 eV) [78]. Yet thiophenes present many advantages [79], not the least of which is their well established and versatile chemistry. Derivatives of thiophene can be synthesized by selective substitution via lithiation chemistry. Thiophene monomers are easily oxidized, either electrochemically or chemically, to form radical cations that polymerize. If thiophene is substituted unsymmetrically, this method produces to a regiorandom polymer. Brominated thiophenes can be polymerized through transition

EBSCOhost - printed on 2/14/2023 1:06 PM via . All use subject to https://www.ebsco.com/terms-of-use

metal-catalyzed cross-coupling reactions to give regioregular homopolymers or to make copolymers [80]. Thiophenes are electron rich and chemically stable, making them good for p-type transport, and they self-assemble with close π–π stacks. Furthermore, the increased polarizability of the sulfur atom compared to carbon helps lower reorganization energies and can lead to intermolecular sulfur–sulfur interactions. These interactions are described in more detail in Section 1.7.

Nitrogen heteroatoms can be incorporated into OSCs in five- or six-membered rings. In five-membered pyrroles, the lone pair on nitrogen contributes to the aromaticity of the ring making the heterocycle electron rich. Conversely, in six-membered pyridine, the lone pair is perpendicular to the π-orbitals of the ring and therefore does not contribute to the aromaticity, but rather enhances basicity. In this case, the electronegativity of the nitrogen atom makes the ring electron poor and lowers the HOMO–LUMO levels of the molecule. As a result OSCs containing nitrogen have been shown to be p-type, ambipolar, or n-type. (See examples in Figure 1.35.)

Thiazoles are five-membered rings containing both sulfur and nitrogen heteroatoms (Figure 1.17). They belong to the azole family of molecules, along with oxazoles and imidazoles. Thiazole is slightly less aromatic than thiophene [81, 82], with sulfur's lone pair contributing to the aromaticity of the ring, while the nitrogen atom is electron withdrawing. This makes thiazole an overall electron-deficient heterocycle in OSCs. (See examples in Figure 1.34.)

1.6.4 Substituents

Introducing substituents is a convenient way to tune the properties of a molecule or polymer since they provide an enormous potential for structural and electronic variation (Figure 1.18). They are also necessary for solution-processable materials. Substituents can affect the energy levels of a material, as well as impact planarity, and reorganization energy.

Long alkyl chains are commonly used to impart solubility to a polymer or large polycyclic molecule. The nature of that chain, linear or branched, and its location, will have an impact on the solid-state packing of the material [44]. In polymers, a large part of the reorganization energy comes from the rotation of the interring dihedral angles between the neutral and charged species. This rotational energy is greatly impacted by the size and type of substituent present on the polymer backbone. Using substituents that form noncovalent interactions that "lock" the conformation of the polymer backbone is advantageous for this reason. One recent example is the use of alkoxy or fluorine substituents on benzotriazole in a benzotriazole–thiophene copolymer (Figure 1.19). The authors attribute tight interchain ordering and improved carrier mobilities on the noncovalent interactions between thiophene's sulfur and the substituents [83]. A computational study on through-space interactions performed by Jackson et al., however, warns that while S–S, O–S, N–S, and

EBSCOhost - printed on 2/14/2023 1:06 PM via . All use subject to https://www.ebsco.com/terms-of-use

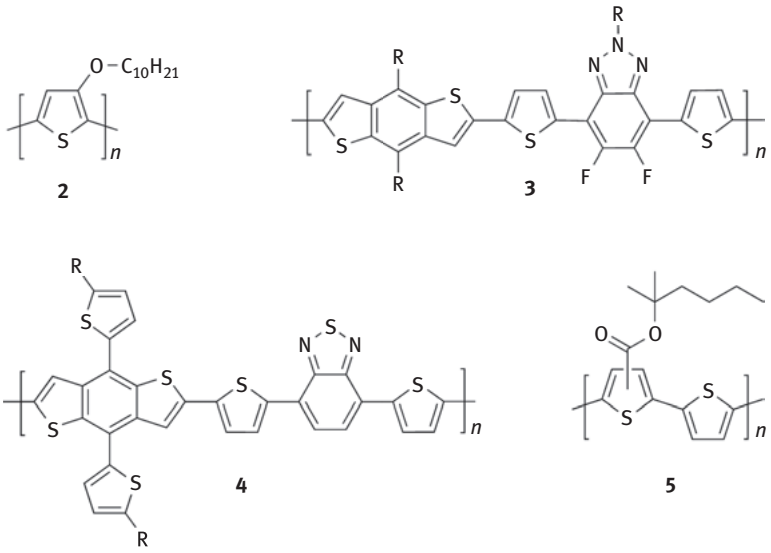

Figure 1.18: A selection polymers illustrating different substituents.

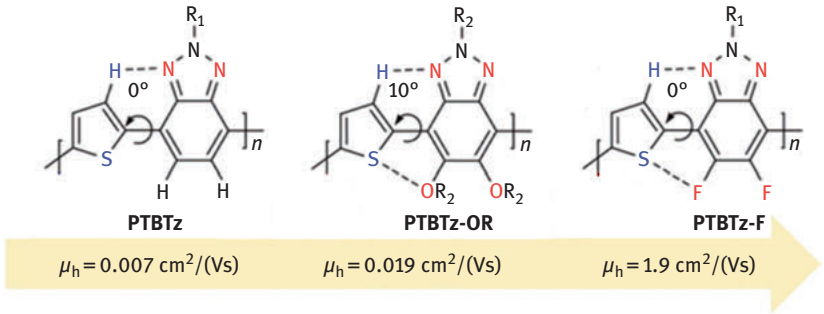

Figure 1.19: Varying the benzotriazole substituents in these copolymers did not affect the band gap, but led to tighter interchain ordering and higher mobilities. Reprinted with permission from Yum et al. [83]. Copyright 2014 American Chemical Society.

F–S interactions all have some stabilizing influence, their noncovalent binding energies might be too low to provide a conformational "lock" in polymers. That study concludes that only hydrogen-bonding interactions, such as CH–N and CH–O, have high enough binding energies (≈ 2 kcal/mol) to act as "locking" mechanisms [84].

Electron-donating or -withdrawing substituents are often used to fine-tune the HOMO and LUMO energy levels of a material. Replacing the hexyl chain in P3HT with an alkoxy chain (see polymer **2**) results in a 0.3 eV increase in the HOMO level, shrinking the band gap of the polymer (1.6 eV compared to 1.9 eV for P3HT) [85].

EBSCOhost - printed on 2/14/2023 1:06 PM via . All use subject to https://www.ebsco.com/terms-of-use

Fluorine is a popular electron-withdrawing substituent because its van der Waals radius is not much larger than hydrogen's (135 pm vs 120 pm) and therefore does not significantly increase torsional twisting when placed on a monomer unit, such as on benzotriazole in polymer **3** [86].

Aromatic substituents can also be used to extend the conjugation pathway orthogonal to the core of the molecule or polymer. Polymer **4** is an example of this strategy. Huo et al. found that when alkylthienyl substituents were used in place of alkoxy groups on benzodithiophene, the resulting material had a smaller band gap, higher hole mobilities, and performed better in BHJ solar cells [87]. Although sometimes improperly called "2D" polymers, polymers with orthogonal aromatic substituents exhibit high molecular ordering with strong π–π stacking and wider absorption bands [88].

Finally, a substituent can be designed to be removable [89], as in polymer **5**. A thermally cleavable ester substituent was used by Fréchet and then Krebs as a sacrificial solubilizing group [90, 91]. Once the material has been solution processed, the ester functionality can be removed to give insoluble, but planar, poly(thiophene).

1.6.5 Donor–Acceptor Strategy

Finally, possibly the most widely explored design strategy for manipulating the band gap of a material is the donor–acceptor strategy, which calls for combining electron-deficient units with electron-rich units. When these units are in conjugation, their orbital splitting results in a narrower band gap with lower HOMO–LUMO levels (Figure 1.20a). This strategy is widely used in polymers for OPVs where broad absorption is desired, but raising the HOMO would be detrimental to the V_{OC}. Using D–A units, the band gap of a material can be fine-tuned, either by altering a unit or by altering its ratio relative to other units. The "push–pull system" in D–A polymers has other benefits as well. As was introduced in Section 1.6.1, BLA can be decreased and polarizability increased by increasing the strength of the donor and acceptor moieties. This has been extensively studied in polyenes [92], as well as other conjugated systems [93, 94]. As a result of their high polarizability, materials with D–A structures can exhibit nonlinear optical properties, such as two-photon absorption [95, 96].

Electron-rich and -deficient aromatics are well known to assemble in a face-to-face manner [98, 99]. The "push–pull" behavior of D–A units promotes intramolecular charge transfer between units, leading to intramolecular dipoles. Thus, the dipole–dipole interactions between polymer chains lead to smaller interchain distances and therefore better charge transport between polymer backbones (Figure 1.20b). Indeed, short π–π distances are frequently observed in X-ray diffraction experiments of D–A polymer films [100, 101]. D–A polymer PTB7, shown in Figure 1.13, has been used in OPVs with PCEs exceeding 9%. Yet when Yu's group attempted to make a similar polymer with a D–A–A structure, their highest

EBSCOhost - printed on 2/14/2023 1:06 PM via . All use subject to https://www.ebsco.com/terms-of-use

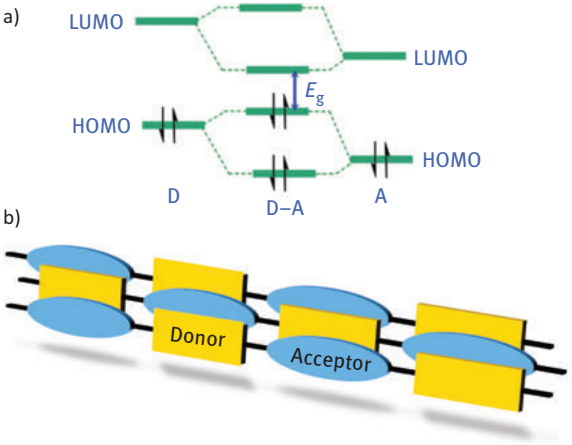

Figure 1.20: (a) The orbital splitting of donor and acceptor units results in a smaller band gap without raising HOMO levels. Reproduced from Ref. [97] with permission of The Royal Society of Chemistry. (b) Tight interchain packing in D–A polymers is favored by alternating donor–acceptor π-stacks.

PCE was only 2%. By using two acceptor units, they lowered the local dipole moment causing charge localization in the A–A unit, and as a result observed faster recombination rates and lower I_{SC}s [102].

Examples of oft-used donor and acceptor units are shown in Figure 1.21. While common in polymer design, the D–A strategy is equally applicable to oligomeric molecules and unimolecular rectifiers, and can be utilized simply through the choice of substituents as well. Examples of D–A copolymers using different building blocks are shown in Figure 1.22. All have shown excellent properties in OPVs or OFETs. Bronstein et al. combined thieno[3,2-*b*]thiophene (TT) and diketopyrrolopyrrole, two particularly well-studied units known for forming crystalline films with good mobilities, in polymer **6**. Although as-spun films of **6** showed no signs of crystallinity in X-ray diffraction or differential scanning calorimetry studies, their charge mobilities were among the highest for polymer FETs ($\mu_h = 1.95\,cm^2/Vs$). Polymer/$PC_{71}BM$ OPV devices gave a max PCE of 5.4% [103]. Higher charge mobilities and PCE values have since been realized in many other diketopyrrolopyrrole copolymers [104]. With polymer **7**, Chen et al. present a heptacyclic unit where the benzodithiophene core is covalently rigidified by two flanking thiophene units. This monomer was copolymerized with thienopyrrolodione. FET devices of **7** exhibited modest mobilities ($\mu_h = 6.8 \times 10^{-2}\,cm^2/Vs$), but OPV devices with $PC_{71}BM$ gave PCEs of 6.6%, a vast improvement compared to the unrigidified analogue with a PCE of 0.2% [105]. Osaka et al. also utilized a fused ring approach with their D–A polymer **8**, which features naphthodithiophene and naphthobisthiadiazole. The first iteration of **8** had no solubilizing chains on the naphthodithiophene units (R′ = 2-decyltetradecyl, R″ = H) and displayed an edge-on orientation with a π-stack distance of

EBSCOhost - printed on 2/14/2023 1:06 PM via . All use subject to https://www.ebsco.com/terms-of-use

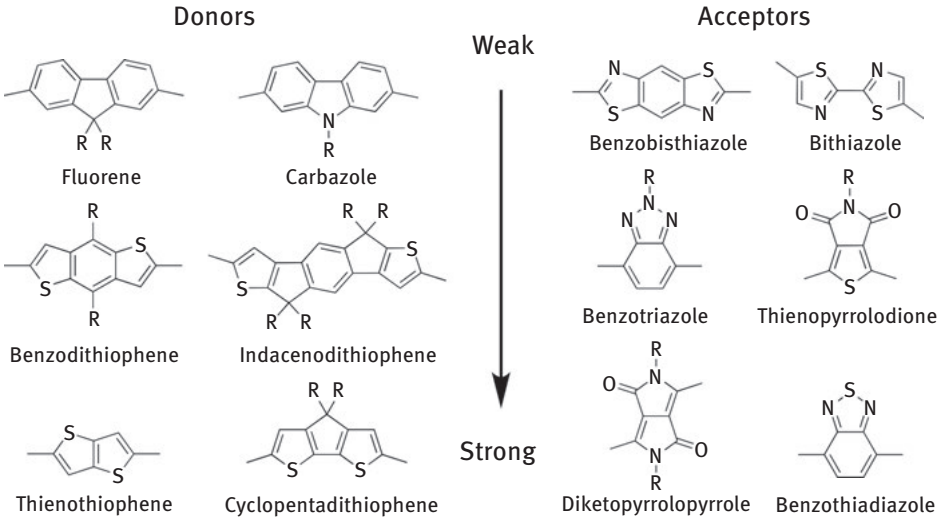

Figure 1.21: A selection of electron-donating and -accepting monomers that have been used in D–A copolymers.

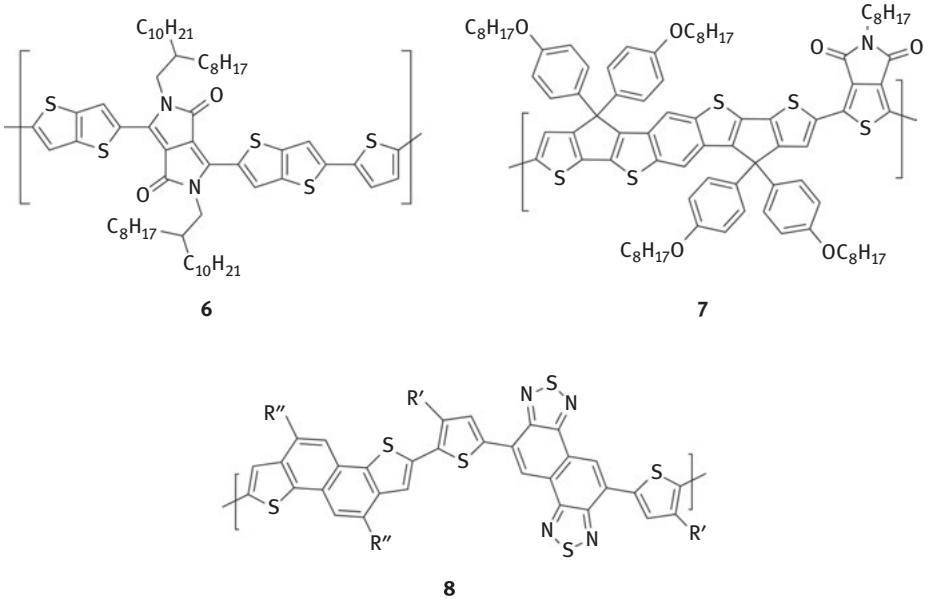

Figure 1.22: Shown are three examples of D–A copolymers with impressive properties in OFET or OPV devices.

EBSCOhost - printed on 2/14/2023 1:06 PM via . All use subject to https://www.ebsco.com/terms-of-use

3.43 Å. This polymer yielded high performing FET and polymer/PCBM OPV devices ($\mu_h = 0.5\,cm^2/Vs$, PCE = 5.2%). Adding linear dodecyl chains to naphthodithiophene changed the orientation of the polymer films to have face-on π-stacks with a distance of 3.51 Å. The improved solubility led to even higher PCEs of 8.0% while only lowering mobilities to $\mu_h = 0.1\,cm^2/Vs$ [106]. Recent years have seen continued progress in the device performance of D–A polymers and small molecules. New materials and processing techniques have led to OPV efficiencies of 10–12% [107–109] and charge mobilities nearing $5\,cm^2/Vs$ [110–112].

1.6.6 Case Study: Band Gap Control of Conjugated Polymers via Alkylsulfanyl Substituents

The design strategies discussed earlier are all utilized in the following study, in which the electronic properties of thienothiophene vinylene polymers are tuned for use as OPV donor polymers. As we have seen from previous examples, thiophene-based conjugated polymers are important semiconducting materials with widespread applications in OLEDs, OFETs, and OPVs [79, 113].

Since P3HT, thiophene-based polymers have been tirelessly modified to create new high-performance materials. The dominant approach has followed the donor–acceptor strategy discussed earlier. This, however, requires the synthesis of two different monomer units, complicates the structure–property relationships, and creates a polarization along the conjugation backbone. Rather than altering the backbone, we tune the polymers' energy levels directly through substituents, a method that is underutilized in conjugated polymer chemistry.

In the past, substituents such as fluorine [114], fluoroalkyl [115], thienyl [116], dicyanoethene [117], alkoxy groups [118], nitro groups [119], and esters [120] have been explored in PTs. We chose to study alkylsulfanyl substituents for several reasons: the van der Waals radius of sulfur (0.18 nm) is smaller than that of $-CH_2$ (0.20 nm), which slightly reduces steric strain compared to alkyl substituents [121]; they impart solubility to the polymer; and, in PTs, they can act as mild electron acceptors, lowering the HOMO levels [122, 123]. Furthermore, their electron withdrawing effect can be tuned by changing the oxidation state of sulfur from sulfanyl (–SR) to sulfoxyl (–SOR) or sulfonyl ($-SO_2R$).

In our comparative analysis of the effect of alkylsulfanyl and alkylsulfonyl substituents on the electronic properties and behavior of conjugated polymers, we chose poly(thieno[3,2-*b*]thiophene vinylene) as the conjugated backbone. Thienothiophene's (TT) fused unit fosters electron delocalization by reducing the BLA (compared to simple thiophene) [124] and its coupling geometry (180° vs ≈ 150° for thiophene) leads to linear rod-like structures, which reduces disorder and increases charge mobilities [125, 126]. A vinylene spacer reduces the twist caused by repulsions between substituents and "dilutes" the aromatic nature of the TT moieties.

EBSCOhost - printed on 2/14/2023 1:06 PM via . All use subject to https://www.ebsco.com/terms-of-use

Both of these effects promote electron delocalization and shrink the band gap of the polymer.

Our study led us to report the synthesis and the spectroscopic, structural, and device characterization of poly(3,6-dialkylsulfanylthieno[3,2-*b*]thiophene vinylene), **S-PTTV**, its oxidized derivative poly(3,6-dialkylsulfonylthieno[3,2-*b*]thiophene vinylene), **SO_2-PTTV**, and the random copolymer incorporating both sulfanyl and sulfonyl units, **S/SO_2-PTTV** (Figure 1.23) [127].

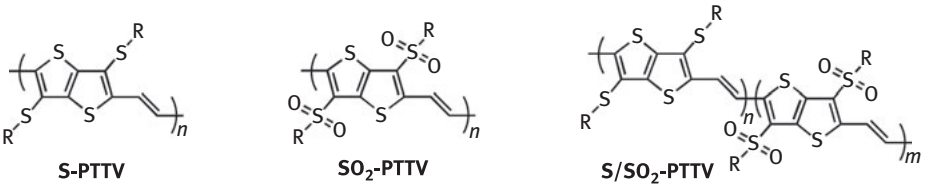

Figure 1.23: Polymer structures discussed in this case study, where R=2-ethylhexyl.

As was discussed earlier, the rigidity of the conjugated backbone is an important factor defining the material properties of PTs and related structures [28]. In our polymers, DFT calculations predict a very shallow rotation barrier (≈ 1.5 kcal/mol) for both TT–TT and SO_2TT-V connections (Figure 1.24). This means that nonplanar **S-PTT** could planarize due to solid-state packing forces (as was in fact observed [121]). Similarly, **SO_2-PTTV**, predicted to be nearly planar in the gas phase, could adopt a twisted conformation under external factors. In fact, the energy penalty for twisting the TT/vinylene dihedral angle in **SO_2-PTTV** by 50° is smaller than RT

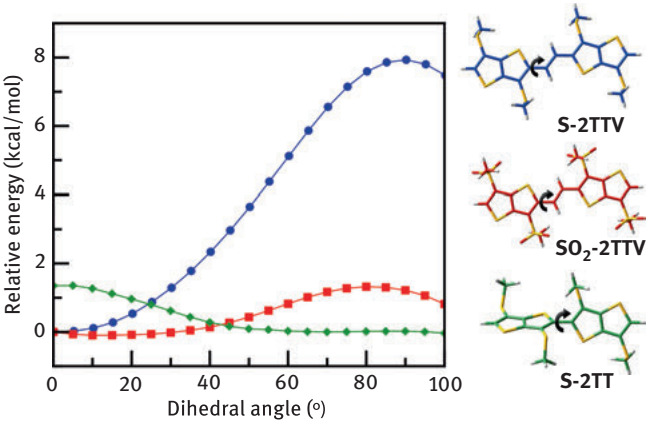

Figure 1.24: Energy barrier of rotation of thiophene/vinylene dihedral angles in model dimers **S-2TTV** (blue dot), **SO_2-2TTV** (red square), and **S-2TT** (green diamond).

EBSCOhost - printed on 2/14/2023 1:06 PM via . All use subject to https://www.ebsco.com/terms-of-use

(0.6 kcal/mol at room temperature). In contrast, a much larger rotation barrier against twisting (7.9 kcal/mol per TT/vinylene connection) is predicted for **S-PTTV**. This can be attributed to the smaller size of the alkylsulfanyl group and perhaps to weak attractive S···H interactions between the substituents and vinylene protons (the calculated S···H distance is 2.80 Å).

The UV–vis absorption spectra of the polymer thin films (Figure 1.25) displayed broad absorption spectra. The absorption of solid **S-PTTV**, λedge = 765 nm (E_g = 1.62 eV), is red-shifted from analogous alkyl-substituted poly(3,6-dihexyl) thieno[3,2-*b*]thiophene vinylene **C_6-PTTV**, which showed a band edge at 700 nm (1.77 eV) [129] and from poly(3,6-dioctylsulfanylthieno[3,2-*b*]thiophene), **SC_8-PTT**, whose band edge appears at 713 nm (1.74 eV) [121]. Evidently, both the sulfanyl substituents and the vinylene spacer play a part in shrinking the band gap. Replacing sulfanyl sides chains with sulfonyl (**SO_2-PTTV**) results in a ≈0.1 eV increase of the optical band gap (720 nm, 1.72 eV). This increase should in part be attributed to the lower molecular weight of the **SO_2-PTTV** polymers, although its lower rigidity (Figure 1.24) should also play a role. Copolymer **S/SO_2-PTTV-1:1** shows a lowered band gap of 1.53 eV, which can be attributed to the donor–acceptor interactions between sulfanyl and sulfonyl-substituted units. The balance between the latter appears important as the increased amount of –SO_2 substituted TT units in **S/SO_2-PTTV-1:2** increases the band gap (1.64 eV), possibly not only due to disrupted solid-state packing, but also due to a lower MW.

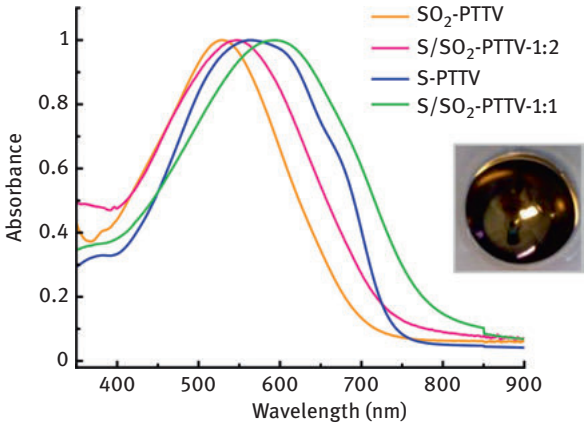

Figure 1.25: Absorption spectra of polymers as thin films on glass. The inset shows the highly reflective, metallic luster of a film of **S-PTTV**.

The effect of the substituents was further analyzed via the redox behavior of the synthesized polymers, as studied by cyclic voltammetry for thin films drop-cast on Pt electrodes (Table 1.1). Compared to the alkyl-substituted **C_6-PTTV** [129], the sulfanyl substituents show a moderate electron withdrawing effect, shifting the

EBSCOhost - printed on 2/14/2023 1:06 PM via . All use subject to https://www.ebsco.com/terms-of-use

Table 1.1: Redox potentials,[a] HOMO–LUMO levels,[b] and band gaps[c] of polymers determined by cyclic voltammetry of thin films.

	E_{red} (V)	E_{ox} (V)	LUMO (eV)	HOMO (eV)	E_g^{CV} (eV)
C_6-PTTV [129]	−1.83	0.24	−2.97	−5.04	2.07
S-PTTV	−1.63	0.32	−3.17	−5.12	1.95
SO_2-PTTV	−1.20	0.91	−3.60	−5.71	2.11
S/SO_2-PTTV-1:1	−1.37	0.50	−3.43	−5.30	1.87
S/SO_2-PTTV-1:2	−1.14	0.74	−3.66	−5.54	1.88

[a]All potentials reported versus Fc/Fc^+ in 0.1 M Bu_4NPF_6/propylene carbonate.
[b]Calculated from the onset of the oxidation and reduction potentials, assuming HOMO of Fc at −4.8 eV [130].
[c]E_g^{CV} = HOMO − LUMO.

oxidation and reduction of **S-PTTV** by 0.08 and 0.20 eV, respectively. A much larger shift is observed for sulfonyl-substituted polymer, **SO_2-PTTV** (0.67 and 0.63 V shifts for oxidation and reduction, respectively). The random copolymers **S/SO_2-PTTV-1:1** and **S/SO_2-PTTV-1:2** show the electronic effects of both their monomer units with reduction and oxidation onsets between those of **S-PTTV** and **SO_2-PTTV**, giving them the smallest electrochemical gaps at 1.87 and 1.88 eV, respectively.

A rather low hole mobility in thin-film transistors of $\approx 1\times10^{-5}\,cm^2/Vs$ was measured for **S-PTTV**, and no further improvement was achieved upon annealing. A likely reason for the poor transistor characteristics of these materials lies in the rotational disorder of the polymer chain and the resultant poor packing, caused by the out-of-plane protrusion of the alkylsulfanyl substituents.

In bulk-heterojunction solar cell devices from polymer:$PC_{70}BM$ blends **S-PTTV** displayed slightly higher open-circuit voltages (V_{OC} = 0.68 V) than reported for **C_6-PTTV** (V_{OC} = 0.60 V), as is expected due to its lower HOMO level. The trend continues for **S/SO_2-PTTV-1:1**, which has the lowest HOMO level and a high V_{OC} of 0.80 V. Thus, we were able to directly tune the open-circuit voltage of the devices by controlling the ratio of the substituents. The performances of both the **S-PTTV** and **S/SO_2-PTTV-1:1** devices were limited, however, by low short-circuit currents (I_{SC}) and FF. Poor mobilities mean more chances for recombination at the interface before holes and electrons can diffuse away, as well as an increase in the serial resistance, resulting in low FFs [131, 132].

In conclusion, the sulfanyl and sulfonyl substituents show moderate and strong electron-withdrawing effects and their combination in random copolymers is a means to fine-tune optoelectronic properties and achieve low band gap polymers (1.5 eV) without affecting the uniformity of the conjugated backbone. This method can be a welcome alternative to designing more complex donor–acceptor motifs for new polymeric semiconductors.

EBSCOhost - printed on 2/14/2023 1:06 PM via . All use subject to https://www.ebsco.com/terms-of-use

1.7 Supramolecular Solid-State Assembly

Although design strategies can be used to tune the energy levels and reorganization energy of a material, the electronic coupling will be dictated by the solid-state assembly of that material. It is the sum of intermolecular π-orbital interactions in three dimensions that will determine the efficacy of charge transport. Most molecular semiconductors display one of four main packing-motifs, shown in Figure 1.26. Close packing that favors strong π–π overlap is beneficial for charge transport, but strong anisotropy may yield poor mobilities in the bulk material, where π–stacks may not align with the direction of current measurement or else be interrupted by point defects or grain boundaries. As a result, 1D π-stacking of coparrallel molecules (such as in Figure 1.26b, c) rarely leads to efficient semiconductors. Rather, 2D herringbone packing (Figure 1.26a) is common for many high mobility semiconductors, despite limited π-overlap of nonparallel molecules.

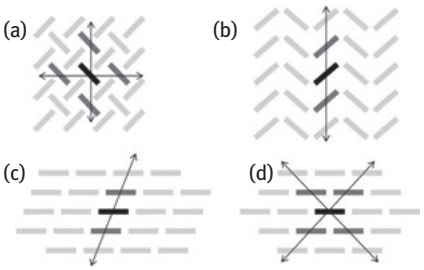

Figure 1.26: The four common packing motifs are (a) herringbone, (b) cofacial herringbone, (c) 1D lamellar "slipped stacks," and (c) 2D lamellar "brickwork" packing. Directions of preferred charge transfer are shown by arrows. Reprinted with permission from Schweicher et al. [21]. Copyright 2014 John Wiley & Sons, Inc.

It is important to remember that the conductance and valence bands are formed by molecular orbital interactions, so not only must the molecules be closely packed, but also their frontier molecular orbitals should be aligned as well. Figure 1.27 maps the electron coupling (t) of two cofacial pentacene molecules with respect to long axis displacement. The molecular overlap is at its maximum when the molecules are perfectly aligned and decreases in an oscillatory pattern that correlates with the nodes of the HOMO orbitals. The electronic coupling (t) in a material can be calculated from the crystal structures. In symmetric systems, t can be approximated by the energy splitting of the frontier orbitals in a dimer (for example, ΔE = (HOMO – HOMO-1)/2 for hole transport) [133]. This approximation, called the energy-splitting-in-dimer approach (ESID), assumes both molecules in the dimer have the same site energies, which will not be the case if the molecules inhabit different environments in the crystal lattice. The energy-splitting-in-dimer method is, therefore, not reliable for extended systems where polarization effects of the crystal environment on the site energies should be taken into account [134]. A better calculation of t is the direct-coupling method, which calculates t from the wave function of each molecule according to eq. (1.6)

EBSCOhost - printed on 2/14/2023 1:06 PM via . All use subject to https://www.ebsco.com/terms-of-use

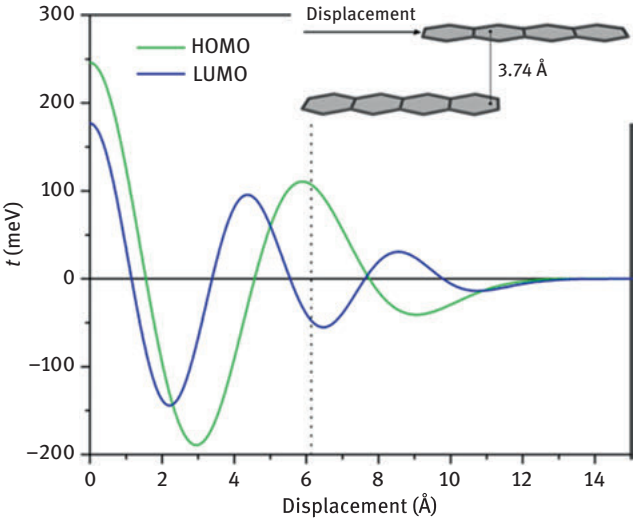

Figure 1.27: Evolution of the HOMO and LUMO intermolecular electronic coupling (t) as a function of displacement for two tetracene molecules with a π-stacking distance of 3.74 Å. The dotted line indicates the magnitude of long-axis displacement found in rubrene crystals. Reprinted with permission from Da Silva Filho al [135]. Copyright 2005 John Wiley & Sons, Inc.

$$t = \frac{J - \frac{1}{2}(\varepsilon_1 + \varepsilon_2)S}{1 - S^2} \tag{1.6}$$

where J is the charge transfer integral, S is the orbital overlap, and ε_1 and ε_2 are the site energies of the molecules.

While predicting exact packing motifs is not generally possible, and the chance of polymorphism is likely, morphological changes can be induced through molecular design. A few recent reviews have addressed this subject as it applies to polymers and small molecules [136, 137]. What follows are a few examples of design strategies based on noncovalent intermolecular interactions.

The solid-state packing of molecules is controlled by noncovalent effects, namely, van der Waals and coulombic interactions. For example, in pentacene, electron density lies in the π-orbitals above and below the plane of the molecule and slightly positively charged hydrogen atoms lie along the periphery of the pentacene backbone. This generates a quadrupole moment, represented as a partial positive charge density sandwiched between two partial negative charge densities (Figure 1.28a). Pentacene has many polymorphs [138], but all of them adopt a herringbone arrangement to maximize electrostatic interactions between its partially negative "face" and partially positive "edge." (Figure 1.28a). This face-to-edge packing still allows for high electronic coupling between the different molecular dimers, leading to high mobilities in pentacene films ($\mu_h \approx 1\,cm^2/Vs$) [139] and single crystals ($\mu_h \approx 40\,cm^2/Vs$) [140].

EBSCOhost - printed on 2/14/2023 1:06 PM via . All use subject to https://www.ebsco.com/terms-of-use

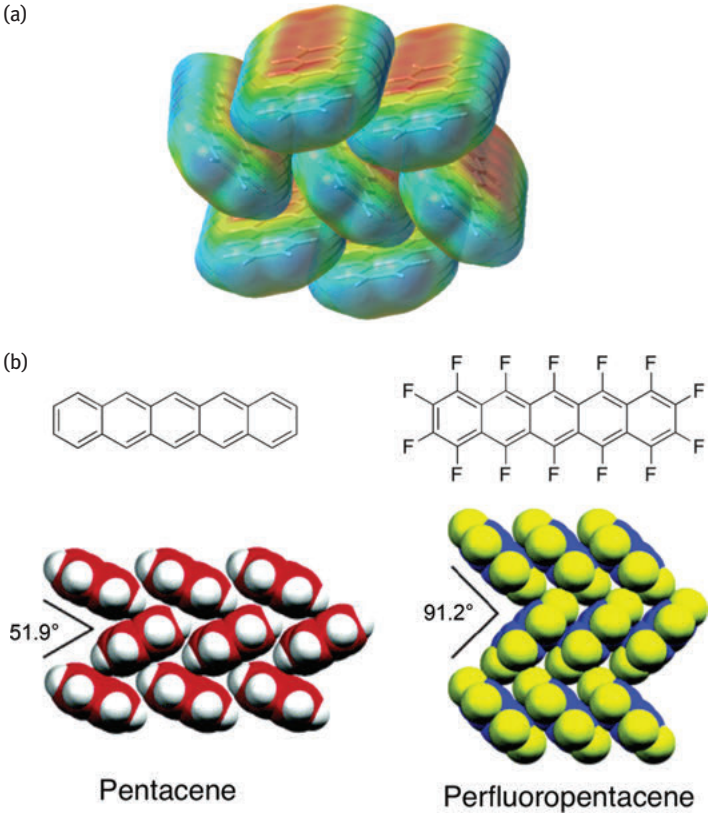

Figure 1.28: (a) Pentacene's herringbone face-to-edge packing is due to its quadrupole moment. (b) In perfluoropentacene the herringbone packing is orthogonal with tighter π–π stacks. Section (b) reprinted with permission from Sakamoto et al. [141]. Copyright 2004 American Chemical Society.

There are several ways to disrupt these electrostatic CH–π interactions and get tighter π–π stacks. One way is to replace the hydrogens with heteroatoms. Perfluoropentacene, for example, has an inverse electron density distribution to pentacene and is a well-known OSC for n-type transport due to the electron-withdrawing nature of fluorine. The fluorine atoms affect the packing of the molecules, in which CH–π interactions are replaced by F–F interactions between nearly perpendicular molecules (Figure 1.28b). The CF–π interactions between molecules of the same π-stack also greatly reduce their short-axis displacement (3.15 Å vs 5.34 Å in pentacene), thereby increasing the electronic coupling between cofacial molecules [141, 142].

The use of bulky substituents is another oft-used strategy for controlling crystal packing. Trialkylsilylethynyl groups have been extensively studied as substituents on oligoacenes because their size can be easily controlled. Anthony et al.

EBSCOhost - printed on 2/14/2023 1:06 PM via . All use subject to https://www.ebsco.com/terms-of-use

found that with smaller alkylsilyl groups (e.g., $SiMe_3$), pentacene derivatives assemble into slipped stacks, but if the size of the substituent is approximately half the length of the acene backbone, then a lamellar "brickwork" arrangement is observed [145]. This type of packing in crystals of bis(triisopropylsilylethynyl)pentacene (TIPS-pentacene) leads to good electronic coupling between overlapping pentacene cores (54 and 65 meV) and high mobilities ($\mu_h = 1.8\,cm^2/Vs$) (Figure 1.29a) [146, 147].

Okamoto et al. designed aryl and perfluoroaryl substituted tetracene as another way to induce face-to-face packing of the acene core. Here, aromatic–fluoroaromatic

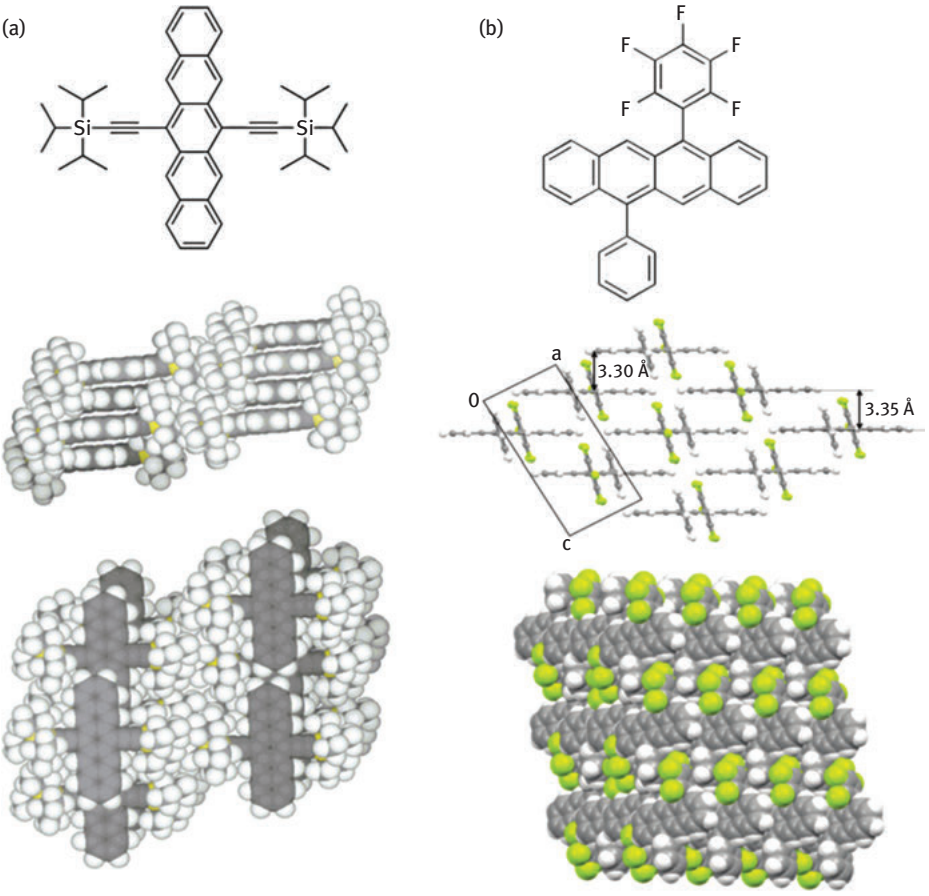

Figure 1.29: (a) Brickwork packing of TIPS-pentacene induced through bulky substituents. Reprinted with permission from Anthony et al. [143]. Copyright 2001 American Chemical Society. (b) Aromatic donor–acceptor interactions between substituents gives a lamellar brickwork assembly in 5-perfluorophenyl-11-phenyltetracene. Reprinted with permission from Okamoto et al. [144]. Copyright 2011 American Chemical Society.

EBSCOhost - printed on 2/14/2023 1:06 PM via . All use subject to https://www.ebsco.com/terms-of-use

(quadrupole) interactions between the substituents of coplanar tetracenes causes lamellar packing and close π–π distances between tetracene layers (Figure 1.29b) [144]. Without such interactions, bis(phenyl)tetracene adopts a herringbone conformation with no π–π stacks.

Alkyl chains placed along the long axis of the molecule, on the other hand, do not disrupt the packing of the molecules, but rather bring them closer together through van der Waals interactions. Inoue et al. studied the crystal packing of phenyl–benzothieno[3,2-*b*]benzothiophene with increasing lengths of alkyl chain substituents [148]. They found that increasing chain length (n = 10) strengthens attractive dispersion forces between the chains, leading to much higher electronic couplings.

CH–π interactions can also be weakened by replacing carbon with heteroatoms along the periphery of the molecule. OSCs containing sulfur, a larger and more polarizable atom than carbon, may benefit from intermolecular interactions through S···S contacts. For such contacts to be useful to hole transport, however, there must be large HOMO orbital coefficients on the sulfur atoms [149]. Even without short S···S distances, having high orbital coefficients over the sulfur atoms can lead to better electronic coupling. Figure 1.30 shows several thiophene containing OSCs, their HOMO orbital contours, and hole transport mobilities in FETs [150, 151]. The intensity of orbital coefficients on sulfur varies with structure. Notably, [5]thienoacene has virtually no orbital coefficients on its sulfurs, so that its HOMO orbital does not extend along its periphery. This explains its relatively low mobility [152]. In DNT-V ($\mu_h = 1.1\,cm^2/Vs$), on the other hand, the HOMO coefficients reside heavily on the central sulfur atom [153]. Unfortunately, other factors may affect charge mobilities. For example, the low lying HOMO of BBBT (−5.6 eV) is thought to cause a large hole injection barrier and limit its mobilities ($\mu_h = 0.01\,cm^2/Vs$) [154, 155].

Some heteroatoms, like O or N, can partake in hydrogen bonding, which could compete for morphological control. The self-assembly of well-defined supramolecular structures requires high-fidelity intermolecular interactions that lead to reversible association and provide predictable intermolecular geometries. In this regard, H-bonding is arguably the most far-reaching interaction for supramolecular control, yet has received surprisingly limited attention in OSCs. Our group has demonstrated efficient charge transport in H-bonded materials, namely, between dipyrrolopyridine donors and imide-functionalized acceptors (Figure 1.31) [156, 157]. The H-bonding interaction not only provides a handle for solid-state structural control, but also leads to electronic perturbation due to H-bonding-mediated charge redistribution in the π-conjugated systems. This affords a stronger D–A pair, enhanced π–π interactions, and facilitates CT interactions between H-bonded complexes.

In Figure 1.32 we see how changes in the linearity of a molecule affect preferences for face-to-edge CH–π interactions versus face-to-face π–stacking. Dinaphtho[2,3-*b*:2′,3′-*f*]thieno[3,2-*b*]thiophene (DNTT) is an excellent p-type semiconductor, due in part to its acene-like structure and electronic coupling in several directions

EBSCOhost - printed on 2/14/2023 1:06 PM via . All use subject to https://www.ebsco.com/terms-of-use

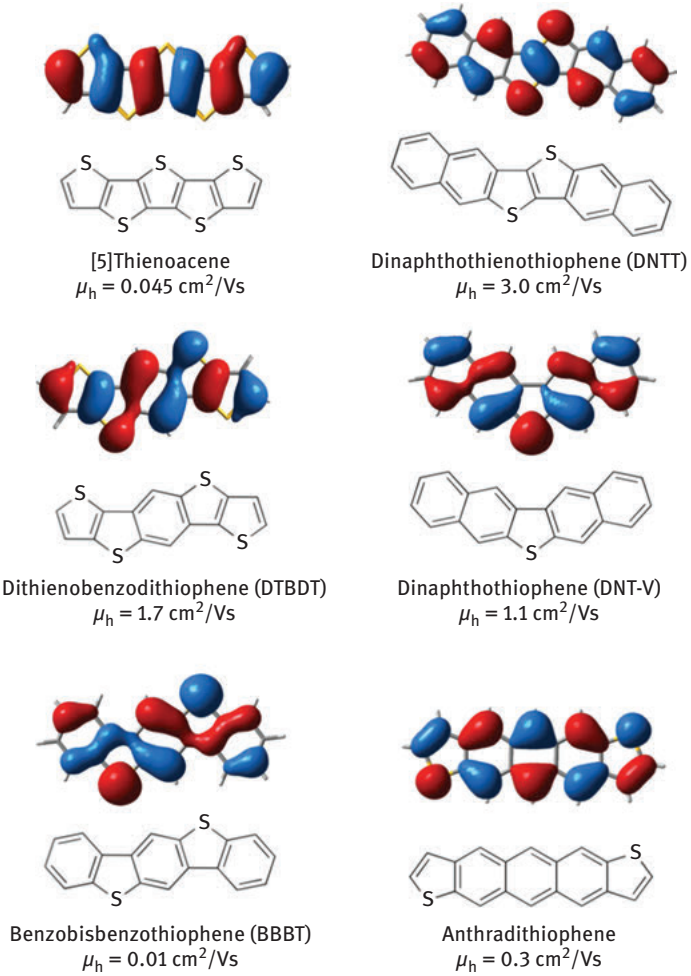

Figure 1.30: Calculated HOMO orbital contours (B3LYP/6-31G(d)) and hole transport mobilities for several thiophene-containing OSCs.

[80, 158]. "Bent" structural isomers of DNTT, however, exhibit much lower charge mobilities due to 1D electronic coupling or electronic coupling between isolated dimers. In addition, of the three isomers, only DNTT shows HOMO orbital coefficients on the sulfur atoms.

Finally, processing techniques can have a huge impact on the morphology of the material [159]. The same molecule will display vastly different electronic properties depending on whether it was drop cast, spin coated, evaporated, annealed, or grown as a single crystal. New solution-processing techniques like solution shearing, in which a top wafer is dragged across the evaporating OSC solution, have succeeded in forming oriented crystalline thin films by physically straining the

EBSCOhost - printed on 2/14/2023 1:06 PM via . All use subject to https://www.ebsco.com/terms-of-use

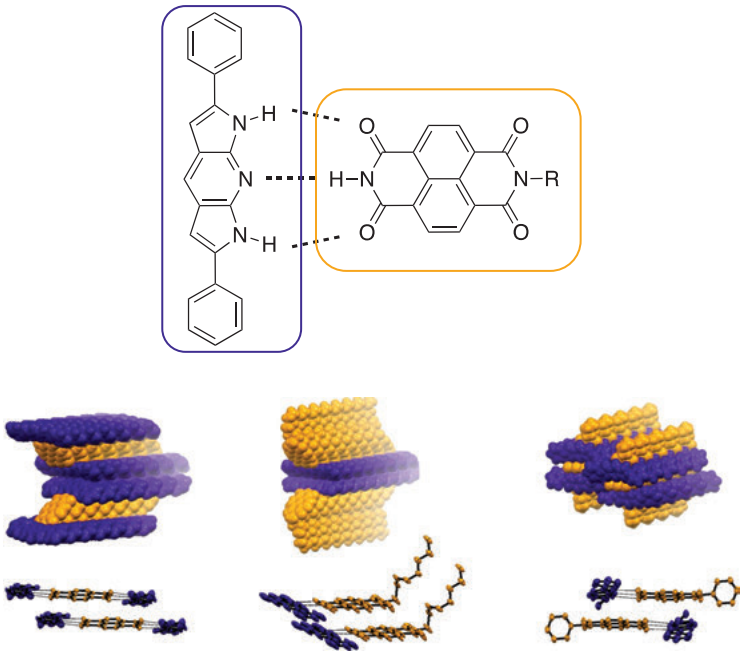

Figure 1.31: Single-cocrystal packing of hydrogen-bonded dipyrrolopyridine and naphthalenediimide derivatives. Reprinted with permission from Black et al. [156] Copyright 2016 John Wiley & Sons, Inc.

molecules as the solvent evaporates. Bao et al. showed closer intermolecular distances and a five-time increase in mobility for thin films of TIPS-pentacene using this solution-shearing technique [160].

1.8 Relevant Small-Molecule OSCs

1.8.1 Sulfur-Containing OSCs

Sulfur-containing molecules were the first high-mobility materials studied in organic electronics (Figure 1.33). It was the metal-like transport properties of TTF complexes, in which TTF forms stable radical cations, that launched the quest for superconductivity in organic materials. In the process, countless derivatives of TTF were synthesized and their conductive properties explored [138]. Crystals of TTF exist as two types of polymorphs: monoclinic or triclinic, each featuring S···S interactions. The monoclinic phase consists of infinite π-stacks, allowing for better charge transport than in the triclinic phase where no π-stacks are formed ($\mu_h = 1.2\,cm^2/Vs$ vs $\mu_h = 0.2\,cm^2/Vs$) [161]. Oligothiophenes were among the first

EBSCOhost - printed on 2/14/2023 1:06 PM via . All use subject to https://www.ebsco.com/terms-of-use

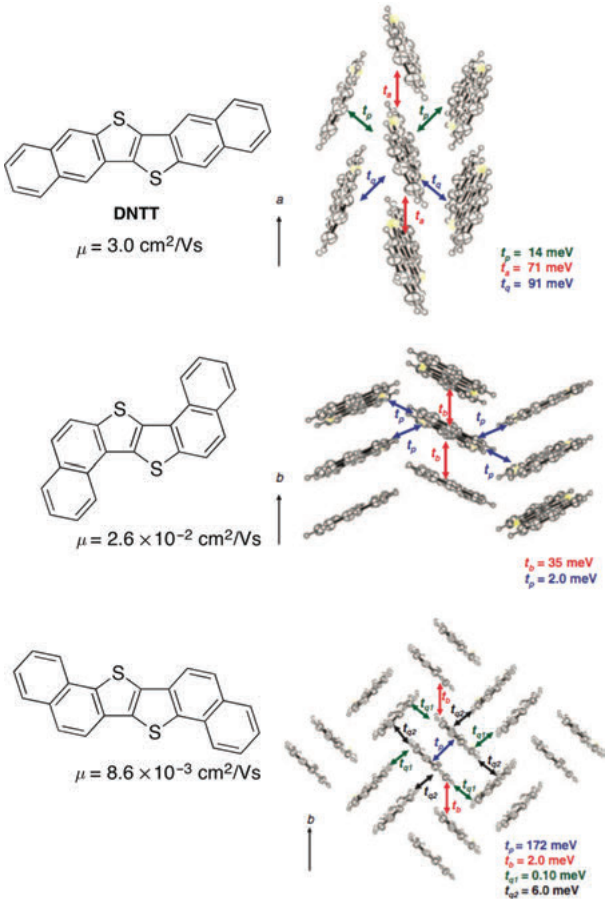

Figure 1.32: Crystal packing of DNTT and two isomers, showing hole mobilities and electronic coupling *t*. Adapted with permission from Yamamoto et al. [158]. Copyright 2010 Chemical Society of Japan.

structures to be used in FETs. Of the unsubstitued oligothiohenes, which are planar and adopt herringbone packing motifs, **α-8T** has the highest reported mobility of 0.33 cm^2/Vs [162]. Many derivatives of oligothiophenes have since been studied, including liquid crystalline **9** with long alkoxy side chains [163]. As spun films of **9** exhibited good hole mobilities of 0.1 cm^2/Vs, but for single crystal devices, mobilities up to 6.2 cm^2/Vs were reported, one of the highest values amongst nonfused oligothiophene semiconductors.

Fused thienoacenes were introduced in the previous section and are a class of high-mobility hole transporting materials. Record high mobilities have been reported for **C8-BTBT**: $\mu_h = 9.1\,cm^2/Vs$ for single crystals [164] and $\mu_h = 43\,cm^2/Vs$ for blends in polystyrene [165]. Average values were lower, however, indicating a preferred pathway for charge carriers in the crystal growth orientation. Anthradithiophene

EBSCOhost - printed on 2/14/2023 1:06 PM via . All use subject to https://www.ebsco.com/terms-of-use

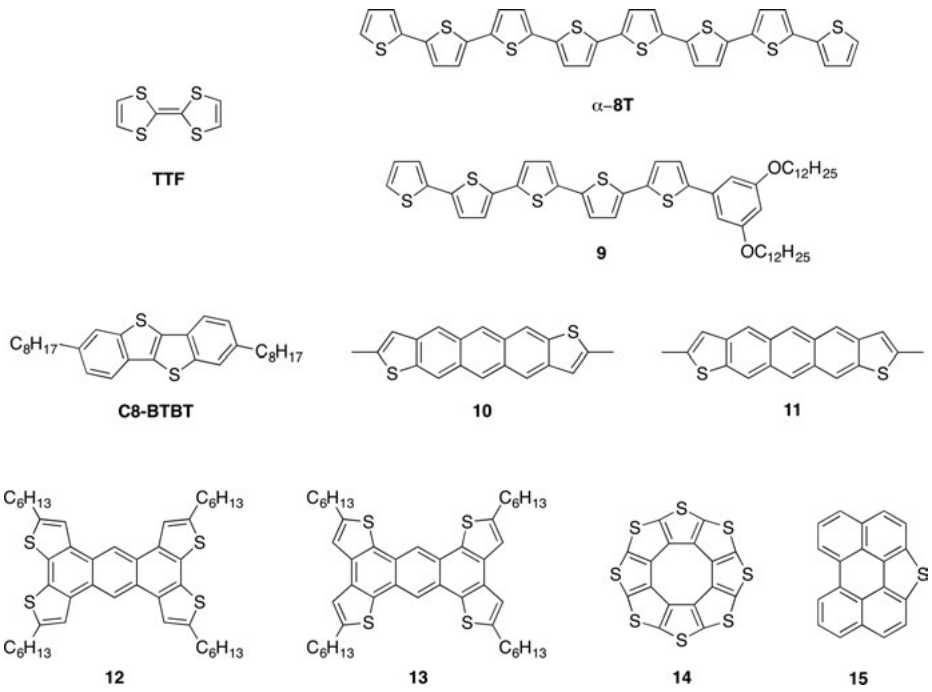

Figure 1.33: A selection of small-molecule OSCs featuring thiophene.

was synthesized as a stable analogue to pentacene and is an example of the effect isomers can have on charge transport. Isomerically pure anti (**10**)- and syn (**11**)-isomers of 2,8-dimethyl-anthradithiophene were synthesized and tested in thin film FET devices [166]. **10** displayed a hole mobility five times higher than **11** (anti $\mu_h = 0.41\,cm^2/Vs$ vs syn $\mu_h = 0.084\,cm^2/Vs$), a fact attributed to its centrosymmetric space group in the crystal structure. Takimiya et al. saw a similar sixfold difference in the mobilities of unsubstituted anthradithiophenes and reported stronger isomer effects in naphthodithiophenes (NDT), where anti-NDT displayed hole mobilities over an order of magnitude higher than in syn-NDT [106]. Contrarily, isomer effects were not observed with silylethynylated thienoacenes, where the large substituents dictate solid-state packing and the heteroatoms are scrambled in the crystal structure [167]. These examples demonstrate the subtler influences molecular structure can have on supramolecular assembly and charge transport.

Many 2D-extended semiconductors have also been studied. Isomers of tetrathienoanthracene, **12** and **13**, for example, have two different conjugation pathways, which only extends into the thiophene moieties in **13**. Both molecules adopt a cofacial herringbone arrangement, but the peripheral sulfur atoms in **12** allow for more close S···S contacts and leads to an order of magnitude higher hole mobilities in **12**, highlighting the importance of these contacts to charge transport [168]. Octathio[8]circulene (**14**), nicknamed "sulflower," synthesized by Chernichenko et al., is

EBSCOhost - printed on 2/14/2023 1:06 PM via . All use subject to https://www.ebsco.com/terms-of-use

entirely composed of peripheral sulfur atoms. Without the possibility of CH–π interactions, the molecule adopts a cofacial herringbone packing motif with very close S···S distances (3.25 Å) [169]. A low hole mobility of $9 \times 10^{-3}\,cm^2/Vs$ was reported for **14**, however, due to pronounced 1D growth in its films, as evidenced by atomic force microscopy [170]. Perylothiophene **15** exhibits a similar packing motif as **14** with short S···S contacts (3.51 Å) between neighboring columns. Sun et al. found that by modifying their SiO_2 substrate they could promote the growth of single-crystal micrometer sized wires. These wires showed better hole transport properties ($\mu_h = 0.8\,cm^2/Vs$) than thin films of deposited **15** ($\mu_h = 0.05\,cm^2/Vs$) [171].

1.8.2 Sulfur and Nitrogen-Containing OSCs

Thiazoles are electron-accepting heterocycles and are often used as acceptors in donor–acceptor polymers [172]. Small molecules with thiazole cores can be tuned to exhibit p- or n-type charge transport by using electron-donating or -withdrawing substituents (Figure 1.34). For example, benzobisthiazole **16**, flanked by alkylated thiophenes displays p-type transport ($\mu_h = 10^{-2}\,cm^2/Vs$) [173]. Single crystals of **16** showed an interesting packing motif consisting of orthogonal π–π stacks with close S···N contacts linking the orthogonal stacks (3.02 Å vs 3.35 Å for the sum of the van der Waals radii). With electron-withdrawing substituents, such as perfluoroalkyl groups, thiazole-containing molecules exhibit n-type charge transport. **17** and **18**, synthesized by Ando et al., have very similar chemical structures, but vastly different conformations in the solid state [174]. While **17** displays excellent electron transport properties ($\mu_e = 1.83\,cm^2/Vs$), devices of **18** showed no transport properties at all. This sharp difference in performance is attributed to small torsional twists in

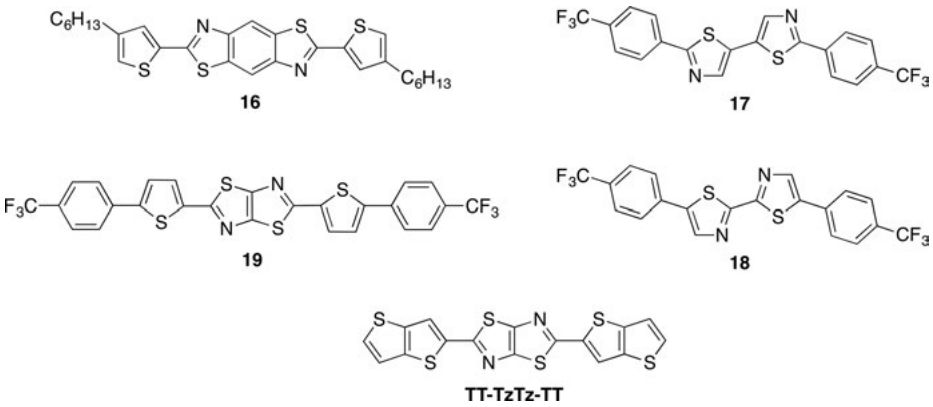

Figure 1.34: A selection of small-molecule OSCs featuring thiazole.

EBSCOhost - printed on 2/14/2023 1:06 PM via . All use subject to https://www.ebsco.com/terms-of-use

18, caused by sterics between the hydrogen atoms on the thiazole unit and the phenyl end group. Thus, while **17** is planar and forms an ordered brickwork network, the unit cell of **18** contains molecules with different torsional angles creating a disordered columnar structure. Fused thiazolothiazole moeties have no hydrogen bonds and are therefore attractive building blocks for planar OSCs. **19**, for example, is nearly planar with thiophene units adopting an all-trans conformation [175]. Short S···S contacts (3.25 Å) were observed between the thiazolo sulfur atoms on neighboring slipped stacks. High electron charge transport with mobilites up to $1.2\,cm^2/Vs$ was measured for thin films of **19** [176]. We synthesized the perfectly planar thienothiophene-substituted molecule **TT–TzTz–TT** and also found short S···S contacts (3.39 Å) and close π–π stacks (3.41 Å) [177]. Interestingly, two polymorphs of **TT–TzTz–TT** were discovered, one displaying semiconducting properties and the other insulating properties. This highlights that molecular structure is only one of the several descriptors of a semiconducting material and that the solid-state packing is at least equally, if not more, important.

1.8.3 Nitrogen-Containing OSCs

Hydrogenated N-heteroacenes, such as **20**, were reported several decades before the synthesis of their hydrocarbon analogue, pentacene, in 1935 (Figure 1.35) [178]. Unlike pentacene, which oxidizes quickly in solutions, hydrogenated N-heteroacenes are stabilized by multiple, isolated Clar's sextets, though they can be oxidized to their fully conjugated forms. In 2003 Miao et al. demonstrated that **20** could serve as an environmentally stable hole transport layer in FETs, exhibiting a mobility of $6\times10^{-3}\,cm^2/Vs$ [179]. In their fully unsaturated forms, N-heteropentacenes have similar band gaps as pentacene, but their frontier molecular orbitals can be lowered according to the number and location of the nitrogen heteroatoms. Two isomers of silylethynylated N-heteropentacene were synthesized by Liang et al. with either internal (**21**) or terminal (**22**) pyrazine units [180]. They found that N-heteroatoms placed internally were twice as effective at lowering the frontier orbitals of the molecule as terminally N-heteroatoms. To date, **21** is still the most effective azaacene for n-type transport, with an electron mobility of $13\,cm^2/Vs$ [181]. The silylethynyl groups on **21** lead to a brickwork packing motif in the solid state, as is seen for TIPS-pentacene in Figure 1.29. Efficient charge transport is observed, however, even in **21**'s precursor, **23. 23** self-assembles into infinite π-stacks with quadruple C–H···N/O hydrogen bonds between stacks in a DDAA–AADD pattern. Thin films of deposited **23** behave as n-type semiconductors with mobilities of $0.04 - 0.12\,cm^2/Vs$ [182].

A few nonlinear azaarene OSCs are known, such as **24**, where each azaacene is separated by a pyrene core [183]. Enantiomerically pure chiral azahelicenes (**25**) have also been studied in OFETs [184]. Although mobilities were low ($\mu_h = 1\times10^{-4}\,cm^2/Vs$), a highly specific photoresponse to circularly polarized light was found [185].

EBSCOhost - printed on 2/14/2023 1:06 PM via . All use subject to https://www.ebsco.com/terms-of-use

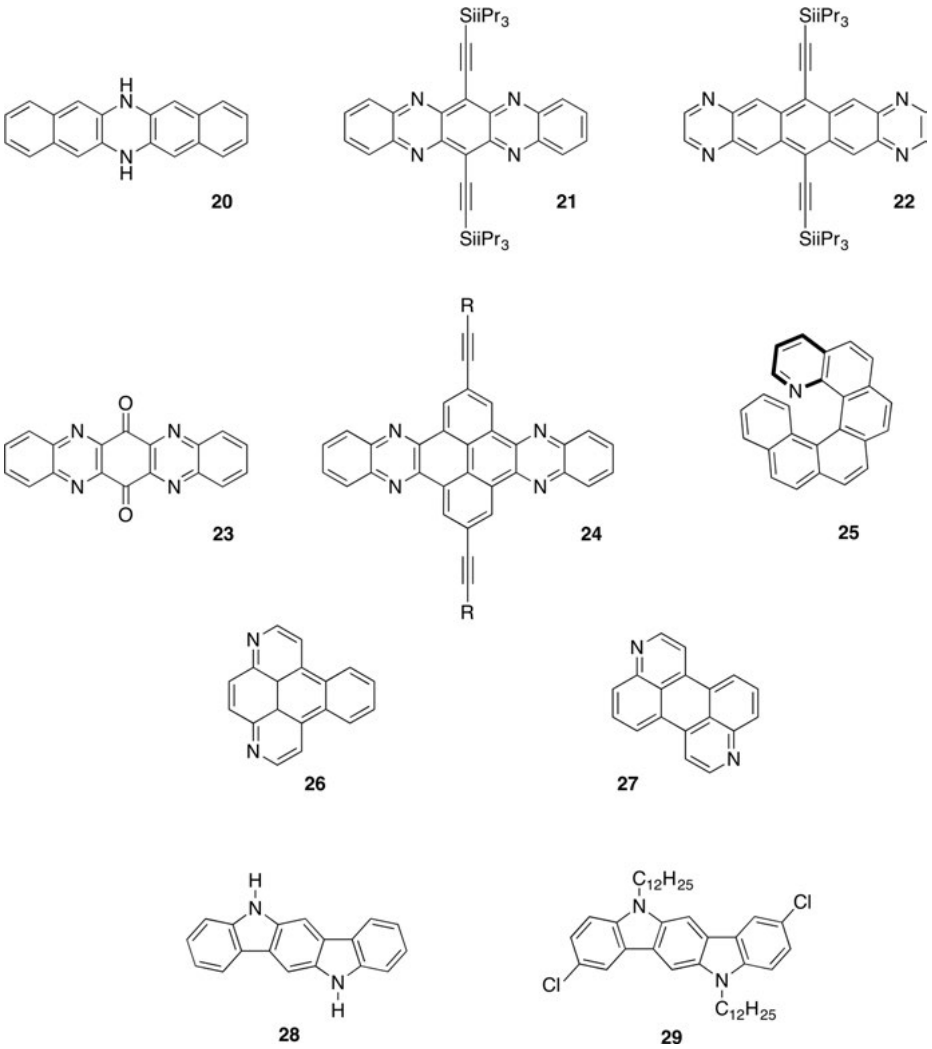

Figure 1.35: A selection of small-molecule OSCs featuring nitrogen heteroatoms.

The synthesis of nonlinear azaarenes, however, is sorely underdeveloped and their examples are limited. Our work on the synthesis of diazabenzopyrene (**26**) and diazaperylene (**27**) aimed at expanding existing synthetic methodologies by utilizing the visible-light photolysis of vinyl azides [186].

OSCs containing pyrrole nitrogens have been extensively studied as well. The carbazole unit has a rich history in the xerographic industry, which used poly(vinyl carbazole) in charge transfer complexes as photoconductors [187]. Carbazoles are attractive units for OSCs because of their chemical and environmental stability, as well as the possibility to tune the energy levels and solid-

EBSCOhost - printed on 2/14/2023 1:06 PM via . All use subject to https://www.ebsco.com/terms-of-use

state packing of the material by altering the substituents on the nitrogen atom. Indolo[3,2-*b*]carbazole **28** crystals, for example, adopt a herringbone arrangement that includes N–H$\cdots\pi$ interactions, as well as C–H$\cdots\pi$ interactions. Thin film devices displayed good hole transport properties with a mobility of 0.1 cm^2/Vs, an order of magnitude more than that was measured for N-substituted analogues in which there were no N–H$\cdots\pi$ interactions [188]. Of the many derivatives of indolo[3,2-*b*]carbazole, the highest hole mobility was measured in thin films of **29** (μ_h = 0.14 cm^2/Vs) [189].

1.9 Conclusions

This chapter has provided a broad, yet detailed, overview of organic electronics, with a focus on design strategies for the synthesis of OSCs. The reader has been introduced to the relevant history, devices (OLEDs, OPVs, and OFETs), and theoretical models used to define charge transport in OSCs. The brief theoretical overview introduces the reader to important variables – electronic coupling and reorganization energy – that are then discussed in detail in terms of molecular design principles. The design principles cover (1) extending conjugation and reducing BLA, (2) introducing heteroatoms, (3) substituents, (4) combining donor–acceptor units, and (5) influencing supramolecular assembly. These strategies were mostly discussed in terms of lowering a material's band gap, yet they can be implemented to achieve a wide range of material properties. The ultimate purpose of a material will dictate what properties to pursue. For example, planarity will certainly be desired for crystalline OFETs, but perhaps not for bulk heterojunction OPVs or OLEDs.

Throughout this chapter a wide range of specific materials were presented, along with discussions about the affects of certain design strategies. An in-depth case study on tuning the band gap of poly(thienothiophene vinylene) utilizes all the presented design strategies and showcases their effects.

Even such a brief survey illustrates a key issue in the study of OSCs: the charge mobilities acquired from devices are far from the intrinsic charge mobility of the material. It is often the case that substrate modifications or different annealing temperatures will lead to orders of magnitude increases in mobility. Charge mobility measurements are therefore more a measure of morphology and supramolecular ordering than of molecular structure properties. That being said, by studying many similar molecules, several structure–property relationships have been elaborated in this chapter. Substituents, for example, tend to dominate solid-state assembly. Long linear alkyl chains can form ordered films through van der Waals interactions allowing for solution-processed devices with mobilities matching those made from vacuum deposition. Planar molecules generally outperform (in terms of charge mobility) those that contain torsional twists, as those lead to disorder in the solid state. Finally, heteroatom

EBSCOhost - printed on 2/14/2023 1:06 PM via . All use subject to https://www.ebsco.com/terms-of-use

placement has been shown to influence not only HOMO/LUMO levels but also supramolecular assembly, with a preference for symmetrical placement.

Overall, this chapter introduced readers to the affects of molecular design on the optoelectronic properties, solid-state assemblies, and device performance of OSCs.

References

[1] Letheby, H. *J. Chem. Soc*. 1862, *15*, 161–163.
[2] Wudl, F., Wobschall, D., Hufnagel, E.J. *J. Am. Chem. Soc*. 1972, *94*, 670–672.
[3] Ferraris, J., Cowan, D.O., Walatka, V., Perlstein, J.H. *J. Am. Chem. Soc*. 1973, *95*, 948–949.
[4] Jérome, D., Mazaud, A., Ribault, M., Bechgaard, K. *J. Phys. Letters* 1980, *41*, 95–98.
[5] Bolto, B., McNeill, R., Weiss, D. *Aust. J. Chem*. 1963, *16*, 1090–1103.
[6] Shirakawa, H., Louis, E.J., MacDiarmid, A.G., Chiang, C.K., Heeger, A.J. *J. Chem. Soc. Chem. Commun*. 1977, 578–580.
[7] Heeger, A., MacDiarmid, A.G., Shirakawa, H. *Stock. Sweden R. Swedish Acad. Sci*. 2000, 1–16.
[8] Tang, C.W., VanSlyke, S.A. *Appl. Phys. Lett*. 1987, *51*, 913–915.
[9] Burroughes, J.H., Bradley, D.D.C., Brown, A.R., Marks, R.N., Mackay, K., Friend, R.H., Burns, P.L., Holmes, A.B. *Nature* 1990, *347*, 539–541.
[10] Burroughes, J.H., Jones, C.A., Friend, R.H. *Nature* 1988, *335*, 137–141.
[11] Horowitz, G., Peng, X., Fichou, D., Garnier, F. *J. Appl. Phys*. 1990, *67*, 528–532.
[12] Berggren, M., Nilsson, D., Robinson, N.D. *Nat. Mater*. 2007, *6*, 3–5.
[13] Myny, K., Steudel, S., Vicca, P., Smout, S., Beenhakkers, J., Aerle, N.A.J.M.V., Furthner, F., Van, B., Putten, D., Tripathi, A.K., Gelinck, G.H., Genoe, J. In *Appl. Org. Print. Electron*.; Cantatore, E., Ed.; Springer US: Boston, MA, 2013; Chapter Organic RF
[14] Huang, W., Diallo, A.K., Dailey, J.L., Besar, K., Katz, H.E. *J. Mater. Chem. C* 2015, *3*, 6445–6470.
[15] Sekine, C., Tsubata, Y., Yamada, T., Kitano, M., Doi, S. *Sci. Technol. Adv. Mater*. 2014, *15*:3, 034203.
[16] Usta, H., Facchetti, A., Marks, T.J. *Acc. Chem. Res*. 2011, *44*, 501–510.
[17] Street, R.A., Northrup, J.E., Salleo, A. *Phys. Rev. B* 2005, *71*, 165–202.
[18] Salleo, A., Kline, R.J., DeLongchamp, D.M., Chabinyc, M.L. *Adv. Mater*. 2010, *22*, 3812–3838.
[19] Warta, W., Karl, N. *Phys. Rev. B* 1985, *32*, 1172–1182.
[20] Kenkre, V.M., Andersen, J.D., Dunlap, D.H., Duke, C.B. *Phys. Rev. Lett*. 1989, *62*, 1165–1168.
[21] Schweicher, G., Olivier, Y., Lemaur, V., Geerts, Y.H. *Isr. J. Chem*. 2014, *54*, 595–620.
[22] Marcus, R.A. *J. Chem. Phys*. 1956, *24*, 966–978.
[23] Marcus, R.A. *Rev. Mod. Phys*. 1993, *65*, 599–610.
[24] Holstein, T. *Ann. Phys. (N. Y)*. 1959, *8*, 343–389.
[25] Bässler, H. *Phys. Status Solidi B* 1993, *175*, 15–56.
[26] Stallinga, P. *Adv. Mater*. 2011, *23*, 3356–3362.
[27] Shur, M., Hack, M. *J. Appl. Phys*. 1984, *55*, 3831–3842.
[28] Horowitz, G., Hajlaoui, M.E., Hajlaoui, R. *J. Appl. Phys*. 2000, *87*, 4456–4463.
[29] Köhler, A., Bässler, H. *Electron. Process. Org. Semicond*., Wiley-VCH Verlag GmbH & Co. KGaA: Weinheim, Germany, 2015, pp 193–305.
[30] Sekitani, T., Zschieschang, U., Klauk, H., Someya, T. *Nat. Mater*. 2010, *9*, 1015–1022.
[31] Barr, M.C., Rowehl, J.A., Lunt, R.R., Xu, J., Wang, A., Boyce, C.M., Im, S.G., Bulovi, V., Gleason, K.K. *Adv. Mater*. 2011, *23*, 3500–3505.

EBSCOhost - printed on 2/14/2023 1:06 PM via . All use subject to https://www.ebsco.com/terms-of-use

[32] Tee, B.C.-K., Chortos, A., Berndt, A., Nguyen, A.K., Tom, A., McGuire, A., Lin, Z.C., Tien, K., Bae, W.-G., Wang, H., Mei, P., Chou, H.-H., Cui, B., Deisseroth, K., Ng, T.N., Bao, Z. *Science* 2015, *350*, 313–316.
[33] Mertens, R., Peleg, R. OLED mobile phones: an introduction and market status. http://www.oled-info.com/oled-mobile-phones (accessed Nov 19, 2015)
[34] Loo, Y.-L., McCulloch, I. *MRS Bull*. 2012, *33*, 653–662.
[35] Lee, J., Chen, H.-F., Batagoda, T., Coburn, C., Djurovich, P.I., Thompson, M.E., Forrest, S.R. *Nat. Mater*. 2016, 15, 92–98.
[36] BELECTRIC OPV GmbH, Solarte. http://www.solarte.de/index.php/en/ (accessed Nov 19, 2015)
[37] Coakley, K.M., McGehee, M.D. *Chem. Mater*. 2004, *16*, 4533–4542.
[38] Qi, B., Wang, J. *J. Mater. Chem*. 2012, *22*, 24315–24325.
[39] Scharber, M.C., Mühlbacher, D., Koppe, M., Denk, P., Waldauf, C., Heeger, A.J., Brabec, C.J. *Adv. Mater*. 2006, *18*, 789–794.
[40] Chen, H.Y., Hou, J.H., Zhang, S.Q., Liang, Y.Y., Yang, G.W., Yang, Y., Yu, L.P., Wu, Y., Li, G. *Nat. Photonics* 2009, *3*, 649–653.
[41] Beaujuge, P.M., Fréchet, J.M.J. *J. Am. Chem. Soc*. 2011, *133*, 20009–20029.
[42] Müller, C., Wang, E., Andersson, L.M., Tvingstedt, K., Zhou, Y., Andersson, M.R., Inganäs, O. *Adv. Funct. Mater*. 2010, *20*, 2124–2131.
[43] Ballantyne, A.M., Chen, L., Dane, J., Hammant, T., Braun, F.M., Heeney, M., Duffy, W., McCulloch, I., Bradley, D.D.C., Nelson, J. *Adv. Funct. Mater*. 2008, *18*, 2373–2380.
[44] Mei, J., Bao, Z. *Chem. Mater*. 2014, *26*, 604–615.
[45] Zardetto, V., Brown, T.M., Reale, A., Di Carlo, A. *Journal of Polymer Science Part B: Polymer Physics* 2011, *49*, 638–648.
[46] Eder, F., Klauk, H., Halik, M., Zschieschang, U., Schmid, G., Dehm, C. *Appl. Phys. Lett*. 2004, *84*, 2673–2675.
[47] Qian, C., Sun, J., Yang, J., Gao, Y. *RSC Adv*. 2015, *5*, 14567–14574.
[48] Fritz, S.E., Kelley, T.W., Frisbie, C.D. *J. Phys. Chem. B* 2005, *109*, 10574–10577.
[49] Melzer, C., von Seggern, H. *Nat. Mater*. 2010, *9*, 470–472.
[50] Dimitrakopoulos, C., Malenfant, P. *Adv. Mater*. 2002, *14*, 99–117.
[51] Noh, Y.-Y., Chang, J.-F., Cheng, X., Baeg, K.-J. In *Polymer electronics*, Meng, H.- f., Ed., CRC Press: Boca Raton, Fl, 2013, Chapter Polymer Fi
[52] Merlo, J.A., Frisbie, C.D. *J. Phys. Chem. B* 2004, *108*, 19169–19179.
[53] Roncali, J. *Macromol. Rapid Commun*. 2007, *28*, 1761–1775.
[54] Pizzoferrato, R., Berliocchi, M., Di Carlo, A., Lugli, P., Venanzi, M., Micozzi, A., Ricci, A., Lo Sterzo, C. *Macromolecules* 2003, *36*, 2215–2223.
[55] Brédas, J.L. *J. Chem. Phys*. 1985, *82*, 3808–3811.
[56] Longuet-Higgins, H.C., Salem, L. *Proc. R. Soc. A Math. Phys. Eng. Sci*. 1959, *251*, 172–185.
[57] Heeger, A., Blanchet, G., Chung, T.-C., Fincher, C. *Synth. Met*. 1984, *9*, 173–184.
[58] Wudl, F., Kobayashi, M., Heeger, A.J. *J. Org. Chem*. 1984, *49*, 3382–3384.
[59] He, Z., Zhong, C., Su, S., Xu, M., Wu, H., Cao, Y. *Nat. Photonics* 2012, *6*, 593–597.
[60] Lu, L., Yu, L. *Adv. Mater*. 2014, *26*, 4413–4430.
[61] Marder, S.R., Beratan, D.N., Cheng, L.T. *Science* 1991, *252*, 103–106.
[62] Marder, S.R., Perry, J.W., Bourhill, G., Gorman, C.B., Tiemann, B.G., Mansour, K. *Science* 1993, *261*, 186–189.
[63] Gorman, C.B., Marder, S.R. *Chem. Mater*. 1995, *7*, 215–220.
[64] Kanibolotsky, A.L., Berridge, R., Skabara, P.J., Perepichka, I.F., Bradley, D.D.C., Koeberg, M. *J. Am. Chem. Soc*. 2004, *126*, 13695–13702.
[65] Brisset, H., Blanchard, P., Illien, B., Riou, A., Roncali, J. *Chem. Commun*. 1997, 569–570.
[66] Roncali, J., Thobie-Gautier, C. *Adv. Mater*. 1994, *6*, 846–848.

EBSCOhost - printed on 2/14/2023 1:06 PM via . All use subject to https://www.ebsco.com/terms-of-use

[67] Trotter, J. *Acta Crystallogr*. 1961, *14*, 1135–1140.
[68] Gerkin, R.E., Lundstedt, A.P., Reppart, W.J. *Acta Crystallogr. Sect. C Cryst. Struct. Commun*. 1984, *40*, 1892–1894.
[69] Watanabe, M., Chang, Y.J., Liu, S.-W., Chao, T.-H., Goto, K., Islam, M.M., Yuan, C.-H., Tao, Y.-T., Shinmyozu, T., Chow, T.J. *Nat. Chem*. 2012, *4*, 574–578.
[70] Sun, Z., Wu, J. *J. Mater. Chem*. 2012, *22*, 4151–4160.
[71] Zhang, L., Fonari, A., Liu, Y., Hoyt, A.L., Lee, H., Granger, D., Parkin, S., Russell, T.P., Anthony, J.E., Bredas, J.L., Coropceanu, V., Briseno, A.L. *J. Am. Chem. Soc*. 2014, *136*, 9248–9251.
[72] Okamoto, H., Kawasaki, N., Kaji, Y., Kubozono, Y., Fujiwara, A., Yamaji, M. *J. Am. Chem. Soc*. 2008, *130*, 10470–10471.
[73] Okamoto, H., Hamao, S., Goto, H., Sakai, Y., Izumi, M., Gohda, S., Kubozono, Y., Eguchi, R. *Sci. Rep*. 2014, *4*, 5–048.
[74] Malloci, G., Cappellini, G., Mulas, G., Mattoni, A. *Chem. Phys*. 2011, *384*, 19–27.
[75] Patra, A., Bendikov, M. *J. Mater. Chem*. 2010, *20*, 422–433.
[76] Dall'Olio, A., Dascola, G., Varacca, V., Bocchio, V. *C. R. Acad. Sci. Paris Série C* 1968, *267*, 433–435.
[77] Diaz, A.F., Kanazawa, K.K., Gardini, G.P. *J. Chem. Soc. Chem. Commun*. 1979, *160*, 635–636.
[78] Zhao, G., He, Y., Li, Y. *Adv. Mater*. 2010, *22*, 4355–4358.
[79] Mishra, A., Ma, C.-Q., Segura, J.L., Bäuerle, P. In *Handb. Thiophene-Based Mater*., Perepichka, I.F., Perepichka, D.F., Eds., John Wiley & Sons, Ltd: Chichester, UK, 2009, Vol. 1, pp. 1–155.
[80] Yamamoto, T., Koizumi, T. *Polymer* 2007, *48*, 5449–5472.
[81] Ramsden, C.A. *Tetrahedron* 2010, *66*, 2695–2699.
[82] Horner, K.E., Karadakov, P.B. *J. Org. Chem*. 2015, *80*, 7150–7157.
[83] Yum, S., An, T.K., Wang, X., Lee, W., Uddin, M.A., Kim, Y.J., Nguyen, T.L., Xu, S., Hwang, S., Park, C.E., Woo, H.Y. *Chem. Mater*. 2014, *26*, 2147–2154.
[84] Jackson, N.E., Savoie, B.M., Kohlstedt, K.L., Olvera De La Cruz, M., Schatz, G.C., Chen, L.X., Ratner, M.a. *J. Am. Chem. Soc*. 2013, *135*, 10475–10483.
[85] Shi, C., Yao, Y., Yang, Y., Pei, Q. *J. Am. Chem. Soc*. 2006, *128*, 8980–8986.
[86] Price, S., Stuart, A., Yang, L., Zhou, H., You, W. *J. Am. Chem. Soc*. 2011, *133*, 4625–4631.
[87] Huo, L., Zhang, S., Guo, X., Xu, F., Li, Y., Hou, J. *Angew. Chem. Int. Ed. Engl*. 2011, *50*, 9697–9702.
[88] Kim, J.H., Song, C.E., Kim, B., Kang, I.N., Shin, W.S., Hwang, D.H. *Chem. Mater*. 2014, *26*, 1234–1242.
[89] Yu, J., Holdcroft, S. *Chem. Commun*. 2001, 1274–1275.
[90] Liu, J., Kadnikova, E.N., Liu, Y., McGehee, M.D., Fréchet, J.M.J. *J. Am. Chem. Soc*. 2004, *126*, 9486–9487.
[91] Gevorgyan, S.a., Krebs, F.C. *Chem. Mater*. 2008, *20*, 4386–4390.
[92] Sheng, Y., Jiang, Y., Wang, X.-C. *J. Chem. Soc. Faraday Trans*. 1998, *94*, 47–52.
[93] Dehu, C., Meyers, F., Bredas, J.L. *J. Am. Chem. Soc*. 1993, *115*, 6198–6206.
[94] Würthner, F., Effenberger, F., Wortmann, R., Krämer, P. *Chem. Phys*. 1993, *173*, 305–314.
[95] An, Z., Odom, S.A., Kelley, R.F., Huang, C., Zhang, X., Barlow, S., Padilha, L.a., Fu, J., Webster, S., Hagan, D.J., Van Stryland, E.W., Wasielewski, M.R., Marder, S.R. *J. Phys. Chem. A* 2009, *113*, 5585–5593.
[96] Ellinger, S., Graham, K.R., Shi, P., Farley, R.T., Steckler, T.T., Brookins, R.N., Taranekar, P., Mei, J., Padilha, L.a., Ensley, T.R., Hu, H., Webster, S., Hagan, D.J., Van Stryland, E.W., Schanze, K.S., Reynolds, J.R. *Chem. Mater*. 2011, *23*, 3805–3817.

EBSCOhost - printed on 2/14/2023 1:06 PM via . All use subject to https://www.ebsco.com/terms-of-use

[97] Zhang, Z., Wang, J. *J. Mater. Chem*. 2012, *22*, 4178–4187.
[98] Martinez, C.R., Iverson, B.L. *Chem. Sci*. 2012, *3*, 2191–2201.
[99] Reczek, J.J., Villazor, K.R., Lynch, V., Swager, T.M., Iverson, B.L. *J. Am. Chem. Soc*. 2006, *128*, 7995–8002.
[100] Tsao, H.N., Cho, D.M., Park, I., Hansen, M.R., Mavrinskiy, A., Yoon, D.Y., Graf, R., Pisula, W., Spiess, H.W., Müllen, K. *J. Am. Chem. Soc*. 2011, *133*, 2605–2612.
[101] Li, Y.N., Sonar, P., Murphy, L., Hong, W. *Energy Environ. Sci*. 2013, *6*, 1684–1710.
[102] Carsten, B., Szarko, J.M., Son, H.J., Wang, W., Lu, L., He, F., Rolczynski, B.S., Lou, S.J., Chen, L.X., Yu, L. *J. Am. Chem. Soc*. 2011, *133*, 20468–20475.
[103] Bronstein, H., Chen, Z., Ashraf, R.S., Zhang, W., Du, J., Durrant, J.R., Tuladhar, P.S., Song, K., Watkins, S.E., Geerts, Y., Wienk, M.M., Janssen, R.A.J., Anthopoulos, T., Sirringhaus, H., Heeney, M., McCulloch, I. *J. Am. Chem. Soc*. 2011, *133*, 3272–3275.
[104] Li, Y., Sonar, P., Murphy, L., Hong, W. *Energy Environ. Sci*. 2013, *6*, 1684–1710.
[105] Chen, Y.L., Chang, C.Y., Cheng, Y.J., Hsu, C.S. *Chem. Mater*. 2012, *24*, 3964–3971.
[106] Osaka, I., Kakara, T., Takemura, N., Koganezawa, T., Takimiya, K. *J. Am. Chem. Soc*. 2013, *135*, 8834–8837.
[107] Kan, B., Li, M., Zhang, Q., Liu, F., Wan, X., Wang, Y., Ni, W., Long, G., Yang, X., Feng, H., Zuo, Y., Zhang, M., Huang, F., Cao, Y., Russell, T.P., Chen, Y. *J. Am. Chem. Soc*. 2015, *137*, 3886–3893.
[108] Zhao, J., Li, Y., Yang, G., Jiang, K., Lin, H., Ade, H., Ma, W., Yan, H. *Nature Energy* 2016, *1*, 15027.
[109] Li, X., Liu, X., Zhang, W., Wang, H.-Q., Fang, J. *Chem. Mater*. 2017, *29*, 4176–4180.
[110] Sung, M.J., Luzio, A., Park, W.-T., Kim, R., Gann, E., Maddalena, F., Pace, G., Xu, Y., Natali, D., de Falco, C., Dang, L., McNeill, C.R., Caironi, M., Noh, Y.-Y., Kim, Y.-H. *Adv. Funct. Mater*. 2016, *26*, 4984–4997.
[111] Gao, Y., Deng, Y., Tian, H., Zhang, J., Yan, D., Geng, Y., Wang, F. *Adv. Mater*. 2017, *29*, 1606217–1606224.
[112] Wang, Y., Hasegawa, T., Matsumoto, H., Mori, T., Michinobu, T. *Adv. Funct. Mater*. 2017, *27*, 1604608–1604623.
[113] Perepichka, I.F., Perepichka, D.F. In *Handbook of Thiophene-Based Materials*, John Wiley & Sons, Ed., 2009
[114] Babudri, F., Farinola, G.M., Naso, F., Ragni, R. *Chem. Commun*. 2007, 1003–1022.
[115] Li, L., Collard, D.M. *Macromolecules* 2005, *38*, 372–378.
[116] Huo, L., Zhang, S., Guo, X., Xu, F., Li, Y., Hou, J. *Angew. Chem. Int. Ed. Engl*. 2011, *50*, 9697–9702.
[117] Casalbore-Miceli, G., Gallazzi, M., Zecchin, S., Camaioni, N., Geri, A., Bertarelli, C. *Adv. Funct. Mater*. 2003, *13*, 307–312.
[118] Dey, T., Invernale, M.A., Ding, Y., Buyukmumcu, Z., Sotzing, G.A. *Macromolecules* 2011, *44*, 2415.
[119] Zhang, Q.T., Tour, J.M. *J. Am. Chem. Soc*. 1998, *120*, 5355–5362.
[120] Liang, Y., Feng, D., Wu, Y., Tsai, S.-T., Li, G., Ray, C., Yu, L. *J. Am. Chem. Soc*. 2009, *131*, 7792–7799.
[121] Cremer, L., De Verbiest, T., Koeckelberghs, G. *Macromolecules* 2008, *41*, 568–578.
[122] Huo, L., Zhou, Y., Li, Y. *Macromol. Rapid Commun*. 2009, *30*, 925–931.
[123] Pozo-Gonzalo, C., Khan, T., McDouall, J.J.W., Skabara, P.J., Roberts, D.M., Light, M.E., Coles, S.J., Hursthouse, M.B., Neugebauer, H., Cravino, A., Sariciftci, N.S. *J. Mater. Chem*. 2002, *12*, 500–510.
[124] Milián-Medina, B., Van Vooren, A., Brocorens, P., Gierschner, J., Shkunov, M., Heeney, M., McCulloch, I., Lazzaroni, R., Cornil, J. *Chem. Mater*. 2007, *19*, 4949–4956.
[125] McCulloch, I., Heeney, M., Bailey, C., Genevicius, K., Macdonald, I., Shkunov, M., Sparrowe, D., Tierney, S., Wagner, R., Zhang, W., Chabinyc, M.L., Kline, R.J., McGehee, M.D., Toney, M.F. *Nat. Mater*. 2006, *5*, 328–333.

EBSCOhost - printed on 2/14/2023 1:06 PM via . All use subject to https://www.ebsco.com/terms-of-use

[126] Lee, J.S., Son, S.K., Song, S., Kim, H., Lee, D.R., Kim, K., Ko, M.J., Choi, D.H., Kim, B., Cho, J.H. *Chem. Mater*. 2012, *24*, 1316–1323.
[127] Schneider, J.A., Dadvand, A., Wen, W., Perepichka, D.F. *Macromolecules* 2013, *46*, 9231–9239.
[128] Zade, S.S., Bendikov, M. *Chem. Eur. J*. 2007, *13*, 3688–3700.
[129] He, Y., Wu, W., Zhao, G., Liu, Y., Li, Y. *Macromolecules* 2008, *41*, 9760–9766.
[130] D'Andrade, B.W., Datta, S., Forrest, S.R., Djurovich, P., Polikarpov, E., Thomson, M.E. *Org. Electron*. 2005, 6, 11–20.
[131] Zhang, Y., Dang, X.-D., Kim, C., Nguyen, T.-Q. *Adv. Energy Mater*. 2011, *1*, 610–617.
[132] Kroon, R., Lenes, M., Hummelen, J.C., Blom, P.W.M., de Boer, B. *Polym. Rev*. 2008, *48*, 531–582.
[133] Newton, M.D. *Chem. Rev*. 1991, *91*, 767–792.
[134] Valeev, E.F., Coropceanu, V., Da Silva Filho, D.A., Salman, S., Brédas, J.L. *J. Am. Chem. Soc*. 2006, *128*, 9882–9886.
[135] Da Silva Filho, D.A., Kim, E.G., Brédas, J. L. *Adv. Mater*. 2005, *17*, 1072–1076.
[136] Noriega, R., Rivnay, J., Vandewal, K., Koch, F.P.V., Stingelin, N., Smith, P., Toney, M.F., Salleo, A. *Nat. Mater*. 2013, *12*, 1038–1044.
[137] Sutton, C., Risko, C., Brédas, J.-L. *Chem. Mater*. 2016, *28*, 3–16.
[138] Bendikov, M., Wudl, F., Perepichka, D.F. *Chem. Rev*. 2004, *104*, 4891–4946.
[139] Gundlach, D., Lin, Y., Jackson, T., Nelson, S., Schlom, D. *IEEE Electron Device Lett*. 1997, *18*, 87–89.
[140] Jurchescu, O.D., Baas, J., Palstra, T.T.M. *Appl. Phys. Lett*. 2004, *84*, 3061–3063.
[141] Sakamoto, Y., Suzuki, T., Kobayashi, M., Gao, Y., Fukai, Y., Inoue, Y., Sato, F., Tokito, S. *J. Am. Chem. Soc*. 2004, *126*, 8138–8140.
[142] Delgado, M.C.R., Pigg, K.R., da Silva Filho, D.A., Gruhn, N.E., Sakamoto, Y., Suzuki, T., Osuna, R.M., Casado, J., Hernández, V., Navarrete, J.T.L., Martinelli, N.G., Cornil, J., Sánchez-Carrera, R.S., Coropceanu, V., Brédas, J.-L. *J. Am. Chem. Soc*. 2009, *131*, 1502–1512.
[143] Anthony, J.E., Brooks, J.S., Eaton, D.L., Parkin, S.R. *J. Am. Chem. Soc*. 2001, *123*, 9482–9483.
[144] Okamoto, T., Nakahara, K., Saeki, A., Seki, S., Oh, J.H., Akkerman, H.B., Bao, Z., Matsuo, Y. *Chem. Mater*. 2011, *23*, 1646–1649.
[145] Anthony, J.E., Eaton, D.L., Parkin, S.R. *Org. Lett*. 2002, *4*, 15–18.
[146] Park, S.K., Jackson, T.N., Anthony, J.E., Mourey, D.a. *Appl. Phys. Lett*. 2007, *91*, 10–13.
[147] Wade, J., Steiner, F., Niedzialek, D., James, D.T., Jung, Y., Yun, D.-J., Bradley, D.D.C., Nelson, J., Kim, J.-S. *J. Mater. Chem. C* 2014, *2*, 10110–10115.
[148] Inoue, S., Minemawari, H., Tsutsumi, J., Chikamatsu, M., Yamada, T., Horiuchi, S., Tanaka, M., Kumai, R., Yoneya, M., Hasegawa, T. *Chem. Mater*. 2015, *27*, 3809–3812.
[149] Osaka, I., Shinamura, S., Abe, T., Takimiya, K. *J. Mater. Chem. C* 2013, *1*, 1297–1304.
[150] Gao, P., Beckmann, D., Tsao, H.N., Feng, X., Enkelmann, V., Baumgarten, M., Pisula, W., Müllen, K. *Adv. Mater*. 2009, *21*, 213–216.
[151] Nakano, M., Niimi, K., Miyazaki, E., Osaka, I., Takimiya, K. *J. Org. Chem*. 2012, *77*, 8099–8111.
[152] Xiao, K., Liu, Y., Qi, T., Zhang, W., Wang, F., Gao, J., Qiu, W., Ma, Y., Cui, G., Chen, S., Zhan, X., Yu, G., Qin, J., Hu, W., Zhu, D. *J. Am. Chem. Soc*. 2005, *127*, 13281–13286.
[153] Okamoto, T., Mitsui, C., Yamagishi, M., Nakahara, K., Soeda, J., Hirose, Y., Miwa, K., Sato, H., Yamano, A., Matsushita, T., Uemura, T., Takeya, J. *Adv. Mater*. 2013, *25*, 6392–6397.
[154] Gao, P., Beckmann, D., Tsao, H.N., Feng, X., Enkelmann, V., Pisula, W., Müllen, K. *Chem. Commun*. 2008, 1548–1550.
[155] Ebata, H., Miyazaki, E., Yamamoto, T., Takimiya, K. *Org. Lett*. 2007, *9*, 4499–4502.
[156] Black, H.T., Yee, N., Zems, Y., Perepichka, D.F. *Chem. Euro. J*. 2016, *22*, 17251–17261.
[157] Black, H.T., Perepichka, D.F. *Angew. Chem. Int. Ed*. 2014, *53*, 2138–2142.
[158] Yamamoto, T., Shinamura, S., Miyazaki, E., Takimiya, K. *Bull. Chem. Soc. Jpn*. 2010, *83*, 120–130.
[159] Virkar, A.a., Mannsfeld, S., Bao, Z., Stingelin, N. *Adv. Mater*. 2010, *22*, 3857–3875.

EBSCOhost - printed on 2/14/2023 1:06 PM via . All use subject to https://www.ebsco.com/terms-of-use

[160] Giri, G., Verploegen, E., Mannsfeld, S.C.B., Atahan-Evrenk, S., Kim, D.H., Lee, S.Y., Becerril, H.a., Aspuru-Guzik, A., Toney, M.F., Bao, Z. *Nature* 2011, *480*, 504–508.
[161] Jiang, H., Yang, X., Cui, Z., Liu, Y., Li, H., Hu, W., Liu, Y., Zhu, D. *Appl. Phys. Lett.* 2007, *91*, 123–505.
[162] Murphy, A.R., Fréchet, J.M.J. *Chem. Rev.* 2007, *107*, 1066–1096.
[163] Dong, S., Zhang, H., Yang, L., Bai, M., Yao, Y., Chen, H., Gan, L., Yang, T., Jiang, H., Hou, S., Wan, L., Guo, X. *Adv. Mater.* 2012, *24*, 5576–5580.
[164] Liu, C., Minari, T., Lu, X., Kumatani, A., Takimiya, K., Tsukagoshi, K. *Adv. Mater.* 2011, *23*, 523–526.
[165] Yuan, Y., Giri, G., Ayzner, A.L., Zoombelt, A.P., Mannsfeld, S.C.B., Chen, J., Nordlund, D., Toney, M.F., Huang, J., Bao, Z. *Nat. Commun.* 2014, *5*, 3–005.
[166] Mamada, M., Minamiki, T., Katagiri, H., Tokito, S. *Org. Lett.* 2012, *14*, 4062–4065.
[167] Lehnherr, D., Waterloo, A.R., Goetz, K.P., Payne, M.M., Hampel, F., Anthony, J.E., Jurchescu, O.D., Tykwinski, R.R. *Org. Lett.* 2012, *14*, 3660–3663.
[168] Brusso, J.L., Hirst, O.D., Dadvand, A., Ganesan, S., Cicoira, F., Robertson, C.M., Oakley, R.T., Rosei, F., Perepichka, D.F. *Chem. Mater.* 2008, *20*, 2484–2494.
[169] Chernichenko, K.Y., Sumerin, V.V., Shpanchenko, R.V., Balenkova, E.S., Nenajdenko, V.G. *Angew. Chemie – Int. Ed.* 2006, *45*, 7367–7370.
[170] Dadvand, A., Cicoira, F., Chernichenko, K.Y., Balenkova, E.S., Osuna, R.M., Rosei, F., Nenajdenko, V.G., Perepichka, D.F. *Chem. Commun. (Camb).* 2008, 5354–5356.
[171] Sun, Y., Tan, L., Jiang, S., Qian, H., Wang, Z., Yan, D., Di, C., Wang, Y., Wu, W., Yu, G., Yan, S., Wang, C., Hu, W., Liu, Y., Zhu, D. *J. Am. Chem. Soc.* 2007, *129*, 1882–1883.
[172] Lin, Y., Fan, H., Li, Y., Zhan, X. *Adv. Mater.* 2012, *24*, 3087–3106.
[173] Pang, H., Vilela, F., Skabara, P., McDouall, J., Crouch, D., Anthopoulos, T., Bradley, D.D.C., de Leeuw, D., Horton, P., Hursthouse, M. *Adv. Mater.* 2007, *19*, 4438–4442.
[174] Ando, S., Murakami, R., Nishida, J.- i., Tada, H., Inoue, Y., Tokito, S., Yamashita, Y. *J. Am. Chem. Soc.* 2005, *127*, 14996–14997.
[175] Ando, S., Nishida, J.- i., Tada, H., Inoue, Y., Tokito, S., Yamashita, Y. *J. Am. Chem. Soc.* 2005, *127*, 5336–5337.
[176] Kumaki, D., Ando, S., Shimono, S., Yamashita, Y., Umeda, T., Tokito, S. *Appl. Phys. Lett.* 2007, *90*, 053506.
[177] Schneider, J.A., Black, H., Lin, H.-P., Perepichka, D.F. *ChemPhysChem* 2015, *16*, 1173–1178.
[178] Hinsberg, O. *Justus Liebig's Ann. der Chemie* 1901, *319*, 257–286.
[179] Miao, Q., Nguyen, T.Q., Someya, T., Blanchet, G.B., Nuckolls, C. *J. Am. Chem. Soc.* 2003, *125*, 10284–10287.
[180] Liang, Z., Tang, Q., Mao, R., Liu, D., Xu, J., Miao, Q. *Adv. Mater.* 2011, *23*, 5514–5518.
[181] Xue, G., Wu, J., Fan, C., Liu, S., Huang, Z., Liu, Y., Shan, B., Xin, H.L., Miao, Q., Chen, H., Li, H. *Mater. Horiz.* 2016, *3*, 119–123.
[182] Tang, Q., Liang, Z., Liu, J., Xu, J., Miao, Q. *Chem. Commun. (Camb).* 2010, *46*, 2977–2979.
[183] More, S., Bhosale, R., Choudhary, S., Mateo-Alonso, A. *Org. Lett.* 2012, *14*, 4170–4173.
[184] Takenaka, N., Sarangthem, R.S., Captain, B. *Angew. Chem. Int. Ed.* 2008, *47*, 9708–9710.
[185] Yang, Y., da Costa, R.C., Fuchter, M.J., Campbell, a. J. *Nat. Photonics* 2013, *7*, 634–638.
[186] Schneider, J.A., Perepichka, D. *J. Mater. Chem. C* 2016, *4*, 7269–7276.
[187] Law, K.Y. *Chem. Rev.* 1993, *93*, 449–486.
[188] Zhao, H., Jiang, L., Dong, H., Li, H., Hu, W., Ong, B.S. *Chemphyschem* 2009, *10*, 2345–2348.
[189] Li, Y., Wu, Y., Gardner, S., Ong, B.S. *Adv. Mater.* 2005, *17*, 849–853.

EBSCOhost - printed on 2/14/2023 1:06 PM via . All use subject to https://www.ebsco.com/terms-of-use

EBSCOhost - printed on 2/14/2023 1:06 PM via . All use subject to https://www.ebsco.com/terms-of-use

Bing Yu, Yue Zhao

2 CO_2-Controlled Polymer Self-Assembly and Application

In this chapter, we present a brief introduction of the synthesis and properties of the CO_2-responsive polymers with different CO_2-responsive functional groups (tertiary amine, amidine, guanidine, imidazole, and carboxylic acid). Then we focus on the self-assembly behaviors of CO_2-responsive polymers and the size, shape, and morphology transformation behaviors of their assemblies as triggered by CO_2. Finally, we provide a review of selected recent studies demonstrating the potential applications of CO_2-responsive polymer assemblies in the field of controllable encapsulation and release, CO_2-induced gelation, and CO_2-switchable surfactants.

Keywords: CO2-responsive polymers, self-assembly, morphology transformation

2.1 Introduction of CO2-Responsive Polymers

Stimuli-responsive polymers exhibit reversible or irreversible alternation in their physical or chemical properties in response to external stimuli such as temperature, pH, light, chemical agent, mechanical force, and electric/magnetic field. In the past years, stimuli-responsive polymers have attracted much attention as a result of their potential applications in many fields, including bio-imaging [1, 2], sensors [3, 4], and drug delivery [5, 6]. However, there are some drawbacks in applying these traditional stimulations for certain applications, especially those used under physiological condition. For example, to achieve a reversible change over cycles, switchable stimuli such as pH and chemical agent require repeated addition of chemical compounds into the polymer solution, which may result in salt accumulation and chemical contamination [7]. Meanwhile, some other stimuli such as light, electrical/magnetic field, as well as mechanical force, may be harmful to biological tissue [8]. Therefore, it is important to discover novel stimulation modes to satisfy the demanding conditions in many applications.

Carbon dioxide (CO_2) is such a novel stimulus developed in recent years. It is interesting not only because it is cheap and abundant but also because it is benign, nontoxic, and thus can be used in physiological conditions. Therefore, CO_2-responsive polymers are potentially useful in many fields, such as CO_2-switchable latexes [9–13], CO_2-induced gelation [14–16], CO_2 monitoring and capturing [17–20], CO_2-responsive

Bing Yu, Yue Zhao, Département de chimie, Université de Sherbrooke, Sherbrooke, Québec, Canada

https://doi.org/10.1515/9783110537734-002

EBSCOhost - printed on 2/14/2023 1:06 PM via . All use subject to https://www.ebsco.com/terms-of-use

materials for separation [21, 22], chemosensor for detection of CO_2 [23–25], CO_2-switchable nano-carriers for encapsulation and release [26], and so on. The most attractive and distinctive feature of CO_2 stimulation is that it can react with some specific functional groups selectively and reversibly, as well as be removed easily through an inert gas (N_2, Ar) bubbling or heating, with those CO_2-responsive functional groups converting back to their initial state. This process is truly mild and green without any chemical contamination and salt accumulation [27]. Meanwhile, compared with other stimuli, the stimulating strength of CO_2 can be continuously and precisely controlled by the amount of CO_2 added in the polymer solution through a continuous flow of CO_2 [28].

Through introducing CO_2-responsive functional groups into the amphiphilic polymers, the obtained polymers can self-assemble into different structures and morphologies from nanoscopic to macroscopic scale when dispersed in water, and these various morphologies are mostly dependent on the balance of the hydrophobic–hydrophilic fractions [29], which can be altered through CO_2 bubbling due to the amphiphilicity changes caused by protonation. As a result, a morphology transformation of the assemblies can be triggered by CO_2. Compared with other stimulations, the continuous, quantitative, and reversible response triggered by CO_2 is beneficial for precisely tuning the morphology and for observing the transition regions during a morphology transformation process of the amphiphilic polymer assemblies.

In this review, we present a brief introduction of the synthesis and properties of the CO_2-responsive polymers with different CO_2-responsive functional groups (tertiary amine, amidine, guanidine, imidazole, and carboxylic acid). Then we focus on the self-assembly behaviors of CO_2-responsive polymers and the size, shape, and morphology transformation behaviors of their assemblies as triggered by CO_2. Finally, we provide a review of selected recent studies demonstrating the potential applications of CO_2-responsive polymer assemblies in the field of controllable encapsulation and release, CO_2-induced gelation, and CO_2-switchable surfactants.

2.2 Some Types of Polymers with CO_2-Responsive Functional Groups

As mentioned above, in order to synthesize polymers responsive to CO_2, the introduction of CO_2-reactive functional groups is necessary, which include tertiary amine, amidine, guanidine, imidazole, and carboxylic acid. These functional groups in aqueous solution can be protonated after CO_2 bubbling, while most of them can also be deprotonated and recover to their initial state by inert gas bubbling or heating (Figure 2.1). In these reversible protonation and deprotonation processes, the polymer polarity or solubility can change, which results in switching the hydrophobic–hydrophilic balance of the CO_2-responsive polymers, and thus affecting their self-assembly morphology of the polymers.

EBSCOhost - printed on 2/14/2023 1:06 PM via . All use subject to https://www.ebsco.com/terms-of-use

2.2.1 CO_2-Responsive Polymers with Tertiary Amino Groups

A weak base is usually a kind of CO_2-responsive functional groups, which can switch from neutral to cationic when reacting with weak acid such as CO_2. However, a base may be too weak to react with CO_2, or too strong to recover even upon heating. As a result, these bases must be neither too strong nor too weak to be regarded as a CO_2-responsive functional group. A common parameter for comparing the basicity is the dissociation constant (pK_a) of the conjugate acid; a stronger base usually possesses a larger pK_a.

Amine is a common base that can be protonated by CO_2, and tertiary amine ($-NR_1R_2$) is one of the simplest and well investigated CO_2-responsive functional groups. In water, tertiary amines can react with CO_2 to form charged ammonium bicarbonate (Figure 2.1). The pK_a values of most tertiary amino groups are between 6.5 and 8.0. As a result, they can react with either strong acids such as HCl or weak acids such as CO_2, and can be regarded as a pH/CO_2 dual-responsive functional group. There are some important advantages of using tertiary amines over other bases. On one hand, tertiary amines can be easily introduced into polymers because several tertiary amine-containing, low-cost, and easily polymerizable monomers such as *N*,*N*-dimethylaminoethyl methacrylate (DMAEMA), *N*,

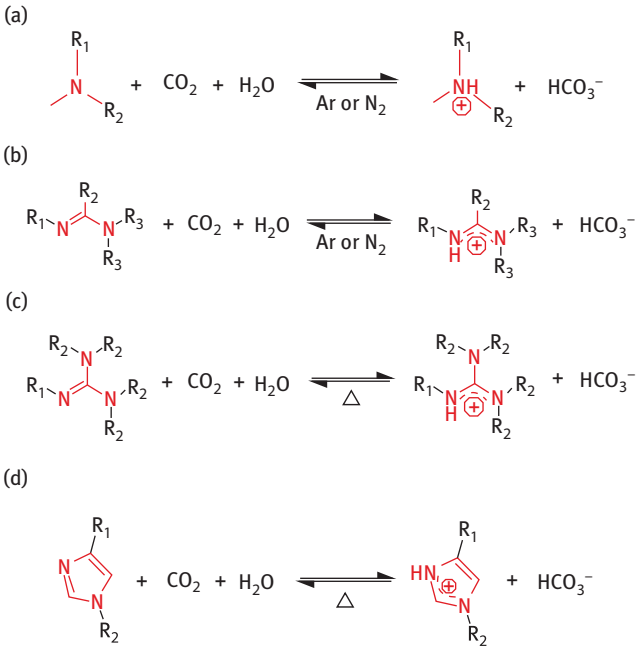

Figure 2.1: The reversible protonation and deprotonation reaction of different base groups upon CO_2 stimulation: (a) tertiary amine, (b) amidine, (c) guanidine, and (d) imidazole. Adapted from Ref. [28] with permission from the RSC.

EBSCOhost - printed on 2/14/2023 1:06 PM via . All use subject to https://www.ebsco.com/terms-of-use

N-diethylaminoethyl methacrylate (DEAEMA), and *N*,*N*-diisopropylaminoethyl methacrylate (DPAEMA) are commercially available. On the other hand, studies in recent years show that polymers bearing tertiary amines display excellent and robust switchability, in addition to the low hydrolysis side effect in aqueous media [28].

However, most tertiary amine-containing polymers cannot be used at elevated temperatures due to thermally activated deprotonation unless using increased CO_2 pressure. But this easily deprotonation property of ammonium bicarbonate is another advantage for applications in which a rapid back-conversion to their initial neutral form is required [30]. Generally, an opposite deprotonation process can be fulfilled through a simple inert gas bubbling with Ar or N_2 in the aqueous media.

DMAEMA and DEAEMA are the two tertiary amine-containing monomers most often used in synthesizing CO_2-responsive polymers. The polymers containing tertiary amino groups are more hydrophobic in their neutral form than in the charged form, or they can simply switch from a hydrophobic polymer to a hydrophilic polymer after the protonation of the tertiary amine groups by bubbling CO_2. This protonation and deprotonation process is reversible through the addition and removal of CO_2 as the pK_a value of DMAEMA and DEAEMA homopolymers (PDMAEMA and PDEAEMA) is ~7.4 and ~7.5, respectively [31].

There is another major difference between using DMAEMA and DEAEMA to prepare CO_2-responsive polymers. The two monomers have very similar chemical structures, but their water solubility is different from each other. While DEAEMA and PDEAEMA are relatively hydrophobic, DMAEMA and PDMAEMA are relatively hydrophilic even in the neutral form. Moreover, PDMAEMA can be more easily precipitated in hexane than PDEAEMA with a similar molecular weight [32]. Though it is possible for both DMAEMA and DEAEMA to hydrolyze, DEAEMA is more resistant to hydrolysis than DMAEMA at a similar temperature and pH as a result of its hydrophobicity [33]. In order to overcome the hydrolysis problem, a more hydrolytically stable CO_2-reactive monomer, dimethylaminopropyl methacrylamide (DMAPMAm) can be used in some special applications.

Besides tertiary amines, bulky secondary amines and bulky primary amines are also responsive to CO_2 because they can also convert into the corresponding bicarbonate salt in water due to the inhabitation of carbamate formation by the bulky groups [34]. Typically, one secondary alkyl group, such as an isopropyl group, attached to the nitrogen atom is sufficient to prevent the carbamate formation. These amines usually possess a faster switch rate as well as a faster biodegradation than the tertiary amines.

2.2.2 CO_2-Responsive Polymers with Amidines

Amidine is a kind of nitrogen analogues of carboxylic esters in which two oxygen atoms are replaced with two nitrogen atoms and also a combination of one amide and one imine functional groups, which can be protonated and deprotonated reversibly by addition and removal of CO_2 in water (Figure 2.1). The pK_a values of

EBSCOhost - printed on 2/14/2023 1:06 PM via . All use subject to https://www.ebsco.com/terms-of-use

amidine groups are between 5 and 12, which are larger than those of the tertiary amino groups. Consequently, amidine is a stronger base than the tertiary amine, which can convert into bicarbonate salts much more quickly and sensitively than tertiary amines when purging with CO_2; however, the reverse process is more difficult and slower, sometimes heating is necessary for its back conversion [10]. Although amidine-containing polymers have been well investigated and exhibit many advantages and interesting features, there are still two drawbacks for its future applications. One of the inevitable problem is the hydrolysis effect in the natural condition even without CO_2, which results in a risk of decomposition of the amidine-containing polymer when dispersed in water. Moreover, compared with the tertiary amine-containing polymer, the synthesis routes of amidine-containing polymer are always complicated and sometimes a multi-step organic reaction is required [35]. However, amidine-containing block copolymer is still very useful in the fields of CO_2-triggered self-assembly and morphology transformation, CO_2-switchable latexes, and purification as well as some biological applications such as biomimetic regulation.

2.2.3 CO_2-Responsive Polymers with Other Functional Groups

Guanidine is also an amine derivative, which possesses two amide and one imine functional groups attached on the same carbon atom. Because of the resonance after protonation, guanidine is a much stronger organic base than tertiary amine and amidine with a pK_a value of ~13.5. After purging with CO_2 in water, guanidines can be protonated and converted into guanidinium species accompanied with bicarbonate (Figure 2.1). But, if there are any N–H bonds in guanidine, carbamates will be formed instead of, or in addition to bicarbonate salts [10]. As a result of its high pK_a value, the deprotonation of guanidine bicarbonate salt is very difficult, and simply N_2 or Ar bubbling is impossible to achieve, which may be realized at a very high temperature for a long time. But this characteristic can turn into an advantage for guanidine-containing CO_2-responsive polymers in applications involving high temperatures. Meanwhile, in order to tune the pK_a value of guanidine, different substitutions are introduced. Alkyl substitution can increase the basicity of the guanidine derivatives, while the introduction of an aromatic substituent can result in a lower basicity [34].

Imidazoles and imidazolines are two types of five-membered ring amidines, which usually exist in many biological compounds, such as histidine (an amino acid), histamine (a hormone), and some drugs. Imidazoles substituted with alkyl chain is also CO_2-reactive in water, which can be protonated and convert into the corresponding bicarbonate imidazolium salt after the addition of CO_2 (Figure 2.1). The alkyl-substituted imidazole also possesses a higher basicity than tertiary amine, whose pK_a value is always between 10 and 14.5 depending on the substituent group. As a result, the obtained imidazolium salt is very stable in water, which is difficult to decompose through inert gas bubbling.

EBSCOhost - printed on 2/14/2023 1:06 PM via . All use subject to https://www.ebsco.com/terms-of-use

Some polymers comprising carboxylic acids or phenols are also shown to be CO_2-responsive in water. Unlike the CO_2-responsive functional groups discussed above, a carboxylic acid can be anionic in its ionized (deprotonated) form, but converted into the neutral form upon protonation in the presence of CO_2 that decreases the pH of the solution. However, this CO_2 response is dependent on the initial pH of the system, which can be affected by concentration, functional group density, and other factors. Generally, to achieve an effective CO_2 response, the initial pH of the system should be at least one pH unit above the pK_a of the weak acid groups. Meanwhile, the reaction of these anionic groups with CO_2 is more sensitive when water solubility of the neutral form is poor [36]. Similarly, McCormick et al. also synthesized a series of pH- and CO_2-responsive methacryloyl sulfonamides (MSAs) that possess pK_a values in the biologically relevant regime (pH = 4.5–7.4) with reversible addition–fragmentation chain-transfer (RAFT) polymerization, where these polymers are also anionic in its deprotonated form and can aggregate after the addition of CO_2 due to the protonation. Moreover, the pK_a value and the aggregation pH of the corresponding pMSA are tunable by the sulfonamide R group of MSA monomers [37].

2.2.4 CO_2-Responsive Copolymers with Dual Stimuli Response

Some CO_2-responsive polymers exhibit dual stimuli response after introduction of polymer chains containing other stimuli-reactive moieties. For instance, Yuan's group synthesized a diblock copolymer composed of PDEAEMA and poly(*N*-isopropylacrylamide) (PDEAEMA-*b*-PNIPAM) through RAFT polymerization, and the polymer assemblies were shown to be responsive to both CO_2 and temperature [38]. This block copolymer is composed of CO_2-responsive PDEAEMA and thermal sensitive PNIPAM. At room temperature and without CO_2, the PDEAEMA block is hydrophobic and the PNIPAM block hydrophilic. As a result, it could self-assemble into vesicles when dispersed in water. However, the PDEAEMA block became hydrophilic after the addition of CO_2, while the PNIPAM block became hydrophobic at a temperature above its LCST, resulting in the formation of spherical particles with a NIPAM core and a DEAEMA shell. Therefore, the morphology change of these diblock copolymer assemblies could be triggered by either temperature or CO_2, which could be unimers, spheres, or vesicles depending on the ratio of the hydrophobic block to the hydrophilic block (Figure 2.2). Similarly, an amphiphilic diblock copolymer PCL-*b*-P(NIPAM-*co*-DMAEMA) terminated with a pyrene group was synthesized by the combination of ring-opening polymerization (ROP) and RAFT [39]. The aggregation behavior of the micelles formed by this diblock copolymer, as well as its fluorescence emission intensity, also exhibited dual-responsiveness to CO_2 and temperature.

EBSCOhost - printed on 2/14/2023 1:06 PM via . All use subject to https://www.ebsco.com/terms-of-use

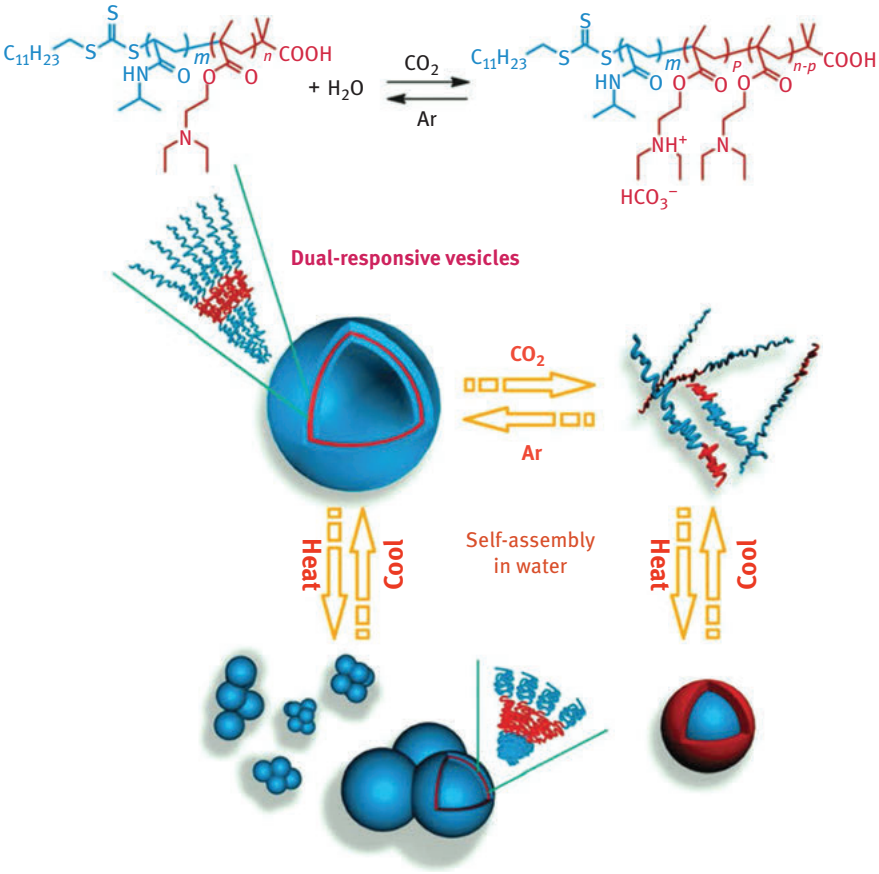

Figure 2.2: Scheme of the morphology transformation of the PDEAEMA-b-PNIPAM diblock polymer triggered by CO_2 and temperature. Reprinted from Ref. [38] with permission from the RSC.

Another interesting type of polymers can be responsive to two different gases, namely, O_2 and CO_2. For instance, Zhu's group developed a diblock copolymer composed of PEG as the hydrophilic block and a random copolymer of DEAEMA and 2,2,2-trifluoroethyl methacrylate (FMA) as the hydrophobic block [40]. This polymer could self-assemble into vesicles with the hydrophobic DEAEMA/FMA block forming the vesicle wall. As FMA can react with O_2, the self-assembled vesicles are dual responsive to both O_2 and CO_2. After the addition of CO_2, the vesicles could be transformed to micelles as a result of the protonation of the tertiary amino groups in DEAEMA and resulting in an increase in interfacial energy. By contrast, the addition of O_2 could only increase the hydrophilicity of the diblock copolymer slightly and, consequently, the vesicles expanded slightly instead of transforming to micelles (Figure 2.3). The same group also designed and prepared a type of microgels through soap-free emulsion copolymerization of another O_2-responsive monomer

EBSCOhost - printed on 2/14/2023 1:06 PM via . All use subject to https://www.ebsco.com/terms-of-use

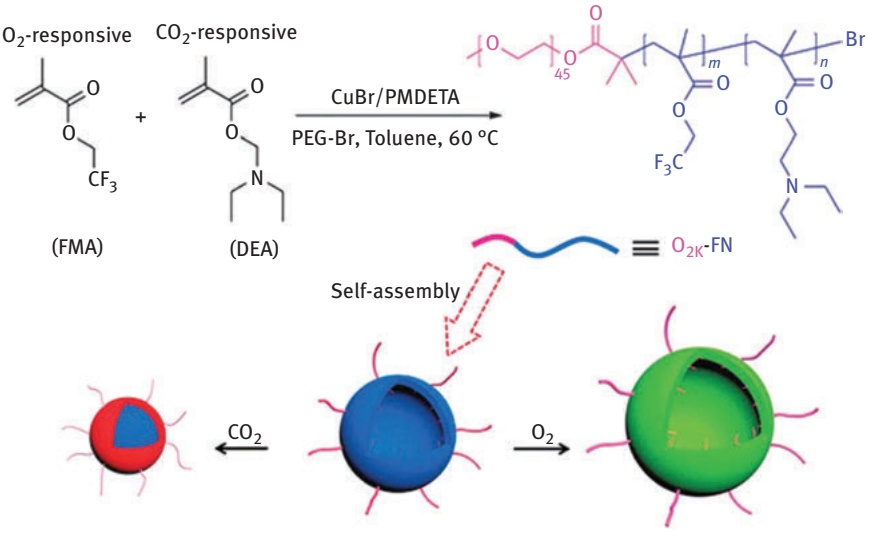

Figure 2.3: Synthesis of the CO_2 and O_2 dual-responsive diblock copolymer, and schematic illustration of the CO_2- and O_2-induced self-assembly and shape transformation process of the diblock copolymer vesicles. Reprinted from Ref. [40] with permission from ACS publications.

2,3,4,5,6-pentafluorostyrene (FS) and DEAEMA with cross-linker [41]. The obtained microgels dispersed in aqueous solution could undergo phase transitions triggered by both O_2 and CO_2, and the levels of the responsivity could be tunable by varying the FS and DEAEMA content in the copolymer. Moreover, the phase transitions were also reversible, and after N_2 bubbling, the microgels could be recovered to their initial states.

Besides the O_2-responsive polymer, NO (nitric acid)-responsive polymer such as poly(2-(3-(2-aminophenyl)-ureido)ethyl methacrylate) (PAPUEMA) can also be introduced into a CO_2-responsive polymer, leading to a polymer with CO_2 and NO dual-response. In this case, a triblock copolymer with a hydrophilic poly(oligo (ethylene glycol) methyl ether methacrylate) (POEGMA) block, a PDEAEMA block, and a NO-reactive PAPUEMA block (POEGMA-*b*-PDEAEMA-*b*-PAPUEMA) was synthesized through RAFT polymerization [42]. The obtained triblock copolymer could self-assemble into micelles with three layers: hydrophilic POEGMA coronas, PDEAEMA middle layer, and PAPUEMA inner layer (Figure 2.4). On one hand, the micelles swelled after the addition of CO_2 as a result of the protonation of PDEAEMA, and then could transform to nanorods upon subsequent purging with NO. This morphology transformation was due to the conversion of the PAPUEMA block into more hydrophobic block bearing benzotriazole moieties. On the other hand, the triblock copolymer micelles could transform into nanorods directly with only NO stimulus.

EBSCOhost - printed on 2/14/2023 1:06 PM via . All use subject to https://www.ebsco.com/terms-of-use

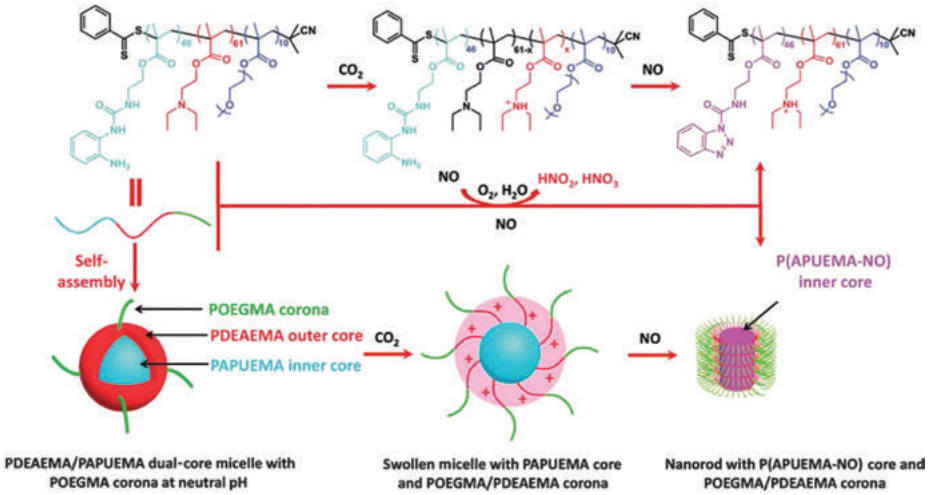

Figure 2.4: Schematic illustration of the self-assembly and morphology transition of dual-responsive triblock copolymer POEGMA-b-PDEAEMA-b-PAPUEMA triggered by CO_2 and NO. Reprinted from Ref. [42] with permission from the RSC.

2.3 Self-Assembly and Morphology Transition of CO_2-Responsive Polymers

2.3.1 Self-Assembly of CO_2-Responsive Polymers

As pointed out above, CO_2-responsive functional groups can be easily introduced into an amphiphilic polymer structure. Through CO_2 bubbling, one or more specific polymer chains can be protonated, resulting in the amphiphilic alternation of the polymers. Moreover, the sensitivity of various CO_2-responsive functional groups to the presence of CO_2 in aqueous solution may be different due to the difference in their pK_a, and the protonation degree of these groups can be continuously and precisely tuned by controlling the amount of CO_2 added into the polymer solution. This easily accessible and continuous variation of the amphiphilicity as well as the robust reversibility make CO_2 an attractive stimulus for the controllable and tunable self-assembly of CO_2-responsive polymers. Compared with other stimuli, this tunable self-assembly of the polymers based on CO_2 is convenient and "green," which is beneficial for different applications.

Zhao's group reported a study on a diblock copolymer composed of a water-soluble poly(*N*,*N*′-dimethylacrylamide) (PDMA) block and a CO_2-responsive PDEAEMA block (PDMA-*b*-PDEAEMA) [43]. As PDEAEMA is hydrophobic in neutral condition and PDMA is hydrophilic, the diblock copolymer can self-assemble into vesicles with a

EBSCOhost - printed on 2/14/2023 1:06 PM via . All use subject to https://www.ebsco.com/terms-of-use

diameter of ~410 nm when dispersed in water. Through the accumulative addition of CO_2 gas into the polymer solution, the PDEAEMA block is gradually protonated and becomes hydrophilic, resulting in a swelling of the vesicle at the beginning and then a dissociation of the vesicle when the polymer is totally water-soluble. In the same work, a number of coumarin units were also introduced into the PDEAEMA chains of another diblock copolymer PEO-*b*-P(DEAEMA-*co*-CMA). In the latter case, the membrane of the vesicles formed by the coumarin-containing block P(DEAEMA-*co*-CMA) can be cross-linked by the photo-dimerization of the chromophore. After purging with CO_2, the crosslinked vesicle wall can only swell instead of being dissociated. That is to say, the swelling of these coumarin-containing diblock copolymer vesicles can be controlled by CO_2 stimulation (Figure 2.5). After bubbling with N_2, the PDEAEMA block is deprotonated and becomes hydrophobic again and the vesicle can shrink back to the initial state. It was also found that the expansion extent of the vesicle was dependent on the cross-linking degree of the vesicles, which is tunable by the photo-dimerization degree of the coumarin groups. By decreasing the cross-linking density and the photo-dimerization degree, the degree of vesicle expansion after CO_2 bubbling gradually became larger. For example, with a coumarin dimerization degree of 30%, the average hydrodynamic volume of the vesicles could be increased by ~2100% after the addition of CO_2. This is possibly the largest swelling degree of the polymer vesicles triggered by an external stimulus.

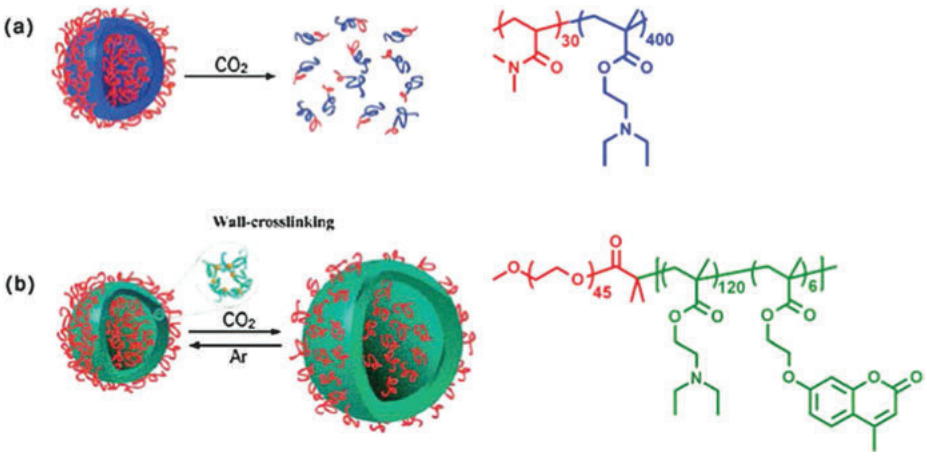

Figure 2.5: (a) Diblock copolymer PDMA-*b*-PDEAEMA and the CO_2-triggered dissociation of its vesicle in aqueous solution. (b) Diblock copolymer PEO-*b*-P(DEAEMA-co-CMA) and the swelling/shrinking of its cross-linked vesicle during the addition and removal of CO_2. Reprinted from Ref. [43] with permission from the RSC.

Host–guest interaction can be used in the synthesis of CO_2-responsive polymers, and the obtained polymer can also self-assemble into CO_2-responsive micelles or

EBSCOhost - printed on 2/14/2023 1:06 PM via . All use subject to https://www.ebsco.com/terms-of-use

vesicles. Yuan's group designed and synthesized a novel CO_2 /thermal dual-responsive triblock copolymer formed by noncovalent host–guest interaction and thiol–ene Michael addition, which was composed of β-cyclodextrin (β-CD) end-capped PDMAEMA, adamantine (Ada)/alkenyl-ended hydrophobic poly(ε-caprolactone) (PCL), and thiol end-capped thermo-responsive PNIPAM [44]. These three homopolymers could self-associate into a supramolecular triblock copolymer through host–guest interaction between Ada and β-CD as well as the thiol–ene Michael addition. The copolymer in water can self-assemble into vesicles with walls of three-layer sandwich-like nanostructure, in which the thermoresponsive PNIPAM blocks act as the outer layer, the hydrophobic PCL blocks act as the middle layer, and the CO_2-responsive PDMAEMA blocks act as the inner layer. After the addition of CO_2, these vesicles can undergo a swelling process as a result of the protonation of the PDMAEMA blocks. Moreover, this process is reversible. After the removal of CO_2 through N_2 gas bubbling, the diameter of the vesicles will recover to its initial state. At the same time, these vesicles are also thermoresponsive due to the existence of PNIPAM block. With increasing temperature above the LCST of PNIPAM, the assemblies transform from vesicles to spherical micelles (Figure 2.6).

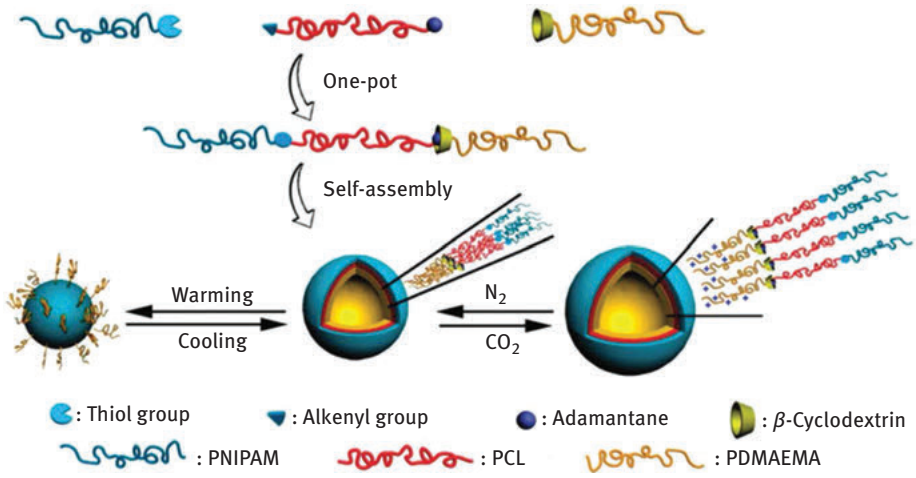

Figure 2.6: The scheme for the synthesis and self-assembly of the supramolecular triblock copolymer of PNIPAM-*b*-PCL-*b*-PDMAEMA, as well as their CO_2/thermo-dual stimuli-responses. Reprinted from Ref. [44] with permission from ACS publications.

Zhao's group also reported a novel supramolecular block, glycol-polypeptide, formed by the host–guest interaction between benzimidazole and β-cyclodextrin, and the obtained block copolymer is cleavable when triggered by CO_2 [45] (Figure 2.7). Two biopolymers, dextran (Dex-CD) and poly(L-valine) (BzI-PVal) were synthesized, which were ended with β-cyclodextrin and benzimidazole, respectively. Therefore, they can

EBSCOhost - printed on 2/14/2023 1:06 PM via . All use subject to https://www.ebsco.com/terms-of-use

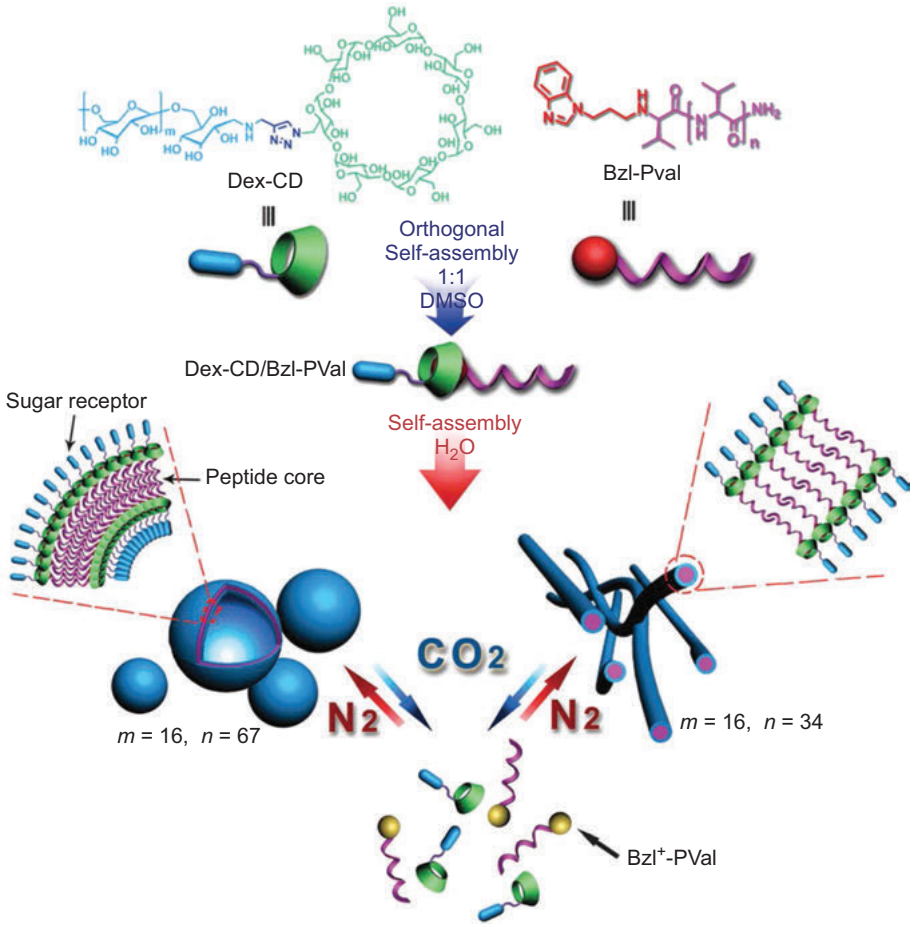

Figure 2.7: The scheme for the CO_2-triggered assembly and disassembly process of the supramolecular block glycol-polypeptides formed by the connection of polysaccharide (Dex-CD) and poly(L-valine) (BzI-PVal) through the host–guest interaction between benzimidazole and β-cyclodextrin. Reprinted from Ref. [45] with permission from ACS publications.

be connected with each other through the host–guest interaction between benzimidazole and β-cyclodextrin, and the resulting supramolecular block copolymer (Dex-CD/BzI-PVal) can self-assemble into either vesicles or nanofibers, depending on the relative block lengths. Moreover, these vesicular and fibrous aggregates can be dissociated and reassembled through the CO_2 "breathing in" and "breathing out" process, which is ascribed to the protonation and deprotonation of the imidazole groups, resulting in a cleavage and reformation of the noncovalent connection between the benzimidazole and β-cyclodextrin groups. This supramolecular self-assembly provides a new method to synthesize CO_2-responsive polymers and use them to construct nanostructures with CO_2-triggered morphology transformation.

EBSCOhost - printed on 2/14/2023 1:06 PM via . All use subject to https://www.ebsco.com/terms-of-use

Besides cyclodextrin, pillar[5]arene can also be used as a kind of CO_2-responsive host in the host–guest self-assembly. Huang's group reported a novel CO_2-responsive pillararene-based molecular recognition fabricated by a water-soluble pillar[5]arene and an anionic surfactant, sodium dodecyl sulfonate (SDS). After the addition of CO_2, the inclusion supramolecular amphiphilic complex self-assembled into spherical bilayer vesicles, and these vesicles would be dissociated upon bubbling N_2 or adding much more SDS to eliminate the inclusion complex [46] (Figure 2.8). The assembly and disassembly of vesicles were successfully triggered by gas and surfactant, resulting in the release of a water-soluble dye, calcein. Compared with cyclodextrin-based CO_2-responsive molecular recognition, this CO_2-responsive pillar[5]arene-based host–guest complex formed with the addition of CO_2, while cyclodextrin-based CO_2-responsive molecular recognition was disrupted after bubbling CO_2. This characteristic makes these vesicles potential to be used in drug delivery and sensors.

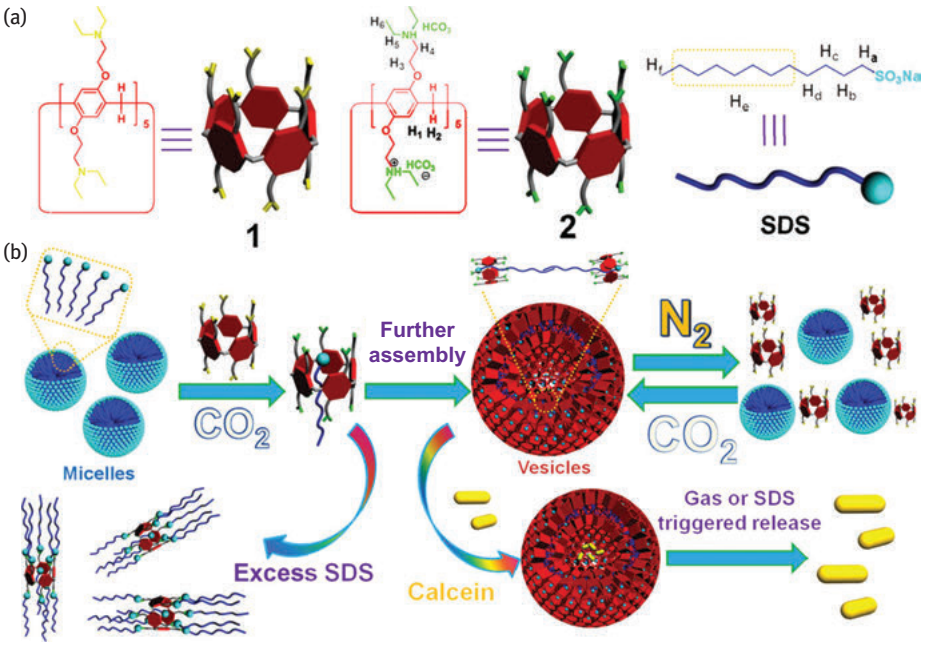

Figure 2.8: (a) The chemical structures and schematic representations of 1, 2, and SDS and (b) schematic representation of gas-controlled self-assembly and dual-triggered release of calcein. Reprinted from Ref. [46] with permission from ACS publications.

In order to tune the volume of each block efficiently, dendrimers can also be introduced into the CO_2-responsive polymers. For instance, dendronized triblock copolymers POEGMA-*b*-P(Gn)-*b*-PDEAEMA were synthesized with Fréchet-type poly(aryl ether) as the dendron (Gn) block and tunable chain "thickness" through the generation of dendronized block [47]. According to the report, the used

EBSCOhost - printed on 2/14/2023 1:06 PM via . All use subject to https://www.ebsco.com/terms-of-use

common solvent, the generation of dendrons, and the CO_2-stimulus could all affect the self-assembly behavior of the triblock copolymers. Yuan et. al. designed and synthesized an amphiphilic dendritic star-block terpolymer with the 'graft onto' strategy using the combination of ring-opening polymerization (ROP), atom transfer radical polymerization (ATRP), and click chemistry, which can form vesicles in aqueous media spontaneously [48]. The size of these vesicles and pierce macropores on the wall were efficiently tunable by the degree of protonation of the PDEAEMA block in the polymer triggered by CO_2 bubbling. These CO_2-breathing and piercing vesicles can also be used as nanocapsules for fluorescent dyes and bioactive molecules in living systems.

2.3.2 Morphology Transition of CO_2-Responsive Polymers

Since CO_2 is an endogenous metabolite molecule, it can also be regarded as a physiological stimulus. In this regard, CO_2 has been used to trigger the morphology transformation or deformation of polymer assemblies in an effort to mimic organelles. Among the reports in the literature, Zhao's group designed and synthesized a triblock copolymer comprising hydrophilic poly(ethylene oxide) (PEO, termed as O) as the outer block, hydrophobic polystyrene (S) as the middle block, and CO_2-responsive PDEAEMA (A) as the inner block [49]. By fixing the length of O block and A block while altering the length of the S block, three different initial nanostructures (giant vesicles, worm-like micelles, and spherical micelles) could be formed by self-assembly of this series of OSA copolymers, in which A blocks constitute the inner part of the hydrophobic region (Figure 2.9). After addition of CO_2, their nanostructures could be altered. The spheres formed by OSA copolymer with the shortest S block could expand their size from 24 nm to 45 nm, the curly and folded nanofibers formed by OSA copolymer with the longer S block could transform into straight and rigid nanowires, while the giant vesicles formed by OSA copolymer with the longest S block could be compartmentalized into several smaller irregular vacuoles. These different morphology transformation behaviors of OSA copolymer are based on the varying lengths of their hydrophobic polymer chains. As CO_2-responsive A block was located inside the hydrophobic core and restricted by the S layer, when the A blocks were gradually protonated and became increasingly hydrophilic during CO_2-purging process, these nanostructures could only adsorb more water instead of being freely dissociated. Therefore, the CO_2-controlled deformations of these OSA triblock copolymer assemblies are mainly attributed to the synergistic effect of core-chain restricted hydration and corona-chain repulsion. In this way, the CO_2-modulated morphology transformations of these triblock copolymer assemblies are able to mimic the shape regulation of different organelles, such as the lipid droplet self-regulated "breathing" phenomenon, the elastic telescopic motion of microfilaments, and the lysosomes' endocytosis behavior.

EBSCOhost - printed on 2/14/2023 1:06 PM via . All use subject to https://www.ebsco.com/terms-of-use

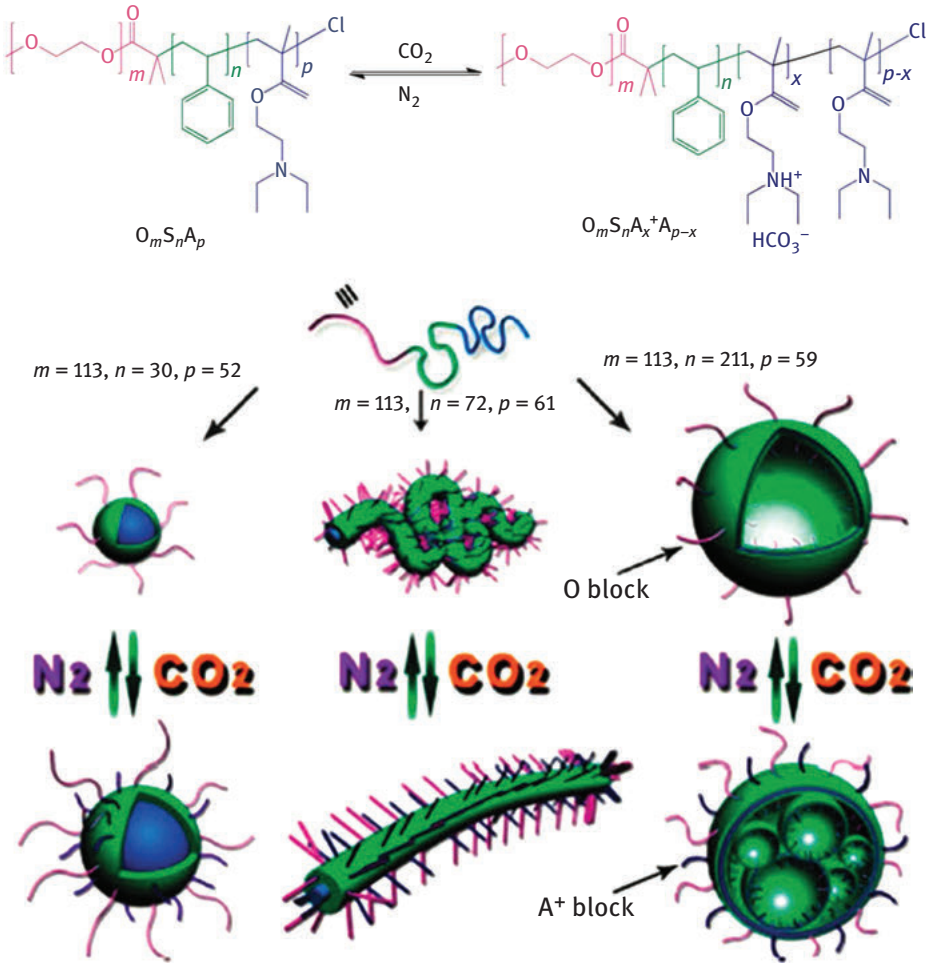

Figure 2.9: CO_2-switchable triblock copolymer PEO-b-PS-b-PDEAEMA (OSA) and their CO_2-induced morphology deformation. Reprinted from Ref. [49] with permission from ASC publications.

The block sequence of the CO_2-responsive block copolymers can also affect the degree of protonation and morphology transformation of the assemblies triggered by CO_2. Sometimes different nanostructures can be obtained from self-assembly of polymers with different sequences but similar composition, and their CO_2-induced morphology transformation processes are also different. A diblock copolymer PEO-*b*-P(DEAEMA-*co*-S) (polymer P_r) was designed and synthesized by Feng's group, which was composed of a hydrophilic PEO block and a CO_2-responsive P(DEAEMA-*co*-S) random copolymer block [50]. This diblock copolymer can self-assemble into vesicles with an initial diameter of ~300 nm when dispersed in water. After purging the aqueous solution with CO_2 gas, the vesicles changed into smaller micelles (Figure 2.10).

EBSCOhost - printed on 2/14/2023 1:06 PM via . All use subject to https://www.ebsco.com/terms-of-use

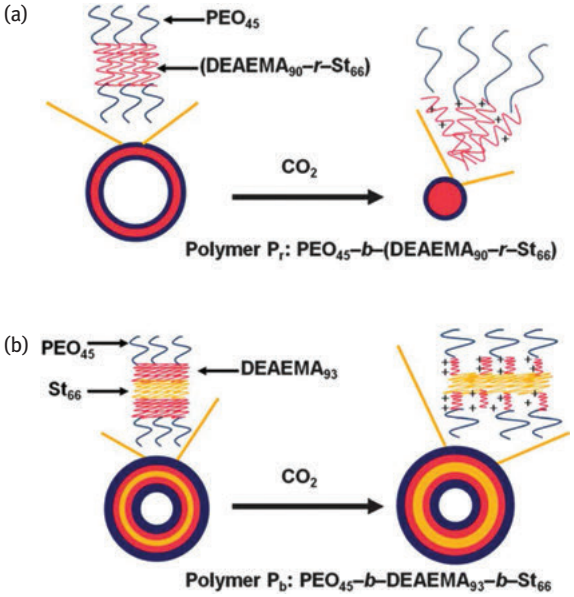

Figure 2.10: Schematic representation of CO_2-triggered transformation from large vesicle to smaller micelle (a) for diblock copolymer P_r and the vesicles expansion for the triblock counterpart P_b (b). Reprinted from Ref. [50] with permission from the RSC.

This phenomenon was ascribed to the protonation of P(DEAEMA-*co*-S) induced by CO_2, resulting in an increasing proportion of the hydrophilic blocks. By contrast, another triblock copolymer PEO-*b*-PDEAEMA-*b*-PS (polymer P_b) was also designed and synthesized in the same study, which possessed a similar composition. P_b could also self-assemble into vesicles in aqueous solution. But after purging with CO_2, the P_b vesicles exhibited only an expansion instead of transforming into smaller micelles (Figure 2.10). This difference was attributed to the limited hydration of P(DEAEMA-*co*-S) block in the diblock copolymer P_r due to the steric hindrance effect of adjacent styrene groups. In fact, the protonation degree of the P(DEAEMA-*co*-S) block in P_r was only 35% after CO_2 bubbling.

There is another example showing the importance of the sequence of blocks in determining the CO_2-triggered morphological transformation. An ABC-type triblock copolymer PEO-*b*-PAD-*b*-PS was designed, where the middle block PAD is CO_2-responsive poly(*N*-amidino) dodecyl acrylamide [51] (Figure 2.11a). This triblock copolymer could self-assemble into rigid nanotubes initially with a diameter between ~320 nm and ~680 nm, and an axial length of several micrometers. After purging the polymer solution with CO_2 for 15 min, the tubular structure disappeared and large vesicles with an average diameter of ~410 nm were generated. After further CO_2 bubbling for 25 min, the large vesicles further transformed into "spring-like"

EBSCOhost - printed on 2/14/2023 1:06 PM via . All use subject to https://www.ebsco.com/terms-of-use

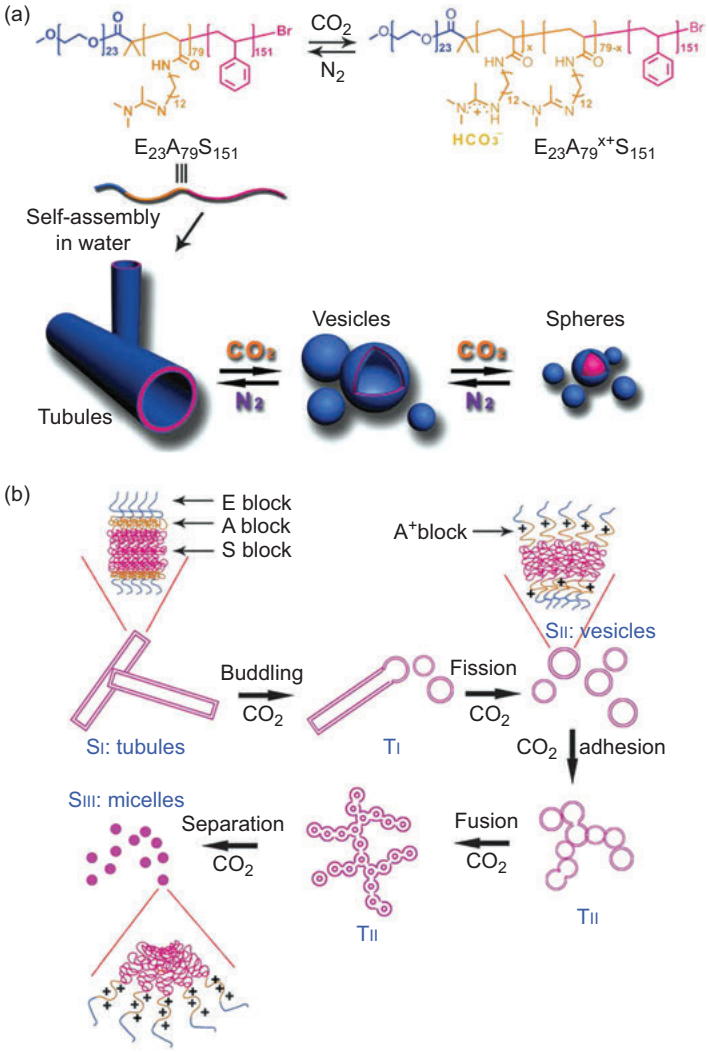

Figure 2.11: (a) CO_2-triggered morphology transformation of the assemblies of PEO-*b*-PAD-*b*-PS from nanotubes to vesicles then to spheres, (b) CO_2-triggered morphology transformation mechanism of the triblock copolymer assemblies in aqueous solution. Reprinted from Ref. [51] with permission from Wiley.

cylinders, then into spherical micelles. The observed tubular-vesicular transformation process is reminiscent of what is known in the Golgi apparatus in cells. The mechanism of this morphology transformation can be explained as follows (Figure 2.11b): the PAD middle block can be gradually protonated by CO_2 and thus the hydrophilic volume fraction of the triblock copolymer will be increased accordingly. At the initial

EBSCOhost - printed on 2/14/2023 1:06 PM via . All use subject to https://www.ebsco.com/terms-of-use

state, the nanotubes formed by self-assembly are rigid and straight as a result of the compact chain arrangement induced by the weak chain interactions. After the addition of CO_2, part of the amidine groups in PAD block are protonated, resulting in increasing electrostatic repulsion among the corona chain and making the tubular structures reduce their volume through bending to minimize the interfacial free energy, and the increased curvature of the membrane leads to large vesicles. Upon continuous CO_2 addition, the hydrophilic fraction and thus the curvature further increase, resulting in further bending of the vesicles and transformation of the morphology into cylinders and spheres. Therefore, the morphology of the assemblies formed by this CO_2-responsive block copolymer can be precisely controlled through the added amount of CO_2, which can alter the morphologies continuously through the changes in protonation degree and the hydrophilic–hydrophobic ratio of the block copolymer.

Besides tubules, vesicles, and core–shell micelles, CO_2-responsive polymers can also self-assemble into a morphology of higher level, such as the multi-compartment micelles (MCMs). Feng et al. reported CO_2-responsive MCMs with a segregated corona formed by a triblock copolymer comprising a hydrophilic PEO block (O), a hydrophobic fluorocarbon block of poly(2,2,3,4,4,4-hexafluorobutyl methacrylate) (F), and a CO_2-reactive PDEAEMA block (E) [52]. This block copolymer could self-assemble into uniform micelles when dispersed in water. After CO_2 bubbling, the E block was protonated, resulting in a segregation of the micelle core into two distinct phases, forming MCMs with a segregated corona. After N_2 gas bubbling, the uniform spherical micelles were reformed, which was due to the deprotonation of the tertiary amino groups in the E block (Figure 2.12).

With the same polymer, it was also found that the solvent composition could change the morphology of CO_2-responsive aggregations [53]. In a mixed solvent of water and ethanol, by increasing the water content from 0% to 50%, the polymer aggregates changed from sphere to short rod, then long cylinder, and finally worm-like micelle. In another work, the same group also discovered a reversible morphology transformation (Figure 2.13) from giant worms to polymersomes triggered by CO_2. In that case, a kind of block-random segmented copolymer comprising a hydrophilic PEO block and a hydrophobic DEAEMA/4-vinyl pyridine (4VP) random copolymer block was synthesized [54]. The obtained block copolymer could self-assemble into giant worm-like micelles that are formed by the fusion of several vesicles when dispersed in water. After purging with CO_2 gas, these giant worm-like micelles were deformed into smaller vesicles. Furthermore, necklace-like aggregates were formed after the removal of CO_2 through N_2 bubbling. Similar to other systems, this morphology transition was also due to the reversible protonation–deprotonation of PDEAEMA moieties in the triblock copolymer, which changes the hydrophilic fraction in the triblock copolymer. Moreover, the hydrogen bonding between 4VP moieties is also beneficial for the stabilization and morphology transformation of the assemblies.

EBSCOhost - printed on 2/14/2023 1:06 PM via . All use subject to https://www.ebsco.com/terms-of-use

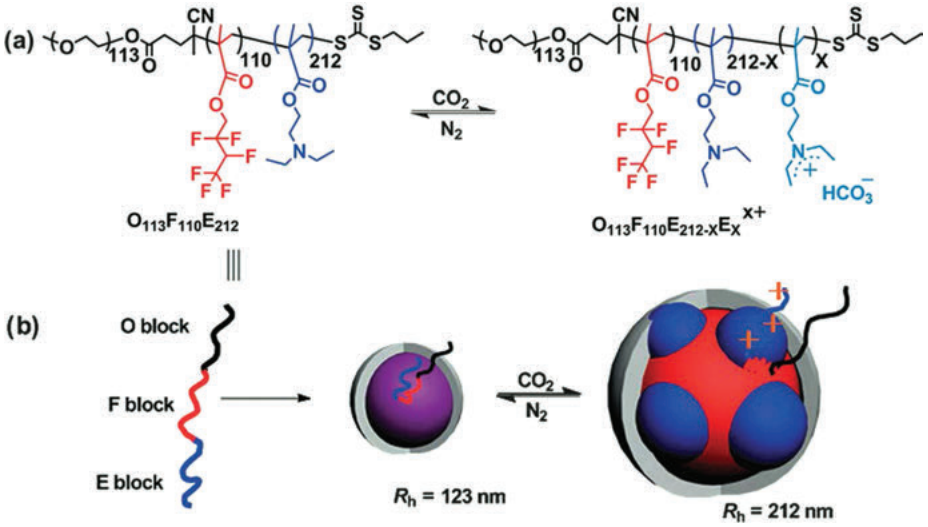

Figure 2.12: (a) The structure of the triblock copolymer (b) The schematic illustration of the morphology transition triggered by CO_2: triblock copolymer (left); spherical micelle with grey hydrophilic "O" corona and purple hydrophobic "E" and "F" core (center); multi-compartment micelle with a red "F" block core and phase-separated corona comprising blue charged "E" domains and gray "O" domains (right). Reprinted from Ref. [52] with permission from the RSC.

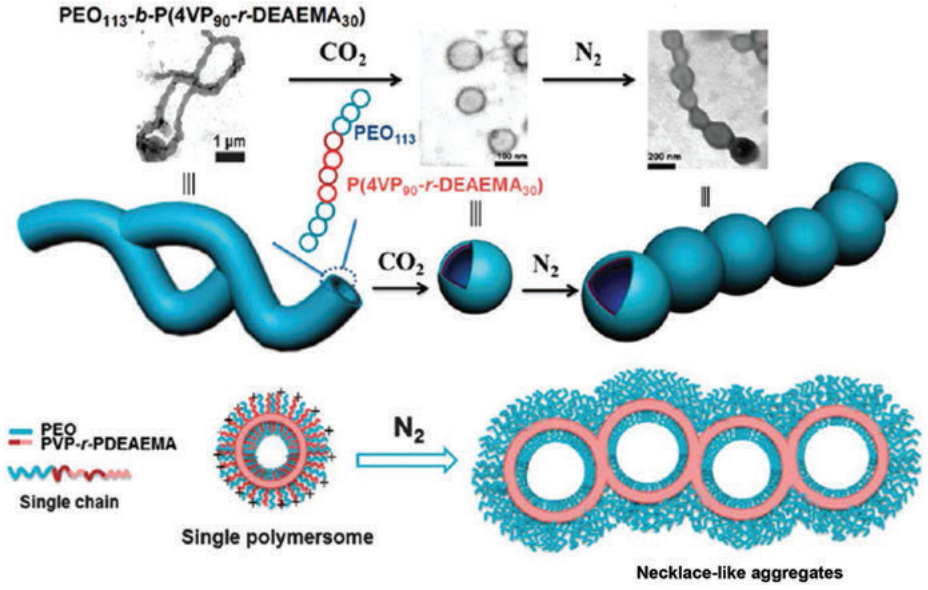

Figure 2.13: The structure of polymersomes formed by the self-assembly of the triblock copolymer after CO_2 bubbling in water and the necklace-like aggregates formed after the removal of CO_2. Reprinted from Ref. [54] with permission from the RSC.

EBSCOhost - printed on 2/14/2023 1:06 PM via . All use subject to https://www.ebsco.com/terms-of-use

2.4 Application of CO_2-Responsive Polymers

Since many properties of CO_2-responsive polymers, such as water solubility, self-assembly, morphology, and inter/intramolecular electrostatic interactions can be altered by simply adding or removing CO_2, many potential applications of this category of polymers have been demonstrated. The following section will review some of the applications based on CO_2-responsive polymers as well as their assemblies.

2.4.1 CO_2-Triggered Release of Guest Molecules from Polymer Assemblies

As shown in Section 2.3, CO_2-responsive polymers can form assemblies with different nanostructures, which could be deformed or dissociated when triggered by CO_2. Meanwhile, both hydrophilic and hydrophobic molecules could be encapsulated in these nanostructures and released when they are deformed. Therefore, the CO_2-responsive polymers can be used in CO_2-triggered release of guest molecules. Yuan et al. first fabricated CO_2-responsive vesicles self-assembled with amidine-containing amphiphilic block copolymer, which possessed a biomimetic "breathing" feature. In their research, a kind of diblock copolymer composed of CO_2 responsive poly((*N*-amidino) dodecyl acrylamide) (PAD) block and hydrophilic PEO block was designed and synthesized by ATRP [55]. In aqueous solution, this diblock copolymer can form vesicles with a diameter of ~60 nm. Upon addition of CO_2, the average diameter of the vesicles can increase up to ~120 nm, and the maximum volume changes are about ~800%, which originates from the CO_2-induced protonation of PAD blocks. Moreover, after the removal of CO_2 by Ar gas bubbling, the vesicle shrank back to its initial size (Figure 2.14). Therefore, the swelling/shrinking process triggered by alternative CO_2/Ar gas bubbling is reversible, which can just mimic the "breathing" behavior of the cells. This type of CO_2-responsive polymer vesicles provide a method to tune the size of the polymer assemblies with gas bubbling in a quantitative way, which can be used as nano-containers for controlled drug delivery, and the release rate of the drugs can be controlled by the cumulative amount of CO_2/Ar bubbling.

During the swelling and shrinking process of these vesicles, the wall thickness of the vesicle membrane will be increased and decreased to adapt to the volume contraction and expansion of the vesicle on the condition that the macromolecular aggregate number (N_{agg}) in each vesicle is a constant. Based on this mechanism, a kind of intelligent polymeric bio-nanoreactor can be designed, which can be used in size-selective biomolecule/nanoparticle separation and delivery as well as biomimicking the size selective molecular permeability of the cell membranes. The same group further reported a study on PEO-*b*-PAD, which can be self-assembled into polymersomes displaying the CO_2-triggered "breathing" ability [56]. A lot of

EBSCOhost - printed on 2/14/2023 1:06 PM via . All use subject to https://www.ebsco.com/terms-of-use

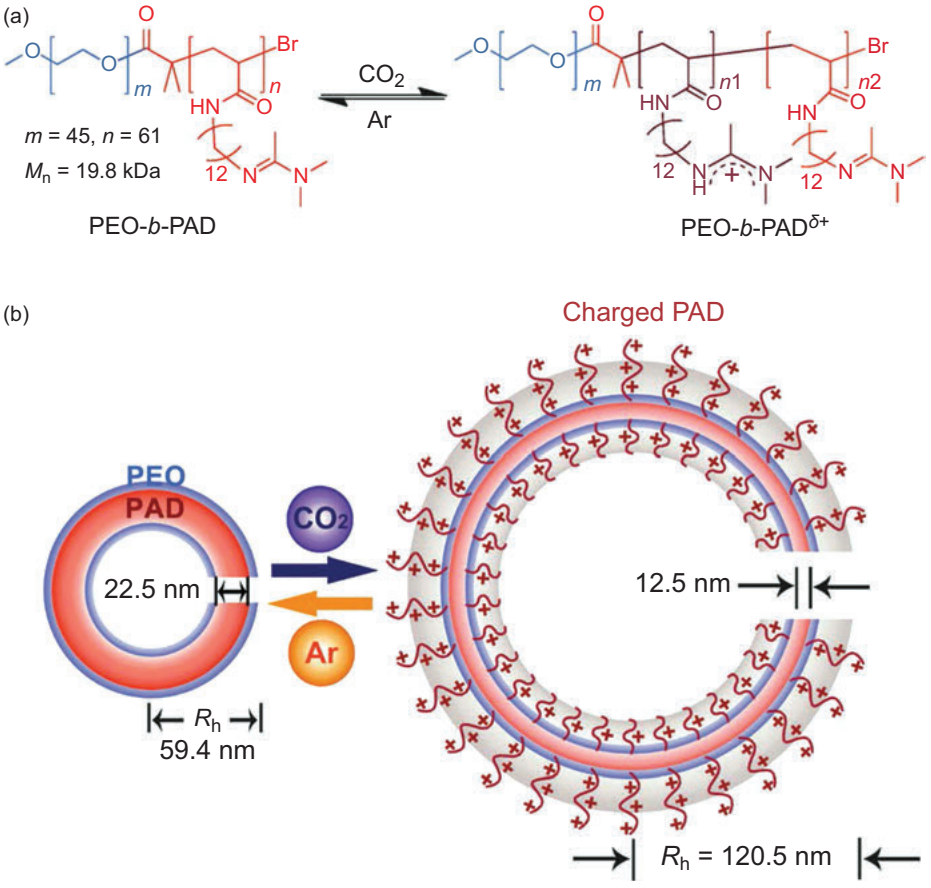

Figure 2.14: CO_2-triggered morphology change of amidine-containing diblock copolymer PEO-*b*-PAD (a) and the scheme of the reversible gas-triggered "breathing" feature of the vesicles in aqueous solution (b). Reprinted from Ref. [55] with permission from Wiley.

nanoholes can be generated in the membrane of the polymersomes during CO_2 purging process, and the size of these nanoholes is tunable by the external CO_2 stimulation strength. As a result, the polymersomes can be used in the size-selective drug release (Figure 2.15a), size-selective nanoparticle separation (Figure 2.15b), and size-selective enzymatic nanoreactor biomimicking (Figure 2.15c).

Another kind of polymer comprising amidine groups (PADS) and PDMAEMA (PADS-*b*-PDMAEMA) was synthesized by Yuan's group through RAFT polymerization and click chemistry [57]. The obtained diblock copolymer can self-assemble into vesicles composed of hydrophilic PDMAEMA as the outer layer and hydrophobic PADS as the inner layer. After purging the solution with CO_2 for 20 min, the average size of the PADS-*b*-PDMAEMA vesicles increased from ~500 nm to more than

EBSCOhost - printed on 2/14/2023 1:06 PM via . All use subject to https://www.ebsco.com/terms-of-use

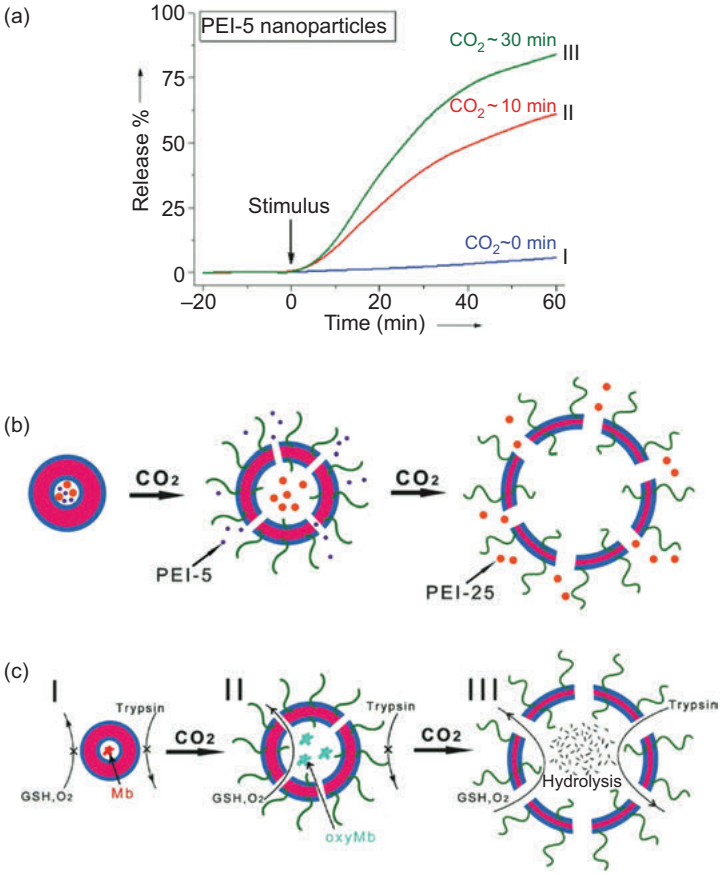

Figure 2.15: Applications of PEO-*b*-PAD polymersomes: (a) rate-tunable release curve for hyperbranched poly(ethylene imide) (PEI) nanoparticles with different CO_2-stimulation levels, (b) size-selective separation of PEI nanoparticles of different size (PEI-5 and PEI-25) by adjusting CO_2-stimulation levels, and (c) biomimetic enzymatic nanoreactors (Mb: myoglobin, an iron-centered endogenous protein; GSH: glutathione, an intracellular reduced agent; trypsin: a common hydrolyzed enzyme). Reprinted from Ref. [56] with permission from Wiley.

~1000 nm due to the protonation of both PDMAEMA and PADS giving rise to an increase in the hydrophilicity of the diblock copolymer (Figure 2.16a). Moreover, the expansion degree of the vesicles was tunable through the amount of CO_2 bubbling. After the removal of CO_2 through Ar bubbling, the vesicles shrank back to their initial state, which was due to the deprotonation of tertiary amines in PDMAEMA and amidines in PADS, and this swelling–shrinking process was reversible. Since PDMAEMA is also a thermo-responsive polymer, the diblock copolymer vesicles could transform into micelles after heating above 45 °C, which is the LCST of the PDMAEMA block in the diblock copolymer. This phenomenon was ascribed to the

EBSCOhost - printed on 2/14/2023 1:06 PM via . All use subject to https://www.ebsco.com/terms-of-use

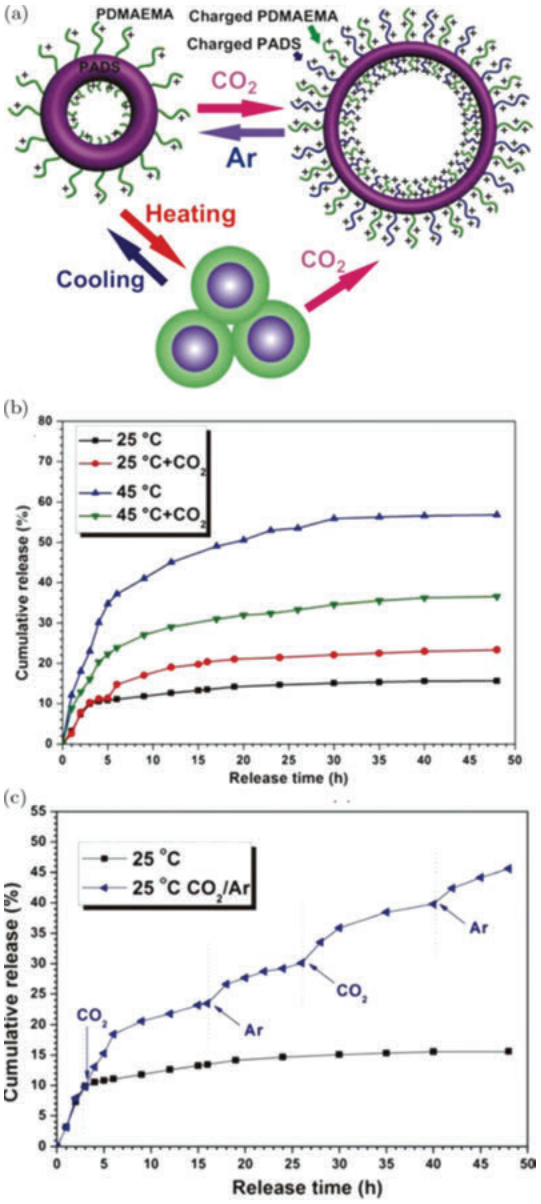

Figure 2.16: (a) Self-assembly of PADS-*b*-PDMAEMA into vesicles and the reversible vesicles-micelles/aggregates transformation triggered by CO_2/Ar and heating/cooling. (b) Controlled release of DOX from PADS-*b*-PDMAEMA vesicles or micelles/aggregates at different temperatures and CO_2 stimuli. (c) Controlled release of DOX from PADS-*b*-PDMAEMA vesicles without stimuli and with alternating CO_2/Ar stimuli. Reprinted from Ref. [57] with permission from the RSC.

EBSCOhost - printed on 2/14/2023 1:06 PM via . All use subject to https://www.ebsco.com/terms-of-use

increasing hydrophobicity of the PDMAEMA block after heating. However, the micelles were not stable and tended to aggregate without CO_2. Owing to the CO_2-triggered swelling-shrinking properties, PADS-*b*-PDMAEMA vesicles can also be used as nanocarriers. DOX, a typical hydrophobic anticancer drug, was encapsulated in the hydrophobic PADS layers of the vesicles, and the controlled release of the drug from the vesicles was investigated. As shown in the release curve at 25 °C (Figure 2.16b, c), the release rate of DOX from the vesicles was tunable through the addition of CO_2, which is ascribed to the swelling–shrinking behavior of the diblock vesicles induced by the alternating CO_2/Ar bubbling.

This kind of CO_2-triggered release of guest molecules can not only be used in the drug delivery mentioned above, but also used in the separation of natural homologues. Zhu's group successfully used the polymeric extractant PEI for the separation of α-tocopherol from the tocopherol homologues [21]. In their research, varieties of PEI solutions were used to extract tocopherols from their hexane solutions. Higher selectivity coefficients and distribution of tocopherols were achieved with PEI–acrylonitrile as the extractant. After extraction, tocopherols could be released from PEI chains after the addition of CO_2, which will induce a precipitation of PEI out from the extract phase, facilitating the recovery of PEI for reuse. These precipitated protonated PEI could be redissolved in the solvent for reuse through N_2 bubbling and heating.

2.4.2 CO_2-Responsive Polymer Surfactants for Emulsion Polymerization

Surfactants are very important components in the emulsion polymerization process, and many types of latex particles at various size scales can be prepared through appropriate use of surfactants, which makes these latex particles stable. However, sometimes the residual surfactant is harmful for the performance of the obtained particles. For instance, the migration of the residual surfactant has a negative effect on the performance of the final products. As a result, how to remove the surfactants after polymerization is an important issue. The conventional method for removing surfactants is just washing, but this method may allow part of the surfactant to remain in the latex particles especially when the surfactant possesses a better particle-stabilizing performance. Therefore, a destabilization of the latex particles is also usually performed by addition of salt, acid, or base depending on the type of surfactant used in the polymerization process. However, for removal of these salt, acid, and base by washing, more water will be required, and a large amount of waste water will be generated in this process that is costly and causes environmental concerns.

In order to overcome these problems, some stimuli-responsive surfactants are designed and synthesized, which can be activated and deactivated as desired. Then

EBSCOhost - printed on 2/14/2023 1:06 PM via . All use subject to https://www.ebsco.com/terms-of-use

the stability of the latex is dependent on the state of these surfactants, which is triggered by the used external stimulus. Many different types of stimuli-responsive surfactants have been developed, which can be reversibly activated and deactivated by adding, for example, oxidant/reductant or acid/base into the system. However, the residual of these chemical compounds bring up some new problems for the application of the obtained materials. In this regard, the utilization of a CO_2-responsive surfactant is an efficient way to solve this problem. After purging with CO_2, the pH of the system can be decreased, resulting in the protonation of the surfactants. Moreover, this process is completely reversible, and the deprotonation of these surfactants can occur by a simple inert gas bubbling process. Therefore, the state changes triggered by CO_2 are green and without any chemical contamination, and the state change degree can be easily controlled by the amount of CO_2 bubbled through the solution. A lot of the CO_2-responsive surfactants, mainly developed by Jessop, Cunningham, and their coworkers are reported [9, 11]. For example, Jessop et al. added *N,N*-dimethylethanolamine (DMEA) as a CO_2-switchable additive to a dodecane/water emulsion, which was prepared using sodium dodecyl sulfate (SDS) surfactant [58]. Without DMEA, CO_2 could not destabilize the emulsion. But after the addition of DMEA, CO_2 bubbling caused dissociation of the emulsion, which was attributed to the increasing ionic strength of the solution. This process was reversible and a stable emulsion can reform after the removal of CO_2 through Ar bubbling (Figure 2.17). They also investigated the effect of the molecular structure

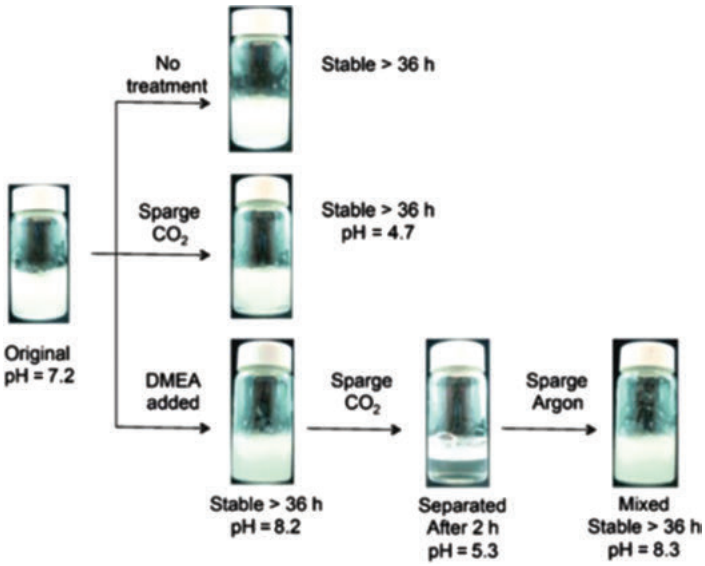

Figure 2.17: Reversible coagulation/redispersion of dodecane/water emulsion (dodecane 5 mL, SDS 0.20 g, and water 5 mL), the amount of DMEA added was 1 mL. Reprinted from Ref. [58] with permission from Wiley.

EBSCOhost - printed on 2/14/2023 1:06 PM via . All use subject to https://www.ebsco.com/terms-of-use

of two CO_2-switchable surfactants *N*'-dodecyl-*N*,*N*-dimethylacetamidinium bicarbonate ($C_{12}N$) and *N*'-(2-(2-(dodecyloxy)ethoxy)ethyl-*N*,*N*-dimethylacetamidinium bicarbonate ($C_{12}E_2N$) on the coagulation and redispersion behavior of PS latexes, and found that PS latexes with $C_{12}E_2N$ surfactant respond to N_2 and CO_2 more quickly and completely than those with $C_{12}N$ surfactant, which was due to the effective higher pK_{aH} of $C_{12}E_2N$ in hydrophobic environment [59]. CO_2-responsive functional groups can also be introduced into an ATRP initiator, which can be used as surfactants to prepare latexes. A type of ATRP initiator 1,1-(diethylamino)undecyl 2-bromo-2-methylpropanoate ($BrC_{11}N$) was synthesized by Jessop's group, and living CO_2-responsive poly(methyl methacrylate) (PMMA) latexes were prepared with this initiator using reverse ATRP emulsion polymerization without addition of other emulsifiers [60]. The resultant latexes can be switched between the dispersed and aggregated states using only CO_2 and inert gas (Ar, air, N_2) as triggers.

Zhu's group reported the study of a diblock copolymer PDMAEMA-*b*-PMMA via RAFT polymerization. It was protonated after the addition of HCl, and used as a CO_2-responsive surfactant to prepare polymer latexes via an emulsion polymerization of MMA (Figure 2.18) [61]. After neutralization with NaOH and washing with deionized water, the resultant PMMA latexes could be dispersed in water by CO_2 bubbling and ultrasonication, while N_2 bubbling with gentle heating can make these PMMA latexes coagulated. The coagulation and dispersion processes could be repeated for many times just by the simple CO_2/N_2 bubbling. They also investigated the relationship between the block copolymer composition and the coagulation/dispersion characteristics of the latexes, and found that the PMMA latexes are stable when the weight fraction of MMA in the diblock copolymer surfactant used in the preparation process is below 58.5% [62]. At the same time, by increasing the content

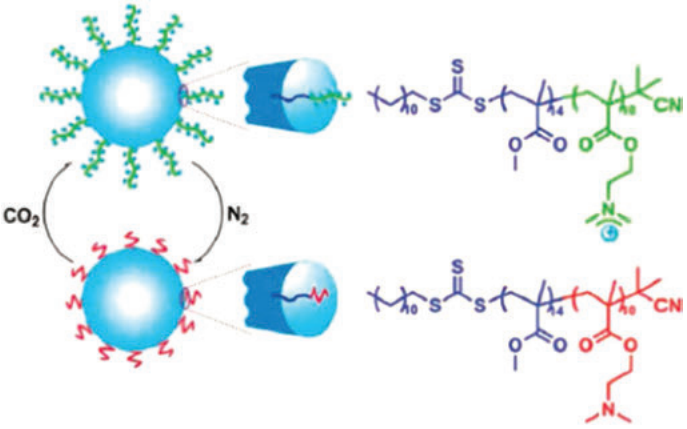

Figure 2.18: Scheme of reversibly coagulatable/dispersible PMMA latexes prepared through emulsion polymerization of MMA using PDMAEMA-*b*-PMMA surfactant. Reprinted from Ref. [61] with permission from Wiley.

EBSCOhost - printed on 2/14/2023 1:06 PM via . All use subject to https://www.ebsco.com/terms-of-use

of MAA, the particle size of the resulting PMMA latexes gradually decreased. Through the CO_2 bubbling and ultrasonication, the PMMA latexes prepared using the surfactants with < 46% of MMA could be well dispersed in water without size changes. While the size of the latex particle prepared using the surfactants with more than 46% of MMA may be increased by more than 20% during the repeatable coagulation/dispersion process.

On the other hand, CO_2-responsive polymers can be used not only as surfactants to prepare polymeric latexes, but also used in the synthesis of CO_2-switchable nanoparticles directly via surfactant-free mini-emulsion RAFT polymerization. Jiang et al. reported the synthesis of PDMAEMA-*b*-PS nanoparticles with a core–shell structure and an average diameter of ~120 nm [63]. The positive-charged tertiary amine in shell can make these nanoparticles well dispersed in water after CO_2 bubbling. While the removal of CO_2 through N_2 bubbling can make these nanoparticles aggregated. Their dispersion/aggregation behavior triggered by CO_2 can be potentially used in the drug delivery system (Figure 2.19). Compared with CO_2-switchable small-molecule surfactants added in emulsion, their surfactants are covalently linked to the nanoparticles, which can resistant to the desorption and migration of the polymer surfactants efficiently in some applications.

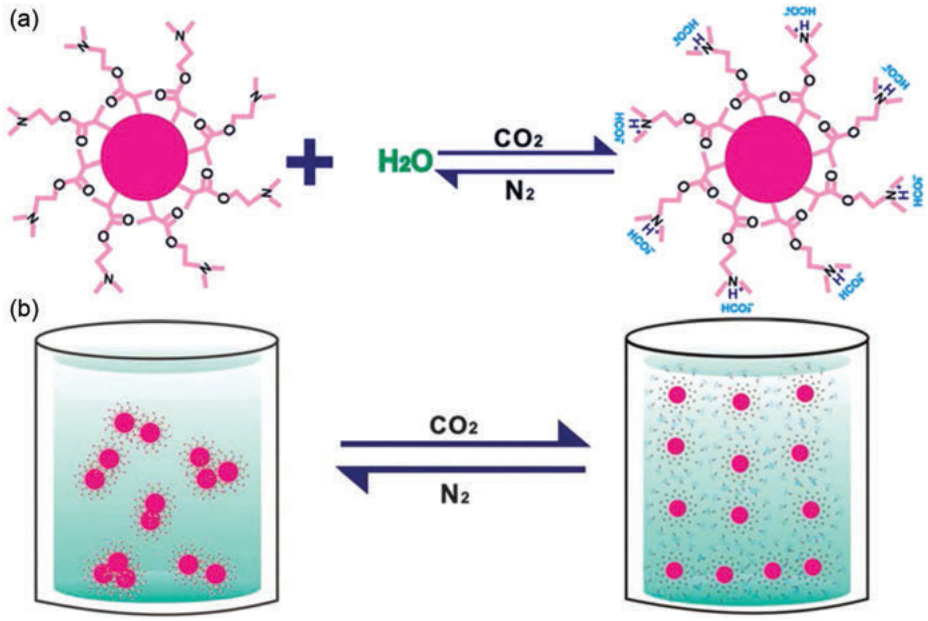

Figure 2.19: (a) The protonation and deprotonation process of PDMAEMA on the surface of the nanoparticles upon CO_2 and N_2 bubbling; (b) schematic illustration of dispersion and aggregation of the nanoparticles triggered by CO_2. Reprinted from Ref. [63] with permission from Elsevier.

EBSCOhost - printed on 2/14/2023 1:06 PM via . All use subject to https://www.ebsco.com/terms-of-use

2.4.3 CO_2-Responsive Polymer Gels and Rheology Modifiers

Polymer systems with a stimuli-triggered rheology alteration have been widely investigated during recent years, which can change from non-viscous liquid to gels or high viscosity solutions induced by the alteration of temperature, pH, or light irradiation. Among those polymer systems, CO_2-responsive polymer gels are particularly interesting as CO_2 is a kind of green stimulus, and there is no salt accumulation during the stimulation process compared with pH stimulus. Meanwhile, the degree of gelation can be tunable by the amount of gas flow. There are a number of CO_2-responsive polymer gels reported. For example, Yan and his group developed a type of poly(ionic liquid) (PIL) gels with CO_2-stimulus responsiveness through the copolymerization of an imidazolium-type ionic liquid monomer with DMAEMA [64]. After the addition of CO_2, the prepared PIL solution can be converted to a stable and transparent gel, which can be turned back to the initial solution state after N_2 bubbling.

In order to obtain polymer gels with a relatively low polymer gelation concentration. ABA-type amphiphilic triblock copolymers with a hydrophilic midblock is often used. Such triblock copolymers can self-assemble into the "flowerlike" micelles in dilute aqueous solution. However, at a high concentration (typically > 5–10 wt%), a three-dimensional network can be generated, as a number of the hydrophilic B blocks can act as "bridges" between the hydrophobic micelle cores formed by the hydrophobic A blocks. Obviously, if the A block in the amphiphilic ABA triblock polymer can switch from hydrophobic to hydrophilic, CO_2 triggered gel–sol transition can be realized. By contrast, if both A and B blocks are initially soluble in water while the A block can be converted into hydrophobic block upon CO_2 bubbling, the opposite sol–gel transition may be possible.

Zhao and his group designed and synthesized a type of CO_2-responsive ABA triblock copolymer with a hydrophilic PEO middle block and CO_2-responsive P(DMAEMA-*co*-MEO_2MA) end blocks [14]. The obtained triblock copolymer can form gels above the LCST of P(DMAEMA-*co*-MEO_2MA) block, which is about 30 °C. But after purging with CO_2, the tertiary amino groups in the P(DMAEMA-*co*-MEO_2MA) block were protonated, resulting in an upward shift of its LCST to above 37 °C, then all the blocks were soluble in water, and a gel–sol transition was observed (Figure 2.20a). The opposite CO_2-induced sol–gel transition was also observed in the same research only by altering the end block of the triblock copolymer. To this end, another ABA triblock copolymer with a hydrophilic PEO middle block and CO_2-responsive P(MAA-*co*-MEO_2MA) end blocks was synthesized. Due to the protonation of some carboxylic acid groups upon the addition of CO_2, the negative charge in P(MAA-*co*-MEO_2MA) was decreased in the CO_2 purging process, resulting in a downward shift of the LCST to 24 °C. Without changing the solution temperature, the triblock copolymer became amphiphilic, and a physical gel was formed due to the aggregation of P(MAA-*co*-MEO_2MA) block in the triblock copolymer and the network formation (Figure 2.20b). Moreover, the transition process

EBSCOhost - printed on 2/14/2023 1:06 PM via . All use subject to https://www.ebsco.com/terms-of-use

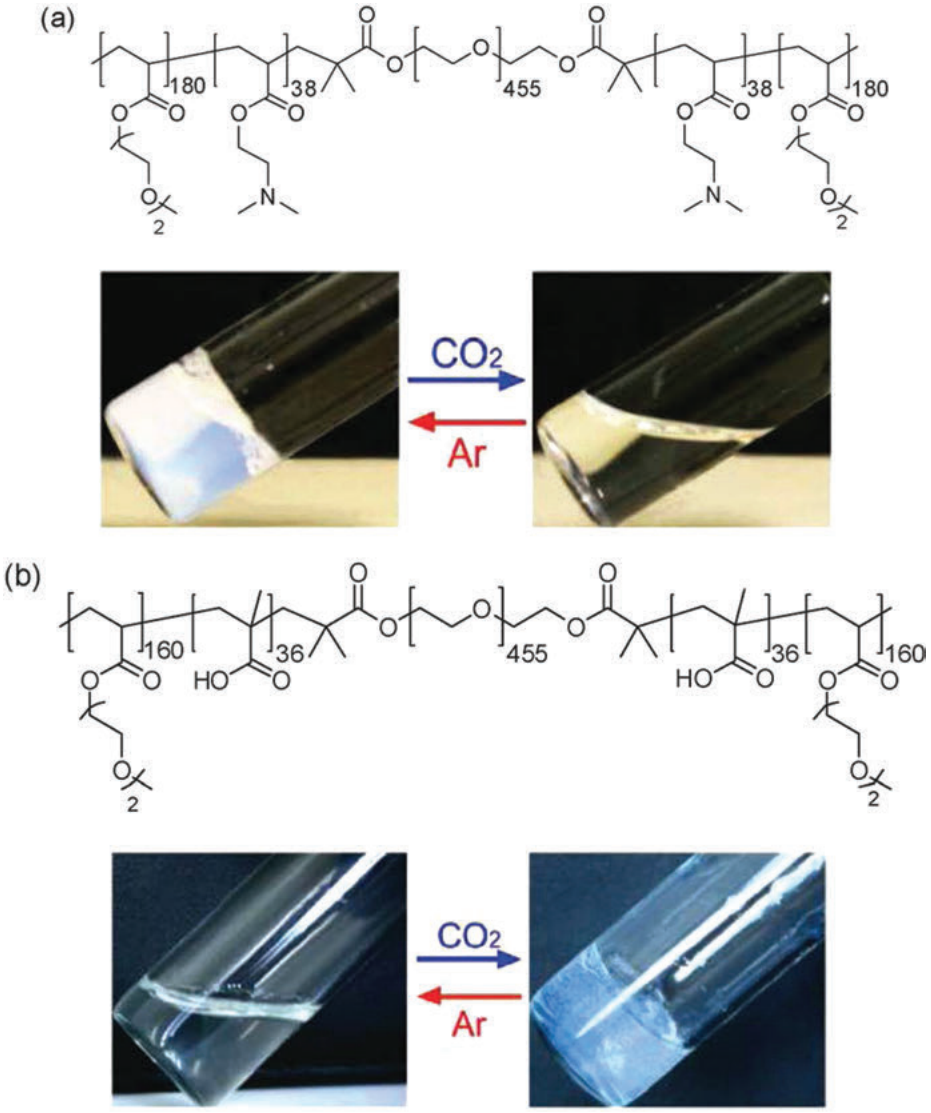

Figure 2.20: (a) The ABA-type triblock copolymer P(DMAEMA-*co*-MEO_2MA)-*b*-PEO-*b*-P(MEO_2MA-*co*-DMAEMA) and its CO_2-induced gel-to-sol transition. (b) The triblock copolymer P(DMAEMA-co-MAA)-*b*-PEO-*b*-P(MEO_2MA-*co*-MAA) and its CO_2-induced sol-to-gel transition. Reprinted from Ref. [14] with permission from ACS publications.

between the sol and gel state is reversible and repeatable upon the CO_2 and Ar purging. This work shows a way to control the rheological properties of polymer systems by CO_2 as a trigger, and this kind of polymer may be potentially used in controlled drug release, biomedical device, and scaffolds for tissue engineering.

EBSCOhost - printed on 2/14/2023 1:06 PM via . All use subject to https://www.ebsco.com/terms-of-use

Another triblock copolymer–based CO_2-switchable gel was also developed [65]. The obtained triblock copolymer was composed of hydrophilic PEO middle block and PDMAEMA end blocks. As shown in Figure 2.21, after dissolving the PDMAEMA-*b*-PEO-*b*-PDMAEMA triblock copolymer into nanoclay aqueous dispersions, the obtained aqueous mixture exhibited a strong response to CO_2, which converted from a low viscous sol to a self-healable gel in the presence of CO_2, and this phenomenon was due to the protonation of PDMAEMA blocks, resulting in a positively charged triblock copolymer bridge across the negatively charged nanoclays and then the formation of a physical network. Upon the removal of CO_2 through N_2 bubbling, a gel-to-sol transition was observed, which was ascribed to the deprotonation of PDMAEMA, resulting due to the weakening of the electrostatic interaction between PDMAEMA blocks and nanoclays. The whole transition process was completely reversible. Moreover, the formed hydrogel possessed excellent self-healing ability and was thus believed to be potentially useful in many areas including the enhanced oil recovery (EOR) triggered by CO_2, the intelligent delivery systems, and other biomaterial fields.

Besides tuning the viscosity of the polymer solution, CO_2 can also tune the viscosity of the assembly systems. For example, Jessop's group reported two CO_2-responsive aqueous solutions possessing switchable viscosity [66], and found that the solution of sodium octadecyl sulfate and 2-(dimethylamino) ethanol could form viscoelastic worm-like micelles in the presence of CO_2, but these micelles will disappear after the removal of CO_2, resulting in a decrease in its viscosity. Another solution of sodium stearate and sodium nitrate possessed high viscosity only if CO_2 is

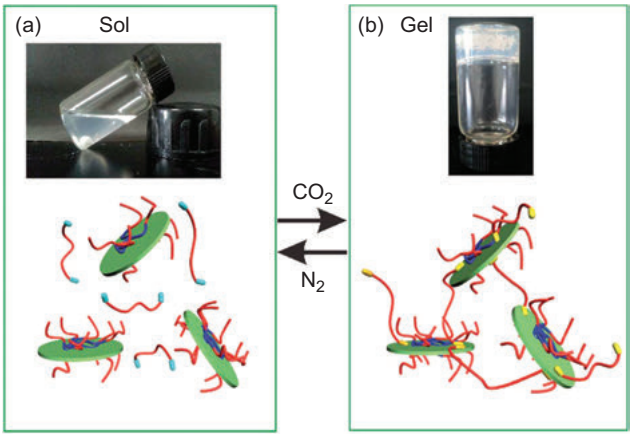

Figure 2.21: CO_2-induced gelation of the triblock copolymer in aqueous clay dispersion. The system is a low-viscous fluid (a), upon CO_2 bubbling, it converts into a viscoelastic gel (b); after N_2 passing through, the gel turns back to the initial sol state (a). Reprinted from Ref. [65] with permission from the RSC.

EBSCOhost - printed on 2/14/2023 1:06 PM via . All use subject to https://www.ebsco.com/terms-of-use

absent. Feng's groups developed a wormlike micellar system that underwent a fully reversible, repeatable "sol–gel" transition upon alternative treatment with CO_2 and N_2 [67–69]. These sol–gel transitions are based on the electrostatic interaction between various amino group–containing surfactant and anionic surfactant. As they are not polymers with large molecular weights, we will not discuss them in detail.

There is another interesting gelation mechanism for CO_2-responsive microgels, which is reported by Han's group. Unlike the CO_2-triggered gelation described above, which is induced by the increasing hydrophobic interaction or electrostatic interaction after the addition of CO_2, the jamming mechanism is the main reason for the gelation of the microgels [70]. In their research, the microgels were composed of PDMAEMA, the size of the microgels increased after addition of CO_2, and the suspension transformed into a glassy state due to the jamming of the particles. After removal of CO_2 by N_2 bubbling, the system recovered to a liquid suspension. As the transition process was rapid and reversible, the system could be applied in the fields of self-supporting detergents, biomaterials, and microfluidic devices.

2.5 Summary and Perspectives

CO_2-responsive polymers are a new type of stimuli-responsive polymers that is very attractive in recent years. Compared with other "more traditional" stimuli-responsive polymers, there are many advantages and unique features for CO_2-responsive polymers. As discussed in the chapter, CO_2 is cheap, mild, and abundant chemical agent, and it can also be easily added into and removed from the polymer system without any contamination and accumulation of salt or other chemicals. At the same time, the stimulation strength of CO_2 is precisely tunable through a quantitative addition of CO_2 gas. In addition, as a key molecule in the body, the stimulus of CO_2 has no problems of toxicity or biocompatibility, which offers new possibilities for applications under physiological conditions.

Since the self-assembly behavior of CO_2-responsive polymers is dependent on their hydrophilic/hydrophobic balance, which is tunable by the protonation/deprotonation degree of the polymers induced by the amount of CO_2, a morphology transformation triggered by CO_2 can be easily achieved. Compared with other stimulations, the continuous, quantitative, and reversible response triggered by CO_2 is beneficial for the observation of the morphology transformation process of the assemblies. These characteristics allow CO_2-responsive polymer assemblies to be explored as a synthetic model system to mimic the deformation, shape changes, or morphological transformations known for organelles.

However, there are still some challenges in controlling the morphology of polymer assemblies under CO_2 stimulation. First, the protonated state of most CO_2-responsive polymers is not very stable at a relatively high temperature, resulting in an instability of the assemblies formed by the polymers. At the same time, some

EBSCOhost - printed on 2/14/2023 1:06 PM via . All use subject to https://www.ebsco.com/terms-of-use

CO_2-reactive functional groups such as amidine and guanidine are stable at the protonated state. However, the removal of CO_2 from the functional groups is very slow, which makes the reversible morphology transformations of the assemblies very difficult, and heating or bubbling of inert gas for a long time is usually required. As a result, the investigation of more CO_2-responsive functional groups of various pK_a and introduction of these functional groups into polymers are very important in future, which can improve the morphology transformation performance of the obtained polymers in terms of both speed and magnitude.

Another big problem of CO_2-responsive polymers is the limited response rate that is restricted by both the solubility of CO_2 in the polymer solution and the diffusion ability of CO_2 through the polymeric structure and the environmental medium to reach the CO_2-reactive groups. Moreover, the long-term stability of the CO_2-responsive polymers as well as their resistance to hydrolysis are also very important parameters for their practical applications when a large number of switching cycles are required. These challenges will be solved by the investigation of novel polymers with different CO_2-responsive functional groups and topological structure in future. A bright future of CO_2-responsive polymers is likely.

References

[1] Shim, M.S. and Kwon, Y.J., Stimuli-responsive polymers and nanomaterials for gene delivery and imaging applications. *Adv. Drug Del. Rev. 64* (11), 1046–1059, (2012).

[2] Dong, R.; Ravinathan, S.P.; Xue, L.; Li, N.; Zhang, Y.; Zhou, L.; Cao, C. and Zhu, X., Dual-responsive aggregation-induced emission-active supramolecular nanoparticles for gene delivery and bioimaging. *Chem. Commun. 52* (51), 7950–7953, (2016).

[3] Yan, Q.; Yuan, J.; Kang, Y.; Cai, Z.; Zhou, L. and Yin, Y., Dual-sensing porphyrin-containing copolymer nanosensor as full-spectrum colorimeter and ultra-sensitive thermometer. *Chem. Commun. 46* (16), 2781–2783, (2010).

[4] Liu, L.; Li, W.; Liu, K.; Yan, J.; Hu, G. and Zhang, A., Comblike thermoresponsive polymers with sharp transitions: synthesis, characterization, and their use as sensitive colorimetric sensors. *Macromolecules 44* (21), 8614–8621, (2011).

[5] Mura, S.; Nicolas, J. and Couvreur, P., Stimuli-responsive nanocarriers for drug delivery. *Nat Mater 12* (11), 991–1003, (2013).

[6] Ge, Z. and Liu, S., Functional block copolymer assemblies responsive to tumor and intracellular microenvironments for site-specific drug delivery and enhanced imaging performance. *Chem. Soc. Rev. 42* (17), 7289–7325, (2013).

[7] de Boer, B.; Stalmach, U.; van Hutten, P.F.; Melzer, C.; Krasnikov, V.V. and Hadziioannou, G., Supramolecular self-assembly and opto-electronic properties of semiconducting block copolymers. *Polymer 42* (21), 9097–9109, (2001).

[8] Wolkoff, P.; Schneider, T.; Kildesø, J.; Degerth, R.; Jaroszewski, M. and Schunk, H., Risk in cleaning: chemical and physical exposure. *Sci. Total Environ. 215* (1–2), 135–156, (1998).

[9] Liu, Y.; Jessop, P.G.; Cunningham, M.; Eckert, C.A. and Liotta, C.L., Switchable surfactants. *Science 313* (5789), 958–960, (2006).

EBSCOhost - printed on 2/14/2023 1:06 PM via . All use subject to https://www.ebsco.com/terms-of-use

[10] Fowler, C.I.; Jessop, P.G. and Cunningham, M.F., Aryl amidine and tertiary amine switchable surfactants and their application in the emulsion polymerization of methyl methacrylate. *Macromolecules 45* (7), 2955–2962, (2012).
[11] Mihara, M.; Jessop, P. and Cunningham, M., Redispersible polymer colloids using carbon dioxide as an external trigger. *Macromolecules 44* (10), 3688–3693, (2011).
[12] Pinaud, J.; Kowal, E.; Cunningham, M. and Jessop, P., 2-(Diethyl)aminoethyl methacrylate as a CO_2-switchable comonomer for the preparation of readily coagulated and redispersed polymer latexes. *ACS Macro Lett. 1* (9), 1103–1107, (2012).
[13] Su, X.; Jessop, P.G. and Cunningham, M.F., Surfactant-free polymerization forming switchable latexes that can be aggregated and redispersed by CO_2 removal and then readdition. *Macromolecules 45* (2), 666–670, (2012).
[14] Han, D.; Boissiere, O.; Kumar, S.; Tong, X.; Tremblay, L. and Zhao, Y., Two-way CO_2-switchable triblock copolymer hydrogels. *Macromolecules 45* (18), 7440–7445, (2012).
[15] Nagai, D.; Suzuki, A. and Kuribayashi, T., Synthesis of hydrogels from polyallylamine with carbon dioxide as gellant: development of reversible CO_2 absorbent. *Macromol. Rapid Commun. 32* (4), 404–410, (2011).
[16] Hoshino, Y.; Imamura, K.; Yue, M.; Inoue, G. and Miura, Y., Reversible absorption of CO_2 triggered by phase transition of amine-containing micro- and nanogel particles. *J. Am. Chem. Soc. 134* (44), 18177–18180, (2012).
[17] Lu, W.; Sculley, J.P.; Yuan, D.; Krishna, R.; Wei, Z. and Zhou, H.-C., Polyamine-tethered porous polymer networks for carbon dioxide capture from flue gas. *Angew. Chem. Int. Ed. 51* (30), 7480–7484, (2012).
[18] Ochiai, B.; Yokota, K.; Fujii, A.; Nagai, D. and Endo, T., Reversible trap–release of CO_2 by polymers bearing DBU and DBN moieties. *Macromolecules 41* (4), 1229–1236, (2008).
[19] Aoyagi, N.; Furusho, Y.; Sei, Y. and Endo, T., Fast equilibrium of zwitterionic adduct formation in reversible fixation–release system of CO_2 by amidines under dry conditions. *Tetrahedron 69* (26), 5476–5480, (2013).
[20] Ma, Y. and Yung, L.-Y.L., Detection of dissolved CO_2 based on the aggregation of gold nanoparticles. *Anal. Chem. 86* (5), 2429–2435, (2014).
[21] Yu, G.; Lu, Y.; Liu, X.; Wang, W.-J.; Yang, Q.; Xing, H.; Ren, Q.; Li, B.-G. and Zhu, S., Polyethylenimine-assisted extraction of α-tocopherol from tocopherol homologues and CO_2-triggered fast recovery of the extractant. *Ind. Eng. Chem. Res. 53* (41), 16025–16032, (2014).
[22] Che, H.; Huo, M.; Peng, L.; Fang, T.; Liu, N.; Feng, L.; Wei, Y. and Yuan, J., CO_2-responsive nanofibrous membranes with switchable oil/water wettability. *Angew. Chem. Int. Ed. 54* (31), 8934–8938, (2015).
[23] Wei, H.; Zhang, J.; Shi, N.; Liu, Y.; Zhang, B.; Zhang, J. and Wan, X., A recyclable polyoxometalate-based supramolecular chemosensor for efficient detection of carbon dioxide. *Chem. Sci. 6* (12), 7201–7205, (2015).
[24] Gao, C.; Lu, S.; Liu, M.; Wu, C. and Xiong, Y., CO_2-switchable fluorescence of a dendritic polymer and its applications. *Nanoscale 8* (2), 1140–1146, (2016).
[25] Xu, L.Q.; Zhang, B.; Sun, M.; Hong, L.; Neoh, K.-G.; Kang, E.-T. and Fu, G.D., CO_2-triggered fluorescence "turn-on" response of perylene diimide-containing poly(*N,N*-dimethylaminoethyl methacrylate). *Journal of Materials Chemistry A 1* (4), 1207–1212, (2013).
[26] Hartmann, L.; Bedard, M.; Borner, H.G.; Mohwald, H.; Sukhorukov, G.B. and Antonietti, M., CO_2-switchable oligoamine patches based on amino acids and their use to build polyelectrolyte containers with intelligent gating. *Soft Matter 4* (3), 534–539, (2008).
[27] Tour, J.M.; Kittrell, C. and Colvin, V.L., Green carbon as a bridge to renewable energy. *Nat Mater 9* (11), 871–874, (2010).

EBSCOhost - printed on 2/14/2023 1:06 PM via . All use subject to https://www.ebsco.com/terms-of-use

[28] Yan, Q. and Zhao, Y., Block copolymer self-assembly controlled by the "green" gas stimulus of carbon dioxide. *Chem. Commun*. *50* (79), 11631–11641, (2014).
[29] Blanazs, A.; Armes, S.P. and Ryan, A.J., Self-assembled block copolymer aggregates: from micelles to vesicles and their biological applications. *Macromol. Rapid Commun*. *30* (4-5), 267–277, (2009).
[30] Jessop, P.G.; Mercer, S.M. and Heldebrant, D.J., CO_2-triggered switchable solvents, surfactants, and other materials. *Energ. Environ. Sci*. *5* (6), 7240–7253, (2012).
[31] van de Wetering, P.; Moret, E.E.; Schuurmans-Nieuwenbroek, N.M.E.; van Steenbergen, M.J. and Hennink, W.E., Structure–activity relationships of water-soluble cationic methacrylate/methacrylamide polymers for nonviral gene delivery. *Bioconj. Chem*. *10* (4), 589–597, (1999).
[32] Darabi, A.; Shirin-Abadi, A.R.; Pinaud, J.; Jessop, P.G. and Cunningham, M.F., Nitroxide-mediated surfactant-free emulsion copolymerization of methyl methacrylate and styrene using poly(2-(diethyl)aminoethyl methacrylate-co-styrene) as a stimuli-responsive macroalkoxyamine. *Polym. Chem*. *5* (21), 6163–6170, (2014).
[33] Darabi, A.; Shirin-Abadi, A.R.; Jessop, P.G. and Cunningham, M.F., Nitroxide-mediated polymerization of 2-(diethylamino)ethyl methacrylate (DEAEMA) in water. *Macromolecules 48* (1), 72–80, (2015).
[34] Darabi, A.; Jessop, P.G. and Cunningham, M.F., CO_2-responsive polymeric materials: synthesis, self-assembly, and functional applications. *Chem. Soc. Rev*. *45* (15), 4391–4436, (2016).
[35] Lin, S. and Theato, P., CO_2-responsive polymers. *Macromol. Rapid Commun*. *34* (14), 1118–1133, (2013).
[36] Ceschia, E.; Harjani, J.R.; Liang, C.; Ghoshouni, Z.; Andrea, T.; Brown, R.S. and Jessop, P.G., Switchable anionic surfactants for the remediation of oil-contaminated sand by soil washing. *RSC Adv*. *4* (9), 4638–4645, (2014).
[37] Abel, B.A.; Sims, M.B. and McCormick, C.L., Tunable pH- and CO_2-responsive sulfonamide-containing polymers by RAFT polymerization. *Macromolecules 48* (16), 5487–5495, (2015).
[38] Feng, A.; Zhan, C.; Yan, Q.; Liu, B. and Yuan, J., A CO_2- and temperature-switchable "schizophrenic" block copolymer: from vesicles to micelles. *Chem. Commun*. *50* (64), 8958–8961, (2014).
[39] Yuan, W.; Shen, J. and Zou, H., Amphiphilic block copolymer terminated with pyrene group: from switchable CO_2-temperature dual responses to tunable fluorescence. *RSC Adv*. *5* (17), 13145–13152, (2015).
[40] Zhang, Q. and Zhu, S., Oxygen and carbon dioxide dual responsive nanoaggregates of fluoro- and amino-containing copolymer. *ACS Macro Lett*. *3* (8), 743–746, (2014).
[41] Lei, L.; Zhang, Q.; Shi, S. and Zhu, S., Oxygen and carbon dioxide dual gas-responsive and switchable microgels prepared from emulsion copolymerization of fluoro- and amino-containing monomers. *Langmuir 31* (7), 2196–2201, (2015).
[42] Hu, J.; Whittaker, M.R.; Li, Y.; Quinn, J.F. and Davis, T.P., The use of endogenous gaseous molecules (NO and CO_2) to regulate the self-assembly of a dual-responsive triblock copolymer. *Polym. Chem*. *6* (13), 2407–2415, (2015).
[43] Yan, B.; Han, D.; Boissiere, O.; Ayotte, P. and Zhao, Y., Manipulation of block copolymer vesicles using CO_2: dissociation or "breathing". *Soft Matter 9* (6), 2011–2016, (2013).
[44] Liu, B.-w.; Zhou, H.; Zhou, S.-t.; Zhang, H.-j.; Feng, A.-C.; Jian, C.-m.; Hu, J.; Gao, W.-p. and Yuan, J.-y., Synthesis and self-assembly of CO_2–temperature dual stimuli-responsive triblock copolymers. *Macromolecules 47* (9), 2938–2946, (2014).
[45] Yan, Q.; Zhang, H. and Zhao, Y., CO2-Switchable Supramolecular Block Glycopolypeptide Assemblies. *ACS Macro Lett*. *3* (5), 472–476, (2014).

EBSCOhost - printed on 2/14/2023 1:06 PM via . All use subject to https://www.ebsco.com/terms-of-use

[46] Jie, K.; Zhou, Y.; Yao, Y.; Shi, B. and Huang, F., CO_2-responsive pillar[5]arene-based molecular recognition in water: establishment and application in gas-controlled self-assembly and release. *J. Am. Chem. Soc. 137* (33), 10472–10475, (2015).
[47] Huo, M.; Ye, Q.; Che, H.; Sun, M.; Yuan, J. and Wei, Y., Synthesis and self-assembly of CO_2-responsive dendronized triblock copolymers. *Polym. Chem. 6* (42), 7427–7435, (2015).
[48] Feng, A.; Liang, J.; Ji, J.; Dou, J.; Wang, S. and Yuan, J., CO_2-breathing and piercing polymersomes as tunable and reversible nanocarriers. *Sci. Rep. 6*, 23624, (2016).
[49] Yan, Q. and Zhao, Y., CO_2-stimulated diversiform deformations of polymer assemblies. *J. Am. Chem. Soc. 135* (44), 16300–16303, (2013).
[50] Liu, H.; Guo, Z.; He, S.; Yin, H.; Fei, C. and Feng, Y., CO_2-driven vesicle to micelle regulation of amphiphilic copolymer: random versus block strategy. *Polym. Chem. 5* (16), 4756–4763, (2014).
[51] Yan, Q. and Zhao, Y., Polymeric microtubules that breathe: CO_2-driven polymer controlled-self-assembly and shape transformation. *Angew. Chem. Int. Ed. 52* (38), 9948–9951, (2013).
[52] Liu, H.; Zhao, Y.; Dreiss, C.A. and Feng, Y., CO_2-switchable multi-compartment micelles with segregated corona. *Soft Matter 10* (34), 6387–6391, (2014).
[53] Liu, H.; Wang, W.; Yin, H. and Feng, Y., Solvent-driven formation of worm-like micelles assembled from a CO_2-responsive triblock copolymer. *Langmuir 31* (32), 8756–8763, (2015).
[54] Wang, W.; Liu, H.; Mu, M.; Yin, H. and Feng, Y., CO_2-induced reversible morphology transition from giant worms to polymersomes assembled from a block-random segmented copolymer. *Polym. Chem. 6* (15), 2900–2908, (2015).
[55] Yan, Q.; Zhou, R.; Fu, C.; Zhang, H.; Yin, Y. and Yuan, J., CO_2-responsive polymeric vesicles that breathe. *Angew. Chem. Int. Ed. 50* (21), 4923–4927, (2011).
[56] Yan, Q.; Wang, J.; Yin, Y. and Yuan, J., Breathing polymersomes: CO_2-tuning membrane permeability for size-selective release, separation, and reaction. *Angew. Chem. Int. Ed. 52* (19), 5070–5073, (2013).
[57] Zou, H. and Yuan, W., CO_2- and thermo-responsive vesicles: from expansion-contraction transformation to vesicles-micelles transition. *Polym. Chem. 6* (13), 2457–2465, (2015).
[58] Su, X.; Robert, T.; Mercer, S.M.; Humphries, C.; Cunningham, M.F. and Jessop, P.G., A conventional surfactant becomes CO_2-responsive in the presence of switchable water additives. *Chem. Eur. J. 19* (18), 5595–5601, (2013).
[59] Su, X.; Jessop, P.G. and Cunningham, M.F., Switchable surfactants at the polystyrene–water interface: effect of molecular structure. *Green Materials 2* (2), 69–81, (2014).
[60] Su, X.; Nishizawa, K.; Bultz, E.; Sawamoto, M.; Ouchi, M.; Jessop, P.G. and Cunningham, M. F., Living CO_2-switchable latexes prepared via emulsion ATRP and AGET miniemulsion ATRP. *Macromolecules 49* (17), 6251–6259, (2016).
[61] Zhang, Q.; Yu, G.; Wang, W.-J.; Li, B.-G. and Zhu, S., Preparation of CO_2/N_2-triggered reversibly coagulatable and redispersible polyacrylate latexes by emulsion polymerization using a polymeric surfactant. *Macromol. Rapid Commun. 33* (10), 916–921, (2012).
[62] Zhang, Q.; Yu, G.; Wang, W.-J.; Yuan, H.; Li, B.-G. and Zhu, S., Switchable block copolymer surfactants for preparation of reversibly coagulatable and redispersible poly(methyl methacrylate) latexes. *Macromolecules 46* (4), 1261–1267, (2013).
[63] Wang, X.; Jiang, G.; Wei, Z.; Li, X. and Tang, B., Preparation and drug release property of CO2 stimulus-sensitive poly(*N,N*-dimethylaminoethyl methacrylate)-*b*-polystyrene nanoparticles. *Eur. Polym. J. 49* (10), 3165–3170, (2013).
[64] Zhang, J.; Xu, D.; Guo, J.; Sun, Z.; Qian, W.; Zhang, Y. and Yan, F., CO_2 responsive imidazolium-type poly(ionic liquid) gels.*Macromol. Rapid Commun. 37* (14), 1194–1199, (2016).
[65] Zhang, L.; Qian, J.; Fan, Y.; Feng, W.; Tao, Z. and Yang, H., A facile CO_2 switchable nanocomposite with reversible transition from sol to self-healable hydrogel. *RSC Adv. 5* (76), 62229–62234, (2015).

EBSCOhost - printed on 2/14/2023 1:06 PM via . All use subject to https://www.ebsco.com/terms-of-use

[66] Su, X.; Cunningham, M.F. and Jessop, P.G., Switchable viscosity triggered by CO_2 using smart worm-like micelles. *Chem. Commun*. *49* (26), 2655–2657, (2013).
[67] Zhang, Y.; Feng, Y.; Wang, Y. and Li, X., CO_2-switchable viscoelastic fluids based on a pseudogemini surfactant. *Langmuir 29* (13), 4187–4192, (2013).
[68] Zhang, Y.; Feng, Y.; Wang, J.; He, S.; Guo, Z.; Chu, Z. and Dreiss, C.A., CO_2-switchable wormlike micelles. *Chem. Commun*. *49* (43), 4902–4904, (2013).
[69] Zhang, Y.; Chu, Z.; Dreiss, C.A.; Wang, Y.; Fei, C. and Feng, Y., Smart wormlike micelles switched by CO_2 and air. *Soft Matter 9* (27), 6217–6221, (2013).
[70] Zhao, C.; Zhang, J.; Yuan, G. and Han, C.C., CO_2-triggered liquid–solid switching through a jamming mechanism. *RSC Adv*. *3* (25), 9645–9648, (2013).

EBSCOhost - printed on 2/14/2023 1:06 PM via . All use subject to https://www.ebsco.com/terms-of-use

M. Nazir Tahir, Michael U. Ocheje, Kacper Wojtkiewicz,
Simon Rondeau-Gagné

3 Self-Healing Materials: Design and Applications

Objects and materials that can regenerate themselves spontaneously and autonomously, and restore their initial properties after suffering from damages (strain, puncture, cracks, etc.) seem to be coming directly out of a Sci-Fi movie. With the recent progress in soft materials, polymer chemistry, and materials chemistry, self-healing materials are becoming a reality, bringing a multitude of exciting opportunities and possibilities for various day-to-day life applications such as healthcare, electronics, telecommunication, transport, infrastructure, and others. In this chapter, we will cover important concepts for self-healing and describe some recent examples of highly efficient self-healing materials. A special emphasis will be put on the chemistry of this class of materials by examining different strategies that can be used to design more efficient and autonomously intrinsic self-healing materials. Finally, examples of applications of self-healing materials for organic electronics will be described, highlighting some of the promises of self-healing materials for the next generation of smart materials.

3.1 Introduction

The human body is an incredible source of innovation and technological advancements. Our body is not only functioning in a precise and perfectly regulated manner, but also has incredible properties and characteristics. Among these, the ability of the body to heal and regenerate itself after an injury is particularly remarkable from a scientific point of view. Regardless of the type of damage suffered, different components of our immune system are activated immediately to repair and rebuild the damaged parts spontaneously and autonomously; everything is done automatically in a relatively short time. The best example is wounds that autonomously stop bleeding, or broken bones that heal after some time. Throughout the ages, nature (especially the human body) has inspired generations of scientists to try and reproduce these incredible self-healing characteristics. This poses a thought: Would it be possible to have materials capable of regenerating themselves spontaneously after being damaged like the human body does? If so, by having such healing abilities, these types of materials could drastically impact and revolutionize many facets of

M. Nazir Tahir, Michael U. Ocheje, Kacper Wojtkiewicz, Simon Rondeau-Gagné, Department of Chemistry and Biochemistry, University of Windsor, Canada

https://doi.org/10.1515/9783110537734-003

EBSCOhost - printed on 2/14/2023 1:06 PM via . All use subject to https://www.ebsco.com/terms-of-use

our world, beginning from the way we design consumer products, all the way to the manufacturing process and conception of new advanced technologies. This may sound like fiction, but the concept of self-healing is currently under the spotlight of material scientists, and new materials with self-healing and improved mechanical properties are continuously being developed and prepared [1–3]. This chapter is intended to present the basic concepts of self-healing and to put into perspective the different strategies of self-healing as well as the recent technological advances in this field of materials chemistry.

3.1.1 A Brief History

Self-healing materials have peaked curiosity since the times of antiquity. For a very long time, humans tried to improve the mechanical robustness and durability of materials. As architectural achievements have grown, new solutions have made their presence to slow down, and even prevent, the degradation of materials utilized for construction. A good example of primitive self-healing comes from the Roman era. As we know, the Romans have been at the forefront of important architectural achievements which, even today, remain in very good condition. This preservation through the ages comes especially from the use of mortar. This mortar, used to bind and stick the bricks together, was made from volcanic ash and lime, and represents one of the first examples of self-healing materials [4]. When this material is exposed to rain, a certain amount of the lime becomes soluble and can move through the brick network. Thus, lime can fill any crack that has formed over time. Upon water evaporation, the lime filling the cracks becomes solid, which reinforces the construction and spontaneously repairs damages. This phenomenon allowed the Roman construction to self-regenerate upon damages, which greatly increased the structure's durability even if mortar is not a highly resistant material. Based on this ancient concept, several contemporary constructions, particularly in Europe and Asia, also relied on the same principle of a self-healing "glue" to increase their durability.

3.2 Concepts in Self-Healing

Self-healing materials are attracting a lot of attention in modern material sciences as exemplified by the growing number of scientific publications in the area, which went from less than 10 in 2007 to almost 500 in 2017 (source: Web of Science). As a result, a lot of different materials with different self-healing properties have been reported using a wide variety of approaches. Before describing these approaches and materials, it is important to understand the basics of self-healing and the concepts that best describe this phenomenon.

EBSCOhost - printed on 2/14/2023 1:06 PM via . All use subject to https://www.ebsco.com/terms-of-use

3.2.1 Types of Self-Healing

Self-healing is best described as the property of a material to recover, fully or partially, a certain function or property lost upon damage or stress. Self-healing is divided in two categories: (1) autonomous healing and (2) nonautonomous healing [5]. As the name suggests, autonomous self-healing occurs without any external trigger and intervention. Healing of a human skin injury generally occurs spontaneously which is a good example of autonomous self-healing. In contrast, nonautonomous self-healing requires external interventions, which can be of several types. For example, if the damaged material requires heat treatment or irradiation in order to regenerate, this behavior is known as nonautonomous self-healing.

Another way to describe and classify self-healing is regarding the intrinsic capacity of the materials to regenerate themselves after being damaged, identified as intrinsic or extrinsic self-healing. In intrinsic self-healing, materials already have all the components necessary for the activation of self-healing. On the contrary, extrinsic self-healing requires the addition of the required healing agents to trigger the healing process. These two types of self-healing are directly related to the approach used and can be modified and tuned directly through the design of the materials. In general, intrinsic self-healing is preferred as it reduces the energy costs and decreases the number of steps required for the material to exhibit self-healing properties.

3.2.2 Self-Healing Mechanism and Efficiency

To get a better understanding of self-healing, it is important to know the different stages of the process. In the case of the self-healing of bulk mechanical properties, healing mechanisms proceed through successive steps, as depicted in Figure 3.1 [6]. First, when materials are strained or stretched, the applied tensile energy will dissipate by the system through the formation of macroscopic, microscopic, and/or nanoscale cracks. This process is known as tensile strain dissipation. Self-healing will be triggered by the formation of a mobile phase in the materials, which can be formed

Figure 3.1: Basic mechanism for crack healing in damaged materials: (a) The bulk self-healing material before being damaged; (b) crack formation through tensile strain dissipation; (c) formation of a mobile phase at the surface of the crack; (d) mass transport of the mobile phase to completely fill the crack; and (e) solidification of the material to restore its initial morphology.

EBSCOhost - printed on 2/14/2023 1:06 PM via . All use subject to https://www.ebsco.com/terms-of-use

spontaneously or via an external intervention. This mobile phase is important and will directly affect the rate and efficiency of the healing. Once the mobile phase is formed at the surface of the cracks, it can migrate into the crack, thus initiating the healing process. This mass transport will allow the reconnection of the damaged parts either chemically or physically. At the final stage, the mobile phase solidifies and becomes an integral part of the material, which is completely (or partially) restored.

Since self-healing applies to a specific property of the material, quantifying the effectiveness of this process can be challenging. To facilitate and quantify self-healing efficiency, the relationship between the properties investigated before and after self-healing must be established. Therefore, the self-healing efficiency (η) is defined by the percent recovery of the property or function *f*, evaluated for the native and healed materials (Figure 3.2).

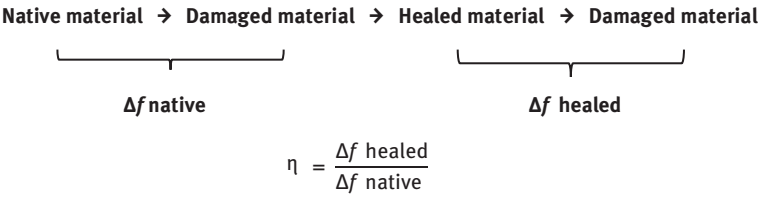

Figure 3.2: Self-healing efficiency calculation and quantification.

Self-healing only applies to a specific property or function, so it is important to consider that not all initial properties of the material are regenerated. The self-healing efficiency must therefore always be considered in relation to the specific property studied. In addition, the properties or functions of the materials are rarely fully restored following self-healing. An example of materials' properties versus time is depicted in Figure 3.3 [7]. A traditional material can be stretched up to its breaking point without a significant loss of performance (green curve). Through several strategies, one might improve the material's performance and tolerance to tensile strain, which pushes back the breaking point. However, the material will suffer from a significant loss of performance once it reaches its failure point (blue curve). In a self-healing material or system, a partial loss of performance will occur upon tensile strain. The performance will then be regenerated upon self-healing, but the initial performance of the materials will not be fully recovered (red curve). Following several self-healing cycles, this hysteresis in the material's maximum performance will ultimately lead to complete degradation. In an ideal self-healing phenomenon, no such hysteresis is observed, which implies fully restored mechanical properties of the materials after failure and self-healing. However, for most of self-healing strategies, full recovery of the material's initial properties is very challenging and is never entirely achieved.

EBSCOhost - printed on 2/14/2023 1:06 PM via . All use subject to https://www.ebsco.com/terms-of-use

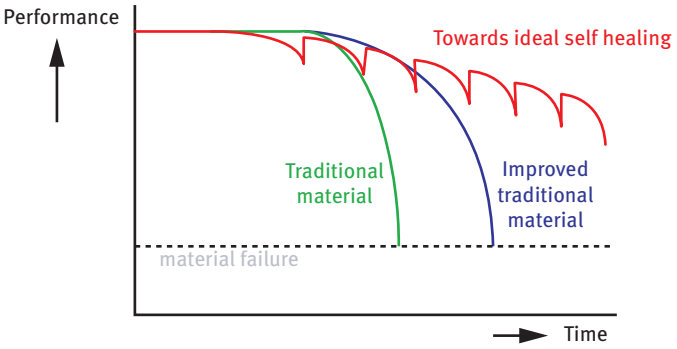

Figure 3.3: Material's performance versus time. After an extended period of use or the addition of stimuli, traditional materials exhibit property failures. For classically improved traditional materials, the mechanisms remain the same. With respect to self-healing materials, they are able to recover their performance and undergo many cycles of stress without exhibiting total mechanical failure. However, the hysteresis in materials performance before and after self-healing ultimately leads to material's degradation.

3.3 Approaches for Self-Healing

Research on the development of new self-healing materials and new concepts has intensified during the last decade, which led to the establishment of various strategies for self-regeneration. Strongly dependent on the types of materials used and their properties (elastic modulus, thermal transitions, surface energy, solubility, etc.), each approach presents important advantages and drawbacks when compared to one another. The following section will present the key approaches for self-healing and an overview of the most recent developments in their utilization.

3.3.1 Encapsulation of Repairing Agents

Polymers are one of the most studied and investigated type of materials for self-healing because of several factors such as the ease of chemical functionalization, an amorphous morphology which allows high mobility of molecules (and polymer chains) at low temperature and good solubility which facilitate their processing in different sizes and shapes. For these reasons, encapsulation of regenerating agents inside a polymer matrix has become a major approach for the development of self-healing polymers, especially for industries and manufacturers. This type of extrinsic self-healing is based on the incorporation of heterogeneities into a polymer matrix, which are composed of active agents (compounds) [8]. Upon damages, these active chemicals are "spilled" from the damaged areas, thus triggering the healing reaction. These heterogeneities can be introduced under different shapes and sizes,

EBSCOhost - printed on 2/14/2023 1:06 PM via . All use subject to https://www.ebsco.com/terms-of-use

but are generally introduced in the matrix as nanoparticles or hollow fibrous structures.

As depicted in Figure 3.4a, the self-healing material is designed and processed to contain heterogeneous pockets of monomers or reagents. Catalytic species are also dispersed in the polymeric matrix uniformly. Upon cracks (or damage), the microcapsules are broken, which liberates reactive agents through the polymer matrix (Figure 3.4b). Upon exposure to the catalyst embedded in the matrix, polymerization occurs, which cross-links the reactive monomers and forms an internal glue. The solid phase then fills the damaged area, regenerating the initial polymer matrix.

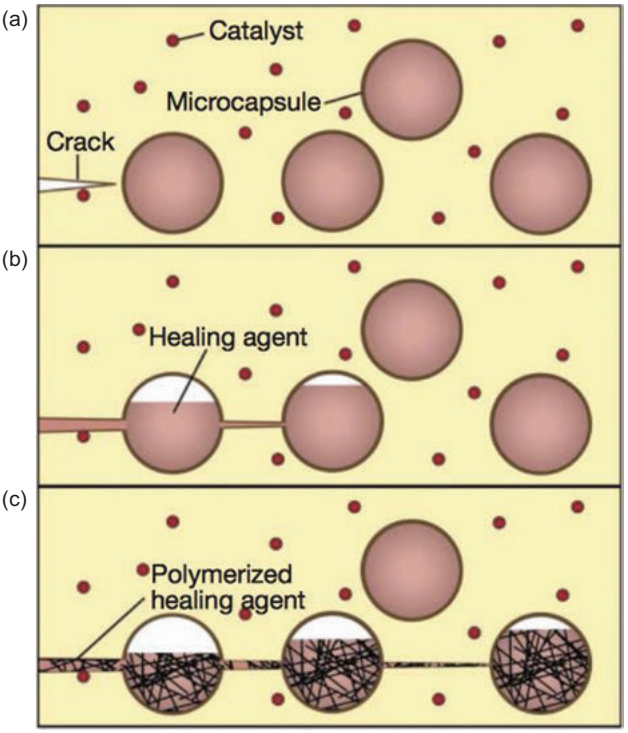

Figure 3.4: Self-healing via encapsulation of healing agent. Adapted with permission from Ref. [8]. Copyright 2001 Nature Publishing Group.

Even though this approach can be straightforward and easily applicable to a multitude of different types of polymers, several parameters must be controlled to maximize self-healing efficiency and allow optimal regeneration of damaged materials. First, the heterogeneities must be stable in the polymer matrix and deliver enough materials to allow for complete healing. This important parameter is particularly challenging to control: large capsules contain more healing agents but can drastically

EBSCOhost - printed on 2/14/2023 1:06 PM via . All use subject to https://www.ebsco.com/terms-of-use

affect the bulk properties of the polymeric matrix by modifying the roughness of the materials and induce crack propagation. In contrast, smaller capsules typically have a limited amount of healing agents available for delivery upon damage but do not modify the bulk properties of the polymer. The heterogeneities also need a membrane fragile enough to rupture when damaged. Therefore, the interface between the polymer and the membrane is important to control and investigate to optimize the release of the healing agent. Similar to the capsules, the incorporation of the catalyst in the polymer matrix must not affect the material's bulk properties. In addition, the healing agent (monomer) must have a low viscosity (mass transport), a good stability, and be immiscible with the native polymer. Finally, to enable an optimal self-healing, the cross-linking reaction must be fast and efficient at room temperature.

One of the most efficient and early demonstrations of the microencapsulation approach for self-healing has been achieved by embedding encapsulated dicyclopentadiene (DCPD) monomers inside an epoxy matrix (Figure 3.5a) [8]. Grubb's catalyst (bis(tricyclohexylphosphine) benzylidene ruthenium (IV) dichloride) was used to trigger a ring-opening metathesis polymerization (ROMP). In this example, DCPD was used because of its low viscosity, which promoted the dispersion of the healing

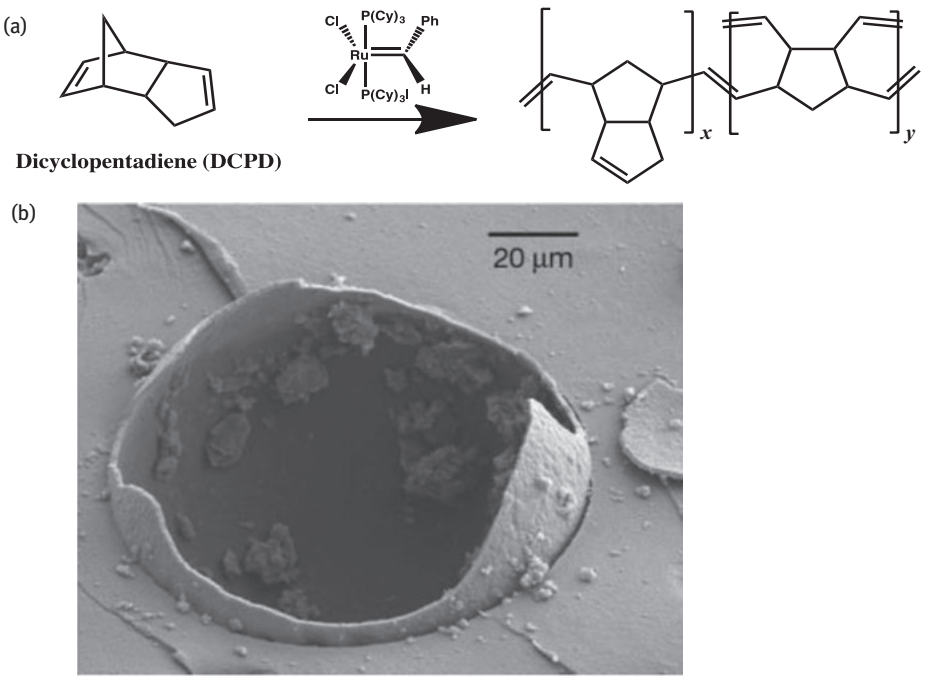

Figure 3.5: (a) Cross-linking reaction of DCPD with Grubb's catalyst and (b) scanning electron microscopy image (SEM) of a fractured capsule containing urea-based healing agents. Adapted with permission from Ref. [8]. Copyright 2001 Nature Publishing Group.

EBSCOhost - printed on 2/14/2023 1:06 PM via . All use subject to https://www.ebsco.com/terms-of-use

agent in the epoxy matrix. Interestingly, the ROMP reaction successfully repaired the damaged epoxy polymers, which recovered 75% of its initial fracture toughness after self-healing. This example clearly demonstrates that the microencapsulation, when carefully designed and controlled, is a very efficient approach for self-healing. The utilization of several cross-linking reactions has also been reported since the last decade. Among others, the polymerization of poly(dimethylsiloxane) (PDMS) triggered by Pt catalyst, the reaction of epoxide with $CuBr_2$/2-methylimidazole complex ($CuBr_2$(2-MeIM)$_4$) and the polymerization of isocyanate in the presence of water (Figure 3.5b) [9], showed great promise for the extrinsic healing of polymeric matrices through microencapsulation.

3.3.2 Dynamic Cross-Linking

Based on the rational chemical design of materials, dynamic cross-linking is one of the most promising approaches in developing intrinsic self-healing materials. Recent developments in the fields of coordination and supramolecular chemistry have given rise to motifs capable of forming intermolecular covalent and noncovalent bonds possessing a dynamic characteristic [10, 11]. Furthermore, these interactions can spontaneously and autonomously break and reform. This means that the incorporation of such dynamic bonds into materials through rational chemical design, which can allow materials to regenerate spontaneously via bond reformation after being damaged, is now feasible. The following pages will cover several types of dynamic bonds used for the design of intrinsically self-healing materials. Each of these interactions possesses several advantages and disadvantages, which will also be highlighted. Figure 3.6 presents the most important noncovalent interactions along with their typical range of binding strength. The comparison between noncovalent and covalent bonds will also be

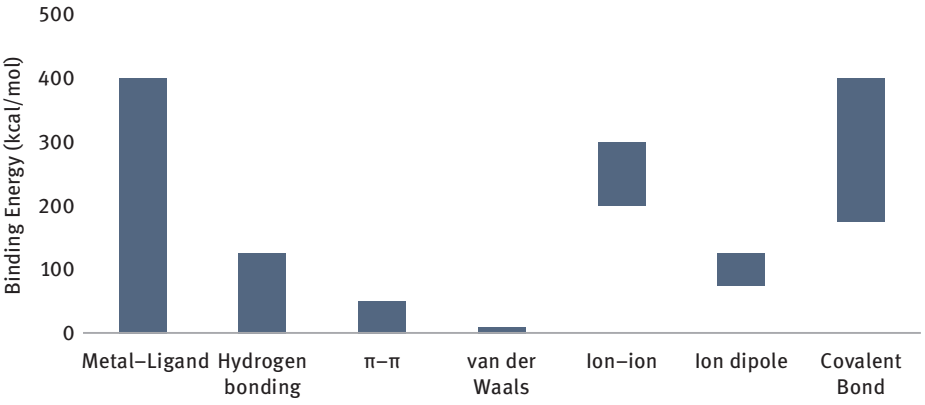

Figure 3.6: Binding energies of different types of covalent and noncovalent bonds.

EBSCOhost - printed on 2/14/2023 1:06 PM via . All use subject to https://www.ebsco.com/terms-of-use

considered. Because of the wide variety of motifs and binding energies, the choice of dynamic bonding used for self-healing depends on the desired bulk properties and chemical design of the materials. The most common methods of producing dynamic bonds that undergo self-healing are covalent bonding, hydrogen bonding, and metal–ligand coordination, principally because of the wide range of energy covered and synthetic ease (Figure 3.7).

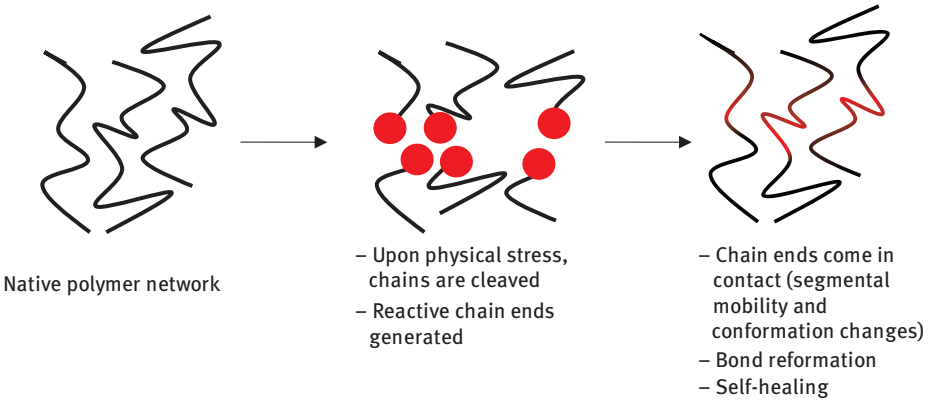

Figure 3.7: Schematic illustration of ideal self-healing mechanism in polymers incorporating dynamic bonding moieties. Upon physical damage, reactive end groups are generated. Upon conformational changes and segmental mobility of the polymer chains, the dynamic moieties get in contact with each other, enabling bond reformation and regeneration of the initial polymer network.

Hydrogen Bonding

Hydrogen bonds (H-bonds) are by far the most common and widely studied type of noncovalent interactions. These supramolecular bonds come from the dipolar interaction of a hydrogen attached to an electron-withdrawing group interacting with a neighboring electronegative atom. These newly formed bonds may not be the most robust nor as strong as noncovalent bonds, but their dynamic behavior can enable remarkable mechanical and chemical resistance in materials. In addition, the presence of various moieties forming H-bonds in natural compounds inspired chemists to develop several synthetic motifs capable of forming such bonds with different orientation and with different strengths. The complementarity of H-bonds, guided by the design of the donor-acceptor (D–A) pairs, also brings an additional level of possibility in terms of design by rationally tuning the bonding strength, and, thus, the mechanical properties of the materials. Various self-healing polymers have been reported to use this type of dynamic bonding, making H-bonds one of the most promising supramolecular interactions for the design of spontaneous self-healing materials [12–14]. Figure 3.8 shows some example of self-healing materials based on H-Bonds, enabled by urea and amide groups.

EBSCOhost - printed on 2/14/2023 1:06 PM via . All use subject to https://www.ebsco.com/terms-of-use

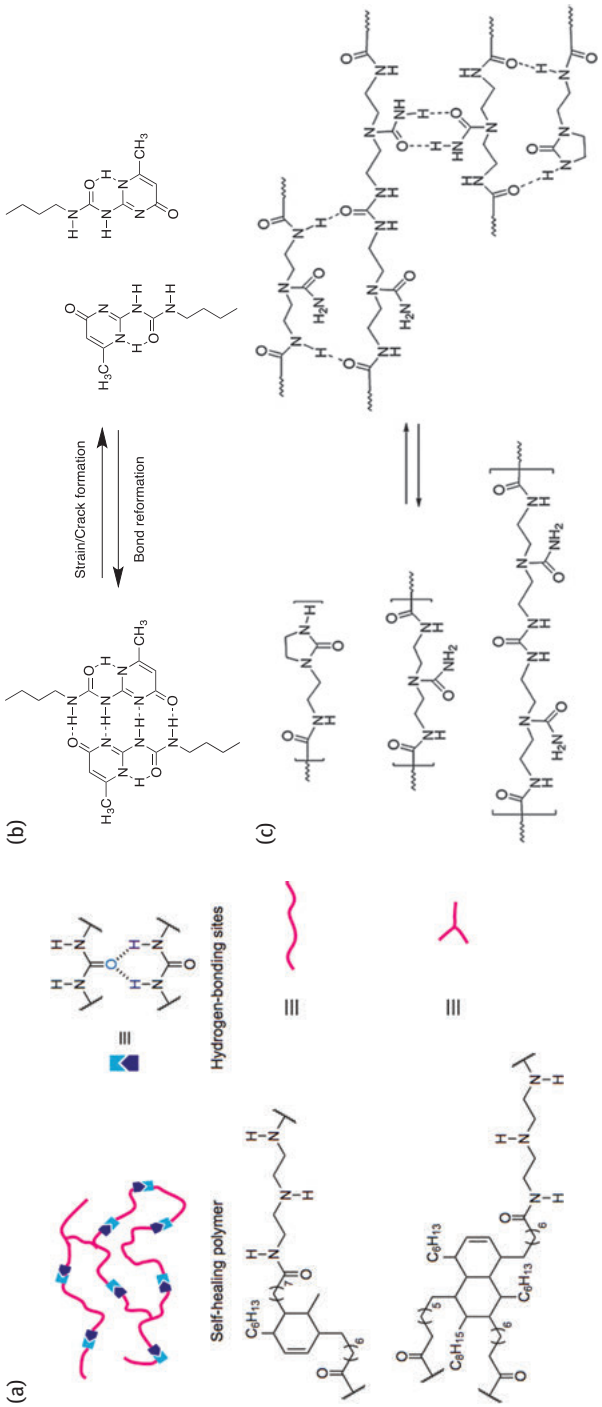

Figure 3.8: Self-healing materials based on hydrogen bonding motifs: (a) complimentary copolymers incorporating urea functionalities, (b) urea isopyrimidone (Upy), and c) polyamides. Adapted with permission from Ref. [12] to [14].

EBSCOhost - printed on 2/14/2023 1:06 PM via . All use subject to https://www.ebsco.com/terms-of-use

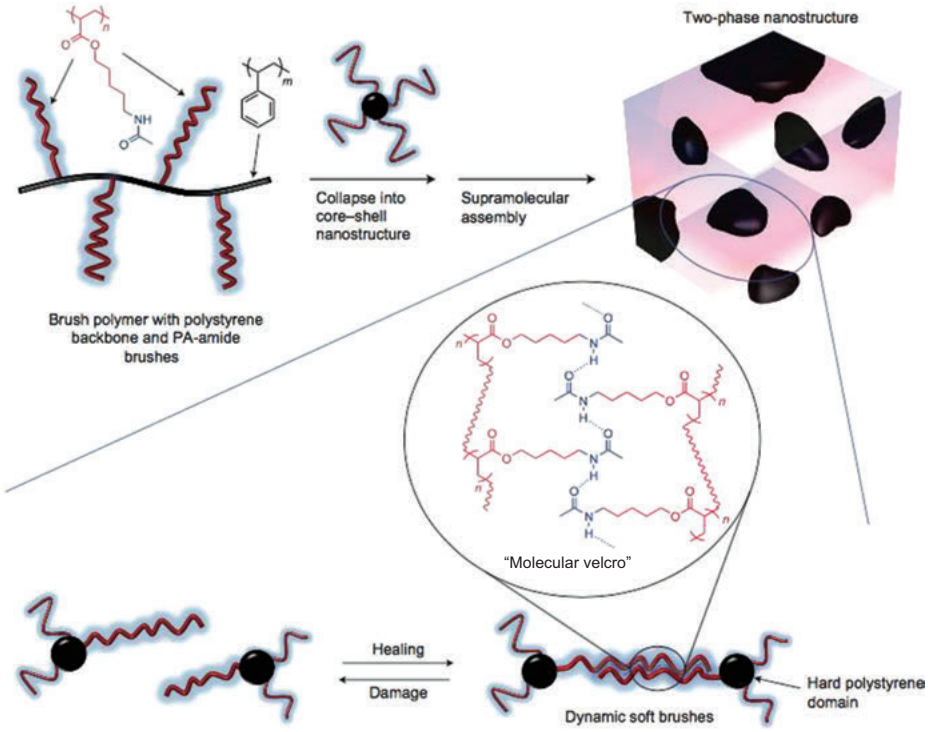

Figure 3.9: A self-healing hybrid polymer based on dynamic hydrogen bonding and phase separation. Adapted with permission from [12]. Copyright 2012 Nature Publishing Group.

Self-healing polymers that rely on H-bonding have the dynamic interactions directly embedded in a polymer matrix. Therefore, various effects can additionally influence the efficiency of self-healing, that is, fiber formation, stacking interactions, phase separation, and crystallization of the polymer chains. Moreover, secondary effects such as dipole–dipole interactions or secondary hydrogen bonding can also be enabled. Because of these additional effects, the molecular design and the choice of hydrogen bonding moieties are crucial parameters to control. A good example of highly efficient self-healing materials based on H-bonds and enhanced by phase separation has been recently reported by Guan and coworkers (Figure 3.9) [12]. In their design, the authors utilized a high glass transition temperature (T_g) polystyrene-based backbone, on to which soft polar H-bonding brushes were grafted with a low T_g, based on polyacrylate amide. This unique design allowed for a phase separation in the bulk state, which enabled an entirely controlled self-healing process. Specifically, when the hybrid polymer was damaged, the weak supramolecular bonds, contained in the polar phase, were preferentially ruptured. Because of the low glass transition of the polyacrylate amide

EBSCOhost - printed on 2/14/2023 1:06 PM via . All use subject to https://www.ebsco.com/terms-of-use

matrix, the polymer network can easily rearrange and reform the dynamic amide H-bonds. This unique design and approach allowed for very efficient self-healing (92% recovery of the initial mechanical properties) after 24 h and represents an important example of the versatility of self-healing via dynamic hydrogen bonding.

As mentioned previously, hydrogen bonding offers great versatility for designing self-healing materials. However, in bulk and large-area applications, they are limited due to the fact that this method is sensitive to moisture and other environmental parameters. Additionally, when compared to different types of dynamic supramolecular interactions, H-bonds are relatively weak.

Metal–Ligand Interactions

Although this method has been extensively studied for different application purposes, coordination chemistry is another particularly attractive approach to implement self-healing to a polymer matrix. Based on the affinity of different coordinating motifs to metal centers, this approach offers multiple design possibilities and great control over the dynamic interaction strength and orientation. By carefully adjusting for the type of metal ion and ligand interaction, it is possible to design a cross-linking network that exhibits appropriate bond strengths with highly stretchable and self-healing properties [15–18]. It is, therefore, not surprising if metal coordination is found in nature in stretchable and self-healable systems, such as the mussels' byssus thread, which utilizes coordination of Fe(III) by pendant catechol units (Figure 3.10) [19].

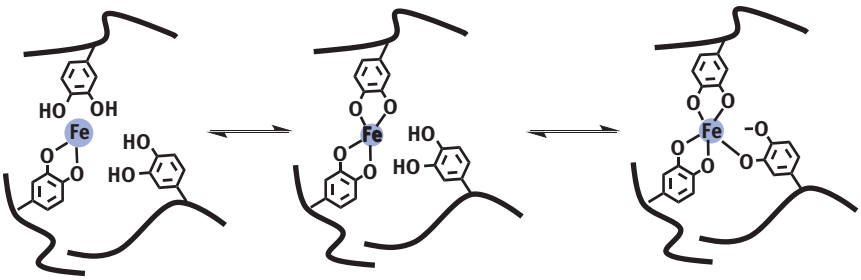

Figure 3.10: Dynamic coordination of Fe(III) by catechol moieties.

Similar to other types of dynamic bonding, the self-healing capabilities of metal–ligand interactions are because of their dynamic behavior and the ability to dissipate energy upon strain through bond breakage/reformation. Furthermore, the wide variety of binding strengths in coordination chemistry enhances the stimuli responsiveness of the materials, changing the ligand and metal centers, allowing for fine tuning of the

EBSCOhost - printed on 2/14/2023 1:06 PM via . All use subject to https://www.ebsco.com/terms-of-use

self-healing process upon different external stimulus, for example, light, heat, and pH. Also, interestingly, this phenomenon can also be tuned by the different approaches used in the preparation of the self-healing metallopolymers. In fact, as depicted in Figure 3.11, depending on the manner that the ligand and metals are inserted in the polymer matrix, different directionality and bonding strength will be achieved.

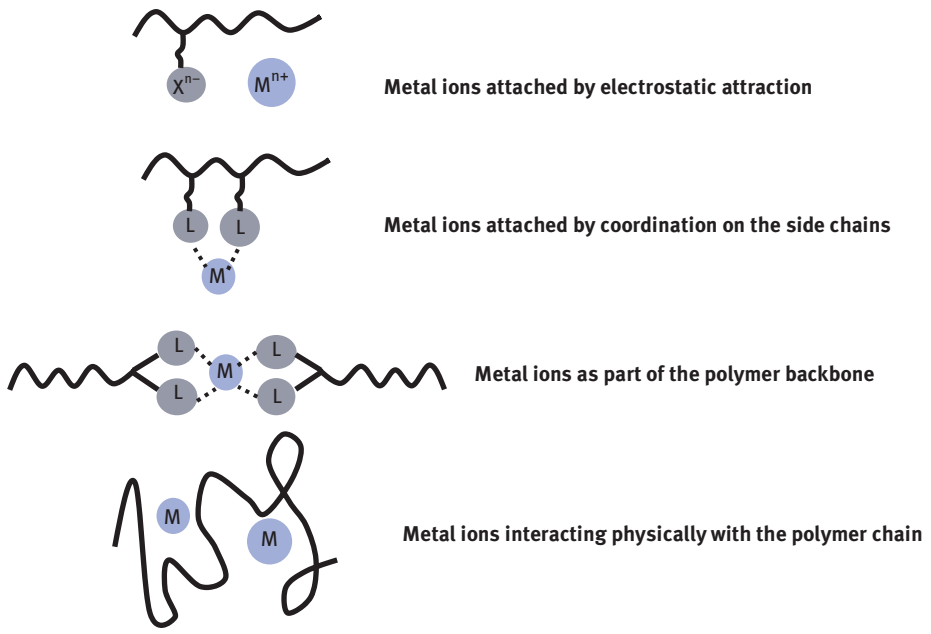

Figure 3.11: Chemical design approaches to prepare self-healing materials by metal coordination and incorporation to polymers.

3.3.3 Dynamic Covalent Bonds

While the two approaches that were previously discussed to achieve self-healing in materials rely on the use of supramolecular bonds, the use of dynamic chemical reactions to generate new covalent bonds is also becoming a popular approach to enable self-regeneration. Unlike supramolecular interactions, covalent bonds have the advantage of being more robust and more stable to external conditions such as temperature, moisture, and solvents. It is therefore not surprising to see an increasing number of reported examples of self-healing materials based on this approach [11, 20, 21]. The type of dynamic reaction incorporated into the material greatly depends on the final application. Among the parameters to carefully control, the energy barrier of the equilibrium (direct reaction vs. inverse reaction), the number of molecules involved and the need for external triggers or reagents, are particularly important factors to consider when designing a technique using dynamic covalent bonding.

EBSCOhost - printed on 2/14/2023 1:06 PM via . All use subject to https://www.ebsco.com/terms-of-use

Several types of reactions have already been proven to be effective for self-healing. Among others, [4+2] cycloaddition reactions (Diels–Alder), are interesting because of their reversibility, by generating retro Diels–Alder adducts. However, in cases where a high activation energy is required, their compatibility with low T_g polymeric matrixes will be limited. Exchange reactions, such as the formation of imine bonds, generated from the condensation of an aldehyde and an amine, have also been shown to be an effective approach for self-healing. This acid-catalyzed spontaneous reaction has been recently used to obtain self-healing materials based on polyethylene glycol (PEG) chains [22]. In addition, another approach that is quickly gaining attention when producing self-healing materials is the reaction that spontaneously allows for the exchange between thiol and disulfide bonds, given the spontaneity of the reaction and the low energy barrier required to influence the chemical equilibrium (Figure 3.12) [23, 24]. Finally, the generation of radicals, resulting from the breakage of a covalent bond under a mechanical force, can also be used to repair materials. In general, the lifetime of radicals is much shorter than the time required for self-healing. However, by carefully developing a method, it is possible to extend the lifetime of the radicals for a period long enough to regenerate the broken covalent bonds, following self-healing steps of rearrangement, diffusion, and randomization, discussed earlier in this chapter. Thiocarbonate, thiuram disulfide derivatives, or alkoxyamines are some examples of motifs that can be used for this type of dynamic cross-linking [25, 26]. The breakdown of NO–C bonds, well known to occur for TEMPO derivatives, is also known to generate self-healing material.

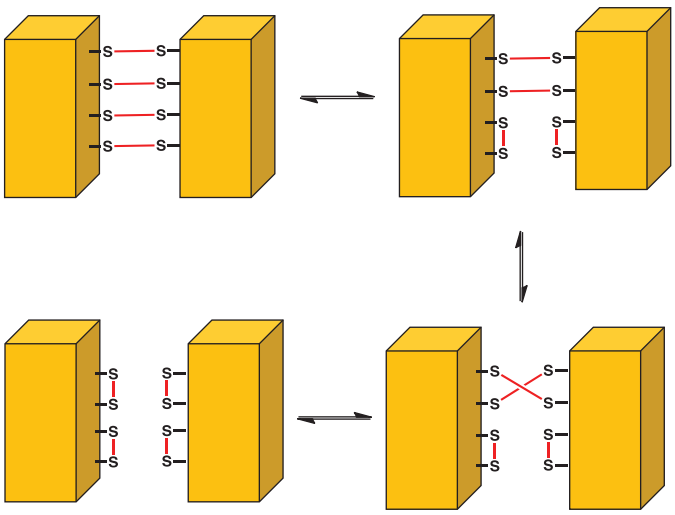

Figure 3.12: Self-healing of materials based on the thiol–disulfide exchange.

EBSCOhost - printed on 2/14/2023 1:06 PM via . All use subject to https://www.ebsco.com/terms-of-use

3.3.4 Other Approaches to Self-Healing

Shape-Memory Effect

Reactive groups and the type of dynamic bonding, as demonstrated previously, are very important to consider for the efficiency of self-healing. Another important aspect to consider is the ability of the physical network to be remodeled. Upon physical damage, the ability of a polymeric network to "remember" its initial shape is a particularly attractive parameter for self-healing, on which the development of shape-memory polymer is based on [27]. This last family of polymers, in most cases, relies on the ability of the materials to react to external stimuli and recover their initial shape and morphology from a temporarily altered physical state. As it is for most self-healing strategies, the shape-memory effect is highly dependent on the material's T_g. At high temperature (above the T_g), the polymer chains are highly mobile and can flow through the materials. At lower temperature, polymer chains are fixed and rigid. Therefore, these competing effects can be used to modulate the segmental mobility of the polymer chains and control the morphology of the materials and self-healing process. It is important to mention that properties other than T_g can be used to enable a shape-memory effect such as cross-linking density (light-triggered) and melting point (temperature-triggered). When used in combination with other self-healing strategies, such as dynamic cross-linking or self-repairing agents, the shape-memory effect is a powerful technique to enhance the efficiency of self-healing by enabling an additional opportunity to drive crack closure. A good example of an efficient, light-triggered, and self-healing shape-memory polymer has been reported by Langer and coworkers [28]. First, a light responsible polymer is stretched and irradiated at a specific wavelength (λ) above 260 nm to fix the polymer network through cross-linking. Upon stress release, the polymer remains in its elongated shape. Interestingly, upon irradiation with $\lambda < 260$ nm, the new cross-linking bonds are cleaved, allowing for the network to recover its memorized, initial shape. As a result, the damages caused by stretching are entirely healed, allowing for the material to endure further strain cycles. This light-triggered shape-memory self-healing is depicted in Figure 3.13.

Migration of Nanoparticles

Another very interesting approach to develop and regenerate a polymer matrix is based on the migration of nanoparticles. Unlike previous approaches based on the mobility of polymer chains and on the linkage of various covalent and dynamic bonds, this approach relies on the incorporation of particles randomly dispersed in a polymer phase and which, depending on the appearance of cracks or deformations, can move and concentrate at the damaged interface, causing self-healing within the material. Based on recent molecular dynamics experiments and confirmed experimentally with CdSe/ZnS nanoparticles embedded in polymethylmethacrylate

EBSCOhost - printed on 2/14/2023 1:06 PM via . All use subject to https://www.ebsco.com/terms-of-use

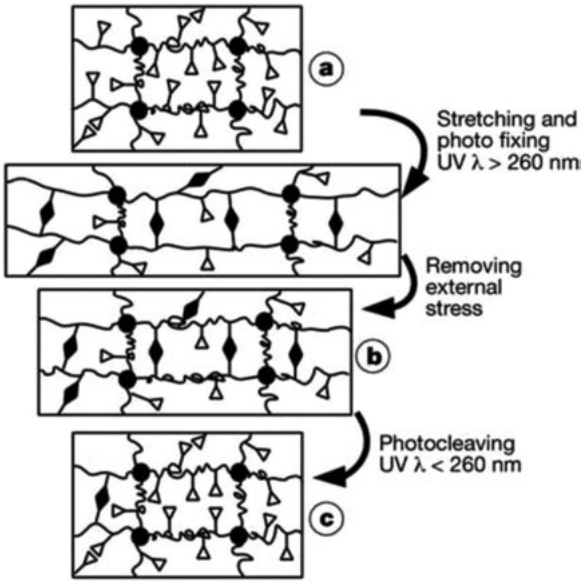

Figure 3.13: Shape-memory effect of a photo-responsive polymer as reported by Langer and coworkers. Adapted with permission from Ref. [28]. Copyright 2005 Nature Publishing Group.

(PMMA), it has been shown that nanoparticles tend to be attracted toward the damaged area in a polymer matrix, at a higher temperature. As soon as one particle begins to move toward the damaged area, another area becomes depleted of nanoparticles, which results in the movement of other localized particles to attain equilibrium again. Upon cooling of the materials, a new and healed morphology can be generated. Interestingly, it has been shown that larger particles are more effective than smaller ones, especially at shorter timescales.

Despite being naturally attracted into the depleted regions of a damaged polymer matrix, material chemists creatively designed a new autonomous system to enhance the migration of functional particles, which as a result will bolster the self-healing ability and stimuli response. One of the most inventive approaches has been reported by Wang and coworkers, using self-propelled nanomotors to autonomously seek and repair cracks in electrical systems [29]. More specifically, Au/Pt Janus spherical nanomotors have been prepared and characterized. These nanomotors can be powered when hydrogen peroxide is introduced in solution as "fuel," which reacts with the Pt surface. Therefore, when a crack is formed on the gold electrode, preventing electrical conductivity, the nanomotors can swim to the damaged area and restore contact. This way, the nanomotors act as conductive "patches" in the broken circuit and can restore the electrical current. This concept of self-healing through self-propelled nanoparticles is illustrated in Figure 3.14..

EBSCOhost - printed on 2/14/2023 1:06 PM via . All use subject to https://www.ebsco.com/terms-of-use

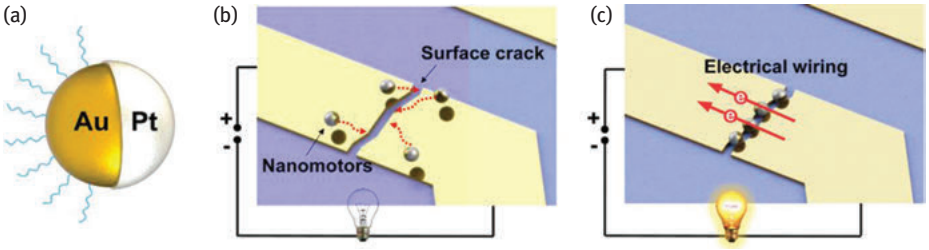

Figure 3.14: Schematic illustration of autonomous self-healing of damaged gold electrodes through migration of self-propelled Janus particles: (a) structure of the Janus Au/Pt nanoparticles, (b) upon damage, the gold circuit is cracked, thus preventing electrical conductivity, and (c) upon adding H_2O_2 fuel, the nanomotors move across the system and concentrate at the crack site, thus restoring a conductive pathway. Adapted with permission from Ref. [29]. Copyright 2015 American Chemical Society.

3.4 Some Applications of Self-Healing Materials

As previously demonstrated, there are multiple design possibilities toward self-healing materials. Therefore, by using the different synthetic tools available, material chemists can now design more efficient self-healing materials for various applications, including regenerative medicine, wearable and stretchable electronics, consumer goods, advance manufacturing, and so on. In order to give a glimpse of these applications, the next pages will cover some new and exciting applications of self-healing materials.

3.4.1 Field-Effect Transistors

Since the last decade, research is being performed to develop new electronic technology, such as wearable/stretchable devices, intelligent robotics, and body-conformable devices [30, 31]. In fact, the demand for such devices has been significantly increasing in the past years with the rise of new portable and compact devices. However, current silicon-based electronics, despite their outstanding efficiency, sometimes suffer from limitations of mechanical compliance and robustness. Therefore, different types of conjugated polymer-based materials have been developed for numerous utilizations in electronics, mainly because of their inherent characteristics including lightweight, flexibility, easy processing, and structural versatility [32, 33]. Furthermore, self-healing properties have been recently implemented to these systems toward electronics that can not only be stretched, but also capable of regenerating themselves after being damaged.

The core units of modern electronic circuits and hardware are field-effect transistors (FET). FETs are small devices that utilize an electric field to control the

EBSCOhost - printed on 2/14/2023 1:06 PM via . All use subject to https://www.ebsco.com/terms-of-use

electrical behavior of the electronic device. FETs are, thus, an integral logic component [34]. In current technology, FETs are based on silicon. However, to develop new stretchable and flexible devices, these devices also need to possess a good mechanical compliance. Generally, fabricated through the combination of multiple functional materials (layered device), FETs incorporating self-healing materials have recently been reported and demonstrated with very interesting properties. First, self-healable dielectrics (insulating materials) have been reported via the utilization of metal–ligand dynamic cross-linking. Based on polydimethylsiloxane (PDMS), a very stretchable polymer, the new dielectric materials contain bipyridine moieties, which are capable of spontaneously coordinating to metal centers, including Fe^{2+} and Zn^{2+} (Figure 3.15a–c) [35]. The resulting polymers showed very good electronic properties, crucial for the fabrication of field-effect transistors including an increased dielectric constant and good scapacitance. Moreover, the different coordinated bipyridine-containing PDMS howed a very high stretchability (up 300% strain) and efficient spontaneous self-healing. Even after a decrease in the stretchability because of the surface aging for 24 h and then self-healing, the materials were still able to exhibit a strain tolerance greater than 200% after healing. Interestingly, the new dielectric materials not only showed good electric and mechanical properties, but also have been used in the fabrication of entirely stretchable FETs. The resulting devices maintained the favorable mechanical properties of a dielectric metal-coordinated self-healing polymer, which opens the door for the development of new electronic materials with autonomous self-healing via dynamic cross-linking with metal–ligand interactions.

Simultaneously reported by Kim et al., a similar strategy, based on metal-coordination, toward self-healing dielectric materials has been utilized (Figure 3.15d–f) [36]. The authors reported the incorporation of catechol units to a stretchable soft polymer based on PMMA. Previously utilized in other self-healing systems, catechol moieties can form highly dynamic complexes with Fe^{3+} and are also easily accessible synthetically. The resulting elastomeric materials demonstrated good electronic properties (dielectric constant and capacitance) and excellent mechanical compliance, crucial for applications in stretchable electronics. Moreover, after a mild healing treatment (55 °C for 33 min.), the healed materials showed almost complete restoration of their initial properties. Despite being nonautonomous, this report highlights the recent efforts toward self-healable dielectrics and fabrication of fully stretchable/self-healing FETs.

FETs not only need highly efficient dielectric materials, but more importantly, require semiconductors with high charge mobility. Therefore, development of self-healing semiconductors is crucial toward self-healing FETs. Conjugated polymers, a specific class of organic macromolecules, are the most promising candidates to achieve these characteristics because they possess all the qualities necessary for the use as the semiconducting layer in stretchable/self-healing FETs, which include high-charge carrier mobility, processability via solution deposition, and potential low cost [32]. However, because of the intrinsic rigidity of conjugated polymeric backbone, the

EBSCOhost - printed on 2/14/2023 1:06 PM via . All use subject to https://www.ebsco.com/terms-of-use

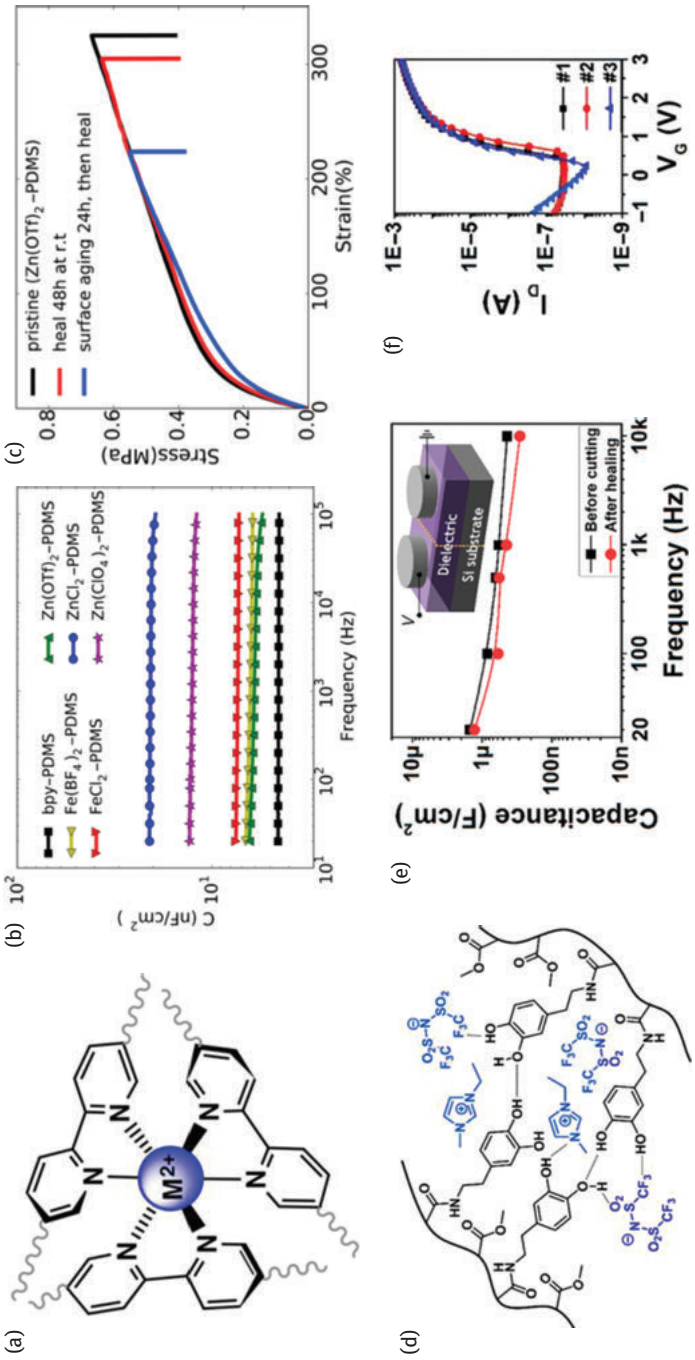

Figure 3.15: (a) Bipyridine-based cross-linked PDMS polymers (polymer chains and counterion have been omitted for clarity); (b) capacitance versus frequency measured for various bipyridine-functionalized PDMS; (c) self-healing test for PDMS–bipyridine polymer cross-linked by coordination to Zn^{2+}. Self-healing has been performed under ambient conditions without any intervention; (d) schematic illustration of catechol-containing PMMA-based elastomers; (e) capacitance value of the catechol-containing dielectric before and after healing from mechanical breakdown; and (f) transfer characteristics of the FET devices built from catechol-containing PMMA-based elastomers after self-healing. Adapted with permission from Ref. [35] and [36]. Copyright 2016 American Chemical Society.

EBSCOhost - printed on 2/14/2023 1:06 PM via . All use subject to https://www.ebsco.com/terms-of-use

development of self-healing conjugated polymers is still challenging. One of the only examples of a self-healing semiconducting polymer has been reported in 2016 by Bao et al. [37]. To enable stretchability and self-healing in a highly π-conjugated system, the authors incorporated pyridine dicarboxamide (PDCA) units into diketopyrrolopyrrole-based polymers, a unit known to lead to high-charge mobility (Figure 3.16). Interestingly, the PDCA units were used because of their capacity of forming intermolecular H-bonds via the amide moieties and also because of the fact that they can act as ligands for various metal centers, including Fe^{3+} [38]. The resulting conjugated polymers, with intermolecular hydrogen bonding, showed an impressive enhancement in molecular stretchability and were shown to maintain their charge transport properties, even at 120% strain. More important, after being damaged, mild thermal and solvent treatments led to a complete restoration of the polymer morphology, which demonstrates the efficiency of dynamic hydrogen bonding to heal the polymer network. Finally, the new semiconducting polymers were used to fabricate fully stretchable FET devices. Interestingly, the devices incorporating the healable conjugated polymers were also able to demonstrate their healing abilities undergoing similar solvent and thermal treatments. Despite being nonautonomous, the healing properties of conjugated polymers and related FETs opened the door to the development of novel electronic devices that can be both stretchable and healable.

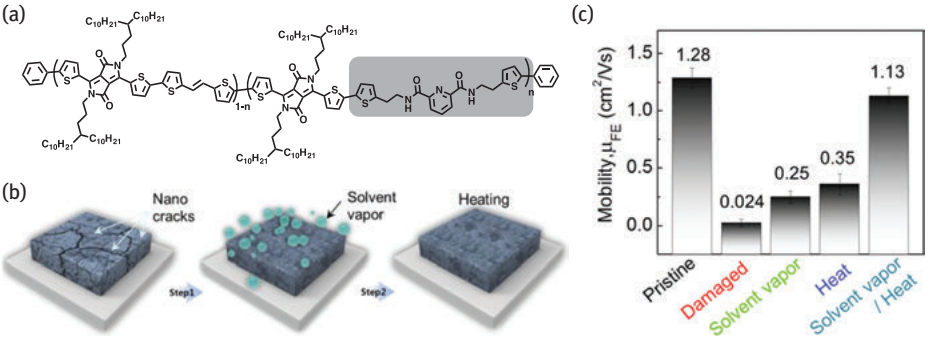

Figure 3.16: (a) Healable semiconducting conjugated polymers based on PDCA-containing DPP-based polymers; (b) treatments used for healing the conjugated polymer thin films after being damaged by strain and (c) charge mobility of the polymers after the different healing treatments. Adapted with permission from Ref. [38]. Copyright 2016 Nature Publishing Group.

Finally, other stretchable FET components have been shown to possess autonomous self-healing ability. For example, conductive carbon nanotube (CNTs) networks have been used as electrodes for the fabrication of fully stretchable FETs [39]. The self-healing ability of CNTs comes from the strong van der Waals interactions between the tubes. Therefore, as soon as the strain is released, adjacent nanotubes will automatically come back into contact with each other restoring an

EBSCOhost - printed on 2/14/2023 1:06 PM via . All use subject to https://www.ebsco.com/terms-of-use

optimal morphology for electric conductivity. Moreover, this carbon-rich material is particularly interesting for large-scale fabrication, given the possibility of performing solution deposition of the CNTs by a method known as spray coating.

In addition to electronics and related areas, the utilization of self-healing materials attracted attention in other areas of application. Among others, new applications for these materials include resistant fabrics, resealing tires, and long-life batteries [40]. In order to give an overview of some new exciting applications for self-healing materials, the following section highlights and describes some selected examples.

3.4.2 Advanced Manufacturing and Technologies

One of the first applications in which self-healing materials are now being investigated is in advanced transportation technologies, especially in jet plane conception and production. In that context, self-healing materials showed great potential for replacing conventional ceramic composites, widely used in current jet engines. Given the fact that these ceramic composites are sensitive to failure and a variety of different types of mechanical impacts, existing ceramic composites in combustion chambers have been replaced by self-healing boron-containing composites [41]. The self-healing properties of these boron composites are attributed to the formation of boron oxide (B_2O_3) that can seal the matrix cracks. The self-healing properties of these materials have been investigated at high temperatures (around 1,350 °C), temperatures typically found in an aircraft engine combustion chamber. Even though this new approach has not yet been optimized, these new self-healing materials showed great potential to enhance the robustness of jet planes and transport technologies in general.

3.4.3 Functional Coatings and Adhesives

Closer to our life, self-healing composites are also promising candidates toward self-healing paints and coatings, capable of spontaneously recovering their function and surface homogeneity after being damaged. The self-healing coatings also showed some promising results for the protection of large structures from corrosion and minor impacts. In order to achieve production such as self-healing coating materials, Yang et al. recently synthesized an epoxy resin composite coating for steel alloys with embedded urea formaldehyde microcapsules [42]. As described in previous sections, microcapsules are highly efficient healing agents and are particularly interesting toward intrinsic and spontaneous self-healing. Therefore, this strategy has been proved to be suitable for paint application. A key factor in their role as epoxy resin composites is that in preparation and application, they did not break apart during the coating step. In addition, the coated steel samples were successfully protected against corrosion even after the coating was damaged and healed. It is important to

EBSCOhost - printed on 2/14/2023 1:06 PM via . All use subject to https://www.ebsco.com/terms-of-use

mention that protection against corrosion is particularly critical for many industries as metallic alloys, including aluminum, titanium, and magnesium, are very important components of many products and if they begin to corrode, the integrity of the structure may be in jeopardy [43]. Another example is the use of self-healing vanadia coatings for aerospace-grade aluminum and magnesium alloys that have been reported recently, opening new opportunities for producing functional self-healing coatings in aerospace and other advanced technology industries [44, 45].

Conductive polymer coatings, based on polyaniline and polypyrrole, also attracted great interest for the design of protective coatings, especially because of their ability to actively store ions. This intrinsic property confers with intrinsic self-healing coatings through a specific process attributed to the reduction and healing of the conductive polymers by releasing anions into the system when they are damaged. This self-healing ability, combined with an eco-friendly nature, make self-healing conductive polymer coatings promising candidates to replace traditional hexavalent chromium coating, which are well known to be toxic and easily damaged. Interestingly, self-healing conductive materials can also be used as adhesives and metal fillers, which act as a channel for charge transport while also mechanically strengthening the solid substrate. These new materials are considered as one of the most promising replacements for Pb-based solders in electronic assembly applications. In a recent report, polystyrene was utilized to generate microcapsules, which were filled with silver nanowires and dimethylbenzylamine. Upon external stimuli and/or damage, the microcapsules are broken, thus releasing a healing agent capable of repairing cracks. In addition to the mechanical healing, the conductive silver nanowires can restore the conductivity, improving the self-healing efficiency and completely restoring the initial functionality of the adhesive.

3.4.4 Biomedical Engineering

Hydrogels are three-dimensional networks composed of hydrophilic polymers, which possess the ability to absorb a large amount of water (up to thousands of times their dry weight), thus generating a mimic of in vivo conditions. Hydrogels with the ability to achieve autonomous self-healing of its initial properties after being damaged are defined as “self-healing hydrogels.” In contrast to conventional hydrogels, self-healing hydrogels exhibit greater potential for application, especially in the biomedical and bioengineering field. These applications include cell therapy, tissue engineering, and drug delivery systems. For example, in the field of cartilage and bone tissue engineering, self-healing hydrogels have shown great promise as hydrogels are considered as good scaffolds for cartilage tissues. When implanted in vivo, classic hydrogels generally suffer from poor integration to the surrounding cartilage tissue, thus increasing the risks of fracture. However, when a dynamic reversible acylhydrazone bond is incorporated into the rational design of

EBSCOhost - printed on 2/14/2023 1:06 PM via . All use subject to https://www.ebsco.com/terms-of-use

the hydrogel, autonomous self-healing is enabled, resulting in an enhanced adhesion to tissues and cartilages. Such adhesion is resulting directly from the dynamic Schiff-base reaction between surface aldehyde moieties of the hydrogel and the amide moieties located at the surface of the cartilaginous tissue. Such dynamic interactions drastically enhance the adhesive strength, capable of reaching a maximum pressure resistance of 10 kPa [44].

3.4.5 Petroleum Extraction

Sealing of wellbores in geothermal and tight oil/gas reservoirs by filling the annulus with cement is a well-established practice during the petroleum extraction process. However, failure of the cement, as a result of physical and/or chemical stress, is a common problem with serious environmental and financial consequences. To address this challenge, a self-healing polymer-cement composite was prepared by combining self-healable thermoset disulfide containing epoxy resins with class H wellbore cement. The thermal stability and mechanical strength of the resulting self-healing polymer–cement composites were drastically improved, which was attributed to the formation of numerous chemical interactions between the polymer and cement matrix, including covalent bonds, hydrogen bonding, and van der Waals interactions. Self-healing properties were demonstrated by sealing fractures with 0.3–0.5 mm apertures, two orders of magnitude larger than typical wellbore fractures. This polymer–cement composite represents a major advance in wellbore cementing that could improve the environmental safety and economics of enhanced geothermal energy and tight oil/gas production [45].

3.5 Conclusion and Perspectives

As discussed in this chapter, self-healing materials are promising candidates for the development of new applications, including the development of new functional devices with robust conformations and long lifetimes, new ultra-durable coatings and also for aerospace technologies. Although the research on self-healing composites and polymers is still in its infancy, over the past decade, this research field of material sciences highly intensified and achieved significant progress. Specifically, various new strategies toward efficient self-healing has been developed and designed. Among others, the incorporation of microcapsules containing repairing agents showed great promise for efficient self-healing in the polymer matrices. In addition, intrinsic spontaneous self-healing can also now be implemented in various materials directly by rational chemical design and, in fact, synthetic chemistry allowed for the incorporation of dynamic cross-linking moieties into materials. These dynamic

EBSCOhost - printed on 2/14/2023 1:06 PM via . All use subject to https://www.ebsco.com/terms-of-use

interactions, for example, hydrogen bonding, dynamic covalent bonds, thiol–disulfide exchange, and metal–ligand interactions, can spontaneously break and reform upon being damaged, which opens the door to the preparation of a whole new library of self-healable materials that can be fine-tuned through rational design.

Despite the accelerating development of self-healing materials with enhanced efficiency, many challenges still remain to be addressed before using these materials in our day-to-day lives. In fact, for both extrinsic and intrinsic self-healing systems, finding high throughput, scalable, and cost-effective methods for mass production and manufacturing still requires highly focused research efforts. Moreover, many self-healing materials currently used and developed require harsh conditions to trigger self-healing properties including high temperatures, light exposure, physical contact, and so on. Therefore, to overcome such problems, materials that promote spontaneous self-healing or self-healing under milder conditions must be developed.

Self-healing materials are a new and important class of materials that will undoubtedly revolutionize many areas, including consumer goods, advanced technologies, and manufacturing. Moreover, as described and exemplified in this chapter, this field of materials chemistry and polymer science opens new and incredible opportunities of applications for chemists, materials scientists, and engineers.

References

[1] Yang, Y. & Urban, M.W. Self-healing polymeric materials. *Chem. Soc. Rev*. 42, 7446–7467 (2013).
[2] Herbst, F., Döhler, D., Michael, P. & Binder, W.H. Self-healing polymers via supramolecular forces. *Macromol. Rapid Commun*. 34, 203–220 (2013).
[3] Zhang, B. *et al*. Self-healing, malleable and creep limiting materials using both supramolecular and reversible covalent linkages. *Polym. Chem*. 6, 7368–7372 (2015).
[4] De Nardi, C., Bullo, S., Cecchi, A. & Ferrara, L. Self-healing capacity of advanced lime mortars. *Adv. Mater. Process. Technol*. 2, 349–360 (2016).
[5] Diesendruck, C.E., Sottos, N.R., Moore, J.S. & White, S.R. Biomimetic Self-Healing. *Angew. Chem. Int. Ed*. 54, 2–22 (2015).
[6] Wu, D.Y., Meure, S. & Solomon, D. Self-healing polymeric materials: A review of recent developments. *Prog. Polym. Sci*. 33, 479–522 (2008).
[7] Brinkman, E. *Self healing materials concept and applications, Second Edition. NL Agency, Focus on Innovation* 100, (2011).
[8] White, S.R. *et al*. Autonomic healing of polymer composites. *Nature* 409, 794–797 (2001).
[9] Yang, J. *et al*. Microencapsulation of Isocyanates for Self-Healing Polymers, *Macromolecules*, 41, 9650–9655 (2008).
[10] Rajput, A. & Mukherjee, R. Coordination chemistry with pyridine/pyrazine amide ligands. Some noteworthy results. *Coord. Chem. Rev*. 257, 350–368 (2013).
[11] Cash, J.J.; Kubo, T.; Bapat, A.P.; Sumerlin, B.S. Room-Temperature Self-Healing Polymers Based on Dynamic- Covalent Boronic Esters. *Macromolecules* 48, 2098–2106 (2015).

EBSCOhost - printed on 2/14/2023 1:06 PM via . All use subject to https://www.ebsco.com/terms-of-use

[12] Chen, Y., Kushner, A.M., Williams, G.a. &Guan, Z. Multiphase design of autonomic self-healing thermoplastic elastomers. *Nat. Chem*. 4, 467–472 (2012).
[13] Sijbesma, R.P. *et al*. Reversible polymers formed from self-complementary monomers using quadruple hydrogen bonding. *Science* 278, 1601–1604 (1997).
[14] Cordier, P., Tournilhac, F., Soulié-Ziakovic, C. & Leibler, L. Self-healing and thermoreversible rubber from supramolecular assembly. *Nature* 451, 977–980 (2008).
[15] Mozhdehi, D. *et al*. Self-Healing Multiphase Polymers via Dynamic Metal-Ligand Interactions Self-Healing Multiphase Polymers via Dynamic Met- al-Ligand Interactions. *J. Am. Chem. Soc*. 136, 16128–16131 (2014).
[16] Tang, Z., Huang, J., Guo, B., Zhang, L. & Liu, F. Bioinspired Engineering of Sacrificial Metal-Ligand Bonds into Elastomers with Supramechanical Performance and Adaptive Recovery. *Macromolecules* 49, 1781–1789 (2016).
[17] Li, C.-H. *et al*. A highly stretchable autonomous self-healing elastomer. *Nat. Chem*. 8, 1–7 (2016).
[18] Sandmann, B. *et al*. The Self-Healing Potential of Triazole. *Macromol. Rapid Commun*. 36, 604–609 (2014).
[19] Holten-Andersen, N. *et al*. Metal-coordination: using one of nature's tricks to control soft material mechanics. *J. Mater. Chem. B* 2, 2467 (2014).
[20] Imato, K. *et al*. Self-healing of chemical gels cross-linked by diarylbibenzofuranone-based trigger-free dynamic covalent bonds at room temperature. *Angew. Chem. Int. Ed*. 51, 1138–1142 (2012).
[21] Nasresfahani, A. & Zelisko, P.M. Synthesis of a self-healing siloxane-based elastomer cross-linked via a furan-modified polyhedral oligomeric silsesquioxane: investigation of a thermally reversible silicon-based cross-link. *Polym. Chem*. 8, 2942–2952 (2017).
[22] Chao, A., Negulescu, I. & Zhang, D. Dynamic Covalent Polymer Networks Based on Degenerative Imine Bond Exchange: Tuning the Malleability and Self-Healing Properties by Solvent. *Macromolecules* 49, 6277–6284 (2016).
[23] Pepels, M., Filot, I., Klumperman, B. & Goossens, H. Self-healing systems based on disulfide–thiol exchange reactions. *Polym. Chem*. 4, 4955 (2013).
[24] Deng, G. *et al*. Dynamic hydrogels with an environmental adaptive self-healing ability and dual responsive Sol-Gel transitions. *ACS Macro Lett*. 1, 275–279 (2012).
[25] Zhang, Z.P., Rong, M.Z., Zhang, M.Q. & Yuan, C. Alkoxyamine with reduced homolysis temperature and its application in repeated autonomous self-healing of stiff polymers. *Polym. Chem*. 4, 4648 (2013).
[26] Yuan, C., Rong, M.Z., Zhang, M.Q., Zhang, Z.P. & Yuan, Y.C. Self-healing of polymers via synchronous covalent bond fission/radical recombination. *Chem. Mater*. 23, 5076–5081 (2011).
[27] Habault, D., Zhang, H. & Zhao, Y. Light-triggered self-healing and shape-memory polymers. *Chem. Soc. Rev*. 42, 7244 (2013).
[28] Lendlein, A., Jiang, H., Jünger, O. & Langer, R. Light-induced shape-memory polymers. *Nature* 434, 879–882 (2005).
[29] Li, J.. *et al*. Self-Propelled Nanomotors Autonomously Seek and Repair Cracks. *Nano Lett*. 15, 7077–7085 (2015).
[30] Wagner, S. & Bauer, S. Materials for stretchable electronics. *MRS Bull*. 37, 207–213 (2012).
[31] Rim, Y.S., Bae, S.H., Chen, H., De Marco, N. & Yang, Y. Recent Progress in Materials and Devices toward Printable and Flexible Sensors. *Adv. Mater*. 28, 4415–4440 (2016).
[32] Guo, X., Baumgarten, M. & Müllen, K. Designingπ-conjugated polymers for organic electronics. *Prog. Polym. Sci*. 38, 1832–1908 (2013).

EBSCOhost - printed on 2/14/2023 1:06 PM via . All use subject to https://www.ebsco.com/terms-of-use

[33] Savagatrup, S., Printz, A.D., O'Connor, T.F., Zaretski, A.V. & Lipomi, D.J. Molecularly stretchable electronics. *Chem. Mater*. 26, 3028–3041 (2014).
[34] Horowitz, G. Organic Field-Effect Transistors. *Adv. Mater*. 10, 365–377 (1998).
[35] Rao, Y.L. *et al*. Stretchable self-healing polymeric dielectrics cross-linked through metal-ligand coordination. *J. Am. Chem. Soc*. 138, 6020–6027 (2016).
[36] Ko, J., Kim, Y.J. & Kim, Y.S. Self-Healing Polymer Dielectric for a High Capacitance Gate Insulator. *ACS Appl. Mater. Interfaces* 8, 23854–23861 (2016).
[37] Oh, J.Y. *et al*. Intrinsically stretchable and healable semiconducting polymer for organic transistors. *Nature* 539, 411–415 (2016).
[38] Bartczak, T.J.; Michalska, Z.M.; Ostaszewski, B.; Sobota, P.; Strzelec, K. Synthesis, characterization and X-ray structures of the model ligand for a coordination polymer: diethyl-2,6-pyridine dicarboxamide and its complex with PdCl2. *Inorg. Chem. Acta* 319, 229–234 (2001).
[39] Lipomi, D.J. *et al*. Skin-like pressure and strain sensors based on transparent elastic films of carbon nanotubes. *Nat. Nanotechnol*. 6, 788–792 (2011).
[40] Das, R., Melchior, C. & Karumbaiah, K.M. *Self-healing composites for aerospace applications*. *Advanced Composite Materials for Aerospace Engineering* (Elsevier Ltd, 2016). doi:10.1016/B978-0-08-100037-3.00011-0
[41] L, G.-H., Cheng, L.-F., Luan, X.-G. & Liu, Y.-S. Self-healing Behavior of 2D-C/[SiC-(B-C)] Composite in Aero-engine Combustion Chamber. *J. Inorg. Mater*. 26, 969–973 (2011).
[42] Zhao, Y., Zhang, W., Liao, L.P., Wang, H.M. & Li, W.J. The self-healing composite anticorrosion coating. *Phys. Procedia* 18, 216–221 (2011).
[43] Hamdy, A.S. & Butt, D.P. Novel smart stannate based coatings of self-healing functionality for AZ91D magnesium alloy. *Electrochim. Acta* 97, 296–303 (2013).
[44] Hamdy, A.S., Doench, I. & Möhwald, H. Smart self-healing anti-corrosion vanadia coating for magnesium alloys. *Prog. Org. Coat.* 72, 387–393 (2011).
[45] Hamdy, A.S., Doench, I. & Möhwald, H. Intelligent self-healing corrosion resistant vanadia coating for AA2024. *Thin Solid Films* 520, 1668–1678 (2011).

EBSCOhost - printed on 2/14/2023 1:06 PM via . All use subject to https://www.ebsco.com/terms-of-use

William L. Odette, Janine Mauzeroll

4 Redox-Responsive Self-Assembled Amphiphilic Materials: Review and Application to Biological Systems

Redox-responsive self-assembled materials comprise a broad and diverse field employing a range of structures including polymers, dendrimers, nanoparticles, and supramolecular nanosheet gels. Such materials may be employed in a range of applications including energy storage, electronics, sensors, catalysis and biomedicine. In this chapter we present a review of redox-responsive lipid (and lipid-like) materials in addition to current developments and future directions in the field. Our discussion focuses primarily micellar and liposomal systems in the context of biomedical applications.

4.1 Introduction

Lipid-based systems (e.g., liposomes) were rapidly identified as promising advanced materials for the delivery of therapeutics following their first description in 1965 [1]. In the ensuing decades, liposomes and other lipidic materials have found broad application in fields such as diagnostic imaging [2], vaccine delivery [3] and cosmetics [4], but delivery of (primarily antitumor and antimicrobial [5]) therapeutics remains the most intense area of lipid nanocarrier research [6]. Mechanistically, the action of lipid-based therapeutics ranges from relatively simple – for example, the increased circulation time of otherwise poorly soluble drugs such as doxorubicin as seen in Doxil®, the first clinically approved liposomal formulation [7] – to increasingly complex stimulus-responsive delivery of therapeutic cargo as seen in ThermoDox®, a heat-responsive liposomal doxorubicin formulation currently in phase III clinical trials [8]. Despite the apparent promise of such materials as medical adjuvants, the significant heterogeneity observed (in the most well-studied case of chemotherapeutic systems) in different cancer cell lines and tumor tissues has led to significant challenges in overcoming the transition from in vitro studies and animal tumor models to clinically relevant preparations for use in humans [9]. Stimuli-responsive systems represent a promising avenue of inquiry in overcoming the implicit shortcomings of nanoparticulate delivery systems; a wide variety of intrinsic and extrinsic stimuli exist which may be exploited including temperature (e.g., heat-responsive ThermoDox®), pH, light, magnetic field, enzymes and redox gradients. Herein the focus is on redox-sensitive lipid-based materials – including nonbilayer forming surfactants – and their potential for application in

William L. Odette, Janine Mauzeroll, Department of Chemistry, McGill University, Canada

https://doi.org/10.1515/9783110537734-004

EBSCOhost - printed on 2/14/2023 1:06 PM via . All use subject to https://www.ebsco.com/terms-of-use

biological systems, primarily in the context of drug delivery. Inherently nontoxic, biodegradable and biocompatible [10], liposomes and other lipid-based systems comprise approximately 50% of clinically approved nanodrugs at present [11, 12]. Coupled with the well-characterized but still largely unexplored redox environment as a source of stimuli-responsive trigger mechanisms, redox-responsive lipidic materials represent a wellspring of potential for the development of clinically relevant therapeutic systems.

4.2 Redox Environment of Disease States

4.2.1 Reactive Oxygen/Nitrogen Species and the Cellular Redox Environment

Background

Cellular redox homeostasis, governed by the production and removal of reactive oxygen and nitrogen species (RONS), is critical for normal cell function. The relationship of RONS to cellular processes is multifaceted, comprising a diverse array of reactive (neutral and radical) species critical to the regulation of redox signaling and maintenance of antioxidant–oxidant balance [13]. RONS are frequently invoked in a general sense in the context of cellular pathophysiology, but it is important to note that the true picture of reactive species in the cell – their identity, production, regulation and function – is far too complex to be summarized with simple umbrella terms, for example, "RO(N)S accumulation" or "RO(N)S induction" (Figure 4.1). Differences in the concentration as well as subcellular localization of a given reactive species may have a profound effect on its function, that is, differentiation between functioning as a toxin or as a signaling molecule [14].

As material chemists it is our aim to provide sufficient background to understand in broad strokes the importance of RONS in normal cellular function as well as the imbalances in cellular redox homeostasis characteristic of certain disease states (discussed in section 2.2) that may be exploited by redox-responsive functional materials. This discussion of the importance of redox chemistry to cellular function underscores the importance of the cellular redox environment as a potential therapeutic target. A summary of some biologically relevant redox couples and their standard potentials is included in Table 4.1, illustrating the broad potential range in which redox reactions occur in a biological context. While efforts to date have focused on a relatively small number of reliable and well-characterized couples (e.g., glutathione/GSSG), there remains significant room for the expansion of the "toolbox" of redox-responsive advanced materials in the broad spectrum of biologically compatible redox couples.

In the intentional design of redox-responsive materials for biological applications, it is important to have at least a passing familiarity with the key aspects of the cellular redox environment at both the component and systems levels, to have

EBSCOhost - printed on 2/14/2023 1:06 PM via . All use subject to https://www.ebsco.com/terms-of-use

a better understanding of the factors influencing redox homeostasis and where these factors may be exploited in the process of material design. A comprehensive overview of cellular redox homeostasis and its component parts is shown in Figure 4.1. The discussion will focus primarily on endogenous sources of intra- and extracellular RONS. Exogenous RONS sources such as UV light represent an irregular and to a large extent unpredictable contribution to the cellular redox environment; they are unattractive from a material design standpoint and will therefore be omitted from this discussion. Antioxidant systems will be considered with regard to their complementary function to RONS-producing systems but will not be elaborated at length in isolation.

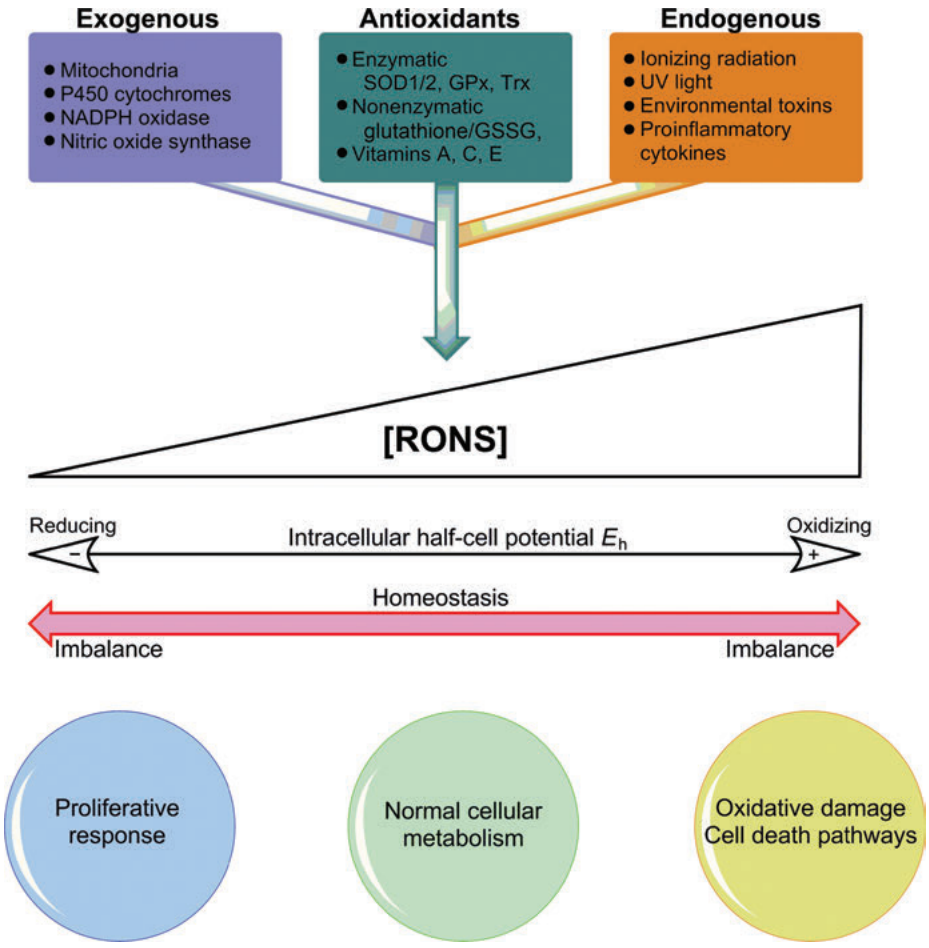

Figure 4.1: The cellular redox environment, contributing systems and physiological outcomes.

EBSCOhost - printed on 2/14/2023 1:06 PM via . All use subject to https://www.ebsco.com/terms-of-use

Table 4.1: Biological and biocompatible redox couples.

Couple	E^o/V (pH if =/=7.0)	Couple	E^o/V (pH if =/= 7.0)
$HO^•, H^+/H_2O$	2.31	Fe(III)/Fe(II) (cytochrome c)	0.26
$H_3CH_2C^•, H^+/CH_3CH_3$	1.9	Semiubiquinone, H^+/ubiquinol ($CoQ^{•-}$, $2H^+/CoQH_2$)	0.20
$O_3^•, 2H^+/H_2O, O_2$			
$RO^•, H^+$/ROH (aliphatic alkoxy radical)	1.8	Fe(III)/Fe(II) (EDTA)	0.12
	1.6	Fe(III)/Fe(II) (aqueous)	0.11
$N_3^•/N_3^-$	1.33	Ubiquinone/ubiquinol ($CoQ/CoQH_2$)	0.1
$^•CH_2OH, H^+/CH_3OH$	1.2	TEMPO ($R_2NO^•, H^+/R_2NOH$)	0.08
$Fe(III)(1,10\text{-phen})_3/Fe(II)(1,10\text{-phen})_3$	1.15	Fe(III)/Fe(II) (cytochrome b)	0.05
$HOO^•, H^+/H_2O_2$	1.06	Fe(III)/Fe(II) (DETAPAC)	0.03
$ROO^•, H^+$/ROOH (alkylperoxy radical)	1.0[a]	Fumarate/succinate	0.03
$Allyl^•, H^+$/allyl-H	0.96	Ubiquinone, H^+/semiubiquinone ($CoQ/CoQ^{•-}$)	–0.036
$O_2^{•-}, 2H^+/H_2O_2$			
$RS^•/RS^-$ (cysteine)	0.94	Oxaloacetate/malate	–0.17
$C_6H_5O^•, H^+/C_6H_5OH$	0.92	Dehydroascorbic acid/$ascorbate^{•-}$	–0.17
$O_3/O_3^{•-}$	0.90	Pyruvate/lactate	–0.19
$O_2, 4H^+/2H_2O$	0.89	Fe(III)/Fe(II) (ferritin)	–0.19
Cyclopentenyl-$3^•, H^+$/cyclopentenyl-H	0.82	FAD, $2H^+/FADH_2$	–0.22
Cyclopentadien-1,3-yl-$5^•, H^+$/H-cyclopentadien-1,3-yl-5	0.70	Duroquinone/$duroquinone^{•-}$	–0.26
	0.65	Riboflavin/$riboflavin^{•-}$	–0.32
O_2 (1Δg)/$O_2^{•-}$	0.65	$NAD^+, 2H^+$/NADH, H^+	–0.32
Pentadien-1,4-yl-$3^•$, H-pentadien-1,4-yl-3	0.60	$NADP^+, 2H^+$/NADPH, H^+	–0.324
	0.60	$O_2/O_2^{•-}$	–0.33
$PUFA^•, H^+$/PUFA-H (polyunsaturated fatty acid, bis-allylic H)	0.59	Adriamycin/$adriamycin^{•-}$	–0.34
	0.54	Fe(III)/Fe(II) (transferrin)	–0.4 (7.3)
$HU^{•-}, H^+/UH_2$– (urate)	0.53	Fe(III)/Fe(II) (ferredoxin)	–0.45
Cu(II)/Cu(I) (hemocyanin)	0.50	Paraquat/$paraquat^{•-}$	–0.45
Catechol-$O^•, H^+$/catechol-OH	0.48	Fe(III)/Fe(II) (desferal)	–0.45
α-Tocopheroxyl$^•, H^+$/α-tocopherol (vitamin E)	0.37	$O_2, H^+/HO_2^•$	–0.46
	0.32	Acetate/pyruvate	–0.7
Trolox C (T-$O^•, H^+$/TOH)[b]	0.28	RSSR/$RSSR^•$ (cystine or GSSG)	–1.5
Fe(III)/Fe(II) (cytochrome f)	0.28	$CO_2/CO_2^•$	–1.8
$H_2O_2, H^+/H_2O, ^•OH$		H_2O/e^-_{aq}	–2.9
Fe(III)/Fe(II) (cytochrome a)			
Ascorbate$^•, H^+$/ascorbate– (vitamin C)			

a Peroxyl radicals may have a wide range of reduction potentials, 0.77 V < E^o < 1.4 V.

b 6-Hydroxy-2,5,7,8-tetramethyl-chromane-2-carboxylic acid, a water-soluble analog of vitamin E.

EBSCOhost - printed on 2/14/2023 1:06 PM via . All use subject to https://www.ebsco.com/terms-of-use

Intracellular RONS Sources and Generation

Oxygen-metabolizing enzymatic systems and the mitochondrial electron transport chain are the primary source of endogenously generated intracellular RONS. The subsequent discussion provides an overview of the most important contributors to the cellular redox environment (shown in Figure 4.2) and will hopefully provide a baseline of information such that chemists designing redox-active materials will have a more thorough picture of redox homeostasis and the elements that might be targeted or exploited in advanced material design.

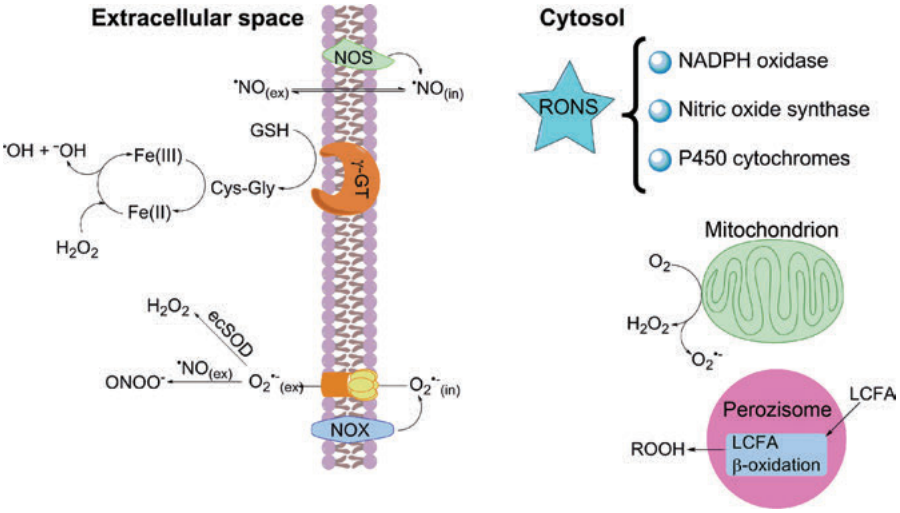

Figure 4.2: Major physiological RONS sources. Certain minor contributors, for example, lipoxygenase, cyclooxygenase and endoplasmic reticulum stress have been omitted for clarity.

Cytochromes P450

P450 cytochromes [15] or CYP450 encompasses a broad family of (primarily but not exclusively) membrane-bound [16] monooxygenase enzymes predominantly localized in the mitochondria and endoplasmic reticulum [17]. Cytochromes P450 catalyze the transfer of a single oxygen atom from molecular oxygen (O_2) to a substrate in a two-electron process that oxidizes one equivalent of NADPH and produces one equivalent of H_2O as a byproduct [18]. The specific process catalyzed by CYP450 enzymes can vary significantly from carbon hydroxylation and heteroatom oxygenation to epoxidation of olefins and aldehyde oxidation [19]. The structure and specific function of CYP450 enzymes vary greatly; they are frequently implicated in metabolism of drugs [20], steroids [21] and carcinogens [22], but the manifold cellular functions of CYP450 and other oxygen-metabolizing enzymatic systems discussed herein exclusive of their ability to generate reactive oxygen species are outside the scope of this chapter.

EBSCOhost - printed on 2/14/2023 1:06 PM via . All use subject to https://www.ebsco.com/terms-of-use

NADPH Oxidases

NADPH oxidases [23] are a family of membrane-bound proteins that facilitate the transport of electrons across biological membranes. NADPH oxidases (NOX) differ from CYP450 enzymes in that the generation of reactive oxygen species is the primary function of NOX [24], while RONS generation by CYP450 occurs via substrate oxygenation. Functionally, NOX enzymes act as transmembrane redox chains that connect the electron donor – cytosolic NADPH – with the terminal acceptor, molecular oxygen in the phagosomal or extracellular space [25]. The prototypical role of NOX enzymes occurs in phagocytic vacuoles in neutrophils, a type of white blood cell. Reduction of molecular oxygen generates superoxide, which results in a transmembrane potential gradient [26], and the compensatory ion flux across the membrane is thought to optimize conditions for the digestive functions of the granule enzymes [27].

Nitric Oxide Synthase

Nitric oxide ($^{\bullet}$NO) is an important signaling compound with a diverse variety of functions ranging from the regulation of vascular tone [28] to posttranslational modification (PTM) of proteins [29]. NO can react with superoxide to generate peroxynitrite ($ONOO^{-}$), a potent oxidant and potential source of oxidative stress in cells [30]. Nitric oxide synthases [31] (NOS) produce NO in a two-step process utilizing L-arginine as the substrate and NADPH and molecular oxygen as cosubstrates and generating L-citrulline as a byproduct [32].

Mitochondria

In addition to cytoplasmic and membrane-bound enzymes, the mitochondrial electron transport chain represents the other major endogenous source of intracellular RONS [33]. Briefly, four enzymatic complexes located in the mitochondrial inner membrane (Figure 4.3) catalyze a series of redox processes with the two-electron reduction of molecular oxygen to water as the terminal step [34]. The process generates a proton gradient across the mitochondrial membrane that drives the synthesis of ATP [35]. Generation of RONS at the inner mitochondrial membrane primarily results from “leakage” of the electron transport chain leading to one-electron reduction of molecular oxygen to produce superoxide [36]. Although it is thermodynamically feasible for a number of mitochondrial small-molecule electron donors to carry out this reduction, formation of superoxide is primarily governed by kinetic factors at redox-active protein functionalities and protein-bound electron carriers such as reduced coenzyme Q [37]. The rate of superoxide production may be approximated by

$$\left(\frac{\mathrm{d}\left[O_2^{\bullet -}\right]}{\mathrm{d}t}\right)_{\text{total}} = [O_2] \sum_i \left(K_E P_R [E]\right)_i \tag{4.1}$$

With the relevant kinetic factors [38] being the concentration of enzyme or protein-bearing redox-active moieties [E], the proportion of electron carriers in the protein in a redox state capable of carrying out the reduction of oxygen to superoxide P_R,

EBSCOhost - printed on 2/14/2023 1:06 PM via . All use subject to https://www.ebsco.com/terms-of-use

EBSCOhost - printed on 2/14/2023 1:06 PM via . All use subject to https://www.ebsco.com/terms-of-use

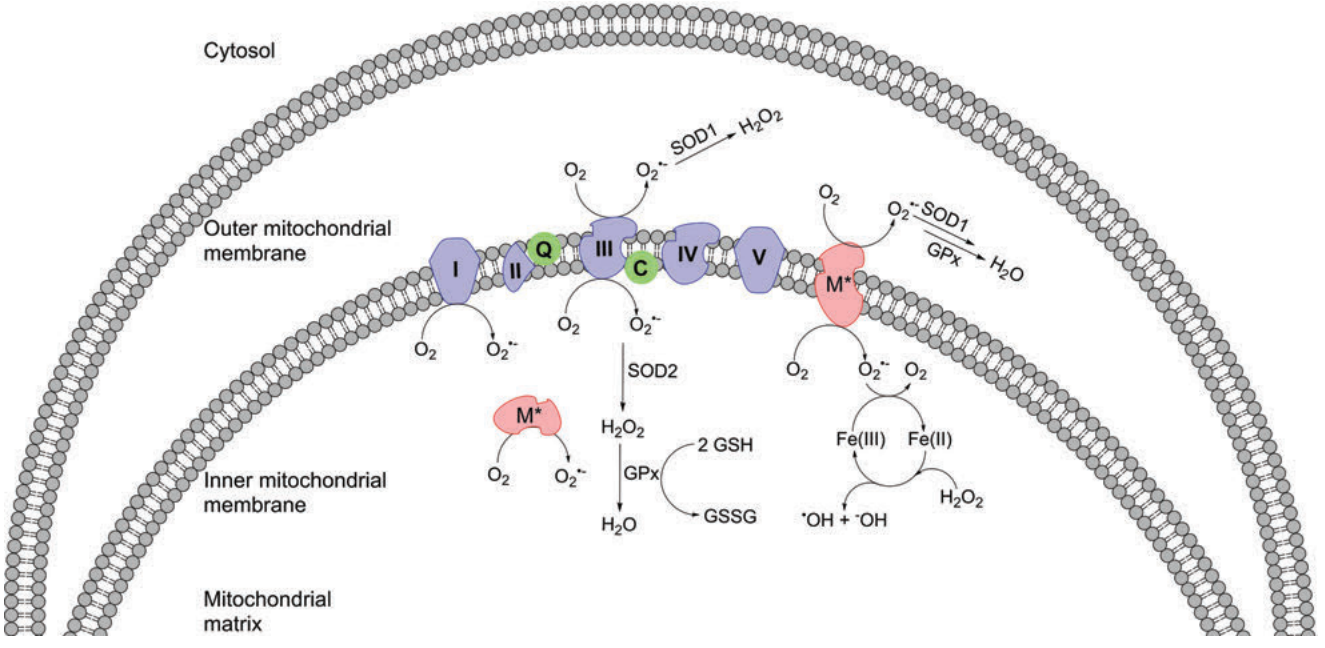

Figure 4.3: RONS production in the mitochondrial electron transport chain. SOD1 and SOD2 refer to Cu–Zn and Mn–superoxide dismutase, respectively. M* represents mitochondrial metabolic enzymes, for example, pyruvate dehydrogenase and ubiquinone oxidoreductase, which contribute to RONS generation in the mitochondrion insufficiently to merit individual elaboration. It should be presumed that Fenton and Haber–Weiss processes occur in the intermembrane space as well as the mitochondrial matrix. Q = coenzyme Q10, C = cytochrome c.

the local $[O_2]$ and the second-order rate constant for the one-electron reduction of oxygen K_E. The kinetic variables are taken as a sum over all possible electron–donor sites within a given environment (e.g., single protein and mitochondrion).

Despite the various mechanisms by which superoxide may be produced in the inner mitochondrial membrane, high local concentrations of manganese superoxide dismutase (MnSOD) in addition to other RONS removal sources (e.g., glutathione) can prevent mitochondria from serving as a net source of RONS under normal nonpathological conditions [39]. However, disproportionation of superoxide to H_2O_2 proximal to free iron atoms released from iron–sulfur clusters or heme groups (iron–sulfur cluster assembly machinery is located in the mitochondrion [40], and electron transport chain complexes contain Fe–S clusters) may also generate hydroxyl radicals by Fenton (eqs. (4.3)–(4.4)) and/or Haber–Weiss (eqs. (4.2)–(4.4), net reaction (4.5)) chemistry:

$$L_nFe^{3+} + O_2^{\bullet -} \rightleftharpoons L_nFe^{2+} + O_2 \tag{4.2}$$

$$L_nFe^{2+} + H_2O_2 \rightleftharpoons L_nFe(H_2O_2)^{2+} \tag{4.3}$$

$$L_nFe(H_2O_2)^{2+} \rightleftharpoons L_nFe^{3+} + \bullet OH + {}^{-}OH \tag{4.4}$$

$$O_2^{\bullet -} + H_2O_2 \rightleftharpoons O_2 + {}^{\bullet}OH + {}^{-}OH \tag{4.5}$$

In addition to the inner membrane-bound mitochondrial electron transport chain, monoamine oxidase enzymes located on the outer mitochondrial membrane produce stoichiometric amounts of H_2O_2 as a byproduct of the oxidative deamination of biogenic amines and therefore represent another source of RONS in the mitochondrion [41].

The Extracellular Redox Environment

In the discussion of redox-responsive materials for biological applications, it is necessary to consider both intra- and extracellular redox environments as the extracellular space will be the first environment encountered by an externally administered nanocarrier.

As discussed earlier, NADPH oxidase and nitric oxide synthase are located in the plasma membrane and contribute to the generation of RONS in both the intra- and extracellular spaces. Superoxide ($O_2^{\bullet -}$) generated by NOX is membrane impermeable but may pass through the pores of ion channels located in the plasma membrane [42]. Enzymatic disproportionation of $O_2^{\bullet -}$ produces H_2O_2, which may lead to the formation of hydroxyl radicals. Superoxide may also react with $^{\bullet}NO$ in the extracellular space to form peroxynitrite ($ONOO^-$). In a similar fashion to superoxide, nitric oxide can be enzymatically generated in both the intra- and extracellular spaces by membrane-bound NOSs. As a neutral compound, $^{\bullet}NO$ may also diffuse freely across the plasma membrane [43]. γ-Glutamyl transferase (GGT) is an another important membrane-bound regulator of the extracellular redox environment that catalyzes the first steps in the degradation of extracellular glutathione (GSH), an important cellular redox mediator [44].

EBSCOhost - printed on 2/14/2023 1:06 PM via . All use subject to https://www.ebsco.com/terms-of-use

The role of GGT in maintenance of redox homeostasis and reduction of oxidative stress is complex; degradation of GSH generates free cysteine which can serve as an antioxidant [45], but cysteinyl glycine (an intermediate product of GSH degradation) can reduce Fe(III) to redox-active Fe(II), leading to lipid peroxidation and generation of hydroxyl radicals [46]. Key components influencing extracellular redox homeostasis are shown in Figure 4.2.

In addition to membrane-bound enzymes, serum proteins comprise the remainder of enzymatic extracellular redox environment modulators. The extracellular form of superoxide dismutase catalyzes the disproportionation of $O_2^{\bullet -}$ to H_2O_2 in the extracellular space to prevent iron reduction and conversion of $^{\bullet}NO$ to peroxynitrite by superoxide. Glutathione peroxidase-3 (GPX3) utilizes GSH to catalyze the reduction of lipid hydroperoxides, although in vitro experiments have suggested that glutaredoxin and thioredoxin (TRX) may function as electron sources for GPX3 due to the low GSH concentration in plasma [47]. Other minor enzymatic contributors to regulation of the extracellular redox environment include a secreted form of thioredoxin reductase-1, extracellular catalase and paraoxonase-1 [48].

While most of the attention has been directed at enzymatic redox regulators, small-molecule redox couples are a critical aspect of redox homeostasis in both the intra- and extracellular environments. In the extracellular space, thiol/disulfide couples are the critical redox regulators; cell surface and extracellular thiols are critical components of cellular functions including signal transduction and ligand binding [49]. Important thiol-disulfide redox regulators include cysteine (CyS)/cystine (CySS), glutathione (GSH)/glutathione disulfide (GSSG) and thioredoxin (TRXSH)/thioredoxin disulfide (TRXSS) [50].

Although its precise role in the overall picture of physiological redox homeostasis is poorly characterized, it is important to consider the contribution of the microbiome as a nontrivial contributing factor. The human body is a host to vast numbers of bacteria [51] comprising a stable and regulated community [52], and the importance of these communities to normal physiological function, especially in the context of the intestines, has only begun to be intensively investigated in recent years. Alterations in both community composition (i.e., relative abundance of bacterial taxa) and microbial function have been linked to a number of pathological conditions including inflammatory bowel disease [53], type 2 diabetes and rheumatoid arthritis [54]. In addition to specific correlation to pathological states, redox-dependent signaling has been implicated as an important factor in the regulation of microbial influence on gut physiology more generally [55]. Taken together, gut microbes and the broader human microbiome represent a relatively unknown metabolic organ whose contribution to the regulation of cellular redox homeostasis should not be neglected.

EBSCOhost - printed on 2/14/2023 1:06 PM via . All use subject to https://www.ebsco.com/terms-of-use

4.2.2 Redox Homeostasis and the Tumor Microenvironment

An imbalance in the cellular redox environment, primarily due to overproduction of RONS or antioxidant deficiency [56], is observed in many disease states including cancer, fibrosis, cardiovascular disease and diabetes [57]. As the application of redox-responsive lipid materials is frequently aimed at the delivery of chemotherapeutic agents for cancer treatment, a brief overview of the corruption of redox homeostasis mechanisms and a general picture of the tumor redox environment will be provided.

As previously described for nonpathological states, the cellular redox environment is described as the net balance of redox couples in dynamic equilibrium in both the intra- and extracellular spaces [58]. This balance is governed by a highly complex network including transcriptional/translational regulation, PTM, RONS production and antioxidant degradation and intracellular signaling pathways. Tumor tissue may exhibit dysregulation in one of several points of this regulatory network, giving rise to the high degree of heterogeneity observed in different cancer cell lines.

Genetic Determinants of the Tumor Redox Environment

Tumor Suppressors, Oncogenes and Antioxidant Enzymes

Oncogene activation and loss of tumor suppressor genes are known to be important factors in carcinogenesis. Generally, oncogenes are the result of gain-of-function mutations in proto-oncogenes and comprise a major factor in the progression of cancer along with the loss-of-function mutations in tumor suppressor genes. The products of oncogenes have diverse functions typically associated with the promotion of cell proliferation; they may serve as transcription factors, growth factors/growth factor receptors, regulators of apoptosis (programmed cell death) or chromatin remodelers, and their function may encompass several such areas [59]. The function of tumor suppressor gene products is typically linked to the suppression of cell proliferation and may include the inhibition of cell division through transcriptional repression, DNA damage repair or induction of apoptosis [60].

The accumulation of mutations in proto-oncogenes and tumor suppressor genes sufficient to overcome normal cellular regulatory function will ultimately result in tumorigenesis and the development of cancer. One of the most important and intensely studied tumor suppressors is p53; some 50% of all malignancies exhibit mutations in the p53 gene, and a large proportion of those lacking a p53 mutation have inactivated it by an alternative mechanism [61]. In vitro studies and animal models of subjects with defective p53 display increased RONS stress in addition to high rates of mutagenesis and tumor growth [62]. Increased RONS production is also associated with expression of several oncogenes including *Ras* and *Myc* [63]. Constitutive activation of Ras, a GTPase implicated broadly in intracellular signaling pathways, is common in a variety of cancers [64]. Ras expression has been shown to promote RONS

EBSCOhost - printed on 2/14/2023 1:06 PM via . All use subject to https://www.ebsco.com/terms-of-use

production [65]; however, evidence suggests that increased RONS production triggered by Ras may trigger either senescence or malignant transformation dependent on the cellular context [66]. Myc is a transcription factor involved in the regulation of genes for many normal cellular functions, including proliferation and apoptosis [67]. Genomic instability may result from abnormal expression of Myc, implicating the *c-Myc* protooncogene in an array of human cancers. Similar to the context-dependent role of Ras, the role of Myc and the increased levels of RONS observed following its activation have a complex relationship to cell death or survival. Overexpression of *c-Myc* has been shown to promote apoptosis through excessive RONS accumulation and inhibition of MnSOD (SOD2) [68], while sensitization of cells to cisplatin was observed following downregulation of *c-Myc* [69].

Aberrant expression of antioxidant enzymes is another important component of altered cellular redox homeostasis in cancer. In mice lacking both Cu-ZnSOD genes, greater than 70% developed tumor nodules and a significantly increased mutation frequency was observed [70]. For heterozygous MnSOD knockout mice, the mitochondrial membrane potential was decreased and mitochondrial oxidative damage was observed; additionally, tumor incidence increased twofold in older animals compared to wild-type mice [71]. Highlighting the importance of the GSH/GSSG redox couple and precise maintenance of the cellular redox environment, transgenic mice overexpressing GPX1 displayed a higher incidence of tumorigenesis in two-stage skin carcinogenesis model studies [72].

Posttranslational Modifications and Epigenetic Changes

PTMs in chromatin (DNA–histone complexes) are the covalent modification of amino acid residues – most commonly serine, threonine, lysine and arginine – in histones, the protein scaffolds around which DNA is organized in the cell and which control the transcriptional activation or repression of a given portion of DNA depending on the chromatin state [73]. Common PTM include methylation, acetylation, phosphorylation and ubiquitination; they influence transcription and protein expression and have been implicated in cancer development and progression [74]. In the context of the altered redox environment of tumors, relevant PTM are those controlled by redox reactions, primarily the oxidation and reduction of thiols (-SH) to disulfides (-SS-) and vice versa. TRX is an important mediator of redox signaling that facilitates reduction of other proteins by cysteine thiol–disulfide exchange [75]. TRX with disulfides at cysteine residues located in the active site is irreversibly inactivated, and data from human prostate and breast cancer cell lines serve to highlight the variable nature of the tumor redox environment: more invasive prostate cancer cell lines show increased TRX oxidation with decreased enzyme activity [76], while studies in breast cancer cells show predominantly the reduced form of TRX with increased enzymatic activity [77]. These data demonstrate that a given tumor may experience either oxidizing or reducing conditions as a consequence of its

EBSCOhost - printed on 2/14/2023 1:06 PM via . All use subject to https://www.ebsco.com/terms-of-use

imbalanced redox environment. Other PTM influenced by redox status in cancer include nitrosylation [78], nitration [79] and glutathionylation [80].

Epigenetic changes include reversible methylation/acetylation of histone proteins as well as DNA methylation/demethylation [81]. As these epigenetic changes have metabolic requirements, for example, the dependence of class III histone deacetylases on NAD^+, redox imbalances have the capacity to drive epigenetic changes through metabolic alterations [82] and are therefore an important component of the tumor redox environment.

Important Features of the Tumor Redox Microenvironment

As carcinogenesis is a feature of tissues and not individual cells, the tumor microenvironment as a whole must be considered in addition to individual cellular factors affecting the tumor redox status. An important physiological parameter of the tumor microenvironment is local hypoxia (chronic or cycling [83]), resulting in increased dependence on anaerobic glycolysis and an acidic local pH (5.6–6.8 compared to 7.2–7.5 intracellularly [84]). Given the plurality of cellular redox couples, it is difficult to obtain a quantitative picture of the tumor redox microenvironment. Due to the high intracellular concentration of glutathione, the GSH/GSSG redox couple is generally accepted as a proxy of the intracellular redox environment [85]. In vivo measurements from animal cancer models have shown a high concentration of intracellular GSH and a shift to more negative (reducing) potentials for the GSH/GSSG couple, a feature of proliferating cells [86]. This observation contrasts with the higher (more positive) redox potential and high oxidizing capacity observed in cells under oxidative stress conditions and in many types of cancer [87]. This apparent contradiction may be resolved by noting that a high reducing capacity will promote electron flux to substrates such as oxygen and iron, leading to superoxide production (and dismutation to H_2O_2) and subsequent generation of hydroxyl radicals via Fenton chemistry. Reduced metal ions themselves such as Fe^{2+} and Cu^+ may serve as electron sources for the reduction of molecular oxygen to $O_2^{\bullet -}$ [88]. Hypoxia-induced acidosis in the extracellular space contributes to liberation of oxidized metal ions (e.g., Fe^{3+} and Cu^{2+}), which are then subject to the reducing tumor microenvironment and RONS generation cascade described previously [89].

In summary, the tumor redox microenvironment cannot be simply described as either oxidizing or reducing. High intracellular concentrations of glutathione lead to an increased reducing capacity, which combined with the hypoxic and acidic extracellular environment create conditions favorable for the generation of high levels of RONS. Genomic instability in cancer cells may facilitate their tolerance of the resulting oxidative stress through overexpression of antioxidant enzymes while the same RONS generation may be highly toxic and/or mutagenic to normal cells in the vicinity of the tumor. While the tumor redox microenvironment is highly complex, the existence of both high

EBSCOhost - printed on 2/14/2023 1:06 PM via . All use subject to https://www.ebsco.com/terms-of-use

oxidizing and high reducing capacities allows for a broad spectrum of mechanisms by which tumors may be targeted by redox-responsive materials for the delivery of therapeutics or imaging agents.

Relevance of Redox Biology in Advanced Material Design

The background information of a relatively detailed overview of the cellular redox environment in a condensed and readily available form is of great utility to material scientists and chemists concerned with the design of redox-responsive materials for application to biological systems. In the context of lipid/surfactant-based materials, the primary application in the biological milieu is drug delivery, especially chemotherapeutic treatments for cancer. As a leading cause of human deaths worldwide (8.8 million in 2015 [90]) and an unavoidable consequence of aging [91] (despite certain factors of aging that contribute to tumor suppression [92]), it seems natural that cancer should receive a significant fraction of attention in the design of nanocarrier-based therapeutics.

The enhanced permeability and retention (EPR) effect has been frequently invoked in the design of chemotherapeutic nanomedicines since its first description 30 years ago [93]. Briefly, the EPR effect refers to the "leaky" nature of tumor vasculature due to vascular fenestrations and aberrant pericyte coverage/extracellular matrix and the consequent extravasation of particles in the size range ca. 10–100 nm [94]. These conditions would promote drug accumulation in tumor tissue and enhance the resultant therapeutic effect. Taken at face value, the EPR effect provides a strong rationale for the design of nanoparticulate drug delivery systems and has often been cited as such, bolstered by promising results in preclinical studies and the clinical success of Doxil®. Recent studies [95] have demonstrated that, in spite of such a promising outlook, the EPR effect generally fails to deliver more than a modest increase in efficacy of drug delivery to tumors compared to normal organs [96]. This failure to translate from preclinical studies and in vivo models is primarily a consequence of differences between murine tumor models and human tumors as well as the high degree of heterogeneity observed in human tumor tissues [97] (e.g., slow vs. fast growing tumors, primary vs. metastatic). Possible strategies to circumvent the limitations in the EPR effect include active targeting of nanomedicines as well as stimuli-responsive activity, taking advantage of endogenous (pH, redox potential, enzyme concentration) stimuli potentially present in the tumor microenvironment or exogenous sources such as temperature, light and magnetic fields [98].

EBSCOhost - printed on 2/14/2023 1:06 PM via . All use subject to https://www.ebsco.com/terms-of-use

4.3 Phosphatidylethanolamine (PE) Lipids and Membrane Fusion

4.3.1 Polymorphic Phase Behavior of Lipids and Surfactants

In the broader context of redox-sensitive lipid-based nanocarriers, the mechanism of cargo delivery typically depends on a redox-triggered disassembly of micellar or bilayer structures. While micelle structures are an important consideration in the context of redox-sensitive lipid-based advanced materials, membrane destabilization and fusion are primarily relevant to bilayer structures.

Polymorphic phase behavior of amphiphilic lipids in aqueous solution is a highly complex process dependent on intermolecular (van der Waals) forces, steric interactions, electrostatics, solution ionic strength and pH, presence of other lipids or proteins and so on. In addition to the commonly encountered micellar and lamellar (bilayer) phases, lipids may adopt a variety of nonlamellar phases including H_I (micellar hexagonal) and H_{II} (inverse micellar hexagonal) and a variety of cubic phases [99] more commonly encountered in the domain of intracellular transport [100]. Despite this complexity, lipid phase behavior can be approximated using relatively simple parameters describing the shape preferences of the individual membrane components [101]. A lipid packing parameter, P, can be assigned ($0 \leq P \leq 1$), given by $P = V/a_e{*}l$ where V and l are the volume and length of the hydrocarbon tail, respectively, and a_e is the cross-sectional headgroup area [102]. A sampling of lamellar and nonlamellar lipid phases and their relation to the lipid packing parameter is shown in Figure 4.4. It is important to note that while a_e is frequently taken to be a simple geometric area corresponding to the chemical structure of the headgroup, more recent calculations have shown that a_e depends directly on the tail packing free energy and is therefore more accurately described as a thermodynamic quantity derived from equilibrium free energy considerations and not a simple geometric quantity [103]. Such thermodynamic considerations are beyond the scope of this review, however, which is only concerned with the relation of the packing parameter to lipid phase dynamics and destabilizing transitions facilitated by redox reactions of lipid materials.

4.3.2 Lipid Phase Behavior and Membrane Stability

From observations in biological systems, a breakdown in lipid membrane integrity is a necessary component of fusion processes. Whether this process proceeds exclusively through formation of nonlamellar phase intermediates or through a less ordered process of local membrane disordering following aggregation is somewhat ambiguous; it has been suggested that smaller lipid vesicles (~50 nm) lack the area necessary for formation of nonlamellar phases and that fusion in these types of

EBSCOhost - printed on 2/14/2023 1:06 PM via . All use subject to https://www.ebsco.com/terms-of-use

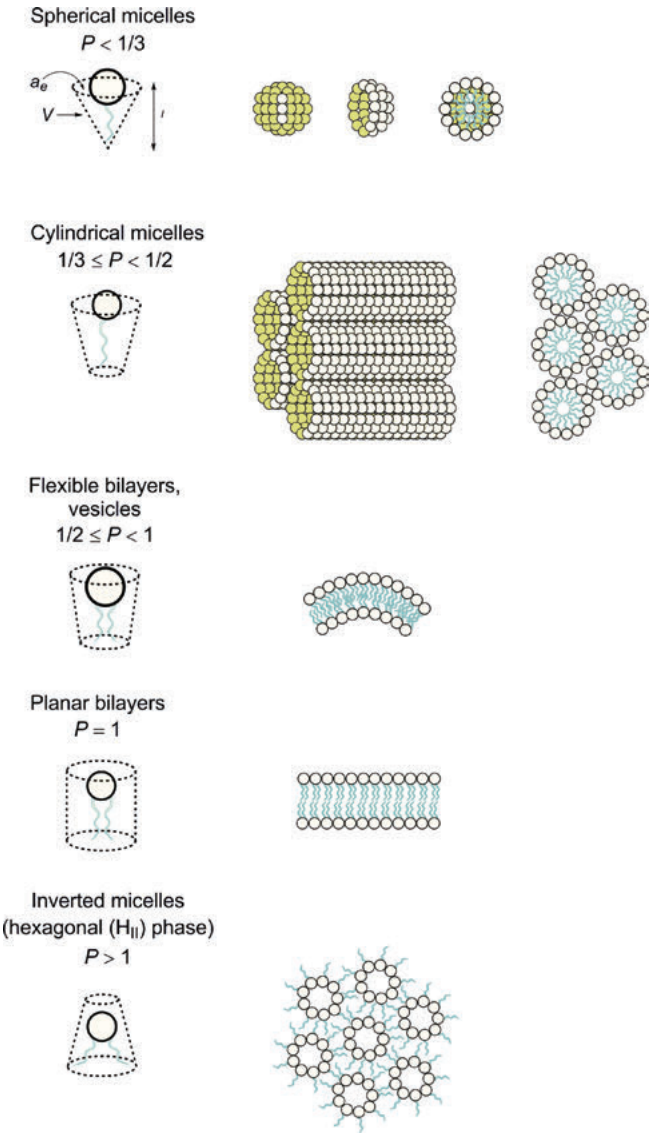

Figure 4.4: Lipid phase polymorphism and relation to packing parameter.

lipid structures may proceed through a simpler aggregation–disordering–fusion process [104]. While the specific mechanics of biological membrane fusion are of less concern in the design of stimuli-responsive lipidic materials, it is necessary to understand the basic principles governing membrane disaggregation or fusion for the design of nanocarriers with the capacity to deliver a specific cargo (e.g., therapeutic compounds).

EBSCOhost - printed on 2/14/2023 1:06 PM via . All use subject to https://www.ebsco.com/terms-of-use

The relationship of P to preferred lipid structures is shown in Figure 4.4 [105]. The optimal interval of P values for bilayer-based materials is [0.5,1], but it is possible for mixtures containing lipids whose P value would dictate a preference for nonbilayer structures to adopt a bilayer conformation provided the mixture is stabilized by (typically) 20–50 mol% bilayer-forming lipid [106]. This observation facilitates the design of lipidic nanostructures containing some fraction of nonbilayer forming lipids, whereby phase transition and membrane destabilization may be induced by oxidation or reduction (i.e., changing a_e and P through redox headgroup alteration [107]) of the destabilizing lipid. This redox-induced disaggregation is the principle underlying the majority of redox-sensitive nanocarriers.

4.4 Principles and Applications of Redox-Sensitive Lipid/Surfactant Materials

4.4.1 (Electro)chemical Principles Underlying Redox-Responsive Materials

The principles underlying the utility of redox-responsive lipidic materials as biological nanocarriers (i.e., intra/extracellular redox gradients and membrane destabilization) have been described in detail in Sections 4.1–4.2. The critical feature of the biological redox environment that facilitates broad application of redox-active materials is its heterogeneity; in addition to the (generally) oxidizing extracellular and reducing intracellular environments, differential redox gradients exist both as a function of subcellular or tissue localization and in response to a variety of pathological conditions, especially cancer [108]. This heterogeneity allows for a variety of oxidation- and reduction-sensitive functional groups to be utilized as redox-active moieties in advanced materials. These functionalities are summarized in Table 4.1. At present, disulfides and quinones represent the most commonly employed reduction-sensitive groups, and ferrocene is the most common oxidatively triggered group utilized in such redox-responsive materials. Despite these preferences, a diverse array of functional groups remain to be explored for this purpose (see examples of biocompatible redox couples in Table 4.1). In combination with the diversity of biological redox environments, there remains significant potential for the application of these materials.

4.4.2 Applications

Early efforts in the development of redox-responsive vesicular lipidic materials utilized viologen derivatives **1–4** as the redox functionality. In the first example of such

EBSCOhost - printed on 2/14/2023 1:06 PM via . All use subject to https://www.ebsco.com/terms-of-use

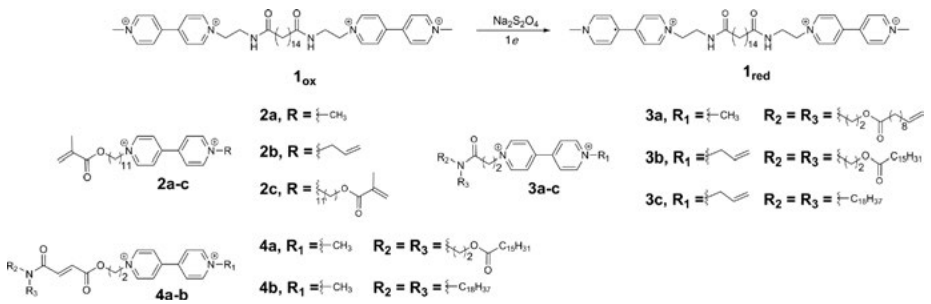

Figure 4.5: Vesicle-forming amphiphilic viologen derivatives.

a system, Fuhrhop [109] prepared unilamellar vesicles with diameters in the range of 10–100 nm from the viologen amphiphiles shown in Figure 4.5. The external solution-oriented bipyridyl units were reduced upon treatment with aqueous dithionite, but this did not lead to membrane disaggregation. In a subsequent report, Fendler and coworkers [110] prepared bilayer vesicles with similar redox functionality but employing an unsaturated single- (micelle-forming) or double-tail alkyl chain is more analogous to a dialkylphospholipid. These vesicles were shown to entrap 2-aminopyridine and the potential of such vesicles as drug delivery vehicles was noted, but their ability to release cargo in a redox-sensitive manner was not investigated.

The next significant advance in redox-sensitive surfactant materials was the development of alkyl ferrocene-based micelles with reversible formation–disaggregation behavior by Saji [111, 112] in Figure 4.6. Complementary alkyl ferrocene surfactants were prepared for micelle formation; (11-ferrocenyl)undecyltrimethylammonium bromide (**5**) with redox-active and cationic functionalities at distal ends of the surfactant, and (ferrocenylmethyl)dodecyldimethylammonium bromide with ferrocene located proximal to the cationic ammonium (**6**). In both examples, formation of micelles was observed, and their ability to encapsulate a guest compound was demonstrated by the solubilization in aqueous media of a dye compound, 1-(*o*-tolylazo)naphthalen-2-ol (TAN), in micellar solutions of **5** and **6**. Addition of $Ce(SO_4)_2$ and subsequent oxidation of the ferrocenyl units induced disaggregation of the micelles and precipitation of TAN, and the reversibility of this behavior was shown by the subsequent addition of $Na_2S_2O_4$ (in the case of **5**) or hydroquinone (**6**). Upon reduction of ferrocene the micelles re-formed and the dye was solubilized. An analogous system comprising a double-tailed surfactant containing two ferrocene alkyl units coupled to a cationic ammonium headgroup [113] (**9a–b**) has also been described. Vesicle formation was observed with ferrocene in the reduced state and destabilization following treatment with $Ce(SO_4)_2$. Entrapment and oxidatively triggered release [114] of both hydrophobic (benzene) and hydrophilic (glucose) guest compounds was demonstrated in this vesicular system.

EBSCOhost - printed on 2/14/2023 1:06 PM via . All use subject to https://www.ebsco.com/terms-of-use

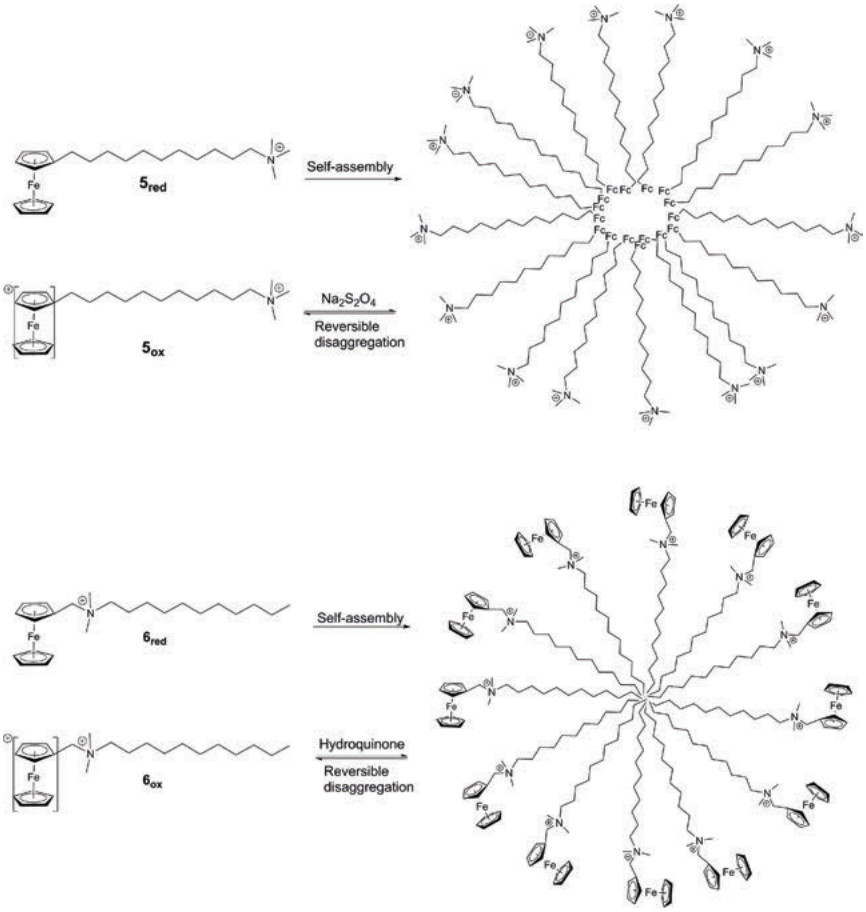

Figure 4.6: Redox-controlled micelle formation and disaggregation by ferrocene/ammonium containing amphiphiles.

In the first example of redox-controlled vesicle formation and disassembly, Gokel [115] reported the synthesis of a ferrocene-dihydrocholesterol (cholestanol) conjugate (**7**) (Figure 4.7). Upon anodic or chemical (with Ce(IV)) oxidation of ferrocene, a cationic amphiphile was generated and stable plurilamellar vesicles formed. Reduction of ferrocene following treatment with aqueous dithionite induced vesicle collapse, and isolation and characterization of the recovered cholestanyl ferrocene by mass spectrometry confirmed that the process was due to ferrocene redox activity and not chemical modification. This reductive destabilization approach was employed in other metalloamphiphiles [116, 117] (**8–11**), demonstrating that the concept of redox-responsive vesicle disassembly was general and not limited to **7**.

EBSCOhost - printed on 2/14/2023 1:06 PM via . All use subject to https://www.ebsco.com/terms-of-use

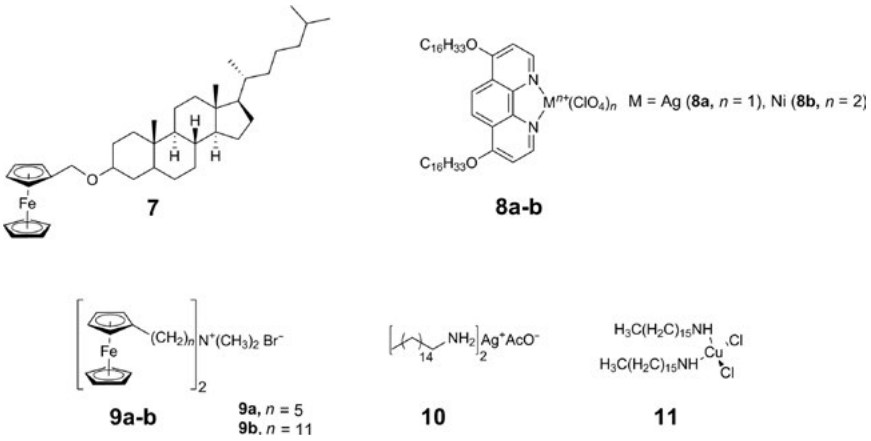

Figure 4.7: Metalloamphiphiles capable of redox-controlled vesicle formation.

In a more recent example of metalloamphiphile-based systems, Mauzeroll and coworkers [118] reported the development of a redox-sensitive giant unilamellar vesicle (GUV) system based on a synthetic ferrocene-functionalized phospholipid (**15**) (Figure 4.9). Spontaneous vesicle disaggregation was observed upon treatment with Ir(IV), and in vitro studies demonstrated increased cytotoxicity in HeLa (human cervical cancer) cells treated with doxorubicin-loaded redox GUVs compared to nonredox liposomes. These redox-active liposomes also displayed a degree of specificity for delivery of doxorubicin to cancerous (HeLa) versus noncancerous (MRC5) cells. It is hypothesized that the oxidizing extracellular environment induces the conversion of ferrocene to ferrocenium in the outer leaflet of the liposomes leading to destabilization and membrane disassembly followed by contents release. Efforts are currently underway to replicate this system in ca. 100 nm liposomes for in vivo evaluation of its therapeutic capacity.

In an important conceptual advance in the area of redox-sensitive liposomal systems, Zalipsky [119] reported the first example of serum-stable liposomes containing a significant fraction of a nonbilayer forming lipid, dioleoylphosphatidylethanolamine (DOPE). Unmodified DOPE adopts an inverted hexagonal micellar (H_{II}) phase, but *N*-acylated DOPE derivatives or mixtures containing bulky hydrophilic groups such as poly(ethylene glycol) PEG are capable of forming stable bilayer structures [120]. Under physiological conditions, DOPE-containing liposomes were prepared by the addition of a distearoylphosphatidylethanolamine-methoxypoly(ethylene glycol) conjugate containing a disulfide linkage (mPEG-SS-DSPE, **12**). These liposomes were able to encapsulate pyranine (a membrane-impermeable solute) without significant leakage in prolonged incubation (36 h) with plasma or serum at physiological temperatures. Treatment with dithiothreitol (DTT), a potent reducing agent, induced thiolytic cleavage of the mPEG-DSPE disulfide linkage and complete release of entrapped pyranine

EBSCOhost - printed on 2/14/2023 1:06 PM via . All use subject to https://www.ebsco.com/terms-of-use

following a short lag time. In a subsequent report, the same DOPE-based liposomal system containing mouse anti-CD19 monoclonal antibody conjugated to maleimide-PEG-DSPE phospholipids and loaded with doxorubicin were applied in in vitro (human B-cell lymphoma) and murine tumor cytotoxicity studies, resulting in a modest increase in therapeutic efficiency compared to free doxorubicin [121]. In vitro drug release experiments showed that DOPE/mPEG-SS-DSPE liposomes were sensitive to DTT-induced thiolytic cleavage and membrane destabilization at pH 5.5 (mimicking endosomal conditions) but not at pH 7.4, providing the first example of a multiple stimulus-responsive redox-active liposomal delivery vehicle as well as the first detailed pharmacokinetic analysis of such a system.

Arbuzova et al. [122] extended this concept, preparing DOPE/phosphatidylcholine (PC) liposomes containing a multifunctional lipid-like synthetic amphiphile containing a disulfide linkage and a headgroup with both biotin and dansyl functionalities (**13**) for streptavidin binding and fluorescent localization to confirm liposomal incorporation, respectively. The nonspecific uptake and release capability of these liposomes were demonstrated in macrophages with calcein-containing liposomes as well as specific uptake of antibody-targeted liposomes by BT-474 (human breast cancer) cells. The liposomes were functionalized with anti-p185HER2 antibody (a receptor known to be overexpressed in many cancer cell types) through streptavidin–biotin binding and loaded with doxorubicin. BT-474 cells were treated with both reduction-sensitive and -insensitive liposomes, and the doxorubicin fluorescence was seen to be significantly greater in the reduction-sensitive treated population, suggesting successful uptake but less efficient drug release by the reduction-insensitive liposomes. Specific uptake of antibody-targeted liposomes and reductively triggered release of contents were the focus of this study, and comparative cytotoxicity measurements relative to free doxorubicin were not performed.

A recent report from Zhang et al. [123] described a similar approach utilizing DOPE/PC liposomes stabilized with a multifunctional synthetic amphiphile, in this case containing a redox-responsive disulfide linkage, a histidine pendant group and an acid-sensitive hexahydrobenzoic (HHB) amide functionality (**14**) (Figure 4.8). The cationic surface charge of these liposomes promotes endosomal uptake, after which the protonation of the histidine imidazole ring and degradation of the HHB linkage increases proton influx into the endosomal vesicle and ultimately its degradation and release of the liposomes into the cytoplasm. In the reducing intracellular environment the disulfide linkage is cleaved, destabilizing the liposomes leading to the release of encapsulated doxorubicin. In vivo studies in mice showed significantly more doxorubicin accumulation in tumor xenografts for the redox-active HHB liposomal preparation compared to analogous systems lacking either the disulfide linkage or the synthetic HHB amphiphile entirely.

The quinone–hydroquinone redox couple is another biologically important pairing (in addition to thiol–disulfide) that has found broad application in the development of redox-sensitive materials for use in biological systems. The redox

EBSCOhost - printed on 2/14/2023 1:06 PM via . All use subject to https://www.ebsco.com/terms-of-use

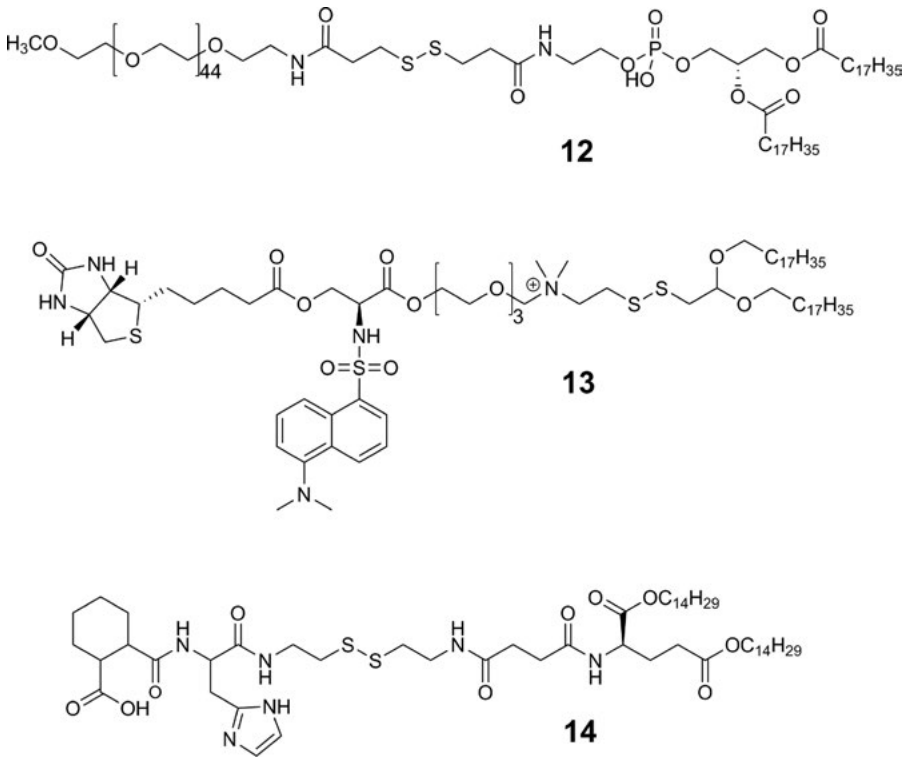

Figure 4.8: Redox-responsive amphiphiles containing disulfide linkages as the redox functionality.

functionality in these materials takes advantage of the observation that "trialkyl locked" quinone propionic esters or amides undergo rapid and facile reductive lactonization [124]. McCarley has provided several reports thoroughly exploring the potential of a trigger-release liposomal delivery system based on reductive lactonization of a quinone propionic acid–DOPE conjugate (Q-DOPE, **16**). Similar to disulfide cleavage, reductive quinone cyclization upon treatment with $Na_2S_2O_4$ liberates the hydroquinone functionality of the DOPE headgroup, and the resulting unstabilized lipid undergoes a lamellar to inverted hexagonal phase transition (L_α–H_{II}), destabilizing the liposomes and releasing their contents. An initial report demonstrated the necessity of the *gem*-dimethyl group β to the lactone carbonyl for kinetically facile cyclization following quinone reduction [125] and the ability of Q-DOPE liposomes to release an encapsulated dye (calcein) upon headgroup reduction.

Subsequent studies of the Q-DOPE liposomal system focused on the effects of anions in solution [126] and lipid composition on the mechanism and kinetics of content release following quinone reduction. The proposed mechanism for the reductively triggered release depends on vesicle aggregation and

EBSCOhost - printed on 2/14/2023 1:06 PM via . All use subject to https://www.ebsco.com/terms-of-use

accumulation of a sufficient concentration of DOPE to facilitate the (L_α–H_{II}) phase transition. Increased hydration of the phosphatidylethanolamine headgroups enlarges their relative area and confers a degree of stability to the vesicles; consistent with this hypothesis, less polarizable and more hydrated anions resulted in faster release of contents from Q-DOPE liposomes due to their dehydrating effect on the PE headgroups, in agreement with the Hofmeister series. The addition of unfunctionalized DOPE or PEG-DOPE conjugates to Q-DOPE liposomes was also shown to have an effect on contents release; addition of DOPE to the membranes lowered the barrier for accumulation of a sufficient concentration of DOPE to promote the (L_α–H_{II}) transition and resulted in a faster efflux of encapsulated calcein. The effect of addition of PEG-DOPE to Q-DOPE liposomes was somewhat less intuitive; at concentrations above 0.5 mol% PEG_{2000}–DOPE, contents release was significantly delayed. This effect is hypothesized to be the result of the formation of stabilized lamellar phase domains from the exclusion of PEG_{2000}–DOPE from liposomal contact areas due to steric effects, preventing further release of calcein once a critical concentration of bilayer-stable lipid is reached. These studies provide valuable insight into the mechanics of bilayer disassembly and represent a significant advance in the intentional design of redox-responsive lipidic nanocarriers.

A novel reduction-sensitive disulfide-based liposomal system was recently described by Kim [127]. Liposomes composed of egg PC were prepared incorporating benzyl disulfide in the bilayer itself; upon treatment with DTT the disulfide linkage was cleaved, generating benzyl thiol. Subsequent reorientation of benzyl thiol in the liposomal membrane was sufficient to cause membrane destabilization and release of encapsulated calcein. While a creative example of a redox-sensitive material, a drug-release strategy that releases reactive sulfur species as a byproduct of its cargo delivery mechanism may encounter toxicity issues in biological systems.

In a somewhat less well-characterized application of redox-responsive surfactant materials than stimulated delivery of small molecules, several systems have been developed for the delivery of nucleic acids. While cationic lipids are well known for their ability to form lipoplexes with DNA, only a few such systems that are redox-responsive have been described. Perhaps the most well-characterized example [128] utilizes the same double-tailed ferrocene alkyl surfactant (**9**) previously shown to form vesicles in a redox-sensitive manner. This compound can also form serum-stable complexes with nucleic acids and is capable of delivering both DNA [129] for transfection and siRNA [130] for gene silencing with increased efficiency in its reduced state. When the ferrocene units are oxidized to ferrocenium, efficiency of nucleic acid delivery with BFDMA is significantly decreased.

EBSCOhost - printed on 2/14/2023 1:06 PM via . All use subject to https://www.ebsco.com/terms-of-use

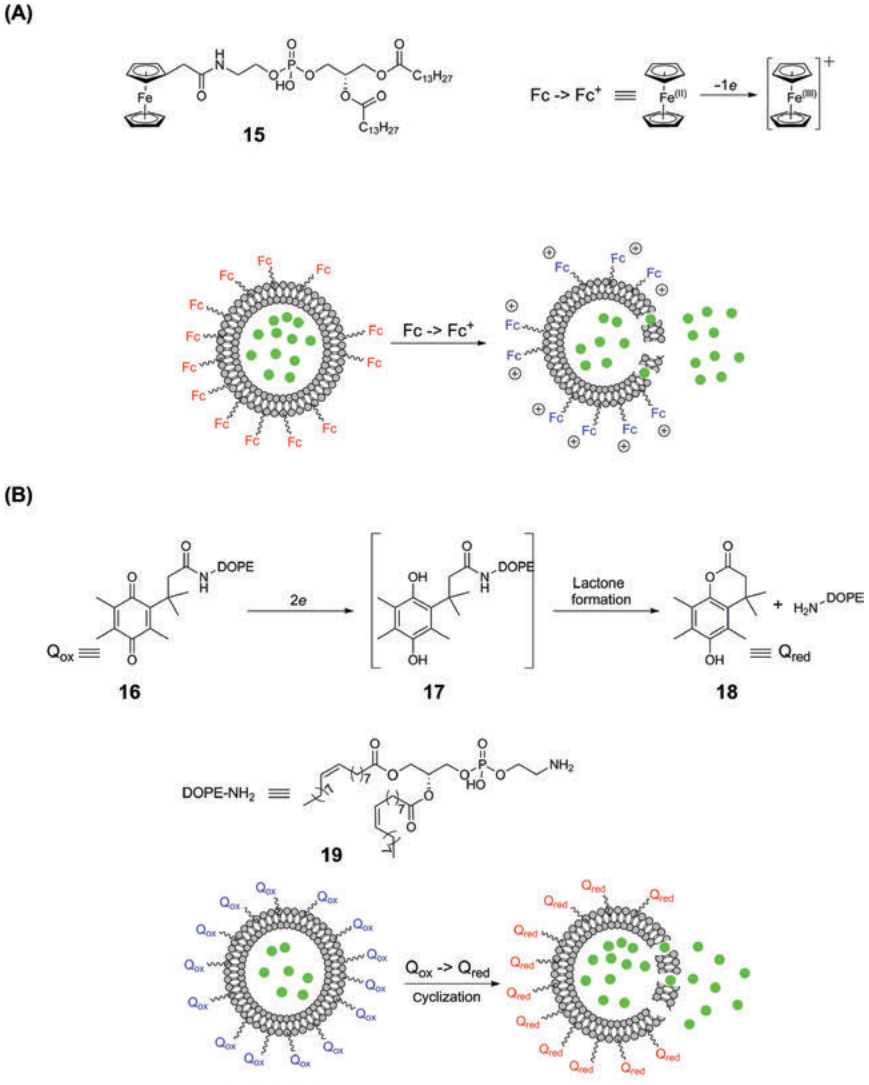

Figure 4.9: (A) Oxidation- and (B) reduction-triggered redox-responsive liposomal systems.

4.5 Conclusions

Redox-responsive surfactant-based materials have demonstrated significant potential for applications to biological systems, in particular the delivery of small-molecule therapeutics. While this remains the best characterized utility of such materials, there remains considerable room for refinement of existing systems and

EBSCOhost - printed on 2/14/2023 1:06 PM via . All use subject to https://www.ebsco.com/terms-of-use

diversification of applications (e.g., diagnostics and imaging). Application of any synthetic advanced material in the biological environment has proven to be an extremely complex task; simply understanding the plurality of factors at play in a given biological system is enormously difficult, to say nothing of trying to replicate those conditions at the bench to rationally design materials that can function in such a complex context while minimizing deleterious side effects. In spite of these challenges, significant progress has been made in this area in its relatively short history and, given our evolving knowledge of biological redox systems, they remain a promising source of endogenous stimuli for redox-responsive materials. As discussed previously, the authors believe that in addition to the principles of organic, physical and supramolecular chemistry that inform the design of such advanced materials at the molecular level, it is important also to consider in detail the relevant features of the environment for which a given material is intended. The so-called rational design could then be seen as comprising hierarchical sets of design principles (e.g., preparation and application) that should all be considered as integral parts of the whole rather than disconnected segments. This approach has been presented in the specific context of redox-sensitive materials for applications to biological systems but should be valid generally in the design of any functional material for application in a given context.

References

[1] Gregoriadis G., Liposome research in drug delivery: The early days, J Drug Target. 16 (7–8), 520–524 (2008).
[2] Goins B.A. and Phillips W.T., The use of scintigraphic imaging as a tool in the development of liposome formulations, Prog. Lipid Res. 40 (1–2), 95–123 (2001).
[3] Gregoriadis G. and Allison A.C., Liposomes as immunological adjuvants, Nature 252, 252 (1974).
[4] Bouwstra J.A. and Honeywell-Nguyen P.L., Skin structure and mode of action of vesicles, Adv. Drug Deliv. Rev. 54 (suppl. 1), S41–S55 (2002).
[5] Weissig V., Pettinger T.K. and Murdock N., Nanopharmaceuticals (part 1): Products on the market, Int. J. Nanomedicine 9, 4357–4373 (2014).
[6] Bulbake U., Doppalapudi S., Kommineni N. and Khan W., Liposomal formulations in clinical use: An updated review, Pharmaceutics 9 (2), 12 (2017).
[7] Barenholz Y., Doxil® — The first FDA-approved nano-drug: Lessons learned, J. Control. Release 160 (2), 117–134 (2012).
[8] Ref. 6.
[9] Danhier F., To exploit the tumor microenvironment: Since the EPR effect fails in the clinic, what is the future of nanomedicine? J. Control. Release 244, 108–121 (2016).
[10] Mallick S. and Choi J.S., Liposomes: Versatile and biocompatible nanovesicles for efficient biomolecules delivery, J. Nanosci. Nanotechnol. 14 (1), 755–765 (2014).
[11] Ref. 6.
[12] Ref. 5.

EBSCOhost - printed on 2/14/2023 1:06 PM via . All use subject to https://www.ebsco.com/terms-of-use

[13] Egea J., et al. European contribution to the study of ROS: A summary of the findings and prospects for the future from the COST action BM1203 (EU-ROS), Redox Biology 13, 94–162 (2017).
[14] Sarsour E.H., Kumar M.G., Chaudhuri L., Kalen A.L., and Goswami P.C., Redox control of the cell cycle in health and disease, Antioxid. Redox Signal. 11 (12), 2985–3011 (2009).
[15] Zangar R.C., Davydov D.R. and Verma S., Mechanisms that regulate production of reactive oxygen species by cytochrome P450, Toxicol. Appl. Pharmacol. 199, 316–331 (2004).
[16] Denisov I.G., Shih A.Y. and Sligar S.G., Structural differences between soluble and membrane-bound cytochrome P450s, J. Inorg. Biochem. 108, 150–158 (2012).
[17] Ghersi-Egea J.F., Perrin R., Leininger-Muller B., Grassiot M.C., Jeandel C., Floquet J., Cuny G., Siest G. and Minn A., Subcellular localization of cytochrome P450, and activities of several enzymes responsible for drug metabolism in the human brain, Biochem. Pharmacol. 45 (3), 647–658 (1993).
[18] Meunier B., de Visser S.P. and Shaik S., Mechanism of oxidation reactions catalyzed by cytochrome P450 enzymes, Chem. Rev. 104, 3947–3980 (2004).
[19] Guengerich F.P., Common and uncommon cytochrome P450 reactions related to metabolism and chemical toxicity, Chem. Res. Toxicol. 14 (6), 611–650 (2001).
[20] Brodie B.B., Gillette J.R. and La Du B.N., Enzymatic metabolism of drugs and other foreign compounds, Annu. Rev. Biochem. 27 (3), 427–454 (1958).
[21] Estabrook R.W., Cooper D.Y. and Rosenthal O., The light reversible carbon monoxide inhibition of the steroid C21-hydroxylase system of the adrenal cortex, Biochem. Z. 338, 741–755 (1963).
[22] Mueller G.C. and Miller J.A., The metabolism of 4-dimethylaminoazobenzene by rat liver homogenates, J. Biol. Chem. 176, 535–544 (1948).
[23] Bokoch G.M., and Knaus U.G., NADPH oxidases : Not just for leukocytes anymore, Trends Biochem. Sci. 28, 502–508 (2003).
[24] Segal A.W., The function of the NADPH oxidase of phagocytes and its relationship to other NOXs in plants, invertebrates, and mammals, Int. J. Biochem. Cell Biol. 40 (4–3), 604–618 (2008).
[25] Bedard K. and Krause K.H., The NOX family of ROS-generating NADPH oxidases : Physiology and pathophysiology, Physiol. Rev. 87, 245–313 (2007).
[26] Henderson L.M., Chappell J.B. and Jones O.T., The superoxide –generating NADPH oxidase of human neutrophils is electrogenic and associated with an H+ channel, Biochem. J. 246 (2),325–329 (1987).
[27] Ref. 19.
[28] Rapoport R.M., Draznin M.B. and Murad F., Endothelium-dependent relaxation in rat aorta may be mediated through cyclic GMP-dependent protein phosphorylation, Nature 306, 174–176 (1983).
[29] Pozdnyakov N., Lloyd A., Reddy V.N. and Sitaramayya A., Nitric oxide -regulated endogenous ADP-ribosylation of rod outer segment proteins, Biochem. Biophys. Res. Commun. 192, 610–615 (1993).
[30] Förstermann U. and Sessa W.C., Nitric oxide synthases: Regulation and function, European Heart Journal 33, 829–837 (2012).
[31] Bredt D.S., Hwang P.M., Glatt C.E., Lowenstein C., Reed R.R. and Snyder S.H., Cloned and expressed nitric oxide synthase structurally resembles cytochrome P-450 reductase, Nature 351, 714–718 (1991).
[32] Ref. 30.

EBSCOhost - printed on 2/14/2023 1:06 PM via . All use subject to https://www.ebsco.com/terms-of-use

[33] Chen Q., Vazquez E.J., Moghaddas S., Hoppel C.L. and Lesnefsky E.J., Production of reactive oxygen species by mitochondria: Central role of complex III, J. Biol. Chem. 278 (38), 36027–36031 (2003).
[34] Hatefi Y., The mitochondrial electron transport and oxidative phosphorylation system, Ann. Rev. Biochem. 54, 1015–1069 (1985).
[35] Ibid.
[36] Rapoport R.M., Draznin M.B. and Murad F., Endothelium-dependent relaxation in rat aorta may be mediated through cyclic GMP-dependent protein phosphorylation, Nature 306, 174–176 (1983).
[37] Murphy M.P., How mitochondria produce reactive oxygen species, Biochem. J. 417, 1–13 (2009).
[38] Ibid.
[39] Andreyev A.Y., Kushnareva Y.E. and Starkov A.A., Mitochondrial metabolism of reactive oxygen species, Biochemistry (Mosc). 70 (2), 200–214 (2005).
[40] Stehling O. and Lill R., The role of mitochondria in cellular iron–sulfur protein biogenesis: Mechanisms, connected processes, and diseases, Cold Spring Harb. Perspect. Biol. 5, a011312 (2013).
[41] Cadenas E. and Davies K.J., Mitochondrial free radical generation, oxidative stress, and aging, Free Radical Biol. Med. 29 (3/4), 222–230 (2000).
[42] Chaiswing L. and Oberley T.D., Extracellular/microenvironmental redox state, Antioxid. Redox Signal. 13 (4), 449–465 (2010).
[43] Ibid.
[44] Whitfield J.B., Gamma glutamyl transferase, Crit. Rev. Clin. Lab. Sci. 38 (4), 263–355 (2001).
[45] Keillor J.W., Castonguay R. and Lherbet C., Gamma-glutamyl transpeptidase substrate specificity and catalytic mechanism, Meth. Enzymol. 401, 449–467 (2005).
[46] Paolicchi A., Tongiani R., Tonarelli P., Comporti M. and Pompella A., Gamma-glutamyl transpeptidase-dependent lipid peroxidation in isolated hepatocytes and HepG2 hepatoma cells, Free Radical Biol. Med. 22 (5), 853–860 (1997).
[47] Ref. 37.
[48] Ottaviano F.G., Handy D.E. and Loscalzo J., Redox regulation in the extracellular environment, Circ. J. 72, 1–16 (2008).
[49] Kemp M., Go Y.M. and Jones D.P., Nonequilibrium thermodynamics of thiol/disulfide redox systems: A perspective on redox systems biology, Free Radical Biol. Med. 44 (6), 921–937 (2008).
[50] Ref. 37.
[51] Sender R., Fuchs S. and Milo R., Revised estimates for the number of human and bacteria cells in the body, PLoS Biology 14 (8), e1002533 (2016).
[52] Faith J.J., Guruge J.L., Charbonneau M., Subramanian S., Seedorf H., Goodman A.L. and Rosenbaum M., The long-term stability of the human gut microbiota, Science 341 (6141), 1237439 (2013).
[53] Palm N.W., de Zoete M.R., Cullen T.W., Barry N.A., Stefanowski J., Hao L. and Ruggiero E., Immunoglobulin A coating identifies colitogenic bacteria in inflammatory bowel disease, Cell 158 (5), 1000–1010 (2014).
[54] Wang J. and Jia H., Metagenome-wide association studies: Fine-mining the microbiome , Nat. Rev. Microbiol. 14, 508–522 (2016).
[55] Neish A.S. and Jones R.M., Redox signaling mediates symbiosis between the gut microbiota and the intestine, Gut Microbes 5 (2), 250–253 (2014).
[56] Trachootham D., Lu W., Ogasawara M.A., Valle N.R.D. and Huang P., Redox regulation of cell survival, Antioxid. Redox Signal. 10 (8), 1343–1374 (2008).
[57] Ref. 14.

EBSCOhost - printed on 2/14/2023 1:06 PM via . All use subject to https://www.ebsco.com/terms-of-use

[58] Salazar-Ramiro A., Ramírez-Ortega D., de la Cruz V.P., Hérnandez-Pedro N.Y., González-Esquivel D.F., Sotelo J. and Pineda B., Role of redox status in development of glioblastoma, Front. Immunol. 7, 156 (2016).
[59] Croce C.M., Oncogenes and cancer, New Engl. J. Med. 358, 502–511 (2008).
[60] Sun W. and Yang J., Functional mechanisms for human tumor suppressors, J. Cancer 1, 136–140 (2010).
[61] Hainaut P. and Hollstein M., p53 and Human Cancer: The First Ten Thousand Mutations, Adv. Cancer Res. 77, 81–137 (2000).
[62] Attardi L.D. and Donehower L.A., Probing p53 biological functions through the use of genetically engineered mouse models, Mutat. Res. 576, 4–21 (2005).
[63] Ref. 56.
[64] Ibid.
[65] Irani K., Xia Y., Zweier J.L., Sollott S.J., Der C.J., Fearon E.R. and Goldschmidt-Clermont P.J., Mitogenic signaling mediated by oxidants in Ras-transformed fibroblasts, Science 275, 1649–1652 (1997).
[66] Serrano M., Lin A.W., McCurrach M.E., Beach D. and Lowe S.W., Oncogenic ras provokes premature cell senescence associated with accumulation of p53 and p16 INK4a, Cell 88, 593–602 (1997).
[67] Ref. 14.
[68] Tanaka H., Matsumura I., Ezoe S., Satoh Y., Sakamaki T., Albanese C. and Kanakura Y., E2F1 and c-Myc potentiate apoptosis through inhibition of NF-κB activity that facilitates MnSOD-mediated ROS elimination, Mol. Cell 9, 1017–1029 (2002).
[69] Biroccio A., Benassi B., Amodei S., Gabellini C., Del Bufalo D. and Zupi G., c-Myc down-regulation increases susceptibility to cisplatin through reactive oxygen species-mediated apoptosis in M14 human melanoma cells, Mol. Pharmacol. 60, 174–182 (2001).
[70] Elchuri S., Oberley T.D., Qi W., Eisenstein.R.S., Roberts L.J., Van Remmen H. and Huang T.T., CuZnSOD deficiency leads to persistent and widespread oxidative damage and hepatocarcinogenesis later in life, Oncogene 24 (3), 367–380 (2005).
[71] Van Remmen H., Ikeno Y., Hamilton M., Pahlavani M., Wolf N., Thorpe S.R. and Nelson J., Life-long reduction in MnSOD activity results in increased DNA damage and higher incidence of cancer but does not accelerate aging, Physiol. Genomics 16, 29–37 (2003).
[72] Lu Y.P., Lou Y.R., Yen P., Newmark H.L., Mirochnitchenko O.I., Inouye M. and Huang M.T., Enhanced skin carcinogenesis in transgenic mice with high expression of glutathione peroxidase or both glutathione peroxidase and superoxide dismutase, Cancer Res. 57, 1468–1474 (1997).
[73] Knorre D.G., Kudryashova N.V. and Godovikova T.S., Chemical and Functional Aspects of Posttranslational Modification of Proteins, Acta Naturae 1 (3), 29–51 (2009).
[74] Sawan C. and Herceg Z., Histone Modifications and Cancer, Adv. Genet. 70, 57-85 (2010).
[75] Holmgren A., Thioredoxin and glutaredoxin systems 264 (24), 13963–13966 (1989).
[76] Shan W., Zhong W., Zhao R. and Oberley T.D., Thioredoxin 1 as a subcellular biomarker of redox imbalance in human prostate cancer progression, Free Radical Biol. Med. 49 (12), 2078–2087 (2010).
[77] Jorgenson T.C., Zhong W. and Oberley T.D., Redox Imbalance and Biochemical Changes in Cancer, Cancer Res. 73 (20), 6118–6123 (2013).
[78] Yakovlev V.A., Nitric Oxide–Dependent Downregulation of BRCA1 Expression Promotes Genetic Instability, Cancer Res. 73 (2), 706–715 (2013).
[79] Dhar S.K. and Clair D.K.S., Manganese superoxide dismutase regulation and cancer, Free Radical Biol. Med. 52 (11-12), 2209–2222 (2012).

EBSCOhost - printed on 2/14/2023 1:06 PM via . All use subject to https://www.ebsco.com/terms-of-use

[80] Townsend D.M., Manevich Y., He L., Hutchens S., Pazoles C.J. and Tew K.D., Novel role for glutathione S-transferase π regulator of protein S-glutathionylation following oxidative and nitrosative stress, J. Biol. Chem. 284 (1), 436–445 (2009).
[81] Ref. 72.
[82] Ibid.
[83] Michiels C., Tellier C. and Feron O., Cycling hypoxia: A key feature of the tumor microenvironment, Biochim. Biophys. Acta 1866 (1), 76–86 (2016).
[84] Chiche J., Brahimi-Horn M.C. and Pouysségur J., Tumour hypoxia induces a metabolic shift causing acidosis: A common feature in cancer, J. Cell. Mol. Med. 14, 771–794 (2010).
[85] Khramtsov V.V. and Gillies R.J., Janus-faced tumor microenvironment and redox , Antioxid. Redox. Signal. 21 (5), 723–729 (2014).
[86] Kuppusamy P., Li H., Ilangovan G., Cardounel A.J., Zweier J.L., Yamada K. and Mitchell J.B., Noninvasive imaging of tumor redox status and its modification by tissue glutathione levels, Cancer Res. 62, 307–312 (2002).
[87] Luanpitpong S., Talbott S.J., Rojanasakul Y., Nimmannit U., Pongrakhananon V., Wang L. and Chanvorachote P., Regulation of lung cancer cell migration and invasion by reactive oxygen species and caveolin-1, J. Biol. Chem. 285, 38832–38840 (2010).
[88] Ref. 72.
[89] Ibid.
[90] Wang H., et al., Global, regional, and national life expectancy, all-cause mortality, and cause-specific mortality for 249 causes of death, 1980–2015: A systematic analysis for the Global Burden of Disease Study 2015, Lancer 388 (10053), 1459–1544 (2016).
[91] Campisi J., Aging, cellular senescence, and cancer, Annu. Rev. Physiol. 75, 685–705 (2013).
[92] Finkel T., Serrano M. and Blasco M.A., The common biology of cancer and ageing, Nature 448, 767-774 (2007).
[93] Matsumura Y. and Maeda H., A new concept for macromolecular therapeutics in cancer chemotherapy: Mechanism of tumoritropic accumulation of proteins and the antitumor agent smancs, Cancer Res. 46, 6387-6392 (1986).
[94] Petros R.A. and DeSimone J.M., Strategies in the design of nanoparticles for therapeutic applications, Nat. Rev. Drug Discovery 9, 615–627 (2010).
[95] Ref. 9.
[96] Maeda H., Toward a full understanding of the EPR effect in primary and metastatic tumors as well as issues related to its heterogeneity, Adv. Drug Deliv. Rev. 91, 3–6 (2015).
[97] Nichols J.W. and Bae Y.H., EPR: Evidence and fallacy, J. Control. Release 190, 451–464 (2014).
[98] Ref. 9.
[99] Seddon, J.M., Templer, R.H., Polymorphism of Lipid-water Systems. In Handbook of Biological Physics; Lipowsky, R., Sackmann, E. Eds.; Elsevier: Amsterdam, 1995, Vol. 1; pp 99–149.
[100] Ellens H., Siegel D.P., Alford D., Yeagle P.L., Boni L., Lis L.J. and Bentz J., Membrane fusion and inverted phases, Biochemistry 28 (9), 3692–3702 (1989).
[101] Cullis P.T. and De Kruijff B., Lipid polymorphism and the functional roles of lipids in biological membranes, Biochim. Biophys. Acta 559, 399–420 (1979).
[102] Kumar V.V., Complementary molecular shapes and additivity of the packing parameter of lipids, PNAS USA 88, 444-448 (1991).
[103] Nagarajan R., Molecular packing parameter and surfactant self-assembly: The neglected role of the surfactant tail, Langmuir 18, 31-38 (2002).
[104] Cevc G. and Richardsen H., Lipid vesicles and membrane fusion , Adv. Drug Deliv. Rev. 38, 207–232 (1999).
[105] Balazs D.A. and Godbey W.T., Liposomes for use in gene delivery, J. Drug Deliv. 2011, 326497 (2011).

EBSCOhost - printed on 2/14/2023 1:06 PM via . All use subject to https://www.ebsco.com/terms-of-use

[106] Cullis P.R., Hope M.J. and Tilcock C.P., Lipid polymorphism and the roles of lipids in membranes, Chem. Phys. Lipids 40, 127–144 (1986).
[107] Barenholz, Y., Lichtenberg, D., Liposomes: Preparation, Characterization, and Preservation. In Methods of Biochemical Analysis; Glick, D., Ed.; Wiley: New York, 2006; Vol. 33; pp 342–346.
[108] Phillips D.J. and Gibson M.I., Redox-sensitive materials for drug delivery: Targeting the correct intracellular environment, tuning release rates, and appropriate predictive systems, Antioxid. Redox Signal. 21 (5), 786–803 (2014).
[109] Baumgartner E. and Fuhrhop J.H., Vesicles with a Monolayer, Redox-Active Membrane, Angew. Chem. Int. Ed. 19 (7), 550–551 (1980).
[110] Tundo P., Kippenberger D.J., Klahn P.L., Nelson E.P., Jao T.C. and Fendler J.H., Functionally polymerized surfactant vesicles. Synthesis and characterization, J. Am. Chem. Soc. 104 (2), 456–461 (1982).
[111] Saji T., Hoshino K. and Aoyagui S., Reversible formation and disruption of micelles by control of the redox state of the surfactant tail group, J. Chem. Soc. Chem. Commun. 13, 865–866.
[112] Saji T., Hoshino K. and Aoyagui S., Reversible formation and disruption of micelles by control of the redox state of the head group, J. Am. Chem. Soc. 107 (24), 6865–6868 (1985).
[113] Yoshino N., Shoji H., Kondo Y. and Kakizawa Y., Syntheses of Cationic Surfactants having Two Ferrocenylalkyl Chains, J. Jpn. Oil Chem. Soc. 45 (8), 769–775 (1996).
[114] Kakizawa Y., Sakai H., Yamaguchi A., Kondo Y., Yoshino N. and Abe M., Electrochemical control of vesicle formation with a double-tailed cationic surfactant bearing ferrocenyl moieties, Langmuir 17 (26), 8044–8048 (2001).
[115] Medina J.C., Li C., Bott S.G., Atwood J.L. and Gokel G.W.,A molecular receptor based on the ferrocene system: Selective complexation using atomic ball bearings, J. Am. Chem. Soc. 113 (1), 366–367 (1991).
[116] Munoz, S S. and Gokel G.W., Redox-switched vesicle formation from two novel, structurally distinct metalloamphiphiles, J. Am. Chem. Soc. 115 (9), 4899–4900 (1993).
[117] Muñoz S., Abel E., Wang K. and Gokel G.W., Control of vesicle formation by chemical switching, Tetrahedron 51 (2), 423–434 (1995).
[118] Noyhouzer T., L'Homme C., Beaulieu I., Mazurkiewicz S., Kuss S., Kraatz H.B., Canesi S. and Mauzeroll J., Ferrocene-Modified Phospholipid: An Innovative Precursor for Redox-Triggered Drug Delivery Vesicles Selective to Cancer Cells, Langmuir 32, 4169-4178 (2016).
[119] Kirpotin D., Hong K., Mullah N., Papahadjopoulos D. and Zalipsky S., Liposomes with detachable polymer coating: Destabilization and fusion of dioleoylphosphatidylethanolamine vesicles triggered by cleavage of surface-grafted poly (ethylene glycol), FEBS Letters 388 (2), 115–118 (1996).
[120] Ong W., Yang Y., Cruciano A.C. and McCarley R.L., Redox-triggered contents release from liposomes , J. Am. Chem. Soc. 130 (44), 14739–14744 (2008).
[121] Ishida T., Kirchmeier M.J., Moase E.H., Zalipsky S. and Allen T.M., Targeted delivery and triggered release of liposomal doxorubicin enhances cytotoxicity against human B lymphoma cells, Biochim. Biophys. Acta 1515 (2), 144–158 (2001).
[122] Goldenbogen B., Brodersen N., Gramatica A., Loew M., Liebscher J., Herrmann A. and Arbuzova A., Reduction-sensitive liposomes from a multifunctional lipid conjugate and natural phospholipids: Reduction and release kinetics and cellular uptake, Langmuir 27 (17), 10820–10829 (2011).
[123] Xu X., Zhang L., Assanhou A.G., Wang L., Zhang Y., Li W. and Zhang C., Acid/redox dual-activated liposomes for tumor-targeted drug delivery and enhanced therapeutic efficacy, RSC Adv. 5, 67803–67808 (2015).

EBSCOhost - printed on 2/14/2023 1:06 PM via . All use subject to https://www.ebsco.com/terms-of-use

[124] Carpino L.A., Triolo S.A. and Berglund R.A., Reductive lactonization of strategically methylated quinone propionic acid esters and amides, J. Org. Chem. 54 (14), 3303–3310 (1989).
[125] Levine M.N. and Raines R.T., Trimethyl lock: A trigger for molecular release in chemistry, biology, and pharmacology, Chem. Sci. 3, 2112–2420 (2012).
[126] McCarley R.L., Forsythe J.C., Loew M., Mendoza M.F., Hollabaugh N.M. and Winter J.E., Release Rates of Liposomal Contents Are Controlled by Kosmotropes and Chaotropes, Langmuir 29 (46), 13991–13995 (2013).
[127] Guo H. and Kim J.C., Reduction-responsive release property of egg phosphatidylcholine liposomes incorporating benzyl disulfide , J. Ind. Eng. Chem. 44, 105–111 (2016).
[128] Abbott N.L., Jewell C.M., Hays M.E., Kondo Y. and Lynn D.M., Ferrocene-containing cationic lipids : Influence of redox state on cell transfection, J. Am. Chem. Soc. 127, 11576–11577 (2005).
[129] Golan S., Aytar B.S., Muller J.P., Kondo Y., Lynn D.M., Abbott N.L. and Talmon Y., Influence of biological media on the structure and behavior of ferrocene -containing cationic lipid/DNA complexes used for DNA delivery, Langmuir 27, 6615–6621 (2011).
[130] Aytar B.S., Muller J.P., Kondo Y., Talmon Y., Abbott N.L. and Lynn D.M., Redox-based control of the transformation and activation of siRNA complexes in extracellular environments using ferrocenyl lipids, J. Am. Chem. Soc. 135, 9111–9120 (2013).

EBSCOhost - printed on 2/14/2023 1:06 PM via . All use subject to https://www.ebsco.com/terms-of-use

Sooran Noroozi, Seyed Mohamad Taghavi

5 Ultrafine Nanofiber Formation by Centrifugal Spinning

Large surface-area-to-volume ratio and special morphology of the nano fibers cause them to have remarkable properties such as excellent mechanical properties, heat transfer capacity and electrical features. However, some barriers in nanofiber fabrication techniques such as low production rate, restrictions on materials, process complexity and high production cost limit the mass production of nanofibers. Increasing demand for nanofibers in many applications such as air and water filtering, sensors and protective masks motivates many efforts for eliminating these barriers. Nanofibers produced through the centrifugal spinning (CS) technique have recently been fabricated with much fewer limitations. Nanofiber production through CS, in which a nozzle or orifice rotates at high speed around its axis of symmetry, can produce high volumes of polymeric fibers with average diameters around 300 nm. Although CS is a very practical alternative and promising technique, production of nanofibers by CS technique is facing a number of critical challenges that need to be addressed. Recently invented, CS is still under substantial developments and much research needs to be performed to explain the exact mechanisms responsible for thinning of the fiber through CS. Many physical and geometrical parameters influence the nanofiber production through CS, for example, spinneret angular velocity, orifice radius, polymer solution rheology, surface tension, evaporation rate or temperature. Here, we first introduce the different methods of nanofiber formations and draw a comparison between CS and the other methods based on the literature. Second, we demonstrate our recent attempts to produce and control the nanofiber production through the CS approach, conducted at the Laboratory of Complex Fluids Research in Laval University.

Keywords: Centrifugal spinning, nanofiber, complex fluids, string model, setup design

Nanofiber materials are the strands with diameters less than 1,000 nm, granting them remarkable properties such as high surface-to-volume ratio and flexible surface functionalities. To date, nanofibers have had significant applications in tissue engineering, wound dressing, filter media, sensors, to name a few (see e.g., Huang et al. [1]). Nanofiber production techniques influence the fiber morphology, radius, the web porosity, and the production rate. Although there exist several methods to produce nanofibers,

Sooran Noroozi, Seyed Mohamad Taghavi, Laboratory of Complex Fluids Research, Department of Chemical Engineering, Université Laval, Canada

https://doi.org/10.1515/9783110537734-005

EBSCOhost - printed on 2/14/2023 1:06 PM via . All use subject to https://www.ebsco.com/terms-of-use

only four of them are used in industrial scale, such as electrospinning (ES), melt blowing (MB), bicomponent fiber spinning and centrifugal spinning (CS) [2]. Here, we briefly compare the advantages and disadvantages of these four methods.

5.1 Nanofiber Fabrication Techniques

5.1.1 Electrospinning

To date, the ES technique is the most common technique to produce nanofibers. In this method, electrostatic force is used to stretch a pendant drop to form a continuous fiber. The stretched fibers can then be assembled through a spinning collector forming a highly porous web. The provided voltage, the spinneret–collector distance, the solution properties and the ambient parameters (e.g. ambient humidity) are known to affect the fiber characteristics when using ES techniques [3]. Based on the type of the polymer exposed to the electrostatic force, the ES techniques are classified into three categories: (i) melt ES, (ii) solution ES and (iii) emulsion ES [4]. Although the ES technique is capable of producing nanofibers with small size (>50 nm), it suffers from some limitations such as a need for high voltage, rather low flow rate and instabilities of the process.

5.1.2 Melt Blowing

In the MB technique, a polymer melt is extruded through small nozzles into converged stream of hot blowing air bringing about small-sized fiber production. Besides stretching the polymer into micro/nano-sized fibers, the air also carries the forming fiber down the stream so that a rotating collector can assemble them as nonwoven web. The quality of the forming fibers is controlled by air speed, air temperature, fiber acceleration, polymer properties, the nozzles diameter and the collector–nozzle distance. Using the hot air is essential to keep the emerging fibers from sudden cooling at the orifice. Despite the high throughput, MB techniques require huge machinery; also the choice of materials is very limited.

5.1.3 Bicomponent Spinning

In the bicomponent spinning (BS) method, one of the two immiscible polymers arranged in the cross section is removed and the other one with nanosized cross

EBSCOhost - printed on 2/14/2023 1:06 PM via . All use subject to https://www.ebsco.com/terms-of-use

section remains. The cross section, formed of the two fluids, usually has shapes such as islands in the sea, segmented pie, and hollow segmented pie. The BS method is very promising for controlling the produced fiber diameter. However, like MB method it needs huge machinery. In addition, only some polymers can be treated to form nanofibers using BS techniques.

5.1.4 Centrifugal Spinning

CS, illustrated schematically in Figure 5.1, is a technique to extrude fibers through high speed, rotating polymer solution jets. The CS system is composed of a chamber (spinneret) attached to a rotor shaft and the nozzles at which polymer solution emanates [5]. In the CS process, the emerging fibers move away from the nozzle under centrifugal force and assembled by the collectors, which are typically vertical stationary rods.

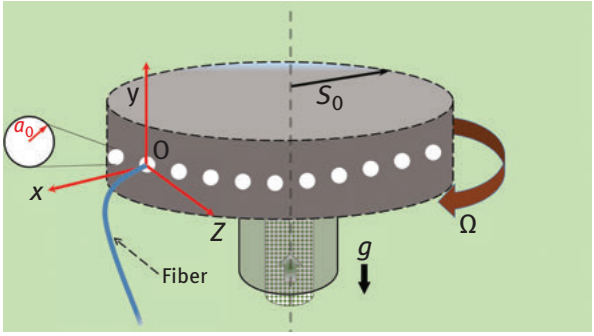

Figure 5.1: Schematic diagram of CS technique.

The high throughput of CS at low cost in industrial scale makes this method a promising alternative for nanofiber fabrication [6]. However, this method suffers from some limitations, for example, corrosion of the device by the solvent. There exists no enough documents to characterize the optimum operational conditions of CS process and beads formation through collecting the fiber. In this chapter, we try to characterize the effects of different parameters on the CS method performance, for example, the effect of rotational speed and surface tension using the experimental and mathematical modeling results.

EBSCOhost - printed on 2/14/2023 1:06 PM via . All use subject to https://www.ebsco.com/terms-of-use

5.2 Experimental Analysis of CS

In this section, at first we introduce the CS setup and the important operational parameters. To understand the most important phenomena involved in the CS process, we briefly show some results on the effects of each parameters on the CS performance based on our experimental data and the literature. Henceforth, we review the different types of spinnable materials to produce centrifugally spun (C-spun) nanofibers. Finally, we go through the effects of material physical properties on the CS performance. It is noted that our experimental work presented here is performed using polyethylene oxide (PEO), 9,00,000 g/mol, solved in deionized water. The concentration of the polymer and rotational speed are 9 wt.% and 10^4 rpm, respectively, unless otherwise specified.

5.2.1 Design Parameters

Here, we introduce the important controlling parameters that affect the producing fiber features such as porosity, fiber size, fiber morphology and defects formation. As discussed in the previous section, in CS a polymeric liquid (solution or melt) is loaded into a spinneret with several nozzles that rotates at a high speed, for example, 10^3–10^4 rpm. The centrifugal force pushes the polymeric liquid through the spinneret nozzles, resulting in continuous polymer jets (Figure. 5.2). These emerging jets have a sharp curvature because of the high centrifugal force which cause them to move away from the spinneret as they are stretched into very thin fibers.

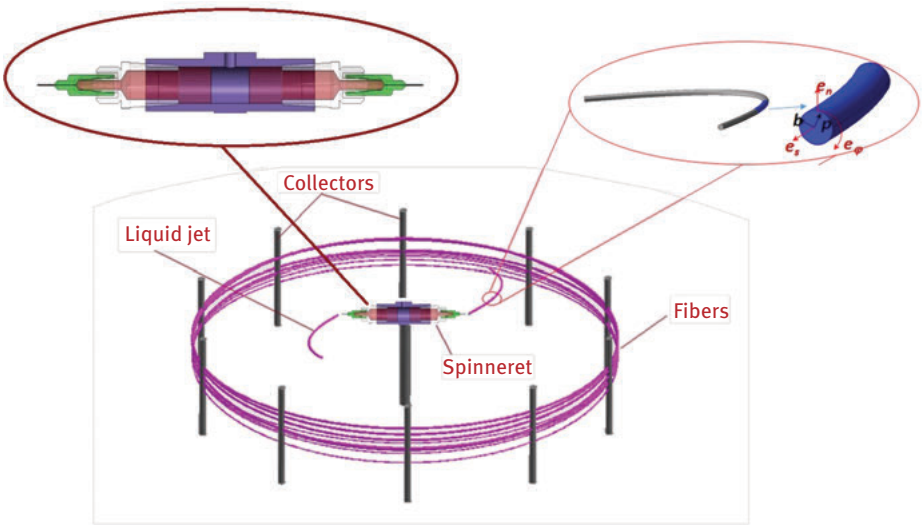

Figure 5.2: Schematic diagram of CS setup.

EBSCOhost - printed on 2/14/2023 1:06 PM via . All use subject to https://www.ebsco.com/terms-of-use

During the process, several parameters consisting of the geometrical design parameters, the spinneret angular velocity, orifice radius, viscosity, shear-thinning and viscoelastic properties, surface tension, temperature, evaporation and ambient humidity play a crucial role on the resultant fiber quality. By controlling these parameters, free beaded fibers with desirable radius and web morphology may be achieved.

5.2.2 Geometrical Parameters

The most important elements of the CS geometry that may impact the fiber trajectory, stretching rate and production rate are the spinneret design, nozzle–collectors distance, fluid fill and diameter of the orifice that polymer solution/melt emerges from.

Geometry of the Spinneret

Generally, there exist two types of spinneret: nozzle-free spinneret and two/multiple nozzles design (see Figure 5.3). The nozzle-free spinneret is composed of a perforated cylinder, which rotates about its axis causing the polymer to emanate from the orifices under the centrifugal force [7]. However, in the two nozzle spinnerets, a cylinder with two nozzles at its ends rotates around its axis to produce nanofibers [8]. In addition, some authors (see e.g. Huttunen and Kellomäki [9] and Wang et al. [10]) used the cotton-candy machine instead of CS-specific designs to produce microfibers and nanofibers. Although the cotton-candy machine is similar to CS in terms of the production technique, its nozzle diameter is relatively large and it rotates at a lower speed [5]. In spite of the fact that the spinneret design may influence the production flow rate, the quality of the produced fiber and controlling the fiber morphology, there is yet no report on the effects of spinneret design on the production quality.

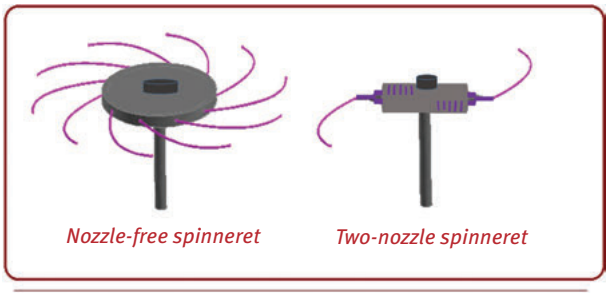

Figure 5.3: Schematic diagram of different spinneret designs.

EBSCOhost - printed on 2/14/2023 1:06 PM via . All use subject to https://www.ebsco.com/terms-of-use

Nozzle–Collectors Distance

By affecting the evaporation time of solvent and thus the solidification time, the gap between nozzle tips and the collectors can influence the fiber morphology and size. Most importantly, it also controls the extension time of the fiber. According to Padron et al. [8], and Lu et al. [11], the fiber extension process fails if the collectors are placed too close to the nozzles due to the very short flight time and hence small solvent evaporation and jet extension. On the other hand, the collector has almost no effect on the production procedure if located at the distance beyond needed for the fiber extension. Our experimental data show that at a certain high rotational speed (9,000–11,000 rpm), increasing the nozzle–collectors distance beyond a certain point, for example, 40 cm with 9,000 rpm, results in production failure; this limitation can be removed with increasing the rotation speed. Zhang and Lu [39], showed that at smaller rotational speed, for example, 4,000 rpm, an increase in the nozzle–collectors distance has no remarkable effect on the fiber diameter.

Fluid Fill

The spinneret feeding process with the polymer solution or melt can be performed continuously or in a batch form in which the polymer solution/melt is placed into the spinneret and then the process starts. In the case of batch feeding, the fluid level in the spinneret may affect the fiber size and the curvature. According to Padron et al. [8], at higher fluid level the size of producing fiber is less than the lower level one and also the fiber emerges further outward. This is attributed to the higher hydrostatic pressure in the spinneret in the case with higher liquid level compared to lower level. However, Mellado et al. [12], declared that due to the very small hydrostatic pressure compared to the centrifugal force, the liquid level in the reservoir does not affect the exit velocity of the jet significantly.

Nozzle Diameter

The orifice diameter plays an important role in the producing fiber size, that is, the initial fiber diameter that emerges from the nozzle is reduced by decreasing the orifice diameter [8, 11]. However, the head loss through the orifice with the smaller diameter is higher and it would be also a source of instability when the rotation speed exceeds a certain point. Additionally, based on our experimental observations, at very small diameters (0.1 mm) the fiber solidifies through the nozzle and causes blockage at small rotation speed (3,000–4,000 rpm). On the other hand, there is a high chance of nozzle failure at high rotational speed. The material properties can have a controlling role to remove such limitations.

EBSCOhost - printed on 2/14/2023 1:06 PM via . All use subject to https://www.ebsco.com/terms-of-use

5.2.3 Operational Parameters

In the CS process, the thinning rate of the fiber is controlled by two mechanisms consisting of stretching the fiber through centrifugal force and the solvent evaporation until the fiber reaches the collecting area [13]. Therefore, the most important operational parameters of the CS that control the quality, shape and size of the producing fibers are the angular velocity of the spinneret, the ambient humidity and the temperature. To understand the effect of these parameters on the fiber formation process, Mellado et al. [12], divided the fiber formation process through CS into three phases which are categorized as (i) jet initiation, (ii) jet extension and (iii) solvent evaporation. Each step can be characterized using its corresponding timescale (see Mellado et al. [12] for the details).

Angular Velocity

Angular velocity of the spinneret acts as the most important parameters in the fiber formation through the CS process. At the jet initiation phase, through overcoming of the surface tension force, the centrifugal force causes the fiber to emerge from the nozzle. Henceforth, during the spinning phase, centrifugal force accelerates the liquid jet by increasing the inertial force. Thus, greater centrifugal force gives rise to more reduction in the fiber size by inducing the greater extension [10]. However, there exists a critical rotation speed at which the fiber starts to break after being expelled from the nozzle and form beads [10].

Figure 5.4 shows the effect of rotation speed on the fiber web porosity, the mean size and fiber morphology based on our experimental data. As observed, at higher rotation speed the mean fiber size is much smaller than the lower speeds. In addition, at lower speed the beads formation is observed. Obviously, the rotation speed limit for beads formation totally depends on the solvent and polymer properties. Moreover, at a certain rotation speed, the jet instabilities start to grow rapidly, causing the jet to break into satellite droplets.

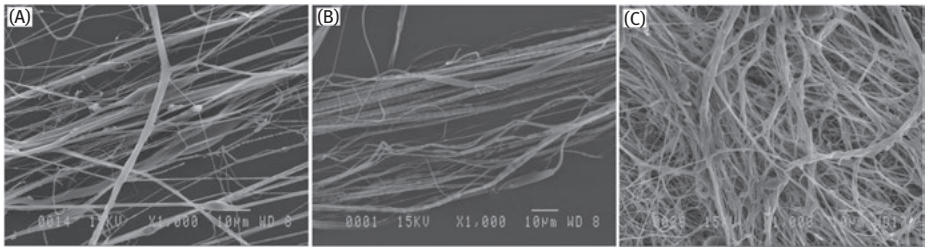

Figure 5.4: SEM image for fiber web formation for 9 wt.% 9,00,000 g/mol solution at (A) 6,000 rpm, (B) 9,000 rpm and (C) 11,000 rpm.

EBSCOhost - printed on 2/14/2023 1:06 PM via . All use subject to https://www.ebsco.com/terms-of-use

Ambient Humidity

The ambient humidity plays a crucial role in solvent evaporation process and thus solidification of the jet by controlling the mass transfer rate of the solvent into the surrounding gas in processes like ES [1]. The effect of humidity has not been profoundly studied on the producing fiber qualities in CS. However, through scaling time method of Mellado et al. [12], one can find that the timescale of solvent evaporation is very large compared to the extension phase. Therefore, the main solvent evaporation may occur once the fiber reaches the collector region.

Temperature

In some cases where the polymer solution/melt viscosity is very high, heat treatment is performed to reduce the viscosity of C-spun fibers. Temperature of the solvent and its change during the CS process may impact the fiber fabrication process through changing the physical properties of the fiber such as density and viscosity. However, there is no report on the temperature effects on the nanofiber fabrication performance using the CS process.

5.2.4 Types of Nanofibers

Through CS, different types of nanofibers can be manufactured consisting of polymer, carbon or ceramic nanofibers. Here, we report the previous attempts to produce different types of nanofibers for various applications using CS.

Polymer Nanofibers

As mentioned, polymer nanofibers can be produced using polymer solutions/melts through CS. To produce a polymer solution, usually polymer is solved in the proper solvent using mixing process and heat treatment simultaneously. There are some authors that have successfully fabricated polymer nanofibers using CS with different types of polymer solution/melts, as listed in Table 5.1.

Carbon Nanofibers

Recently, carbon nanofibers (CNFs) have attracted much attention in aerospace and energy sectors due to their lightweight, large surface area, very high adsorption capacity and electrical conductivity. Producing CNF is a four-step process. At first, a precursor polymer such as polyacrylonitrile is treated by a spinning method like ES or CS to produce precursor fibers. Afterward, using subsequent heat treatment followed by stabilization in air, CNFs can be attained by carbonization in an inert

EBSCOhost - printed on 2/14/2023 1:06 PM via . All use subject to https://www.ebsco.com/terms-of-use

Table 5.1: List of studies on producing polymer nanofibers from polymer solutions/melts using CS along with their applications.

Author	Polymer solution/melt	Desired application
Weitz et al. [13]	poly(methyl methacrylate)	As a prototype system
Badrossamay et al. [7]	PEO-water, PLA-chloroform	Tissue-engineering scaffolds
Huttunen and KelLomäki [9]	Polylactide melt	Tissue-engineering scaffolds
Mellado et al. [14]	Poly(lactic acid)	As a prototype system
McEachin and Lozano [14]	Polycaprolactone	Biomedical applications
Vazquez, Vasquez, and Lozano [33]	Polyvinylidene fluoride	Fuel cells and filtration
Mary et al. [15]	Polycaprolactone blended polyvinyl pyrrolidone	Biomedical applications
Lu et al. [13]	Polyacrylonitrile	Tissue engineering, sensing, battery separators
Ren et al. [25]	Poly(L-lacticacid)	Tissue-engineering scaffolds
Padron et al. [21]	Polyethylene oxide	Filtration and wound dressing

Table 5.2: List of studies on producing ceramic nanofibers using CS along with their applications.

Author	Ceramic nanofiber	Desired application
Sedaghat, Taheri-Nassaj, and Naghizadeh [30]	Alumina mat	Insulating due to low thermal conductivity
Liu et al. [11]	Titanium dioxide (TiO_2) nanofibers	Environmental pollution problems
Liu et al. [12]	Zirconia (ZrO_2) nanofibers	Optical sensors, thermal insulation, solid oxide fuel cells, composite reinforcement

atmosphere [39]. In an experimental work, Zhang and Lu [39], succeeded to produce CNF using poly(methyl methacrylate) through CS.

Ceramic Nanofibers

Using the calcination process, C-spun precursor nanofibers can be synthesized. The process of producing ceramic nanofibers is much more complicated than the polymer nanofibers [11]. Few studies that have been conducted to fabricate ceramic nanofibers using C-spun precursor nanofibers are listed in Table 5.2.

EBSCOhost - printed on 2/14/2023 1:06 PM via . All use subject to https://www.ebsco.com/terms-of-use

Physical Properties

Physical properties of the polymer solutions/melts remarkably affect the extension, trajectory and the size of the emerging fiber during CS process. In this section, we review the impacts of physical properties and the type of the polymer solutions/melts on CS performance. The most effective property of the polymer solution/melt in CS process is polymer viscosity, which is controlled by molecular weight and the solution concentration. Here, we review the effects of these parameters on the CS performance.

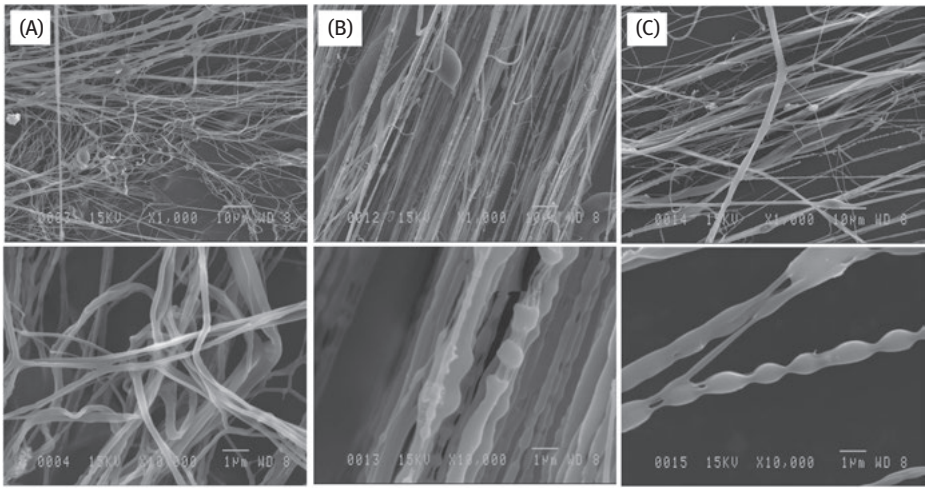

Figure 5.5: SEM image for fiber web formation at 6,000 rpm with polymer molecular weight of 9,00,000 g/mol at (A) 6 wt.%, (B) 8 wt.% and (C) 9 wt.%. Bottom row shows the closer view.

Solution Viscosity

The molecular weight and solution concentration are two controlling parameters of solution viscosity in nanofiber fabrication and define the polymer chains pattern as separated or entangled [21]. The chain entanglement degree determines the resistance of the fiber against centrifugal force and thus fiber extension. At critical value of the chain entanglement density, a phenomenon called the Rayleigh instability occurs in which the jet breaks due to small resistance against the fiber extension. However, at higher values the chain entanglement subdues the Rayleigh instability resulting in the formation of continuous fibers [21]. If the chain entanglement cannot damp the Rayleigh instability completely, beaded fibers are produced. The degree of entanglement of polymer chains in a solution can be described by the number of entanglement per chain (or the Berry number, Be) [22].

Figure 5.5 depicts the scanning electron microscopic (SEM) images of the resultant fiber webs at different polymer concentrations. As seen, with increasing the polymer concentration the mean fiber size increases. The beaded fibers are also

EBSCOhost - printed on 2/14/2023 1:06 PM via . All use subject to https://www.ebsco.com/terms-of-use

observed at higher concentrations. This is attributed to very high resistance against the fiber extension due to high molecular entanglement density.

Surface Tension

Two main forces, namely viscous and surface forces, balance the centrifugal force in the CS process. During CS, the centrifugal force makes the fiber emanate from the orifice and causes the jet surface to increase. By increasing the jet surface area, surface tension force increases causing jet instabilities and beads formation through the CS process. There is no experimental report on the effect of surface tension force variation on the CS performance in the literature. Although some attempts so far have been made to characterize the fiber formation process through CS, the effects of many parameters such as surface tension, evaporation rate and rheological effects have not been fully understood yet and their effects are needed to be scrutinized.

5.3 Mathematical Modeling of CS

Despite the effectiveness of the experimental approach to find the impacts of controlling parameters on the CS process performance, the experimental approach is very time-consuming. Furthermore, it is very hard if not impossible to have a comprehensive understanding of each parameter on the CS process performance in which many parameters are involved using the experimental approach. At this condition, mathematical modeling can help us to understand the physics of such a complex process. In this section, we first introduce the mathematical approaches that have been so far used to model the CS process along with their limitations. Afterward, we show the effects of some important parameters on the nanofiber fabrication performance in the CS process based on our simulation results 5.

5.3.1 Mathematical Modeling Techniques

To date, some authors have tried to model the CS process using different methods including asymptotic method [23–27], rod method [28–31] and regularized asymptotic method [32, 33]. Here, we first briefly introduce the asymptotic method and its limitations. Afterward, we go through our attempts to develop the regularized asymptotic method to remove the singularity problem of asymptotic method. Finally, we focus on the results of our works based on the regularized asymptotic method to consider the effects of controlling parameter on the fiber size.

EBSCOhost - printed on 2/14/2023 1:06 PM via . All use subject to https://www.ebsco.com/terms-of-use

Asymptotic Method

The asymptotic or string models are developed using the zeroth-order slender body theories. In these methods, it is assumed that the jet is a long and thin object with a very small aspect ratio $\varepsilon = a_0/s_0$ (ratio of the nozzle diameter to the spinneret diameter, see Figure 5.1), also known as slenderness parameter. The very small slenderness parameter ε allows us to use the leading and first-order behaviors as a reasonable estimate of the fiber behaviors [34, 35]. Asymptotic model equations are relatively simple and including the fiber non-Newtonian rheological properties and surface tension in the equations is much easier compared to its counterparts known as rod models.

5.3.2 Governing Equations

To derive the governing equations of the CS process, a rotating reference frame with the angular speed of Ω in the Cartesian coordinate system (x, y, z) with the fixed nozzle is assumed. The equations of motion and continuity can therefore be obtained as

$$\begin{gathered}\frac{\partial \mathbf{u}}{\partial t} + \mathbf{u}.\nabla\mathbf{u} = -\frac{1}{\rho}\nabla p + \frac{1}{\rho}\nabla.\mathbf{T} + \mathbf{g} - 2\,\omega\times\mathbf{u} - \omega\times\left(\omega\times\mathbf{r}'\right), \\ \nabla.\mathbf{u} = 0,\end{gathered} \tag{5.1}$$

where t stands for time, ρ the fluid density, and p the pressure within the liquid jet. Also, $\mathbf{g} = (0, -g, 0)$, $\mathbf{\Omega} = (0, \Omega, 0)$, $\mathbf{r'} = (x + s_0, y, z)$. $\mathbf{u}$ and $\mathbf{T}$ denote the velocity field and the shear stress tensor, respectively [24]. These equations along with stress balance equations at the jet–air interface form a set of equations. Due to the highly curved fiber in CS process, analyzing the jet behavior in a Cartesian coordinate is too difficult. Thus, to ease the numerical modeling of the CS process, the governing equations are transformed into a curvilinear coordinate system (s, n, ϕ), where s is the arc length along the jet centerline and (n, ϕ) are the plane polar coordinates, showing the radial and azimuthal directions of the jet cross section [24]. The unit vectors in such a coordinate system are indicated by $\boldsymbol{e_s}$, $\boldsymbol{e_n}$ and $\boldsymbol{e_\phi}$. The origin of the coordinate system is located at the orifice center (denoted by O in Figure 5.1). Moreover, the centerline location is described by the Cartesian coordinates $(X(s, t), Y(s, t), Z(s, t))$. In this chapter, we do not present the procedure to derive the final equations; however, they can be found in complete form in 3D and 2D frames in Parau et al. [36], and Noroozi et al. [33], respectively for Newtonian and non-Newtonian jets. It is noted that the subscripts s and t denote the derivatives with respect to the arc length and time.

Final Set of Equations

After transporting the conservation equations into curvilinear coordinate system and substituting the asymptotic series into each quantity followed by keeping the leading and first-order terms we arrive at the final set of equations as

EBSCOhost - printed on 2/14/2023 1:06 PM via . All use subject to https://www.ebsco.com/terms-of-use

$$
\begin{aligned}
N_{2s} &= \frac{Re}{u}u_t + Re\left(\frac{uN_2}{3}\right)\left(1+\frac{1}{2u^{\frac{3}{2}}We}\right) + \frac{Re}{Fr^2}\frac{\cos(\beta)}{u} \\
&\quad - \frac{Re}{Rb^2}\frac{[(X+1)\cos(\alpha) - Z\sin(\alpha)]\sin(\beta)}{u}, \\
\kappa_1 &= \frac{1}{q}\left(-\frac{2}{Rb} - \frac{1}{u\sin(\beta)Rb^2}((X+1)\sin(\alpha) + Z\cos(\alpha))\right), \\
\kappa_2 &= \frac{1}{q}\left(\frac{\sin(\beta)}{uFr^2} + \frac{\cos(\beta)}{uRb^2}((X+1)\cos(\alpha) + Z\sin(\alpha))\right), \\
q &= uRe - N_2 - \frac{Re}{u^{1/2}We}
\end{aligned}
\tag{5.2}
$$

where N_2 is the tensile force and q stands for the internal energy; α and β are two fiber angles. It is noted that all the quantities are dimensionless here. The important nondimensional numbers here are Rossby (*Rb*), Reynolds (*Re*), Weber (*We*) and Froude (*Fr*) numbers, denoting the ratio of inertial to rotational (centrifugal and Coriolis), viscous, surface and gravitational forces, respectively.

Although the string models are straightforward, they suffer from some limitations (e.g., near-orifice singularities), that is, their applicability is only constrained to certain parameter ranges. Götz et al. [37] and Arne et al. [31] proved that if $ReRb^2 < 1$ the string models have no physically relevant stationary solutions. The singularity problem of asymptotic methods comes from the dominant effects of viscous and surface force terms at the regions near to the nozzle at which the internal energy of the fiber (q in eq. (5.2)) becomes zero or minus. This results in the spurious jet curvature behavior at the vicinity of the jet. This behavior occurs due to eliminating some responsible terms for the fiber bending through keeping just the leading and first-order terms in the curvature equations (see Noroozi et al. [33]). Keeping the responsible terms in the equations, Taghavi and Larson [32] and Noroozi et al. [33] could eliminate the singularity problem of the string model and used the regularized string method for a wide variety of the parameter ranges. Here, we try to show the effects of some important parameters on the CS performance using our mathematical modeling results.

Effect of Rotation Speed

Figure 5.6 illustrates the effect of *Rb* number on the fiber trajectory (Figure 5.6A) and resultant fiber size (Figure 5.6B). It is vividly seen that when rotation speed is small ($Rb = 1$) the fiber falls down after emerging from the nozzle under the gravitational force. At higher speed, on the other hand, the fiber curves and extends until it meets the collectors without remarkably falling down due to the high rotational speed which causes the resultant fiber size much thinner compared to the large

EBSCOhost - printed on 2/14/2023 1:06 PM via . All use subject to https://www.ebsco.com/terms-of-use

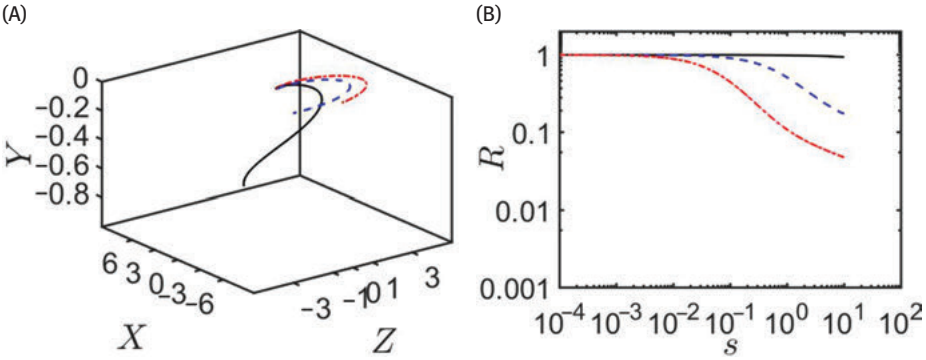

Figure 5.6: Simulation results for $Re = 0.1$ and $Fr = We = 10$ in different Rb numbers: (A) fiber trajectory and (B) fiber radius, $Rb = 1$ (solid line), $Rb = 0.1$ (dashed line) and $Rb = 0.01$ (dash-dot line).

Rb (see Figure 5.6(B)). The simulation results here show that if the fiber does not rupture due to jet instability we can have the fiber 10 times smaller than the nozzle size at relatively small Rb.

Effect of Viscosity

The influence of viscosity variation on the fiber trajectory and size is depicted through Figure 5.7(A) and (B), respectively. As observed, with increasing viscosity (or Re reduction), the fiber curves more toward the spinneret. Furthermore, the resultant fiber size at all three cases meets the same value ($R \approx (Rb^2/2s)$) at sufficiently large distances from the nozzle. This shows that if the collectors are located far enough from the spinneret, the fiber size will be the same regardless of the fiber viscosity. In practice, viscosity damps the jet instability and keeps the jet from rupturing and thus at higher viscosities the jet is more stable.

Effect of Surface Tension

Figure 5.8 illustrates the fiber trajectory and size when the We number (or surface tension) changes. As shown, the We number reduction (or surface tension increase) causes the jet to curve more toward the spinneret. On the other hand, the fiber size is not remarkably affected by We variation.

However, in practice, an increase in surface tension gives rise to jet instability. This phenomenon can be predicted through stability analysis of the jet [38, 39].

EBSCOhost - printed on 2/14/2023 1:06 PM via . All use subject to https://www.ebsco.com/terms-of-use

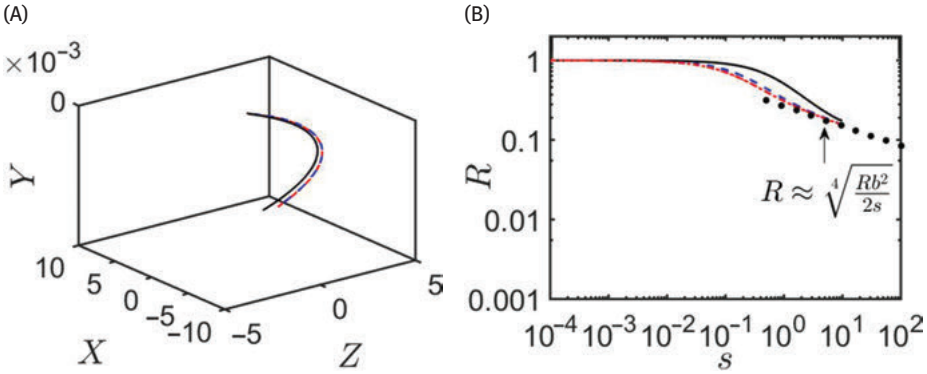

Figure 5.7: Simulation results for *Rb* = 0.1 and *Fr* = *We* = 10 in different *Re* numbers: (A) fiber trajectory and (B) fiber radius, *Re* = 0.1 (solid line), *Re* = 1 (dashed line) and *Re* = 2 (dash-dot line).

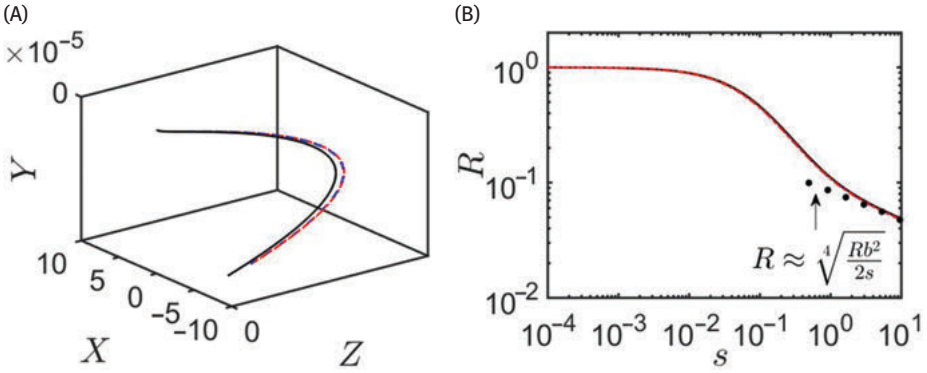

Figure 5.8: Simulation results for *Rb* = 0.01, *Re* = 0.1 and *Fr* = 10 in different *We* numbers: (A) fiber trajectory and (B) fiber radius, *We* = 0.01 (solid line), *We* = 0.1 (dashed line) and *We* = 1 (dash-dot line).

5.4 Conclusion

This chapter introduced a very novel technique called CS to produce nanofibers with high throughput and low cost. We discussed about some advantages of the method compared to other existing methods including ES and MB techniques such as low operating costs, higher production rate and the material choice compatibility. We also introduced the important flaws of the CS process like beads formation and insufficient documentation to characterize such a method. We then went through the controlling parameters of CS process and considered the effects of each

EBSCOhost - printed on 2/14/2023 1:06 PM via . All use subject to https://www.ebsco.com/terms-of-use

parameter on CS process performance based on our experimental and mathematical modeling results conducted in our laboratory. Our study so far shows that there is a lack of data to characterize and map the CS process to produce nanofiber. In near future, our team will try to examine some numerical and experimental tests to fill this gap and successfully characterize the CS process.

References

[1] Huang, Z.M. et al. (2003). "A review on polymer nanofibers by electrospinning and their applications in nanocomposites". In: *Compos. Sci. Technol.* 63.15, pp. 2223–2253.

[2] Nayak, R. et al. (2011). "Recent advances in nanofibre fabrication techniques". In: *Text. Res. J.* 82.2, pp. 129–147.

[3] Feng, C., K.C. Khulbe, and T. Matsuura (2010). "Recent progress in the preparation, characterization, and applications of nanofibers and nanofiber membranes via electrospinning/interfacial polymerization". In: *J. Appl. Polym. Sci.* 115.2, pp. 756–776.

[4] Persano, L. et al. (2013). "Industrial upscaling of electrospinning and applications of polymer nanofibers: a review". In: *Macromol. Mater. Eng.* 298.5, pp. 504–520.

[5] Zhang, X. and Y. Lu (2014). "Centrifugal spinning: an alternative approach to fabricate nanofibers at high speed and low cost". In: *Polym. Rev.* 54.4, pp. 677–701.

[6] Sarkar, K. et al. (2010). "Electrospinning to force spinning TM". In: *Mater. Today* 13.11, pp. 12–14.

[7] Badrossamay, M.R. et al. (2010). "Nanofiber assembly by rotary jet-spinning". In: *Nano. Lett.* 10.6, pp. 2257–2261.

[8] Padron, S. et al. (2013). "Experimental study of nanofiber production through force spinning". In: *J. Appl. Phys.* 113.2, p. 024318.

[9] Huttunen, M. and M. Kellomäki (2011). "A simple and high production rate manufacturing method for submicron polymer fibres". In: *J. Tissue Eng. Regen. Med.* 5.8, e239–e243.

[10] Wang, L. et al. (2011). "Fabrication of polymer fiber scaffolds by centrifugal spinning for cell culture studies". In: *Microelectro. Eng.* 88.8, pp. 1718–1721.

[11] Lu, Y. et al. (2013). "Parameter study and characterization polyacrylonitrile nanofibers fabricated via centrifugal spinning process". In: *Eur. Polym. J.* 49.12, pp. 3834–3845.

[12] Mellado, P. et al. (2011). "A simple model for nanofiber formation by rotary jet spinning". In: Appl. Phys. Lett. 99.20, p. 203107.

[13] Weitz, R.T. et al. (2008). "Polymer nanofibers via nozzle-free centrifugal spinning". In: *Nano Lett.* 8.4, pp. 1187–1191.

[14] McEachin, Z. and K. Lozano (2012). "Production and characterization of polycaprolactone nanofibers via force spinning^{TM} technology". In: *J. Appl. Polym. Sci.* 126.2, pp. 473–479.

[15] Vazquez, B., H. Vasquez, and K. Lozano (2012). "Preparation and characterization of polyvinylidene fluoride nanofibrous membranes by force spinning". In: *Polymer Engineering and Science* 52.10, pp. 2260–2265.

[16] Mary, L.A. et al. (2013). "Centrifugal spun ultrafine fibrous web as a potential drug delivery vehicle". In: *Express Polym. Lett.* 7.3, pp. 238–248.

[17] Ren, L. et al. (2013). "Large-scale and highly efficient synthesis of micro-and nanofibers with controlled fiber morphology by centrifugal jet spinning for tissue regeneration". In: *Nanoscale* 5.6, pp. 2337–2345.

[18] Liu, H. et al. (2013a). "Preparation of nanocrystalline titanium dioxide fibers using sol–gel method and centrifugal spinning". In: *J. Sol-Gel. Sci. Techn.* 65.3, pp. 443–451.

EBSCOhost - printed on 2/14/2023 1:06 PM via . All use subject to https://www.ebsco.com/terms-of-use

[19] Sedaghat, A., E. Taheri-Nassaj, and R. Naghizadeh (2006). “An alumina mat with a nano microstructure prepared by centrifugal spinning method”. In: *J. Non-Cryst. Solids* 352.26, pp. 2818–2828.
[20] Liu, H.Y. et al. (2013b). “Preparation of high-quality zirconia fibers by super-high rotational centrifugal spinning of inorganic sol”. In: *Mater. Manuf. Process*. 28.2, pp. 133–138.
[21] Moghe, A.K. and B.S. Gupta (2008). “Co-axial electrospinning for nanofiber structures: preparation and applications”. In: *Polym. Rev*. 48.2, pp. 353–377.
[22] Sarac, A.S. (2016). Nanofibers of Conjugated Polymers. CRC Press.
[23] Wallwork, I.M. (2001). “The trajectory and stability of a spiraling liquid jet”. *PhD thesis*. University of Birmingham.
[24] Wallwork, I.M. et al. (2002). “The trajectory and stability of a spiralling liquid jet. Part 1. Inviscid theory”. In: *J. Fluid Mech*. 459, pp. 43–65.
[25] Parau, E.I. et al. (2006). “Nonlinear travelling waves on a spiralling liquid jet”. In: *Wave Motion* 43.7, pp. 599–618.
[26] Uddin, J., S.P. Decent, and M.J.H. Simmons (2008). “Non-linear waves along a rotating non-Newtonian liquid jet”. In: *Int. J. Eng. Sci*. 46.12, pp. 1253–1265.
[27] Decent, S.P. et al. (2009). “The trajectory and stability of a spiraling liquid jet: Viscous theory”. In: *Appl. Math. Model*. 33.12, pp. 4283–4302.
[28] Mahadevan, L. and J.B. Keller (1996). “Coiling of flexible ropes”. In: *Proc. R. Soc. A*. 452.1950, pp. 1679–1694.
[29] Ribe, N.M. (2004). “Coiling of viscous jets”. In: *Proc. R. Soc. A*. 460.2051, pp. 3223–3239.
[30] Ribe, N.M., M. Habibi, and D. Bonn (2006). “Stability of liquid rope coiling”. In: *Phys. Fluids* 18.8, p. 084102.
[31] Arne, W. et al. (2010). “Numerical analysis of Cosserat rod and string models for viscous jets in rotational spinning processes”. In: *Math. Mod. Meth. Appl*. S. 20.10, pp. 1941–1965.
[32] Taghavi, S.M. and R.G. Larson (2014). “Regularized thin-fiber model for nanofiber formation by centrifugal spinning”. In: *Phys. Rev. E*. 89.2, 023011, Erratum 89 (5), 059903.
[33] Noroozi, S. et al. (2017). “Regularized string model for nanofibre formation in centrifugal spinning methods”. In: *J. Fluid Mech*. 822, 202–234.
[34] Eggers, J. (1997). “Nonlinear dynamics and breakup of free-surface flows”. In: *Reviews of Modern Physics* 69.3, p. 865.
[35] Hohman, M.M. et al. (2001). “Electrospinning and electrically forced jets. II. Applications”. In: *Phys. Fluids*. 13.8, pp. 2221–2236.
[36] Părău, E.I. et al. (2007). “Nonlinear viscous liquid jets from a rotating orifice”. In: *J. Eng. Math*. 57.2, pp. 159–179.
[37] Götz, T. et al. (2008). “Numerical evidence for the non-existence of stationary solutions of the equations describing rotational fiber spinning”. In: *Math. Mod. Meth. Appl. Sci*. 18.10, pp. 1829–1844.
[38] Wong, D.C.Y. et al. (2004). “Break-up dynamics and drop size distributions created from spiralling liquid jets”. In: *Int. J. Multiphas. Flow*. 30.5, pp. 499–520.
[39] Bassi, R. (2011). “Absolute instability in curved liquid jets”. *PhD thesis*. University of Birmingham.

EBSCOhost - printed on 2/14/2023 1:06 PM via . All use subject to https://www.ebsco.com/terms-of-use

EBSCOhost - printed on 2/14/2023 1:06 PM via . All use subject to https://www.ebsco.com/terms-of-use

Qiliang Wei, Gaixia Zhang, Shuhui Sun

6 Rational Design of Highly Efficient Non-precious Metal Catalysts for Oxygen Reduction in Fuel Cells and Metal–Air Batteries

Exploring inexpensive and high-performance non-precious metal catalysts (NPMCs) to replace the rare and expensive platinum-(Pt)-based catalyst for oxygen reduction reaction (ORR) is crucial for future low-temperature fuel cell and metal–air battery devices. So far, Fe/N/C-based catalysts exhibiting superior ORR performance than the other NPMCs have received intensive exploration. Especially, a breakthrough for NPMCs has been made by the Dodelet group, with catalyst activity approaching that of Pt in a polymer electrolyte membrane fuel cell (PEMFC). However, commercialization has been mainly hampered by its poor stability during chronoamperometry experiment. Recently, as the work of torch relay, we investigated the possible mechanisms for the poor stability of the Fe/N/C in a PEMFC and also explored some novel structured efficient Fe/N/C electrocatalysts for ORR, which hold great potential for use in PEMFC and metal–air battery.

Keywords: PEM fuel cells, metal-air batteries, non-precious metal catalysts, Fe/N/C, stability mechanisms, novel nanostructures

6.1 Introduction

Nowadays, the rising global energy demand and environmental pollution of traditional fossil fuels have become serious global problems. Practical and environmentally sustainable energy sources to replace traditional fossil fuels are urgently needed. Fuel cells and metal–air batteries, in particular the proton exchange membrane (or polymer electrolyte membrane) fuel cells (PEMFCs) and rechargeable Zn–air batteries, are regarded among the most promising candidates [1, 2]. As a vital part, the oxygen reduction reaction (ORR) on the cathode is particularly more difficult to carry out and more responsible for the performance of fuel cells and metal–air batteries. Platinum (Pt) nanoparticles (NPs) dispersed on carbon material catalysts are currently considered as offering the best ORR performance. However, the high cost and low abundance of Pt hinder the widespread and commercialization of these promising devices. Moreover,

Qiliang Wei, Gaixia Zhang, Shuhui Sun, Institut National de la Recherche Scientifique-Énergie Matériaux et Télécommunications, Varennes, Canada

https://doi.org/10.1515/9783110537734-006

EBSCOhost - printed on 2/14/2023 1:06 PM via . All use subject to https://www.ebsco.com/terms-of-use

Pt-based catalysts suffer from susceptibility to methanol crossover, carbon monoxide (CO) poisoning, carbon corrosion, and Pt particles agglomeration. Therefore, rational design of highly active, extremely stable, and methanol (and CO) tolerance catalysts with low Pt usage and non-Pt nanomaterials remains a critical issue in the development of fuel cells and metal–air batteries. Considerable efforts have been directed toward (1) decreasing Pt content in the catalysts by developing either Pt–metal alloy or their novel structured materials [3–12], and (2) replacing Pt-based catalysts by non-precious metal catalyst (NPMC) and ORR catalysts (Figure 6.1a) [13–20]; among the latter, catalysts based on Fe/N/C are particularly promising because of their superior ORR performance than the other NPMCs. Especially, in 2009, the Dodelet group at Institut National de la Recherche Scientifique (INRS) made a breakthrough, with activities (the kinetics) of Fe–N/C catalyst comparable to that of Pt or C (Figure 6.1a) [20]. Then the synthetic method was further optimized by the same group using a metal organic framework (MOF, ZIF-8) instead of carbon black and the catalyst (here named as NC

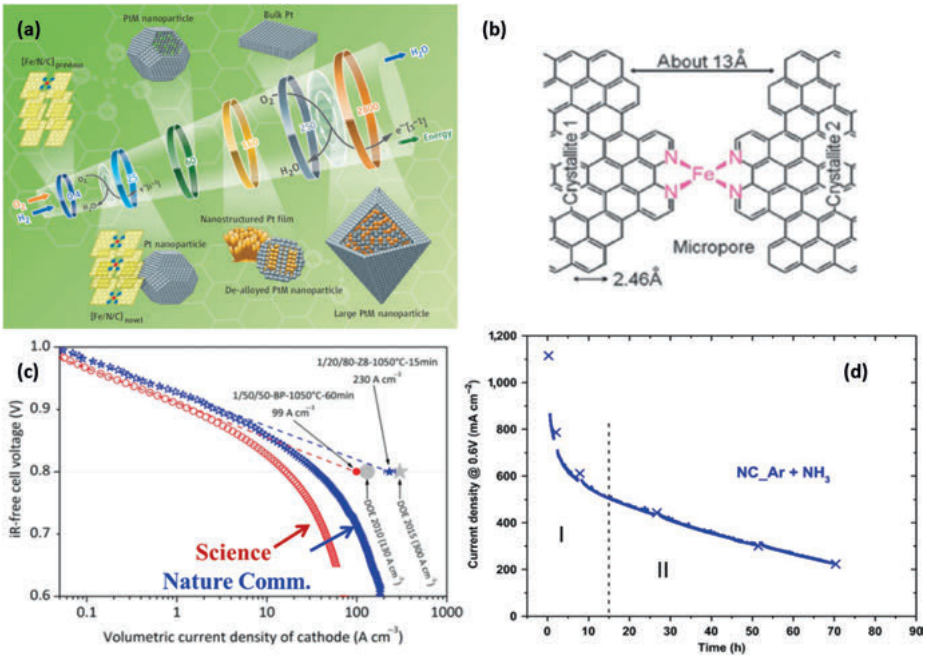

Figure 6.1: (a) The development scheme of Pt and Pt-free catalysts for PEMFC, (b) scheme of the FeN_4 active sites in micropores, (c) polarization curves for membrane electrode assembly (MEAs) comprising a cathode made with 1/20/80-Z8-1,050 °C–15 min the most active Fe/Phen/ZIF8-derived catalyst [19] (blue stars) and 1/50/50-BP-1050 °C-60 min^{20} (red circles) developed in Dodelet group, (d) chronoamperometry curves showing two decay rates (I and II) for the current density at 0.6 V and 80 °C in H_2/O_2 fuel cell for NC_Ar+NH_3. The cathode catalyst loading is 4 mg cm^{-2} and the MEA membrane is Nafion 211. Reproduced with permission from Refs. [19, 22].

EBSCOhost - printed on 2/14/2023 1:06 PM via . All use subject to https://www.ebsco.com/terms-of-use

catalyst) has the same level of power density as Pt/C [19, 20]. The active sites are believed to be FeN_4 existing in the micropores [21] (Figure 6.1b). The catalyst was labeled NC_Ar+NH_3 (or sometimes NC_Phen_Ar+NH_3). It is made by first ball milling a mixture of ZIF-8 (a MOF containing zinc nodes and 2-methylimidazole ligands) and the complex formed between Fe(II) acetate and 1,10 phenanthroline (Fe(II)$[Phen]_3$. $2Ac^-$). The resulting material is first pyrolyzed in Ar at 1,050 °C, then in pure NH_3 at 950 °C. Although NC_Ar+NH_3 performs well initially at 0.6 V in H_2/O_2 fuel cell (Figure 6.1c), the poor stability is a definite constraint that limits it into becoming serious contenders to Pt (at least for automotive applications). Therefore, unveiling the reasons of the instability of the active Fe/N/C catalysts and exploring novel structured active and stable Fe/N/C catalysts have become our research interest.

6.2 Investigating Decay Mechanism of MOF-Based NC_Ar+NH_3 Catalysts

6.2.1 Whether Iron is Involved in the Lack of Stability Catalysts

From Figure 6.1d, there are two decay rates that can be observed on the curve representing the current density decay at 0.6 V: a fast decay lasting about 15 h, followed by a much slower decay lasting up to the end of the chronoamperometry experiment. Our first hypothesis is to verify if iron in the catalyst could be at the origin of the first rapid decay of NC_Ar+NH_3 through a Fenton reaction with some H_2O_2 generated by an incomplete reduction of O_2 in fuel cell [22]. To do so, the strategy was simple: produce a MOF_Ar+NH_3 catalyst using the same ZIF-8, but without deliberate addition of an iron precursor, and compare its stability to that of NC_Ar+NH_3. However, this has been impossible to achieve since there is a native iron impurity in ZIF-8 leading to an increase of Fe content after each pyrolysis step. In order to circumvent this problem, we produced several MOF_Ar+NH_3 (t) catalysts, varying (t), and the pyrolysis time in NH_3 (and therefore also the Fe content). This enabled us to determine, by extrapolation to 50 ppm Fe on a log i versus log Fe content, the initial current density at 0.6 V of a catalyst (MOF_CNx_Ar+NH_3) for which the current density would essentially be attributable to CNx catalytic sites.

RRDE experiments were performed on four selected catalysts: three of them being NC_Ar+NH_3, MOF_Ar+NH_3 (20 min), and MOF_ Phen Ar+NH_3. The other catalyst (NC_Ar) is an intermediate toward NC_Ar+NH_3. The Rotating ring disk electrode (RRDE) results are presented in Figure 6.2a. The disk currents versus potential indicate that the catalytic activity of these four catalysts decrease from NC_Ar+NH_3>NC_Ar>MOF_Ar+NH_3 (20 min)>MOF_ Phen Ar+NH_3. The selectivity of the same catalysts evolves in the reverse order since MOF_ Phen Ar+NH_3

EBSCOhost - printed on 2/14/2023 1:06 PM via . All use subject to https://www.ebsco.com/terms-of-use

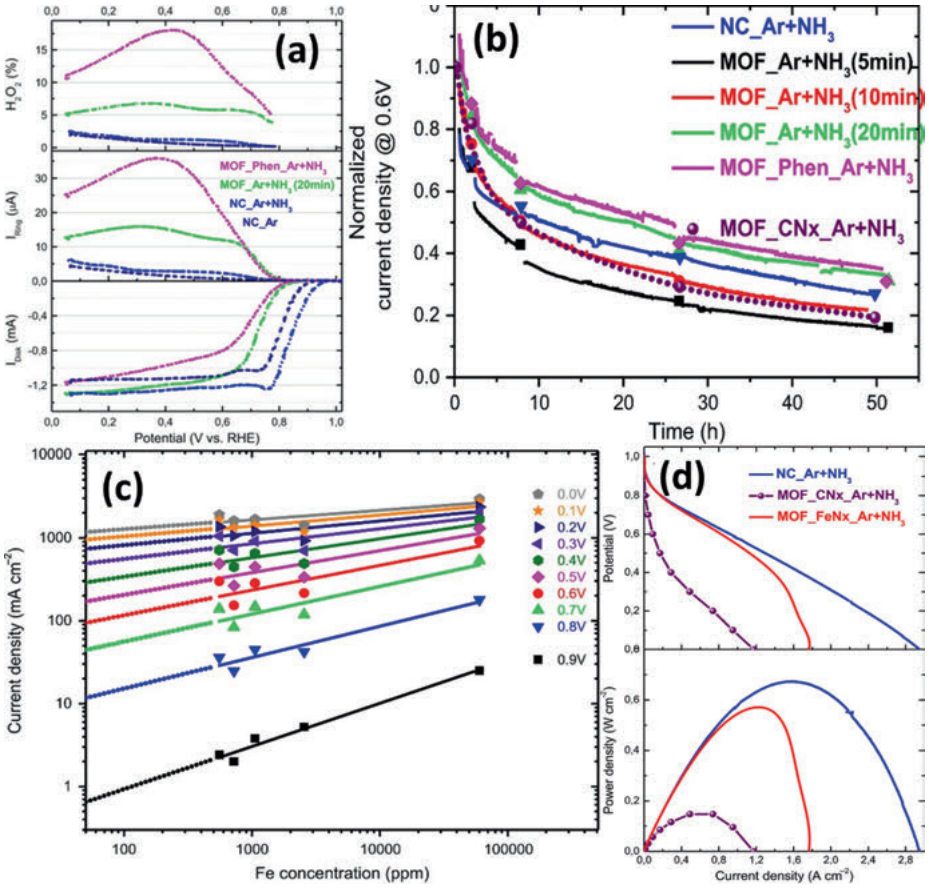

Figure 6.2: (a) RRDE experiments performed on five selected cathode catalysts at 1,500 rpm and at room temperature in a H_2SO_4 solution at pH 1. The catalyst loading onto the glassy carbon disk is 817 μg cm^{-2}. (b) Normalized current density at 0.6 V and 80 °C in H_2/O_2 fuel cell for either NC_Ar+NH_3 or various MOF_Ar+NH_3 cathode catalysts. (c) Log–log plot of the initial current density at 80 °C for various potentials (from 0.9 V to 0.0 V) in H_2/O_2 fuel cell of various MOF–Ar+NH_3 cathode catalysts, including NC_Ar+NH_3 (solid lines) and their extrapolation at 50 ppm Fe (dotted lines) in order to obtain what would be the initial current density at the same potential in fuel cell of a MOF–CNx_Ar+NH_3 catalyst that would contain a large majority of CNx sites active for ORR. All cathode catalyst loadings are~4 mg cm^{-2} and the membranes used in all MEAs is Nafion 211. (d) Initial experimental polarization curve and corresponding power curves obtained at 80 °C in H_2/O_2 fuel cell for NC_Ar+NH_3 cathode catalyst (blue line). Reproduced with permission from Ref. [22].

generates a much larger amount of peroxide than the other catalysts. It is followed by MOF_Ar+NH_3 (20 min), then by the two other catalysts that practically reduce O_2 to H_2O below 0.8 V in an acid solution. The efficiency of the Fenton reaction depends mainly on H_2O_2 concentration, pH, and temperature. Here, the last two parameters were the same for all the catalysts. When Fe is present, Fe

EBSCOhost - printed on 2/14/2023 1:06 PM via . All use subject to https://www.ebsco.com/terms-of-use

ions act as catalyst for HO• generation, according to the reaction of Fe^{2+} with H_2O_2 ($Fe^{2+} + H_2O_2 + H^+ \rightarrow Fe^{3+} + HO\bullet + H_2O$). This reaction becomes the dominant source of HO• when Fe impurity > 40 ppm. If H_2O_2 or HO• radicals were causing the current degradation during the first 15 h of durability test at 0.6 V in fuel cell, the current decay would certainly be different from one catalyst to another on the basis of the large differences in the amount of peroxide release and of iron content attributed to these catalysts. However, the normalized current decay curves shown in Figure 6.2b for the three catalysts tested for peroxide in solution (NC_Ar + NH_3, MOF_Ar + NH_3 (20 min), and MOF_Ar_Phen + NH_3) behave very similarly on the entire decay range tested (about 50 h). One may therefore conclude that it is neither the chemical oxidation of the catalysts by H_2O_2 nor by HO• (or ferryl ions) that is causing their fast current decay during their first 15 h of durability test.

Figure 6.2c displays the linear extrapolations to 50 ppm Fe at all potentials from 0.9 to 0.0 V of the fuel cell measurement. The values of current density, extrapolated at 50 ppm Fe at each potential in Figure 6.2c, are used to plot the purple symbols in Figure 6.2d. This is the catalyst MOF_CNx_Ar+NH_3, with the initial polarization curve in H_2/O_2 fuel cell essentially containing CNx catalytic sites (plus a few FeNx sites derived from the 50 ppm Fe content). The initial power density curve of MOF_CNx_Ar+NH_3 is the purple curve in Figure 6.2d. The polarization and power density curves for NC_Ar+NH_3 are also given for comparison (blue curves in Figure 6.2d). The red curve in Figure 6.2d is obtained by subtracting, at each potential, the contribution of MOF_CNx_Ar+NH_3 from the total current density curve of NC_Ar+NH_3, which is the blue curve in Figure 6.2d. Assuming that the only sites contributing to the total current density in the NC_Ar+NH_3 catalyst are FeNx and CNx sites, the red curve is therefore an expression of what would be the initial polarization curve in H_2/O_2 fuel cell of the exclusive contribution of FeNx sites to the total current density. Its power contribution is given by the red curve in the bottom of Figure 6.2d. As one may see in Figure 6.2d, the individual contribution of CNx and FeNx sites to the total current density is not in a constant ratio at all potentials. FeNx sites are already very active at high potential where their contribution dominates the total current density. However, being mainly located in micropores, these sites strongly suffer from transport limitations when the total current density increases. Near 0 V, they practically reach a limiting current density, while the contribution of the CNx sites always increases as the applied potential decreases.

6.2.2 A Specific Demetalation of Fe–N_4 Catalytic Sites in the Micropores [23]

In order to find the real reason for the fast initial current density decay of the NC_Ar+NH_3 catalyst, a series of experiments in which recording of polarization

EBSCOhost - printed on 2/14/2023 1:06 PM via . All use subject to https://www.ebsco.com/terms-of-use

curves alternates with chronoamperometries at different potentials were conducted. Figure 6.3a shows the results of the first MEA (MEA#1) analyzed at 500 mV. It starts with the recording of a first polarization curve (PC#1). During this measurement, the current density is measured from open circuit voltage (OCV) to 0 V versus reversible hydrogen electrode (RHE). Then the cell potential is set at 500 mV and the current density is recorded for 25 h after which a second polarization curve (PC#2) is measured from OCV to 0 V versus RHE. Then the cell potential is again set at 500 mV and the current density is recorded for another 25 h until the total elapsed time reaches 50 h. The same alternation in the polarization curve and chronoamperometry is repeated three more times until the total duration of the experiment reaches 125 h.

Figure 6.3b displays six polarization curves (Figure 6.3c, in Tafel representation) recorded during the entire 125 h of chronoamperometry experiments at 500 mV. It is possible on Figure 6.3b to read the evolution with elapsed time of the current density of MEA#1 at different potentials. Here only potential of 0.8 V is given. The current density at 0.8 V is probed by the magenta color horizontal lines crossing all polarization curves at 0.8 V. By reading the current density, it can be drawn as shown in Figure 6.3d, which represents the change in current density at 0.8 V. Figure 6.3e shows how current density at 0.8 V changes with the elapsed time when chronoamperometries were performed at seven different potentials from 800 to 200 mV on seven different MEAs. There are six experimental points on each curve in Figure 6.3e because five chronoamperometry segments were recorded at each potential as may be seen in Figure 6.3f. The same results were obtained at different potentials from 0.8, 0.7, 0.6 V... to 0.2 V, that the change of current density with elapsed time at a given potential is practically the same for that given potential (in V), indicating that the fast initial current decay of the MEAs was insensitive to the potential used during the chronoamperometry steps.

Figure 6.3h shows the decrease in both current densities measured at 0.8 V in a fuel cell run at 80 and 25 °C. The curve with the black symbols in Figure 6.3h was obtained for a first MEA in a H_2/air fuel cell at 80 °C, while that with the red symbols was obtained at 25 °C for a second MEA. Figure 6.3i shows the same results with Figure 6.3h, but this time, it is the logarithm of the current density versus time. In this representation, a large fraction of the experimental points follows a linear function (black straight line at 80 °C and a red one at 25 °C). By extrapolating the straight line to $t = 0$, it is possible to follow the entire current decrease from $t = 0$ in zone 2 and also to calculate $t_{1/2}$, the half-life for the exponential current decay as a function of time in zone 2. In the example shown in Figure 6.3, $t_{1/2}$ = 2,360 min at 0.8 V and 80 °C, while $t_{1/2}$ = 6,000 min at 0.8 V and 25 °C. The difference in Figure 6.3i between the experimental points and the straight line at the same temperature represents the decrease in the current density in zone 1. The latter is plotted in Figure 6.3j at 80 and 25 °C. Figure 6.3k presents the same results as in Figure 6.3j, but this time the logarithm of the current density is again expressed as a function of time. In this representation, one may see that the

EBSCOhost - printed on 2/14/2023 1:06 PM via . All use subject to https://www.ebsco.com/terms-of-use

experimental points are again following a linear function, at both 80 and 25 °C, from which $t_{1/2}$ may be calculated at both temperatures for the current density decrease in zone 1. In the example of Figure 6.3k, $t_{1/2}$ = 102 min at 0.8 V and 80 °C, while it is 144 min at 0.8 V and 25 °C. Both the current density decrease shown in Figure 6.8h are therefore the sum of two kinetics of current decrease. The same operation may be repeated for 0.7, 0.6, . . .0.2 V with the same conclusion: that of a superposition at each potential of two first-order kinetics, a fast one and a slow one for the decrease in current density in H_2/air fuel cell. The conclusion drawn from these two temperature experiments was that $t_{1/2}$ for the fast initial exponential decay of the current density (relative to the initial current density of the MEA) was practically the same at all potentials and also at both temperatures used. On the contrary, $t_{1/2}$ for the slow exponential decay of the current density (relative to the initial current density of the MEA) greatly differed with the potential and the temperature. Indeed, $t_{1/2}$, second decay at 80 °C went from 2,360 min at 0.8 V to 25,000 min at 0.2 V, while at 25 °C, $t_{1/2}$, second decay increases from 6,000 min at 0.8 V to infinity at 0.2 V.

From the adsorption–desorption isotherm of NC_Ar+NH_3, it is deduced that the Fe/N/C carbonaceous catalyst is characterized by interconnected open-end slit-shaped micropores in which water (with dissolved H^+ and O_2) quickly flows under the pressure differential of a working cathode if their width is ≥ 0.7 nm, as it has no interaction with the micropore hydrophobic walls. Although FeN_4-like sites are thermodynamically stable in a closed system, they are not stable anymore when they are located in the open system of a micropore network through which there is a fast transport of water (and dissolved protons and oxygen). In that case, Le Chatelier principle applies, and the equilibrium between the iron ion in and out of the FeN_4-like site cannot be established because the iron ion as soon as it leaves the site located in the micropore, is first flushed out of the micropore network by the rapid flow of water prevailing in these nanostructures to finally end up out of the MEA. The loss of iron is confirmed by the combination of Mossbauer spectroscopy and neutron activation analysis (NAA) (Figure 6.3l). The empty black points in Figure 6.3l present the relative decrease (in %) of the current density measured at 0.6 V in H_2/air fuel cell running at 80 °C during a maximum of 50 h. Six different MEAs, prepared with a NC_Ar+NH_3 catalyst synthesized with a ^{57}FeAc precursor, were used to obtain this figure. The first MEA (reference) was used without running any fuel cell test. For the remaining five MEAs, the fuel cell test of the second MEA was stopped after 1 h, while that of the third MEA was stopped after 2 h; after 6 h for the fourth MEA; after 18 h for the fifth one; and after 50 h for the sixth one. After completion of the electrochemical tests, each MEA was analyzed by NAA to measure their iron content. They were also analyzed by Mossbauer spectroscopy to determine the changes, from t = 0 to t = 50 h, in relative proportions of "inorganic" and "organic" iron species. NAA and Mossbauer spectroscopy of the first MEA were used as reference (t = 0 h). The decrease of the sum of the FeN_4 sites (D1 + D2) is shown as colored triangles in Figure 6.3l, where it is seen that the relative number of

EBSCOhost - printed on 2/14/2023 1:06 PM via . All use subject to https://www.ebsco.com/terms-of-use

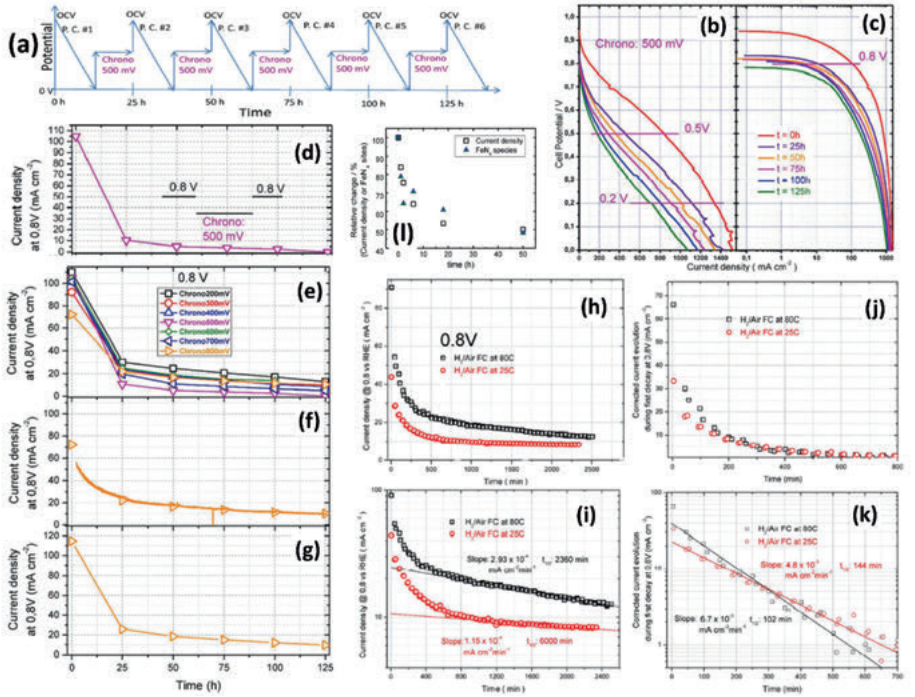

Figure 6.3: (a) Sequence of experiments for MEA#1 analyzed by recording polarization curves (PC) at a sweep rate of 0.5 mV s^{-1} in alternation with chronoamperometries at 500 mV; (b) classical and (c) Tafel representations of the six polarization curves for MEA#1 recorded initially (t = 0 h) and after each of the five chronoamperometry segment of 25 h at 500 mV. The change in current density with elapsed time for MEA#1 is probed by horizontal lines at three potentials: (1) 0.8, (2) 0.5, and (3) 0.2 V. (d) Punctual evolution at 0.8 V of the current density read for MEA#1 on the sequence of polarization curves recorded at t = 0 h and after each of the 25 h five chronoamperometry segments at 500 mV. (e) Current density values read at 0.8 V on each of the six polarization curves recorded during the entire 125 h experiment for all seven MEAs used in this work, each MEA having been maintained at a different chronoamperometric potential (between 200 and 800 mV) during the stability experiment; (f) change in current density at 0.8 V during the five 25 h chronoamperometry segments at 800 mV; the symbols are the current density values read at 0.8 V on each polarization curve; (g) average current density values of Figure 6.3e at t = 0 h and after 25, 50, 75, 100, and 125 h for all seven MEAs used in this work, each MEA having been maintained at a different potential (from 200 to 800 mV) during the stability experiment. (h) Time evolution of current densities in zones 1 and 2 at 0.8 V in H_2/air PEM fuel cell and at 80 °C (black symbols) and 25 °C (red symbols); (i) half-life determination for the exponential decay of the current density in zone 2; (j) exponential decay of the current density in zone 1; (k) half-life determination for the exponential decay in zone 1. (l) Relative changes versus time of (i) the number of FeN_4-like sites (filled colored triangles) at the cathode of MEAs using a NC_Ar+NH_3 catalyst and (ii) of the current density provided by the same MEA (empty black squares) in H_2/Air fuel cells running at 0.6 V and 80 °C. The numbers of FeN_4-like sites were obtained from the absorption areas in the Mossbauer spectra and from the iron contents at the cathode of MEAs as determined by neutron activation analysis. Reproduced with permission from Ref. [23].

EBSCOhost - printed on 2/14/2023 1:06 PM via . All use subject to https://www.ebsco.com/terms-of-use

FeN_4 sites (the colored triangles) decreases in a similar way than that of the relative current density measured at 0.6 V (the empty black points in Figure 6.3l). During the same period of 50 h, the amount of "inorganic iron species" remains almost constant (not shown). The duration of the 50 h test covers the entire duration of the first decrease in the current density (the fast decay) but only a very small part of the slow decay. The latter is characterized by a value of $t_{1/2}$ at 0.6 V of about two orders of magnitude larger than that of the fast decay at the same potential. It can be assigned the fast decrease in the number of FeN_4 sites observed by Mössbauer spectroscopy to the disappearance of these active sites in the micropores. In conclusion, this specific demetalation of the FeN_4-like catalytic sites located in the micropores, is the cause of the initial loss of ORR activity of NC_Ar+NH_3 catalysts in fuel cells assigned to the first, fast current decay.

6.3 Novel Structured Non-precious Metal Catalyst Electrocatalytst

6.3.1 Core–Shell Structured Electrocatalysts

The core–shell structured NPMC was prepared by a synthetic approach via pyrolysis of evaporation-induced self-assembled iron(III) porphyrin molecules uniformly deposited on templating carbon black [24]. FeTMPPCl has been chosen as precursor of NPMCs for three reasons. First, FeTMPPCl and carbon support are both hydrophobic and the hydrophobic–hydrophobic interaction will be beneficial for FeTMPPCl to be dispersed on carbon easily. Second, FeTMPPCl contains FeN_4 sites and are active for ORR. Third, FeTMPPCl is relatively cheap and readily available. In a typical synthesis, initially, the acid-treated carbon black was well dispersed in chloroform containing FeTMPPCl with the aid of brief mild sonication in a water bath. Next, chloroform was slowly rotary evaporated under vacuum to induce the self-assembly of FeTMPPCl templated on carbon black as shown in Figure 6.4a. In the following, FeTMPPCl-coated carbon black was treated in argon to form graphene-like layers wrapping the carbon template and iron species coming from FeTMPPCl precursor. Finally, the sample was treated in acid to remove iron species and other by-products.

Transmission electron microscopy (TEM) images (Figure 6.4b, c) reveal that before and after FeTMPPCl molecules coated on the carbon black, there is no noticeable structural difference. As expected, no large FeTMPPCl agglomerations were formed during the self-assembly process. After heat treatment, it is found that graphene-like layers have fully coated on the carbon black mixed with 20–50 nm particles covered with thin graphene-like layers (1–2 nm) as shown in Figure 6.4d. After being leached in 0.5 M aq. H_2SO_4, TEM images reveal that Fe_3O_4 NPs have been completely removed likely because of insufficient protection of the 1–2 nm thin graphene-like layers.

EBSCOhost - printed on 2/14/2023 1:06 PM via . All use subject to https://www.ebsco.com/terms-of-use

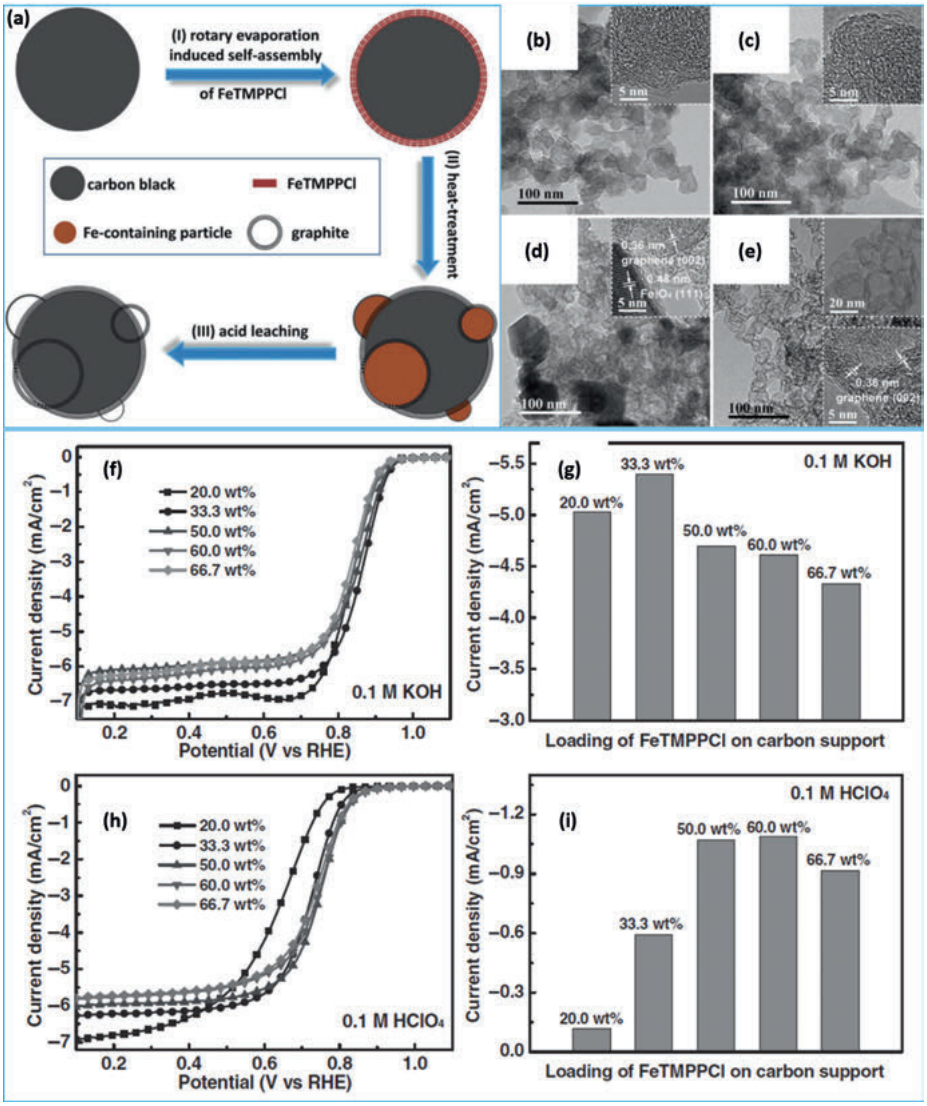

Figure 6.4: (a) Schematic synthetic route of NPMCEs: (I) rotary evaporation-induced self-assembly, (II) heat-treatment of FeMTPPCl-coated carbon, (III) acid leaching step for the removal of unstable species and by-products. (b–e) TEM image of samples obtained at different synthetic stage. (f–i) ORR polarization curves measured in O_2-saturated 0.1 m KOH with a positive sweep rate of 5 mV s^{-1} at 1,600 rpm for NPMCs synthesized with 20.0–66.7 wt% loading of (f) FeTMPPCl on carbon and (g) their corresponding current density at 0.8 V (vs. RHE); ORR polarization curves measured in O_2-saturated 0.1 m $HClO_4$ with a positive sweep rate of 10 mV s^{-1} at 1,600 rpm for (h) NPMCs synthesized with 20.0–66.7 wt% loading of FeTMPPCl on carbon and (i) their corresponding current density at 0.8 V (vs. RHE). Reproduced with permission from Ref. [24].

EBSCOhost - printed on 2/14/2023 1:06 PM via . All use subject to https://www.ebsco.com/terms-of-use

Interestingly, the obtained NPMC turns out to be composed of multiple graphene-like layers fully coated on the carbon black (Figure 6.4e and insets) mixed with hollow spheres with only 1–2 nm of graphene-like layers formed by the removal of central Fe_3O_4 particles.

The electrochemical properties of resultant NPMCs were evaluated in both alkaline (0.1 M KOH) and acidic (0.1 M $HClO_4$) solution using rotating disk electrode (RDE) technique. ORR polarization curves of NPMCEs synthesized with different FeTMPPCl loading on carbon are shown in Figure 6.4f–i. It turns out that the ORR activity varies to a large extent in both alkaline and acidic solutions relative to the FeTMPPCl loading on the carbon in terms of the current density at 0.8 V (vs. RHE) as the describer of ORR activity. Under alkaline conditions, at the loading of 33.3 wt%, the highest current density at 0.8 V (vs. RHE) is achieved. At either a higher or lower loading, the obtained current density at 0.8 V (vs. RHE) decreases (Figure 6.4f, g). It is likely that there is not enough ORR active sites formed below the 33.3 wt% of FeTMPPCl loading and some of the ORR active sites have been covered up above the 33.3 wt% loading. In contrast, in 0.1 M $HClO_4$ aqueous solution, the relationship between the current density at 0.8 V (vs. RHE) and FeTMPPCl loading shows a trend different from that occurring in alkaline media (Figure 6.4h, i). The current density at 0.8 V (vs. RHE) continuously increases from 0.12 to 0.59 to 1.07 mA cm^{-2} as the FeTMPPCl loading changes from 20.0 to 33.3 to 50.0 wt%. Further enlargement of the FeTMPPCl loading from 50.0 to 60.0 wt% merely results in an almost constant current density at 0.8 V (vs. RHE) (1.07 and 1.09 mA cm^{-2}), and further increase to 66.7 wt%, the current density at 0.8 V (vs. RHE) again decreases to 0.91 mA cm^{-2}. There are not enough ORR active sites created, as the FeTMPPCl loading is less than 50.0 wt%. At the loading of 50.0 wt%, the number of ORR active sites reaches the maximum value. When the FeTMPPCl loading is even larger than 50.0 wt%, the ORR active sites appear to remain almost unchanged. It seems that the reaction media is a critical factor for the ORR performance of the same type of NPMCs.

Besides ORR activity, the durability of NPMCs is also critical for practical applications. The durability test was carried out by cycling NPMC and commercial Pt/C-coated RDE in O_2-saturated 0.1 M KOH or 0.1 M $HClO_4$ solution. Figures 6.5a, b exhibit the durability of NPMCs synthesized with different FeTMPPCl loadings on carbon black in both alkaline and acidic electrolyte. In 0.1 M KOH, the NPMCs obtained at various FeTMPPCl loadings on carbon demonstrate remarkable durability during the potential cycling process. There is nearly no degradation observed for each NPMC after durability test. In contrast, commercial Pt/C loses 74.3% of the original activity in terms of current density at 0.9 V (vs. RHE) after 2,500 cycles of potential cycling. Interestingly, in 0.1 M $HClO_4$, when the FeTMPPCl loading on the carbon increases from 20.0 to 50.0 wt%, the durability in terms of current density at 0.7 V (vs. RHE) continuously gets improved. As the loading of FeTMPPCl on the carbon further increases to 60.0 wt%, the durability gains no additional improvement (Figure 6.5b). In contrast, commercial Pt/C shows the same durability as the NPMC synthesized

EBSCOhost - printed on 2/14/2023 1:06 PM via . All use subject to https://www.ebsco.com/terms-of-use

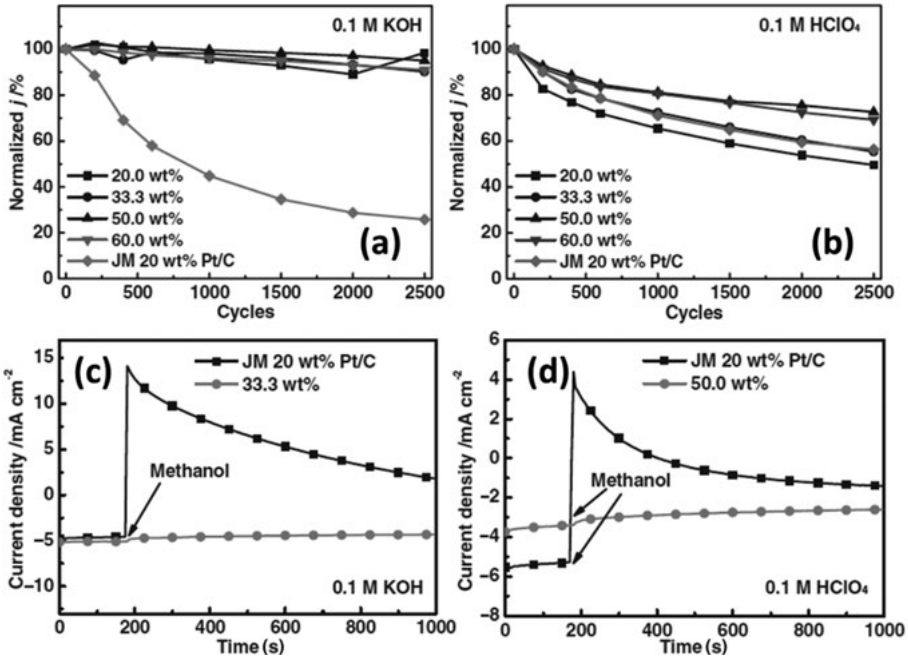

Figure 6.5: (a) Current density degradation of the NPMCs synthesized at different FeTMPPCl loading (20.0, 33.3, 50.0, and 60.0 wt%) and commercial Pt/C at 0.9 V (vs. RHE) in 0.1 M KOH during potential cycling process; (b) current density degradation of NPMCs synthesized at different FeTMPPCl loading (20.0, 33.3, 50.0, and 60.0 wt%) and commercial Pt/C at 0.9 V (vs. RHE) in 0.1 M $HClO_4$ during potential cycling process. (c) Chronoamperometric response of the NPMCE synthesized with 33.3 wt% FeTMPPCl loading on carbon and commercial Pt/C at 0.8 V (vs. RHE) in O_2-saturated 0.1 M KOH at 1,600 rpm, (d) chronoamperometric response of the NPMCE synthesized with 50.0 wt% FeTMPPCl loading on carbon and commercial Pt/C and at 0.7 V (vs. RHE) in O_2-saturated 0.1 M $HClO_4$ at 1,600 rpm. The arrow indicates the introduction of 10 vol% methanol. Reproduced with permission from Ref. [24].

using 33.3 wt% of FeTMPPCl loading on the carbon. Furthermore, the NPMCs obtained with higher FeTMPPCl loading on the carbon exhibit much better durability than commercial Pt/C. In acidic media, the degradation of NPMCs is possibly caused by the formation of the relatively large amount of H_2O_2 that can damage the ORR active sites. Owing to the core–shell structure of NPMCs, when the outer ORR active sites are destroyed during potential cycling, the inner sites would be exposed to maintain the ORR activity. This strategy points out a promising avenue for the design of durable NPMCs in acid.

Except for the high activity and durability, methanol tolerance is also an important issue for cathode electrocatalysts in direct methanol fuel cells and it is an apparent shortcoming for commercial Pt/C electrocatalyst. For commercial Pt/C, the original negative ORR current density shifts to positive current density in a short

EBSCOhost - printed on 2/14/2023 1:06 PM via . All use subject to https://www.ebsco.com/terms-of-use

time after the methanol addition both in alkaline and acidic solutions, suggesting a serious poisoning effect by methanol. Remarkably, the current density of NPMCs only shows a small change as methanol is added into the electrolyte (Figure 6.5c, d). The excellent methanol tolerance of NPMCs should come from the inertness of the NPMCs to methanol oxidation reaction.

6.3.2 3D Porous Fe/N/C Spherical Nanostructures

The carbon support or host for the catalytic sites plays a crucial role in fabricating highly efficient Fe/N/C ORR catalysts. Spherical structure has the advantages of close packed arrays and high volume density for active sites. So we explored the use of spherical phenolic resol-F127 monomicelles (SPRMs) [25] as the host for impregnating FeAc and 1, 10-Phen to form a catalyst precursor that is subsequently heat treated in Ar and NH_3, respectively. By adjusting the content of FeAc, the pyrolysis temperature in Ar, and pyrolysis time in NH_3, a series of Fe/N/C samples (specifically named as Fe*x*NC-Ar*T*-NH_3-*y*%, in which, *x* means the content of FeAc added in the experiment, *T* means the pyrolysis temperature in Ar, and *y* means the weight remaining after the NH_3 pyrolysis) were prepared. The content of Fe and surface area of the catalysts can be controllably adjusted by the quantity of FeAc and the pyrolysis time in NH_3 atmosphere. Accordingly, the optimized catalyst is obtained showing outstanding ORR activity, stability, and methanol crossover tolerance both in alkaline and acidic conditions[26].

We investigated the factors which affect the activity of the Fe/N/C catalysts, such as Brunauer, Emmett and Teller (BET) surface area (micropores, mesopores, and their ratio), and the Fe content. As shown in Figure 6.6, it can be seen that (i) the BET surface area (from ~400, ~500, to ~700 m^2/g) of the samples increases with the increase in FeAc content (from 20, 30, to 50 mg) in raw materials; (ii) for the samples in the same FeAc content group, the BET surface area decreases with the increase in the Fe amount (Fe_{cal}) in the final catalyst, that is, during NH_3 pyrolysis process, the Fe content kept constant, while the carbon lost more weight with prolonged pyrolysis time, in the catalysts; (iii) the optimized Fe% in the final catalysts is in the range of 5.5–8 wt% (Figure 6.6a); (iv) the optimized micropore surface area is around 450 $m^2\,g^{-1}$ (Figure 6.6b); (v) the activity of our catalyst increases as the ratio of mesopores increases (Figure 6.6c), so the optimal ratio of micro-/mesopore in these catalysts is around 4–5 (Figure 6.6d). In summary, the ORR activity can be optimized by the proper balance of Fe content and surface area (microspore and mesopore). For example, the most active Fe30NC-Ar700-NH_3-45% possesses Fe content of 7.02 wt% and the micropore/mesopore ratio of 4.33.

Figure 6.7a shows the typical RRDE voltammograms of Fe30NC-Ar700-NH_3-45% and commercial Pt/C catalyst obtained at room temperature in O_2-saturated 0.1 M KOH solution. It can be seen that the current density at 0.85 V can be achieved at

EBSCOhost - printed on 2/14/2023 1:06 PM via . All use subject to https://www.ebsco.com/terms-of-use

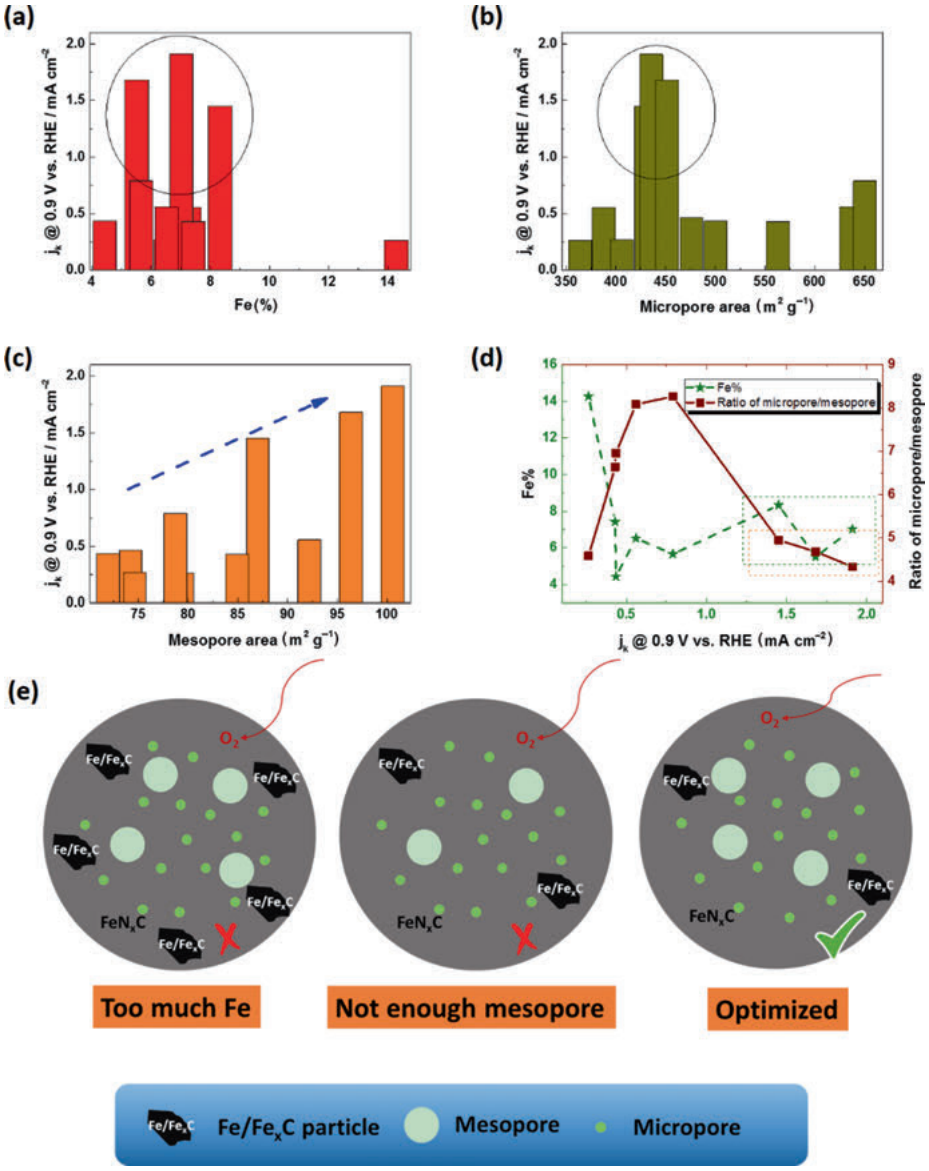

Figure 6.6: (a) Histogram of j_k@0.9 V with the Fe content in the catalysts, (b, c) histogram of j_k@0.9 V with the micropore and mesopore surface area, and (d) relationships of Fe content, ratio of micropore/mesopore, and j_k@0.9 V. (e) Schematic images of the optimal microstructure of Fe/N/C catalysts. Reproduced with permission from Ref. [26].

3.43 mA cm^{-2} for Fe30NC-Ar700-NH_3-45% versus 1.15 mA cm^{-2} for Pt/C (with higher loading for NPMC). Furthermore, the methanol tolerance of the Fe30NC-Ar700-NH_3-45% and Pt/C catalysts was evaluated by adding 1.0 M methanol into 0.1 M KOH

EBSCOhost - printed on 2/14/2023 1:06 PM via . All use subject to https://www.ebsco.com/terms-of-use

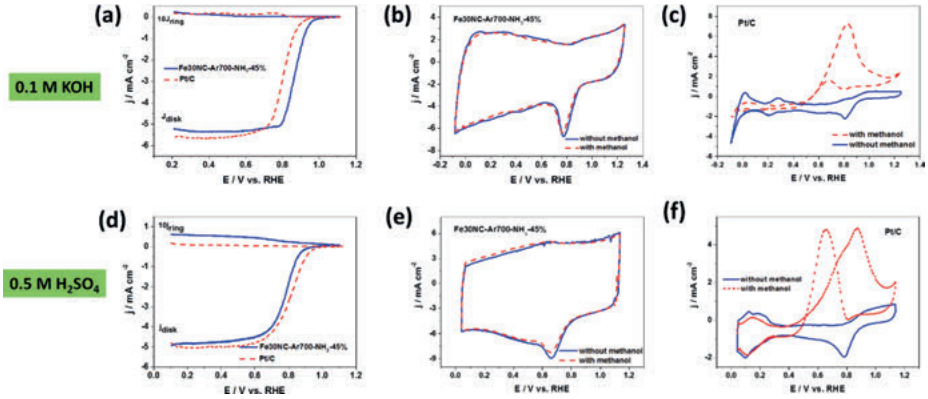

Figure 6.7: (a) RRDE voltammograms of Fe30NC-Ar700-NH_3-45% and Pt/C in O_2-saturated 0.1 M KOH at a scan rate of 10 mV s^{-1}, rotation rate = 1,600 rpm. (b–c) CV curves of (c) Fe30NC-Ar700-NH_3-45% and (d) Pt/C in O_2-saturated 0.1 M KOH without and with 1.0 M methanol. Scan rate: 50 mV s^{-1}. (d) RRDE voltammograms of Fe30NC-Ar-NH_3-45% and Pt/C in O_2-saturated 0.5 M H_2SO_4 at a scan rate of 10 mV s^{-1}, rotation rate = 1,600 rpm. (e–f) CV curves of (c) Fe30NC-Ar700-NH_3-45% and (d) Pt/C in O_2-saturated 0.5 M H_2SO_4 without and with 1.0 M methanol. Scan rate: 50 mV s^{-1}. Reproduced with permission from Ref. [26].

electrolyte. After addition of methanol, there is almost no change in the ORR peak current for Fe30NC-Ar700-NH_3-45% (Figure 6.7b); however, the typical inverse methanol oxidation peaks in CVs were observed (Figure 6.7c) for the Pt/C catalyst. These results suggest that Fe30NC-Ar700-NH_3-45% has much better methanol tolerance (i.e, catalytic selectivity toward ORR) than the commercial Pt/C catalyst in alkaline media.

Most important, Fe30NC-Ar700-NH_3-45% catalyst is also active and stable for ORR in acidic media. As shown in Figure 6.7d, in 0.5 M H_2SO_4 electrolyte, Fe30NC-Ar700-NH_3-45% shows slightly negative shift (~30 mV), in terms of the onset potential and half-wave potential, compared with those of Pt/C. From the methanol crossover test, we can see that in the presence of 1.0 M methanol, there is only a slight change of peak current for Fe30NC-Ar700-NH_3-45% (Figure 6.7e), whereas significant methanol oxidation peaks in CVs for the Pt/C catalyst (Figure 6.7f) can be observed, suggesting that Fe30NC-Ar700-NH_3-45% also has excellent selectivity for ORR with strong tolerance to methanol crossover effect in acidic media.

6.3.3 Litchi-like Highly Porous Fe/N/C Spheres

The fabrication of carbon-based electrocatalysts that is highly active and stable as well with plenty of pores for the mass transport is essential for high-performance metal–air batteries [27]. A simple route involving sulfur (S) as a "promoter" was developed to achieve a litchi-like porous Fe/N/C catalyst with abundant FeN_x species [28]. The

EBSCOhost - printed on 2/14/2023 1:06 PM via . All use subject to https://www.ebsco.com/terms-of-use

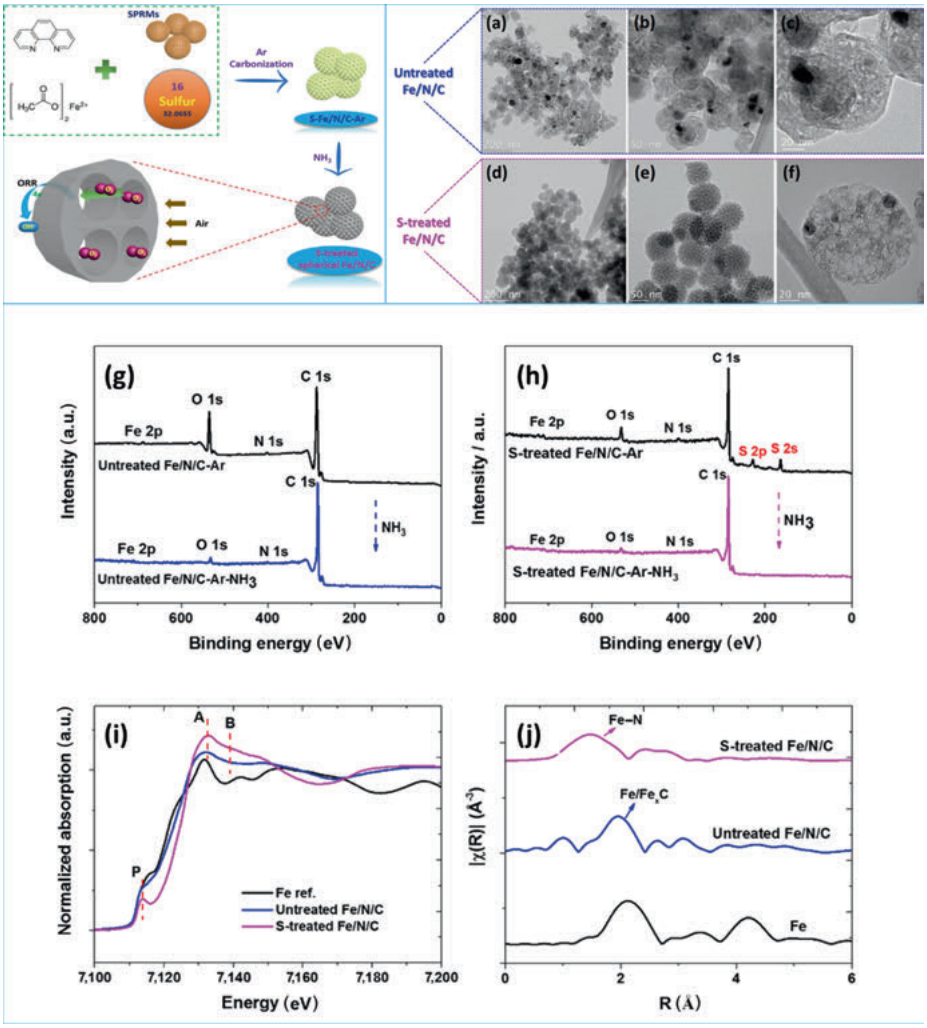

Figure 6.8: Top left scheme is the illustration of the formation of the litchi-like highly porous S-treated Fe/N/C catalysts. TEM images of untreated Fe/N/C (a–c) and S-treated Fe/N/C (d–f) catalysts at different magnifications. (g) XPS spectrum of untreated Fe/N/C (before and after ammonia pyrolysis), and (h) S-treated Fe/N/C catalysts (before and after ammonia pyrolysis). (i) Normalized Fe K-edge XANES spectra and (j) the magnitude of Fourier-transformed EXAFS oscillations $k^2\chi$ (k) spectra of untreated Fe/N/C, S-treated Fe/N/C, and reference Fe foil. Reproduced with permission from Ref. [28].

obtained electrocatalyst exhibits a large surface area with a high pore volume, and shows high activity for ORR. The fabrication of the litchi-like S-treated Fe/N/C spheres can be illustrated in the upper left scheme of Figure 6.8. After the Ar carbonization process, S was doped into the Fe/N/C spheres. During the stage of ammonia pyrolysis,

EBSCOhost - printed on 2/14/2023 1:06 PM via . All use subject to https://www.ebsco.com/terms-of-use

S would react with ammonia as $3S + 2NH_3 = 3H_2S + N_2$; as a result, only Fe, N, and C elements were obtained after the pyrolysis. However, during the first Ar pyrolysis stage, the addition of S is expected to (i) be doped into the carbon framework to increase the surface area [29], (ii) help dispersing the Fe–N_x active sites more evenly, and (iii) buffer the carbon-based spheres from collapsing.

X-ray photoelectron spectroscopy (XPS) measurements were performed to elucidate the changes of the states of elements and chemical speciation for untreated Fe/N/C and S-treated Fe/N/C catalysts. For both samples, it shows only the presence of C, N, O, and Fe elements. However, if we analyze peaks for these two samples before and after the ammonia pyrolysis (Figure 6.8g, h), we can find that (i) the oxygen peaks decrease a lot for both samples after the ammonia pyrolysis, because of the reactions between the oxygen-containing groups and NH_3, (ii) there is S existing for the S-treated Fe/N/C sample after the carbonization under Ar, indicating that part of the S was doped inside the carbon framework, (iii) after the ammonia pyrolysis, the S peaks disappear (Figure 6.8h), indicating that NH_3 is playing multifunctional roles, that is, further activation of Fe/N/C, expanding the surface area, etching off carbon, and elimination of S species. As a result, these obtained S-treated Fe/N/C spheres show greatly improved pore volumes and surface area, consisting with the BET analysis [28]. To unravel the local and electronic structure of Fe/N/C samples, X-ray absorption near edge structure (XANES) and extended X-ray absorption fine structure (EXAFS) were analyzed. As indicated by the Fe K-edge XANES in Figure 6.8i, the pre-edge peak (peak P) is caused by the forbidden 1s → 3d transition, its intensity in the XANES spectra could reflect the distortion degree from the perfect octahedral symmetry [30], a stronger peak indicates a higher degree of Fe local structure distortion; in addition, the intensity ratio of the peak A to peak B (Figure 6.8i) is also attributed to the enhanced distortion of the Fe–N_4 local structure [31]. From the results shown in Figure 6.8i, a stronger peak P and higher intensity ratio of peak A/peak B are observed in S-treated Fe/N/C, so it can be deduced that because of the function of S, the Fe–N_x active sites in S-treated Fe/N/C has a higher degree of distortion. The experimental Fourier transforms (FT) at the Fe K-edge of the EXAFS data of the samples were further analyzed and displayed in Figure 6.8j. The signal at ~1.6 Å in S-treated Fe/N/C should be attributed to the Fe–N scattering because of a nitrogen shell surrounding Fe, corroborating the existence of the Fe–N_x configurations in the graphitic carbon framework [32–34]; interestingly, without S treatment, the dominant signal in untreated Fe/N/C is characterized instead by a peak at around 2.0–2.2 Å, which could be assigned to metallic Fe and Fe_3C [35]; this indicates that with the existence of S, the elements of Fe, N, and C tend to form Fe–N_x-coordinated active sites, while, without S, they are mainly inclined to form Fe/Fe_xC NPs, consisting well with the TEM observation.

The ORR activity of S-treated Fe/N/C and untreated Fe/N/C was first accessed by cyclic voltammetry (CV). In N_2-saturated 0.1 M KOH, both Fe/N/C samples exhibited a featureless CV curve, while S-treated Fe/N/C shows a

EBSCOhost - printed on 2/14/2023 1:06 PM via . All use subject to https://www.ebsco.com/terms-of-use

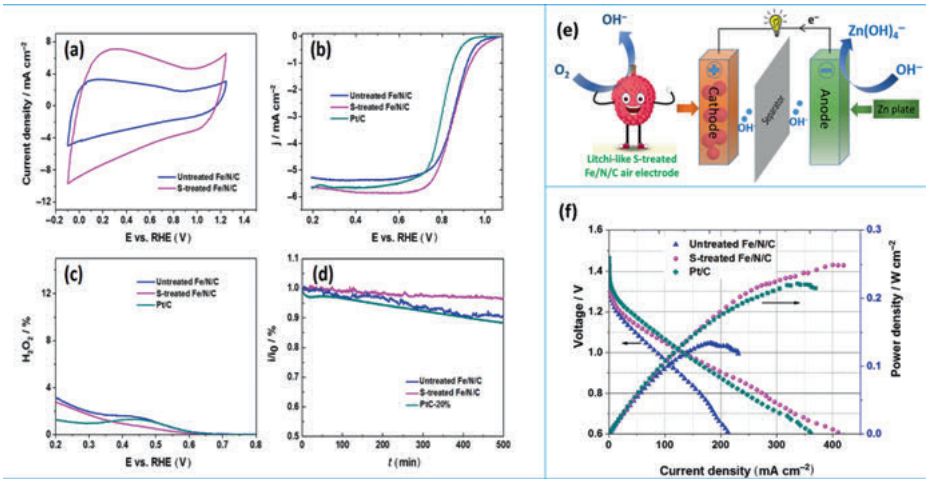

Figure 6.9: (a) CV curves in N_2-saturated 0.1 M KOH at a scan rate of 50 mV s^{-1}, (b) RRDE voltammograms of untreated Fe/N/C, S-treated Fe/N/C, and Pt/C in O_2-saturated 0.1 M KOH at a scan rate of 10 mV s^{-1}, rotation rate = 1,600 rpm. (c) H_2O_2 yield calculated from the RRDE voltammograms in (b), (d) Chronoamperometric responses (at 0.7 V vs. RHE) of untreated Fe/N/C, S-treated Fe/N/C, and commercial Pt/C catalysts in O_2-saturated 0.1 M KOH. (e) Schematic of the discharge process for the rechargeable Zn–air battery. (f) Discharge polarization curves and corresponding power density plots. Reproduced with permission from Ref. [28].

much larger capacitance because of the much higher surface area (Figure 6.9a). Figure 6.9b shows the typical rotating disk electrode (RDE) voltammograms of untreated Fe/N/C, S-treated Fe/N/C, and commercial Pt/C catalysts in O_2-saturated 0.1 M KOH solution; interestingly, both untreated Fe/N/C and S-treated Fe/N/C have higher activity than commercial Pt/C, indicating that Fe/Fe_xC might be also active for ORR in alkaline. The current density at 0.8 V of untreated Fe/N/C, optimal S-treated Fe/N/C, and commercial Pt/C are 4.4 mA cm^{-2}, 4.7 mA cm^{-2}, and 3.2 mA cm^{-2}, respectively. The calculated H_2O_2 yield according to the RRDE test results of the S-treated Fe/N/C catalyst remained below untreated Fe/N/C samples at all potentials in 0.1 M KOH (Figure 6.9c). This negligible H_2O_2 yield clearly confirms that the S-treated Fe/N/C has extremely high ORR catalytic efficiency. The durability of the S-treated Fe/N/C and commercial Pt/C catalysts in a half-cell condition was evaluated by chronoamperometric measurements at 0.7 V (vs. RHE) in O_2-saturated 0.1 M KOH solution with a rotation speed of 1,600 rpm. Figure 6.9d shows that the current density of the litchi-like S-treated Fe/N/C catalyst remains ~96% after 500 min, which is apparently higher than that of the untreated Fe/N/C (~90%) and commercial Pt/C catalyst (~88%) in the same condition, suggesting its excellent durability of the litchi-like porous S-treated Fe/N/C spheres. To explore

EBSCOhost - printed on 2/14/2023 1:06 PM via . All use subject to https://www.ebsco.com/terms-of-use

the potential use of these litchi-like porous S-treated Fe/N/C spheres for real energy devices, a homemade Zn–air battery was assembled using untreated Fe/N/C, S-treated Fe/N/C, and Pt/C as the air cathode and a polished zinc plate as the anode filled with the (6 M KOH + 0.2 M $Zn(Ac)_2$) electrolyte (Figure 6.9e). Figure 6.9f depicted the polarization curves and corresponding power density plots of a single Zn–air battery constructed by untreated Fe/N/C, S-treated Fe/N/C, and Pt/C, at the same condition. Impressively, the litchi-like S-treated Fe/N/C sample displays >1.5 times of the untreated Fe/N/C in terms of current density at 1.0 V and almost double of the peak power densities (~250 mW cm^{-2} vs. ~125 mW cm^{-2}), and even outperforms the commercial Pt/C catalyst (~220 mW cm^{-2}) with the same loading (Figure. 6.5c). Considering the similar ORR activity of the untreated Fe/N/C ($E_{1/2}$=0.87 V) and S-treated Fe/N/C ($E_{1/2}$=0.88 V), the critical role of hierarchical porous structure to the single-cell devices is highlighted.

6.4 Conclusion

We have summarized our recent work about NPMCs for ORR in PEMFC and metal–air battery in this chapter. In the first part, based on the outstanding NPM catalyst (NC_Ar+NH_3 catalyst), which has initially high activity and power density comparable to commercial Pt/C for ORR, we conducted a series of study, aiming to find out the real reason for the initial fast current density decay. We demonstrated that (1) the release of the H_2O_2 by the catalysts during ORR is not the cause of the fast decay, either by reacting directly with the catalytic sites or by participating to a Fenton's reaction with iron present in the catalysts; (2) the behaviors of the active sites of CNx and FeN_4 for ORR, including activity, power density, and stability, have been identified; and (3) the specific demetalation of the FeN_4-like catalytic sites located in the micropores, is the cause of the initial loss of ORR activity of the catalyst in fuel cells. The second part is the novel structured NPMC catalysts we have explored, including core–shell structures, 3D porous spherical structure, and litchi-like highly porous Fe/N/C spheres. We hope this will pave new ways for the design and synthesis of high-efficient NPMCs toward ORR applicable to various fuel cells and metal–air batteries.

Acknowledgements: This work is supported financially by the Natural Sciences and Engineering Research Council of Canada (NSERC), the Fonds de Recherche du Québec-Nature et Technologies (FRQNT), Centre Québécois sur les Materiaux Fonctionnels (CQMF), Ballard Power Systems Inc., Canada Foundation for Innovation (CFI), and Institut National de la Recherche Scientifique (INRS).

EBSCOhost - printed on 2/14/2023 1:06 PM via . All use subject to https://www.ebsco.com/terms-of-use

References

[1] Jaouen F., Proietti E., Lefèvre M., Chenitz R., Dodelet J.-P., Wu G., Chung H.T., Johnston C.M. and Zelenay P., *Energy & Environmental Science*, 2011, 4, 114–130.

[2] Fu J., Cano Z.P., Park M.G., Yu A., Fowler M. and Chen Z., *Advanced Materials*, 2017, 29, 1604685.

[3] Sun S., Jaouen F. and Dodelet J.P., *Advanced Materials*, 2008, 20, 3900–3904.

[4] Sun S., Zhang G., Gauquelin N., Chen N., Zhou J., Yang S., Chen W., Meng X., Geng D. and Banis M.N., *Scientific Reports*, 2013, 3, 1775.

[5] Sun S., Zhang G., Geng D., Chen Y., Banis M.N., Li R., Cai M. and Sun X., *Chemistry-A European Journal*, 2010, 16, 829–835.

[6] Sun S., Zhang G., Geng D., Chen Y., Li R., Cai M. and Sun X., *Angewandte Chemie*, 2011, 123, 442–446.

[7] Sun S., Zhang G., Zhong Y., Liu H., Li R., Zhou X. and Sun X., *Chemical Communications*, 2009, 0, 7048–7050.

[8] Wang Y.-J., Zhao N., Fang B., Li H., Bi X.T. and Wang H., *Chemical reviews*, 2015, 115, 3433–3467.

[9] Yang X., Roling L.T., Vara M., Elnabawy A.O., Zhao M., Hood Z.D., Bao S., Mavrikakis M. and Xia Y., *Nano Letters*, 2016, 16, 6644–6649.

[10] Escudero-Escribano M., Malacrida P., Hansen M.H., Vej-Hansen U.G., Velázquez-Palenzuela A., Tripkovic V., Schiøtz J., Rossmeisl J., Stephens I.E.L. and Chorkendorff I., *Science*, 2016, 352, 73–76.

[11] Tong X., Zhang J., Zhang G., Wei Q., Chenitz R., Claverie J.P. and Sun S., *Chemistry of Materials*, 2017, 29, 9579–9587.

[12] Zhang G., Sun S., Cai M., Zhang Y., Li R. and Sun X., *Scientific Reports*, 2013, 3, 1526.

[13] Hong W.T., Risch M., Stoerzinger K.A., Grimaud A., Suntivich J. and Shao-Horn Y., *Energy & Environmental Science*, 2015, 8, 1404–1427.

[14] Sahraie N.R., Kramm U.I., Steinberg J., Zhang Y., Thomas A., Reier T., Paraknowitsch J.-P. and Strasser P., *Nature Communications*, 2015, 6, 8618.

[15] Lin L., Zhu Q. and Xu A.-W., *Journal of the American Chemical Society*, 2014, 136, 11027–11033.

[16] Dombrovskis J.K. and Palmqvist A.E.C., *Fuel Cells*, 2016, 16, 4–22.

[17] Wu G. and Zelenay P., *Accounts of Chemical Research*, 2013, 46, 1878–1889.

[18] Wei Q., Tong X., Zhang G., Qiao J., Gong Q. and Sun S., *Catalysts*, 2015, 5, 1574–1602.

[19] Proietti E., Jaouen F., Lefèvre M., Larouche N., Tian J., Herranz J. and Dodelet J.-P., *Nature communications*, 2011, 2, 416.

[20] Lefèvre M., Proietti E., Jaouen F. and Dodelet J.-P., *Science*, 2009, 324, 71–74.

[21] Kramm U.I., Herranz J., Larouche N., Arruda T.M., Lefèvre M., Jaouen F., Bogdanoff P., Fiechter S., Abs-Wurmbach I. and S. Mukerjee, *Physical Chemistry Chemical Physics*, 2012, 14, 11673–11688.

[22] Zhang G., Chenitz R., Lefèvre M., Sun S. and Dodelet J.-P., *Nano Energy*, 2016, 29, 111–125.

[23] Chenitz R., Kramm U.I., Lefevre M., Glibin V., Zhang G., Sun S. and Dodelet J.-P., *Energy & Environmental Science*, 2018, 11, 365–382.

[24] Li J., Song Y., Zhang G., Liu H., Wang Y., Sun S. and Guo X., *Advanced Functional Materials*, 2017, 27, 1604356.

[25] Wei Q., Fu Y., Zhang G., Wang Y., Wang X., Mohamedi M. and Sun S., *RSC Advances*, 2016, 6, 84149–84154.

[26] Wei Q., Zhang G., Yang X., Chenitz R., Banham D., Yang L., Ye S., Knights S. and Sun S., *ACS Applied Materials & Interfaces*, 2017, 9, 36944–36954.

[27] Wei Q., Fu Y., Zhang G. and Sun S., *Current Opinion in Electrochemistry*, 2017,4 (1) 45–59.

EBSCOhost - printed on 2/14/2023 1:06 PM via . All use subject to https://www.ebsco.com/terms-of-use

[28] Wei Q., Zhang G., Yang X., Fu Y., Yang G., Chen N., Chen W. and Sun S., *Journal of Materials Chemistry A*, 2018, 6, 4605–4610.
[29] Herrmann I., Kramm U.I., Radnik J., Fiechter S. and Bogdanoff P., *Journal of The Electrochemical Society*, 2009, 156, B1283–B1292.
[30] Khalil M., Marcus M.A., Smeigh A.L., McCusker J.K., Chong H.H.W. and Schoenlein R.W., *The Journal of Physical Chemistry A*, 2006, 110, 38–44.
[31] Jia Q., Ramaswamy N., Hafiz H., Tylus U., Strickland K., Wu G., Barbiellini B., Bansil A., Holby E.F. and Zelenay P., *ACS nano*, 2015, 9, 12496–12505.
[32] Jiang W.-J., Gu L., Li L., Zhang Y., Zhang X., Zhang L.-J., Wang J.-Q., Hu J.-S., Wei Z. and Wan L.-J., *Journal of the American Chemical Society*, 2016, 138, 3570–3578.
[33] Zitolo A., Goellner V., Armel V., Sougrati M.-T., Mineva T., Stievano L., Fonda E. and Jaouen F., *Nature materials*, 2015, 14, 937–942.
[34] Zhu Q.-L., Xia W., Zheng L.-R., Zou R., Liu Z. and Xu Q., *ACS Energy Letters*, 2017, 2, 504–511.
[35] Strickland K., Miner E., Jia Q., Tylus U., Ramaswamy N., Liang W., Sougrati M.-T., Jaouen F. and Mukerjee S., *Nature Communications*, 2015, 6, 7343.

EBSCOhost - printed on 2/14/2023 1:06 PM via . All use subject to https://www.ebsco.com/terms-of-use

EBSCOhost - printed on 2/14/2023 1:06 PM via . All use subject to https://www.ebsco.com/terms-of-use

Janane F. Rahbani, Hanadi F. Sleiman

7 Toward the Assembly of Dynamic and Complex DNA Nanostructures

Keywords: DNA nanotechnology, Dynamic nanostructures, DNA origami, DNA nanotubes, Higher-order DNA based nanoarchitectures

During the past 30 years, the field of DNA nanotechnology has witnessed significant development and has been applied in various other fields such as biology, physics, chemistry, and engineering [1–3]. The number of laboratories working on this topic has expanded immensely, leading to the generation of a variety of two- (2D) and three-dimensional (3D) nanostructures. These novel constructs were incorporated in the creation of nanomechanical devices and contributed in the advancement of medical applications [4, 5].

7.1 Introduction

DNA (deoxyribonucleic acid) is the molecule that encodes our genetic information. Since Watson and Crick revealed the recognition motifs of DNA, biologists have been further exploiting the chemical basis underlying our genes. In particular, the hydrogen bonding between adenine (A)/thymine (T) and guanine (G)/cytosine (C) is called Watson–Crick base pairing (Figure 7.1). However, biology is no longer the sole area of science in which DNA is playing a crucial role. According to Professor Nadrian Seeman, founder of DNA nanotechnology: "It is now possible to exploit DNA complementarity to control the structure of matter."

In the last few decades, researchers have focused on building materials and technologies on the nanometer size regime (1–100 nm) [6]. Working at this length scale offers a variety of appealing opportunities since the properties of nanoparticles can be highly dependent on their sizes [7]. Indeed, the shape and length of nanoparticles can significantly manipulate their electronic, optical, chemical, and magnetic properties. Since nanomaterials are generally smaller than 100 nm, their structural properties are influenced by their surrounding molecules and the interaction between the particles often generate unique optical and electronic properties.

Despite the existence of two common approaches, top-down and bottom-up, in building nanomaterials, it is still challenging to construct materials at this scale. The top-down strategy refers to breaking down large structures into smaller dimensions

Janane F. Rahbani, Hanadi F. Sleiman, Quebec Centre for Advanced Materials, Department of Chemistry, McGill University, Montreal, Canada

https://doi.org/10.1515/9783110537734-007

EBSCOhost - printed on 2/14/2023 1:06 PM via . All use subject to https://www.ebsco.com/terms-of-use

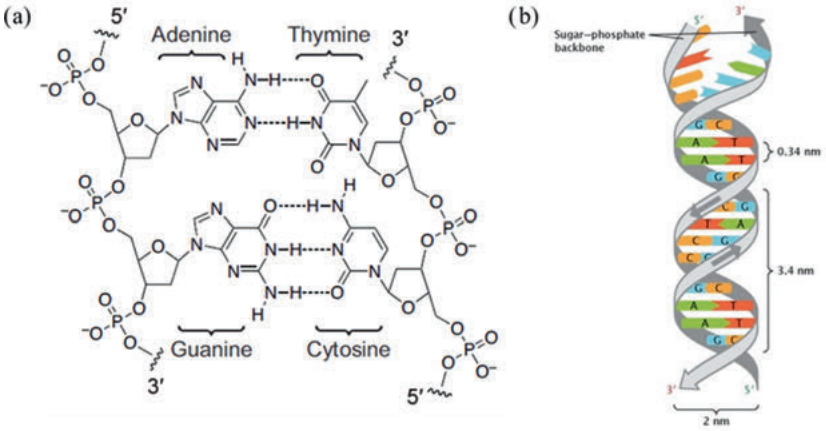

Figure 7.1: Watson–Crick base pairing. (a) Three hydrogen bonds linking nucleobases G and C versus two hydrogen bonds linking nucleobases A and T. (b) B-DNA: right-handed helical sense, a 3.4 Å helical rise per base pair, a width of 2 nm and a 10.5 base pairs per helical turn. Adapted with permission from Reference 8 (Nature Publishing Group, 2008) [8].

required for processing [9]. This method is widely used in fabricating nanodevices, yet it requires external and expansive tools to achieve smaller sizes in the molecular scale. Alternatively, bottom-up techniques are able to produce devices through the autonomous self-assembly of small building blocks [10]. Indeed, the idea of supramolecular self-assembly involves the creation of novel materials with unique chemical compositions and properties (Figure 7.2) [11]. This concept is mainly based on noncovalent interactions such as hydrogen bonding, π–π stacking, the hydrophobic effect, and so on. The self-assembly of DNA is the result of these interactions through Watson–Crick base pairing.

Inspired by the helical structure of DNA and aiming at designing periodic lattices from short oligonucleotides, Nadrian Seeman established the field of DNA nanotechnology in 1982 [12]. Because DNA is inherently linear, he introduced specific geometrical motifs that can dictate the final size and shape of the nanostructures. Figure 7.3 shows early examples of branched junctions reported in literature. To better understand how these nanostructures assemble, it is important to define concepts such as nonnatural hybridization and stable stick-ends and explain appropriate strategies to design sequences. For instance, the Holliday junction presents a simple example of unusual arrangement of two helices to produce a four-way junction [13]. When the 5′- and/or 3′-ends of the junctions are extended by a defined number of unhybridized bases (sticky ends or overhangs), a 2D/3D lattice can be produced depending on the complementarity of the sticky-ends. Figure 7.3 depicts the formation of a quadrilateral from a sticky-ended branched junction.

EBSCOhost - printed on 2/14/2023 1:06 PM via . All use subject to https://www.ebsco.com/terms-of-use

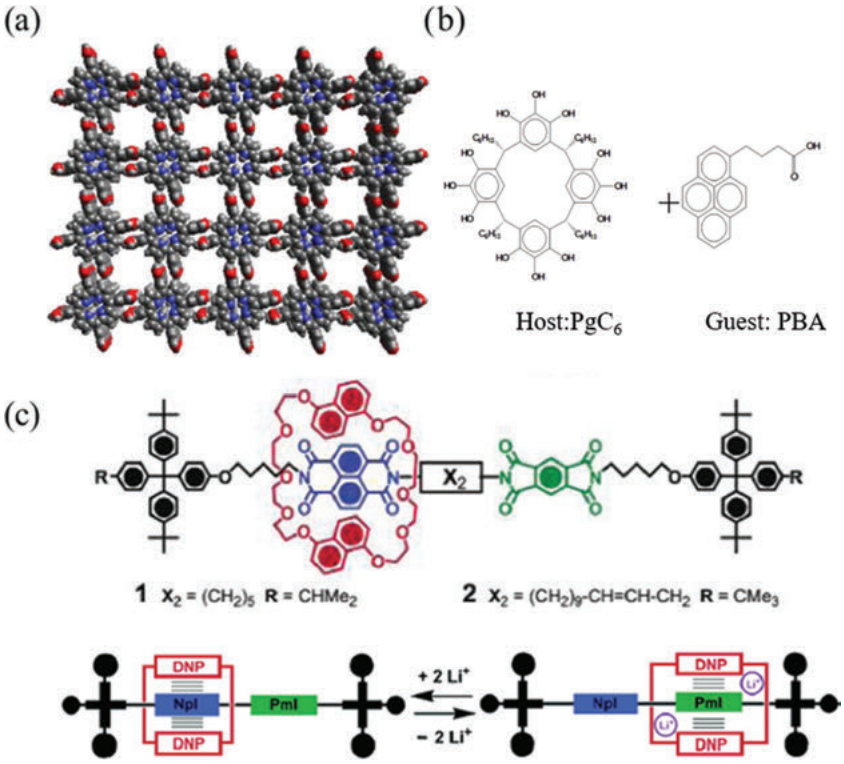

Figure 7.2: (a) Crystal structure of an octahydroxy porphyrin network: 5,10,15,20-tetrakis(3′,5′-dihydroxy-phenyl) porphyrin. On the basis of the position of hydroxyl groups and the nature of metals, the size of the pores varies. Adapted with permission from Reference 14 (Taylor and Francis, 1998) [14]. (b) Crystal structure of resolved pyrene fragments inside a hexameric assembly. Adapted with permission from Reference 15 (Science, 2005) [15]. (c) Schematic representation of a switchable bistable rotaxane. The blue and green colored docking sites are π-electron poor, whereas the red ring is π-electron rich. The addition/removal of lithium cations induce the switching between the two docking sites. Adapted with permission from Reference 16 (ACS Publishing, 2004) [16].

7.2 Structural DNA Nanotechnology

Following the invention of the Holliday junction, Seeman found that the construction of larger patterns requires more rigid geometrical motifs. Thus, he developed double crossover motifs (DX) to build defined 2D networks [18]. The DX motif was shown to be approximately twice as rigid as equivalent linear double-stranded DNA due to the two crossover points, the points at which individual strands cross between two domains, that provide a defined orientation of DNA and confine their mobility. Triple crossover (TX) motifs [19] were developed to further increase the rigidity of branched junctions, yet they were not as widely used as DX motifs.

EBSCOhost - printed on 2/14/2023 1:06 PM via . All use subject to https://www.ebsco.com/terms-of-use

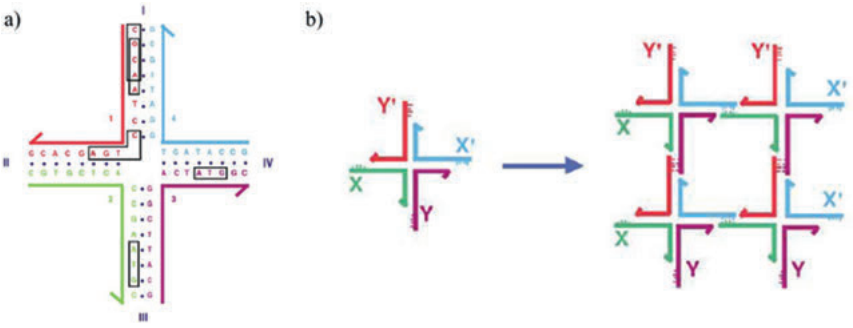

Figure 7.3: (a) A stable branched junction composed of four DNA strands. (b) A four-way sticky-ended branched junction induces the assembly of a quadrilateral. Adapted with permission from Reference 18 (Elsevier Publishing, 2003) [17].

Figure 7.4c displays the assembly of a 2D array due to the interaction between two DX motifs programmed to come together via Watson–Crick base pairing [20]. Note that changing the number of bases between crossovers or modifying the size and/or sequences of sticky-ends leads to the formation of nanotubes instead of planar sheets (Section 7.4). Therefore, it is critical to consider the helicity of DNA when designing any structure.

Because of its ease of synthesis and programmability, DNA has been used to produce a wide range of structures. Several geometrical motifs and branching junctions have been created to assemble cubes [21], nanotubes [22, 23], tetrahedral [24, 25], and so on. Other factors including stochiometric ratios between DNA strands, annealing temperatures, stepwise versus one-pot assemblies play an important role in determining the final geometry and shape of the structures. For example, Sleiman and coworkers reported the assembly of DNA cubes made up of four strands mixed and annealed together at 95 °C then cooled down to 4 °C for 6 h (Figure 7.5) [27]. Changing the conditions of assembly by adding one component in excess or mixing the strands at room temperature leads to the formation of other byproducts and significantly affects the yield of the desired discrete shape. DNA tetrahedron is another geometry reported by Turberfield's research group constituting of four strands (Figure 7.5) [28]. The latter example illustrates how the shape of the nanostructure is determined by the designed sequences of the original motif.

Following the successful generation of large 2D arrays and a wide range of 3D systems based on DNA molecules, researchers have employed DNA nanostructures to arrange proteins [29, 30], small molecules [31], and nanoparticles [32, 33] with nanoscale precision, optimize biological probes [34], create novel drug delivery vehicles [35, 36], and combine the traditional synthesis of DNA with lithographic techniques [37, 38]. Knowing that real-world applications require a large-scale production of DNA, ongoing efforts have been focusing on developing inexpensive

EBSCOhost - printed on 2/14/2023 1:06 PM via . All use subject to https://www.ebsco.com/terms-of-use

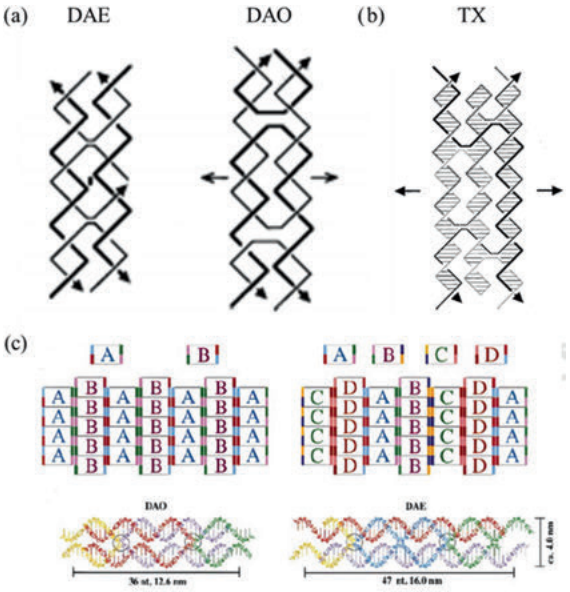

Figure 7.4: (a) Schematic representation of two types of double-crossover structures (D). A: antiparallel refers to the orientation of the two helical domains. E: even and O: odd refer to the number of helical turns between the two crossover points. Adapted with permission from Reference 18 (ACS Publishing, 1993) [18]. (b) Scheme of a triple-crossover complex consisting of three helices having coplanar axes. The complex is made up of four strands. Adapted with permission from Reference 26 (ACS Publishing, 2000) [26]. (c) Generation of 2D networks from DX tiles bearing different overhang address abilities. Adapted with permission from Reference 20 (Nature Publishing Group, 1998) [20].

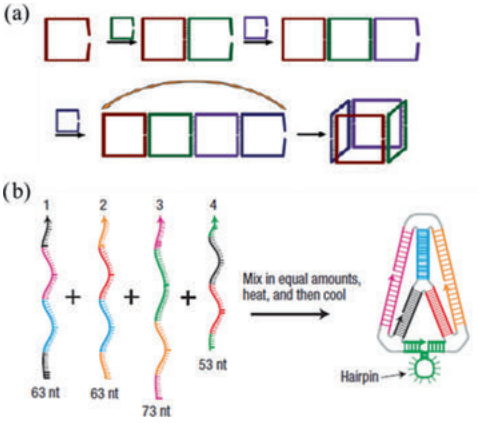

Figure 7.5: (a) Scheme showing the clip-by-clip approach for the synthesis of DNA cubes from four strands. Adapted with permission from Reference 27 (ACS Publishing, 2016). (b) Scheme representing the synthesis of a DNA tetrahedron from four strands. The hairpin region acts as a toehold for further strand displacement experiments. Adapted with permission from Reference 28 (Nature Publishing Group, 2008).

EBSCOhost - printed on 2/14/2023 1:06 PM via . All use subject to https://www.ebsco.com/terms-of-use

routes such as on-chip DNA synthesis to produce oligonucleotides in high yields [39]. Finally, because DNA is limited by the four-letter genetic code, it becomes extremely difficult to assemble a large number of strands without avoiding undesired secondary interactions. To solve this problem, various orthogonal interactions such as the hydrophobic effect were introduced to increase the complexity and functional range of DNA structures. In the following sections, we will further elaborate on different strategies employed to create higher-order nanostructures and will discuss their impact on the field.

7.3 DNA Origami

Two decades after the generation of the initial geometrical motifs, Paul Rothemund revolutionized the field of DNA nanotechnology by using a long strand of DNA to build nanostructures [40]. He used a strand of genomic viral DNA M13mp18 and folded it around more than 200 short strands (called staples strands) obtained synthetically to form various DNA geometries and shapes with the aid of a computer software (Figure 7.6). Unlike Seeman's 2D arrays, the assembly of DNA origami does not rely on sticky-end cohesion of DX motifs. Instead, crossover points were generated through the assembly of these short and unique strands at predesigned positions with the long scaffold. Compared to other assembly modes of DNA nanostructures, DNA origami offers many advantages: (i) based on the locations/sequences of staples strands, a wide range of morphologies can be created; (ii) origami structures are more rigid than DX tiles since crossovers are continuously connected by a single backbone; and (iii) because of their structural robustness, it is easy to characterize origami tiles and study their assemblies via AFM, TEM, single-molecule fluorescence, and so on. In this section, we will be describing some of the origami designs and their emerging applications ranging from nanodevices to drug delivery.

On the basis of the origami approach developed by Rothemund, Shih and coworkers aimed at designing 3D origami structures. They put together an innovative software named "cadnano" to improve the production of random 3D nanostructures through a user-friendly interface [41]. The Shih group reported the assembly of square lattices using this program (Figure 7.7a) [42]. Besides designing stable and rigid nanostructures, curvature of origami tiles was introduced by Yan et al. They found that adding/erasing bases between crossover points drastically alters the planarity of the structure (Figure 7.7b) [43]. However, while the surface area of a single origami can provide around ~200 templating sites, it remains a challenge to assemble higher-order nanostructures that are capable of accomplishing complicated functions. For most of practical applications, assembling larger origami is required to allow wiring of multicomponent electronic devices [44, 45], to amplify optical effects as observed in optical metasurfaces [46], or

EBSCOhost - printed on 2/14/2023 1:06 PM via . All use subject to https://www.ebsco.com/terms-of-use

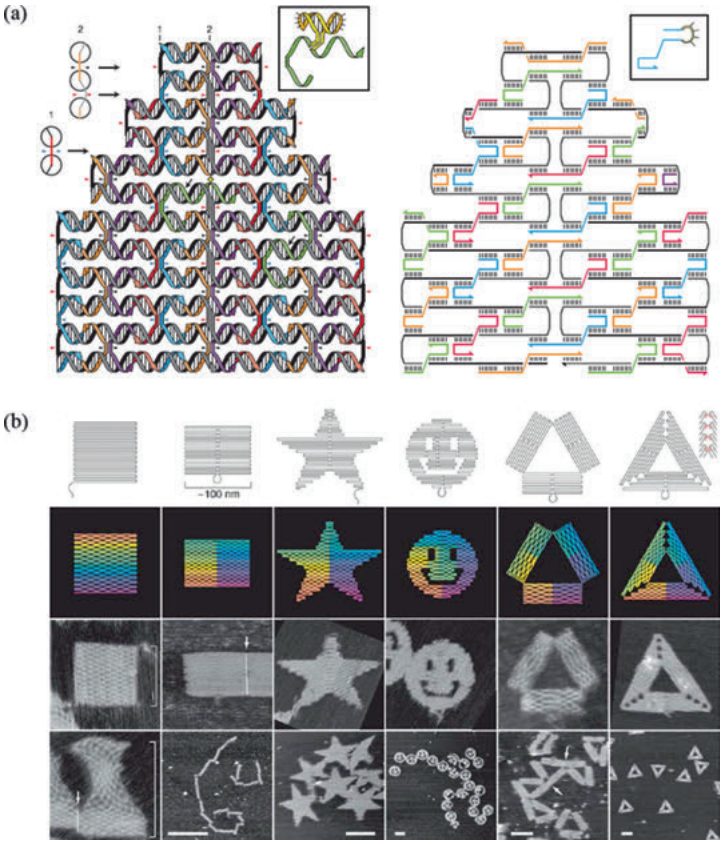

Figure 7.6: (a) A long strand (7249-nt) is folded into various shapes through hybridization to staples strands of unique sequences. While running through every helix, crossover points are generated to increase the rigidity of the final structure. (b) Images of some 2D structures produced using this technique. Adapted with permission from Reference 40 (Nature Publishing Group, 2006).

simply to template proteins and nanoparticles over bigger areas. The main limitation arises from the scarce sources for long single-stranded DNA scaffolds of different lengths and random sequences at a large scale. To overcome this problem, ongoing efforts have been focusing on exploring the folding of DNA origami into 2D arrays by means of multiple tiles [47, 48, 49]. Other promising strategies include the self-assembly of individual origami tiles into superorigami through surface diffusion on a solid substrate [50] or by gold nanoparticle (AuNP) bridges [51]. While it is important to balance construct simplicity with complex function, higher-order nanostructures should maintain their addressability and geometric versatility.

EBSCOhost - printed on 2/14/2023 1:06 PM via . All use subject to https://www.ebsco.com/terms-of-use

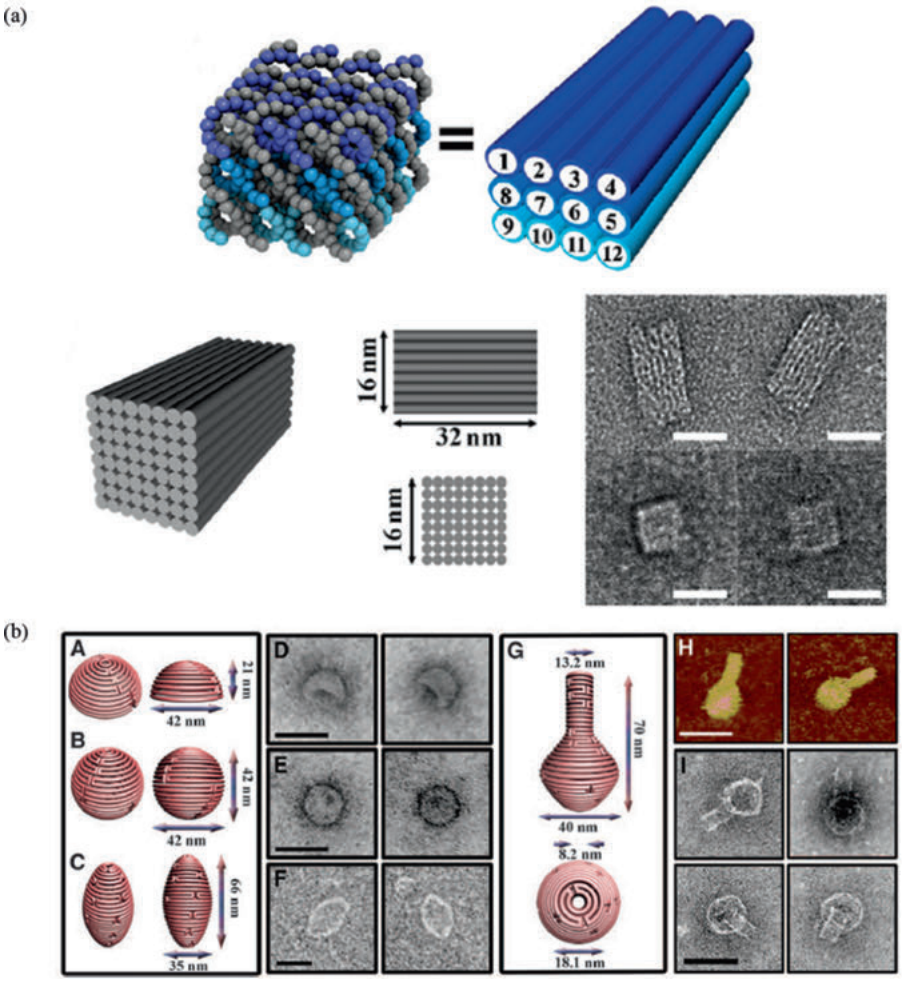

Figure 7.7: (a) Schematic representation of 3D DNA origami square-lattice structure. The gray color refers to the scaffold strand and the blue colors refer to the staple strands. To simplify the scheme, each cylindrical rod on the right represents one double helix. The eight-layer structure is visualized by TEM (scale bar is 20 nm). Adapted with permission from Reference 42 (ACS Publishing, 2009). (b) Complex curvatures were introduced in the design of origami structures. A: hemisphere, B: sphere, C: ellipsoid, D: TEM micrographs of the hemisphere, E: TEM micrographs of the sphere, F: TEM micrographs of the ellipsoid (scale bar is 50 nm), G: nanoflask, H: AFM micrographs of the nanoflask (scale bar is 75 nm), and I: TEM micrographs of the nanoflask (scale bar is 50 nm). Adapted with permission from Reference 43 (Science 2011).

To increase the utility of DNA origami, many researchers have been labeling DNA with nanoparticles [52], enzymes [53], polymers [54] or small molecules [55], and so on. These units either direct the assembly of higher-order origami structures or the origami platforms are used to control their positions in 2D and 3D. The main goal in

EBSCOhost - printed on 2/14/2023 1:06 PM via . All use subject to https://www.ebsco.com/terms-of-use

both cases is building efficient systems capable of displaying new properties at the macroscopic level. For example, AuNPs and nanorods have been commonly used in the fabrication of novel materials due to their unique optical properties. In this regard, DNA nanostructures are employed to manipulate light by controlling the distance between nanoparticles. Since AuNPs are easily conjugated to thiolated DNA strands, Gang and coworkers reported the assembly of a network of AuNPs captured inside a cross-shaped DNA origami (Figure 7.8a) [56]. Turberfield et al. organized AuNPs via DNA nanoflowers to control photonic properties (Figure 7.8b) [57]. Molecular patterning onto AuNPs was demonstrated by Wei and coworkers after attaching the nanoparticles to origami at defined positions then removing the template under specific conditions [58]. It is noteworthy that this strategy was reported first by Sleiman's group on nanocubes [59]. Furthermore, DNA origami presents an ideal tool to build plasmonic materials since the distance between particles can be addressed within a nanoscale precision. This concept was demonstrated by Schmidt's research group who was able to template AuNPs on nanotubes by tuning various parameters affecting the interaction of DNA with the gold surface (Figure 7.8c) [60].

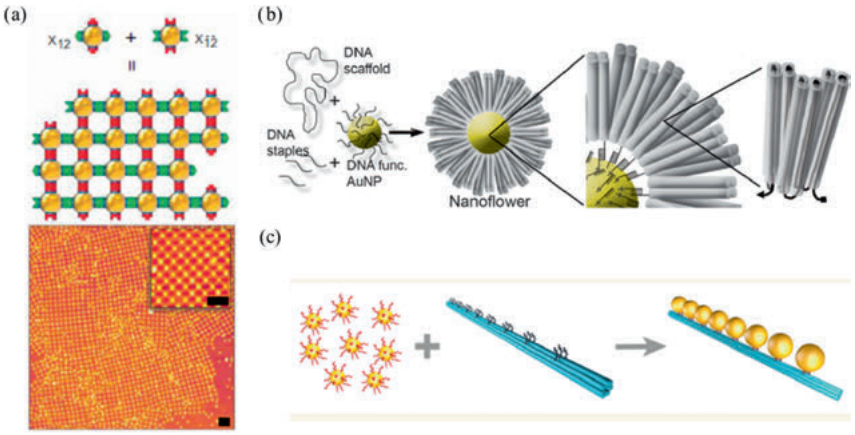

Figure 7.8: (a) Formation of a 2D network of DNA origami mediated by AuNP. Adapted with permission from Reference 56 (Nature Publishing Group, 2016). (b) Assembly of nanoflowers mediated by DNA origami. In a one-pot reaction, staples strands, scaffold, and 15 nm AuNP were mixed. Adapted with permission from Reference 57 (ACS Publishing, 2016). (c) Scheme showing the assembly of AuNP on DNA nanotubes (six helical bundles) through Watson–Crick base pairing. Adapted with permission from Reference 60 (ACS Publishing, 2016).

Alternatively, researchers envisioned the use of DNA origami as a tool to better understand complex biological systems. As such, a variety of macromolecules were

EBSCOhost - printed on 2/14/2023 1:06 PM via . All use subject to https://www.ebsco.com/terms-of-use

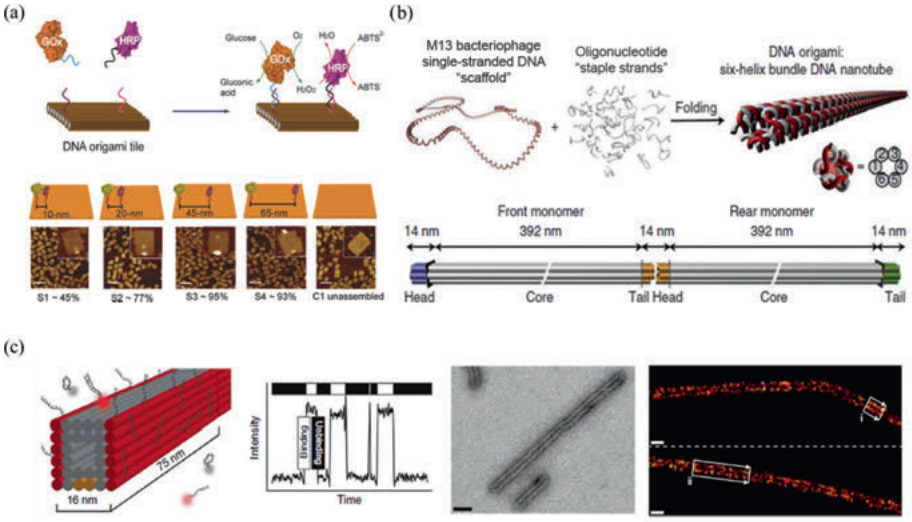

Figure 7.9: (a) DNA origami mediated assembly of glucose oxidase and horseradish peroxidase enzymes with a defined interenzyme distances. The spacing between the two enzymes was observed by AFM (scale bar: 200 nm). Adapted with permission from Reference 64 (ACS Publishing, 2012). (b) Scheme showing the formation of a six-helix bundle DNA nanotube using DNA origami approach. The cartoon represents an 800 nm long six-helix tube. The proteins were later properly aligned on these structures for NMR studies. Adapted with permission from Reference 65 (Nature Publishing Group, 2013). (c) From left to right: Schematic representation of a DNA origami looking similar to a microtubule. The distance separating the single-stranded overhangs (9 bases) is 16 nm. The transient binding reaction between these strands and their complementary fluorescent strands generates fluorescence blinking leading to a stochastic superresolution imaging. The TEM micrograph displays the morphology of the origami polymers. The origami tubes were also observed via PAINT technique where two well-resolved lines are visible. Adapted with permission from Reference 67 (Nature Publishing Group, 2014).

templated on the origami surface to (i) develop enzymatic nanoreactors [61], (ii) build more efficient drug delivery vehicles [62], and (iii) improve current biosensing devices [63]. Yan and coworkers employed origami tiles in an attempt to examine the activity of two enzymes as a function of the distance between them (Figure 7.9a) [64]. Shih's group used the ordering provided by origami nanotubes to aid in the NMR characterization of membrane proteins (Figure 7.9b) [65]. Moreover, various publications described the interaction of functionalized DNA nanostructures with lipid membranes. A study conducted by Walter et al. has shown that the number/position of cholesterol barges on origami tiles play a significant role in controlling their dynamics on the bilayer surface. Therefore, these systems can be labeled with fluorescent dyes and used as probes to characterize biological membranes [66]. In addition to their usage as templating platforms, DNA origami

EBSCOhost - printed on 2/14/2023 1:06 PM via . All use subject to https://www.ebsco.com/terms-of-use

are considered exceptional substrates to perform super-resolution single-molecule experiments based on DNA PAINT (a variation of super-resolution fluorescence microscopy) [67]. Jungman and coworkers reported the successful imaging of biomolecules within 5 nm resolution using this technique. Briefly, DNA-PAINT is based on the transient interaction between one or more short DNA strands labeled with dyes, typically 9 bases, with specific staple strands on origami (Figure 7.9c).

For the fabrication of nanomaterials using DNA origami, the size limitations of the origami substrates present once again the main challenge in developing large-scale assemblies. It seems unlikely that practical devices can be produced from the examples reported in literature. Hence, it is essential to focus on overcoming this limitation while optimizing the structures of DNA origami and their assembly conditions. Furthermore, it is noteworthy to mention that the majority of origami structures are inherently static. An ideal optimization to promote the generation of nanomaterials based on DNA at the macroscopic level is to program their dynamics at the nanoscale level [68].

7.4 DNA Nanotubes and Other Dynamic Nanostructures

The necessity to simplify assembly while preserving programmability and dynamic character is illustrated by the construction of DNA nanotubes. Several strategies based on DX motifs, DNA origami, and single-stranded DNA were adopted to build tubes with different shapes and geometries. One of the first methods involved the formation of 2D sheets that fold into nanotubes. The size of these tubes depends highly on the number of bases between two crossover points within the DX motif and the length/position of the sticky ends [22, 69]. For example, Seeman et al. demonstrated the assembly of six- and eight-helix bundles of different inner cavities (Figure 7.10a) [23]. They showed that the connection between two helices at particular positions significantly affects the angles between DX portions, hence leading to the growth/disassembly of micron-sized tubes. Yin's research group reported the assembly of nanotubes and other complex shapes from single-stranded tiles made up of 42 bases (Figure 7.10b) [70]. Each strand consisted of four domains and was able to bind four other strands during assembly. Another strategy to build nanotubes from a single-stranded oligonucleotide was demonstrated by Mao and coworkers [71]. Inspired by the natural folding of microtubules, the authors aimed at reducing the number of DNA strands by increasing sequence symmetry. They synthesized a strand made up of 52 bases and divided into four palindromic domains (same sequences when read from 5′- to 3′-end or 3′- to 5′-end). Because of this self-complementarity, 2D lattices were

EBSCOhost - printed on 2/14/2023 1:06 PM via . All use subject to https://www.ebsco.com/terms-of-use

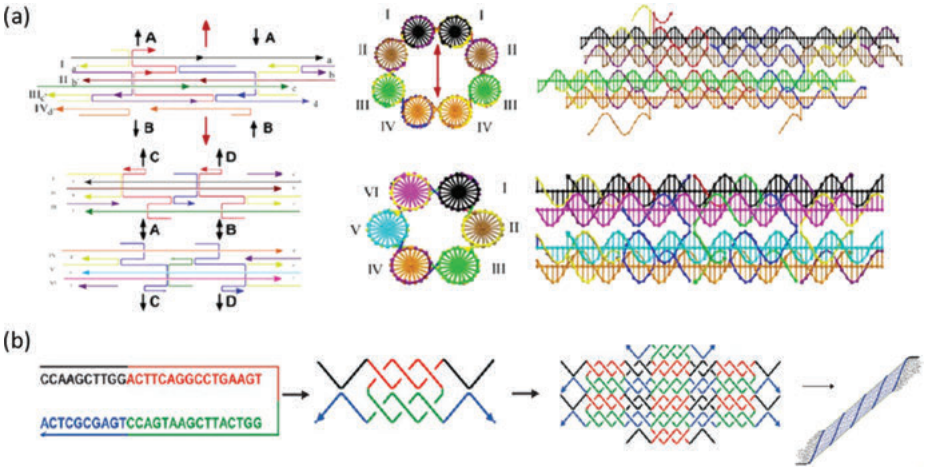

Figure 7.10: (a) Schematic representations of eight-helix (top) and six-helix (bottom) bundles. The connection between crossovers is illustrated in the left through the letters and arrows. The cross-sections of the tubes are displayed in the center and the helices appear to the right of the panels. Adapted with permission from Reference 23 (ACS Publishing, 2007). (b) Scheme showing the formation of DNA nanotubes based on single-stranded tile strategy. Left: 3D illustration of tubes with programmed circumferences. Right: A possible kinetic product (12-helix bundle) during the assembly of six-helix bundles. Adapted with permission from Reference 70 (Science 2008). (c) Schematic drawing of a single-stranded DNA nanotube composed of hour palindromic domains. A two-stranded complex is formed first, followed by the assembly of 2D sheets that will fold into tubes. Adapted with permission from Reference 71 (RSC Publishing 2006).

assembled upon the hybridization of the sticky ends, followed by the formation of tubes due to the flexibility of the lattices (Figure 7.10c).

Using the DNA origami approach, another generation of DNA nanotubes with defined diameters and lengths was produced. A six-helix bundle tube was achieved when the M13mp18 scaffold was folded around 168 staple strands [30]. Each short oligonucleotide consisted of 42 bases and interacted with the scaffold in three regions of 14 bases each. Shih and colleagues showed that such interactions led to the assembly of tubes instead of 2D sheets. Schulman's group made DNA nanotubes via an origami approach tiles and used them as seeds to control the growth of tubes based on DX motifs [72]. According to the authors, the origami seeds act as nucleation templates, hence accelerating the growth of the tubes with controlled dimensions.

The production of DNA nanotubes is a central area in nanobiotechnology. Besides controlling the dimensions of the tubes, it is crucial to regulate their movements to build multicomponent devices. Thus, it is worthwhile to shed more light on a variety of dynamic DNA nanostructures reported in literature before discussing some of the attempts to build dynamic DNA nanotubes.

EBSCOhost - printed on 2/14/2023 1:06 PM via . All use subject to https://www.ebsco.com/terms-of-use

The idea of isothermal DNA strand displacement was introduced by Neumann and coworkers to construct one of the first molecular machines made up of DNA (Figure 7.11a) [73]. The nanomechanical switch in this case was based on the interaction between an extended single-stranded overhang (toehold) with its complement component. As a result, the complement strand was able to remove the targeted strand from the machine and allowed the DNA tweezer to open. Since the discovery of strand displacement approach, a variety of DNA walkers have been demonstrated [74–76]. Another type of DNA-based robots was generated by Yan and coworkers by allowing three deoxyribozymes "legs" to interact with prescriptive landscapes (Figure 7.11b) [77]. The directional progress of the robots on the track was followed via single-molecule fluorescence. The authors believed that the potential interaction between these robots might lead to collective behavior as a means of performing more complex tasks.

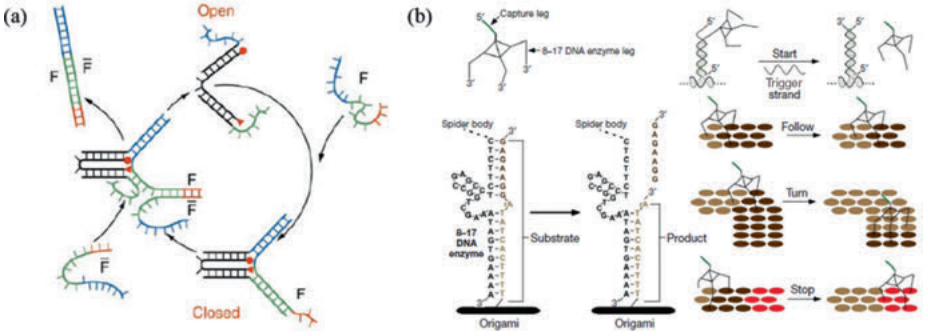

Figure 7.11: (a) Schematic representation of a DNA tweezer. The machine closes upon binding of strand F to the sticky ends of strands B and C. Then, the complement of strand F induces the re-opening of the tweezer. Adapted with permission from Reference 73 (Nature Publishing Group, 2000). (b) Scheme showing the movement of a DNA walker in the presence of deoxyribozyme enzyme. The enzyme breaks the substrate specifically at an RNA base, generating two short strands. Following the dissociation of these strands, a new substrate can bind the machine. Adapted with permission from Reference 77 (Nature Publishing Group, 2010).

The generation of dynamic DNA nanostructures is becoming more essential to build practical devices. Since the introduction of the new cellular membrane model in the 1970s, researchers have been developing novel techniques to examine membrane's heterogeneity [78]. Various agents have been implemented to the lipid bilayers to optimize imaging quality via confocal microscopy and flow cytometry [79, 80]. In this regard, DNA nanostructures offer a remarkable platform to functionalize the membranes and/or generate artificial nanopores. Howorka and coworkers built a

EBSCOhost - printed on 2/14/2023 1:06 PM via . All use subject to https://www.ebsco.com/terms-of-use

molecular valve able to control the transportation of cargos across the membrane. The valve was demonstrated to be selective toward small charged organic molecules and to experience nanomechanical changes upon binding to the cargo (Figure 7.12a) [4]. Another study published by Seelig et al. employed strand displacement approach to detect collisions between compartments on the cellular membrane (Figure 7.12b) [81]. This analysis is supposed to help understanding the dynamic behavior of some of the molecules present in the lipid bilayers. Alternatively, DNA nanostructures have been created to deliver cargos to the cells. Ricci and coworkers reported the assembly of DNA nanosystems that are able to encapsulate/release cargo upon binding to antibodies [82]. One of the antigens used in this study included HIV-related antigen and is suggested to improve future diagnosis of HIV in vivo. A simple DNA-based nanomachine was reported by Liu's research group. The authors employed a C-rich sequence called "i-motif" to build a nanomotor [83]. Briefly, an oligonucleotide containing CCC stretches forms a quadruplex structure at a pH lower than 5 due to the intramolecular hydrogen bonding between protonated and unprotonated cytosines. The process is reversible since the duplex

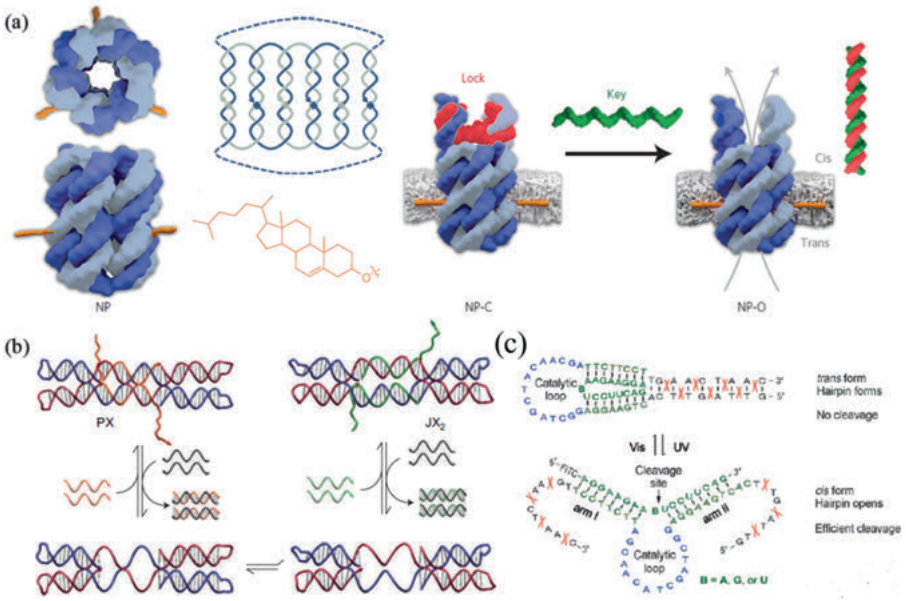

Figure 7.12: (a) Schematic representation of a DNA nanopore that opens upon the hybridization of the key strand (green) to the lock strand (red). Adapted with permission from Reference 4 (Nature Publishing Group, 2016). (b) Another DNA switch based on exchanging strands between PX and JX_2 tile motifs. Adapted with permission from Reference 81 (Nature Publishing Group, 2011). (c) Scheme displaying a light-responsive DNA-based machine. Azobenzene molecules were incorporated in the DNA sequences. The hairpin opens under UV light allowing DNAzymes to cleave the RNA target. Adapted with permission from Reference 84 (Wiley-VCH, 2010).

EBSCOhost - printed on 2/14/2023 1:06 PM via . All use subject to https://www.ebsco.com/terms-of-use

form can be easily achieved under neutral or basic pH. However, the incorporation of C-rich stretches within nanostructures remains challenging since some systems are not stable at acidic pH. Light-driven DNA nanomachines were demonstrated by Asanuma's research group [84]. They incorporated two azobenzene-modified sequences to open/close a hairpin structure in response to UV light. Once the hairpin opened, the enzymes found the correct topology to cleave protected RNA segments (Figure 7.12c).

The importance of forming dynamic DNA nanotubes, similar to the aforementioned examples, lies in their ability to amplify motion, hence acting as biophysical probes or efficient drug delivery vehicles. However, methods based on DX or TX motifs, single-stranded tiles, and origami generate rigid systems that are fully double stranded and are not inherently dynamic. Therefore, Sleiman's research group has assembled a variety of DNA nanotubes of tunable geometry and rigidity based on sticky end cohesion of DNA polygons on top of one another via linking strands (Figure 7.13a) [85]. Since the linking strands are able to switch between single- and double-stranded forms through strand displacement strategy, the resulting tubes were ideal for loading/releasing cargos (Figure 7.13b) [86].

7.5 Higher-Order DNA Nanostructures

Natural systems combine many different supramolecular interactions in a hierarchical manner to build functional structures. In contrast, DNA nanotechnology relies almost exclusively on DNA base pairing for structure generation. Introducing other supramolecular interactions can significantly expand the structural and functional range of DNA assemblies, but this requires an understanding of the interplay between these different interactions within DNA nanostructures. On the other hand, the production of DNA-based nanodevices with a resolution on the nanoscale requires the combination of standard nanofabrication methods with bottom-up assembly techniques. Ongoing efforts have been investigating a variety of strategies to assemble higher-order DNA systems and to scale them up. In this section, two main strategies will be discussed: (i) DNA patterning on surfaces and (ii) assembly of supramolecular DNA structures.

Organizing DNA into long-range assemblies in 2D/3D holds great potential for encapsulating/releasing small molecules for drug delivery, arranging nanoparticles to promote the creation of electronic devices, and engineering novel biosensors. Ideally, to employ oligonucleotides in any device, the DNA motifs must be geometrically well aligned before the beginning of the processing step [87]. One of the strategies reported to organize DNA involves lithography [88]. Briefly, a substrate is patterned via lithography (soft lithography involving patterned poly(dimethyl siloxane), for example, can be used to organize biomaterials under mild conditions),

EBSCOhost - printed on 2/14/2023 1:06 PM via . All use subject to https://www.ebsco.com/terms-of-use

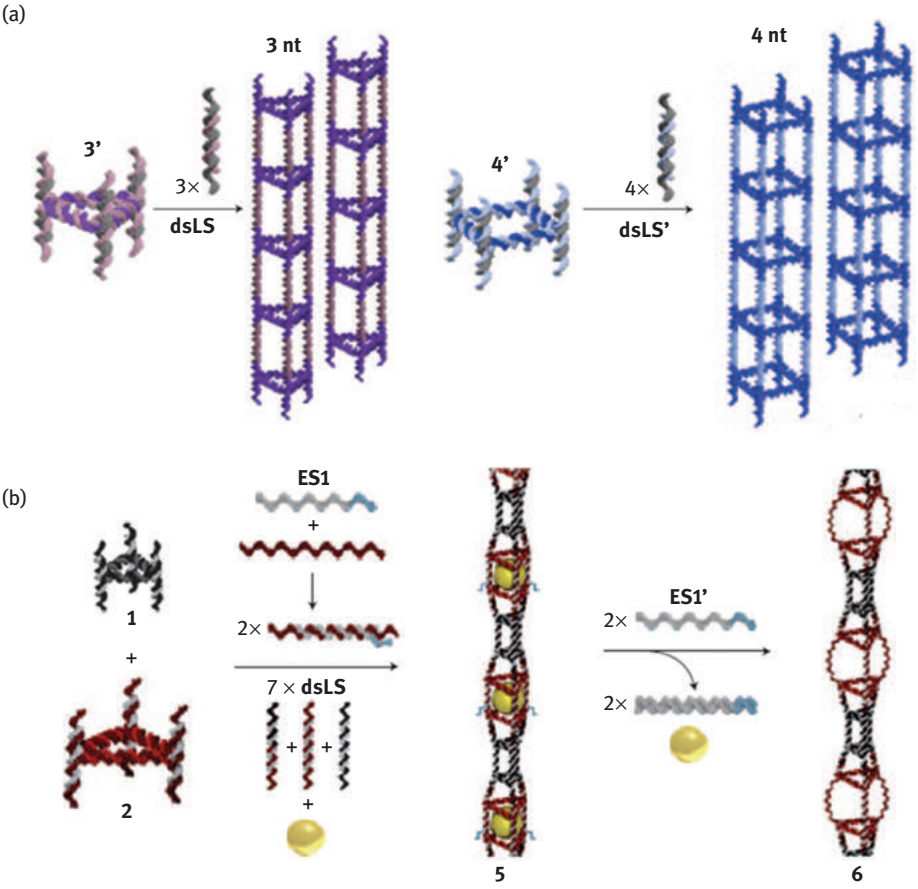

Figure 7.13: (a) Self-assembly of triangular and square nanotubes through sticky-end cohesion between triangular/square units and 3/4 linking strands, respectively. Adapted with permission from Reference 85 (Nature Publishing Group, 2009). (b) Scheme showing the construction of triangular tubes that are able to encapsulate 15 nm AuNPs, followed by the selective release of these particles through strand displacement strategy. Adapted with permission from Reference 86 (Nature Publishing Group, 2010).

followed by the addition of a solution containing DNA strands that are generally integrated into defined areas on the etched surface. The oligonucleotides can be later functionalized with other materials, including AuNPs [88] (Figure 7.14a) or used to grow other materials [89]. Alternatively, Rothemund and coworkers reported the organization of origami tiles on a mica surface by controlling the diffusion of cations on the surface [50]. The authors demonstrated that gradually replacing magnesium by sodium cations induced the self-assembly of origami tiles into periodic lattices. According to previous studies, the interaction of negatively

EBSCOhost - printed on 2/14/2023 1:06 PM via . All use subject to https://www.ebsco.com/terms-of-use

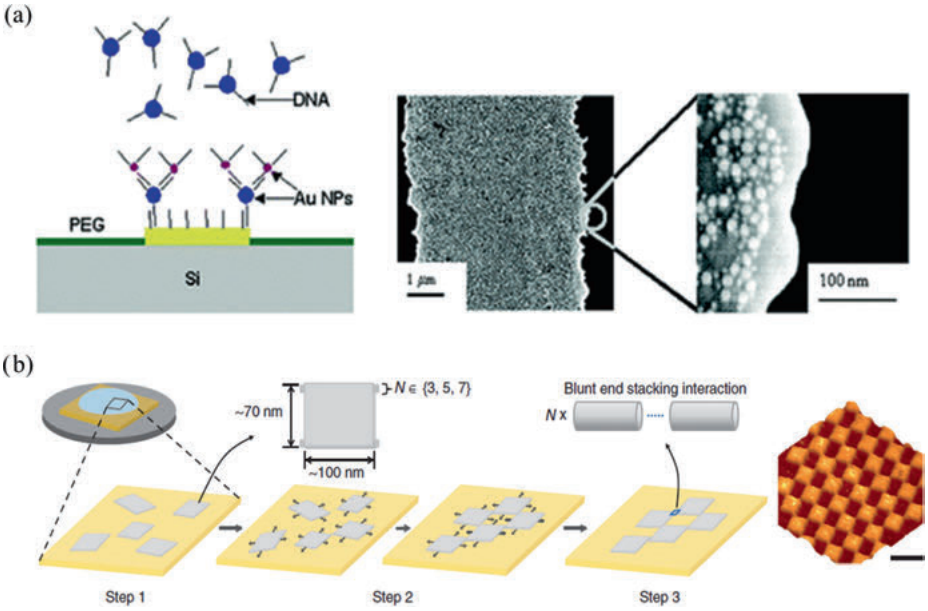

Figure 7.14: (a) Schematic representation of the assembly of two layers of AuNPs on a gold film patterned by photolithography. Adapted with permission from Reference 88 (ACS Publishing, 2004). (b) Organization of 2D origami lattices through controlling the diffusion of cations on mica surface. The tiles are immobilized on the surface in the presence of magnesium buffer (step 1). During the second step, sodium buffer was added to allow the diffusion of origami tiles. Finally, the tiles are immobilized again upon the addition of nickel and magnesium buffers. To the right is an AFM micrograph of the resulting structure. Scale bar, 200 nm.

charged oligonucleotides with the negatively charged mica surface is highly dependent on the concentration and type of cations. In this paper, the diffusion of cations was suggested to play a key role in controlling the dynamic behavior of origami rectangular tiles and to build a higher-order assembly (Figure 7.14b). Using the AFM cantilever, Liu's research group generated a pattern of DNA following a specific path [90]. Typically, the material on the surface can be replaced by DNA at particular areas while the AFM tip is travelling across the surface. Note that complex patterns can be created via other techniques such as dip-pen nanolithography [91], yet these strategies remain expensive for the high-scale production of nanodevices. Moreover, the generation of error-free assembly procedures via similar approaches still require to be optimized in a more efficient manner. Therefore, other routes including the usage of nonnatural bases and various orthogonal interactions were examined to produce higher-order DNA nanostructures.

Noncovalent interactions primarily mediate the supramolecular assembly of basic building blocks within biological systems. This approach is mimicked synthetically to

EBSCOhost - printed on 2/14/2023 1:06 PM via . All use subject to https://www.ebsco.com/terms-of-use

provide a powerful platform for the organization of various nanostructures, including nanoparticles [92], proteins [93], and small molecules [94]. In DNA nanotechnology, Watson—Crick base pairing has mainly been used as a model for the assembly of DNA nanostructures, although their complexities are inherently limited by the genetic code. Ongoing efforts have been focusing on introducing orthogonal interactions to increase the complexity of the systems without compromising structural integrity. For instance, synthetic modifications incorporated in DNA double helices such as geometric vertices have a great impact on the rigidity and stability of duplexes [95]. They are able to alter the linearity of DNA, hence producing new geometries without modifying DNA sequences. Sleiman and coworkers synthesized an m-terphenyl-based vertex and attached it to DNA overhangs at both ends (Figure 7.15) [96]. The resulting final structure was rigidified by the inserted vertex and was used to organize six AuNPs. Using the same concept, Richert's research group examined the formation of tetrahedral lattices by inserting four-way junctions within duplexes [97]. Similarly, large networks of DNA were created after incorporating six-way insertions [98].

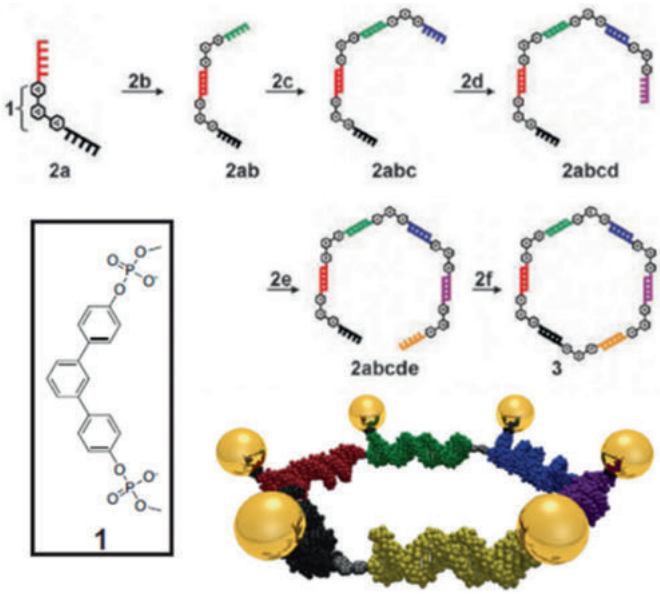

Figure 7.15: Organization of AuNPs into a hexagonal pattern. Adapted with permission from Reference 96 (Wiley-VCH, 2006).

The desire to further expand the DNA "alphabet" while preserving the ability to predict the geometry of DNA-based structures encouraged scientists to combine coordination chemistry and DNA. Similar to the field of metallosupramolecular

EBSCOhost - printed on 2/14/2023 1:06 PM via . All use subject to https://www.ebsco.com/terms-of-use

chemistry, the inserted ligands can precisely arrange metal complexes and provide DNA nanostructures with new functionalities for applications in nanoelectronics, optics, charge transport, and catalysis. In turn, nucleic acids are one of the few materials that are suited for controlling the position of transition metals and the assembly of 3D metal frameworks. A variety of approaches were reported to incorporate metals into DNA such as metal binding to artificial or natural nucleic acids [99, 100], addition of metal complexes to DNA [101], and integration of ligands to DNA for subsequent coordination to transition metals [102]. Through metal binding to natural nucleobases, a molecular logic gate (Figure 7.16a), for example, was generated [103]. DNA polymerases were only activated in the presence of specific mismatches and Hg^{2+}/Ag^{+} cations. Hannon and coworkers produced bimetallic helicate structures, preassembled metallosupramolecular structures, that can bind DNA similar to other natural DNA binders (Figure 7.16b) [104]. Sleiman's research group reported the addition of diphenylphenanthroline ligands into a prism. Subsequent to the addition of metals, the metal–DNA cages were found to be more stable, hence more suitable for future applications (Figure 7.16c) [102].

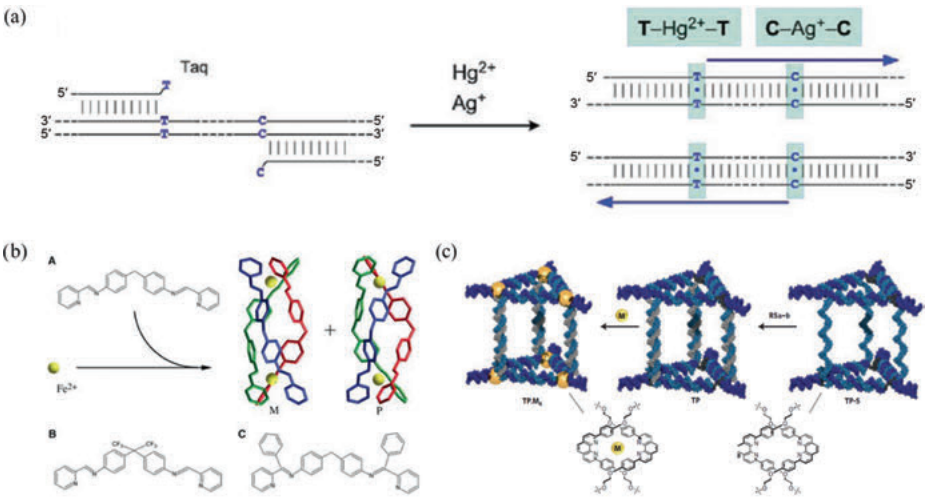

Figure 7.16: (a) Generation of an AND logic gate through T–Hg^{2+}–T and C–Ag^{+}–C base pairs. Adapted with permission from Reference 103 (ACS Publishing, 2012). (b) 3D representation of the metallosupramolecular structures obtained by X-ray crystallography. M: $[Fe_2L_3]^{4+}$ and P-$[Fe_2L_3]^{4+}$; L=$C_{25}H_{20}N_4$. Adapted with permission from Reference 104 (Oxford Press, 2008). (c) Schematic drawing of the production of 3D DNA prism followed by site-specific metalation. Adapted with permission from Reference 102 (Nature Publishing Group, 2009).

One of the main advantages of the method used in our lab is its ability to introduce a wide range of orthogonal interactions into DNA in a sequence-controlled manner. In

EBSCOhost - printed on 2/14/2023 1:06 PM via . All use subject to https://www.ebsco.com/terms-of-use

particular, hydrophobic modifications have been employed to trigger DNA assembly into higher-order structures [105]. For instance, Simmel and coworkers have shown the formation of DNA-sandwiched structures through the hydrophobic aggregation of cholesterol-modified DNA origami (Figure 7.17a) [106]. Lipid–DNA conjugates have been employed to improve the stability of nanostructures in cells, to facilitate vesicle fusion, and to create synthetic membrane nanopores [107–109]. In addition, hydrophobic chains were attached to individual nucleobases to form "nucleolipids" capable of self-assembling into spherical micelles in an aqueous buffer [110]. Yanagawa and coworkers reported the creation of helical fibers from nucleolipids at certain conditions [111]. Long-range assembly of amphiphilic DNA polymers were demonstrated by Herrmann et al. through microphase separations. The authors described the formation of a large 1D morphology via microphase separation of a long DNA strand attached to a hydrophobic polymer made up of polypropylene oxide (Figure 7.17b)

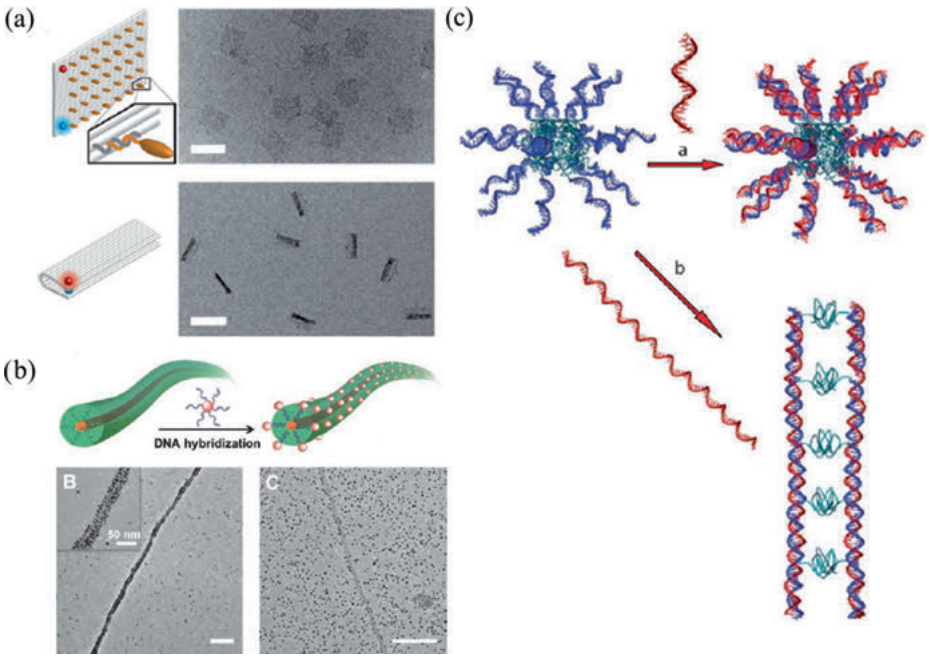

Figure 7.17: (a) Top: TEM micrograph of origami tiles consisting of 24 double helices. The positions of the strands functionalized with cholesterol are displayed in orange. Bottom: TEM image showing the intramolecular hydrophobic interaction between cholesterol moieties attached on origami. Scale bar, 100 nm. Adapted with permission from Reference 106 (Wiley-VCH, 2014). (b) Schematic representation of the interaction between DNA nanofibers (made up of single-stranded DNA amphiphile) and functionalized AuNPs. TEM B: oligonucleotide on AuNPs is complementary to nanofibers. TEM C: complementarity is absent. Scale bar, 200 nm. Adapted with permission from Reference 113 (RSC Publishing 2011). (c) Schematic drawing of hybridization of short versus long ssDNA to micelles made up of DNA amphiphiles. Adapted with permission from Reference 112 (Wiley-VCH, 2007).

EBSCOhost - printed on 2/14/2023 1:06 PM via . All use subject to https://www.ebsco.com/terms-of-use

[113]. Moreover, attaching dentritic polybenzylether to DNA induced the generation of long fibers as reported by Liu's research group (Figure 7.17c) [112].

Recently, Sleiman's group devised a method for positioning sequence-controlled hydrophobic polymers on small DNA cages to direct their assembly [31, 114] The length and placement of the hydrophobic chains on the small cages were important determinants of their hydrophobically driven assembly, defining whether it is intra- or intermolecular, and how large the aggregation number is [115].

7.6 Conclusion

Since the establishment of the field, researchers have been extensively exploring the usage of DNA nanostructures to develop progressively functional systems for a wide range of applications. Extended DNA nanostructures, for example, DNA nanotubes, with important aspect ratio can amplify DNA distortions and respond to external stimuli as a means to develop smart nanomechanical devices. In particular, DNA nanotubes made up of repeating domains over micron sizes offer an effective platform to organize a wide range of entities using a restricted amount of initial materials. Furthermore, besides using Watson–Crick base pairing as a model to build DNA nanostructures, other orthogonal interactions such as metal coordination and hydrophobic interactions were introduced to increase the complexity of the assemblies without affecting structural integrity. Remarkably, DNA-based structures with chemically modified moieties have been developed for applications ranging from biomedicine to material sciences. Finally, the use of DNA origami approach to construct various 2D/3D nanostructures plays a significant role in the evolving area of DNA nanotechnology. This strategy provides an ideal tool to specifically position functional objects and study their interactions at the nanoscale level.

References

[1] Zhang F., Nangreave J., Liu Y., Yan H., *J. Am. Chem. Soc*. 2014, *136*, 11198–11211.
[2] Chen Y.-J., Groves B., Muscat R.A., Seelig G., *Nature nanotechnology* 2015, *10*, 748.
[3] Pan J., Li F., Cha T.-G., Chen H., Choi J.H., *Curr. Opin. Biotechnol*. 2015, *34*, 56–64.
[4] Burns J.R., Seifert A., Fertig N., Howorka S., *Nature nanotechnology* 2016, *11*, 152.
[5] Angell C., Xie S., Zhang L., Chen Y., *Small* 2016, *12*, 1117–1132.
[6] Hashimoto M., Tong R., Kohane D.S., *Mol. Pharm*. 2013, *10*, 2127–2144.
[7] Hobson D.W., *Wiley Interdisciplinary Reviews: Nanomedicine and Nanobiotechnology* 2009, *1*, 189–202.
[8] Pray L., *Nat. Education* 2008, *1*, 100.
[9] Seeman N.C., *Nature* 2003, *421*, 427–431.
[10] Seeman N.C., Belcher A.M., *Proceedings of the National Academy of Sciences* 2002, *99*, 6451–6455.

EBSCOhost - printed on 2/14/2023 1:06 PM via . All use subject to https://www.ebsco.com/terms-of-use

[11] Lehn J.-M., *Science* 1993, *260*, 1762–1763.
[12] Seeman N.C., *J. Theor. Biol.* 1982, *99*, 237–247.
[13] Mao C., Sun W., Seeman N.C., *Journal of the American Chemical Society* 1999, *121*, 5437–5443.
[14] Bhyrappa P., Wilson S. R., Suslick K.S., *Supramol. Chem.* 1998, *9*, 169–174.
[15] Dalgarno S.J., Tucker S.A., Bassil D.B., Atwood J.L., *Science* 2005, *309*, 2037–2039.
[16] Vignon S.A., Jarrosson T., Iijima T., Tseng H.-R., Sanders J.K., Stoddart J.F., *Journal of the American Chemical Society* 2004, *126*, 9884–9885.
[17] Seeman N.C., *Chem. Biol.* 2003, *10*, 1151–1159.
[18] Fu T.J., Seeman N.C., *Biochemistry* 1993, *32*, 3211–3220.
[19] Mao C., LaBean T.H., Reif J.H., Seeman N.C., *Nature* 2000, *407*, 493.
[20] Winfree E., Liu F., Wenzler L.A., Seeman N.C., *Nature* 1998, *394*, 539.
[21] Aldaye F.A., Palmer A.L., Sleiman H.F., *science* 2008, *321*, 1795–1799.
[22] Rothemund P.W., Ekani-Nkodo A., Papadakis N., Kumar A., Fygenson D.K., Winfree E., *Journal of the American Chemical Society* 2004, *126*, 16344–16352.
[23] Kuzuya A., Wang R., Sha R., Seeman N.C., *Nano letters* 2007, *7*, 1757–1763.
[24] Walsh A.S., Yin H., Erben, Wood M.J., Turberfield A.J., *ACS nano* 2011, *5*, 5427–5432.
[25] Goodman R.P., Berry R.M., Turberfield A.J., *Chemical Communications* 2004, 1372–1373.
[26] LaBean T.H., Yan H., Kopatsch J., Liu F., Winfree E., Reif J.H., Seeman N.C., *Journal of the American Chemical Society* 2000, *122*, 1848–1860.
[27] McLaughlin C.K., Hamblin G.D., Hänni K.D., Conway J.W., Nayak M.K., Carneiro K.M., Bazzi H.S., Sleiman H.F. , *Journal of the American Chemical Society* 2012, *134*, 4280–4286.
[28] Goodman R.P., Heilemann M., Doose S., Erben C.M., Kapanidis A.N., Turberfield A.J., *Nature nanotechnology* 2008, *3*, 93–96.
[29] Yan H., Park S.H., Finkelstein G., Reif J.H., LaBean T.H., *Science* 2003, *301*, 1882–1884.
[30] Douglas S.M., Chou J.J., Shih W.M., *Proceedings of the National Academy of Sciences* 2007, *104*, 6644–6648.
[31] Edwardson T.G., Carneiro K.M., McLaughlin C.K., Serpell C.J., Sleiman H.F., *Nature chemistry* 2013, *5*, 868–875.
[32] Zhao Z., Jacovetty E.L., Liu Y., Yan H., *Angewandte Chemie International Edition* 2011, *50*, 2041–2044.
[33] Sharma J., Chhabra R., Liu Y., Ke Y., Yan H., *Angewandte Chemie International Edition* 2006, *45*, 730–735.
[34] Pei H., Lu N., Wen Y., Song S., Liu Y., Yan H., Fan H., *Advanced Materials* 2010, *22*, 4754–4758.
[35] Lu C.-H., Willner B., Willner I., *ACS nano* 2013, *7*, 8320–8332.
[36] Labhasetwar V., *Curr. Opin. Biotechnol.* 2005, *16*, 674–680.
[37] Deng Z., Mao C., *Angewandte Chemie International Edition* 2004, *43*, 4068–4070.
[38] Diagne C.T., Brun C., Gasparutto D., Baillin X., Tiron R., *ACS nano* 2016, *10*, 6458–6463.
[39] Marchi A.N., Saaem I., Vogen B.N., Brown S., LaBean T.H., *Nano letters* 2014, *14*, 5740–5747.
[40] Rothemund P.W., *Nature* 2006, *440*, 297–302.
[41] Douglas S.M., Marblestone A.H., Teerapittayanon S., Vazquez A., Church G.M., Shih W.M., *Nucleic acids research* 2009, *37*, 5001–5006.
[42] Ke Y., Douglas S.M., Liu M., Sharma J., Cheng A., Leung A., Liu Y., Shih W.M., Yan H., *Journal of the American Chemical Society* 2009, *131*, 15903–15908.
[43] Han D., Pal S., Nangreave J., Deng Z., Liu Y. , Yan H., *Science* 2011, *332*, 342–346.
[44] Maune H.T., Han S.-P., Barish R.D., Bockrath M., Goddard W.A. III, Rothemund P.W., Winfree E., *Nature nanotechnology* 2010, *5*, 61–66.

EBSCOhost - printed on 2/14/2023 1:06 PM via . All use subject to https://www.ebsco.com/terms-of-use

[45] Bui H., Onodera C., Kidwell C., Tan Y., Graugnard E., Kuang W., Lee J., Knowlton W.B., Yurke B., Hughes W.L., *Nano letters* 2010, *10*, 3367–3372.
[46] Holloway C.L., Kuester E.F., Gordon J.A., O'Hara J., Booth J., Smith D.R., *IEEE Antennas and Propagation Magazine* 2012, *54*, 10–35.
[47] Wu N., Willner I., *Nano letters* 2016, *16*, 2867–2872.
[48] Chen H., Zhang H., Pan J., Cha T.-G., Li S., Andréasson J., Choi J.H., *ACS nano* 2016, *10*, 4989–4996.
[49] Liu W., Zhong H., Wang R., Seeman N.C., *Angewandte Chemie* 2011, *123*, 278–281.
[50] Woo S., Rothemund P.W., *Nature communications* 2014, *5*, 4889.
[51] Yao G., Li J., Chao J., Pei H., Liu H., Zhao Y., Shi J., Huang Q., Wang L., Huang W., *Angewandte Chemie International Edition* 2015, *54*, 2966–2969.
[52] Shen X., Song C., Wang J., Shi D., Wang Z., Liu N., Ding B., *Journal of the American Chemical Society* 2011, *134*, 146–149.
[53] Numajiri K., Yamazaki T., Kimura M., Kuzuya A., Komiyama M., *Journal of the American Chemical Society* 2010, *132*, 9937–9939.
[54] Krissanaprasit A., Madsen M., Knudsen J.B., Gudnason D., Surareungchai W., Birkedal V., Gothelf K.V., *ACS nano* 2016, *10*, 2243–2250.
[55] Song S., Fan C., in *Rolling Circle Amplification (RCA)*, Springer, 2016, pp. 151–159.
[56] Liu W., Halverson J., Tian Y., Tkachenko A.V., Gang O., *Nature chemistry* 2016, *8*, 867–873.
[57] Schreiber R., Santiago I., Ardavan A., Turberfield A.J., 2016.
[58] Zhang Y., Chao J., Liu H., Wang F., Su S., Liu B., Zhang L., Shi J., Wang L., Huang W., *Angewandte Chemie* 2016, *128*, 8168–8172.
[59] Edwardson T.G., Lau K.L., Bousmail D., Serpell C.J., Sleiman H.F., *Nature chemistry* 2016, *8*, 162.
[60] Gür F.N., Schwarz F.W., Ye J., Diez S., Schmidt T.L., 2016.
[61] Linko V., Eerikäinen M., Kostiainen M.A., *Chemical Communications* 2015, *51*, 5351–5354.
[62] Zhang Q., Jiang Q., Li N., Dai L., Liu Q., Song L., Wang J., Li Y., Tian J., Ding B., *Acs Nano* 2014, *8*, 6633–6643.
[63] Tintoré M., Gállego I., Manning B., Eritja R., Fàbrega C., *Angewandte Chemie International Edition* 2013, *52*, 7747–7750.
[64] Fu J., Liu M., Liu Y., Woodbury N.W., Yan H., *Journal of the American Chemical Society* 2012, *134*, 5516–5519.
[65] Bellot G., McClintock M.A., Chou J.J., Shih W.M., *Nature protocols* 2013, *8*.
[66] Johnson-Buck A., Jiang S., Yan H., Walter N.G., *ACS nano* 2014, *8*, 5641–5649.
[67] Jungmann R., Avendaño M.S., Woehrstein J.B., Dai M., Shih W.M., Yin P., *Nat. Methods* 2014, *11*, 313–318.
[68] Wang P., Meyer T.A., Pan V., Dutta P.K., Ke Y., *Chem* 2017, *2*, 359–382.
[69] Mathieu F., Liao S., Kopatsch J., Wang T., Mao C., Seeman N.C., *Nano letters* 2005, *5*, 661–665.
[70] Yin P., Hariadi R.F., Sahu S., Choi H.M., Park S.H., LaBean T.H., Reif J.H., *Science* 2008, *321*, 824–826.
[71] Liu H., Chen Y., He Y., Ribbe A.E., Mao C., *Angewandte Chemie International Edition* 2006, *45*, 1942–1945.
[72] Mohammed A.M., Schulman R., *Nano letters* 2013, *13*, 4006–4013.
[73] Yurke B., Turberfield A.J., Mills A.P., Simmel F.C., Neumann J.L., *Nature* 2000, *406*, 605–608.
[74] Yan H., Zhang X., Shen Z., Seeman N.C., *Nature* 2002, *415*, 62–65.
[75] Dirks R.M., Pierce N.A., *Proc. Natl. Acad. Sci. U.S.A.* 2004, *101*, 15275–15278.
[76] Sherman W.B., Seeman N.C., *Nano Letters* 2004, *4*, 1203–1207.
[77] Lund K., Manzo A.J., Dabby N., Michelotti N., Johnson-Buck A., Nangreave J., Taylor S., Pei R., Stojanovic M.N., Walter N.G., *Nature* 2010, *465*, 206.

EBSCOhost - printed on 2/14/2023 1:06 PM via . All use subject to https://www.ebsco.com/terms-of-use

[78] Singer S.J., Nicolson G.L., *Science* 1972, *175*, 720–731.
[79] Korlach J., Schwille P., Webb W.W., Feigenson G.W., *Proceedings of the National Academy of Sciences* 1999, *96*, 8461–8466.
[80] Dive C., Watson J.V., Workman P., *Cytometry Part A* 1990, *11*, 244–252.
[81] Zhang D.Y., Seelig G., *Nature chemistry* 2011, *3*, 103–113.
[82] Ranallo S., Prévost-Tremblay C., Idili A., Vallée-Bélisle A., Ricci F., *Nature Communications* 2017, *8*.
[83] Liu D., Balasubramanian S., *Angewandte Chemie International Edition* 2003, *42*, 5734–5736.
[84] Zhou M., Liang X., Mochizuki T., Asanuma H., *Angewandte Chemie* 2010, *122*, 2213–2216.
[85] Aldaye F.A., Lo P.K., Karam P., McLaughlin C.K., Cosa G., Sleiman H.F., *Nature nanotechnology* 2009, *4*, 349–352.
[86] Lo P.K., Karam P., Aldaye F.A., McLaughlin C.K., Hamblin G.D., Cosa G., Sleiman H.F., *Nature chemistry* 2010, *2*, 319–328.
[87] Hung A.M., Noh H., Cha J.N., *Nanoscale* 2010, *2*, 2530–2537.
[88] Kannan B., Kulkarni R.P., Majumdar A., *Nano Letters* 2004, *4*, 1521–1524.
[89] Becerril H.A., Woolley A.T., *Chemical Society Reviews* 2009, *38*, 329–337.
[90] Liu M., Amro N.A., Chow C.S., Liu G.-y., *Nano letters* 2002, *2*, 863–867.
[91] Piner R.D., Zhu J., Xu F., Hong S., Mirkin C.A., *science* 1999, *283*, 661–663.
[92] Daniel M.-C., Astruc D., *Chem. Rev.* 2004, *104*, 293–346.
[93] Liu G.-Y., Amro N.A., *Proceedings of the National Academy of Sciences* 2002, *99*, 5165–5170.
[94] Liu Z., Sun X., Nakayama-Ratchford N., Dai H., *ACS nano* 2007, *1*, 50–56.
[95] Shi J., Bergstrom D.E., *Angewandte Chemie International Edition* 1997, *36*, 111–113.
[96] Aldaye F.A., Sleiman H.F., *Angewandte Chemie International Edition* 2006, *45*, 2204–2209.
[97] Meng M., Ahlborn C., Bauer M., Plietzsch O., Soomro S.A., Singh A., Muller T., Wenzel W., Bräse S., Richert C., *ChemBioChem* 2009, *10*, 1335–1339.
[98] Singh A., Tolev M., Meng M., Klenin K., Plietzsch O., Schilling C.I., Muller T., Nieger M., Bräse S., Wenzel W., *Angewandte Chemie International Edition* 2011, *50*, 3227–3231.
[99] Kuklenyik Z., Marzilli L.G., *Inorg. Chem.* 1996, *35*, 5654–5662.
[100] Miyake Y., Togashi H., Tashiro M., Yamaguchi H., Oda S., Kudo M., Tanaka Y., Kondo Y., Sawa R., Fujimoto T., *Journal of the American Chemical Society* 2006, *128*, 2172–2173.
[101] Bond P., Langridge R., Jennette K., Lippard S., *Proceedings of the National Academy of Sciences* 1975, *72*, 4825–4829.
[102] Yang H., McLaughlin C.K., Aldaye F.A., Hamblin G.D., Rys A.Z., Rouiller I., Sleiman H.F., *Nature chemistry* 2009, *1*, 390–396.
[103] Takezawa Y., Shionoya M., *Acc. Chem. Res.* 2012, *45*, 2066–2076.
[104] Malina J., Hannon M.J., Brabec V., *Nucleic acids research* 2008, *36*, 3630–3638.
[105] Börjesson K., Lundberg E.P., Woller J.G., Nordén B., Albinsson B., *Angewandte Chemie International Edition* 2011, *50*, 8312–8315.
[106] List J., Weber M., Simmel F.C., *Angewandte Chemie International Edition* 2014, *53*, 4236–4239.
[107] Langecker M., Arnaut V., Martin T.G., List J., Renner S., Mayer M., Dietz H., Simmel F. C., *Science* 2012, *338*, 932–936.
[108] Burns J.R., Stulz E., Howorka S., *Nano letters* 2013, *13*, 2351–2356.
[109] Wilks T.R., Bath J., de Vries J.W., Raymond J.E., Herrmann A., Turberfield A.J., O'Reilly R.K., *ACS nano* 2013, *7*, 8561–8572.
[110] Kwak M., Herrmann A., *Chemical Society Reviews* 2011, *40*, 5745–5755.
[111] Yanagawa H., Ogawa Y., Furuta H., Tsuno K., *Journal of the American Chemical Society* 1989, *111*, 4567–4570.

EBSCOhost - printed on 2/14/2023 1:06 PM via . All use subject to https://www.ebsco.com/terms-of-use

[112] Ding K., Alemdaroglu F.E., Börsch M., Berger R., Herrmann A., *Angewandte Chemie International Edition* 2007, *46*, 1172–1175.
[113] Wang L., Feng Y., Sun Y., Li Z., Yang Z., He Y.-M., Fan Q.-H., Liu D., *Soft Matter* 2011, *7*, 7187–7190.
[114] Chidchob P., Edwardson T.G., Serpell C.J., Sleiman H.F., *Journal of the American Chemical Society* 2015.
[115] Serpell C.J., Edwardson T.G., Chidchob P., Carneiro K.M., Sleiman H.F., *Journal of the American Chemical Society* 2014, *136*, 15767–15774.

EBSCOhost - printed on 2/14/2023 1:06 PM via . All use subject to https://www.ebsco.com/terms-of-use

EBSCOhost - printed on 2/14/2023 1:06 PM via . All use subject to https://www.ebsco.com/terms-of-use

Theo G.M. van de Ven, M.A. (Tony) Whitehead

8 Alternating Copolymer Nanotubes

Keywords: alternating copolymers, nanotubes, self-assembly, molecular modeling, nanotube imaging, neutron scattering

Linear alternating copolymers with one phenyl group per repeat unit self-assemble by π–π stacking, provided the phenyl groups are favorably orientated. Two molecules can zip together, with the phenyl groups acting as the teeth (or elements) of the zipper. An example of a macromolecule that can act as a molecular zipper is poly(styrene *alt*. maleic anhydride), referred to as SMA. In water, the maleic anhydride group is hydrolyzed, resulting in maleic acid that contains two carboxyl groups. When two SMA molecules are zipped together, only a fraction of the phenyl groups is engaged in the zipper, while others are free and available for further π–π stacking. This leads to additional self-assembly into sheets of SMA, consisting of parallel SMA molecules, all zipped together side by side. These sheets roll up to minimize their energy, forming hollow nanotubes. We review the experimental evidence for SMA nanotube formation and summarize the quantum mechanical calculations that predict their formation. The results of SMA are compared to those of SMI, a styrene–maleimide copolymer, formed by reacting SMA with 3-(dimethylamino)-1-propylamide. Since SMA is an alternating copolymer, SMI is an alternating copolymer as well. For certain alternating copolymers, the chirality of the copolymer is extremely important. This led to the investigation of alternating copolymers made from natural molecules, such as oligopeptides and oligosaccharides, which have an inherent chirality. Finally we discuss how these nanotubes can act as templates to make advanced materials.

8.1 Introduction

In contrast to the large literature on the self-assembly of block copolymers, the literature on the self-assembly of alternating copolymers is scarce. Block copolymers can self-assemble in a large number of structures, such as spherical or cylindrical micelles, vesicles, lamellae, and so on [1], and can form 2D crystalline nanosheets [2]. Alternating copolymers can self-assemble in nanotubes or nanosheets, either by hydrogen bonding or by π-stacking. An example of an alternating copolymer that can self-assemble into nanotubes by hydrogen bonding is poly(2,3-dihydroxybutylene-alt-butylene di-thioether) (P(DHB-a-BDT)), synthesized using an epoxy-thiol click-chemistry reaction,

Theo G.M. van de Ven, M.A. (Tony) Whitehead, Pulp & Paper Research Centre and Quebec Centre for Advanced Materials Department of Chemistry McGill University, Montreal QC, Canada

https://doi.org/10.1515/9783110537734-008

EBSCOhost - printed on 2/14/2023 1:06 PM via . All use subject to https://www.ebsco.com/terms-of-use

which forms ultrathin nanotubes that are 30 nm in diameter and several microns long [3]. Examples of alternating copolymers that form nanotubes by π-stacking are discussed in this chapter.

SMA, an alternating copolymer, is used industrially in the surface treatment of paper (so-called surface sizing) to control printing and coating. An interesting property of SMA is that it performs this task very well when applied as an aqueous solution at pH 7. At low and high pH, SMA performs poorly [4]. The reason for this intriguing behavior is in the conformations of SMA molecules, which differ at different pHs. When dissolved in water, the maleic anhydride moieties in SMA are hydrolyzed maleic acid moieties, formed by opening the ring of the anhydride that creates two carboxyl groups (cf. Figure 8.1).

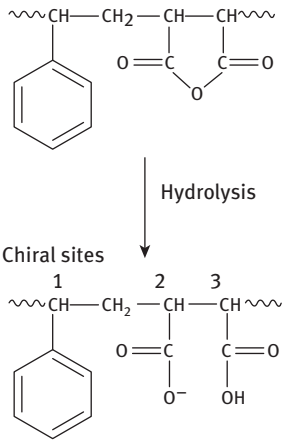

Figure 8.1: Structure of alternating copolymer SMA (top) and structure of SMA, after hydrolysis in water (bottom). Each repeat unit in SMA has one phenyl group, two carboxyl groups, and three chiral sites.

Depending on pH, these carboxyl groups can be protonated or dissociated. At low pH (around 3), both carboxyl groups are protonated, which follows from the dissociation constant (pK_a value) of the first carboxyl group, which is 4.9. At high pH (around 12) both carboxyl groups are dissociated, which follows from the pK_a of the second carboxyl group, which is 10.2 [4]. At pH 7 one carboxyl group is protonated and one is dissociated (cf. Figure 8.2).

At pH 7 the maleic acid ring is closed by the formation of a hydrogen bond between the protonated and dissociated carboxyl groups (Figure 8.2, bottom right). This ring closure leads to a rather rigid linear conformation of SMA [5]. At low and high pH, the SMA molecules behave like semiflexible chains [6]. In its linear form (at pH 7) the phenyl groups are oriented in such a way that two SMA molecules can self-associate by π–π stacking, as shown in Figure 8.3.

As indicated in Figure 8.1, SMA has three optically active centers per repeat unit, which are distributed randomly along the chain, and one might expect that the configuration of an SMA molecule is affected by its chirality. As we will see

EBSCOhost - printed on 2/14/2023 1:06 PM via . All use subject to https://www.ebsco.com/terms-of-use

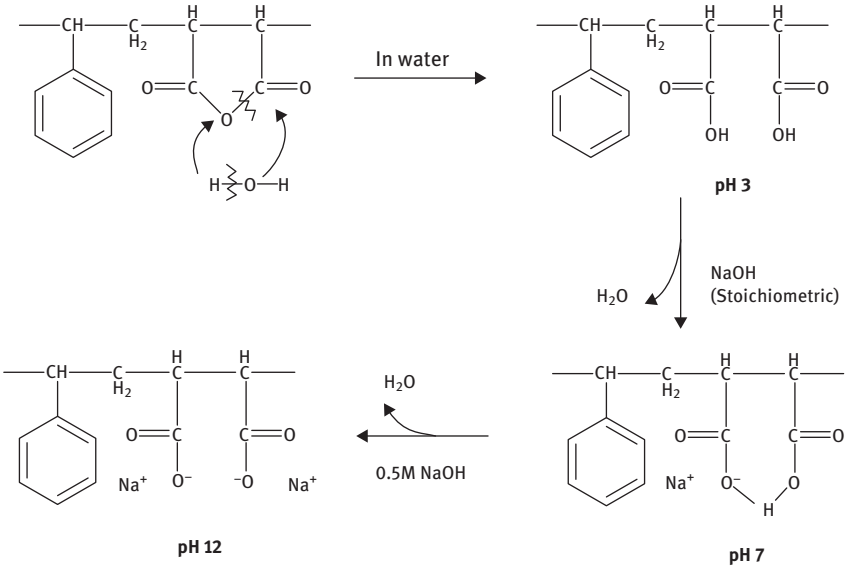

Figure 8.2: Primary structure of SMA depends on pH, which determines how many carboxylic groups are protonated or dissociated.

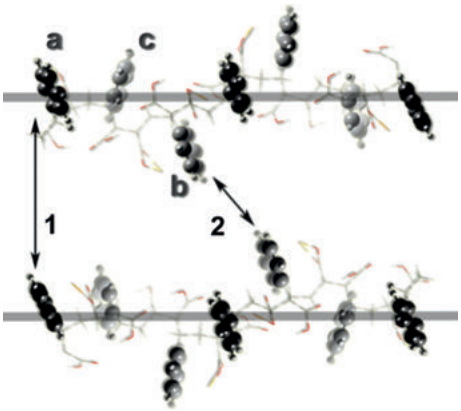

Figure 8.3: π–π stacking interactions between two SMA heptamers. The darker phenyl groups are in front of the plane and the lighter ones behind the plane (adapted from [7]).

later, most SMA chains self-assemble into nanotubes, which implies that chirality plays a minor role.

The first evidence of self-association of SMA came from dynamic light scattering (DLS) experiments [8], which showed large complexes at pH 7, but not at low and high pH. However, DLS tells us little about the nature of the self-assembly.

EBSCOhost - printed on 2/14/2023 1:06 PM via . All use subject to https://www.ebsco.com/terms-of-use

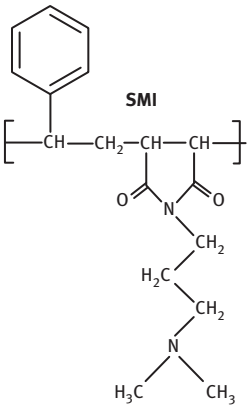

Figure 8.4: Structure of SMI.

A second alternating copolymer containing phenyl groups is poly(styrene *alt*. maleimide) (SMI), which can be produced by reacting SMA with 3-(dimethylamino)-1-propylamide. SMI is used industrially as a coating agent [9]. Its structure is shown in Figure 8.4. Similar to SMA at pH 7, the ring in the imide is closed, resulting in a rigid structure at all pHs. SMI is soluble in water at low pH, due to the protonation of the tertiary amine group at the end of the side chain.

Here we will review the experimental evidence for the formation of SMA and SMI nanotubes, followed by theoretical explanations and predictions from quantum mechanics.

8.2 Experimental Evidence for SMA and SMI Nanotubes

8.2.1 Small Angle Neutron Scattering

Small-angle neutron scattering (SANS) is an ideal tool to study the structure in aqueous solutions. One of its greatest advantages is that we can control the contrast by varying the ratio of water to heavy water (H_2O/D_2O). The scattering length density (SLD) of the $H_2O)/D_2O$ mixture can be made the same as, for example, that of styrene, making styrene invisible to neutrons. Figure 8.5 shows the neutron scattering intensity as a function of scattering vector Q for SMA solutions in water at pH 7 and 12. It can be seen that the scattering intensity is very different for these two pH values. At pH 12, the scattering intensity decreases monotonically with Q, indicating that no self-assembly takes place. At pH 7, a peak in the scattering intensity plot is seen, implying the occurrence of structure.

EBSCOhost - printed on 2/14/2023 1:06 PM via . All use subject to https://www.ebsco.com/terms-of-use

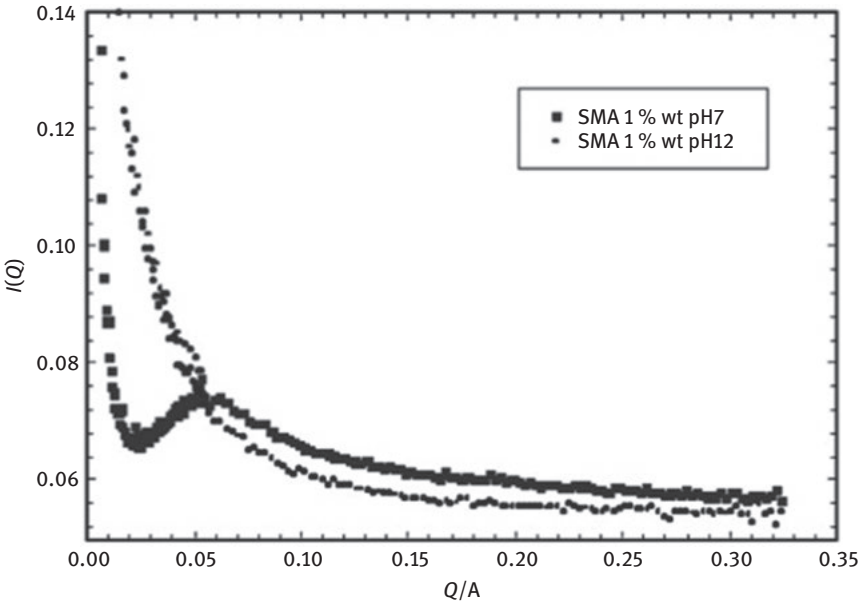

Figure 8.5: Neutron scattering intensity as a function of scattering vector for SMA solutions at pH 7 and 12 (after [10]).

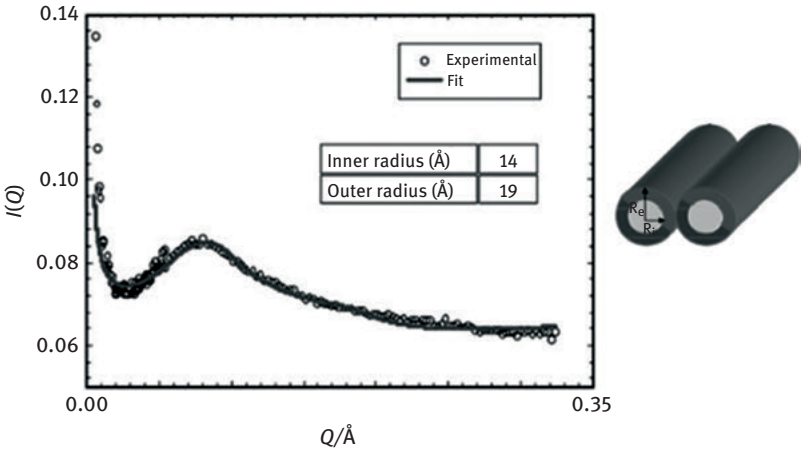

Figure 8.6: Best fit of experimental scattering data for 1% SMA solution at pH7 (adapted from [10]).

Fitting the data to a model of hollow cylinders with inner and outer radii R_1 and R_2, using the SLD of the solvent and the measured SLD of the nanotube wall (determined by varying the H_2O/D_2O ratio till the scattering is (near) zero), shows

EBSCOhost - printed on 2/14/2023 1:06 PM via . All use subject to https://www.ebsco.com/terms-of-use

excellent agreement with experiment (cf. Figure 8.6), with values of the inner and outer radii of 1.4 and 1.9 nm [10].

One can probe the self-assembly of SMA in more detail by varying the contrast. When the (deuterated) styrene is made invisible to neutrons, by matching the SLD of the H_2O/D_2O mixture to that of styrene, the peak in the scattering intensity plot disappears [6]. From this one can conclude the self-association at pH 7 is due to π–π stacking.

The inside wall of an SMA nanotube is hydrophobic and it is possible to fill the nanotubes with hydrophobic molecules, for example, pyrrole, followed by polymerization. SANS data on suspensions of SMA nanotubes filled with polypyrrole show very similar structures as suspensions of empty nanotubes, proving that filling the nanotubes does not alter their structure to any measurable extent [11, 12]. The data also prove that without polypyrrole the tubes are hollow.

8.2.2 Cryo-TEM of SMA Nanotubes

In sample preparation for cryo-TEM, a drop of an aqueous solution of SMA octamers at pH 7 was refrigerated in liquid nitrogen. The frozen sample was cut and a replica of the top surface was made by first spraying a platinum–carbon mixture at a 45° angle of incidence, followed by spraying carbon normal to the surface. In preparing samples this way, the surface often fractures at locations were discontinuities in structure occur. An example of a cryo-TEM image is shown in Figure 8.7a, which

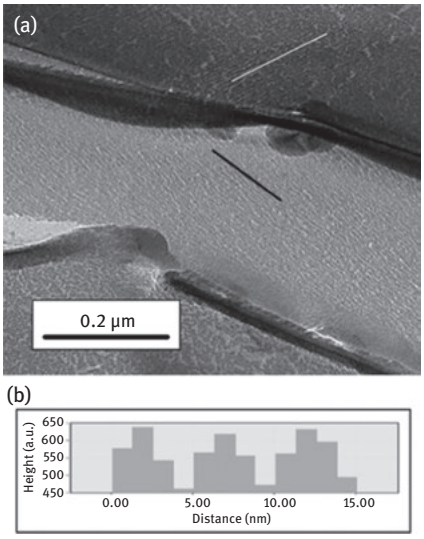

Figure 8.7: (a) Cryo-TEM of a 1% solution of SMA at pH 7. The lines are to guide the eyes and represent the direction of the linear SMA structures. (b) Height profiles of three lines across the linear structures, showing that their diameter is about 5 nm (after [13]).

EBSCOhost - printed on 2/14/2023 1:06 PM via . All use subject to https://www.ebsco.com/terms-of-use

shows long linear structures side by side. Two lines are shown to indicate the direction of the observed linear structures.

In Figure 8.7b the height profiles of three lines across the linear structures are presented, showing that the diameter of these linear structures is about 5 nm. These values are consistent with the diameters deduced from SANS, considering that the 5 nm in cry-TEM includes the spacing between the nanotubes. At pH 3 and pH 12 no linear structures were seen with cryo-TEM [13].

8.2.3 TEM of SMA Nanotubes Filled with Polypyrrole

SMA nanotubes filled with polypyrrole are easier to image with TEM than empty ones, likely because they are sturdier. The polymerization of pyrrole inside SMA nanotubes has been studied in detail [14]. A schematic representation of this reaction is shown in Figure 8.8.

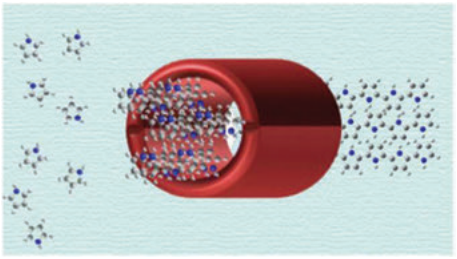

Figure 8.8: Schematic representation of polymerization of pyrrole under confinement (after [14]).

A TEM image of SMA nanotubes filled with polypyrrole is given in Figure 8.9. No linear structures are observed at pH 3 and 12. It can be seen that SMA nanotubes are bundled into larger structures. This is also predicted theoretically (see below), since SMA nanotubes have protruding phenyl groups that

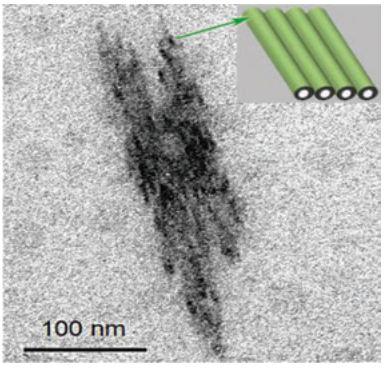

Figure 8.9: TEM of bundles of SMA nanotubes (pH = 7 (after [7])).

EBSCOhost - printed on 2/14/2023 1:06 PM via . All use subject to https://www.ebsco.com/terms-of-use

can lead to additional self-assembly. Hence, we can distinguish primary, secondary, and tertiary structures of SMA. The primary structure at pH 7 is a linear macromolecule. The secondary structure is a nanotube and the tertiary structure is a bundle of aligned nanotubes. Measuring the edge-to-edge distance of the parallel stripes in Figure 8 yields a distance of 4.6±1.6 nm, consistent with SANS and cryo-TEM.

When adding $AgNO_3$ to a suspension of SMA nanotubes filled with polypyrrole, and reducing Ag+ to Ag^0 by adding the reducing agent $NaBH_4$, silver deposits on the nanorods, making them easier to image. An example is shown in Figure 8.10, showing a striped Ag pattern. The diameter of these stripes was found to be 4.4±1.0 nm.

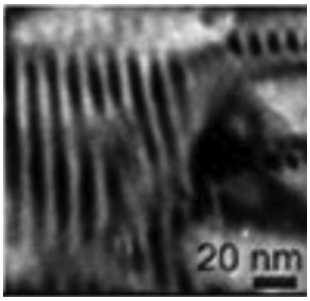

Figure 8.10: TEM image of Ag-SMA-polypyrrole nanorods (adapted from [7]).

8.2.4 AFM Images of SMA and SMI Nanotubes

Examples of SMA nanotubes, filled with polypyrrole, observed by AFM are shown in Figure 8.11. Height measurements give a height of 2–3 nm, which is less than that observed by SANS, cryo-TEM, and TEM. The difference is likely due to the fact that the SMA nanotubes were deposited on a glass surface coated by polylysine. This coating renders the surface positive, thus facilitating the deposition of negatively charged nanotubes. SMA nanotubes might have been partially embedded in the surface coating, and thus only the height of the part protruding from the surface coating is seen in AFM height measurements. It can be seen from Figure 8.11 that

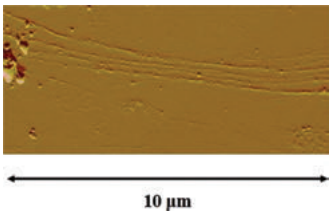

Figure 8.11: AFM of SMA nanotubes, showing that nanotubes can grow to a great length (after [15]).

EBSCOhost - printed on 2/14/2023 1:06 PM via . All use subject to https://www.ebsco.com/terms-of-use

SMA nanotubes can grow to very large lengths, up to 10 μm. Again no linear structures were seen at pH 3 and 12.

A second alternating copolymer chosen to study self-assembly by π–π stacking was SMI. Because of the closed ring (cf. Figure 8.4) in the maleimide moiety, SMI is expected to be rigid and to behave similar as SMA at pH 7, for which the ring is closed by a hydrogen bond. The presence of a long side chain is expected to prevent tertiary structure formation in the form of bundles, due to steric hindrance. Thus, one expects to see only individual nanotubes. Both these predictions were confirmed. SMI forms nanotubes and no bundling of nanotubes was observed. Examples of SMI nanotubes, filled with polypyrrole, are shown in Figure 8.12. The height of these nanostructures was found to be about 4.5 nm.

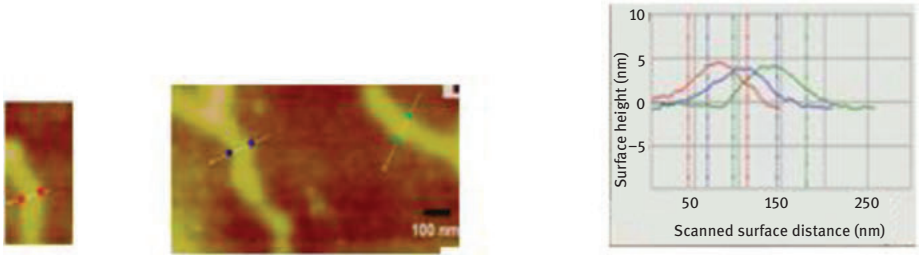

Figure 8.12: AFM of SMI nanotubes filled with polypyrrole on mica. Because most SMI molecules do not self-assemble, the surface of mica is likely covered with a monolayer of SMI. Picture on the right shows three height profiles indicated by the colored dots in the picture. The average height of the scanned nanorods is about 4.5 nm (after [17].

In contrast with SMA, for which the yield of nanotubes is very large, the yield of nanotubes for SMI is extremely small (≪ 1%). As shown later in the theoretical section, this is due to the fact that for SMI only molecules with the same chirality self-assemble.

8.2.5 Neutron Reflectivity

SMA is an amphilic molecules and adsorbs on an air–water interface. Neutron reflectivity data show that SMA forms a monolayer on water, with a surface coverage of about 1.2 mg/m^2 [13]. Indirect evidence that SMA molecules self-assemble at pH 7 and not at other pHs comes from surface tension and neutron reflectivity measurements. Both techniques show that at pH 7 it takes a long time to establish equilibrium conditions, whereas at pH 3 or 12, the equilibrium surface tension is established almost instantaneously. An example of neutron reflectivity data on an

EBSCOhost - printed on 2/14/2023 1:06 PM via . All use subject to https://www.ebsco.com/terms-of-use

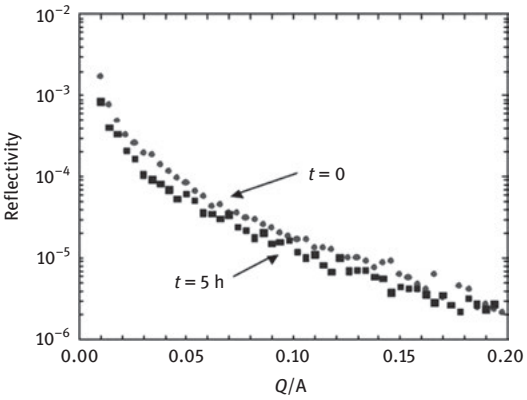

Figure 8.13: Neutron reflectivity as a function of the scattering vector Q at an air–water interface saturated with SMA. Data were taken at a 5 h interval (after [13]).

air–water surface covered with SMA is shown in Figure 8.13. The figure shows reflectivity data on a freshly prepared SMA solution and data taken 5 h afterward on the same sample. It can be seen that the neutron reflectivity has been decreased during the 5 h period. Such behavior was not seen at pH 3 and 12.

The time dependence of surface tension and neutron reflectivity at pH 7 is likely due to the slow establishment of a dynamic equilibrium between SMA nanotubes and molecules at the interface and in solution. Since nanotubes are more hydrophilic on the outside than on the inside, it is likely that SMA molecules have a larger affinity for the air–water interface than SMA nanotubes. Initially both accumulate on the surface, but with time adsorption of SMA molecules is preferred.

Taken together, there is strong evidence for SMA and SMI self-association. Indirect evidence comes from DLS, surface tension, neutron reflectivity, and SANS. SANS data can be modeled by comparing them with predictions for hollow cylinders, which show that SANS data are consistent with the presence of nanotubes with inner and outer diameters of about 3 and 4 nm. Direct evidence comes from cryo-TEM, TEM, and SMA imaging. All these techniques show linear structures with diameters of about 4–5 nm. Evidence that they are hollow structures comes from the observation that they can be filled. SANS data can be modeled by hollow cylinders filled with either water or polypyrrole. All these observations prove that SMA forms nanotubes at pH 7 with a diameter in the range 4–5 nm. SMA nanotubes can further self-associate into bundles of nanotubes and can grow to a length of several microns. SMA forms nanotubes with a high yield, implying that the chirality of SMA plays a minor role. No self-association takes place at pH 3 or 12. Similarly, SMI forms nanotubes of comparable dimensions. Here the tertiary structure of bundles of nanotubes is absent, due to the steric hindrance of the long side chain of SMI. The main

EBSCOhost - printed on 2/14/2023 1:06 PM via . All use subject to https://www.ebsco.com/terms-of-use

difference between SMA and SMI is the yield: Most SMA molecules self-assemble into nanotubes, independent of chirality, whereas very few SMI molecules self-assemble, presumably because only isotactic molecules can self-associate. Very few SMI molecules are isotactic in a population of oligomers with a random chirality.

8.3 Theoretical Predictions from Quantum Mechanical Calculations

8.3.1 Structure of SMA Monomers

The structure of SMA oligomers was calculated, starting from SMA monomers, followed by the calculation of dimers and n-mers up to dodecamers. The conformation of the monomer was obtained by two methods: (i) the tree branch method and (ii) by a series of energy scans [5]. These two methods are complementary and allow a complete description of the possible conformations of the monomers. Both methods gave identical structures. To simulate the dissociation/protonation of the two carboxyl groups in maleic acid, calculations for pH 3, 7, and 12 were performed with the two carboxyl groups protonated (pH 3), one group protonated and one dissociated (pH 7) and both groups deprotonated (pH 12). The conformation at pH 7 depends on whether the counter ion of the carboxyl group is a proton or a Na^+ ion.

The conformational search was performed at the (semiempirical) PM3 level of theory and the structures with minimal energy were subsequently optimized at the RHF/6-31G** and DFT-B3LYP/6-31G** level of theory. The parameters for sodium used in the optimization of SMA at pH 7 and 12 using PM3 were those developed by Brothers and Merz [17]. The calculations were performed using Gaussian [18] and HyperChem [19].

At pH 7 there are two possibilities, depending on which one of the two carboxyl groups is protonated and which one is dissociated. The two resulting structures have very similar energies. The structure with the second carboxyl group deprotonated (closest to the styrene) is the most stable one when Na^+ is the counter ion, with a difference in enthalpy of 7 kJ/mol. At pH 7 an internal hydrogen bond is formed between the hydrogen of the protonated carboxyl group and the oxygen of the deprotonated group. This hydrogen bond closes the ring in maleic acid and changes the geometry of the ground state. This internal hydrogen bond is very strong, with a bond length of 1.68 Å. In comparison, the hydrogen bond between two water molecules is 1.80 Å. This hydrogen bond is stabilized by the presence of Na^+. When H^+ is the counter ion the bond is weaker and the bond length increases to 1.83 Å. Figure 8.14a shows the optimized structure of the SMA monomer at pH 7, with the second carboxyl group deprotonated. Figure 8.14b and

EBSCOhost - printed on 2/14/2023 1:06 PM via . All use subject to https://www.ebsco.com/terms-of-use

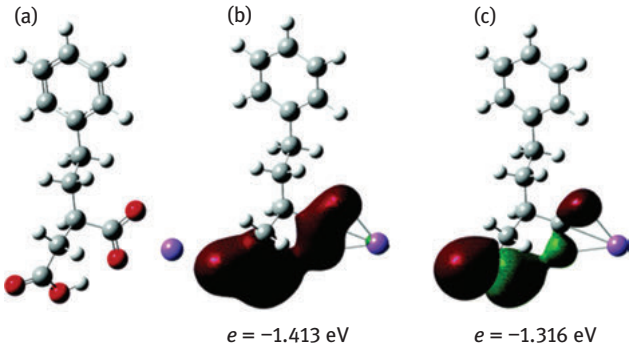

Figure 8.14: (a) Most stable conformation of SMA monomer at pH 7 (white =H, grey = C, red = O, and purple = Na). (b) and (c) Delocalized molecular orbitals 22 and 24 covering the internal hydrogen bond of SMA (adapted from [5]).

c shows the presence of the internal hydrogen bond, as evidenced by two delocalized molecular orbitals covering the bond. This hydrogen bond is stable in an aqueous environment [15, 20].

At pH 3 the monomer of SMA can also form an internal hydrogen bond, but the strength of this bond is much weaker than the bond between two water molecules (bond lengths of 1.87 and 1.80 Å, respectively), implying that this bond is not being formed in an aqueous environment.

The conformations of SMA monomers were also studied when surrounded by water molecules [20]. It was found that water had a negligible effect on the SMA conformations.

8.3.2 Structure of SMA Dimer and Trimer

The dimer of SMA possesses four chiral centers, two of which, the ones at the junction between the two monomers, affect the conformation of the polymer. This results in four possible conformations: RR, RS, SR, and SS. The structures of these four enantiomers were optimized at the PM3 level of theory using series of scans of energy and then optimized with ab initio calculations using RHF/6-31G**. Very different conformations were obtained at pH 3, 7, and 12. At pH 3 and 12, the angle between the monomers is close to 90°, whereas at pH 7 the structure is linear. Results for the optimized structure of the four dimers at pH 7 are shown in Figure 8.15.

It is interesting to note that in the most stable dimer conformation the order of protonation of the carboxyl groups is reversed (compared to the monomer), with the first carboxyl group being the most stable. Another interesting observation is

EBSCOhost - printed on 2/14/2023 1:06 PM via . All use subject to https://www.ebsco.com/terms-of-use

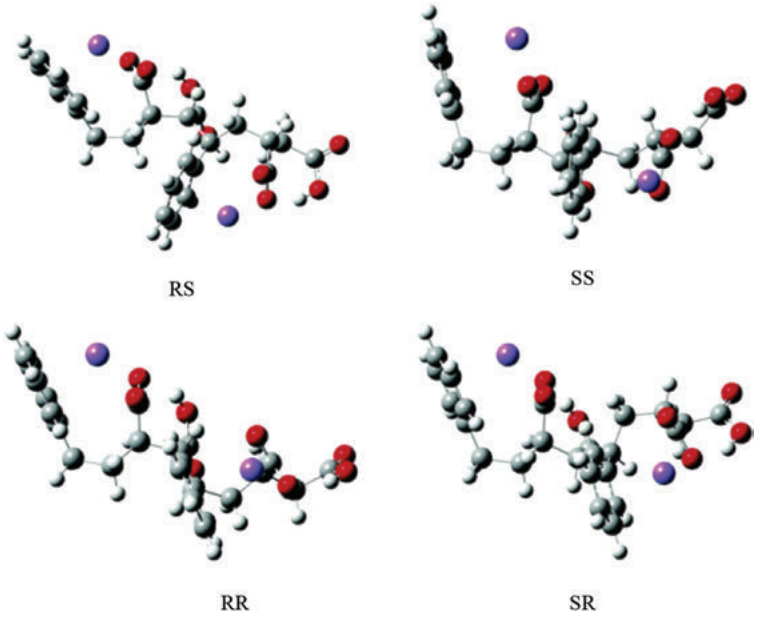

Figure 8.15: Four conformations of the dimer of SMA with different chiralities at pH 7 (after [5]).

that all conformations are linear and that the orientation of the phenyl groups is similar for all four enantiomers.

For the trimer, there are 16 different chiral structures. Similar to that for the dimer, conformations at pH 3 and 12 have 90° steps, whereas the conformations of the trimer at pH 7 are all linear. Four out of the 16 possible structures are shown in Figure 8.16. As for the dimer, the orientation of the phenyl groups is very similar for all enantiomers.

8.3.3 Structure of Quadrimers and Larger Oligomers

In the optimization of the SMA quadrimer structure, two methods were used: (i) energy scans, where all degrees of freedom were optimized, and (ii) a substitution method using two trimers. In the substitution method, two optimized trimers are combined after removing the head of one trimer and the tail of the other. In this way, the second monomer is constrained by the first and the third one and has the same constraint and interaction as a monomer in the middle of a polymer chain. The substitution and energy scans methods gave very similar results, but the substitution method is much faster and can easily be extended to longer oligomers.

EBSCOhost - printed on 2/14/2023 1:06 PM via . All use subject to https://www.ebsco.com/terms-of-use

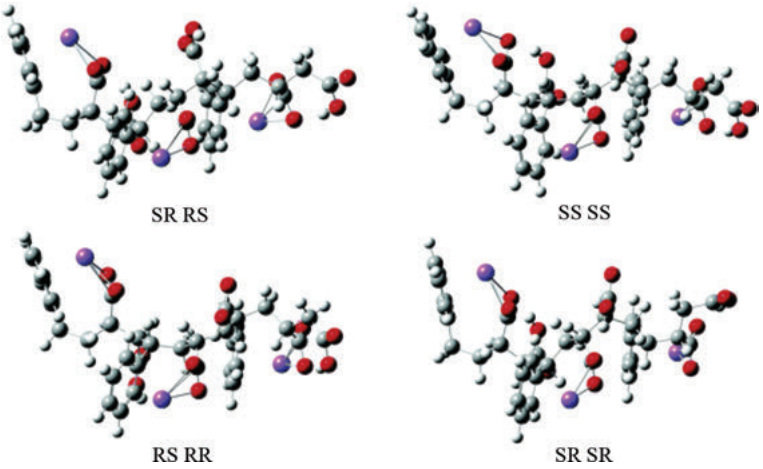

Figure 8.16: Four different trimer conformations of SMA at pH 7 among the 16 possible chiralities (after [5]).

Similar to dimers and trimers, it is found that the structure of larger oligomers is linear at pH 7, whereas they have step-like conformations at pH 3 and 12. For all oligomers, at pH 7 the phenyl groups have very similar orientations independent of chirality (favorable for π–π stacking between chains). An example of the optimized structure of a hexamer at pH 7 is shown in Figure 8.17.

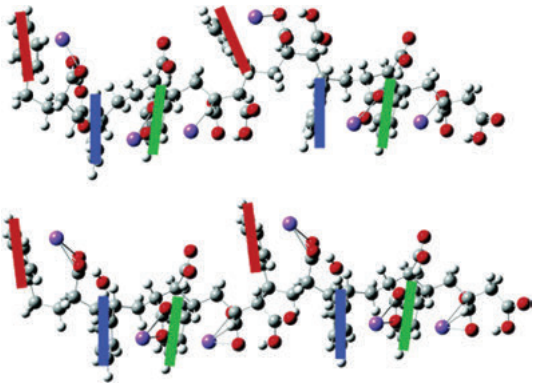

Figure 8.17: Conformation of the hexamer of chirality SR–SS–RS–RR–SS (a) compared to the conformation of the hexamer of regular chirality SS–SS–SS–SS–SS (b). The red rectangles show the orientation of the first and fourth phenyl groups of each oligomer, the blue rectangles show the orientation of the second and fifth phenyl groups, and the green rectangles show the orientation of the third and sixth phenyl groups (after [5]).

EBSCOhost - printed on 2/14/2023 1:06 PM via . All use subject to https://www.ebsco.com/terms-of-use

8.3.4 π–π Stacking Between SMA Chains into Sheets and Nanotubes at pH 7

We have seen that SMA molecules at pH 7 have linear conformations with phenyl groups sticking out in similar directions. This allows for π–π stacking between SMA chains. This π–π stacking protects the phenyl groups from unfavorable interactions with water molecules. An example of self-association between two hexamers is shown in Figure 8.18. This example clearly shows that SMA molecules can zip together, with the phenyl groups acting as the teeth of the zipper.

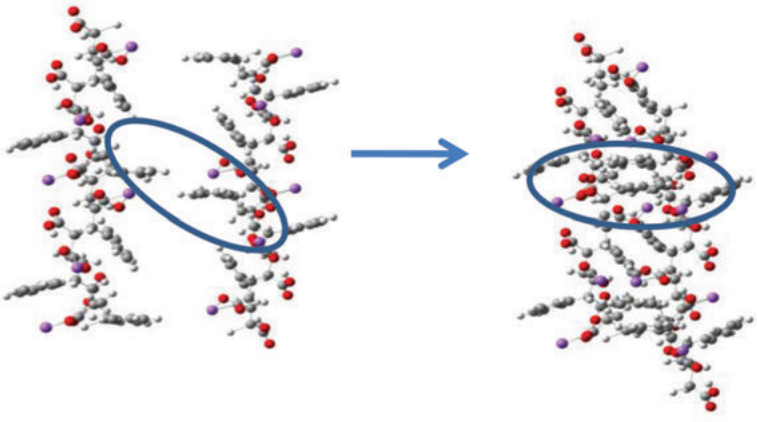

Figure 8.18: Self-association of two SMA hexamers at pH 7 due to π–π stacking. Ellipse on the left shows two phenyl groups prior to association and on the right after association. Optimized SMA structures are shown.

When viewing a linear SMA molecule end-on, we can see that the phenyl groups are located on one of three axes, which we can label α, β, and γ. A schematic representation of π–π stacking between two SMA oligomers can be seen in Figure 8.19, which shows cross-sectional views of two SMA oligomers. The association can either be flexible or rigid, leading to nanosheets or nanotubes.

The nature of the π–π stacking was studied in detail with PM3 and MP2 single-point energy calculations, which show that there is a minimum in the stabilization energy per π-stacking pair of 13 kJ/mol at a center-to-center distance between phenyl groups of about 5 Å. This stabilizing energy is comparable to other π-stacking energies reported in the literature [7]. Nanotubes with the lowest energy consist of eight chains zipped together in a cylinder. Nanotubes of four, five, and six chains can also be formed, but are less stable.

As can be seen from Figure 8.19, association between several SMA chains can lead to SMA sheets, in which all SMA molecules are zipped together in a parallel

EBSCOhost - printed on 2/14/2023 1:06 PM via . All use subject to https://www.ebsco.com/terms-of-use

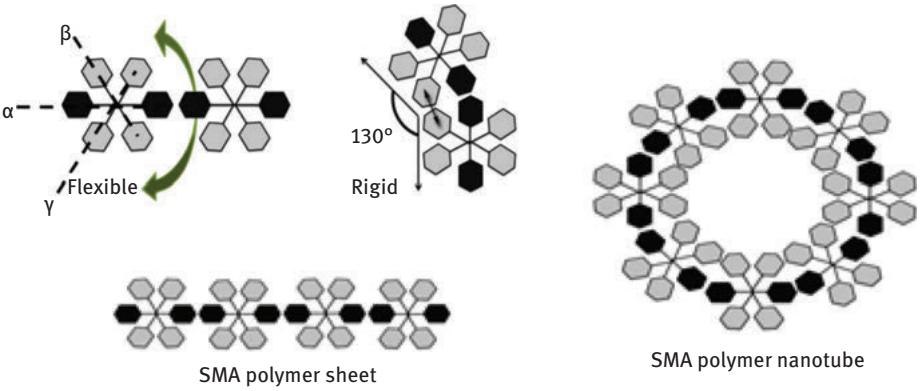

Figure 8.19: Depending on how much π–π stacking occurs between two SMA chains, the association can be flexible or rigid (top left). When more SMA molecules self-associate, this can lead to sheets (bottom left) or nanotubes (right) (adapted from [21]).

orientation, or in tubes, which can be considered as rolled up sheets. The self-association of SMA chains into a nanotube results in a tube with a twist, leaving free phenyl groups at both ends, allowing tubes to grow in length, This is shown in Figure 8.20. Nanotubes can grow to several microns, as shown, for example, in Figure 8.11. The length is much longer than the length of the oligomers from which the nanotubes are made. For instance, the long tubes in Figure 8.11 were made from SMA octamers, which have a length of about 5 nm.

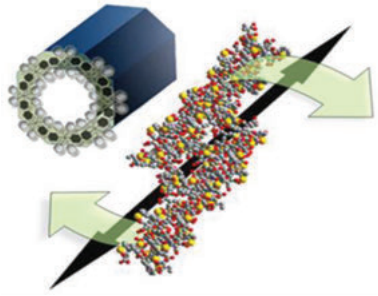

Figure 8.20: Self-association of SMA can lead to nanotubes that have a twist, which allows them to grow in length.

Calculating the structure of long oligomers becomes progressively more demanding. The largest oligomer for which calculations were performed is a dodecamer. The optimized structure of a nanotube consisting of eight chains of SMA dodecamers at pH 7 is shown in Figure 8.21. The nanotube has an inner diameter of 2.8 nm and an outer diameter of 4.1 nm. By inspecting the number of hydrophobic and hydrophilic groups

EBSCOhost - printed on 2/14/2023 1:06 PM via . All use subject to https://www.ebsco.com/terms-of-use

on the inner and outer surface, one can conclude that the inner surface is predominantly hydrophobic and the outer surface hydrophilic.

8.3.5 Tertiary Structure of SMA

Molecular modeling of SMA has shown that at pH 7 the primary structure of SMA oligomers consists of linear conformations, whereas the secondary structure consists of sheets or nanotubes. Inspection of Figure 8.21 shows that SMA nanotubes have many protruding phenyl groups available for further π–π stacking. This association between SMA nanotubes is shown schematically in Figure 8.22. The self-association between nanotubes can lead to the formation of stacks or bundles

Figure 8.21: Front view and side view of the configuration of a tubular self-association of SMA dodecamers at pH 7 (after [13]).

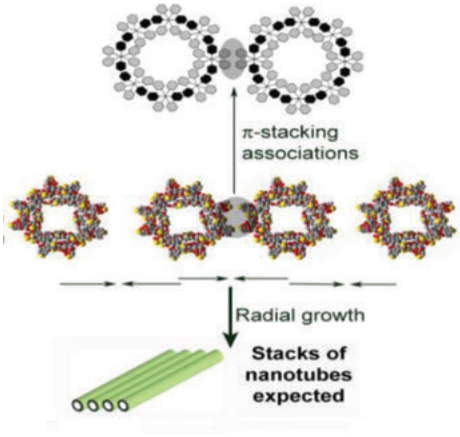

Figure 8.22: Self-association between SMA nanotubes can lead to the formation of SMA stacks or bundles, as observed experimentally.

EBSCOhost - printed on 2/14/2023 1:06 PM via . All use subject to https://www.ebsco.com/terms-of-use

of nanotubes, as seen, for example, in Figure 8.8 and schematically represented in Figure 8.22.

8.3.6 Structure of SMI Monomers, Dimers, and Oligomers

The structure of SMI monomers, dimers, and oligomers was calculated in the same way as the structure of SMA monomers, dimers, and oligomers described earlier. In SMI the maleimide ring is covalently closed (Figure 8.4) and the tertiary amine can be protonated at low pH, making SMI soluble in water. To simulate the effect of pH, both protonated (low pH) and nonprotonated SMI molecules (high pH) were studied. When protonated, the Cl^- ion was chosen as counter-ion for the protonated tertiary amine group of SMI. For the monomer, besides calculations in the gas phase, calculations with SMI surrounded by water molecules were performed as well. It was found that water did not appreciably change the geometry of SMI (cf. Figure 8.23). As in the case of SMA, a variety of chiral SMI structures were optimized for dimers and oligomers.

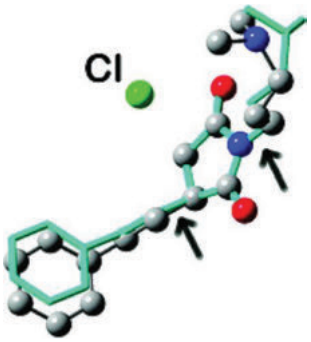

Figure 8.23: Optimized structure of SMI monomer with hydrogens not shown for clarity. The tube model is the optimized structure in the gas phase (calculated with PM3) and the ball and stick model is the optimized structure for a solvated SMI monomer (optimized with DFTLYP/6-31G**). The arrows show differences at the maleimide ring of 8° at the styrene side and 20° at the maleimide side (after [9]).

Like SMA, SMI has three chiral centers per repeat unit. For oligomers with chirality S for site 1 and SS for sites (2,3), referred to as [S, racemo(SS)] and with chiralities [R, racemo(RR)], can be described as racemo-diisotactic, where the oligomer is isotactic with respect to site 1 and racemo-isotactic with respect to sites (2,3). It was found that racemo-diisotactic oligomers have regularly symmetric monomer distributions. Making a single change in the chirality of one of the chiral sites destroys this regularity, producing conformations unable to π-stack. Although an exhausting search with all chiral possibilities was not performed, all chiral structures investigated, other than racemo-diisotactic, showed irregular structures. Because there are

EBSCOhost - printed on 2/14/2023 1:06 PM via . All use subject to https://www.ebsco.com/terms-of-use

very few racemo-diisotactic chiral structures in a population of SMI oligomers with random chirality, only very few molecules will π-stack.

Figure 8.24 shows an example of an SMI hexamer that does not have a recemo-diisotactic conformation. Although the hexamer is linear, the front view shows that there is no symmetry as phenyl groups overlap maleimide moieties. This hexamer is unable to self-associate with other mers in any regular manner.

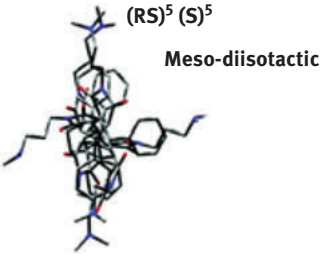

Figure 8.24: Front view of hexamer with a random chiral sequence, showing no symmetry (adapted from [9]).

Figure 8.25 shows a lateral view of a racemo-diisotactic SMI hexamer [S, racemo (SS)]. It can be seen that the phenyl groups point in favorable orientations for π–π staking.

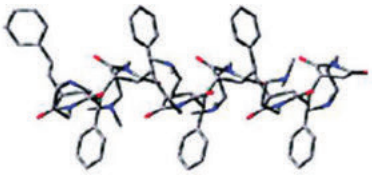

Figure 8.25: Lateral view of optimized structure of racemo-diisotactic SMI hexamer [S, racemo(SS)]. The phenyl groups are in favorable orientations for π–π staking (adapted from [9]).

8.3.7 Self-Association Between Racemo-Diisotactic SMI Oligomers

Racemo-diisotactic SMI oligomers can π-stack in two different ways: head-to-head and head-to-tail. These confirmations are shown in Figure 8.26. The energies per π-stacking pair and center-to- center distances between phenyl groups were calculated. The results show that the minimum energy for head-to-head conformations is –12.6 kJ/mol at a distance of 4.5 Å and that for head-to-tail conformations the minimum energy is –13.6 kJ/mol at a distance of 5.2 Å. The difference in energy is small enough that both conformations can be considered equally stable.

EBSCOhost - printed on 2/14/2023 1:06 PM via . All use subject to https://www.ebsco.com/terms-of-use

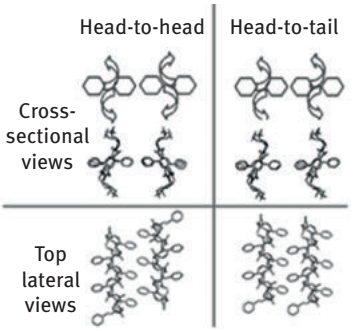

Figure 8.26: Association geometries between racemo-diisotactic SMI hexamers. Shown are the schematic representation of cross-sectional views and tube models viewed from the top lateral view (adapted from [9]).

From the optimized structures of racemo-diisotactic SMI oligomers, we can conclude that two or more of such oligomers can zip together to form sheets or nanotubes. The most stable structures are nanotubes consisting of eight SMI oligomers. An example of such a structure is shown in Figure 8.27 for oligomers in the head-to-head conformation. From the dimensions shown in the figure, it can be seen that the outer diameter of the nanotube is 4.8 nm, similar to that of SMA nanotubes.

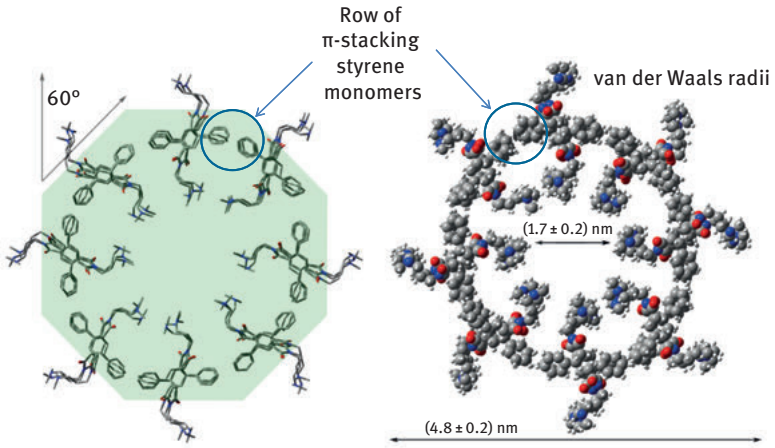

Figure 8.27: Nanotube made from eight racemo-diisotactic SMI oligomers in the head-to-tail conformation. On the right same nanotube, shown with van der Waals radii (adapted from [16]).

As in the case of SMA, SMI nanotubes have a twist, which allows them to grow to any length. In contrast with SMA, SMI does not form tertiary structures, because the presence of the side chains of SMI prevents further π–π stacking between phenyl groups.

EBSCOhost - printed on 2/14/2023 1:06 PM via . All use subject to https://www.ebsco.com/terms-of-use

The discovery of SMA and SMI nanotubes is an excellent example of the interplay between experiment and theory. SMA was used industrially for some 50 years, before it was realized that SMA can form nanotubes. When we started to characterize SMA, we found out quickly from DLS measurements that SMA associates, but only around pH 7. In reporting this finding [8], we postulated that two or more SMA oligomers could zip together, without any evidence, simply because it was the only way we could imagine self-association to occur. This postulate started the theoretical work on the molecular modeling of SMA, which gave rise to the notion that only at pH 7 SMA oligomers are linear with phenyl groups in orientations favorable for π-stacking. Subsequent calculations confirmed our hypothesis that SMA oligomers can indeed zip together and moreover showed that the most stable self-association is a nanotube made up of eight SMA oligomers, with an outer diameter of about 4 nm. This theoretical prediction was subsequently confirmed, first by cryo-TEM and subsequently with other methods, described earlier.

Because it was observed that SMA nanotubes form stacks or bundles of nanotubes (predicted theoretically as SMA nanotubes have protruding phenyl groups), we started to look for alternating copolymers with side chains that could prevent bundling by steric hindrance, and hence would produce only individual isolated nanotubes. This started our work on SMI. We found, as predicted by molecular modeling, that SMI can indeed form nanotubes and no evidence was found of tertiary structures.

The big surprise was the effect of chirality. Because SMA and SMI (an SMA derivative) have three chiral sites per repeat unit, which are randomly distributed along the chain, we expected the effects of chirality on the self-association of SMA and SMI to be similar. Instead we found a large effect of chirality for SMI and a minor effect of chirality for SMA, since the yield of SMA nanotubes is large and that of SMI nanotubes extremely small. It is interesting to note that these large differences in the effects of chirality are predicted by quantum mechanical modeling, which shows the tremendous predicting power of semiempirical molecular orbital calculations. The reason for the difference might be the way the maleic ring is closed: by a hydrogen bond in SMA and a covalent bond in SMA. The covalent bond results in a more rigid structure for SMI, in which the phenyl groups have less freedom to orient.

The prediction that only racemo-diisotactic conformations of SMI can π-stack led us to investigate alternating copolymers made from natural monomers, which all have the same handedness. Provided their phenyl groups are favorably oriented, the prediction is that such alternating copolymers will form nanotubes with a high yield. As an example we studied oligopeptides (a string of left-handed amino acids), which have a phenyl group and two carboxyl groups per repeat unit (resembling SMA) and natural polysaccharides with substituted phenyl groups (resembling SMI). These alternating copolymers will be discussed in the next section.

EBSCOhost - printed on 2/14/2023 1:06 PM via . All use subject to https://www.ebsco.com/terms-of-use

8.4 Nanotubes Made from Oligopeptides

8.4.1 Oligopeptide Conformations

An amino acid with a phenyl group is L-phenylalanine, referred to as F, and an example of an amino acid with two carboxyl groups is L-glutamic acid, referred to as E. The structure of these amino acids is shown in Figure 8.28. All amino acids have the same terminating group, shown in red. When combining two amino acids, a peptide bond is formed between the primary amine of one amino acid and the carboxyl group of the other. Thus in combining F with E, one carboxyl group of E has reacted and hence $(FE)_n$ has only one carboxyl group per repeat unit. The simplest oligopeptide with one phenyl group and two carboxyl groups per repeat unit is $(FEE)_n$. The structure of this repeat unit is shown in Figure 8.29. Similar to SMA, an internal hydrogen bond can be formed between the two carboxylic acids.

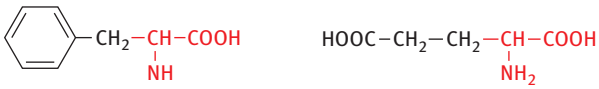

Figure 8.28: Chemical structure of phenylalanine (F) and glutamic acid (E).

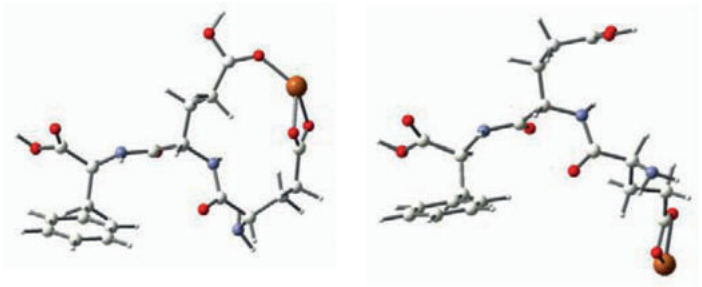

Figure 8.29: Two FEE conformations with (left) and without (right) an internal hydrogen bond. The structures are optimized with the tree branch method (after [22]).

Before optimizing the structure of FEE, the structures of phenylalanine and glutamic acid were optimized with PM3, DFT, and ab initio RHF [22]. Differences in structure obtained with these methods were small. Surrounding F, E, and FE with water molecules did not affect their structure in any appreciable way. After F, E, and FE, FEE was optimized. Two optimized structures of FEE are shown in Figure 8.29, with the structure with the internal hydrogen bond being the most stable. The conformations of dimers, trimers, and oligomers of FEE were calculated in the same way as oligomers of SMA and SMI described earlier. Two examples of a trimer, one with a

EBSCOhost - printed on 2/14/2023 1:06 PM via . All use subject to https://www.ebsco.com/terms-of-use

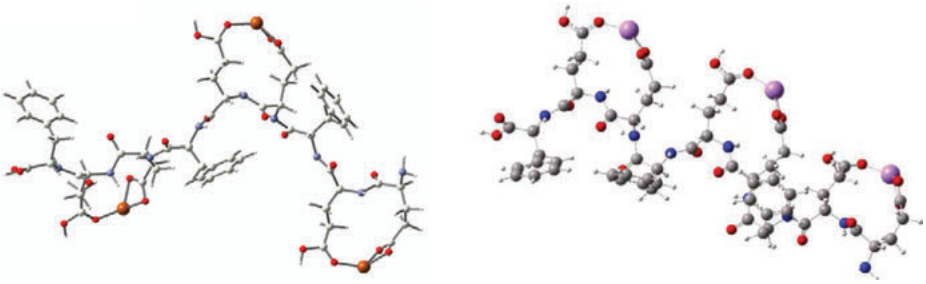

Figure 8.30: Two trimer conformations $(FEE)_3$, with different orientations of phenyl groups (after [22]).

propeller-like conformation and one with all phenyl groups on the same side, are shown in Figure 8.30.

The two conformations in Figure 8.30 were found to have almost identical energies. When solvating these structures, their conformations are hardly affected, but now the trimer with all three phenyl groups on one side has a slightly lower energy.

The optimized conformation of the octamer $(FEE)_8$, build with the substitution method, is shown in Figure 8.31.

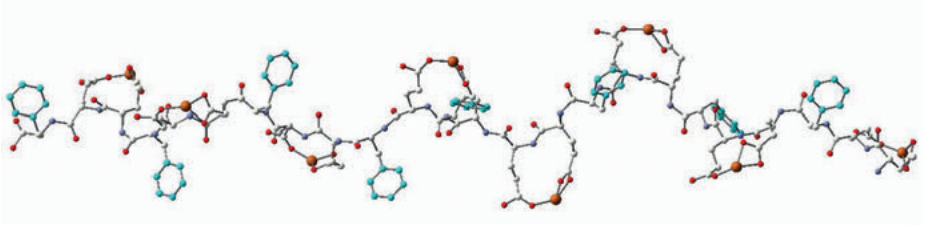

Figure 8.31: Conformation of $(FEE)_8$ with propeller-like orientations of phenyl groups (after [22]).

8.4.2 π–π Stacking Between $(FEE)_n$ Oligomers

An example of two solvated $(FEE)_3$ conformations with all three phenyl groups on the same side is shown in Figure 8.32. It can be seen that the orientation of the phenyl groups is favorable for π- stacking. Such association cannot, however, lead to the formation of nanotubes, since no more phenyl groups are available for further π-stacking.

In contrast, trimers with a propeller-like conformation can self-associate into structures with more than two $(FEE)_3$ molecules. Hence, the formation of $(FEE)_n$

EBSCOhost - printed on 2/14/2023 1:06 PM via . All use subject to https://www.ebsco.com/terms-of-use

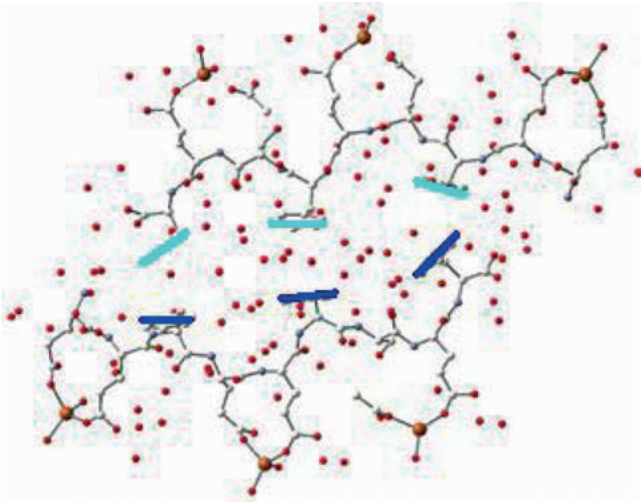

Figure 8.32: Two solvated $(FEE)_3$ trimers, ready for π–π stacking (after [22]). Hydrogen atoms are omitted for clarity.

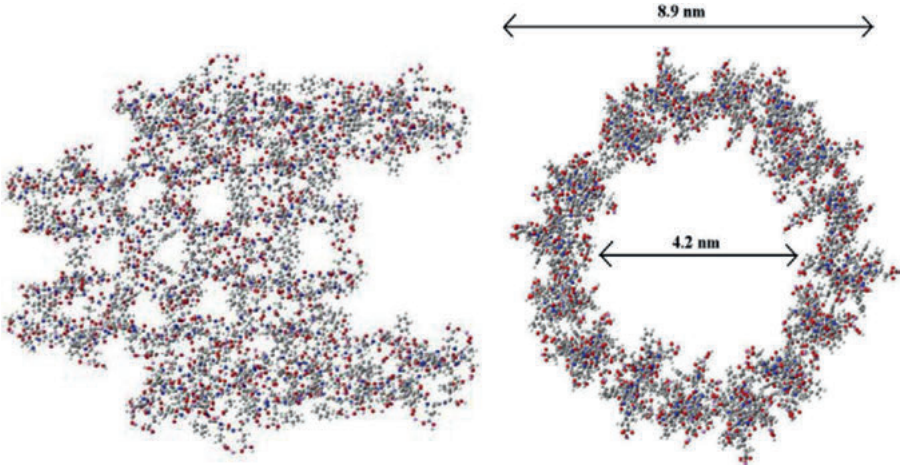

Figure 8.33: Nanotube made from 16 $(FEE)_6$ hexamers. Left: side view; right: front view (after [22]).

nanotubes is only possible for $(FEE)_3$ and larger oligomers in the propeller-like conformation. That propeller-like conformations can form indeed nanotubes is shown in Figure 8.33, which shows the self-association of 8 $(FEE)_6$ hexamers into a nanotube with an outer diameter of about 9 nm. Like SMA and SMI nanotubes, $(FEE)_n$ nanotubes can grow to any length.

EBSCOhost - printed on 2/14/2023 1:06 PM via . All use subject to https://www.ebsco.com/terms-of-use

8.4.3 Experimental Evidence for $(FEE)_6$ Nanotubes

At first we tried to order $(FEE)_6$ oligopeptides from two companies in the business of selling polypeptides, but both were unable to provide us with such oligomers. We subsequently collaborated with Prof. Yingfu Li (McMaster University, Hamilton, ON), who agreed to make the DNA that codes for $(FEE)_6$ oligopeptides. After injecting this DNA in *E. coli* bacteria, the bacteria did not produce any measurable quantities of $(FEE)_6$ oligopeptides. It could be that $(FEE)_6$ oligopeptides form nanotubes inside the bacteria, which are destroyed by the bacteria as soon as they are formed. Eventually we found a supplier able to supply us with $(FEE)_6$. As predicted they form nanotubes, as seen in Figure 8.34. It can be seen that they form linear structures several hundreds of nanometers long.

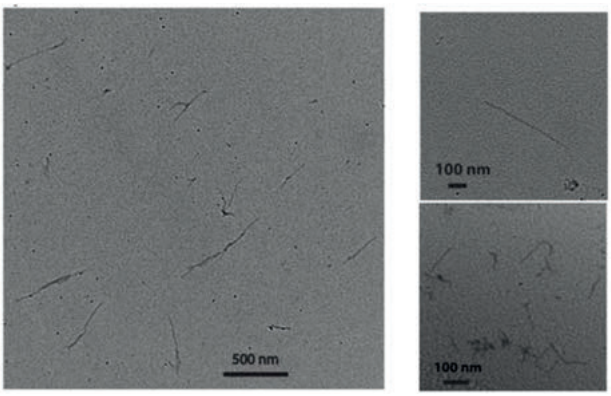

Figure 8.34: TEM images of $(FEE)_6$ nanotubes at various magnifications (after [23]).

The nanotube formation of $(FEE)_6$ shows the predictive power of semiempirical quantum mechanical calculations. The theory predicted nanotubes, which were subsequently observed experimentally.

8.4.4 Advanced Materials Templated from Nanotubes

Alternating copolymer nanotubes are not only interesting advanced materials in their own right, but can also be used as templates for additional advanced materials. One of the potential applications of SMA-based nanotubes is drug delivery. SMA nanotubes are only stable at pH 7 and fall apart at other pHs. Thus, it is possible to load a nanotube with a drug, which is released when the nanotube breaks up when entering an acidic environment, such as a stomach or acidic tumor environment. A pH-responsive,

EBSCOhost - printed on 2/14/2023 1:06 PM via . All use subject to https://www.ebsco.com/terms-of-use

active targeting delivery system was designed using folic acid functionalized amphiphilic alternating copolymer poly(styrene-*alt*-maleic anhydride) (FA-DABA-SMA) via a biodegradable linker 2,4-diaminobutyric acid (DABA) [24].

Nanotubes can also be used to study chemical reactions in confined spaces. In principle this can be done with all types of nanotubes, including single-wall carbon nanotubes. The advantage of alternating copolymer nanotubes is that the interior surface of the nanotubes can be controlled by chemical modification of the alternating copolymers. We already mentioned the polymerization of pyrrole inside SMA. Another example is the formation of a monolayer of gold nanoparticles, formed within the confined space of lamellae of SMA nanosheets. Such novel gold monolayers are expected to be highly catalytically active. Alternating copolymer nanotubes can act as nanoreactors for a number of reactions [25].

Fabrication of 1D metallic nanostructures is an important activity within nanoscience. Among the variety of nanomaterials available, silver nanostructures are especially important in the development of nanotechnology devices: silver is a low-cost and highly conductive metal. Alternating copolymer nanotubes are ideal templates for making silver nanowires. In our first attempt to make silver nanowires, we reduced Ag^+ ions in the presence of SMA nanotubes with the reducing agent $NaBH_3CN$ [26]. However, we produced AgCN nanorods instead of silver nanorods, as confirmed by energy-dispersive X-ray spectroscopy and IR spectroscopy. Examples of AgCN nanowires are shown in Figures 8.35–8.37.

Figure 8.35: TEM of AgCN nanorods made from SMA templates (adapted from [26]).

The AgCN nanorods can be further reduced by a stronger reducing agent into silver nanorods. SEMs of AgCN nanorods before and after reduction by $NaBH_4$ are shown in Figure 8.37. Enlargements of one silver nanowire are shown in Figure 8.38. These silver nanorods were shown to conduct electricity [26]. This opens the door to using these nanostructures in a number of applications in nanoelectronics.

EBSCOhost - printed on 2/14/2023 1:06 PM via . All use subject to https://www.ebsco.com/terms-of-use

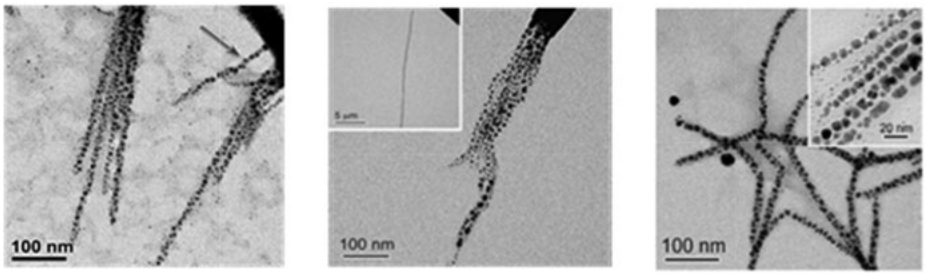

Figure 8.36: AgCN nanorods, made of bundles of smaller nanotubes, as seen by their ends (left and middle). The inset in the middle figure shows that these nanorods can grow to very long lengths. TEM at the right shows a sonicated sample, which shows thinner bundles. The inset shows that these bundles are made of nanorods about 5 nm in diameter, similar to the size of the SMA nanotubes used as templates [26].

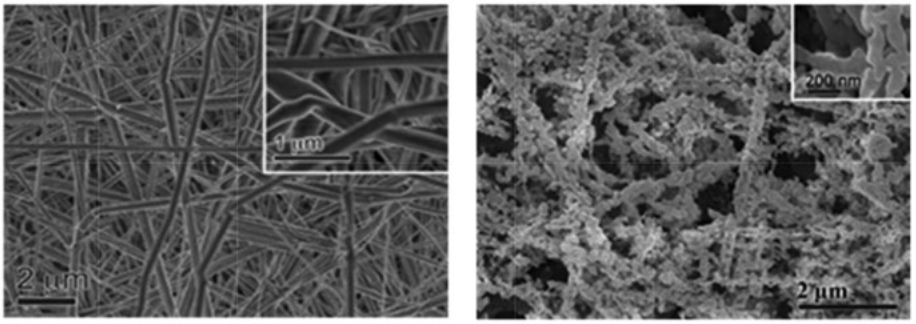

Figure 8.37: SEMs of AgCN nanorods (left) and reduction of these rods to Ag nanorods by NaBH4 (right) 2 µm (after [26]). Inset shows magnified views 1 µm, and 200 nm.

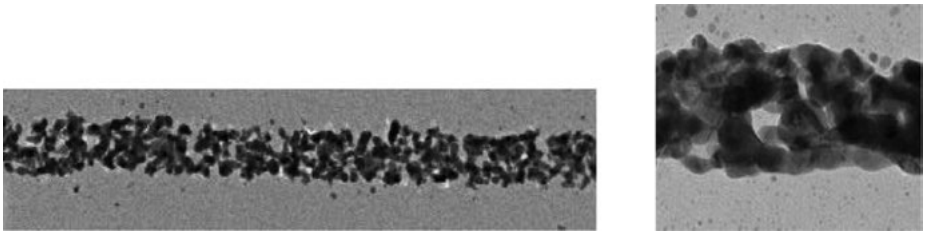

Figure 8.38: Part of silver nanowire with a diameter of 75 nm, shown at two different magnifications, made from SMA template (adapted from [26]).

EBSCOhost - printed on 2/14/2023 1:06 PM via . All use subject to https://www.ebsco.com/terms-of-use

8.5 Conclusions

Alternating copolymers containing regularly spaced phenyl groups have fascinating properties. In this chapter we have discussed three examples, SMA, SMI, and an alternating oligopeptide $(FEE)_6$. All of these oligomers form spontaneously nanotubes by π–π stacking, provided the structures are linear, which for SMA and $(FEE)_6$ is achieved by adjusting the pH, so that a hydrogen bond is formed between two neighboring carboxyl groups. (SMI is linear at all pHs.) SMA and SMI have optically active centers that are randomly distributed along the chain. For SMA most chiralities lead to nanotube formation, whereas for SMI only isotactic molecules self-assemble. This strong effect of chirality is predicted by quantum mechanical calculations. Quantum mechanical calculations predict nanotube formation for all three oligomers and predict that the nanotubes can grow to any length. The calculations also predict that SMA forms tertiary structures by bundling, and the absence of bundling for SMI.

Alternating copolymer nanotubes are not only interesting advanced materials in their own right, but can be also used for a number of applications, such as drug delivery, nanoreactors and templates for conducting nanorods and other advanced nanomaterials.

Acknowledgements: We acknowledge all the graduate students who have worked on self-assembled nanotubes: Renata Vyhnalkova, Cécile Malardier-Jugroot, Thomas Lazzara, Gilles Bourret, and Kevin Conley. The support from CSACS (FRQNT Quebec Centre for Advanced Materials) and NSERC is gratefully acknowledged.

References

[1] Zhang, L. and A. Eisenberg, Multiple Morphologies of "Crew-Cut" Aggregates of Polystyrene-b-poly(acrylic acid) Block Copolymers, Science 268 (5218), 1728–1731 (1995).

[2] Rizis, G., T.G.M. van de Ven and A. Eisenberg, "Raft" formation by two-dimensional self-assembly of block copolymer rod micelles in aqueous solution, Angewandte Chemie, International Edition, 126, 9146–9149 (2014).

[3] Chen, J., C. Yu, Z. Shi, S. Yu, Z. Lu, W. Jiang, M. Zhan, W. H, Y. Zhou and D. Yan, Ultrathin alternating copolymer nanotubes with readily tunable surface functionalities, Angew Chem Int Ed Engl. 54 (12), 3621–3625 (2015).

[4] van de Ven, T.G.M., T.D. Lazzara and M.A. Whitehead, from sizing agents to advanced nanomaterials, Proc. Fund. Appl. Pulp Paper Mod. Symp. August 27–29, 2008, CIPP, UQTR, Trois-Rivières QC Canada, pp. 63–76, UQTR Publishing, Jan 2009.

[5] Malardier-Jugroot, C., T.G.M. van de Ven and M.A. Whitehead, Linear conformation of poly (styrene-*alt*. maleic anhydride) capable of self-assembly: a result of chain stiffening by internal hydrogen bonds, J. Phys. Chem. B. 109, 7022–7032 (2005).

[6] Malardier-Jugroot, C., T.G.M. van de Ven, T. Cosgrove, R.M. Richardson and M.A. Whitehead, Novel self-assembly of amphiphilic copolymers into nanotubes: characterization by small-angle neutron scattering, Langmuir, 21, 10179–10187 (2005).

EBSCOhost - printed on 2/14/2023 1:06 PM via . All use subject to https://www.ebsco.com/terms-of-use

[7] Lazzara, T.D., M.A. Whitehead and T.G.M. van de Ven, Linear nano-templates of styrene and maleic anhydride alternating copolymers, European Polymer Journal, 45, 1883–1890 (2009).
[8] Garnier, G., M. Duskova-Smrckova, R. Vyhnalkova, T.G.M. van de Ven, J-F. Revol, Association in solution and adsorption at an air-water interface of alternating copolymers of maleic anhydride and styrene. Langmuir 16(8),3735–3763 (2000).
[9] Lazzara, T.D., M.A. Whitehead and T.G.M. van de Ven, Effect of chirality on π-stacking in styrene and maleimide alternating copolymers, J. Phys. Chem. B. 112, 4892–4899 (2008).
[10] Malardier-Jugroot, C., T.G.M. van de Ven and M.A. Whitehead, Characterization of a novel self-association of an alternating copolymer into nanotubes in solution. Molecular Simulation, 31(2–3), 173–178 (2005).
[11] Malardier-Jugroot, C., M.A. Whitehead and T.G.M. van de Ven, Polymeric nanotubes and nanorods made from poly(styrene alt. maleic anhydride) and poly(pyrrole), The Proceedings of the First Applied Pulp & Paper Molecular Modelling Symposium (August 24–26, 2005, McCord Museum, McGill University, Montreal, Canada). p. 279, Editors: R. Gaudreault, M.A. Whitehead and T.G.M. van de Ven, Design and Desktop Publishing, Montreal, 2006.
[12] Whitehead, M.A., C. Malardier-Jugroot, T.G.M. van de Ven and T.D. Lazzara, 2007 "Fabrication of intrinsically conducting polymer nanorods for making electrical nanocircuits involves filling nanotubes with monomer to obtain well-defined, packed, defect-free nanorods" Patent Number: WO2005118688-A1; US2008265219-A1.
[13] Malardier-Jugroot, C., T.G.M. van de Ven and M.A. Whitehead, Characterisation of a novel self-assembly of an alternating copolymer into nanotubes in solution, NSTI-Nanotech, 3, 276–279 (2004).
[14] Li, X. and Malardier-Jugroot, C., Confinement effect in the synthesis of polypyrrole within polymeric templates in aqueous environments, Macromolecules, 46(6),2258–2266 (2013).
[15] Malardier-Jugroot, C., T.G.M. van de Ven and M.A. Whitehead, Theoretical characterisation of the self-association of poly(styrene maleic anhydride) chains in water at the nanoscale level, The Proceedings of the First Applied Pulp & Paper Molecular Modelling Symposium (August 24–26, 2005, McCord Museum, McGill University, Montreal, Canada). pp. 257–270, Editors: R. Gaudreault, M.A. Whitehead and T.G.M. van de Ven, Design and Desktop Publishing, Montreal, 2006.
[16] Lazzara, T.D., T.G.M. van de Ven and M.A. Whitehead, Nanotube self-assembly of a styrene and maleimide alternating copolymer, Macromolecules, 41, 6747–6751 (2008).
[17] Brothers, E. and K. Merz, Sodium parameters for AM1 and PM3 optimized using a modified genetic algorithm. J. Phys. Chem. B, 106, 2779 (2002).
[18] Frisch, M.J. *et al*. Gaussian 98W (Revision A.5); Gaussian, Inc. Pittsburgh, 1998.
[19] HyperChem release 5.11, for Windows molecular modelling system, Hypercube Inc., Ont., Canada, 1999.
[20] Malardier-Jugroot, C., T.G.M. van de Ven and M.A. Whitehead, Study of the water conformation around hydrophilic and hydrophobic parts of styrene-maleic anhydride. J. Mol Structure (THEOCHEM) 679, 171–177 (2004).
[21] Lazzara, T.D., "Self-assembled styrene-based alternating copolymer nanotubes: Modelling and experiment", M.Sc. Thesis, 2007, Dept. Chemistry, McGill University, Montreal, Canada.
[22] Conley, K., C.H. Ryu, T.G.M. van de Ven and M.A. Whitehead, Molecular modelling of proteins into nanotubes: a theoretical approach, Proc. Fund. Appl. Pulp Paper Modelling Symposium, Aug. 25, 2011, Concordia Univ. Montreal, Canada, pp. 117–136, Design and desktop publishing, Trois-Rivières, 2012.
[23] Conley K., T.G.M. van de Ven and M.A. Whitehead, Molecular Simulations (in press).

EBSCOhost - printed on 2/14/2023 1:06 PM via . All use subject to https://www.ebsco.com/terms-of-use

[24] Li, X., M.R. Szewczuk and C. Malardier-Jugroot, Folic acid-conjugated amphiphilic alternating copolymer as a new active tumor targeting drug delivery platform, Drug Design, Development and Therapy 10, 4101–4110 (2016).
[25] Malardier-Jugroot, C., From Surface Sizing Agents to Nanotechnology, J-FOR, 5 (4), 24–29 (2016).
[26] Lazzara, T.D., G. Bourret, B. Lennox and T.G.M. van de Ven, Polymer templated synthesis of AgCN and Ag nanowires, Chem. Mater. 21, 2020–2026 (2009).

EBSCOhost - printed on 2/14/2023 1:06 PM via . All use subject to https://www.ebsco.com/terms-of-use

Olivier Lebel, Armand Soldera

9 Molecular Glasses: Emerging Materials for the Next Generation

Despite their ubiquity, glasses remain a misunderstood class of materials, in part, because of the random arrangement of their constituent atoms or molecules. In particular, because small organic molecules tend to naturally crystallize, instances of glass formation are even more esoteric, despite sucrose glass eliciting the delight of confectionery aficionados for over a century. In recent years, glass-forming small molecules, also known as molecular glasses, have received increasing attention beyond the candy store into the pharmaceutical and organic electronics fields. Structural elements responsible for preventing the crystallization of organic compounds were outlined, and it has become easier to predictably synthesize compounds that spontaneously form glasses and do not crystallize. Simulation tools have also evolved to allow simulation of the glass transition of arrays of small molecules. The following chapter provides an overview of the progress made with molecular glasses in the last 25 years, from their synthesis, their characterization, the computational simulation of their properties, and to their target applications.

Keywords: molecular glasses, glassy phase, glass transition, amorphous materials, molecular materials

9.1 Introduction

Solids are usually classified according to the symmetrical arrangement of their constituents: atoms or molecules. The symmetry of crystalline systems is organized according to 230 space groups.[1] Conversely, amorphous solids are commonly characterized by their absence of symmetry. This is true only if a picture of the material is taken (Figure 9.1) at one moment, and later this arrangement is completely modified. It means that an amorphous material is actually highly symmetrical in average, even though it may not appear as such at the supramolecular level. The radial distribution function depicts variations of the atomic density with respect to a distance from a reference atom, and can be extracted from X-ray scattering function. It actually reveals the intimate isotropy of such systems (Figure 9.1). Glasses are described by such an arrangement, and exhibit high rigidity (high Young's modulus).

Olivier Lebel, Department of Chemistry and Chemical Engineering, Royal Military College of Canada, Kingston, ON, Canada
Armand Soldera, Département de Chimie, Université de Sherbrooke, Sherbrooke, QC, Canada

https://doi.org/10.1515/9783110537734-009

EBSCOhost - printed on 2/14/2023 1:06 PM via . All use subject to https://www.ebsco.com/terms-of-use

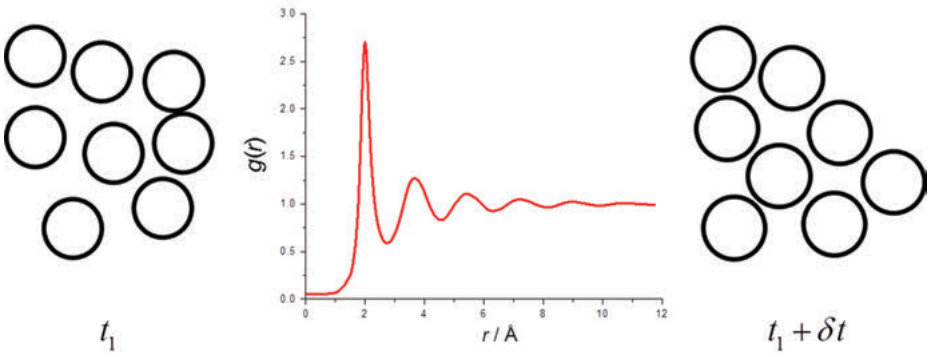

Figure 9.1: Schematic representation of an amorphous materials at two different times, and their common radial distributions function.

Surprisingly, when a glass is heated, it undergoes a transition to another amorphous state, the rubbery (or viscous) state. This transition occurs at one temperature, the so-called glass transition temperature, T_g [2]–[3]. Despite that this transition temperature is known from pharaonic times, it still intrigues a great number of scientists, and is not yet fully understood [4]–[6]. Reaching the glassy state from the rubbery state can be done by quenching from the melt. In fact, for most organic compounds, it is necessary to use such very fast cooling rates to prevent crystallization [4]–[6]. However, because of their molecular structure, inorganic materials (e.g., SiO_2) and polymers lead to this particular state also at very low cooling rates. Unexpectedly, some small organic molecules also possess the ability to reach this glassy state at low cooling rates. Nevertheless, because of their high diffusion rate, they tend to converge quickly toward the more stable crystalline state. Even if the glassy state is attained upon slow cooling, in most cases, crystallization will occur on standing at ambient temperature, typically within a few hours.

The purpose of this chapter is to discuss small molecules that display a higher propensity to form glassy phases, and to remain in the glassy state for extended periods of time. These compounds are called molecular glasses, or amorphous molecular materials [7]–[11]. This class of materials has proved invaluable toward understanding the glassy state and glass formation, as they constitute appealing model systems to study the relationships between their molecular structures and their glass-forming properties, their supramolecular organization in the glassy state, and their bulk physical and mechanical properties.

Unfortunately, our knowledge on glass formation by small molecules remains largely incomplete, partially because of the metastable aspect of the glassy phase, but also because most instances of glass formation are not adequately reported in the literature. For example, a vast number of experimental synthetic procedures mention that the desired product was obtained “as an oil that crystallized on standing.” It is likely that a significant portion of these “oils” was in fact the amorphous compounds above their glass transition temperatures. Nonetheless, considering all glass-forming compounds ever synthesized, isolated, and characterized as such, a few structural elements

EBSCOhost - printed on 2/14/2023 1:06 PM via . All use subject to https://www.ebsco.com/terms-of-use

have emerged as decelerating crystallization kinetics, instead favoring glass formation. Before discussing specifically about their molecular structure, the ways to describe such molecular glasses are first introduced.

The glass-forming properties of molecular glasses can be distinguished according to four main parameters: (1) glass transition temperature (T_g), (2) critical cooling rate (R_c), (3) glass-forming ability (GFA), and (4) kinetic glass stability (GS) [12]–[13]. T_g is defined as the temperature at which a glassy material undergoes transition from the glassy state to the rubber (or viscous) state, and will be discussed more in detail later in the text. R_c is the slowest rate at which a given compound will form a glassy phase, as opposed to crystallization, when cooled from the melt. GFA is typically a qualitative classification of molecular glasses according to their relative R_c and is used for a quick comparison of different glass-forming compounds. GS is also a qualitative comparison of crystallization kinetics, typically at either ambient temperature or at a temperature relative to T_g, when comparing molecular glasses.

9.2 Structural Elements Favoring Glass Formation

As crystals are characterized by long-range positional and directional orders where molecules are packed efficiently, when engineering organic compounds designed to avoid crystallization, it is crucial to introduce structural elements that will hinder this process. Molecular glasses are thus often compounds with irregular shapes that lead to an irregular packing and thus cannot maintain a long-range order.

9.2.1 Non-planarity

Molecular shape is the first structural element, which may account for glass formation, such as simple twisted aromatic compounds such as *o*-terphenyl (**1**) [14] or 1,3,5-trinaphthylbenzene (**2**) [15]. In these two compounds, the aromatic rings are modified in a fashion that makes them deviate from planarity, perturbing the usual π-stacking. Although both *o*-terphenyl and trinaphthylbenzene only form glasses upon fast cooling, research efforts to synthesize polyaromatic compounds with more globular and irregular shapes have eventually yielded analogous compounds capable of spontaneously forming glasses.

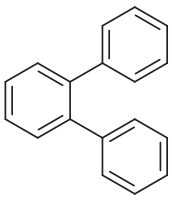

1

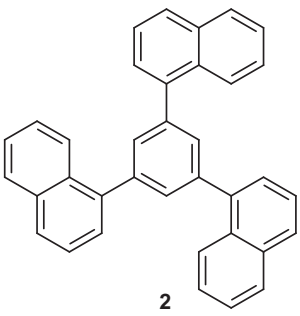

2

EBSCOhost - printed on 2/14/2023 1:06 PM via . All use subject to https://www.ebsco.com/terms-of-use

Two of the first families of aromatic compounds thus studied are triarylamines and 1,3,5-triphenylbenzenes. Although both parent compounds (**3** and **4**, respectively) are propeller-shaped, they do not deviate enough from planarity and readily crystallize. Further substituting these cores with diphenylamino groups, however, increases both the steric hindrance and irregularity of the structures, thereby increasing the propensity of derivatives **5**–**6** to form glasses [16]–[17]. This family of molecular glasses has been named "π-starburst" compounds.

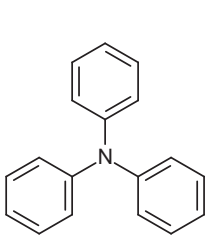

3

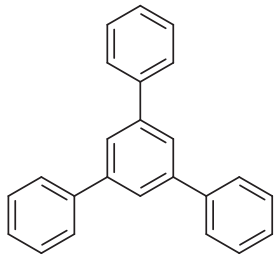

4

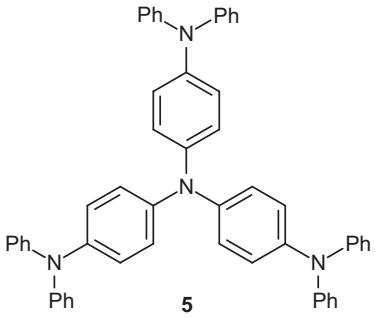

5

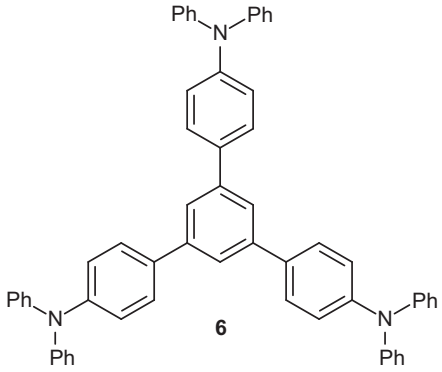

6

Other tridimensional moieties have been successfully used as scaffolds to synthesize glass-forming derivatives, including adamantane (**7**) [18], tetraphenylmethane (**8**) [19], spirobifluorene (**9**) [20], as well as calix[4]arene (**10**) [21]–[23]. In every case, the molecular structures are not flat, but rather either tetrahedral, propeller, or cone-shaped.

7

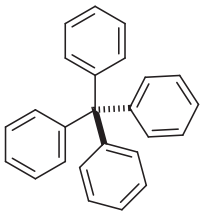

8

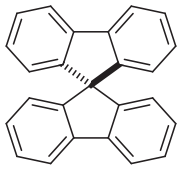

9

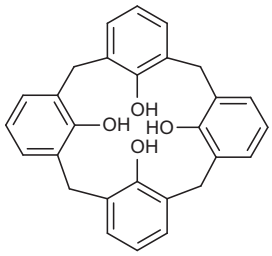

10

EBSCOhost - printed on 2/14/2023 1:06 PM via . All use subject to https://www.ebsco.com/terms-of-use

9.2.2 Symmetry

Lowering the symmetry elements in a molecular structure will decrease its crystallization kinetics, because there are less available redundant ways for the molecules to pack in an ordered fashion. A common way to achieve this in a symmetrically substituted compound is to introduce slightly different substituents at different positions. For example, if diarylaminogroups are introduced, using two different aryl groups on the substituent, such as phenyl and tolyl (**11**) [16], or phenyl and naphthyl groups (**12**–**13**) [24]–[25], will lower molecular symmetry, and therefore decrease the propensity of the compound to crystallize.

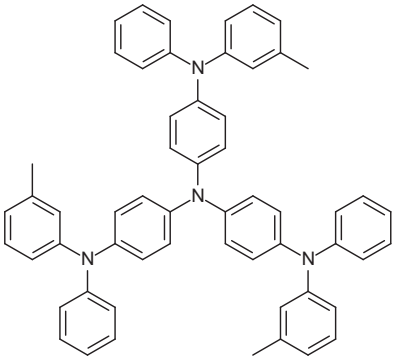

11

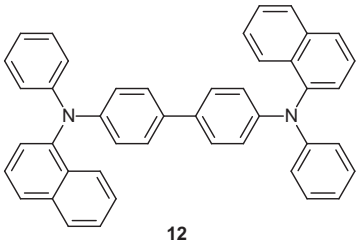

12

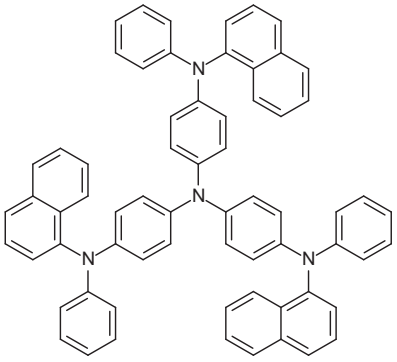

13

As most pharmaceutically relevant compounds possess irregular structures with low degrees of symmetry, glass formation is present in several drugs, and is relevant for amorphous drug formulations, to increase the bioavailability of drugs that are poorly soluble in water, for example [26]–[32]. The compounds known to form the most stable glasses, including felodipine (**14**), nifedipine (**15**), griseofulvin (**16**), indomethacin (**17**), miconazole (**18**), and ketoconazole (**19**) [33], all possess nonplanar molecular structures where there is at most one symmetry axis.

EBSCOhost - printed on 2/14/2023 1:06 PM via . All use subject to https://www.ebsco.com/terms-of-use

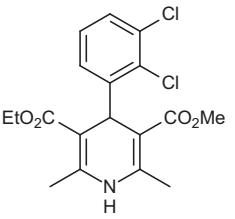

14

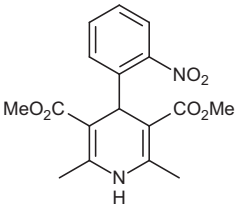

15

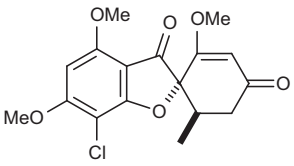

16

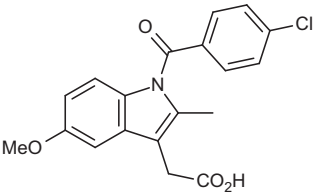

17

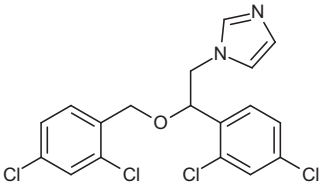

18

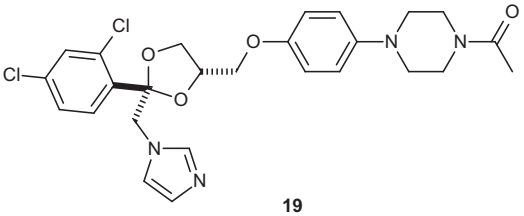

19

9.2.3 Conformational Equilibria

As all symmetry-equivalent molecules in a crystal must adopt the same conformation, this process can be readily hindered by the presence of several conformations that are close in energy. This way, nearly equivalent populations of various conformers exist in the liquid state (or in solution), thereby making it difficult for all molecules to order themselves. When the interconversion of those conformers is hindered by a high-energy barrier (e.g., conjugation and steric hindrance), the crystallization process is slowed even further [34]. Calixarenes can adopt various conformations, which can explain the propensity of some of their derivatives to form glasses [35]. For example, calix[4]arene **10** can adopt the cone as well as various alternate conformations, with a hindered rotation as the result of steric hindrance or hydrogen bonding. Glass-forming aminotriazines, such as example **20** were also found to show high rotational barriers for their substituents as a result of strong conjugation between the amino groups and the triazine ring, giving rise to various conformers that are similar in energy, and therefore exist in closely similar populations [36].

EBSCOhost - printed on 2/14/2023 1:06 PM via . All use subject to https://www.ebsco.com/terms-of-use

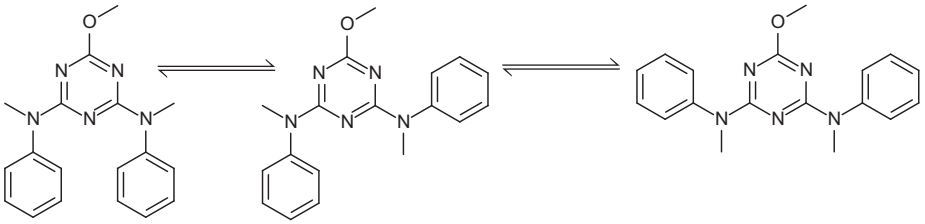

20

9.2.4 Intermolecular Interactions

Although intermolecular noncovalent interactions are often strategically used in crystal engineering to attempt to influence crystal packing, they are not necessarily incompatible with hindering crystallization as well. However, not every type of noncovalent interactions equally contribute to frustrate crystallization. Noncovalent interactions must not otherwise constrain the degrees of freedom of the molecules.

Hydrogen bonds, in particular, are one type of intermolecular interactions often encountered in molecular glasses. Despite what common knowledge would suggest, hydrogen bonds are ideal interactions for promoting glass formation for several reasons: (1) they are relatively strong interactions and contribute to limit molecular diffusion in the solid, (2) they use a small portion of the molecules, thereby preserving the degrees of freedom of the rest of the molecule, (3) they can adopt a wide range of angles, and (4) the presence of multiple groups that can participate in hydrogen bonding can offer several competing motifs that are close in energy. There are several examples in the literature of compounds that can readily form stable glasses and that can form multiple hydrogen bonds. Sugars, especially di- or trisaccharides, such as sucrose (**21**), lactose (**22**), or trehalose (**23**) are the most common examples [34], but several polyalcohols or polycarboxylic acids, such as citric acid (**24**), can also form glasses with varying degrees of stability [37].

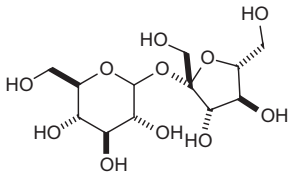

21

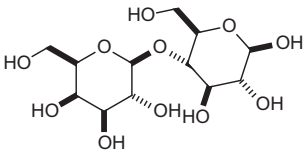

22

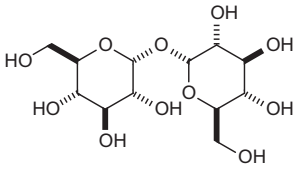

23

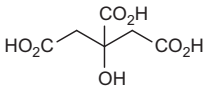

24

EBSCOhost - printed on 2/14/2023 1:06 PM via . All use subject to https://www.ebsco.com/terms-of-use

Amides can also readily form glasses, depending on their geometry and substituents, for example, isophthalyl and trimesyl amides with acetamidophenyl substituents **25**–**26.**[38] Various aminotriazine derivatives, in particular with mexylamino groups (such as representative series **27a**–**i**), readily form stable glasses, and hydrogen bonding has been shown to be present, even at temperatures above T_g [39]–[42].

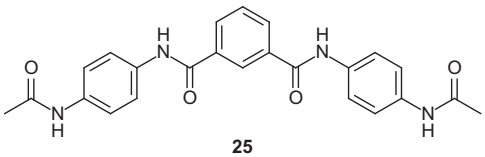

25

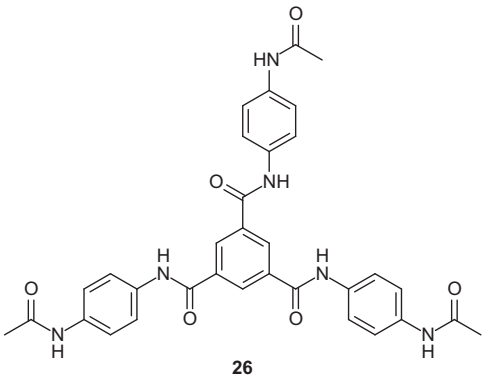

26

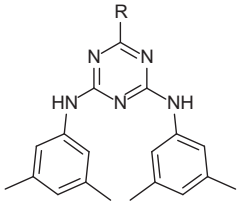

27

27a: R = Et
27b: R = CH_2Cl
27c: R = SMe
27d: R = OMe
27e: R = CH_2OH
27f: R = NC_4H_8
27g: R = CO_2Me
27h: R = CONHMe
27i: R = NHMe

The electrostatic interactions associated with ion pairs can also be present in the glassy state. Usually, ion pairs that do not participate in other additional interactions (e.g., hydrogen bonding) do not associate in a directional fashion, and therefore do not significantly impact the crystallization process. Several organic cations, including quaternary ammonium, alkylpyridinium, or alkylimidazolinium salts, do not interact with their counterions in a strongly directional fashion, and are therefore compatible with glass formation. In fact, several room temperature ionic liquids, including various dialkylimidazolium salts (such as representative compound **28**) [43] and quaternary ammonium salts (example **29** shown) [44], can readily form glassy phases, though with very low (and sub-ambient) T_g values. Even in cases where hydrogen bonding is possible, a wide variety of possible motifs can mitigate the rate of crystallization, and can still result in glass formation. For example, 1,5-dimexylbiguanide (**30**) can form glass-forming salts with a wide range of larger organic carboxylic and dicarboxylic acids, while salts with smaller counterions (halides, small carboxylates, phosphate, and sulfate) readily crystallize [45].

EBSCOhost - printed on 2/14/2023 1:06 PM via . All use subject to https://www.ebsco.com/terms-of-use

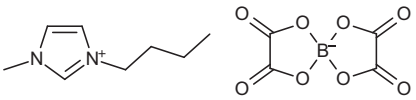

28

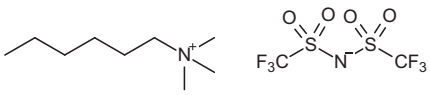

29

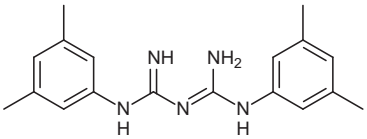

30

Van der Waals interactions are individually weak, and are present in most organic compounds. However, long linear alkyl chains, which can stack into arrays through multiple van der Waals interactions, are often detrimental for GS. Such chains are often used to introduce liquid crystalline behavior [46], and as a result, compounds often show relatively low melting transitions, which also translate into lower glass transitions [40]. This, coupled with the fact that the multiple van der Waals interactions promote cohesion among the alkyl chains, results in an increased propensity to crystallize, coupled with a higher molecular mobility. For these reasons, branched alkyl chains, because they interact more weakly and do not pack as closely and regularly, typically yield more stable glasses. Cholesteryl groups constitute one such example [18], [47].

Strong π–π stacking, especially in a face-to-face geometry, which is often encountered in fused polyaromatics, strongly promotes crystallization. The principal driving force toward crystallization in this case is the fact that the interaction requires a significant portion of the van der Waals surfaces of the molecules to overlap, leading to homogenization of both the conformations and the orientations of the molecules [48]. The interaction thus severely limits the degrees of liberty available to the molecules. Glass formation in compounds possessing moieties that form face-to-face π–π stacking interactions is possible, but requires the introduction of several groups that will introduce more degrees of liberty to the system.

9.3 Groups That Can Induce Glass Formation

While it is widely accepted that irregular structures that pack poorly will show a higher propensity to form glasses and remain in the glassy state, trying to accurately predict the GFA of a given structure based on structure alone is not guaranteed to be successful, as the interplay of structural elements can easily tip the scales toward crystallization. Although initial efforts to design and synthesize optimal molecular glasses was first largely based on trial and error, strategies exist nowadays to accurately promote glass formation using common functional groups that are known to reliably form glasses and that can readily be used to functionalize

EBSCOhost - printed on 2/14/2023 1:06 PM via . All use subject to https://www.ebsco.com/terms-of-use

compounds of interest. While such strategies are often incompatible with biologically relevant compounds such as pharmaceuticals because of the specificity between their structures and the targeted biological receptors (e.g., proteins), they can be used for materials destined for photonic or optoelectronic applications.

While diarylamino groups with various aryl substituents are commonly used as building blocks to successfully engineer glass-forming compounds with specific chromophores, such as azobenzene derivative **31** and spirooxazole glass **32** [49]–[51], they are often integrated within the compounds' structures instead of used as peripheral moieties. This means that the synthesis of such derivatives can require several steps, and in most cases a certain degree of screening is necessary to identify the optimal aryl substituents for the suppression of crystallization. This strategy is still commonly used, especially when the presence of the triarylamine moiety is desirable; for example, for hole transport materials, but for other cases, other glass-inducing moieties have been reported and successfully used.

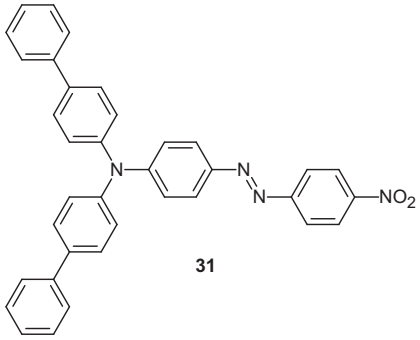

31

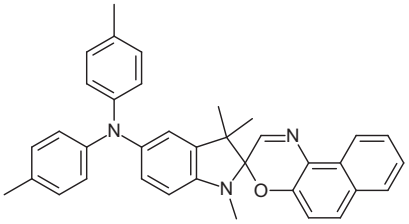

32

Diphenylhydrazines are one such example of a building block that can be readily reacted in a modular with various aromatic aldehydes or ketones to yield glass-forming adducts. For example, 4-formyltriphenylamine **33** readily crystallizes, but its *N,N*-diphenylhydrazone **34** forms a stable glass with a T_g of 50 °C [52]. 9-Alkylcarbazole or phenothiazine derivatives functionalized with a diphenylhydrazone moiety (examples **35** and **36** shown) have been also shown to form stable glasses [11], [53]–[54].

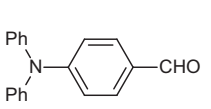

33

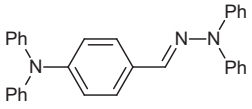

34

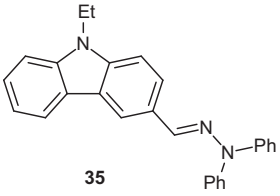

35

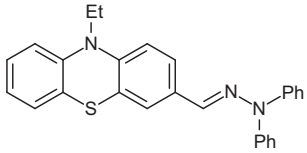

36

EBSCOhost - printed on 2/14/2023 1:06 PM via . All use subject to https://www.ebsco.com/terms-of-use

Triphenylmethyl groups are also bulky, tridimensional aromatic moieties that can be readily introduced to increase the propensity of target compounds (e.g., chromophores) to form glasses. They can be readily introduced by reacting hydroxy or amino groups with triphenylmethyl chloride, although in this case the triphenylmethyl groups that are highly sensitive to acidic conditions can be readily hydrolyzed [55]. This problem has been circumvented by using 1,1,1-triphenylalkyl groups with longer chains, which can still be reacted by simple reactions including nucleophilic substitutions, but are stable toward acids. This approach has been demonstrated with *N*,*N*-bis(5,5,5-triphenylpentyl)aniline, which was used to prepare various chromophores with nonlinear optical properties, including azo derivative **37** [56].

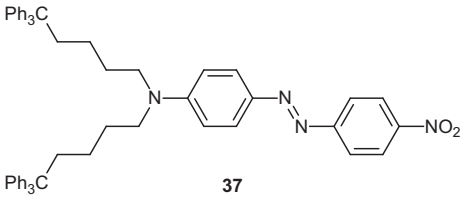

37

As mexylaminotriazine derivatives can readily form glasses, it is possible to prepare derivatives with various reactive groups, including amino (**38**), thiol (**39**), carboxy (**40**), bromomethyl (**41**), or aldehyde (**42**) groups [57], and also use them as peripheral moieties to generate glass-forming adducts with various compounds. This approach is also modular and allows reactions with a wide range of functional groups. However, in some cases, the solubility of the adducts can be limited to highly polar solvents, and the NH groups introduced are incompatible with strong bases. Alternatively, *N*-methyl analogs (**43**) exist where there are no NH groups that can participate in hydrogen bonding, which also leads to higher solubility, but their synthesis is often more complicated and costly [36].

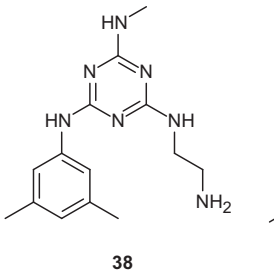

38

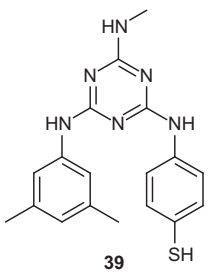

39

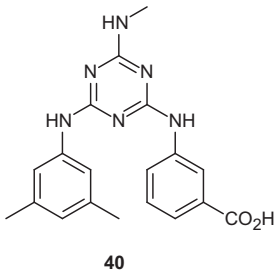

40

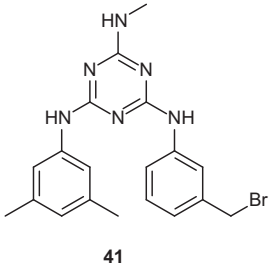

41

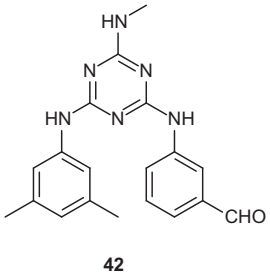

42

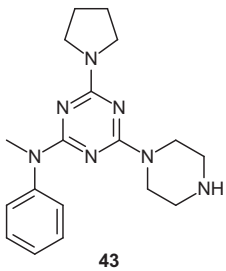

43

EBSCOhost - printed on 2/14/2023 1:06 PM via . All use subject to https://www.ebsco.com/terms-of-use

These derivatives were used to generate glass-forming azo chromophores (representative compound **44** shown) [58]–[60] as well as both electron donors (**45**) [61] and acceptors (**46**) [62] for organic photovoltaics.

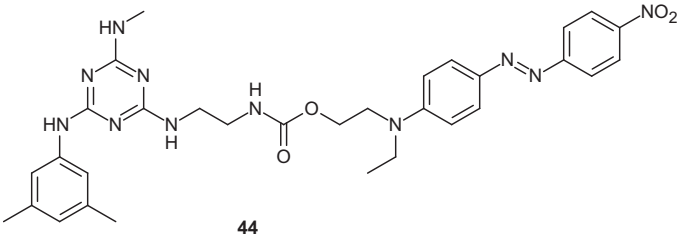

44

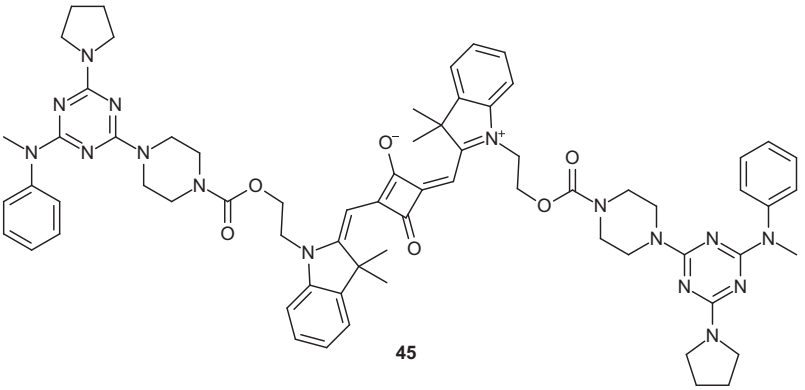

45

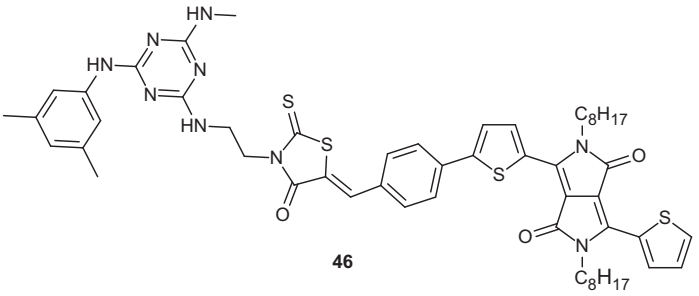

46

9.4 In Silico Design of Molecular Glasses

Molecular simulation is becoming a third way of approaching science as pointed out by Berendsen [63] or Allen and Tildesley [64]. It is now considered as an integral part of a laboratory. However, there are so many simulation techniques that it can become very difficult to select the optimal way to study a specific property. The glass transition is one such case study. It has always been considered as a long-range phenomenon that cannot be captured locally. Consequently, simulation at the atomistic level was not considered as a serious approach to deal with this tricky transition. However,

EBSCOhost - printed on 2/14/2023 1:06 PM via . All use subject to https://www.ebsco.com/terms-of-use

since the seminal work of Rigby and Roe [65] who revealed that a T_g can be determined for polymers with full-atomistic simulation, a huge number of simulations dealing with the glass transition of polymers have been carried out [66]–[68]. In the case of the simulation of molecular glasses, such a technique is certainly the most appropriate way to unveil the effect of various structural elements on the value of the T_g.

The principle of molecular dynamics (MD) is to animate atoms, which are then considered as beads in interactions [69]. These interactions are implemented inside a forcefield, which is characterized by a set of equations and parameters. A forcefield is actually built in order to exhibit the greater transferability between compounds. Nevertheless, its equations and parameters can vary depending on the kind of systems that are simulated. For instance, AMBER (Assisted Model Building with Energy Refinement) is usually employed to characterize biopolymers, while *pcff* (Polymer Consistent Force Field) is used mainly to deal with polymers. These forcefields are abundantly discussed in the literature. The selection of a forcefield is important since the simulated properties greatly depend on its accuracy. As an example, the difference between the AMBER and AMBER/OPLS (Optimized Potentials for Liquid Simulations) forcefields lies principally in the Coulomb potential term whose partial charges are different [70]. This difference leads to inaccurate T_g values for PMMA (poly (methyl methacrylate) in the case of AMBER [71]. This validation step is mandatory during simulation since it is an empirical method, comparison with experimental data must be carried out as regularly as possible. Once the forcefield selection is completed, MD can be carried out. It consists in integrating Newton's equations to animate atoms. To simulate molecular glasses, all the atoms must be considered. As a consequence, to represent all the atomic motions properly, the time step used for the integration should be 1 fs, thereby making very long simulations difficult to attain, and thus experimental times are usually not achievable.

To determine the T_g of molecular glasses, simulated dilatometry, the same method as the one employed to determine the T_g of polymers, can be employed. It consists of reporting the specific volume with respect to the temperature. This volume comes from the knowledge of the molecular weight of the system, and the initial density. However, to represent the amorphous system, this cell is replicated in all the dimensions. Thanks to the periodic boundary conditions, one atom exiting from one side automatically enters through the opposite side, preserving the density of the system. The use of thermostat and barostat (Nosé-Hoover) enables to keep the system at an appropriate temperature and pressure, respectively [72]. Accordingly, when the temperature is changed, the volume of the cell reaches an equilibrium value. This value is reported in a graph with respect to the temperature. By cooling, a change in the slope is an indication of a change in the state, and the occurrence of the glass transition (an example is shown in Figure 9.2). The simulated dilatometry was applied to a series of analogous mexylaminotriazine molecular glasses (**27a**–**h**), which can be differentiated by their functional group [73].

EBSCOhost - printed on 2/14/2023 1:06 PM via . All use subject to https://www.ebsco.com/terms-of-use

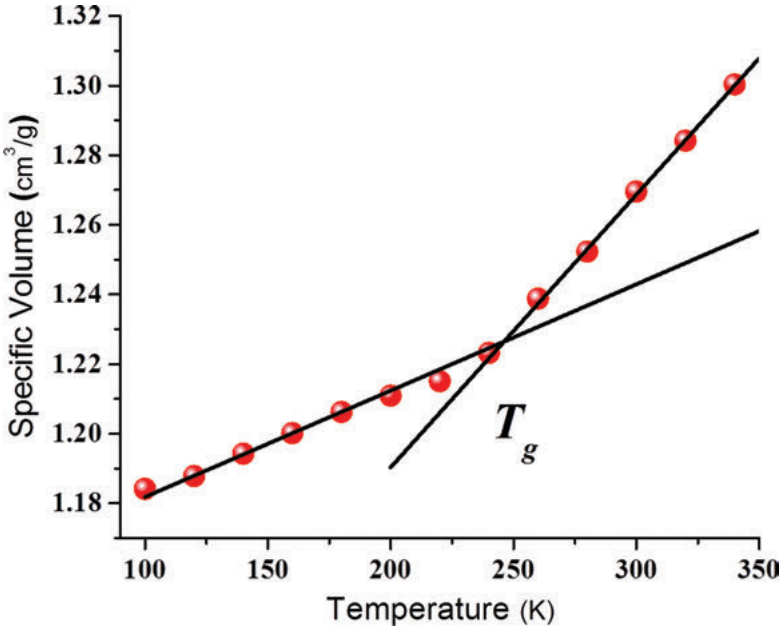

Figure 9.2: Simulated dilatometry: The specific volume is reported with respect to the temperature.

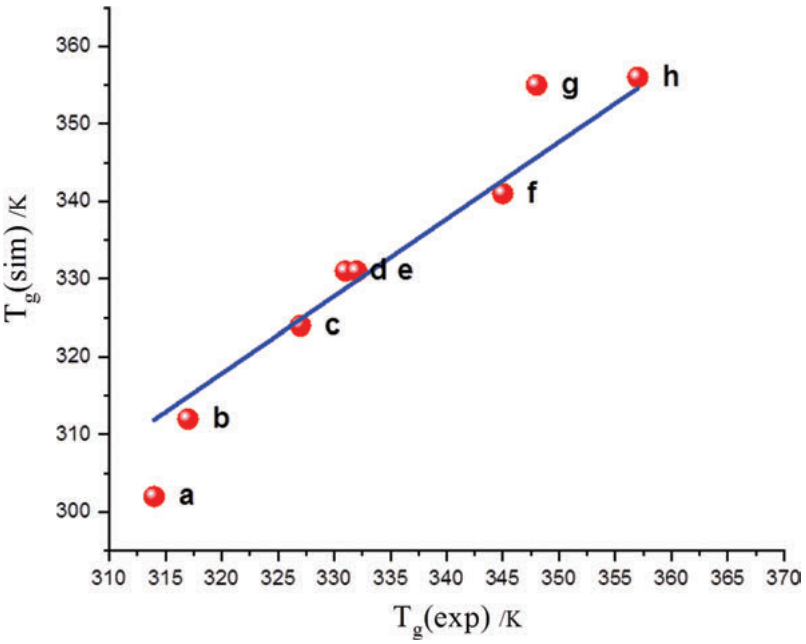

Figure 9.3: Compariso€n between simulated and experimental T_g of compounds **27a–h.**

EBSCOhost - printed on 2/14/2023 1:06 PM via . All use subject to https://www.ebsco.com/terms-of-use

For each molecule, eight different cells have been generated allowing the computation of error bars. The values of the T_g for the different groups are shown in the graph of Figure 9.3 with respect to experimental values. A linear relationship was definitively retrieved showing that the simulated dilatometry procedure can correctly be applied to unveil the glass transition of molecular glasses. Because of this strong agreement, hints about the reasons of the occurrence of such a transition can be definitively grasped. It was observed that conformers of the main core of compounds **27a–h** (which are similar to that shown for compound **20**) are equally probable, that is, they exhibit comparable energy. Consequently, by decreasing the temperature, there is no reason why one stable configuration is preferred to another one, leading to a glass instead of a crystal. This is exacerbated by the high rotational barrier of the mexylamino substituents, which prevents conformers to equilibrate from one to another.

9.5 Physical Properties of Molecular Glasses

As mentioned previously, the most common physical parameter to study molecular glasses is their glass transition temperature (T_g), which represents the transition between two amorphous states of different viscosity, the glassy state to the viscous, or rubbery, state. It becomes a second-order transition at an infinitely slow cooling rate. Under classical cooling rate, the transition is marked by a change in the heat capacity of the material as it reaches the solid glassy state from the supercooled liquid state. Moreover, if one was to extrapolate the heat capacity of the liquid below the glass transition temperature, it would be possible to reach a temperature where the entropy of the supercooled liquid is equal to that of the crystalline solid. This temperature has been called the Kauzmann temperature (T_K), which also corresponds to the temperature at which all molecular translational motion would cease. However, this would indicate that cooling the liquid further would yield an entropy lower to that of the crystalline solid, which constitutes a paradox, known as the Kauzmann paradox [2]–[3]. The resolution of this paradox is not yet confirmed and is still debated.

The glass transition temperature can be measured by several ways. Differential scanning calorimetry (DSC) is the most commonly used method to measure T_g by detecting the change in heat capacity occurring at the glass transition, and it possesses the additional advantages of detecting the presence or absence of crystallization upon heating. Rheology can also be used to measure T_g, which is denoted by a sharp decrease in the viscosity of the material. Dynamical mechanical analysis (DMA) is also greatly employed since difference in viscoelasticity is a characteristic of this tricky phase transition [74].

Besides T_g and crystallization, DSC can be used to elucidate the crystallization kinetics of molecular glasses. By varying the heating and cooling rate, it is possible to determine the kinetic GS by measuring the critical cooling rate (R_c) of the material, which is the slowest cooling rate at which the compound will form a

EBSCOhost - printed on 2/14/2023 1:06 PM via . All use subject to https://www.ebsco.com/terms-of-use

glass instead of crystallizing. Furthermore, it is possible to monitor the presence of crystallization upon heating at various rates. Ideally, a molecular glass should not display any sign of crystallization with heating or cooling rates as low as 0.01 °C/min, though few known molecular glasses display such kinetic stability [75].

Another important parameter to consider with glasses (including polymers and inorganic glasses) is the fragility index, which corresponds to the linearity of the relationship between viscosity and temperature relative to T_g [37], [76]. When the data is plotted in an Arrhenius plot with the log of the viscosity as a function of T_g/T, a linear relationship is characteristic of "strong" glasses (including mainly inorganic glasses), while increasing deviation from linearity denotes more "fragile" glasses, as is the case with most small molecules. It was long believed that there was a correlation between fragility and crystallization kinetics, but as small molecules are typically fragile, such a correlation is difficult to rationalize. However, recent studies have shown that measuring the ratio between viscosity at a given temperature and the viscosity of the melt (η/η_{melt}) as a function of undercooling temperature ($T_{melt}-T$) yields insight into a compound's propensity to crystallize: compounds in which viscosity increases sharply once they are cooled from the melt tend to crystallize slower than compounds in which viscosity increases more progressively [77]. This is likely due to the fact that a lower viscosity translates to a higher molecular mobility, which in turn facilitates the molecules to rearrange in an ordered fashion.

To end this section, it is worthy to introduce the free volume concept to explain variation of T_g qualitatively according to the molecular systems. The transition from the rubber to the glassy states can be actually deciphered in terms of changes in free volume. This volume is defined as the space not occupied by molecules. The different motions of the molecules must be taken into account. Below T_g, this free volume remains constant since there no long-range motions. As the temperature increases, the occurrence of T_g is defined when a critical free volume is reached allowing molecules to move freely. According to Shima Boyer, this value is fixed.

9.6 Application of Molecular Glasses

As sucrose and most sugars are molecular glasses, the control of glass formation versus crystallization has been used extensively in the food industry; for example, in the confection of sugar-based candy, but also to give ice cream the correct texture [78]. However, in these cases, naturally occurring molecular glasses are used, and the emphasis has been placed on their processing to yield the desired products, rather than the development of new molecular glasses.

More recent applications of molecular glasses include amorphous drug formulations [26]–[32]. As drugs are introduced mainly in the crystalline form, it is crucial to screen possible polymorphs to find the form that yields optimal values for several parameters, including compressability, bioavailability, and so on. In cases where

EBSCOhost - printed on 2/14/2023 1:06 PM via . All use subject to https://www.ebsco.com/terms-of-use

bioavailability is low because of poor water solubility, the drugs can be formulated in their amorphous forms, as their kinetics of dissolution are typically orders of magnitude higher because of the metastability of the glassy state. Alternatively, if drugs undergo decomposition in the crystalline state because of the proximity of reactive groups, the respective amorphous forms may actually show longer shelf lives because of random orientation of the molecules. In some of these cases, the compounds can naturally access the glassy state because of their highly irregular molecular structures. In other cases, the drugs may be dispersed within an amorphous material, which is often a di- or trisaccharide because of their low toxicity and availability.

Molecular glasses have also started to be used as substitutes for polymers in some photonic and optoelectronic applications, as well as micro- and nanofabrication processes. Because of their large size and polydisperse nature, specialized polymers containing chromophores are tedious and expensive to synthesize on large scales. Molecular glasses may offer similar performances in several applications, with the added benefits associated with their smaller sizes and monodispersity, which leads to easier synthesis and characterization, and higher batch homogeneity. Furthermore, as the European Union plans to remove from the market all nonrecyclable polymers by 2030 [79], it will become crucial to find appropriate small-molecule materials to replace polymers for these applications.

Azobenzenes are often used in photonics because of their photomechanical properties, which include spontaneous surface patterning processes, such as surface relief gratings (SRG). The initial studies in the mid-1990s on SRG writing have involved polymers with azobenzene derivatives as side chains [80]–[81]. However, azo molecular glasses have later been successfully synthesized by several groups, and using various glass-promoting structural elements, including triarylamine (**31**), triphenylmethane (**37**), and mexylaminotriazine (**44**) groups [49]–[50], [56], [58]. These glasses can be processed into amorphous thin films in a fashion similar to their polymer counterparts and typically show photomechanical properties similar to that of their polymer analogs.

Besides photomechanics, some azobenzene chromophores are known for their nonlinear optical properties. Molecular glasses containing other nonlinear optical chromophores, such as benzylidene-1,3-indandione (**47**) or 5,5-dimethylfuran-2-ylidenemalononitrile (**48**) derivatives have also been reported. Thin films of molecular glasses incorporating these chromophores (or azo chromophores) have shown similar behavior as their polymer analogs [56], [82].

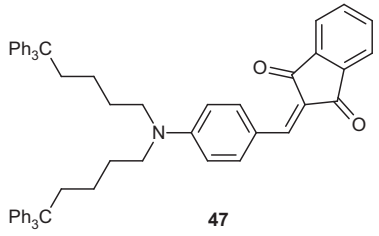

47

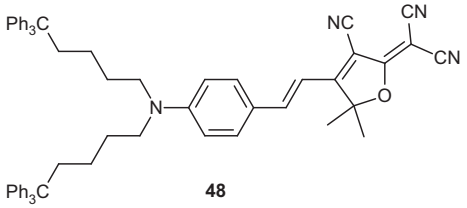

48

EBSCOhost - printed on 2/14/2023 1:06 PM via . All use subject to https://www.ebsco.com/terms-of-use

Molecular glasses are also appealing as alternatives to polymers for nanolithography applications. Molecular glass photoresists are smaller than polymers, therefore they can form smoother patterns with higher resolution and without protruding chain segments. Calixarene derivatives substituted with tert-butylcarbonate groups, such as derivative **49**, are often used for these purposes, in blends with a photoacid generator and a cross-linking agent. Irradiation activates the photoacid generator, leading to the cleavage of the carbonate groups, thereby deprotecting the hydroxy groups of the calixarene, which then react with the cross-linking agent, giving rise to a cross-linked polymer in irradiated areas [22]–[23].

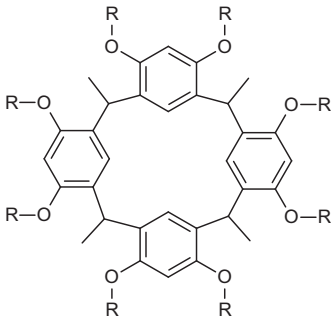

R = H, Boc (random)

49

The hole-transport layers in organic light-emitting diodes (OLEDs) are typically amorphous, and are often constituted of triarylamine derivatives. While polymers incorporating triarylamino groups have been used successfully for this purpose, small molecules are more commonly used because of the aforementioned advantages. Examples of molecular glasses used in OLEDs include 4,4′-(*N*-phenyl-*N*-(1-naphthyl)amino)biphenyl (α-NPD, **12**) [24] and 4,4′,4′-tricarbazolyltriphenylamine (TCTA, **50**) [83].

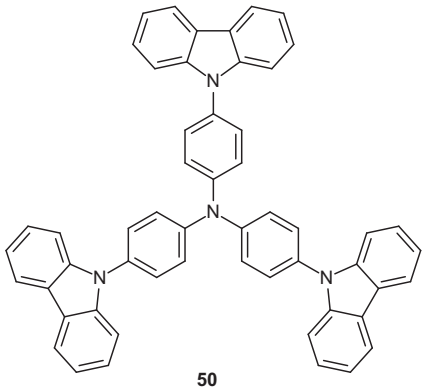

50

EBSCOhost - printed on 2/14/2023 1:06 PM via . All use subject to https://www.ebsco.com/terms-of-use

Bulk heterojunction photovoltaic cells are an emerging field where molecular glasses may be used. In this type of photovoltaic cells, the electron donor and acceptor used as active layer materials are typically polycrystalline in nature. However, amorphous blends offer the advantage of being less dependent on crystalline morphology, and consequently, on processing conditions. Initial attempts to incorporate molecular glasses as one of the active layer materials (often the acceptor, as most commonly used donors are polymers) have been successful, though conversion efficiencies were modest [84]–[86]. However, a glass-forming diketopyrrolopyrrole (DPP) derivative (**46**) was shown to yield conversion efficiencies up to 2.5% with benchmark donor polymer poly(3-hexylthiophene) (P3HT), which is close to the average value reported with benchmark fullerene-based acceptor Phenyl-C61-butyric acid methyl ester ($PC_{61}BM$) (**51**) (2.7%) [62]. Interestingly, this molecular glass, while remaining amorphous in the blend with P3HT, showed a conversion efficiency approximately 50% higher than that of a crystalline analog with a similar chromophore. Moreover, this DPP glass was shown to improve conversion efficiency by 36% when used as a ternary acceptor in the P3HT:$PC_{61}BM$ system, by improving light harvesting while not perturbing the polycrystalline morphology of the P3HT and PCBM domains [87]. Instead, the material remains amorphous and is located at the interfaces between the crystalline domains.

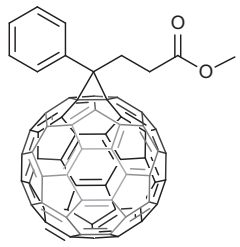

51

9.7 Conclusion

Significant progress has been achieved to attempt to understand glass formation by small organic molecules. The structural elements contributing to impede crystallization are understood enough to provide a working knowledge on how to engineer small-molecule materials that spontaneously form glasses and remain in the glassy state for extended periods of time. The impact of molecular structure on glass transition temperature is also understood to a point where it is possible to design molecular glasses with T_g close to the desired values. However, much remains to be elucidated about the actual glass transition phenomenon itself.

Molecular glasses have found niche applications, mostly in pharmaceutical, photonic, and optoelectronic applications, often as substitutes for specialized polymers, though further advances will likely pave the way for other emerging applications.

EBSCOhost - printed on 2/14/2023 1:06 PM via . All use subject to https://www.ebsco.com/terms-of-use

References

[1] Nye, J.F. *Physical Properties of Crystals*.; Oxford University Press, New York, NY, 1985.
[2] Donth, E.-J. *The Glass Transition*; Springer Series in MATERIALS SCIENCE, Vol. 48; Springer Berlin Heidelberg: Berlin, Heidelberg, 2001.
[3] Gutzow, I. S., Schmelzer, J. W. P. *The Vitreous State – Thermodynamics, Structure, Rheology, and Crystallization 2nd Ed.*; Springer: Heidelberg, Germany, 2013.
[4] Ediger, M.D., Harrowell, P. *J. Chem. Phys*. 2012, *137*, 080901.
[5] Biroli, G., Garrahan, J.P. *J. Chem. Phys*. 2013, *138*, 12A301.
[6] Berthier, L., Ediger, M.D. *Phys. Today* 2016, *69*, 40.
[7] Shirota, Y. *J. Mater. Chem*. 2000, *10*, 1.
[8] Strohriegl, P., Grazulevicius, J.V. *Adv. Mater*. 2002, *14*, 1439.
[9] Shirota, Y. *J. Mater. Chem*. 2005, *15*, 75.
[10] Shirota, Y., Kageyama, H. *Chem. Rev*. 2007, *107*, 953.
[11] Lygaitis, R., Getautis, V., Grazulevicius, J.V. *Chem. Soc. Rev*. 2008, *37*, 770.
[12] Lu, Z.P., Liu, C.T. *Acta Mater*. 2002, *50*, 3501.
[13] Baird, J.A., Van Eerdenbrugh, B., Taylor, L.S. *J. Pharm. Sci*. 2010, *99*, 3787.
[14] Greet, R.J., Turnbull, D. *J. Chem Phys*. 1967, *46*, 1243.
[15] Magill, J.H., Plazek, D.J. *Nature* 1966, *209*, 70.
[16] Shirota, Y., Kobata, T., Noma, N. *Chem. Lett*. 1989, 1145.
[17] Inada, H., Shirota, Y. *J. Mater. Chem*. 1993, *3*, 319.
[18] Chen, S.W., Mastrangelo, J.C., Shi, H., Bashir-Hashemi, A., Li, J. *Macromolecules* 1995, *28*, 7775.
[19] Oldham, W.J., Jr., Lachicotte, R.J., Bazan, G.C. *J. Am. Chem. Soc*. 1998, *120*, 2987.
[20] Salbeck, J., Yu, N., Bauer, J., Weissörtel, F., Bestgen, H. *Synth. Met*. 1997, *91*, 209.
[21] Nakayama, T., Ueda, M. *J. Mater. Chem*. 1999, *9*, 697.
[22] Young-Gil, K., Kim, J.B., Fujigaya, T., Shibasaki, Y., Ueda, M. *J. Mater. Chem*. 2002, *12*, 53.
[23] Nishikubo, T., Kudo, H. *J. Photopolym. Sci. Technol*. 2011, *24*, 9.
[24] Van Slyke, S.A., Chen, C.H., Tang, C.W. *Appl. Phys. Lett*. 1996, *69*, 2160.
[25] Shirota, Y., Kuwabara, Y., Okuda, D., Okuda, R., Ogawa, H., Inada, H., Wakimoto, T., Nakada, H., Yonemoto, Y., Kawami, S., Imai, K. *J. Lumin*. 1997, *72–74*, 985.
[26] Hancock, B.C., Zografi, G. *J. Pharm. Sci*. 1997, *86*, 1.
[27] Yu, L. *Adv. Drug Deliv. Rev*. 2001, *48*, 27.
[28] Timpe, C. *Am. Pharm. Rev*. 2007, *10*, 104.
[29] Gao, P. *Mol. Pharm*. 2008, *5*, 903.
[30] Willart, J.F., Descamps, M. *Mol. Pharm*. 2008, *5*, 905.
[31] Bhugra, C., Pikal, M.J. *J. Pharm. Sci*. 2008, *97*, 1329.
[32] Yu, L. *Adv. Drug Deliv. Rev*. 2016, *100*, 3.
[33] Mao, C., Prasanth Chamarthy, S., Byrn, S.R., Pinal, R. *Pharm. Res*. 2006, *23*, 2269.
[34] Kim, S-J., Karis, T.E. *J. Mater. Res*. 1995, *10*, 2128.
[35] Gataullina, K.V., Ziganshin, M.A., Stoikov, I.I., Gubaidullin, A.T., Gorbatchuk, V.V. *Phys. Chem. Chem. Phys*. 2015, *17*, 15887.
[36] Laventure, A., De Grandpré, G., Soldera, A., Lebel, O., Pellerin, C. *Phys. Chem. Chem. Phys*. 2016, 1681.
[37] Angell, C.A. *Science* 1995,
[38] Naito, K. *Chem. Mater*. 1994, *6*, 2343.
[39] Lebel, O., Maris, T., Perron, M.-E., Demers, E., Wuest, J.D. *J. Am. Chem. Soc*. 2006, *128*, 10372.
[40] Wuest, J.D., Lebel, O. *Tetrahedron*, 2009, *65*, 7393.
[41] Plante, A., Mauran, D., Carvalho, S.P., Pagé, J.Y.S.D., Pellerin, C., Lebel, O. *J. Phys. Chem. B*., 2009, *113*, 14884.

EBSCOhost - printed on 2/14/2023 1:06 PM via . All use subject to https://www.ebsco.com/terms-of-use

[42] Wang, R., Pellerin, C., Lebel, O. *J. Mater. Chem*. 2009, *19*, 2747.
[43] Xu, W., Cooper, E.I., Angell, C.A. *J. Phys. Chem. B* 2003, *107*, 11749.
[44] Sun, J., Forsyth, M., MacFarlane, D.R. *J. Phys. Chem. B* 1998, *102*, 8858.
[45] Carvalho, S.P., Wang, R., Wang, H., Ball, B., Lebel, O. *Cryst. Growth Des*. 2010, *10*, 2734.
[46] Demus, D., Goodby, J., Gray, G.W., Spiess., H.-W., Vill, V. *Handbook of Liquid Crystals*; Wiley-VCH; Weinheim: 1998.
[47] Wei, R., Xu, Z., Liu, X., He, Y., Wang, X. J. *Mater. Chem. C* 2015, *3*, 10925.
[48] Laventure, A., Maris, T., Pellerin, C., Lebel, O. *Cryst. Growth Des*. 2017, *17*, 2365.
[49] Nakano, H., Takahashi, T., Kadota, T., Shirota, Y. *Adv. Mater*. 2002, *14*, 1157.
[50] E. Ishow, B. Lebon, Y. He, X. Wang, L. Bouteiller, L. Galmiche and K. Nakatani, *Chem. Mater*. 2006, *18*, 1261.
[51] Nagahama, D., Nakano, H., Shirota, Y. *J. Photopolym. Sci. Technol*. 2008, *21*, 755.
[52] Nishimura, K., Inada, H., Kobota, T., Matsui, Y., Shirota, Y. *Mol. Cryst. Liq. Cryst*. 1992, *217*, 235.
[53] Ostrauskaite, J., Voska, V., Antulis, J., Gaidelis, V., Jankauskas, V., Grazulevicius, J.V. *J. Mater. Chem*. 2002, *12*, 3469.
[54] Danilevicius, A., Ostrauskaite, J., Grazulevicius, J.V., Gaidelis, V., Jankauskas, V., Tokarski, Z., Jubran, N., Sidaravicius, J., Grevys, S., Dzena, A. *J. Photochem. Photobiol. A: Chem*. 2004, *163*, 523.
[55] Traskovskis K, Mihailovs I, Tokmakovs A, Jurgis A, Kokars V, Rutkis M. *J. Mater. Chem*. 2012, *22*, 11268.
[56] Traskovskis, K., Lazdovica, K., Tokmakovs, A., Kokars, V., Rutkis, M. *Dyes Pigm*. 2013, *99*, 1044.
[57] Eren, R.N. Plante, A., Meunier, A., Laventure, A., Huang, Y., Briard, J.G., Creber, K.J., Pellerin, C., Soldera, A., Lebel, O. *Tetrahedron*, 2012, *68*, 10130.
[58] Kirby, R., Sabat, R.G., Nunzi, J.-M., Lebel, O. *J. Mater. Chem. C* 2014, *2* 841.
[59] Bennani, O.R., Al-Hujran, T.A., Nunzi, J.-M., Sabat, R.G., Lebel, O. *New J. Chem*. 2015, 9162.
[60] Tofini, A., Levesque, L., Lebel, O., Sabat, R.G. *J. Mater. Chem. C* 2018, *6*, 1083.
[61] Adhikari, T., Nunzi, J.-M., Lebel, O. *Org. Electron*. 2017, *49*, 382.
[62] Adhikari, T., Nunzi, J.-M., Lebel, O. *Org. Electron*. 2017, *48*, 230.
[63] Berendsen, H.J.C. *Simulating the Physical World: Hierarchical Modeling from Quantum Mechanics to Fluid Dynamics*; 2007.
[64] Allen, M.P., Tildesley, D.J. *Computer Simulation of Liquids and Liquid Crystals - 2nd Edition*; Oxford University Press: New York, 2017.
[65] Rigby, D., Roe, R.-J. *J. Chem. Phys*. 1988, *89*, 5280.
[66] Soldera, A., Metatla, N. *Phys. Rev. E* 2006, *74* (6), 61803.
[67] Wu, C. *J. Mol. Model*. 2017, *23*, 270.
[68] Lyulin, A.V., de Groot, J.J., Michels, M.A.J. *Macromol. Symp*. 2003, *191*, 167.
[69] Leach, A. R. *Molecular Modelling : Principles and Applications*, 2nd ed.; Prentice Hall: Harlow, England; New York, 2001.
[70] Jorgensen, W. L., Maxwell, D. S., Tirado-Rives, J. *J. Am. Chem. Soc*. 1996, *118*, 11225.
[71] Soldera, A., Metatla, N. *Internet Electron. J. Mol. Des*. 2005, *4*, 721.
[72] Kotelyanskii, M., Theodorou, D.N. *Simulation Methods for Polymers*, Marcel Dekker Inc.; New-York: 2004.
[73] Plante, A., Palato, S., Lebel, O., Soldera, A. *J. Mater. Chem. C* 2013, *1*, 1037.
[74] Halary, J.L., Lauprêtre, F., Monnerie, L. *Polymer Materials: Macroscopic Properties and Molecular Interpretations*, Wiley: Singapore, 2011.
[75] Laventure, A., Soldera, A., Pellerin, C., Lebel, O. *New J. Chem*. 2013, *37*, 3881.
[76] Ediger, M.D., Angell, C.A., Nagel, S.R. *J. Phys. Chem*. 1996, *100*, 13200.

EBSCOhost - printed on 2/14/2023 1:06 PM via . All use subject to https://www.ebsco.com/terms-of-use

[77] Baird, J.A., Santiago-Quinonez, D., Rinaldi, C., Taylor, L.S. *Pharm. Res*. 2011, *29*, 271.
[78] Hartel, R.W. *Crystallization in Foods*, Springer-Verlag, New York, NY, 2001.
[79] Scott, A. *C&EN* 2018, *96*(12), 16–18.
[80] Rochon, P., Batalla, E., Natansohn, A. *Appl. Phys. Lett*. 1995, *66*, 136.
[81] Viswanathan, N.K., Kim, D.Y., Bian, S., Williams, J., Liu, W., Li, L., Samuelson, L., Kumar, J., Tripathy, S.K. *J. Mater. Chem*. 1999, *9*, 1941.
[82] Umezawa, H., Jackson, M., Lebel, O., Nunzi, J.-M., Sabat, R.G. *Opt. Mater*. 2016, *60*, 258.
[83] Kuwabara, Y., Ogawa, H., Inada, H., Noma, N., Shirota, Y. *Adv. Mater*. 1994, *6*, 677.
[84] Li, Z., Dong, Q., Xu, B., Li, H., Wen, S., Pei, J., Yao, S., Lu, H., Li, P., Tian, W. *Sol. Energy Mater. Sol. Cells* 2011, *95*, 2272.
[85] Bulut, I., Lévêque, P., Heinrich, B., Heiser, T., Bechara, R., Zimmermann, N., Méry, S., Ziessel, R., Leclerc, N. *J. Mater. Chem. A* 2015, *3*, 6620.
[86] Li, W., Wang, D., Wang, S., Ma, W., Hedström, S., James, D.I., Xu, X., Persson, P., Fabiano, S., Berggren, M., Inganäs, O., Huang, F., Wang, E. *ACS Appl. Mater. Interfaces* 2015, *7*, 27106.
[87] Adhikari, T., Bobbara, S.R., Nunzi, J.-M., Lebel, O. *Org. Electron*. 2018, *53*, 74.

EBSCOhost - printed on 2/14/2023 1:06 PM via . All use subject to https://www.ebsco.com/terms-of-use

Raymond Tran, Christopher Moraes, Corinne A. Hoesli

10 Production of Pluripotent Stem Cell-Derived Pancreatic Cells by Manipulating Cell-Surface Interactions

Cellular therapies involve the transplantation of human cells to treat illness caused by the loss or dysfunction of tissue or cells in the patient. Many cell-based therapies are limited by access to reliable, cost-effective cell sources. With allogenic cell therapies, issues arise with donor-to-donor variability and in the supply chain toward the transplantation site. Some examples of these treatments include mesenchymal stem cell-based therapies or cancer-targeting chimeric antigen receptor (CAR) T-cell therapies. Some of these therapies require significant and expensive cell expansion after isolation from the donor before the treatment can be administered to the patient.

One example of a currently approved cellular therapy is islet transplantation for the treatment of diabetes. Type 1 diabetes (T1D) is an autoimmune disease where the insulin-producing cells of the pancreas – the pancreatic beta cells – are targeted by the immune system. The treatment consists in replacing these cells by introducing islets, which contain beta cells, into the liver of an immunosuppressed diabetic recipient. To address the sporadic, limited supply of donor islets, one attractive cell source is pluripotent stem cells (PSCs), which can theoretically differentiate into any somatic cell lineage and proliferate indefinitely. In theory, these cells would provide an infinite supply of various cell types on demand with minimal variability and reduced complications from organ or tissue harvesting steps. Although the cells would still be targeted by autoimmune rejection, concerns related to allograft rejection could be alleviated through the use of induced PSCs (iPSCs) derived from the patient himself. Consistently producing safe, mature, and functionally differentiated beta cells from PSCs in a cost-effective manner is highly challenging. Conventional differentiation protocols leverage signaling pathways through timed addition of soluble factors and small molecules. However, other signals relayed by the microenvironment such as mechanical signals also impact cell fate decisions. Controlling and tuning these stimuli can be achieved by rational and strategic design of the supporting biomaterial to present cells with appropriate cues for optimal differentiation toward specific lineages.

Advanced cell culture substrates, including functional materials, are being studied to guide cell behavior and efficiently promote differentiation toward a mature

Raymond Tran, Christopher Moraes, Corinne A. Hoesli, Department of Chemical Engineering, McGill University, Montreal, QC, Canada

https://doi.org/10.1515/9783110537734-010

EBSCOhost - printed on 2/14/2023 1:06 PM via . All use subject to https://www.ebsco.com/terms-of-use

phenotype. The main purpose of this chapter is to provide an overview of current approaches to guide stem cell differentiation using advanced biomaterials. While this field is extremely broad and thoroughly reviewed by several authors [1–3]; in this chapter, we draw attention to the applications of such biomaterial design strategies in differentiating pancreatic cells for cellular therapy of diabetes. In particular, we first look at the work done in directed differentiation using purely soluble factors and continue with advances made by controlling cell–substrate and cell–cell interactions.

10.1 Introduction

10.1.1 Type 1 Diabetes

Diabetes is characterized by the dysregulation of blood glucose levels by the endocrine hormone insulin. In healthy patients, beta cells found in the islets of Langerhans of the pancreas secrete insulin to regulate blood glucose levels. T1D is characterized by the autoimmune destruction of beta cells, while type 2 diabetes is mainly associated with insulin resistance by peripheral tissues as well as beta cell dysfunction [4, 5]. As a result, the body is unable to maintain tight glucose control. It is estimated that ~10% of diabetic patients have T1D [6]. T1D patients need to vigilantly monitor their blood glucose level and administer exogenous insulin as required, either through injections or using a pump. If left unattended, acute symptoms include fatigue and excessive thirst. Chronic complications include increased risks of developing cardiovascular disease, neuropathy, nephropathy, retinopathy, and Alzheimer's disease. Significant strides have made engineering closed-loop insulin pumps such as the MiniMed™ systems by Medtronic. However, it is difficult, if not impossible, to match the fine and autoregulated control provided by pancreatic beta cells even with closed-loop control. Islet transplantation has emerged as a promising cellular therapy approach to reintroduce the missing beta cells and reestablish blood glucose control.

10.1.2 Islet Transplantation

The first successful report of islet transplantation was in the 1970s [7, 8] but islet transplants did not lead to robust insulin independence until 2000, with the publication of "Edmonton Protocol" – a method that utilizes high islet doses and a different immunosuppressive regimen [9]. Several studies have further improved the effectiveness and availability of islet transplantation [10]. Recently, the first phase III multicenter trial reported 71% of patients achieving normal glucose levels after 2 years [11]. In Canada, islet transplantation is an accepted standard-of-care therapy in Alberta, British

EBSCOhost - printed on 2/14/2023 1:06 PM via . All use subject to https://www.ebsco.com/terms-of-use

Columbia, and Ontario. One limitation to islet transplantation is that patients require lifelong immunosuppression to prevent immune rejection. To address this, several groups are working on encapsulation methods to protect the donor islets [12–14]. Despite several advances in islet harvesting and culture [15], the limited supply of donor cells is still a fundamental drawback. Transplantation requires approximately 6,000 to 10,000 islet equivalents (IE)/kg of the recipient. Typically, 2 to 3 donors (and transplant procedures) are required to reach this dose for each patient [16]. Therefore, a cost-effective, sustainable source is required for widespread adoption of the treatment. One potential solution is using PSCs to generate insulin-producing cells.

10.1.3 Pluripotent Stem Cells

PSCs, including embryonic stem cells (ESCs) and (iPSCs) can theoretically proliferate indefinitely and give rise to all adult somatic cell types [17]. ESCs were first derived from the epiblasts (found in the inner cell mass) of the preimplantation embryo [18]. In 2006, Shinya Yamanaka and his group developed a technique to revert adult somatic murine cells into a pluripotent state (i.e., into iPSCs) through the forced expression of four transcription factors: (1) Oct4, (2) c-Myc, (3) Sox2, and (4) Nanog using retroviral transfection [19]. Later, this was achieved with human cells [20]. Since then, alternative approaches to induce pluripotency have been investigated. Such approaches include the use of chemical [21], microRNA [22], recombinant proteins [23], and more [24]. The iPSC technology circumvents some of the ethical concerns associated with the use of preimplantation embryos to generate ESCs. The discovery of methods to generate iPSCs from simple skin biopsies or blood samples opened several research avenues in areas ranging from drug testing to personalized cell therapies, tissue engineering, and the study of rare genetic disorders.

Recently, clinical trials have begun to test the safety and efficacy of PSCs in cellular therapies. For example, Viacyte has developed a macroencapsulation device with human ESC-derived pancreatic endoderm cells to be implanted under the patient's skin. The encapsulation device serves as a physical barrier against immune rejection as well as a method to potentially retrieve cells from the recipient if needed. These cells are expected to mature once implanted into the recipient to produce beta cells, replacing those lost in T1D [25].

PSCs are extremely versatile but safely and effectively producing a desired cell source remains a challenge. Administering a small dose of an undesired cell type can be fatal and yet most differentiation protocols do not yield a pure cell population. Furthermore, there is often significant batch-to-batch variation, thus requiring additional cell separation or immunoisolation steps for safety. The cGMP maintenance and differentiation of PSCs is also an expensive, laborious process because of the reagents used and traceability required. By precisely optimizing differentiation protocols, the

EBSCOhost - printed on 2/14/2023 1:06 PM via . All use subject to https://www.ebsco.com/terms-of-use

economic strain of these therapies can be greatly reduced. By precisely controlling the timing and concentration of soluble factors, and advanced engineering materials to precisely control cell behavior, the yield and efficacy of current differentiation protocols can be further improved to reduce the economic burden of the process.

10.2 Differentiation of Pluripotent Stem Cells

PSCs give rise to more specialized, adult cells in a process called differentiation. Stimuli that induce differentiation are presented by the cellular microenvironment and include soluble factor signaling, cell–cell interactions, cell–extracellular matrix (ECM) interactions, and biophysical forces (Figure 10.1) [26]. Among these, a soluble signaling factor has been most thoroughly investigated in the field of diabetes, while information on the impact of cell-matrix and biophysical forces remains scarce.

10.2.1 Classical Directed Differentiation Toward Beta Cells Using Soluble Factors

The first approaches to produce insulin-producing cells from PSCs relied on the formation of embryoid bodies via stochastic differentiation in the presence of serum. This was first demonstrated in 2001 by two individual groups using ESCs, albeit at low efficiency [27, 28]. In 2006, D'Amour et al. pioneered directed differentiation into pancreatic endocrine cells via timed addition of soluble signaling factors to replicate

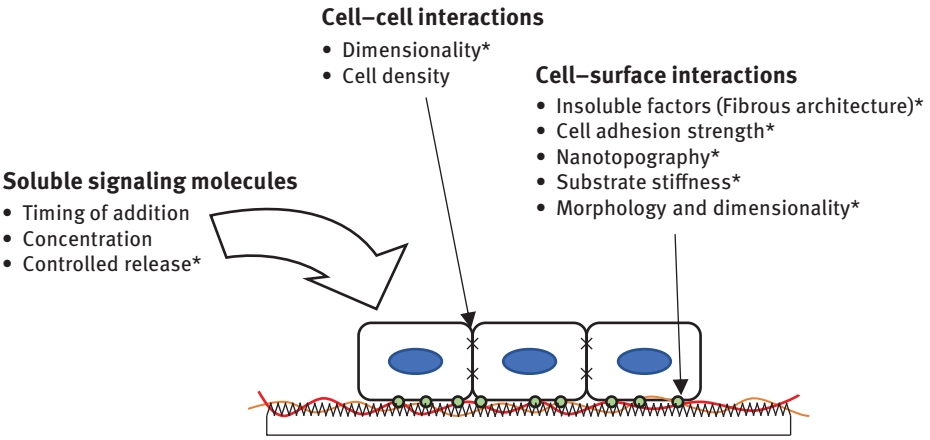

Figure 10.1: General outline of some controllable parameters, which can affect the efficacy of directed differentiation protocols.
* Indicates a parameter which can be controlled by engineering advanced materials.

EBSCOhost - printed on 2/14/2023 1:06 PM via . All use subject to https://www.ebsco.com/terms-of-use

key stages of development (Figure 10.2b). The early differentiation protocols resulted in immature and polyhormonal cells, but more recent protocols describe the production of functional glucose-responsive insulin-secreting cells from both ESCs and iPSCs [29–32] toward the pancreatic lineage is ascertained by the expression of a transcription factor called PDX1 and further commitment toward beta cell lineage is determined by the expression of NKX6.1 [33, 34].

Directed differentiation protocols can vary widely in efficiency, depending on the PSC source, the duration of each differentiation step, and the factors applied [35]. While PDX1-expressing pancreatic progenitor (PP) cells can generally be obtained with high efficiencies, achieving robust differentiation at later stages has been more challenging. This may be because of incorrect pathways to initiate PP commitment that affects downstream pancreatic maturation [36]. Many protocols lead to the production of polyhormonal cells rather than functional monohormonal insulin-producing cells. Recent reports detail the generation of monohormonal insulin-producing beta-like cells but at low efficiency and with impaired glucose sensing [37, 31]. When NKX6.1^{+} cells were transplanted into immunocompromised mice, PPs matured fully [38, 39]. Conversely, the insulin-expressing cells produced in vitro, solely using soluble factors, were more similar to immature fetal beta cells based on transcriptional profiling [40]. It stands to reason that key aspects of the in vivo microenvironment are required but not captured in current directed differentiation protocols.

10.2.2 The Developmental Landscape – A Complex Microenvironment to Capture

Directed differentiation protocols are inspired by detailed information gained from studies of developmental biology. Using this information, the protocols aim to reach each of the main developmental stage through stimuli mimicking developmental cues before progressing to the next stage. This approach has had success with organs such as the heart [41], liver [42], kidney [43], and lungs [44]. However, the cells obtained often lack key functional hallmarks, as is the case with PSC-derived pancreatic beta cells. The field has started to examine other aspects of the cellular microenvironment to increase functionality. For the heart in particular, aspects such as 3D structure [45], mechanical stress [46], electrical conditioning [47], cyclic stretch [48], or communication with other cell types [49] have been investigated. In pancreatic islets, beta cells are in close proximity to blood vessels, which transport nutrients such as oxygen. High oxygen tension promotes beta cell differentiation in cultured fetal pancreatic tissue [50]. Rezania et al. [31] used air–liquid interface culture after producing PPs to expose the cells to atmospheric oxygen levels and to allow apical and basal polarity of the cells. The beta cell-containing islets of Langerhans are also found as aggregates in vivo, prompting many differentiation protocols to be done in cellular aggregates [30, 51].

EBSCOhost - printed on 2/14/2023 1:06 PM via . All use subject to https://www.ebsco.com/terms-of-use

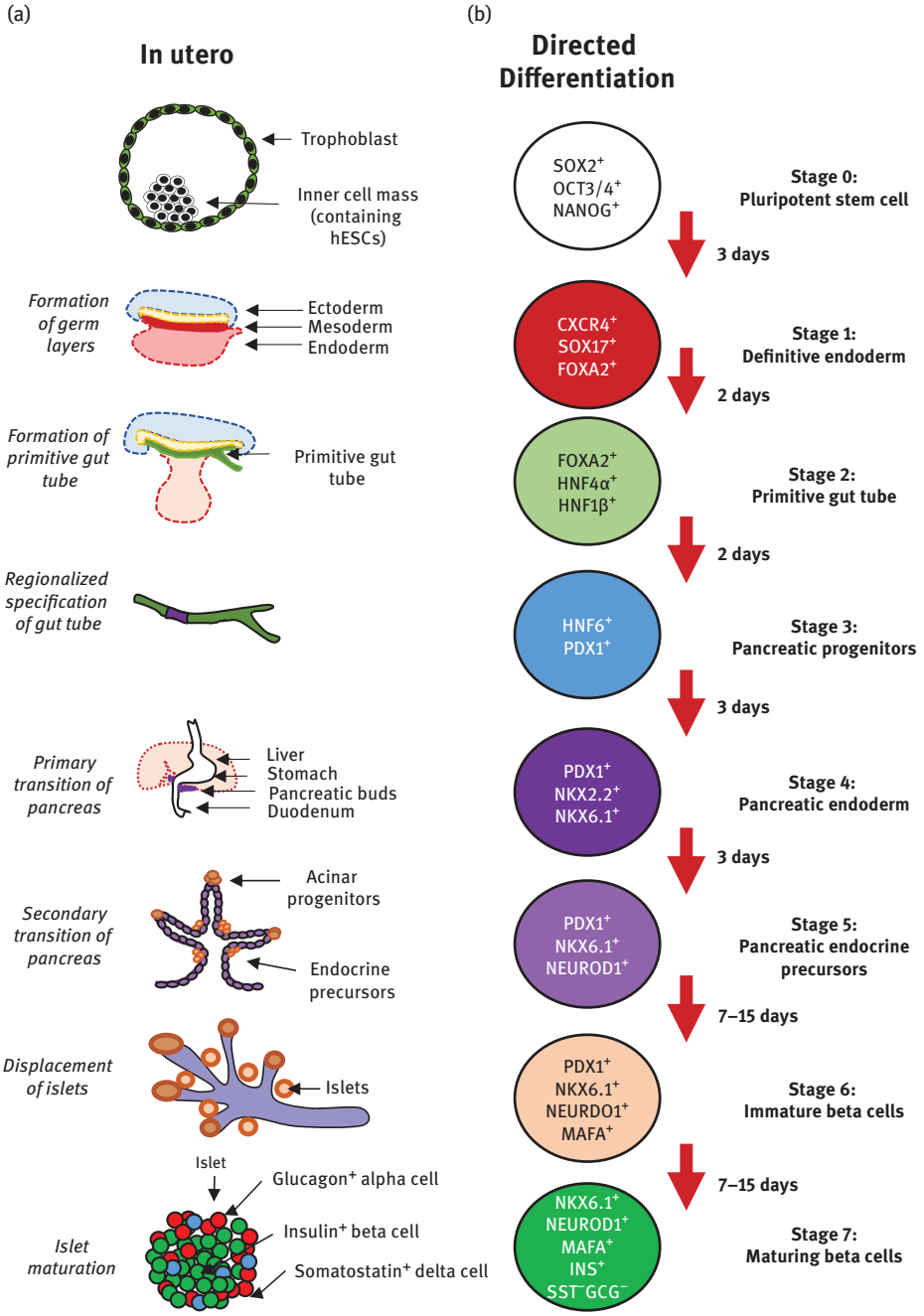

Figure 10.2: Directed differentiation protocols (b) mimic stages of pancreatic development, which are identified by a stage-specific transcription factor profile(a) to produce insulin-secreting beta cells [120, 31].

EBSCOhost - printed on 2/14/2023 1:06 PM via . All use subject to https://www.ebsco.com/terms-of-use

The in vivo microenvironment is fundamentally more complex than our current in vitro systems can capture. In utero, development occurs with remarkable precision through dynamic guidance from the surrounding cellular microenvironment. As cells differentiate, they relay different signals to their neighbors via soluble factors and the deposition of ECM proteins. Various biochemical and biophysical cues from surrounding organs affect nearby organogenesis in various feedback mechanisms. Biophysical forces play a large role in guiding cell behavior, especially during early embryogenesis [52]. Morphological changes impart dynamic biomechanical forces developing tissues. For example, a simplified model of pancreas development is shown in Figure 11.1a.is shown in Figure 11.1a.

Early embryologists investigated the role of mechanical forces in the developmental control [53], but interest waned with the advent of biochemistry and molecular biology. As a result, most recent work on tissue patterning focuses on gene expression and cell signaling [54]. Cells feel their surroundings in a process called mechanotransduction by converting mechanical stimuli into biochemical signals. Cells respond to forces by cytoskeletal reorganization and changes in biochemistry (via concentration, activity, and localization of intracellular proteins) and gene expression [55]. Therefore, proper designing of advanced cell culture substrates to better control cell behavior and interactions can promote more efficient differentiation processes. Biomechanical cues can potentially replace or reduce the doses of expensive soluble factors added to guide differentiation. To efficiently produce fully functional pancreatic beta cells, we require a comprehensive understanding of biophysical components of the microenvironment and how cells interact with these components.

10.2.3 Recapitulating the Interactions Found in Native Tissues

The ECM provides cues to cells via biochemical signals, presentation of growth factors, biophysical signals, and combinations thereof [56]. During development, the ECM composition is constantly changing. The ECM interacts with the developing cells directly as well as indirectly, that is, by sequestering growth factors. As ECM is deposited, the biophysical cues it presents to cells also changes [57]. The presence of ECM can produce more functional cells. For example, islets encapsulated in hydrogels with ECM proteins (particularly collagen IV and laminin) displayed increased insulin secretion when challenged with high glucose concentrations [58]. The mechanical scaffold provided by the ECM plays a role in guiding stem cell differentiation through a cell-generated force feedback mechanism [59]. Understanding how these ECM cues affect the cell behavior and recapitulating this in vitro can be a key to optimizing stem cell differentiation approaches. An example illustrating the role of ECM on stem cell fate is the preferential differentiation of MSCs toward osteogenic lineages in hyaluronic acid-based gels versus chondrogenic lineages in collagen-based gels [60]. The ECM found in vivo contains hundreds of different proteins with varying

EBSCOhost - printed on 2/14/2023 1:06 PM via . All use subject to https://www.ebsco.com/terms-of-use

composition. Combinatiorial protein arrays have been used to study the interactive and additive effects of different ECM components on stem cell behavior [61–64]. The synergistic role of ECM proteins, such as collagen I, can be screened in a combinatorial fashion using protein arrays to optimize endoderm differentiation [65]. Better understanding of which proteins are present in pancreas development and their role in differentiation can help guide efficient production of functional insulin-secreting cells.

10.2.4 Engineering Cell–Surface Interactions

The presence of external ECM, as well as ECM produced within the cell, is paramount for successful differentiation. In particular, external fibronectin downregulates pluripotency of PSCs and defined combinations of fibronectin and laminin enhance definitive endoderm differentiation, which leads to the pancreatic lineage [66]. The ECM surrounding human adult islets is composed mainly of laminin, collagen IV, fibronectin, and other types of collagen. In the embryonic pancreas, the islet ECM composition is different and consists mainly of vitronectin, fibronectin, and collagen IV [67]. The specific roles of the constituent proteins and their effect on cell behaviour during differentiation is relatively unknown. Certain ECM components can influence survival, adhesion, proliferation, and also change stem cell fate decisions. ECM components such as fibronectin, collagen IV, and laminin can promote ESC differentiation into pancreatic lineages [68, 69]. The specific integrin–fibronectin and ECM interactions play an important role in specification of the pancreas [70]. Stress propagation is another function of the surrounding ECM matrix [71]. The cells then sense biomechanical cues by mechanosensors such as ECM-bound integrins that span the cell membrane [72]. The ECM can provide biomechanical stimuli through both the fibrous architecture and the apparent stiffness. Therefore, it is important to try to decouple the specific ECM protein effects from the structural or mechanical stimuli provided by the ECM.

ECM-Mimicking Fibrous Architecture

The ECM provides structural adhesive binding sites that influence the shape the cells adopt on a substrate. A variety of scaffolds have been employed to manipulate stem cell fate decisions. Electrospun nanofibers can mimic the nanotopograpy and fibrous nature of the ECM proteins. To provide adhesion signals required to avoid anoikis of adherent cells, scaffolds can be coated with ECM proteins such as collagen. These nanofibers can direct the cell fate of MSCs by modulating alignment, density, material, and composition [73–76]. Scaffolding and nanotopography can also affect endodermal differentiation. Human ESCs differentiated toward endoderm on 200 nm poly(ε-caprolactone) (PCL) fibers had increased expression of endodermal genes. Cells cultured on thin fibers adopted a clumped, rounded morphology, while those on fibers greater

EBSCOhost - printed on 2/14/2023 1:06 PM via . All use subject to https://www.ebsco.com/terms-of-use

than 800 nm were more spread and anchored which may result in altered interactions with their environment (more cell–cell than cell–substrate) [77]. Integrin–ECM signaling also regulates collective cell migration in pancreas branching during the development and function, which may reveal an important role in future studies [78–80]. Further, integrin signaling mediating traction forces is required for endoderm specification [81].

Decellularized Pancreatic Matrices

Though separating the principal components of the ECM may lead to more cost-effective differentiation techniques, synergistic effects of the matrix may be lost. Decellularized matrix can maximize the differentiation potential resultant from ECM effects. The importance of these cues has prompted some groups to design a bioartificial pancreas and improve islet functionality with decellularized pancreas matrix [82, 83, 84]. Overall, both the biochemical and biophysical cues presented by ECM proteins can facilitate a more mature phenotype, which warrants further inquiry into other microenvironmental stimuli such as the stiffness of the surrounding substrate.

Biophysical Forces Presented Through Culture Substrate Stiffness

Cells interact with their ECM, probing mechanical aspects such as stiffness that contribute largely to numerous cell functions in vivo. For example, MSCs will differentiate into different lineages depending on the stiffness of the culture substrate. More specifically, MSCs cultured on polyacrylamide hydrogels with stiffness values corresponding to that of the brain, bone, and muscle will correspondingly differentiate toward neural, osteogenic, and myogenic lineages, respectively [85]. Stiffness is a fundamental design consideration in material design for cell culture and the key to optimizing pancreatic differentiation may be found in controlling culture substrate stiffness to mimic that of the pancreas. Cells probe the stiffness of their culture substrate by anchoring and pulling on the surface. Through mechanotransduction, these mechanical signals are transmitted through intracellular structures to affect their behavior . The stiffness of the native human pancreas is within the range of $1.4 \pm 2.1 - 4.4 \pm 5.1$ kPa [86]. This is much softer than tissue culture plastic, which has a stiffness of around 3 GPa [87]. The culture of pancreatic progenitors on substrates that are of several orders of magnitude stiffer than the native environment of the pancreas can negatively impact differentiation. Indeed, when human ESCS (hESCs) undergo pancreatic differentiation on relatively softer surfaces, the expression of pancreatic associated markers is increased. This held true at the global level, through changes in bulk stiffness, and also at the local level, by changing the stiffness of nanofibers [88, 89].

EBSCOhost - printed on 2/14/2023 1:06 PM via . All use subject to https://www.ebsco.com/terms-of-use

The bulk stiffness of biomaterials is often modulated by the density of polymer or cross-linking density. Proper controls are required to distinguish if observed effects are simply because of increased attachment of cells because of increased binding ligands. For example, decreased anchorage of keratinocytes to collagen fibers resulted in decreased differentiation irrespective of substrate stiffness [59]. To decouple these mechanisms, deformable pillars can be used to modulate the perceived stiffness while maintaining substrate composition. Specifically, pillars with a high aspect ratio are more flexible and perceived to have a softer apparent modulus while maintaining substrate chemistry. When hESCs undergo differentiation on high aspect ratio pillars, definitive endoderm commitment is improved and resulted in a more cluster-like morphology [90]. Similarly, hESCs encapsulated in a soft 3D alginate matrix were more viable, proliferative, and directed toward pancreatic lineage [91].

The developing embryo is much more complicated and involves dynamic changes in ECM stiffness, architecture, and composition. Optimizing substrates for one stage of differentiation may result in decreasing the differentiation efficiency to a desired lineage downstream. Although high aspect ratio pillars promote definitive endoderm differentiation, pancreatic differentiation is worse compared to flat, tissue culture polystyrene [90]. The system used to study stiffness effects itself must be selected carefully, as each system has its limitations. The classification of "soft" versus "stiff" substrates in relation to the native microenvironment as well as the type of material and ECM coatings used must be kept in mind when comparing different systems. Some of these differences are summarized in Table 10.1. Altogether, these studies demonstrate the need to consider substrate stiffness when optimizing PSC differentiation into pancreatic lineages. In general, increased pancreatic differentiation is observed when cell aggregation is promoted. Therefore, pancreatic differentiation can be improved by controlling both cell–substrate and cell–cell interactions in three-dimensional matrices.

10.2.5 Cell Aggregation and Three-dimensional Cell Culture

Increased cell density may play a key role in pancreatic differentiation. In most protocols, the later stages of directed differentiation involve culturing the PSC-derived cells as aggregates. Typically, aggregation into organoid structures can reveal more realistic drug response, better function in vitro, as well as providing a more realistic 3D environment that better emulates the cell–cell signaling seen in vivo (Figure 10.3) [92, 93]. To provide context, pancreatic development involves a budding step where the epithelium is stratified and protrudes into the surrounding mesenchyme to produce a dense three-dimensional aggregate of cells (Figure 10.2a). Furthermore, in native islets, paracrine signaling is vital for proper cross talk between the various hormonal cells (alpha, beta, delta, and gamma cells) [94]. This cross talk includes synchronized insulin secretion through calcium-driven electrical coupling of cells

EBSCOhost - printed on 2/14/2023 1:06 PM via . All use subject to https://www.ebsco.com/terms-of-use

EBSCOhost - printed on 2/14/2023 1:06 PM via . All use subject to https://www.ebsco.com/terms-of-use

Table 10.1: Comparison of pancreatic differentiation studies from pluripotent stem cells on different substrate platforms.

Author	Cell type	Platform	Condition	ECM coating	Apparent modulus (kPa)	Impact on Differentiation
Sugimoto et al.		Native pancreas			1.4 ± 2.1 – 4.4 ± 5.1	
Electrospinning						
Ghanian et al. [77]	hESCs	poly(ε-caprolactone)	–	Matrigel™	Not reported	hESCs cultured on small diameter nanofibers adopted a clumped morphology and had improved definitive endoderm differentiation.
		Tissue culture polystyrene (control)				
Maldonaldo et al.	iPSCs	Poly(ε-caprolactone)	"Soft"	Col I	20	"Soft" nanofibers promoted posterior foregut and pancreatic differentiation. "Stiff" surfaces promoted mesodermal differentiation while downregulating pancreatic differentiation.
		Polyether–ketone–ketone	Stiff	Col I	300	
		Tissue culture polystyrene (control)		Col I		
Substrate stiffness						
Narayanan et al.	hESCs	Hyaluronic acid hydrogels	Soft	Col IV, fibronectin, laminin	1.3–3.5	Optimal differentiation with 2.1 kPa gels and a 1/3/3 mixture of ColIV, fibronectin, and laminin.
		Tissue culture polystyrene (control)		RIN5F ECM		

(continued)

EBSCOhost - printed on 2/14/2023 1:06 PM via . All use subject to https://www.ebsco.com/terms-of-use

Table 10.1 (continued)

Author	Cell type	Platform	Condition	ECM coating	Apparent modulus (kPa)	Impact on Differentiation
Rasmussen et al. [90]	hESCs	High aspect ratio polycarbonate nanopillars	"Soft"	Fibronectin	34.6	Poor hESC adhesion. "Soft" surfaces promoted endoderm differentiation and rounded morphology. Control had significantly higher pancreatic differentiation compared to test conditions.
		Low aspect ratio polycarbonate nanopillars	Stiff	Fibronectin	2,800	
		Tissue culture polystyrene (control)				
Richardson et al. [91]	hESCs	Low-concentration barium alginate capsules	Soft	N/A	3.9 ± 1.3	"Soft" capsules increase hESC proliferation and supports pancreatic differentiation. Localized ECM deposition in "soft" capsules. "Stiff" capsules support endodermal differentiation but downregulates pancreatic differentiation.
		High-concentration barium alginate capsules	Stiff	N/A	73.2 ± 22.4	

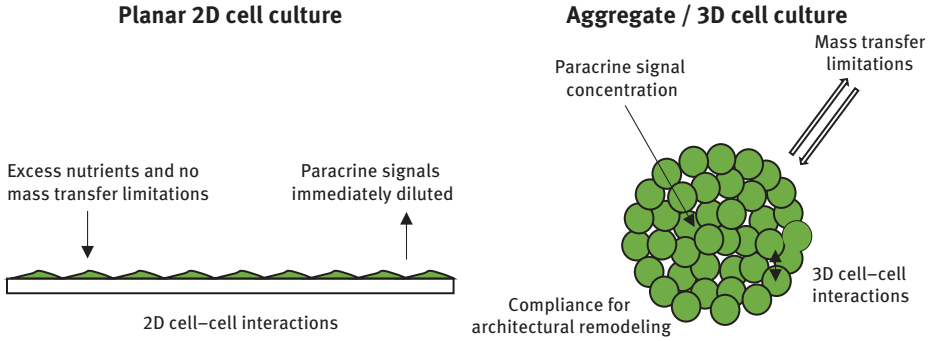

Figure 10.3: Comparison of 2D versus 3D cell culture techniques.

[95]. High initial cell seeding densities promote the differentiation of PSCs into definitive endoderm cells, PP cells, and downstream endocrine lineages including beta cells [96, 97]. The increased differentiation efficiency associated with high cell density may better recapitulate the local cell density in the developing pancreas.

Increase in cell culture density can affect the cell behavior by increasing local concentrations of paracrine or juxtacrine factors [98]. Conventional cell seeding methods produce a nonuniform cell distribution on culture substrates, which results in the stochastic, nonuniform distribution of cell aggregates. The design of novel materials and methods to better control the cell density can play a key role in obtaining consistent differentiation results. For example, uniform, controlled seeding facilitated by an injection molded device, results in the formation of evenly distributed PP aggregates through the culture surface [99].

A common aspect of many 2D in vitro differentiation cultures is the stochastic formation of PP cell clusters [100]. The forced aggregation of PP cells also promotes further differentiation by maximizing the local cell density [101]. Moreover, cell aggregation in high-density culture may lead to changes in the mechanical microenvironment that can also impact differentiation. Native islets are aggregate structures containing mainly beta cells and alpha cells. This knowledge has guided most of the research in the behavior of pancreatic cells in aggregate culture. Aggregation is known to be key for proper functionality and survival of beta cells. In the mouse insulinoma (MIN6) cell line, aggregation increases insulin response to glucose challenges [102]. This is thought to be because of improved paracrine signaling in aggregates. When islet cells are dispersed and reaggregated, they retain glucose responsiveness similar to native islets [103].

Cell aggregation can be done stochastically in stirred bioreactor systems [104, 30] or by culture on nonadhesive surface to allow self-organization [102]. These approaches typically create nonuniform aggregate sizes, which can lead to significant variation in the produced cells. The size of these aggregates plays an important role in their viability and function. Increasing aggregate size can lead

EBSCOhost - printed on 2/14/2023 1:06 PM via . All use subject to https://www.ebsco.com/terms-of-use

to mass transport limitations and potentially core necrosis in cell types with high metabolic demands such as islets [105, 106]. The average diameter of islets is around 100–200 μm [107, 108] and when reaggregated, the optimal diameter to maintain viability and function was 100–150 μm [103]. Proper design of devices to uniformly aggregate cells in a scalable matter may be the key to producing mature cells for cell therapies. Agarose microwells [103] or pyramid-shaped polystyrene wells [109] have been used to generate cell aggregates of controlled size. However, scaling these technologies to therapeutic doses (500,000 ~ 1 million IE/patient) has not yet been demonstrated.

10.2.6 Spatial Confinement of Stem Cells

Though more physiologically and clinically relevant, 3D models are laced with increased complexity. One factor not previously discussed is cell shape, which varies depending on the cell type, culture substrate, and health. The shape of a cell can determine the proliferation, differentiation, and function of cells through mechanotransduction mechanisms [110–112]. To delineate effects of cell shape, paracrine factor gradients or cell–cell interactions, micropatterned substrates where cells are selectively confined within relevant geometries are used. For example, when cultured in selectively adhesive substrates, MSCs will preferentially differentiate into osteoblasts in areas of high tension and into adipocytes in areas of low tension. On the larger scale, MSCs cultured in shapes with concave edges and sharp points preferentially differentiated into osteoblasts, while shapes with large convex edges were more conducive to adipocyte specification [113]. By changing the cell geometry, these effects were revealed to be because of cellular tension and independent of cell number [114]. The role of geometric confinement and endogenous tension in guiding progenitor cells is an active area of investigation. During early embryogenesis, the presence of differential forces is key in spatial patterning of the three germ layers [115, 116]. When ESCs are cultured in circular micropatterns, the expression levels of pluripotency markers are increased at the edge of the patterns. When these confined cells were presented with BMP4, which is greatly involved in early embryonic signaling [117], spatial patterning of the germ layers was observed. In circular patterns, trophectoderm markers were upregulated near the edge, followed by endoderm, mesoderm, and ectoderm markers in the center [118]. Moreover, hESCs cultured on micropatterned Matrigel™ islands will preferentially differentiate into definitive endoderm cells in smaller diameter patterns but mesoderm cells in larger diameter patterns [119]. Limited work has been done in this regard with respect to pancreas and diabetes. However, previous findings from controlling cell shape to controlling differentiation suggest that this may also play a role in specifying pancreatic differentiation.

EBSCOhost - printed on 2/14/2023 1:06 PM via . All use subject to https://www.ebsco.com/terms-of-use

Micropatterned cell culture is a facile method to control cell shape to delineate confounding cell–cell and cell–substrate interactions.

10.3 Conclusions and Perspectives

Significant advances have been made in directed differentiation protocols by solely manipulating cell signaling through timed addition of soluble factors and small molecules . These protocols have the potential to be improved by introducing and emulating other aspects of the cellular microenvironment during development. Biomechanical stimuli provided by surrounding ECM, cells, and tissues may act synergistically with soluble factors in guiding stem cell fate decisions. Recent work has tried to delineate various aspects of the microenvironment of the developing pancreas to improve differentiation into pancreatic cells as summarized in Figure 10.4. Although the initial stages of pancreatic differentiation are relatively well understood, later in vitro differentiation stages remain less robust and efficient. A comprehensive understanding of human pancreatic development and differentiation will help produce functional insulin-secreting beta cells for cell therapies. To accomplish this, a multifaceted, interdisciplinary approach is required to (1) design platforms to mimic pancreas development and study developmental biology in vitro, and (2) design and optimize novel substrates to guide pancreatic differentiation.

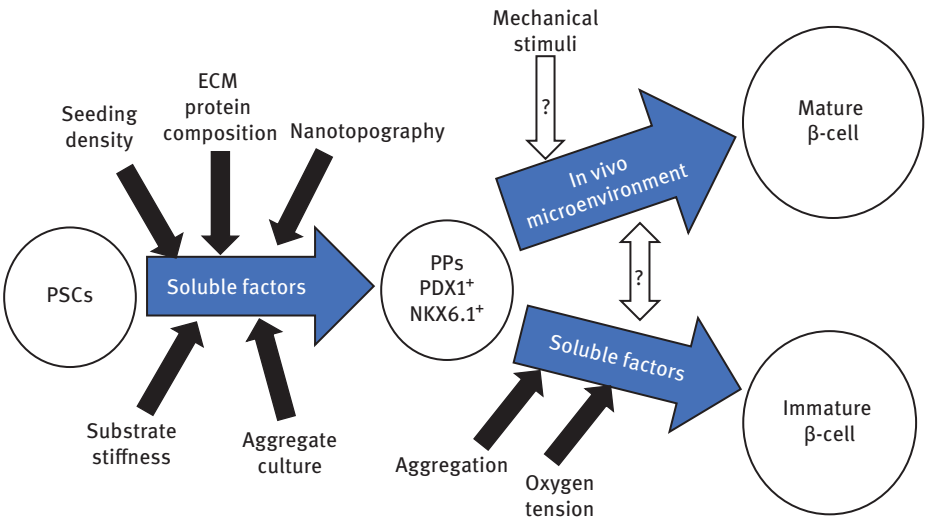

Figure 10.4: Summary of microenvironmental factors known to affect pancreatic differentiation.

The development of tailored functional materials will likely play a key role in the production of safe and abundant cells for therapeutic use. Moreover, functional

EBSCOhost - printed on 2/14/2023 1:06 PM via . All use subject to https://www.ebsco.com/terms-of-use

materials can be developed to tackle other limitations of cell therapies, such as the engineering of devices or delivery vehicles for transplantations. Utilizing advanced materials to investigate cell–surface interactions can help to optimize existing cell production protocols by precisely guiding the cell behavior. Combining soluble factors with tailored materials to guide cell differentiation may be much economical compared to differentiation strategies solely using soluble factors. After the cells are produced, transplantation devices or biomaterials must then be engineered to administer the cells and provide a suitable local environment shortly after implantation. Proper design of these materials should allow long-term therapeutic cell retention and function in vivo. In most cases, where long-term cell retention is needed, strategies must be developed to protect the generated cells from the immune response. This can be done by cell encapsulation with immunoisolating materials or by materials that facilitate controlled release of immunomodulating factors. Furthermore, additional design may be required to ensure long-term viability and function of the transplanted cells in a non-vascularized environment. This entails the engineering of devices or materials containing or promoting the formation of blood vessels. The design of advanced materials has many applications in advancing cell therapies toward the market. Furthermore, knowledge gained from these research areas may reveal novel insights into drug testing or other fundamental studies.

References

[1] Li, D., Zhou, J., Chowdhury, F., Cheng, J., Wang, N., and Wang, F. (2011). Role of mechanical factors in fate decisions of stem cells. Regen. Med. *6*, 229–240.

[2] Lutolf, M.P., Gilbert, P.M., and Blau, H.M. (2009). Designing materials to direct stem-cell fate. Nature *462*, 433.

[3] Shao, Y., Sang, J., and Fu, J. (2015). On human pluripotent stem cell control: The rise of 3D bioengineering and mechanobiology. Biomaterials *52*, 26–43.

[4] DeFronzo, R.A., Ferrannini, E., Groop, L., Henry, R.R., Herman, W.H., Holst, J.J., Hu, F.B., Kahn, C.R., Raz, I., Shulman, G.I., et al. (2015). Type 2 diabetes mellitus. Nature Reviews Disease Primers *1*, 15019. https://www.nature.com/articles/nrdp201519

[5] Katsarou, A., Gudbjörnsdottir, S., Rawshani, A., Dabelea, D., Bonifacio, E., Anderson, B. J., Jacobsen, L.M., Schatz, D.A., and Lernmark, Å. (2017). Type 1 diabetes mellitus. *3*, 17016.

[6] You, W.-P., and Henneberg, M. (2016). Type 1 diabetes prevalence increasing globally and regionally: the role of natural selection and life expectancy at birth. BMJ Open Diabetes Res. Amp Care. *4*. 1–7.

[7] Kemp, C.B., Knight, M.J., Scharp, D.W., Lucy, P.E., and Ballinger, W.F. (1973). Transplantation of isolated pancreatic islets into the portal vein of diabetic rats. Nature *244*, 447–447.

[8] Scharp, D.W., Murphy, J.J., Newton, W.T., Ballinger, W.F., and Lacy, P.E. (1975). Transplantation of islets of Langerhans in diabetic rhesus monkeys. Surgery *77*, 100–105.

[9] Shapiro, A.M.J., Lakey, J.R.T., Ryan, E.A., Korbutt, G.S., Toth, E., Warnock, G.L., Kneteman, N.M., and Rajotte, R.V. (2000). Islet transplantation in seven patients with type 1 diabetes mellitus using a glucocorticoid-free immunosuppressive regimen. N. Engl. J. Med. *343*, 230–238.

EBSCOhost - printed on 2/14/2023 1:06 PM via . All use subject to https://www.ebsco.com/terms-of-use

[10] Bruni, A., Gala-Lopez, B., Pepper, A.R., Abualhassan, N.S., and Shapiro, A.J. (2014). Islet cell transplantation for the treatment of type 1 diabetes: recent advances and future challenges. Diabetes Metab. Syndr. Obes. Targets Ther. *7*, 211–223.
[11] Shapiro, A.M.J., Pokrywczynska, M., and Ricordi, C. (2017). Clinical pancreatic islet transplantation. Nat Rev Endocrinol *13*, 268–277.
[12] Hoesli, C.A., Kiang, R.L.J., Mocinecová, D., Speck, M., Mošková, D.J., Donald-Hague, C., Lacík, I., Kieffer, T.J., and Piret, J.M. (2012). Reversal of diabetes by βTC3 cells encapsulated in alginate beads generated by emulsion and internal gelation. J. Biomed. Mater. Res. B Appl. Biomater. *100B*, 1017–1028.
[13] Lim, F., and Sun, A. (1980). Microencapsulated islets as bioartificial endocrine pancreas. Science *210*, 908.
[14] Scharp, D.W., and Marchetti, P. (2014). Encapsulated islets for diabetes therapy: History, current progress, and critical issues requiring solution. Cell Encapsulation Drug Deliv. *67*, 35–73.
[15] Daoud, J., Rosenberg, L., and Tabrizian, M. (2010). Pancreatic islet culture and preservation strategies: Advances, challenges, and future outlook. Cell Transplant. *19*, 1523–1535.
[16] Lehmann, R., Zuellig, R.A., Kugelmeier, P., Baenninger, P.B., Moritz, W., Perren, A., Clavien, P.-A., Weber, M., and Spinas, G.A. (2007). Superiority of small islets in human islet transplantation. Diabetes *56*, 594.
[17] Wesselschmidt, R.L. (2011). The Teratoma Assay: An In Vivo Assessment of Pluripotency. In Human Pluripotent Stem Cells: Methods and Protocols, P.H. Schwartz, and R.L. Wesselschmidt, eds. (Totowa, NJ: Humana Press), pp. 231–241.
[18] Thomson, J.A., Itskovitz-Eldor, J., Shapiro, S.S., Waknitz, M.A., Swiergiel, J.J., Marshall, V.S., and Jones, J.M. (1998). Embryonic stem cell lines derived from human blastocysts. Science *282*, 1145.
[19] Takahashi, K., and Yamanaka, S. (2006). Induction of pluripotent stem cells from mouse embryonic and adult fibroblast cultures by defined factors. Cell *126*, 663–676.
[20] Takahashi, K., Tanabe, K., Ohnuki, M., Narita, M., Ichisaka, T., Tomoda, K., and Yamanaka, S. (2007). Induction of pluripotent stem cells from adult human fibroblasts by defined factors. Cell *131*, 861–872.
[21] Huangfu, D., Osafune, K., Maehr, R., Guo, W., Eijkelenboom, A., Chen, S., Muhlestein, W., and Melton, D.A. (2008). Induction of pluripotent stem cells from primary human fibroblasts with only Oct4 and Sox2. Nat Biotech *26*, 1269–1275.
[22] Subramanyam, D., Lamouille, S., Judson, R.L., Liu, J.Y., Bucay, N., Derynck, R., and Blelloch, R. (2011). Multiple targets of miR-302 and miR-372 promote reprogramming of human fibroblasts to induced pluripotent stem cells. Nat Biotech *29*, 443–448.
[23] Kim, D., Kim, C.-H., Moon, J.-I., Chung, Y.-G., Chang, M.-Y., Han, B.-S., Ko, S., Yang, E., Cha, K.Y., Lanza, R., et al. (2009). Generation of human induced pluripotent stem cells by direct delivery of reprogramming proteins. Cell Stem Cell *4*, 472–476.
[24] Malik, N., and Rao, M.S. (2013). A review of the methods for human ipsc derivation. Methods Mol. Biol. Clifton NJ *997*, 23–33.
[25] Agulnick, A.D., Ambruzs, D.M., Moorman, M.A., Bhoumik, A., Cesario, R.M., Payne, J.K., Kelly, J.R., Haakmeester, C., Srijemac, R., Wilson, A.Z., et al. (2015). Insulin-producing endocrine cells differentiated in vitro from human embryonic stem cells function in macroencapsulation devices in vivo. Stem Cells Transl. Med. *4*, 1214–1222.
[26] Discher, D.E., Mooney, D.J., and Zandstra, P.W. (2009). Growth factors, matrices, and forces combine and control stem cells. Science *324*, 1673.
[27] Assady, S., Maor, G., Amit, M., Itskovitz-Eldor, J., Skorecki, K.L., and Tzukerman, M. (2001). Insulin production by human embryonic stem cells. Diabetes *50*, 1691.

EBSCOhost - printed on 2/14/2023 1:06 PM via . All use subject to https://www.ebsco.com/terms-of-use

[28] Jacobson, L., Kahan, B., Djamali, A., Thomson, J., and Odorico, J. (2001). Differentiation of endoderm derivatives, pancreas and intestine, from rhesus embryonic stem cells. Transplant. Proc. *33*, 674.
[29] Bose, B., Shenoy, S.P., Konda, S., and Wangikar, P. (2012). Human embryonic stem cell differentiation into insulin secreting β-cells for diabetes. Cell Biol. Int. *36*, 1013–1020.
[30] Pagliuca, F.W., Millman, J.R., Gürtler, M., Segel, M., Van Dervort, A., Ryu, J.H., Peterson, Q.P., Greiner, D., and Melton, D.A. (2014). Generation of functional human pancreatic β cells in vitro. Cell *159*, 428–439.
[31] Rezania, A., Bruin, J.E., Arora, P., Rubin, A., Batushansky, I., Asadi, A., O'Dwyer, S., Quiskamp, N., Mojibian, M., Albrecht, T., et al. (2014). Reversal of diabetes with insulin-producing cells derived in vitro from human pluripotent stem cells. Nat Biotech *32*, 1121–1133.
[32] Russ, H.A., Parent, A.V., Ringler, J.J., Hennings, T.G., Nair, G.G., Shveygert, M., Guo, T., Puri, S., Haataja, L., Cirulli, V., et al. (2015). Controlled induction of human pancreatic progenitors produces functional beta-like cells in vitro. Embro J. *34*, 1759–1772.
[33] Offield, M.F., Jetton, T.L., Labosky, P.A., Ray, M., Stein, R.W., Magnuson, M.A., Hogan, B.L., and Wright, C.V. (1996). PDX-1 is required for pancreatic outgrowth and differentiation of the rostral duodenum. Development *122*, 983.
[34] Schaffer, A.E., Taylor, B.L., Benthuysen, J.R., Liu, J., Thorel, F., Yuan, W., Jiao, Y., Kaestner, K.H., Herrera, P.L., Magnuson, M.A., et al. (2013). Nkx6.1 controls a gene regulatory network required for establishing and maintaining pancreatic beta cell identity. PLOS Genet. *9*, e1003274.
[35] Nostro, M.C., Sarangi, F., Ogawa, S., Holtzinger, A., Corneo, B., Li, X., Micallef, S.J., Park, I.-H., Basford, C., Wheeler, M.B., et al. (2011). Stage-specific signaling through TGFβ family members and WNT regulates patterning and pancreatic specification of human pluripotent stem cells. Development *138*, 861.
[36] Jaramillo, M., Mathew, S., Task, K., Barner, S., and Banerjee, I. (2014). Potential for Pancreatic maturation of differentiating human embryonic stem cells is sensitive to the specific pathway of definitive endoderm commitment. PLOS One *9*, e94307.
[37] Abdelalim, E.M., and Emara, M.M. (2015). Advances and challenges in the differentiation of pluripotent stem cells into pancreatic β cells. World J. Stem Cells *7*, 174–181.
[38] Kroon, E., Martinson, L.A., Kadoya, K., Bang, A.G., Kelly, O.G., Eliazer, S., Young, H., Richardson, M., Smart, N.G., Cunningham, J., et al. (2008). Pancreatic endoderm derived from human embryonic stem cells generates glucose-responsive insulin-secreting cells in vivo. Nat Biotech *26*, 443–452.
[39] Rezania, A., Bruin, J.E., Riedel, M.J., Mojibian, M., Asadi, A., Xu, J., Gauvin, R., Narayan, K., Karanu, F., O'Neil, J.J., et al. (2012). Maturation of Human Embryonic Stem Cell–Derived Pancreatic Progenitors Into Functional Islets Capable of Treating Pre-existing Diabetes in Mice. Diabetes *61*, 2016–2029.
[40] Hrvatin, S., O'Donnell, C.W., Deng, F., Millman, J.R., Pagliuca, F.W., DiIorio, P., Rezania, A., Gifford, D.K., and Melton, D.A. (2014). Differentiated human stem cells resemble fetal, not adult, β cells. Proc. Natl. Acad. Sci. U. S. A. *111*, 3038–3043.
[41] Kattman, S.J., Witty, A.D., Gagliardi, M., Dubois, N.C., Niapour, M., Hotta, A., Ellis, J., and Keller, G. (2011). Stage-Specific optimization of Activin/Nodal and BMP signaling promotes cardiac differentiation of mouse and human pluripotent stem cell lines. Cell Stem Cell *8*, 228–240.
[42] Cai, J., Zhao, Y., Liu, Y., Ye, F., Song, Z., Qin, H., Meng, S., Chen, Y., Zhou, R., Song, X., et al. (2007). Directed differentiation of human embryonic stem cells into functional hepatic cells. Hepatology *45*, 1229–1239.

EBSCOhost - printed on 2/14/2023 1:06 PM via . All use subject to https://www.ebsco.com/terms-of-use

[43] Xia, Y., Nivet, E., Sancho-Martinez, I., Gallegos, T., Suzuki, K., Okamura, D., Wu, M.-Z., Dubova, I., Esteban, C.R., Montserrat, N., et al. (2013). Directed differentiation of human pluripotent cells to ureteric bud kidney progenitor-like cells. Nat Cell Biol *15*, 1507–1515.
[44] Wong, A.P., Bear, C.E., Chin, S., Pasceri, P., Thompson, T.O., Huan, L.-J., Ratjen, F., Ellis, J., and Rossant, J. (2012). Directed differentiation of human pluripotent stem cells into mature airway epithelia expressing functional CFTR protein. Nat. Biotechnol. *30*, 876–882.
[45] Xiao, Y., Zhang, B., Liu, H., Miklas, J.W., Gagliardi, M., Pahnke, A., Thavandiran, N., Sun, Y., Simmons, C., Keller, G., et al. (2014). Microfabricated perfusable cardiac biowire: a platform that mimics native cardiac bundle. Lab. Chip *14*, 869–882.
[46] Ruan, J.-L., Tulloch, N.L., Saiget, M., Paige, S.L., Razumova, M.V., Regnier, M., Tung, K.C., Keller, G., Pabon, L., Reinecke, H., et al. (2015). Mechanical stress promotes maturation of human myocardium from pluripotent stem cell-derived progenitors. Stem Cells *33*, 2148–2157.
[47] Eng, G., Lee, B.W., Protas, L., Gagliardi, M., Brown, K., Kass, R.S., Keller, G., Robinson, R.B., and Vunjak-Novakovic, G. (2016). Autonomous beating rate adaptation in human stem cell-derived cardiomyocytes. *7*, 10312.
[48] Mihic, A., Li, J., Miyagi, Y., Gagliardi, M., Li, S.-H., Zu, J., Weisel, R.D., Keller, G., and Li, R.-K. (2014). The effect of cyclic stretch on maturation and 3D tissue formation of human embryonic stem cell-derived cardiomyocytes. Biomaterials *35*, 2798–2808.
[49] Amano, Y., Nishiguchi, A., Matsusaki, M., Iseoka, H., Miyagawa, S., Sawa, Y., Seo, M., Yamaguchi, T., and Akashi, M. (2016). Development of vascularized iPSC derived 3D-cardiomyocyte tissues by filtration Layer-by-Layer technique and their application for pharmaceutical assays. Acta Biomater. *33*, 110–121.
[50] Heinis, M., Simon, M.-T., Ilc, K., Mazure, N.M., Pouysségur, J., Scharfmann, R., and Duvillié, B. (2010). Oxygen tension regulates pancreatic β-cell differentiation through hypoxia-inducible factor 1α. Diabetes *59*, 662–669.
[51] Schulz, T.C., Young, H.Y., Agulnick, A.D., Babin, M.J., Baetge, E.E., Bang, A.G., Bhoumik, A., Cepa, I., Cesario, R.M., Haakmeester, C., et al. (2012). A scalable system for production of functional pancreatic progenitors from human embryonic stem cells. Plos One *7*, e37004.
[52] Heisenberg, C.-P., and Bellaïche, Y. (2013). Forces in tissue morphogenesis and patterning. Cell *153*, 948–962.
[53] Thompson, D.W. (1942). On Growth and Form. Camb. Univ Press. Cambridge, England. *1*, 7.
[54] Mammoto, T., and Ingber, D.E. (2010). Mechanical control of tissue and organ development. Dev. Camb. Engl. *137*, 1407–1420.
[55] Wang, N., Tytell, J.D., and Ingber, D.E. (2009). Mechanotransduction at a distance: mechanically coupling the extracellular matrix with the nucleus. Nat Rev Mol Cell Biol *10*, 75–82.
[56] Nakayama, K.H., Hou, L., and Huang, N.F. (2014). Role of extracellular matrix signaling cues in modulating cell fate commitment for cardiovascular tissue engineering. Adv. Healthc. Mater. *3*, 628–641.
[57] Rozario, T., and DeSimone, D.W. (2010). The Extracellular Matrix In Development and Morphogenesis: A Dynamic View. Dev. Biol. *341*, 126–140.
[58] Weber, L.M., and Anseth, K.S. (2008). Hydrogel encapsulation environments functionalized with extracellular matrix interactions increase islet insulin secretion. Matrix Biol. *27*, 667–673.
[59] Trappmann, B., Gautrot, J.E., Connelly, J.T., Strange, D.G.T., Li, Y., Oyen, M.L., Cohen Stuart, M.A., Boehm, H., Li, B., Vogel, V., et al. (2012). Nature Materials: Extracellular-matrix tethering regulates stem-cell fate. Nature Materials *11*, 642–649.
[60] Hwang, N.S., Varghese, S., Li, H., and Elisseeff, J. (2011). Regulation of osteogenic and chondrogenic differentiation of mesenchymal stem cells in PEG-ECM hydrogels. Cell Tissue Res. *344*, 499–509.

EBSCOhost - printed on 2/14/2023 1:06 PM via . All use subject to https://www.ebsco.com/terms-of-use

[61] Alberti, K., Davey, R.E., Onishi, K., George, S., Salchert, K., Seib, F.P., Bornhauser, M., Pompe, T., Nagy, A., Werner, C., et al. (2008). Functional immobilization of signaling proteins enables control of stem cell fate. Nat Meth *5*, 645–650.

[62] Flaim, C.J., Chien, S., and Bhatia, S.N. (2005). An extracellular matrix microarray for probing cellular differentiation. Nat. Methods *2*, 119.

[63] Guilak, F., Cohen, D.M., Estes, B.T., Gimble, J.M., Liedtke, W., and Chen, C.S. (2009). Control of stem cell fate by physical interactions with the extracellular matrix. Cell Stem Cell *5*, 17–26.

[64] LaBarge, M.A., Nelson, C.M., Villadsen, R., Fridriksdottir, A., Ruth, J.R., Stampfer, M.R., Petersen, O.W., and Bissell, M.J. (2009). Human mammary progenitor cell fate decisions are products of interactions with combinatorial microenvironments. Integr. Biol. *1*, 70–79.

[65] Rasmussen, C.H., Petersen, D.R., Moeller, J.B., Hansson, M., and Dufva, M. (2016a). Collagen type I Improves the differentiation of human embryonic stem cells towards definitive endoderm. PLOS ONE *10*, e0145389.

[66] Taylor-Weiner, H., Schwarzbauer, J.E., and Engler, A.J. (2013). Defined extracellular matrix components are necessary for definitive endoderm induction. STEM CELLS *31*, 2084–2094.

[67] Stendahl, J.C., Kaufman, D.B., and Stupp, S.I. (2009). Extracellular matrix in pancreatic islets: Relevance to scaffold design and transplantation. Cell Transplant. *18*, 1–12.

[68] Malta, D.F.B., Reticker-Flynn, N.E., da Silva, C.L., Cabral, J.M.S., Fleming, H.E., Zaret, K.S., Bhatia, S.N., and Underhill, G.H. (2016). Extracellular matrix microarrays to study inductive signaling for endoderm specification. High Throughput Approaches Screen. Biomater. *34*, 30–40.

[69] Narayanan, K., Lim, V.Y., Shen, J., Tan, Z.W., Rajendran, D., Luo, S.-C., Gao, S., Wan, A.C.A., and Ying, J.Y. (2013a). Extracellular matrix-mediated differentiation of human embryonic stem cells: Differentiation to insulin-secreting beta cells. Tissue Eng. Part A *20*, 424–433.

[70] Brafman, D.A., Phung, C., Kumar, N., and Willert, K. (2013). Regulation of endodermal differentiation of human embryonic stem cells through integrin-ECM interactions. Cell Death Differ *20*, 369–381.

[71] Wang, H., Abhilash, A., Chen, C.S., Wells, R.G., and Shenoy, V.B. (2014). Long-range force transmission in fibrous matrices enabled by tension-driven alignment of fibers. Biophys. J. *107*, 2592–2603.

[72] D'Angelo, F., Tiribuzi, R., Armentano, I., Kenny, J.M., Martino, S., and Orlacchio, A. (2011). Mechanotransduction: Tuning stem cells fate. J. Funct. Biomater. *2*, 67–87.

[73] Fujita, S., Shimizu, H., and Suye, S. (2012). Control of differentiation of human mesenchymal stem cells by altering the geometry of nanofibers. J. Nanotechnol. *2012*.

[74] Kim, J., Kim, H.N., Lim, K.-T., Kim, Y., Seonwoo, H., Park, S.H., Lim, H.J., Kim, D.-H., Suh, K.-Y., Choung, P.-H., et al. (2013). Designing nanotopographical density of extracellular matrix for controlled morphology and function of human mesenchymal stem cells. *3*, 3552.

[75] Luo, Y., Shen, H., Fang, Y., Cao, Y., Huang, J., Zhang, M., Dai, J., Shi, X., and Zhang, Z. (2015). Enhanced proliferation and osteogenic differentiation of mesenchymal stem cells on graphene oxide-incorporated electrospun poly(lactic-co-glycolic acid) nanofibrous mats. ACS Appl. Mater. Interfaces *7*, 6331–6339.

[76] Xin, X., Hussain, M., and Mao, J.J. (2007). Continuing differentiation of human mesenchymal stem cells and induced chondrogenic and osteogenic lineages in electrospun PLGA nanofiber scaffold. Biomaterials *28*, 316–325.

[77] Ghanian, M.H., Farzaneh, Z., Barzin, J., Zandi, M., Kazemi-Ashtiani, M., Alikhani, M., Ehsani, M., and Baharvand, H. (2015). Nanotopographical control of human embryonic stem cell differentiation into definitive endoderm. J. Biomed. Mater. Res. A *103*, 3539–3553.

[78] Hammar, E., Parnaud, G., Bosco, D., Perriraz, N., Maedler, K., Donath, M., Rouiller, D.G., and Halban, P.A. (2004). Extracellular matrix protects pancreatic β-cells against apoptosis. Diabetes *53*, 2034.

EBSCOhost - printed on 2/14/2023 1:06 PM via . All use subject to https://www.ebsco.com/terms-of-use

[79] Shih, H.P., Panlasigui, D., Cirulli, V., and Sander, M. (2016). ECM signaling regulates collective cellular dynamics to control pancreas branching morphogenesis. Cell Rep. *14*, 169–179.
[80] Wang, R., and Rosenberg, L. (1999). Maintenance of beta-cell function and survival following islet isolation requires re-establishment of the islet-matrix relationship. J. Endocrinol. *163*, 181–190.
[81] Taylor-Weiner, H., Ravi, N., and Engler, A.J. (2015). Traction forces mediated by integrin signaling are necessary for definitive endoderm specification. J. Cell Sci. *128*, 1961.
[82] Goh, S.-K., Bertera, S., Olsen, P., Candiello, J., Halfter, W., Uechi, G., Balasubramani, M., Johnson, S., Sicari, B., Kollar, E., et al. (2013). Perfusion-decellularized pancreas as a natural 3D scaffold for pancreatic tissue and whole organ engineering. Biomaterials *34*, 6760–6772.
[83] Guruswamy Damodaran, R., and Vermette, P. (2018). Decellularized pancreas as a native extracellular matrix scaffold for pancreatic islet seeding and culture. J. Tissue Eng. Regen. Med. *0*, 1–8.
[84] Salvatori, M., Katari, R., Patel, T., Peloso, A., Mugweru, J., Owusu, K., and Orlando, G. (2014). Extracellular matrix scaffold technology for bioartificial pancreas engineering: State of the art and future challenges. J. Diabetes Sci. Technol. *8*, 159–169.
[85] Engler, A.J., Sen, S., Sweeney, H.L., and Discher, D.E. (2006). Matrix elasticity directs stem cell lineage specification. Cell *126*, 677–689.
[86] Sugimoto, M., Takahashi, S., Kojima, M., Gotohda, N., Kato, Y., Kawano, S., Ochiai, A., and Konishi, M. (2014). What is the nature of pancreatic consistency? Assessment of the elastic modulus of the pancreas and comparison with tactile sensation, histology, and occurrence of postoperative pancreatic fistula after pancreaticoduodenectomy. Surg. U. S. *156*, 1204–1211.
[87] Gilbert, P.M., Havenstrite, K.L., Magnusson, K.E.G., Sacco, A., Leonardi, N.A., Kraft, P., Nguyen, N.K., Thrun, S., Lutolf, M.P., and Blau, H.M. (2010). Substrate elasticity regulates skeletal muscle stem cell self-renewal in culture. Science *329*, 1078.
[88] Narayanan, K., Lim, V.Y., Shen, J., Tan, Z.W., Rajendran, D., Luo, S.-C., Gao, S., Wan, A.C.A., and Ying, J.Y. (2013). Extracellular Matrix-Mediated Differentiation of Human Embryonic Stem Cells: Differentiation to Insulin-Secreting Beta Cells. Tissue Eng. Part A 20, 424–433.
[89] Maldonado, M., Luu, R.J., Ico, G., Ospina, A., Myung, D., Shih, H.P., and Nam, J. (2017). Lineage- and developmental stage-specific mechanomodulation of induced pluripotent stem cell differentiation. Stem Cell Res. Ther. *8*, 216.
[90] Rasmussen, C.H., Reynolds, P.M., Petersen, D.R., Hansson, M., McMeeking, R.M., Dufva, M., and Gadegaard, N. (2016b). Enhanced Differentiation of Human Embryonic Stem Cells Toward Definitive Endoderm on Ultrahigh Aspect Ratio Nanopillars. Adv. Funct. Mater. *26*, 815–823.
[91] Richardson, T., Barner, S., Candiello, J., Kumta, P.N., and Banerjee, I. (2016). Capsule stiffness regulates the efficiency of pancreatic differentiation of human embryonic stem cells. Acta Biomater. *35*, 153–165.
[92] Antoni, D., Burckel, H., Josset, E., and Noel, G. (2015). Three-dimensional cell culture: A breakthrough in vivo. Int. J. Mol. Sci. *16*, 5517–5527.
[93] Hohwieler, M., Illing, A., Hermann, P.C., Mayer, T., Stockmann, M., Perkhofer, L., Eiseler, T., Antony, J.S., Müller, M., Renz, S., et al. (2017). Human pluripotent stem cell-derived acinar/ductal organoids generate human pancreas upon orthotopic transplantation and allow disease modelling. Gut *66*, 473.
[94] Caicedo, A. (2013). Paracrine and autocrine interactions in the human islet : More than meets the eye. Semin. Cell Dev. Biol. *24*, 11–21.
[95] Pedersen, M.G., Bertram, R., and Sherman, A. (2005). Intra- and inter-islet synchronization of metabolically driven insulin secretion. Biophys. J. *89*, 107–119.

EBSCOhost - printed on 2/14/2023 1:06 PM via . All use subject to https://www.ebsco.com/terms-of-use

[96] Gage, B.K., Webber, T.D., and Kieffer, T.J. (2013). Initial cell seeding density influences pancreatic endocrine development during in vitro differentiation of human embryonic stem cells. PLOS One *8*, e82076.
[97] Takizawa-Shirasawa, S., Yoshie, S., Yue, F., Mogi, A., Yokoyama, T., Tomotsune, D., and Sasaki, K. (2013). FGF7 and cell density are required for final differentiation of pancreatic amylase-positive cells from human ES cells. Cell Tissue Res. *354*, 751–759.
[98] Blagovic, K., Gong, E.S., Milano, D.F., Natividad, R.J., and Asthagiri, A.R. (2013). Engineering Cell-Cell Signaling. Curr. Opin. Biotechnol. *24*, 940–947.
[99] Rasmussen, C.H., and Rønn Petersen, D. (2016). Manipulation of the extracellular microenvironment by micro- and nanotechnology approaches to improve the generation of pancreatic endocrine cells from human embryonic stem cells (DTU Nanotech). http://orbit.dtu.dk/en/publications/manipulation-of-the-extracellular-microenvironment-by-micro-and-nanotechnology-approaches-to-improve-the-generation-of-pancreatic-endocrine-cells-from-human-embryonic-stem-cells(7cd5163f-c12c-4f74-a53d-139f3012d727).html
[100] Nostro, M.C., Sarangi, F., Yang, C., Holland, A., Elefanty, A.G., Stanley, E.G., Greiner, D.L., and Keller, G. (2015). Efficient generation of NKX6-1(+) pancreatic progenitors from multiple human pluripotent stem cell lines. Stem Cell Rep. *4*, 591–604.
[101] Toyoda, T., Mae, S.-I., Tanaka, H., Kondo, Y., Funato, M., Hosokawa, Y., Sudo, T., Kawaguchi, Y., and Osafune, K. (2015). Cell aggregation optimizes the differentiation of human ESCs and iPSCs into pancreatic bud-like progenitor cells. Stem Cell Res. *14*, 185–197.
[102] Chowdhury, A., Dyachok, O., Tengholm, A., Sandler, S., and Bergsten, P. (2013). Functional differences between aggregated and dispersed insulin-producing cells. Diabetologia *56*, 1557–1568.
[103] Hilderink, J., Spijker, S., Carlotti, F., Lange, L., Engelse, M., van Blitterswijk, C., de Koning, E., Karperien, M., and van Apeldoorn, A. (2015). Controlled aggregation of primary human pancreatic islet cells leads to glucose-responsive pseudoislets comparable to native islets. J. Cell. Mol. Med. *19*, 1836–1846.
[104] Mihara, Y., Matsuura, K., Sakamoto, Y., Okano, T., Kokudo, N., and Shimizu, T. (2017). Production of pancreatic progenitor cells from human induced pluripotent stem cells using a three-dimensional suspension bioreactor system. J. Tissue Eng. Regen. Med. n/a-n/a.
[105] Avgoustiniatos, E.S., and Colton, C.K. (2006). Effect of external oxygen mass transfer resistances on viability of immunoisolated tissuea. Ann. N. Y. Acad. Sci. *831*, 145–166.
[106] Komatsu, H., Cook, C., Wang, C.-H., Medrano, L., Lin, H., Kandeel, F., Tai, Y.-C., and Mullen, Y. (2017). Oxygen environment and islet size are the primary limiting factors of isolated pancreatic islet survival. PLOS One *12*, e0183780.
[107] Hellman, B. (1959). Actual distribution of the number and volume of the islets of Langerhans in different size classes in non-diabetic humans of varying ages. Nature *184*, 1498–1499.
[108] Ionescu-Tirgoviste, C., Gagniuc, P.A., Gubceac, E., Mardare, L., Popescu, I., Dima, S., and Militaru, M. (2015). A 3D map of the islet routes throughout the healthy human pancreas. Sci. Rep. *5*, 14634.
[109] Ungrin MD, Joshi C, Nica A, Bauwens C, Zandstra PW (2008) Reproducible, Ultra High-Throughput Formation of Multicellular Organization from Single Cell Suspension-Derived Human Embryonic Stem Cell Aggregates. PLOS ONE 3(2): e1565. https://doi.org/10.1371/journal.pone.0001565
[110] Chen, C.S., Mrksich, M., Huang, S., Whitesides, G.M., and Ingber, D.E. (1997). Geometric control of cell life and death. Science *276*, 1425.
[111] Ingber, D.E. (1990). Fibronectin controls capillary endothelial cell growth by modulating cell shape. Proc. Natl. Acad. Sci. *87*, 3579.

EBSCOhost - printed on 2/14/2023 1:06 PM via . All use subject to https://www.ebsco.com/terms-of-use

[112] Théry, M. (2010). Micropatterning as a tool to decipher cell morphogenesis and functions. J. Cell Sci. *123*, 4201.
[113] Kilian, K.A., Bugarija, B., Lahn, B.T., and Mrksich, M. (2010). Geometric cues for directing the differentiation of mesenchymal stem cells. Proc. Natl. Acad. Sci. *107*, 4872–4877.
[114] Ruiz, S.A., and Chen, C.S. (2008). Emergence of patterned stem cell differentiation within multicellular structures. Stem Cells *26*, 2921–2927.
[115] Poh, Y.-C., Chen, J., Hong, Y., Yi, H., Zhang, S., Chen, J., Wu, D.C., Wang, L., Jia, Q., Singh, R., et al. (2014). Generation of organized germ layers from a single mouse embryonic stem cell. *5*, 4000.
[116] Zoldan, J., Karagiannis, E.D., Lee, C.Y., Anderson, D.G., Langer, R., and Levenberg, S. (2011). The influence of scaffold elasticity on germ layer specification of human embryonic stem cells. Biomaterials *32*, 9612–9621.
[117] Kishigami, S., and Mishina, Y. (2005). BMP signaling and early embryonic patterning. Bone Morphog. Proteins *16*, 265–278.
[118] Warmflash, A., Sorre, B., Etoc, F., Siggia, E.D., and Brivanlou, A.H. (2014). A method to recapitulate early embryonic spatial patterning in human embryonic stem cells. Nat. Methods *11*, 847–854.
[119] Lee, L.H., Peerani, R., Ungrin, M., Joshi, C., Kumacheva, E., and Zandstra, P. (2009). Micropatterning of human embryonic stem cells dissects the mesoderm and endoderm lineages. Stem Cell Res. *2*, 155–162.
[120] Pan, F.C., and Wright, C. (2011). Pancreas organogenesis: From bud to plexus to gland. Dev. Dyn. *240*, 530–565.

EBSCOhost - printed on 2/14/2023 1:06 PM via . All use subject to https://www.ebsco.com/terms-of-use

EBSCOhost - printed on 2/14/2023 1:06 PM via . All use subject to https://www.ebsco.com/terms-of-use

Nadi Braidy

11 Phase Diagram of an Au–Pt Solid Core–Liquid Shell Nanoparticle

Binary equilibrium phase diagrams are ubiquitous tools for predicting the behavior of multiphase systems. For a binary mixture with fixed global composition and temperature, a equilibrium phase diagram predicts the number and type of phases in equilibrium, and their respective fraction and composition. Equilibrium phase diagrams are computed from empirical thermodynamic properties of the existing phases and solutions. The calculations does not take into account energy terms that may arise because of surface, interface, strain, etc. With the emergence of nanoparticles (NPs) research, several attempts were made to compute binary nano-phase diagram. These studies consider only the energy term of the outer surface, which scales with the inverse of the radius of the NP. However, three important factors are typically omitted from the calculations: first, the shape and the energy of the solid-solid or solid-liquid interface; second, a mass balance constraint that can limit the phase composition of a nanoparticle and third the relative stability of a single, supersatured phase against a two-phase NP system. In this Chapter, we compute the nano-phase diagram of a binary mixture of Au and Pt, with a solid core-liquid shell configuration by incorporating these three principles. We demonstrate that the liquidus and solidus phase boundaries of an Au-Pt nano-phase diagram for a two-phase core-shell configuration is restricted to a much smaller compositional range than the phase composition. Of note, we show that the stability of the two-phase region shrinks significantly with decreasing size, even for NPs as large as 100 nm in diameter, and disappears below ~41.5 nm, where the NP no longer sustains an interface.

Keywords: Equilibrium Phase Diagram, Thermodynamics, Nano-phase diagram, Nanoparticles, Core-shell, Binary mixture

11.1 Introduction

One of the most spectacular and well-documented impact associated with nanoparticles (NPs) is the depression of their phase transition temperature and their increased

Notes: This chapter was adapted from Chapter 10 of author's PhD thesis Phase Stability of Nanoparticles (2008), McMaster University.

Nadi Braidy, Chemical and Biotechnological Engineering, Canada Research Chair in Synthesis and Charaterization in Multifunctional Nanomaterials, Université de Sherbrooke, Canada

https://doi.org/10.1515/9783110537734-011

EBSCOhost - printed on 2/14/2023 1:06 PM via . All use subject to https://www.ebsco.com/terms-of-use

solubility compared to their bulk counterpart. The extent of the temperature depression and solubility increase typically scales with the inverse of the size (or curvature) and the surface energy (γ). Calculating the effect of radius (r) of an NP on the stability of binary systems is more challenging; however, a few approaches were developed. Tanaka and coworkers [1, 2] used the thermodynamic data of a system to redraw the phase diagrams of hypothetical and real binary systems for various particle sizes. To recalculate the size-dependent solidus and liquidus, the authors simply added to the molar Gibbs energy of the solid and the liquid the capillarity functions ($2\gamma V_j/r$, with V_j, the molar volume and j = liquid or solid), with respect to a reference surface state. The strength of their calculations lies in the effort of including a temperature and composition dependence to various physical properties. For example, the surface energy of the liquid is solved using Butler's equations [3] and is temperature dependent; the molar volume of the liquid is considered to vary linearly with temperature and composition; the molar volume contraction upon solidification is also taken into account. The approach offers a quick and easy method to evaluate the impact of adding the capillarity terms to Gibbs energy on the phase diagram. Part of the method, namely the computation of surface energy using Butler's formulae, has been incorporated into a software [4] that can retrieve the thermodynamic functions from existing databases (the approach referred to as CALPHAD: computer CALculation of PHAse Diagrams) [5].

A number of "nano-phase diagrams" were computed using this technique, ranging from systems showing complete solubility (e.g., Au–Ag [6–8], Cu–Ni [9–11]), a miscibility gap (e.g., Ge–Si [12], Au–Ni [13], Au–Pt [14]), simple eutectics or peritectics (e.g., Au–Si [12], Ag–Cu [15], CeO_2–CoO [16]), to complex intermetallic systems (e.g., Sb–In [17], Al–Cu [12], Ni–Sn [18], Ag–Sn [19]). In all these studies, when the surface energy term is added to Gibbs energy, the liquidus, solidus, and invariant points all offset to lower temperatures and can shift toward one of the constituents. Despite the increasing popularity of this method to compute nano-phase diagrams, several issues must be addressed before it can translate into a useful tool:

1. The report consider a system made of a well-defined NP, which can modulate its composition by drawing from an infinite reservoir. This is not the case for isolated NPs for which the constraint of mass balance must be respected.
2. If multiple phases are stable, they must not only be in equilibrium within the NPs, but their stability must consider the energy of the interface in addition to that of the surface. This forces the assumption of a particular phase arrangement and, consequently, an interface shape (e.g., core-shell, spherical cap, straight interface).
3. Now that the interface (and not just the surface) contributes to the total Gibbs energy of an NP, its stability must be compared against a supersaturated, single-phased system for a given composition and temperature. This implies that the phase solubilities and stabilities can no longer be represented by a single line in the phase diagram, but must be represented by separate curves.

EBSCOhost - printed on 2/14/2023 1:06 PM via . All use subject to https://www.ebsco.com/terms-of-use

Very few reports have addressed or explicitly referred to these issues [11, 20–22]. There is a definite need to bridge the various models to the experimental data in a systematic and coherent manner. Apart from the scientific interest, there is an obvious technological incentive to predict the state of multi-component NPs of a given size and take into account the intrinsic physical characteristics of isolated NPs. We have chosen to explore the effect of size on Au–Pt NPs because the Au–Pt phase diagram contains many features arising from the positive enthalpy of mixing of the solid and the liquid phases, such as a miscibility gap in the solid and a large solid–liquid partition gap. The purpose of this work is thus to explore the effect of particle size on the phase diagram of isolated Au–Pt NPs.

Here, we compute equilibrium under the constraint of mass balance assuming the system adopts either a single-phase configuration or one composed of a solid core surrounded by a liquid shell. Note that this core–shell geometry was observed experimentally [22] for other system of bimetallic NPs upon heating and cooling. The method presented here is based on a simplified version of Jesser's approach [22]: we will consider the surface energy to be a linear function of composition and ignore surface segregation. In particular, we will apply to the calculations the constraints of mass–balance and phase stability by considering a core–shell geometry with the liquid on the surface. We replot each of the solidus and liquidus as a set of two curves: one for the phase solubility limit and another for the single-phase stability limit. Of note, we demonstrate that the presence of an interface has a significant impact on the stability of a nanosystems, even for NPs as large as 100 nm.

11.2 Methodology: Model and Governing Equations

Let us first consider an A–B spherical particle of radius R_0 and nominal molar B content X_0^B. Suppose that initially the homogeneous alloy transforms into a solid core of radius r and composition X_S^B surrounded by a liquid sheath of radius R and composition X_L^B. We consider a closed system with two constituents where the number of atoms is finite. The total number of moles of species A and B, n^A and n^B, respectively can be written as

$$n^i = C^i \Gamma \tag{11.1a}$$

$$n^i = X_0^i \frac{\Gamma}{V} \quad i = A,\ B \tag{11.1b}$$

where C^i is the number of moles of species A or B per unit volume of the alloy, X_0^i its molar fraction, and Γ the volume of the alloy and V its corresponding molar volume. For a binary system, $X^B = 1 - X^A = X$, where we now drop the superscript, X will hereafter refer to the molar fraction of B.

EBSCOhost - printed on 2/14/2023 1:06 PM via . All use subject to https://www.ebsco.com/terms-of-use

Using eqs. (11.1), geometric considerations require that

$$X_S r^3 / V_S = X_0 R_0^3 / V_0 \tag{11.2a}$$

$$r^3 / V_S = R_0^3 / V_0 \tag{11.2b}$$

where the Vs are the temperature-dependent molar volumes of the solid and liquid phases. Molar volumes are approximated by a linear combination of the molar volumes of the pure species

$$V_j = \left(1 - X_j\right) V_j^A + X_j V_j^B \quad j = L,\ S \tag{11.3a}$$

$$V_0 = \left(1 - X_p\right) V_p^A + X_p V_p^B \quad p = L \text{ or } S \tag{11.3b}$$

where the subscript p refers to either solid or liquid, depending on the starting phase of the homogeneous particle. Furthermore, we consider that the molar volume of the liquid varies linearly with temperature such that

$$V_L^i = V_{\text{mp}}^i \left[1 + \alpha^i \left(T - T_{\text{mp}}^i\right)\right] \quad i = A,\ B \tag{11.4}$$

where T is the temperature, T_{mp}^i is the melting temperature of the pure bulk component, α^i is the thermal expansion coefficient, and V_{mp}^i is the molar volume at the melting point for $i = A, B$. We approximate the molar volume of pure solid components to be proportional to their respective liquid counterparts

$$V_S^i = V_L^i / \left(1 + \beta^i\right) \quad i = A,\ B \tag{11.5}$$

where β^i can be viewed as the contraction coefficient upon solidification of metals [23].

We wish to find the temperature and nominal composition ranges at which a configuration composed of a solid core and a liquid shell is thermodynamically stable, with respect to a completely solid or liquid NP. At a given R_0, X_0, and T, r and R are determined by the equilibrium between the solid and liquid phases through eqs. (11.2–11.5).

We denote the molar Gibbs energy of the liquid by G_L. The molar Gibbs free energy of a completely solid NP is referred to as G_{S1} (which implies a one-phase NP), while that of the solid core, G_{S2} (which implies a two-phase NP). These molar free energies are equal to

$$G_L = G_L^M + S_{LV} + G_L^A(1 - X_L) + G_L^B(X_L) \tag{11.6a}$$

$$G_{S2} = G_S^M + S_{SL} + G_S^A(1 - X_S) + G_S^B(X_S) \tag{11.6b}$$

$$G_{S1} = G_S^M + S_{SV} + G_S^A(1 - X_S) + G_S^B(X_S) \tag{11.6c}$$

EBSCOhost - printed on 2/14/2023 1:06 PM via . All use subject to https://www.ebsco.com/terms-of-use

where G_S^M and G_L^M are the energy of mixing of the solid and liquid alloy, respectively. S_{LV}, S_{SL}, and S_{SV} are the energy per mole of surface associated with a liquid–vacuum, solid–liquid, and solid–vacuum interface, respectively. G_p^A and G_p^B are the lattice stabilities of elements A and B, respectively, in phase p, (with respect to the liquid reference state)

$$G_L^i = 0 \tag{11.7a}$$

$$G_S^i = H_m^i + S_m^i T \quad i = A,\ B \tag{11.7b}$$

The molar energies of mixing of a regular solution are commonly written as the sum of an ideal term, G_j^{ID}, and an excess term, G^E

$$G_j^M = G_j^{ID} + G_j^E \tag{11.8a}$$

$$G_j^{ID} = R_g T \left[X_j \ln\left(X_j\right) + \left(1 - X_j\right) \ln\left(1 - X_j\right)\right] \tag{11.8b}$$

$$G_j^E = X_j\left(1 - X_j\right)\Omega_j \qquad j = L,\ \ S \tag{11.8c}$$

where R_g is the gas constant and Ω_j is the interaction parameter.

To deduce the surface contributions S_{LV}, S_{SV}, and S_{SL}, let us first consider the free-body diagram of half the composite solid (core)–liquid (shell) particle, as shown in Figure 11.1. The net pressure applied on the outer surface of the particle is the difference between the external pressure P_{ext} and the inner pressure P_L of the liquid phase. If we consider the horizontal projection of the pressure applied to the liquid surface, we obtain that the pressure $P_{\text{ext}} - P_L$ is exerted on a disc of radius R. The force resulting from the projected pressure in the horizontal direction is in equilibrium with the line tension σ_{LV} applied on a circle of radius r. Since the membrane is at rest, we can write

$$(P_{\text{ext}} - P_L)\pi R^2 = 2\pi R\sigma_{LV} \tag{11.9}$$

Similarly, considering a force balance on the inner surface leads to

$$(P_L - P_S)\pi R^2 = 2\pi R\sigma_{SL} \tag{11.10}$$

Adding eqs. (11.9) and (11.10) and simplifying gives

$$(P_{\text{ext}} - P_S) = 2\left(\frac{\sigma_{SL}}{r} + \frac{\sigma_{LV}}{R}\right) \tag{11.11}$$

Finally, by recognizing that the capillarity contribution can be expressed in terms of a pressure difference (e.g., only the two first terms of eq. 11.8), we can write the molar surface energy contribution of the surfaces or interfaces as

EBSCOhost - printed on 2/14/2023 1:06 PM via . All use subject to https://www.ebsco.com/terms-of-use

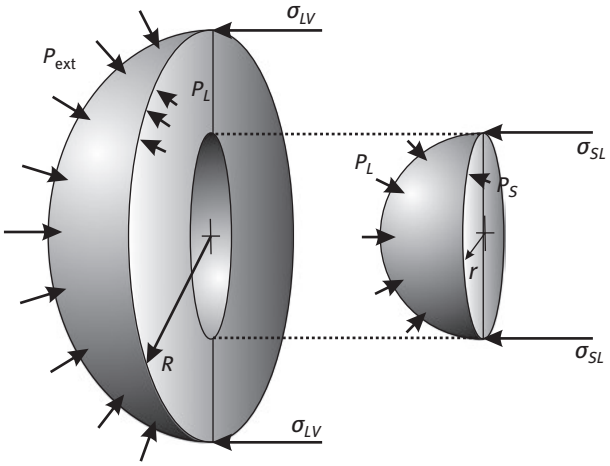

Figure 11.1: Free-body diagram of a composite NP cut in two hemispheres, where the core is detached. r and R are the radii of the solid core and the liquid shell, respectively. σ_{LV} and σ_{SL} refer to the surface tension of the outer and inner shell, respectively. P_{ext} is the external pressure applied on the outer shell while P_L and P_S are the pressures within the liquid and the solid phases, respectively.

$$S_{LV} = 2\sigma_{LV} V_L / R \tag{11.12a}$$

$$S_{SL} = 2\sigma_{LV} V_L / R + 2\sigma_{SL} V_S / r \tag{11.12b}$$

$$S_{SV} = 2\sigma_{SL} V_S / R \tag{11.12c}$$

We approximate the surface energy of an alloy as a linear combination of the surface energies of its pure components

$$\sigma_{LV} = (1 - X_L)\sigma^A_{LV} + X_L \sigma^B_{LV} \tag{11.13a}$$

$$\sigma_{SL} = (1 - X_S)\sigma^A_{SV} + X_S \sigma^B_{SL} \tag{11.13b}$$

$$\sigma_{SV} = (1 - X_S)\sigma^A_{SV} + X_S \sigma^B_{SV} \tag{11.13c}$$

Because the surface energy is temperature dependent and the available data on surface energy is typically given at the melting point of the metal, we will consider the following relation

$$\sigma^i_{LV} = \sigma^i_{LV\ mp} - \kappa^i_{LV}\left(T - T^i_{mp}\right) \tag{11.14}$$

$\sigma^i_{LV\ mp}$ is the surface energy of component i at the melting point and κ^i_{LV} is a temperature coefficient. The solid–liquid interfacial energies are observed to be about 25% larger than their liquid–vapor counterpart [24–26] and are considered to follow the same temperature dependence as their liquid counterpart. Therefore, we can write

EBSCOhost - printed on 2/14/2023 1:06 PM via . All use subject to https://www.ebsco.com/terms-of-use

$$\sigma_{SV}^{i} = 1.25\sigma_{LV}^{i} \; i = A, \; B \tag{11.15}$$

Finally, we will consider that the surface energy of the pure solid component, σ_{SV}^{i}, is temperature independent.

We demonstrate that there exists a limited range of temperatures and nominal compositions over which the core–shell configuration is stable for a given size. The core–shell configuration must fulfill the following conditions to be stable (we will subsequently refer to these conditions by their number):

1. If multiple phases are stable, they must be in equilibrium, that is, the chemical potential must be equal for both phases (one can draw a common tangent to the Gibbs energy curves).
2. Mass balance (eqs. 11.2) must be fulfilled with a core radius that is strictly positive and smaller than the shell radius (i.e., $0 < r < R$). Furthermore, the nominal composition of the NP, X_0, must be within the range defined by the composition of the liquid shell, X_L, and that of the solid core, X_S.
3. The Gibbs free energy of the core–shell system, G_{S2}, must be lower than that of a completely solid (G_{S1}) or liquid (G_L) NP. In other words, a two-phase NP must be more stable than a single-phase NP.

The main assumptions are listed as follows:

- The NP properties are isotropic, which is a reasonable approximation for the liquid phase and for solids at high temperatures. This approximation can be relaxed by considering a surface torque term. This would also allow one to estimate the contribution of faceting, expected to be important for small NP (for R typically below 10 nm, at low temperatures).
- The core is not considered under compression and the overall stress state of the NP does not affect the equilibrium. The model can be further refined by following, for example, the method described by Jesser et al. [27]
- No nucleation barrier is set for the formation of a solid core. However, if the core is too small, the surface contribution of the solid eventually raises the Gibbs energy curve of the solid phase to a point where only a single-phase NP is stable (either G_L or G_{S1}). This phenomenon indirectly acts as a "nucleation barrier."
- Surface or interface segregation is not considered, for simplicity. This could be added to the computation by considering the Gibbs adsorption isotherm as described by Huh et al [22].
- The phases are homogeneous and the solid–liquid interface is sharp [28].
- The surface energy of the alloy is a linear combination of the surface energy of the pure component. This can be further refined by the use of Butler's equations [1–3] that can be computed *via* the thermodynamic properties of a liquid alloy. Note that Butler's equations are not experimentally verified for solids.

EBSCOhost - printed on 2/14/2023 1:06 PM via . All use subject to https://www.ebsco.com/terms-of-use

We apply this method to the solid–liquid equilibrium within a Au–Pt NP. Okamoto [29] has provided the most up-to-date thermodynamic assessment of the Au–Pt system. The thermodynamic parameters of the system are listed in Table 11.1. All the additional parameters and physical properties are listed in Table 11.2.

Table 11.1: Thermodynamic functions for the liquid and solid Au–Pt phases and lattice stability of solid Au and Pt with respect to the liquid reference state [29].

Phase	Enthalpy of mixing $\frac{\Delta H}{X(1-X)}$, J/mol	Entropy of mixing $\frac{\Delta S^E}{X(1-X)}$, J/mol·K
Liquid	$23500 + 4000\,X$	0
Solid	$30000X$	$13.00 + 14.183X$
Element	**Lattice stability G_s^0, J/mol**	
Au	$-13000 + 9.7190T$	
Pt	$-19650 + 9.6224T$	

Table 11.2: Physical properties of Au and Pt and parameters used in the computation of equilibrium.

Parameter	Symbol	Value	Reference
Melting temperature (K)			
Au	T_{mp}^{Au}	1336.15	[29]
Pt	T_{mp}^{Pt}	2047.15	
Thermal expansion coefficient (K^{-1})			
Au	α^{Au}	6.9×10^{-5}	[30]
Pt	α^{Pt}	15.2×10^{-5}	
Molar volume at melting point (m^3/mol)			
Au	V_{mp}^{Au}	11.3×10^{-6}	[30]
Pt	V_{mp}^{Pt}	10.3×10^{-6}	
Contraction coefficient (m^3/mol)			
Au	β^{Au}	0.055	[23]
Pt	β^{Pt}	0.063	
Surface energy temperature coefficient ($Jm^{-2} \cdot K^{-1}$)			
Au	κ^{Au}	2.5×10^{-4}	[31]
Pt	κ^{Pt}	1.2×10^{-4}	[24, 32][a]
Liquid surface energy at melting point (J/m^2)			
Au	σ_{LVmp}^{Au}	1.169	[31]
Pt	σ_{LVmp}^{Pt}	1.8	[24]
Solid surface energy at melting point (J/m^2)			
Au	σ_{SVmp}^{Au}	1.39	[33]
Pt	σ_{SVmp}^{Pt}	2.28	

a Average between experimental data: 1.7×10^{-4} [24] and 0.7×10^{-4} [32].

EBSCOhost - printed on 2/14/2023 1:06 PM via . All use subject to https://www.ebsco.com/terms-of-use

The objective of these simulations is to (i) explore the limits of stability of a core–shell configuration in terms of temperature and composition with respect to a single-phase NP (either liquid or solid) and (ii) for conditions (T, X_0, and R) in which the core–shell configuration is stable, the composition and radius of the solid core (X_S) and the liquid shell (X_L) are determine.

11.3 Results

11.3.1 Gibbs–Thomson Curves and Phase Equilibria (Condition 1)

We shall first consider the Gibbs energy curves related to an NP of 50 nm radius at 1,400 K (Figure 11.2). The curve labeled G_L is associated with the liquid phase and is invariant to the size of the solid core. The other curves (black) are associated with the solid and can be used to demonstrate the Gibbs–Thomson effect. G_{S2}, $r \to R$ represents the case where the NP is almost completely solid but still shares an interface with an infinitely thin liquid shell. The NP adopts this core–shell configuration, the open squares in Figure 11.2a indicate the equilibrium composition of the

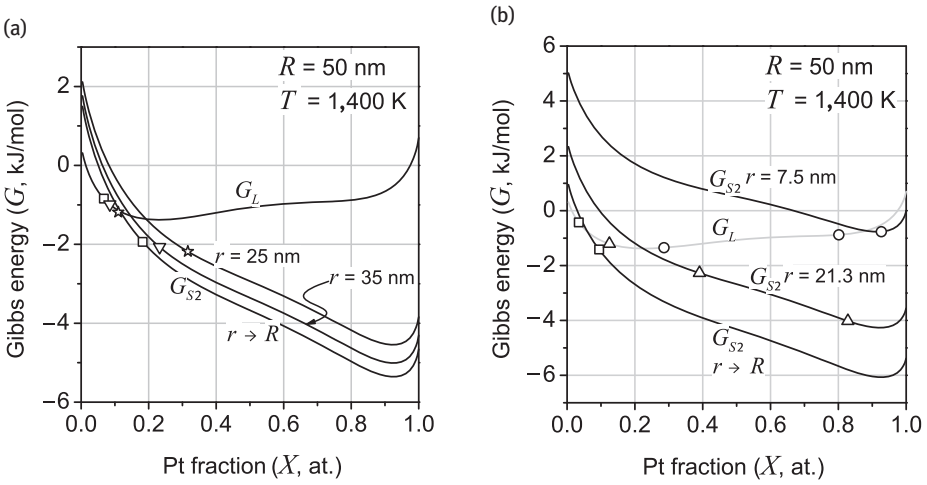

Figure 11.2: Demonstration of the Gibbs–Thomson effect with Gibbs energy curves associated with an NP of 50 nm radius at 1, 400K. Liquid: G_L, gray line. Solid core: G_{S2}, $r \to R$, bottom black line. (a) G_{S2} is also plotted for a solid core with inner radius of (r) 35 nm and 25 nm: center and upper black curves, respectively. Symbols correspond to the equilibrium composition between the energy curves of the solid and the liquid, as specified by the common tangent construction. By decreasing the inner radius of the solid phase, the energy curve rises to increase the equilibrium composition of both the liquid and the solid phases (indicated by squares, down triangles and stars, for $r \to R$, 35 and 25nm, respectively). (b) The values of the inner radii were chosen to match the particular case of a peritectic ($r = 21.3$ nm, triangle) and monotectic ($r = 7.5$nm, circle) transformation.

EBSCOhost - printed on 2/14/2023 1:06 PM via . All use subject to https://www.ebsco.com/terms-of-use

liquid and the solid phases. As the inner core radius, r, decreases, the Gibbs energy curve associated with the solid will rise to higher energies. Consequently, the equilibrium composition of both, the liquid and the solid, will shift to higher Pt fractions, as determined by the common tangent construction. The intercepts of the common tangents are respectively marked by open down triangles and stars for $r =$ 35 nm and 25 nm.

The thermodynamic functions of the liquid and the solid phases both exhibit a double well (at low temperatures) because of their large and positive enthalpy of mixing. Consequently, as the Gibbs energy curve of the solid is increased and the compositions shift to higher Pt content, there will exist two critical inner radii corresponding to a monotectic and a peritectic transformation. The case where $r = 21.3$ nm, in Figure 11.2b illustrates a peritectic transformation: the tangent construction intercepts twice the solid phase curve and once the liquid phase curve (open triangles). Similarly, a monotectic transformation is reached for $r = 7.5$ nm: an equilibrium is obtained between the solid and the liquid phases with two possible compositions (open circles).

The variation of the composition of the solid (X_S) and liquid (X_L) phases as a function of inner core radius (r) are plotted in Figure 11.3 for an NP of 50 nm radius.

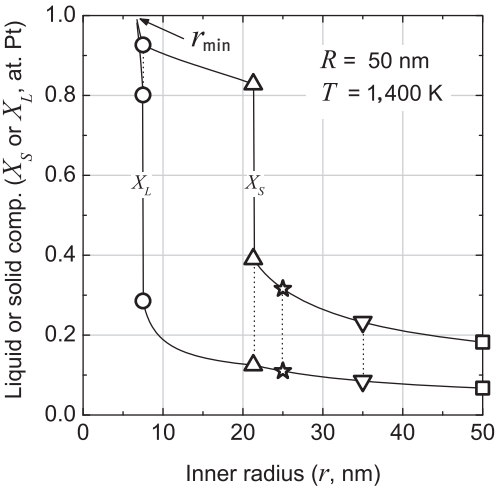

Figure 11.3: Variation of the equilibrium composition of the liquid (X_L) and the solid (X_S) with the inner core radius (r) at various temperatures for a $R = 50$ nm NP. These types of functions are referred to in the text as "Gibbs–Thomson curves." The discontinuities in the variation of the liquid phase composition are associated with a monotectic transformation while those of the solid phase are attributed to a peritectic transformation. Open symbols (square, down triangles, stars, up triangles, and circles correspond to $r \rightarrow R$, 35 and 25, 21.3, and 7.5 nm, respectively) refer to the tangency points of the solid- and liquid-phase energy curves shown in Figure 11.2. The dotted lines between the symbols are tie-lines.

EBSCOhost - printed on 2/14/2023 1:06 PM via . All use subject to https://www.ebsco.com/terms-of-use

We will subsequently refer to these types of curves as "Gibbs–Thomson curves" or "Gibbs–Thomson branch" when referring to either of the curves. The radius at which discontinuities occur are marked by open square and triangle symbols, which correspond to those of Figure 11.2b. The other symbols refer to those of Figure 11.2a. For any given temperature or NP size, X_S and X_L form a pair of Gibbs–Thomson curves that merge for a small value of r, $r_{\min}$, at which $X_S = X_L = 1$. This corresponds to the case where the Gibbs energy curve associated with the solid core raises to a point where it intersects only the liquid phase curve at $X = 1$.

The Gibbs–Thomson branches are composed of segments, each roughly following an exponential decay. If the axes of the Gibbs–Thomson curves were interchanged, X_S and X_L curves could be considered as liquidus and solidus lines. This would result in a meaningless exercise, unless we take into account mass balance, as it will be shown below.

The Gibbs–Thomson curves are drawn at various temperatures (Figure 11.4) for an NP of radii (a) 50 nm and (b) 20nm. As the temperature is increased, the discontinuities disappear above a critical temperature, which corresponds to the consolute point (temperature and composition above which the two inflexion points of the double-well Gibbs energy curve degenerate). At higher temperatures, we also note that the curves shift to larger inner radii and higher compositions. Indeed, at a high temperature, the Gibbs energy curve of the liquid phase is

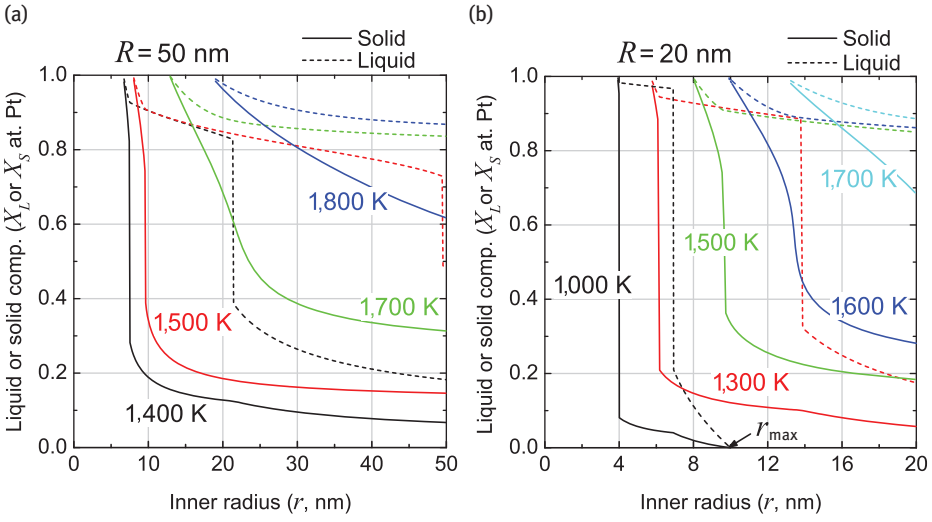

Figure 11.4: Variation of the equilibrium composition of the liquid (X_L, full lines) and the solid (X_S, dashed lines) with the inner core radius (r) at various temperatures for an NP of (a) 50 nm and (b) 20 nm. These types of functions are referred to in the text as "Gibbs–Thomson curves." The discontinuity in the liquid branch is associated with a monotectic transformation while the one in the solid branch is attributed to a peritectic transformation.

EBSCOhost - printed on 2/14/2023 1:06 PM via . All use subject to https://www.ebsco.com/terms-of-use

stabilized with respect to that of the solid phase. Therefore, at high temperatures, the interfacial energy can easily promote the Gibbs energy curve of the solid core to higher energies, where equilibrium with the liquid is forbidden (i.e., $G_{S2} > G_L$ for the whole composition range).

When the size of the NP is decreased to $R = 20$ nm (Figure 11.4b), the Gibbs–Thomson curves remain unchanged but are truncated at a smaller inner radius, since r must be lower than R (note the abscissa scale change). This can be understood by inspection of eqs (11.12a) and (11.12b). When decreasing the overall size, R, of the NP, a common term, $2\sigma_{LV}V_S/R$, raises both the liquid and solid Gibbs energy curves by the same amount, leading to an unchanged equilibrium. The consequence of such a construction is that the liquid phase can be stabilized even at very low temperatures, as seen in Figure 11.4b at 1,000 K. At this temperature, the Gibbs energy curve associated with a solid core with an inner radius smaller than ~4 nm will be higher than that of the liquid for all X, thus stabilizing the liquid phase for such a low temperature (as we will discuss subsequently, this situation will be prevented by invoking Condition 3). Alternatively, at 1,000 K, for a solid core with an inner radius larger than ~10 nm, the Gibbs energy curve of the solid is lower than that of the liquid for all X. In this situation, we can define an upper limit for the inner radius, $r_{\max}$, at which $X_S = X_L = 0$. If the core–shell geometry of an NP is fixed with an inner radius above $r_{\max}$, the NP will be completely solid at 1,000 K. As we will discuss subsequently, this situation will never be encountered as we demonstrate that a core–shell configuration is not stable for such small NPs ($R = 20$ nm). The existence of $r_{\min}$ and $r_{\max}$ was noted here only for the sake of completion and won't be part of future discussions .

11.3.2 Mass–Balance Restriction (Condition 2)

The restriction of mass balance is demonstrated by first expressing X_L as a function of r through the mass–balance equation (eqs. 11.2) and comparing the resulting curve with the Gibbs–Thomson X_L branch. Figure 11.5 shows the Gibbs–Thomson curves for a 50 nm NP at 1,650 K together with X_L (as defined by eqs. 11.2) plotted for various nominal compositions (inward curves). When X_L is plotted for a nominal composition $X_0 = 0.55$ (dotted curve), it intersects the Gibbs–Thomson X_L branch at two positions marked by open squares. This implies that there exist two possible configurations, which satisfy both the mass balance and the equilibrium restrictions for an NP of radius 50 nm at 1,650K: (i) $r = 17.05$ nm with $X_S = 0.53$ and $X_L = 0.88$ and (ii) $r = 37.5$ nm with $X_S = 0.27$ and $X_L = 0.83$. It is important to note that the solution with the largest inner radius is always the most stable one, because its total energy is lower. As the nominal composition decreases, the two solutions move closer together and eventually become degenerated. For $X_0 = 0.398$, defined hereafter as $X_0^{\min}$, there exists only one solution that satisfies both restrictions imposed by

EBSCOhost - printed on 2/14/2023 1:06 PM via . All use subject to https://www.ebsco.com/terms-of-use

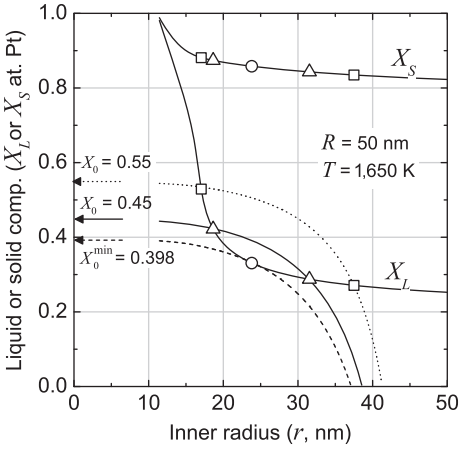

Figure 11.5: Variation of the equilibrium composition of the liquid phase (X_L) and the solid phase (X_S) with the inner core radius (r) at 1, 650K for an NP of radius 50 nm. The composition of the liquid (X_L), as derived from the mass balance (eqs. 11.2), is plotted for nominal compositions of $X_0 = 0.55$ (dotted line), 0.45 (full line) and 0.398 (dashed line). The intersection of these curves with the equilibrium liquid composition (as specified by the double tangent construction) are marked by symbols. For $X_0 > 0.398$, two solutions exist while for $X_0 = 0.398$, these solutions become degenerated. For $X_0 < 0.398$, the amount of Pt in the system is not sufficient for the liquid (shell)/solid (core) configuration to exist.

mass–balance and phase equilibrium of solutions for $r = 23.8$ nm, $X_S = 0.86$ ($X_S^{\min}$) and $X_L = 0.33$ ($X_L^{\min}$). For the values $X_0 < X_0^{\min}$, the coexistence of the liquid and solid phase is impossible since the amount of Pt in the system is not sufficient for a core–shell configuration to form.

The solid, $X_S^{\min}$, and liquid, $X_L^{\min}$, composition (open circles) corresponding to the case $X_0 = X_0^{\min}$ (closed circle) that are plotted on a phase diagram in Figure 11.6a, for an NP of 50 nm radius at 1,650 K. The bulk liquidus and solidus of the Au–Pt system are also displayed in light gray as a reference. Note that the phase diagram serves two purposes here: for a given temperature, it displays the minimal nominal composition that a core–shell configuration can sustain and shows the corresponding composition of the liquid shell and the solid core.

We can construct a "mass balance phase boundary" by computing $X_0^{\min}$ for an array of temperatures (closed circles, Figure 11.6b). If the nominal composition is below $X_0^{\min}$, the NP will be in the liquid state. If $X_0 = X_0^{\min}$, the NP will adopt the core-shell configuration with a solid core and a liquid shell having a composition $X_S^{\min}$ and $X_L^{\min}$ (open circles), respectively.

EBSCOhost - printed on 2/14/2023 1:06 PM via . All use subject to https://www.ebsco.com/terms-of-use

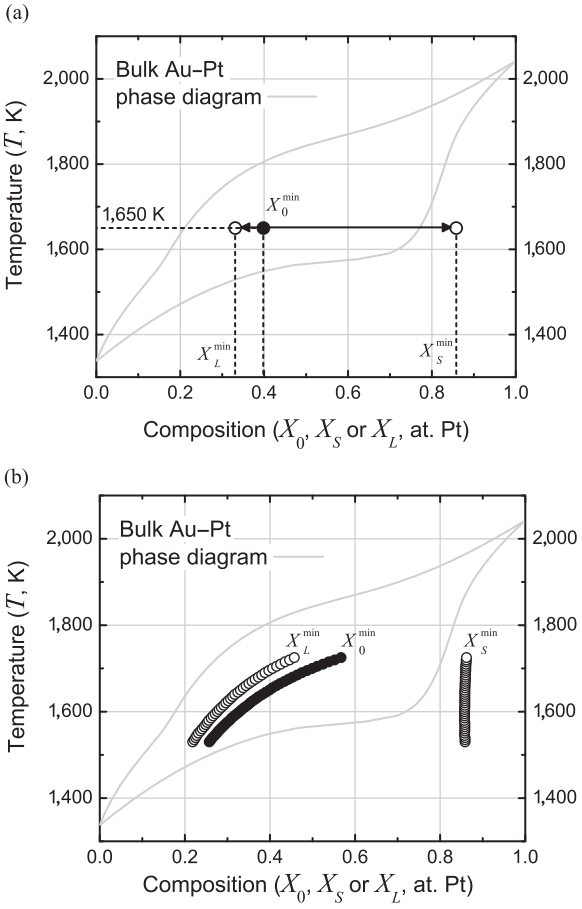

Figure 11.6: (a) Temperature-composition graph showing the minimal nominal composition (X_0^{min}) necessary for a core–shell configuration to exist, for an NP with 50 nm radius at $T = 1,650$ K (closed circle, $X_0 = 0.398$, see Figure 11.5). For this nominal composition, the corresponding composition of the solid (X_S^{min}) and liquid (X_L^{min}) partitions are shown (open circles). (b) The minimal nominal composition, X_0^{min} (closed circles) calculated at various temperatures for a 50 nm NP with corresponding partition composition (open circles). The bulk liquidus and solidus are shown for comparison purposes (gray lines).

11.3.3 Relative Stability of a Two-Phase NP with Respect to a Single-Phase NP (Condition 3)

Condition 3 requires that the core–shell configuration must have a lower energy than a single-phase NP. This condition is illustrated in Figure 11.7a, which displays the Gibbs energy curves of the possible phases associated with an NP of 50 nm radius at 1,650 K with an inner radius of 32.8 nm. The equilibrium compositions

EBSCOhost - printed on 2/14/2023 1:06 PM via . All use subject to https://www.ebsco.com/terms-of-use

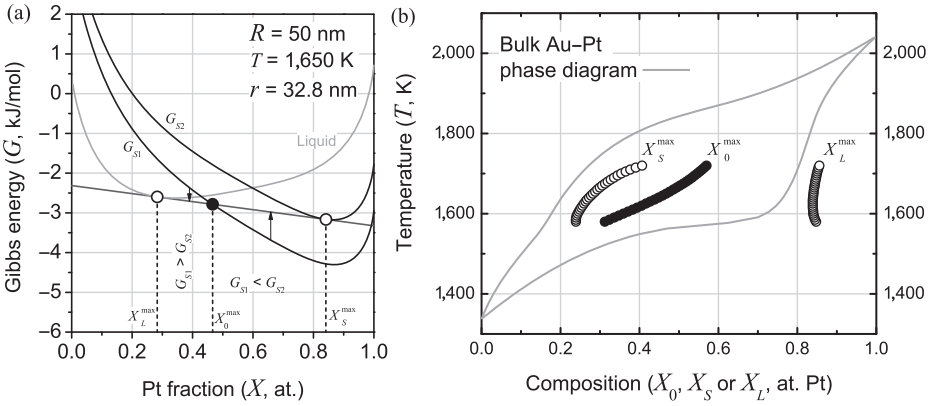

Figure 11.7: (a) Gibbs energy curves computed for an NP with 50 nm radius at 1650 K for the liquid phase (G_L, gray curve), a solid NP (G_{S1}, lower black curve), and a solid core having a 32.8 nm radius (G_{S2}, upper black curve). The double tangent (gray line) specifies the composition of the solid core and a liquid shell (open circles). The intersection between G_{S1} and the double tangent (closed circle) marks the composition above which the energy of a single solid phase is lower, X_0^{max}. For an NP having an overall content $X_L^{max} < X < X_0^{max}$, a core–shell configuration is stabilized when the solid and liquid phase compositions are X_S^{max} and X_L^{max}, respectively. (b) X_0^{max} (closed circles) calculated at various temperatures with corresponding X_L^{max} and X_L^{max} (open circles). The bulk liquidus and solidus are shown for comparison purposes (gray lines).

between the liquid shell and the solid core (upper black line) are dictated by the double tangent construction (gray line) and are marked by open circles. X_0^{max} is defined as the composition where the Gibbs energy curve of the solid NP (G_{S1}, black curve) intersects the double tangent (marked by a closed circle). A common tangent construction cannot be drawn between a completely solid phase, G_{S1} and G_L, since this implies equilibrium between the two phases. As noted previously, equilibrium between solid and liquid necessarily creates an interface, which raises the Gibbs energy curve associated with the solid core. Consequently, the solid–liquid equilibrium can only be considered between G_{S2} and G_L. As seen in Figure 11.7a, for $X_L^{max} < X < X_0^{max}$, the energy of a solid NP is higher than that of a core–shell NP of the same nominal composition (downward arrow). Alternatively, for $X > X_0^{max}$, the most stable configuration is a single-phase solid solution.

The exact composition of X_0^{max} is found by successive iterations since it varies with r. We start the iteration process with X_0 slightly larger than X_0^{min} and find the radius at which the Gibbs–Thomson liquid curve intersects X_L as computed using the mass–balance equation. Gibbs energy curves are then generated with those conditions and the intersection point between the double tangent and G_{1S} becomes the new X_0 and the process is repeated until convergence. This iterative procedure is then finally carried out for an array of temperatures. Another phase

EBSCOhost - printed on 2/14/2023 1:06 PM via . All use subject to https://www.ebsco.com/terms-of-use

boundary can be constructed with the values of $X_0^{\max}$ (closed circles), as shown in Figure 11.7b in which the corresponding values of $X_L^{\max}$ and $X_S^{\max}$ are also reported.

For the situation where $X_0 < X_0^{\min}$ or $X_0 > X_0^{\max}$, the NP can either be completely in liquid ($G_L(X_0) < G_{S1}(X_0)$) or a completely solid phase ($G_{S1}(X_0) < G_L(X_0)$). For example, Figure 11.8a shows the Gibbs energy curves associated with an NP of 50 nm radius at 1500 K with an inner radius core of 19.6 nm. In this situation, the intersection between G_L and G_{S1}, hereafter defined to as X_0^{SL}, occurs at a composition smaller than X_L (as defined by the double tangent construction between G_L and G_{S2}). If $X_0 < X_0^{SL}$, the NP is completely liquid because the G_{S1} energy curve is lower than the double tangent for any composition between X_0^{SL} and 1. For nominal composition larger than X_0^{SL}, the NP is completely solid. Figure 11.8 plots X_0^{SL} for the whole composition range for an NP of 50 nm radius by solving the nominal composition in equation $G_{S1} = G_L$. The molar energy of the alloy NP can therefore be regarded as a lower envelope of G_L, G_{S1}, and the common tangent between G_L and G_{S2}. For the case of pure components, this curve appropriately describes the expected melting point depression when decreasing the size of NPs [34]. However, it

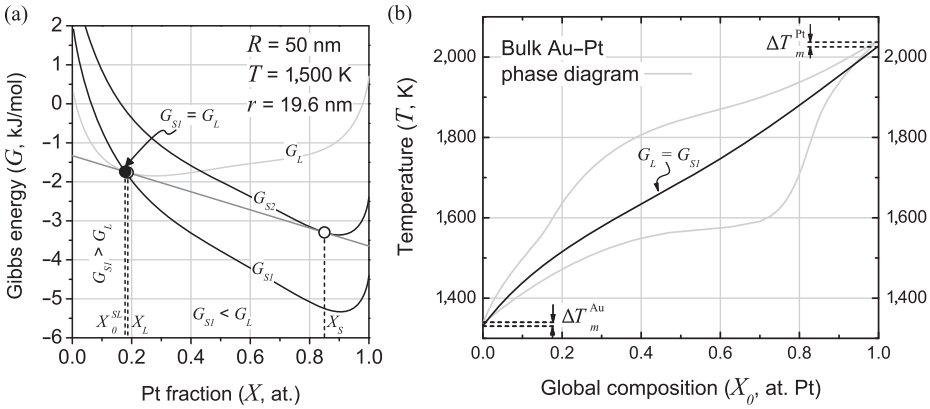

Figure 11.8: (a) Gibbs energy curves associated to an NP of 50 nm radius at 1500 K. Gray line: G_L, liquid phase. Lower black line: G_{S1}, single phase NP. Upper black line: G_{S2}, 19.6 nm radius of the solid core. Open circles marks the solid (X_S) and liquid (X_L) composition of the liquid (G_L) and the solid core (G_{S2}), as specified by the double tangent construction (gray line). Because the composition at which G_L intersects G_{S2} (X_0^{SL}) is smaller than X_L, the solid(core)/lquid(shell) configuration cannot be stable. In this case, the solid and liquid phases shall not coexist within the same NP: the NP is in a liquid state for $X_0 < X_0^{SL}$, and completely solid otherwise. (b) The critical point X_0^{SL} is calculated by letting $G_{S1} = G_L$ for the whole temperature range of interest. The magnitude of the melting points depression of Au (T_m^{Au}) and of Pt (T_m^{Pt}) for an NP of 50 nm radius are in agreement with experimental observations [34]. The bulk liquidus and solidus are shown for comparison purposes (gray lines).

EBSCOhost - printed on 2/14/2023 1:06 PM via . All use subject to https://www.ebsco.com/terms-of-use

should be noted that the model does not predict the appearance of a liquid sheath upon melting of pure NPs.

11.3.4 Temperature-Composition Diagram of Au–Pt NP

We can now combine on the same plot (Figure 11.9a) all the constraints (Conditions 1–3) and infer on the stability of a core–shell configuration. It is surprising to realize that the only region of the phase diagram where a liquid and a solid phase can coexist in a core–shell configuration for a NP having a 50 nm radius is contained in a small lens-shaped region defined by $X_0^{\min}$ and $X_0^{\max}$. Note that the phase boundary, X_0^{SL}, is meaningless in the two-phase region. The inset of Figure 11.9a shows a magnified view of a region of the phase diagram where the phase boundaries appear to intersect. One can note that the phase boundary defined by X_0^{SL} is secant with the phase boundary defined by $X_0^{\min}$. This implies that if the temperature of an NP having a nominal composition of 0.57 decreases from the liquid phase, it will transform first to the solid phase over the small temperature range $X_0^{SL} - X_0^{\min}(1,726 - 1,730\ \text{K})$. Lowering the temperature further in the range $1,720 - 1,726$ K will stabilize the solid (core)–liquid (shell) configuration. The NP would be solid at lower temperatures. This counterintuitive transformation (liquid → solid → 2 phases → solid) is not a consequence of numerical instabilities or precision but is a phenomenon that is predicted on the basis of this model.

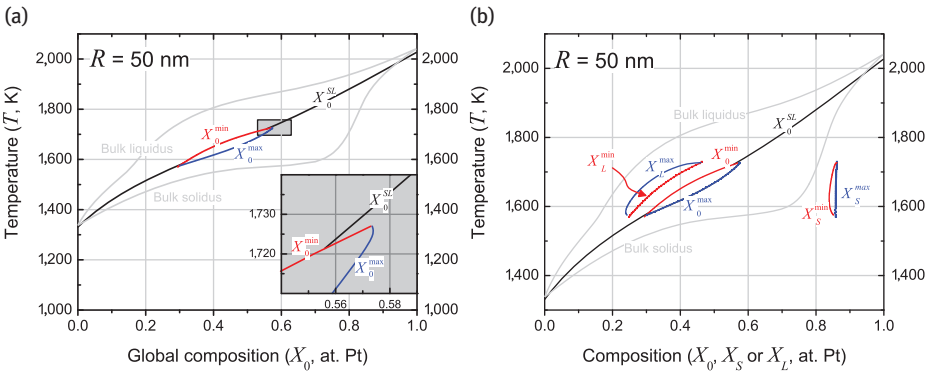

Figure 11.9: (a) Stability limit of a core–shell configuration of an NP of 50 nm radius. The solid and the liquid phases can coexist in a core–shell configuration only for temperatures and compositions of the phase diagram enclosed within $X_0^{\min}$ (red) and the $X_0^{\max}$ (blue) curves. For other regions of the phase diagram, the NP will be completely liquid for $X_0 < X_0^{SL}$ or solid for $X_0 > X_0^{SL}$. The inset shows the details of the intersection of the limiting curves. (b) Same as (a) but the extent of the new liquidus (bounded by $X_L^{\min}$ and $X_L^{\max}$) and solidus (bounded by $X_S^{\min}$ and $X_S^{\max}$) are shown.

EBSCOhost - printed on 2/14/2023 1:06 PM via . All use subject to https://www.ebsco.com/terms-of-use

The transformation sequence related to a partitionless transition from liquid to solid would be kinematically forbidden at the predicted temperatures. We rather expect an undercooling associated with the solidification of a NP. Consequently, a smaller undercooling would be associated with smaller NPs, in agreement with the nucleation theory (see for instance [35]) and shares some similarity with the conclusions of Shirinyan's model [36] (and in a more recent paper [11]). The kinetics of the transformation in small-scale system falls outside this Chapter's scope.

The stability limits of the core–shell configuration are drawn again in Figure 11.9b. If the solid and liquid phases coexist within the NP, then the composition of the solid and liquid phases are expected to be included between $X_S^{\min}$ and $X_S^{\max}$ and between $X_L^{\min}$ and $X_L^{\max}$, respectively. These can be understood as the liquidus and solidus of a NP in the sense that they predict the composition of the phases, but are by no means considered as *phase stability boundaries*. We stress that the phase stability boundaries are rather predicted by X_0^{SL}, $X_0^{\min}$, and $X_0^{\max}$.

The bulk liquidus and solidus are shown for comparison purposes (gray lines). The effect of increasing the outer radius, R, is demonstrated in Figure 11.10a. The stability limits, $X_0^{\min}$ and $X_0^{\max}$, of NP of 50 nm and a 100 nm are shown. The two-phase region of the NP with 100 nm radius extends on a much larger composition and temperature range than for the 50 nm radius case. Note that the limit X_0^{SL} is slightly raised to higher temperatures, consistent with the small variation of the melting point associated with larger NPs. The liquidus and solidus corresponding to the 100 nm NP (blue curves, Figure 11.10b) are compared with those of a 50 nm NP. Overall, as the NP stability limits are expected to approach the bulk liquidus and

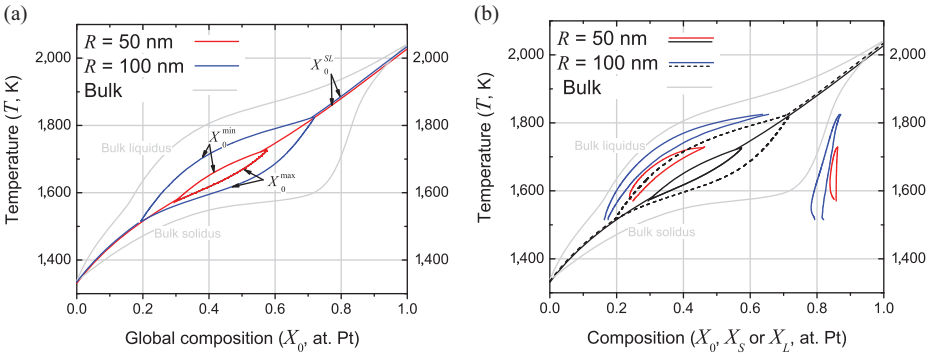

Figure 11.10: (a) Phase diagram comparing the stability limits of the core–shell configuration of NPs of 50 nm (red) and 100 nm (blue) radii. (b) Stability limits of the core-shell configuration of NPs of 50 nm (black curve) and a 100 nm (dashed black curve) radii along with their respective liquidus and solidus. The bulk liquidus and solidus are shown for comparison purposes (gray lines).

EBSCOhost - printed on 2/14/2023 1:06 PM via . All use subject to https://www.ebsco.com/terms-of-use

solidus for larger NPs, the liquidus and solidus approach those of the bulk. These trends are consistent with the expected asymptotic behavior: as $R \to \infty$, the stability limits $X_0^{\min}$ and limiting curves defined by $X_L^{\min}$ and $X_L^{\max}$ will all merge with the bulk liquidus. Similarly, $X_0^{\max}$ and the limiting curves defined by $X_S^{\min}$ and $X_S^{\max}$ will merge with the bulk solidus.

As the NP size decreases, $X_0^{\min}$ and $X_0^{\max}$ will collapse to a single point where the coexistence of liquid and solid phase in a core–shell configuration within an NP will not be possible for sizes smaller than a critical radius. This critical radius is estimated to be $R \sim 41.5$ nm and, for this radius, a core-shell configuration is only possible at a temperature of 1, 645 K. At this temperature, the NP will partition into a 86.4% Pt core with a radius of 21.5 nm and a 35.6% Pt-rich shell. Interestingly, below a diameter of ~83 nm, the NP cannot support a solid–liquid interface and will seek to adopt a lower energy configuration, either completely solid or liquid.

11.4 Conclusion

In this Chapter, we have explored the effect of size on the possible equilibria of the Au–Pt system. The method proposed to compute sections of the size-dependent phase diagram can be considered as a hybrid of Tanaka [1, 2] and Jesser's [22] approaches. We have given a special consideration to illustrate in a graphical manner the effects of surface energy on the Gibbs energy curves. Using "Gibbs–Thomson" curves, the size-induced phase transition and the constraint of mass balance could be described using an intuitive and graphical approach.

Given the high energy cost of the interface, it was found that the solid and liquid phases could not coexist in a core–shell configuration within an NP whose diameter is below ~83 nm. The phase boundaries of the stability region on a temperature-composition diagram for which a solid core could coexist with a liquid shell would approach those of the bulk phase diagram as the size of the NP increased. However, for a given size and nominal Pt composition, the liquid and solid phase Pt compositions are expected to be substantially lower than those of the bulk.

In retrospect, we can state that the Au–Pt system was the ideal example to demonstrate the concepts introduced herein. Indeed, this system allows one to explore the effect of size on the occurrence of various phase transformations that are highlighted by the discontinuities in the Gibbs–Thomson curves. The large partition of the solidus and liquidus facilitates the display of the phase diagram topological changes associated with the size of the system. In addition, the calculations presented here showed that these concepts can be applied to systems having a complex thermodynamic description.

Suggestion of further work includes using Butler's equations to compute the solid–liquid equilibrium. In general, it would be useful to evaluate the stability of a system in

EBSCOhost - printed on 2/14/2023 1:06 PM via . All use subject to https://www.ebsco.com/terms-of-use

another configuration than a core–shell, as suggested by Weissmüler [37]. For example, we can imagine an A–B particle where each phase (α and β) is segregated in two spherical caps separated by an interface, ω. If the system is subject to the constraint of mass balance and adopts an equilibrium shape, it is possible to demonstrate that the curvature of the two phases and the interface will be determined by the relative surface energy: $\sigma_\alpha/\sigma_\omega$ and $\sigma_\beta/\sigma_\omega$. Once the curvatures are known, then the capillarity terms would need to be determined by variational calculus (as opposed to simply taking the product of the area of the spherical cap and the surface energy per volume of moles). The capillarity energy of each phase could then be added to their Gibbs energy and the contribution of the interface can be treated as an energy penalty to the molar energy, referred to a standard state of a two-phase equilibrium mixture.

References

[1] Tanaka, T., Hara, S., Thermodynamic evaluation of nano-particle binary alloy phase diagrams, Zeitschrift Fur Met. 92 (2001) 1236–1241. http://ir.library.osaka-u.ac.jp/dspace/bitstream/11094/26514/1/ZM92_11_1236.pdf.

[2] Tanaka, T., Hara, S. , Thermodynamic evaluation of binary phase diagrams of small particle systems, Zeitschrift Fur Met. (2001).

[3] Butler, J.A. V., The Thermodynamics of the Surfaces of Solutions, Proc. R. Soc. A Math. Phys. Eng. Sci. 135 (1932) 348–375. doi:10.1098/rspa.1932.0040.

[4] Tanaka, T., Hack, K., Hara S., Cermak, Calculation of surface tension of liquid Bi-Sn alloy using thermodynamical application library Chemapp, Calphad. 24 (2000) 465–474.

[5] Kaufman, L.B.H., Computer calculation of phase diagrams with special reference to refractory metals, Academic Press, New York, 1970.

[6] Park, J., Lee, J., Phase diagram reassessment of Ag-Au system including size effect, Calphad Comput. Coupling Phase Diagrams Thermochem. 32 (2008) 135–141. doi:10.1016/j.calphad.2007.07.004.

[7] Lee, J., Sim, K.J., General equations of CALPHAD-type thermodynamic description for metallic nanoparticle systems, Calphad Comput. Coupling Phase Diagrams Thermochem. 44 (2014) 129–132. doi:10.1016/j.calphad.2013.07.008.

[8] Monji, F., Jabbareh, M.A., Thermodynamic model for prediction of binary alloy nanoparticle phase diagram including size dependent surface tension effect, Calphad Comput. Coupling Phase Diagrams Thermochem. 58 (2017) 1–5. doi:10.1016/j.calphad.2017.04.003.

[9] Sopousek, J., Vrestal, J., Pinkas, J., Broz, P., Bursik, J., Styskalik, A., Skoda, D., Zobac, O., Lee, J., Cu-Ni nanoalloy phase diagram – Prediction and experiment, Calphad Comput. Coupling Phase Diagrams Thermochem. 45 (2014) 33–39. doi:10.1016/j.calphad.2013.11.004.

[10] Shirinyan, A., Wautelet, M., Belogorodsky, Y., Solubility diagram of the Cu – Ni nanosystem, J. Physics-Condensed Matter. 18 (2006) 2537–2551. doi:10.1088/0953-8984/18/8/016.

[11] Shirinyan, A., Wilde, G., Bilogorodskyy, Y., Solidification loops in the phase diagram of nanoscale alloy particles: from a specific example towards a general vision, J. Mater. Sci. 53 (2018) 2859–2879. doi:10.1007/s10853-017-1697-y.

EBSCOhost - printed on 2/14/2023 1:06 PM via . All use subject to https://www.ebsco.com/terms-of-use

[12] Bajaj, S., Haverty, M.G., Arróyave, R., Goddard, W.A. III FRSC, Shankar, S., Phase stability in nanoscale material systems: extension from bulk phase diagrams, Nanoscale. 7 (2015) 9868–9877. doi:10.1039/C5NR01535A.
[13] Sopoušek, J., Kryštofová, A., Premović, M., Zobač, O., Polsterová, S., Brož, P., Buršík, J., Au-Ni nanoparticles: Phase diagram prediction, synthesis, characterization, and thermal stability, Calphad Comput. Coupling Phase Diagrams Thermochem. 58 (2017) 25–33. doi:10.1016/j.calphad.2017.05.002.
[14] Braidy, N., Purdy, G.R., Botton, G.A., Equilibrium and stability of phase-separating Au–Pt nanoparticles, Acta Mater. 56 (2008) 5972–5983. doi:10.1016/j.actamat.2008.08.024.
[15] Garzel, G., Janczak-Rusch, J., Zabdyr, L., Reassessment of the Ag-Cu phase diagram for nanosystems including particle size and shape effect, Calphad Comput. Coupling Phase Diagrams Thermochem. 36 (2012) 52–56. doi:10.1016/j.calphad.2011.11.005.
[16] Ivas, T., Grundy, A.N., Povoden-Karadeniz, E., Gauckler L.J., Phase diagram of CeO2CoO for nano-sized powders, Calphad Comput. Coupling Phase Diagrams Thermochem. 36 (2012) 57–64. doi:10.1016/j.calphad.2011.10.005.
[17] Ghasemi, M., Zanolli, Z., Stankovski, M., Johansson, J., Size- and shape-dependent phase diagram of In–Sb nano-alloys, Nanoscale. 7 (2015) 17387–17396. doi:10.1039/C5NR04014K.
[18] Kroupa, A., Káňa, T., Buršík, J., Zemanová, A., Šob, M., Modelling of phase diagrams of nanoalloys with complex metallic phases: application to Ni–Sn, Phys. Chem. Chem. Phys. 17 (2015) 28200–28210. doi:10.1039/C5CP00281H.
[19] Sim K., Lee J., Phase stability of Ag-Sn alloy nanoparticles, J. Alloys Compd. 590 (2014) 140–146. doi:10.1016/j.jallcom.2013.12.101.
[20] Kaptay, G., Nano-Calphad: Extension of the Calphad method to systems with nano-phases and complexions, J. Mater. Sci. 47 (2012) 8320–8335. doi:10.1007/s10853-012-6772-9.
[21] Shirinyan, A.S., Wautelet, M., On phase changes in nanosystems, Mater. Sci. Eng. C. 26 (2006) 735–738. doi:10.1016/j.msec.2005.09.084.
[22] Jesser, W.A., Shneck, R.Z., Gile, W.W., Solid-liquid equilibria in nanoparticles of Pb-Bi alloys, Phys. Rev. B - Condens. Matter Mater. Phys. 69 (2004) 144121. doi:10.1103/PhysRevB.69.144121.
[23] Wittenberg, L., Dewitt, R., Volume contraction during melting: Emphasis on lanthanide and actinide metals, J. Chem. Phys. 56 (1972) 4526. doi:10.1063/1.1677899.
[24] Allen, B.C., Liquid Metals: Chemistry and physcis, Marcel Dekker, New York, 1972.
[25] Murr, L.E., Interfacial phenomena in metals and alloys, Reading, Mass. : Addison-Wesley Pub. Co., Advanced Book Program, 1975.
[26] Kumikov, V.K., Khokonov, K.B., On the measurement of surface free energy and surface tension of solid metals, J. Appl. Phys. 54 (1983) 1346–1350. doi:10.1063/1.332209.
[27] Huh, J.Y., Lee, H., Johnson, W.C., Particle Size Effects on the Coherent Phase Equilibria of Binary Nanoparticles, Met. Mater. Int. 11 (2005) 2005.
[28] Howe, J.M., Saka, H., In situ transmission electron microscopy studies of the solid-liquid interface, Mrs Bull. 29 (2004) 951–957. doi:10.1557/mrs2004.266.
[29] Okamoto, H., Massalski, T.B., The Au-Pt (Gold-Platinum) System, Bull. Alloy Phase Diagrams. 6 (1985) 46–56.
[30] Iida, T., Guthrie R.I.L., The Physical Properties of Liquid Metals, Clarendon Press., Oxford, 1988.
[31] Kasama, A., Iida, T., Morita, Z., Temperature Dependence of Surface Tension of Liquid Pure Metals, 日本金属学会誌. 40 (1976) 1030–1038.
[32] Morita, Z., No Title, Bull. Japan Inst. Met. 125 (1976) 743-.
[33] Jones, H., The Surface Energy of Solid Metals, Met. Sci. J. 5 (1971) 15–18. doi:10.1179/030634571790439342.

EBSCOhost - printed on 2/14/2023 1:06 PM via . All use subject to https://www.ebsco.com/terms-of-use

[34] Buffat, P., Borel, J.P., Size effect on melting temperature of gold particles, Phys. Rev. A At., Mol., Opt. Phys. 13 (1976) 2287–2298.
[35] Porter, D., Easterling K., Phase transformations in metals and alloys, Chapman Hall. (1992). doi:10.1007/s13398-014-0173-7.2.
[36] Shirinyan, A.S., Gusak, A.M., Phase diagrams of decomposing nanoalloys, Philos. Mag. 84 (2004) 579–593. doi:10.1080/14786430310001635431.
[37] Weissmüller, J., Bunzel, P., Wilde, G., Two-phase equilibrium in small alloy particles, Scr. Mater. 51 (2004) 813–818. doi:10.1016/j.scriptamat.2004.06.025.

EBSCOhost - printed on 2/14/2023 1:06 PM via . All use subject to https://www.ebsco.com/terms-of-use

Serene S. Bayram, Amy Szuchmacher Blum

12 Directing the Self-Assembly of Nanoparticles for Advanced Materials

In this chapter, we present an overview of different methods and techniques used for directing the self-assembly of nanoparticles. For exploiting nanoparticle self-assembly in technological applications, both a high level of direction and control as well as an extended assembly size are required to guarantee an efficient scale-up. We focus on tools used for controlling the interparticle forces responsible for triggering self-assembly, outlining both templated and non-templated assembly techniques, including the most common templates used for guiding nanoparticles, as well as externally imposed directing fields that enhance the inherent thermodynamic forces driving the self-assembly process. In addition, we discuss interfacial or surface tension effects that direct the assembly at interfaces or in thin films. *Internal* and *external* self-assembly methods are distinguished, where the former relies on modulating the intrinsic properties of the nanoparticles and the latter employs extrinsic fields and forces to guide the assembly. Finally, we also review the application of rod-shaped and sphere-like viruses in organizing molecules and nanoparticles.

12.1 Introduction

Self-assembly is the process by which nanoparticles and other discrete components spontaneously organize into ordered structures. Self-assembled systems are microscopic or macroscopic structures associated with thermodynamic equilibrium characterized by an energy minimum [1]. As a high level of direction, control and extended assembly size range are typically required for scale-up and technological relevance, the careful design of the assembly methodology is essential. In other words, the thermodynamic forces and kinetic factors driving the assembly need to be modulated, and this is done by the rational choice of template, chemistry, and external field. Directed self-assembly (DSA) is dictated by a predetermined construction of building blocks before applying the assembling forces without a need for advanced or sophisticated techniques. This is a great advantage of bottom–up self-assembly approaches, as they support a spontaneous mass scale production of coherent spatiotemporally organized constructs under a minimal cost and time. Ordered assemblies can be created by using the chemistry concepts of molecular

Serene S. Bayram, Amy Szuchmacher Blum, Department of Chemistry, McGill University, Montreal, QC Canada

https://doi.org/10.1515/9783110537734-012

EBSCOhost - printed on 2/14/2023 1:06 PM via . All use subject to https://www.ebsco.com/terms-of-use

interactions developed for supramolecular chemistry. Stimuli-responsive interparticle interactions as well as nanoparticles' morphological and functional features are tailored to drive ordered assemblies. The interparticle forces can alternatively be enhanced by external intervening electric or magnetic fields, manipulated by geometric confinement, or at directed surfaces and interfaces, depending on their physical properties.

12.2 Directing Self-Assembly by Molecular Interactions

Aggregation-driven self-assembly is based on employing weak and specific interaction forces to achieve the desired structures and functionalities. Colloidal stability is achieved by minimizing attractive forces between colloidal particles. Thus, nanoparticle self-assembly from a stable solution should be driven by an appropriate choice of molecular interaction in order to avoid undesirable and uncontrolled flocculation caused by van der Waals interactions. From a chemical point of view, the interactions between the molecules located at the colloidal interfaces are controlled using stimuli such as temperature, light, pH, solvent polarity, or redox activity. Upon exposure to the triggering stimulus, the particles are spatially organized either via straight intermolecular interactions between capping agents or predesigned templates. In this approach, the assembly is modulated by controlling the periodicity or by the reversibility of the process [1].

12.3 Template Directed Self-Assembly

Templates are surface-modified substrates designed to deposit nanoparticles specifically on surface in a complementary morphology. Template size ranges from below to well above the nanoparticle sizes (Figure 12.1e, f, and g), so templates can be any scaffold onto which particles can be arranged. Microstructures (Figure 12.1f) or block copolymers (Figure 12.1g) are potential templates for organizing nanoparticles. Templates are classified into soft (e.g., DNA, linear polymers, and biomolecules) and hard templates (e.g., carbon nanotubes [CNTs] with modifiable surfaces).

Temperature [2] and pH-sensitive [3] small molecules are inexpensive and widely available tools for DSA through applying principles from supramolecular chemistry such as exploiting weak and reversible interactions between the small molecules and nanoparticle capping agents. When templates are employed, strategies to modulate the nanoparticle assembly involve either using the distribution

EBSCOhost - printed on 2/14/2023 1:06 PM via . All use subject to https://www.ebsco.com/terms-of-use

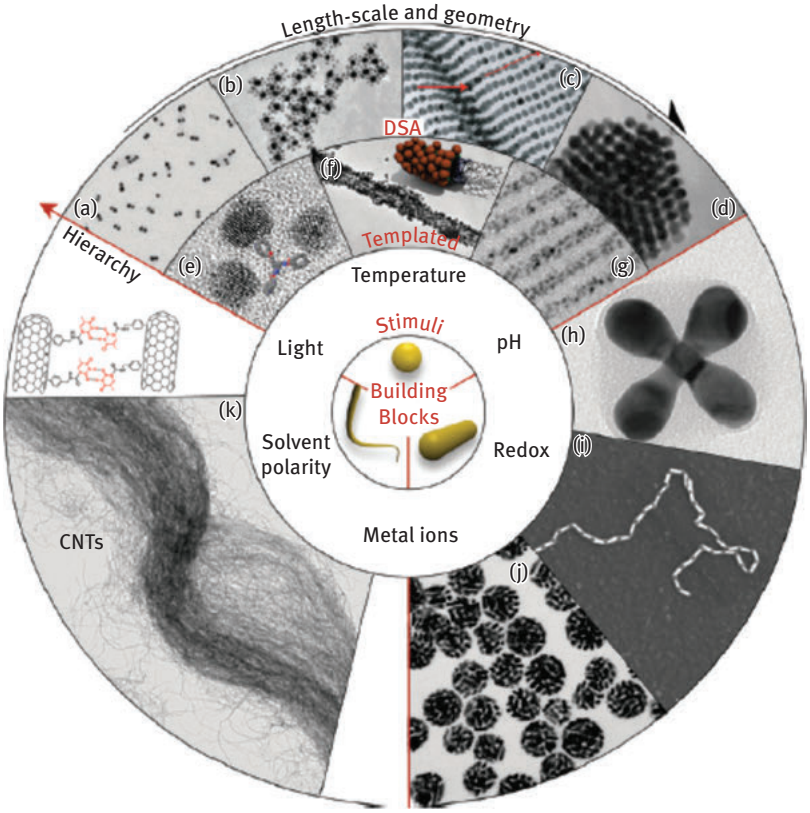

Figure 12.1: A schematic diagram summarizing the directed self-assembly methodologies of gold nanoparticles by molecular interactions. (a, b) Nanoparticle clustering by temperature-sensitive DNA via H-bonding; (c) two-dimensional superlattices of gold organized by DNA; (d) colloidal crystals induced by light-sensitive azobenzenes by dipole–dipole interactions; (e), (f) and (g) depict template-driven assembly of gold nanoparticles by macromolecules, carbon nanotubes, and block copolymers, respectively; (h), (i), and (j) depict the hydrophobic interaction-driven assembly of gold nanorods into low-symmetry clusters, chain-like structures, and spherical objects, respectively; (k) assembly of CNTs into bundles by hydrophobic interactions induced by changes in medium polarity. Image reprinted with permission from Ref. [18].

and chemistry of the coordination sites on the template molecule [4] or varying the initial symmetry of the template [5]. For example, DNA-controlled nanocrystal self-assembly has been widely and popularly reported because of high versatility and specificity in hybridization [6–14]. Because of melting properties of DNA, disassembly of nanoparticles can be triggered by heating. In addition, the DNA helical geometry gives access to large-scale chiral assemblies in the solution phase, which finds potential applications in the fields of chiral nanoplasmonics and metamaterials. Furthermore, the DNA origami folding technique has allowed the exquisite design

EBSCOhost - printed on 2/14/2023 1:06 PM via . All use subject to https://www.ebsco.com/terms-of-use

of highly complex DNA curved surfaces in 3D space [15]. These origami structures were successfully and elegantly utilized for rigidly assembled gold nanoparticles into dimers of a very precise and fixed interparticle gap (down to 5 nm), enabling the investigation of plasmonic antenna effects in precisely positioned optically active molecules [16–17].

The assembly strategies mentioned so far generate assemblies that range in size from nanometers to micrometers. For many technological applications, longer length scales are required. Templates that can themselves organize as block copolymers, which can readily assemble into nanostructured arrays over macroscopic size scales, provide excellent templates in this pursuit. To render the copolymer–nanoparticles network to be modular and reversible, pH- or temperature-responsive molecules are introduced between the nanoparticles and the copolymer that weakly interact with both the ends through noncovalent bonds [19]. CNTs are another material that can be used for larger scale assemblies. For hard templates as CNTs, their surface chemistry is a determining factor in directing the assembly. For example, nanoparticle position and density can be controlled via electrostatic interactions driven by polyelectrolyte surface wrapping of the tubes [20]. Although CNTs do not allow a controlled spacing between the nanoparticles, subsequent processing such as incorporation of nanoparticle–CNT assemblies in thermoresponsive polymers results in more versatile composite structures that are capable of particle alignment [21]. Alternatively, CNTs can be modified by magnetic particles that can be aligned by external magnetic fields, resulting in a more spatially ordered assembly [22].

12.3.1 Biological Templates for Self-Assembly

A variety of biological templates have been widely explored and reported in literature as organizing vectors for nanoparticles. These include bacterial colonies [1], diatoms [23], proteins [24], and DNA [25]. Proteins and DNA are a particularly interesting set of materials to use, as they inherently possess their own assembly properties, which impart additional tuning parameters to the composite organic–inorganic constructs. The hierarchical complexity can thus be achieved by a multistep assembly.

DNA and Protein Template Self-Assembly

Using the H-bonding-driven base-pairing rules in DNA with its four-letter code, both two-dimensional [26–29] and three-dimensional [25, 30–32] DNA scaffold geometries were realized using the DNA origami technique – a process where long DNA strands are folded in predetermined positions using shorter DNA strands called “staple strands.” The DNA scaffold system is highly versatile because of the

EBSCOhost - printed on 2/14/2023 1:06 PM via . All use subject to https://www.ebsco.com/terms-of-use

programmability of its structure, where specific and nanometer-precise binding sites can be designed to anchor complementary strands bound to inorganic nanoparticles' surfaces achieving exquisite assemblies of predetermined spatial geometries.

Within the same rationale, it is unquestionable why proteins can provide a comparable if not a better versatile system for bioengineering. Proteins consist of a 21-amino acid alphabet, each possessing an inherent propensity for chemical functionalization or mutation allowing them to function as templates in a wider variety of conditions. Protein's ability to endure harsh conditions like extreme acidic or basic environments is an added value that allows expanding the scope of their composite counterparts' applications.

Viruses and their capsids have lately garnered a lot of attention as protein templates because of their rigidity, high monodispersity, their interesting and variant geometries, and the ease by which they can be produced in large quantities, rendering them and their composites exceptionally open to scale-up and industrialization.

Introduction to Viruses

Viruses are macromolecules that, by evolution, *learnt* how to propagate themselves through host cells by incorporating their genome into the host cells' molecular machinery. The mechanisms of their function as well as their geometries are explored and well-studied, aided by advances in electron microscopy and scanning probe microscopy. The structure–function correlations of viruses that were developed throughout the years have greatly inspired biochemists to understand biological systems and materials scientists to devise targeted engineered nanostructures. To date, many different viruses have been used, including the bacteriophages M13 and MS2, the plant viruses CPMV, *cowpea chlorotic mottle virus* (CCMV), *red clover necrotic mosaic virus* (RCNMV), and *brome mosaic virus* (BMV), and the animal virus *chilo iridescent virus* (CIV). Viruses are unique bionanoparticles because of their high degree of symmetry and polyvalency and also because of their advantageous size that can range, for spherical particles, from 30 nm (CPMV) to 140 nm (CIV) and reach a length up to microscale (M13). In addition, their surface properties can be altered decisively by mutagenesis to offer peptide display platforms, modified charge densities, and desired amino acid functionalities.

A virus consists of a genetic material contained in a capsid or a coat protein, which may be further enveloped by a lipid bilayer [33]. The capsid represents the quaternary structure of protein subunits in the form of a hollow oligomer that houses the genetic information. The main role of virus capsids is protection of the genetic material as they are rigid and robust, rendering them excellent targets for applications in bionanotechnology. Plant viruses are usually used as platforms for self-assembly, as they are benign to humans and they can usually be used without

EBSCOhost - printed on 2/14/2023 1:06 PM via . All use subject to https://www.ebsco.com/terms-of-use

their genetic material. In fact, they can assemble independently into charged colloid [34] or polymer [35] particles, which are termed as virus-like particles (VLPs). VLPs assemble into a variety of geometries and can respond to a variety of chemical and physical signals like temperature and pH. Because of their robustness, they can tolerate high temperatures and endure wide pH ranges and various organic solvent–water mixtures, which allow their interfacing with the chemistry world.

Viruses and VLPs in Nanotechnology

Viruses and VLPs have been widely applied for the nanofabrication of novel nanomaterials. The most common application is the encapsulation of drug material benefiting from the virus's inherent assembly–disassembly behavior. A model example is CCMV, which is a T=3 icosahedral virus with a capsid consisting of 180 identical coat protein subunits that can be separately expressed in yeast or *E.coli* without its genetic material [36–37]. It undergoes a reversible transition controlled by pH and ionic strength where it develops 60 perforations during the process, thus acting as a molecular gating mechanism allowing ions and small molecules to diffuse in and out through its internal cavity during this structural transition [38]. The encapsulation of large molecules or colloids inside the capsid interior is also possible as long as they meet the electrostatic requirements. CCMV has a positively charged interior and will assemble around negatively charged polyelectrolytes such as polyferrocenylsilane [35].

A second prominent utilization of virus capsids in nanotechnology is in driving the self-assembly of nanoparticles by making use of the particular chemical functionalities displayed on the outer and inner surface. These sites offer addressable handles to bind inorganic nanoparticles, antibodies, or polymers either through their chemical modification or through site mutation, with the latter guaranteeing a 100% yield of evenly spread mutation for the capsids. Cysteine mutation of the CPMV has allowed the specific positioning of gold nanoparticles on predetermined sites via thiol–gold interactions [39]. A selective metal precipitation on virus capsids is also possible because of the electrostatic affinity of negatively charged residues to metal precursors that can deposit and get biomineralized [40]. The rich chemistry of viral capsids is derived from their carboxylate groups in aspartic and glutamic acid residues, amine groups in lysine residues, and phenol groups in tyrosine residues. Chemical modification of the capsids can be orthogonal, and does not compromise their structural integrity; however, it is usually followed by purification steps because of incomplete yield.

The Tobacco Mosaic Virus

The tobacco mosaic virus (TMV) is a 300 nm long rod-shaped virus with an 18 nm diameter and a 4 nm diameter channel that runs through its central axis. It has a helical arrangement of 2,130, 17.5 kDa identical protein subunits, which pack the

EBSCOhost - printed on 2/14/2023 1:06 PM via . All use subject to https://www.ebsco.com/terms-of-use

RNA between its turns (Figure 12.2). The RNA-free protein capsid aggregates into different phases based on pH, ionic strength, and temperature [41]. These aggregates can be distinguished into three classes of structures that interconvert reversibly and are named by their sedimentation coefficients [42]: 4S A-protein, 20S disk, and helix (Figure 12.3). The A-protein is a mixture of small aggregates of protein subunits that predominate at basic conditions. The helix, on the other hand, occurs at an acidic pH. The 20S disk is a two-layer aggregate consisting of 34 subunits with a diameter of 18 nm and possesses a 4-nm pore in its center. It occurs in the pH range of 6.5 to 7.5 under a wide range of ionic strengths and has been closely examined because of its role in the assembly of the complete virion.

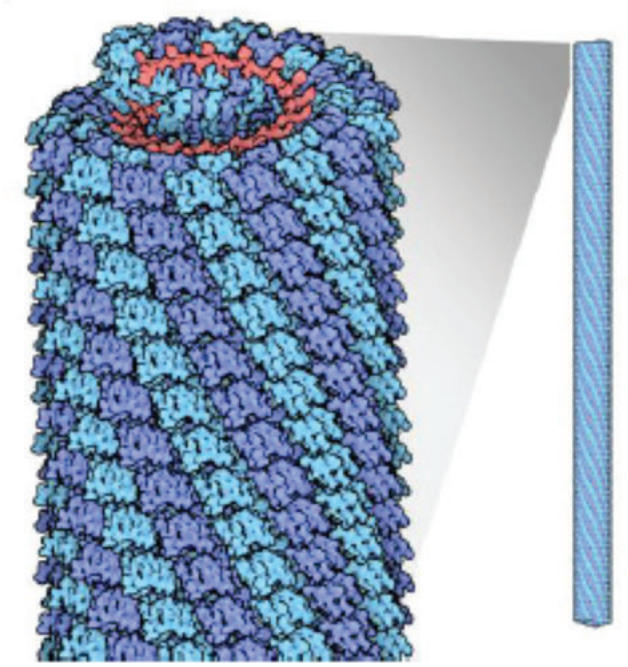

Figure 12.2: Cartoon showing the TMV coat protein (blue) containing RNA (red). © 2014 Reprinted with permission from David Goodsell & RCSB Protein.

The RNA-free TMV coat protein has been extensively studied [43] and has been treated as a paradigm for the self-assembly of biological materials [44]. The self-assembly of TMV is determined by the interplay between hydrophobic forces, electrostatic interactions, and hydrogen bonding. Scanning calorimetry studies prove that the assembly is an endothermic process, which is favored as temperature is increased [45–46]. The assembly of 20S disks is thus entropy-driven and occurs because of

EBSCOhost - printed on 2/14/2023 1:06 PM via . All use subject to https://www.ebsco.com/terms-of-use

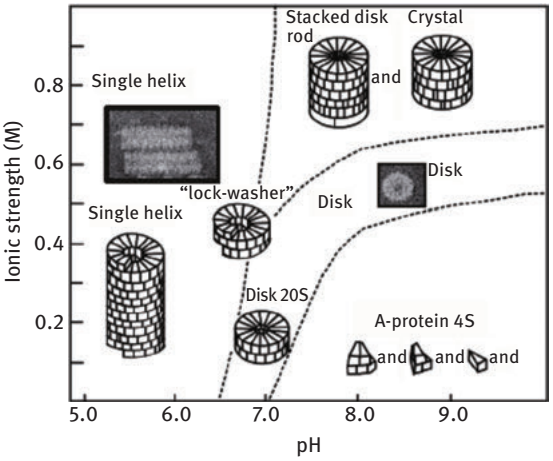

Figure 12.3: Pseudo-phase diagram of TMV coat protein showing the various assembly states with superimposed TEM images. All three states exist in dynamic equilibrium [49] © 2006 Reprinted with permission from Elsevier.

side-to-side hydrophobic interactions between protein subunits that overcome mutual electrostatic repulsions [44]. The charge screening at high ionic strength conditions drives the hydrophobic patches closer to each other as the electrostatic repulsion is suppressed. Repulsion is also reduced by protonating carboxyl groups at lower pH values, which explains the disk formation at lower pH values. However, the helical rod arrangement decreases the contact between hydrophobic surface groups and cannot be explained by electrostatic screening. The axial interaction between Glu50 and Asp77 and lateral one between Asp95 and Asp106 were revealed by high-resolution X-ray diffraction and thought to cause the helical geometry [47]. Further evidence was provided when the site-directed mutagenesis of Asp and Glu into glutamine (Gln) and asparagine (Asn) impaired the helical assembly [48].

TMV and TMV Capsids as Bioscaffolds and Applications in Bionanotechnology

Nearly all previous methods developed to utilize TMV as a bioscaffold have employed the complete virion or the helical rod form of the capsid protein as the templating platform. The inner channel and outer surfaces of the virus surface are hydrophilic displaying glutamic and aspartic acid, lysine and arginine to the solvent. The differential pKa values of the outer surface residues, mainly lysines and *N*-termini, from those in the inner channel like glutamic and aspartic acid were used to selectively complex and mineralize several mineral salts [50]. The relative positive and negative charge of the TMV outer and inner surfaces can be altered by tuning pH allowing for surface-specific metallization [51–54]. The isolated coat protein has been utilized to

EBSCOhost - printed on 2/14/2023 1:06 PM via . All use subject to https://www.ebsco.com/terms-of-use

create functional assemblies by virtue of its inherent self-assembly properties. A Ser123 to Cys TMV mutant was used for binding thiol-reactive dyes to the mutant. The helical assembly of the protein then served the incorporation of FRET donor and acceptor dyes within the geometry to behave as a light-harvesting entity [55]. The tyrosine residues on the TMV surface have also been modified into diazonium salts by electrophilic substitutions to incur new functionalities such as alkynes [56]. Alkynes can then be reacted with azide-containing molecules by the highly specific copper catalyzed azide–alkyne cycloaddition. Tyrosines were targeted to create TMV-based enhanced MRI contrast agents [57], multifunctional viral nanoparticles [58–59], thermally stable virus–polymer conjugates in hydrophobic solvents [60] and thin film sensors for volatile organic compounds [61]. The TMV rods themselves acted as self-assembling units when they were assembled into hyperstructures by the in situ polymerization of aniline [62]. The TMV coat protein mutated with a hexahistidine tag at the C-terminus has been assembled side-by-side through pi-stacking into long fibers or hexagonal disk arrays depending on the conditions of assembly [63]. Tunable thin TMV film assemblies were also fabricated by layer-by-layer assembly with polyelectrolytes [64]. TMV-based composite materials have found a broad spectrum of applications, including drug delivery [65–68], energy and catalysis [69–74], electronics [75–78], and optical resonators [79].

TMV has also served as a biomineralization template to generate tubular inorganic structures by spatially controlled deposition of metals such as nickel, copper, cobalt, palladium, platinum, gold and silver, as well as metal oxides like TiO_2 and Al_2O_3 either on the outer surface or along the inner channel [52, 71, 80–85]. The TMV system can also find applications in photovoltaic and photocatalytic processes as it has been demonstrated as a light harvesting array [55]. Centimeter-scale electrically conductive wire arrays of silver were constructed using TMV assemblies owing to their liquid-crystalline properties and length scales that bridge up the gap between bottom–up and top–bottom fabrication schemes [86]. The spatial and orientation control of TMV assembly on solid supports was further accomplished via nucleic acid hybridization of complementary oligonucleotides after exposing the RNA at the 5′ end of TMV, allowing the generation of on-demand micropatterned arrays [87]. While biomolecules do not support charge transport that limits their utilization in electronic devices, conjugating TMV with platinum allowed the construction of a digital memory device with demonstrated ON–OFF conductance switching [88] (Figure 12.4). Recent studies have employed the inherent self-assembly properties of RNA-free TMV coat protein to fabricate sub-30 nm gold and silver nanorings by using its disk-assembled form as a biotemplate [89–90].

Sphere-Like VLPs in Nanotechnology

Several virus particles bearing an icosahedral symmetry have also been studied and their X-ray structures have been resolved to atomic resolution. The distinct

EBSCOhost - printed on 2/14/2023 1:06 PM via . All use subject to https://www.ebsco.com/terms-of-use

geometries they possess along with the well-understanding of their surface and the self-assembly of their subunits make them good candidates for cargo encapsulation, stimulus-triggered drug release, size-controlled metallization, and site-specific chemical modifications. Large-scale production of the wild type and genetically mutated virus capsids with or without the genetic material is possible by heterologous expression systems. Intact and empty CCMV monomers can be produced in yeast and assembled in vitro into sphere-like particles that undergo structural swollen/non-swollen transition at high/low pH, respectively. In the swollen state, polyoxometalate ion precursors like tungstate, vanadate, and molybdate can diffuse into the virus cavity where they can undergo, upon lowering the pH, oligomerization into polyoxometallic forms. Lowering the pH also contracts the virus cage, thus selectively encapsulating the minerals in the interior side [91–93]. Cationic ion precursors like ferrous and ferric species can be also electrostatically entrapped within the CCMV cage by reversing the inner vessel positive charge. This was achieved via substituting the *N*-termini by glutamate residues, to which the positive ions can bind, thus forming size-constrained iron oxide nanoparticles [94]. CCMV was also used for displaying paramagnetic species like terbium(III) and gadolinium(III) ions on its inherent metal-binding sites [95–96]. On-surface lysines and carboxylate groups as well as cysteine mutants provided a high-yield multivalent display platform for diverse dyes on their surface [97]. Cysteine mutation also served in the immobilization of CCMV on gold surfaces [98]. Other immobilization protocols of multilayer films of the virus involved electrostatic interactions [99, 100].

Like CCMV, BMV exhibits a pH- and ion-dependent swelling behavior allowing the incorporation of gold and quantum dot nanoparticles of sizes up to 16 nm [101–105]. Such hybrids can serve as single plasmonic and spectroscopic tools for biosensing. RCNMV monomers require an assembly initiating site on the RNA; yet, gold nanoparticles were successfully used as artificial initiators for their in vitro assembly, thus forming similar capsules for a slightly broader gold core size ranging from 5 to 15 nm [106]. CPMV has been the subject of different bioconjugation strategies that mainly addressed the solvent-exposed lysine and carboxylate groups installing up to 240 dyes per one wild-type viral particle [107]. Two tyrosine sites were also successfully targeted and oxidized on the exterior of CPMV [108]. As the native form of CPMV does not possess solvent-exposed cysteines [109], cysteine mutants were engineered to precisely nanopattern gold nanoparticles in a 3D arrangement on the outer surface [39, 110]. A mutation-free alternative protocol to introduce addressable thiol functionalities into CPMV was to modify the exposed lysines by thioacetate groups bearing protected thiols, thus preventing unwanted disulfide aggregation events and prolonging safe storage periods [111]. Internal cysteine residues are reachable and could be reacted with small thiol-reactive molecules [112–113]. Larger molecules, such as peptides, proteins, carbohydrates, and polymers were also attached to CPMV using the click-chemistry technique or the copper(I)-catalyzed azide–alkyne cycloaddition [3+2]

EBSCOhost - printed on 2/14/2023 1:06 PM via . All use subject to https://www.ebsco.com/terms-of-use

[114–116]. CPMV could also be made electroactive by decorating it with independent and electrically isolated ferrocene molecules [117] or a redox-active organic viologen derivative [107], and thus could mediate electrocatalytic processes of industrial and biological relevance [117].

Besides their biocompatibility, the VLPs afford multivalence and concentrate the reporter molecules or nanoparticles such as dyes, MRI contrast agents, redox-active species, or larger molecular tags that can behave independently increasing the signal-to-noise ratio and boosting detection sensitivity. However, more studies are still needed to inspect their toxicity, biodistribution, and ways to reduce their immunogenicity.

12.4 Template-Free Directed Self-Assembly

Template-free assembly relies mostly on stimuli-responsive capping agents passivating the nanoparticle surface without the need for a template molecule. Colloidal crystals can be formed by oppositely charged nanoparticles [118], but for additional control, external stimuli can modulate interparticle forces such as H-bonding, molecular dipole forces, hydrophobic forces, and $\pi - \pi$ stacking under equilibrium and nonequilibrium conditions [119]. One example is the assembly of complementary DNA (cDNA)-modified nanoparticle batches, whose assembly dynamics are dictated by temperature, depending on the DNA melting point. This strategy has been successfully applied on spherical, rod-like, and CNT nanoparticles [6–9]. $\pi - \pi$ stacking interactions are also common in controlling the aggregation of nanoparticles, with the ability to induce disassembly at elevated temperatures [120–121]. Light-sensitive organic molecules that can chemisorb to nanoparticle surfaces via thiol linkages were successfully employed to control electromagnetic coupling between gold [122] and silver [123] nanoparticles, owing to their optical switching under UV light. Thus, the choice, chemistry, and geometry of the capping molecules are key factors to control the assembly as desired, as long as global flocculation is avoided.

Other factors that can influence nanoparticle assembly include the nanoparticle concentration, the ionic strength, and the pH. Solvent polarity can also considerably modulate the assembly process as well. For instance, increasing solvent mixtures' polarity enforces the $\pi - \pi$ stacking between aromatic ligands [124]. Solvent mixtures can also modulate hydrophobic and H-bonding forces, controlling the strength of nanoparticle interactions. The former was manifested in the work of Nie et al., where increasing the polarity of the solvent mixtures led to chain-like structures [125]. Template-free assembly approaches do not require complex compositions, additive molecules, or templates, but rather rely on a variety of stimulus interventions, including some inspired by nature.

EBSCOhost - printed on 2/14/2023 1:06 PM via . All use subject to https://www.ebsco.com/terms-of-use

12.5 Self-Assembly Directed by External Fields

Self-assembly directed by external electric and magnetic fields, fluid flows, and spatially patterned optical trap electromagnetic fields has been widely reported, and has demonstrated good potential for scale-up, allowing for bottom–up fabrication of novel functional nanostructures from solution precursor particles. Magnetically and electrically polarizable colloids can undergo field-induced interactions via several polarization mechanisms [126] The main interparticle forces are anisotropic dipole–dipole interactions induced in the far-field. For sufficiently strong interactions surpassing Brownian motion, the dipolar chains formed can coarsen by coalescence. This underlies the mechanism of liquid to solid transitions; however, under weaker field strengths, the dipolar interactions lead to ordered phases of two- and three-dimensional colloidal crystals that are reversible, where disordered states can be reinstated upon field withdrawal. Cycling the fields thus can *anneal* structural defects because of the switchable nature of the assemblies. Some studies on DSA driven by electric or magnetic fields have shown that shape can influence the spatial configuration of the particles. Both translational and orientational orders of anisotropic particles lead to structures that are unattainable using spherical nanoparticles [127–128]. Electric fields have been shown to be excellent directors of assembly for novel and more unique complex particle geometries [129]. A number of factors can be tuned to control interactions between particles and these include the field strength and frequency, the particle shape, the particle and solvent dielectric properties, as well as the choice of capping agents.

The external fields can also reconfigure an existing self-assembly [130]. They can also be incorporated with other forms of directed assembly such as flow fields, which are macroscopic viscous flows capable of directing a disordered particle suspension into ordered crystals. In polymeric matrices or a complex surfactant matrix, flow can induce viscoelastic stresses that can direct the self-assembly, which does not necessarily happen in the direction of the flow but may occur orthogonal to it or in a cascade of orientational transitions like in CNT suspensions [131–132]. Complex fluid flow-directed assembly of nanoparticle suspensions is of great importance in industrial processes where nanoparticles will be subject, in one or more steps, to complex flow fields. Capillary-force-induced convective flows are also used for assembling particles in a variety of flow geometries [133–134]. Combined with lithographic templates, these techniques can direct the assembly of particles down to the size of 2 nm [135].

12.6 Self-Assembly at Liquid Interfaces

Nanoparticle assembly at liquid–liquid interfaces has been demonstrated for a wide range of nanoparticles, especially nonspherical ones, particles modified with

EBSCOhost - printed on 2/14/2023 1:06 PM via . All use subject to https://www.ebsco.com/terms-of-use

special ligands or with Janus-type particles. The main driving force behind trapping the particles at the interface is the reduction in the interfacial energy. Larger particles tend to be preferentially trapped irreversibly at interfaces as shown for CdSe nanoparticles [136]. Controlling the assembly of anisotropic structures at interfaces is tuned by varying the aspect ratio, chemical characteristics of the ligands, concentration, and solvent evaporation rates [137]. The interfacial and capillary forces drive assembly in preferred orientations. For example, rod-like particles achieve an end-to-end direction [138], whereas ellipsoidal particles achieve complex triangular lattices [139]. The orientation of an assembly of ellipsoidal particles can be dictated by externally applied magnetic and AC electric fields during controlled evaporation of deposition protocols [140–141]. In brief, externally assisted directed assembly allows tuning of order–disorder transitions as well as enabling the employment of pulsed fields, which can physically and neatly anneal constructs without generating jammed states.

References

[1] Whitesides, G.M., Grzybowski, B., Self-assembly at all scales. *Science* 2002, *295*(5564), 2418–2421.

[2] Naka, K., Itoh, H., Chujo, Y., Temperature-dependent reversible self-assembly of gold nanoparticles into spherical aggregates by molecular recognition between pyrenyl and dinitrophenyl units. *Langmuir* 2003, *19*(13), 5496–5501.

[3] Ni, W., Mosquera, R.A., Pérez-Juste, J., Liz-Marzán, L.M., Evidence for hydrogen-bonding-directed assembly of gold nanorods in aqueous solution. *The Journal of Physical Chemistry Letters* 2010, *1*(8), 1181–1185.

[4] Kaminker, R., Lahav, M., Motiei, L., Vartanian, M., Popovitz-Biro, R., Iron, M.A., Van Der Boom, M.E., Molecular structure–function relations of the optical properties and dimensions of gold nanoparticle assemblies. *Angewandte Chemie* 2010, *122*(7), 1240–1243.

[5] Olson, M.A., Coskun, A., Klajn, R., Fang, L., Dey, S.K., Browne, K.P., Grzybowski, B.A., Stoddart, J.F., Assembly of polygonal nanoparticle clusters directed by reversible noncovalent bonding interactions. *Nano letters* 2009, *9*(9), 3185–3190.

[6] Kim, J.-Y., Lee, J.-S., Synthesis and thermally reversible assembly of DNA– Gold nanoparticle cluster conjugates. *Nano letters* 2009, *9*(12), 4564–4569.

[7] Pal, S., Sharma, J., Yan, H., Liu, Y., Stable silver nanoparticle–DNA conjugates for directed self-assembly of core-satellite silver–gold nanoclusters. *Chemical Communications* 2009, (40), 6059–6061.

[8] Dujardin, E., Hsin, L.-B., Wang, C.C., Mann, S., DNA-driven self-assembly of gold nanorods. *Chemical Communications* 2001, (14), 1264–1265.

[9] Chen, Y., Liu, H., Ye, T., Kim, J., Mao, C., DNA-directed assembly of single-wall carbon nanotubes. *Journal of the American Chemical Society* 2007, *129*(28), 8696–8697.

[10] Nykypanchuk, D., Maye, M.M., Van Der Lelie, D., Gang, O., DNA-guided crystallization of colloidal nanoparticles. *Nature* 2008, *451*(7178), 549–552.

[11] Park, S.Y., Lytton-Jean, A.K., Lee, B., Weigand, S., Schatz, G.C., Mirkin, C.A., DNA-programmable nanoparticle crystallization. *Nature* 2008, *451*(7178), 553–556.

EBSCOhost - printed on 2/14/2023 1:06 PM via . All use subject to https://www.ebsco.com/terms-of-use

[12] Xu, X., Rosi, N.L., Wang, Y., Huo, F., Mirkin, C.A., Asymmetric functionalization of gold nanoparticles with oligonucleotides. *Journal of the American Chemical Society* 2006, *128* (29), 9286.
[13] Maye, M.M., Nykypanchuk, D., Cuisinier, M., Van Der Lelie, D., Gang, O., Stepwise surface encoding for high-throughput assembly of nanoclusters. *Nature materials* 2009, *8*(5), 388–391.
[14] Loweth, C.J., Caldwell, W.B., Peng, X., Alivisatos, A.P., Schultz, P.G., DNA-based assembly of gold nanocrystals. *Angewandte Chemie International Edition* 1999, *38*(12), 1808–1812.
[15] Han, D., Pal, S., Nangreave, J., Deng, Z., Liu, Y., Yan, H., DNA origami with complex curvatures in three-dimensional space. *Science* 2011, *332*(6027), 342–346.
[16] Acuna, G., Möller, F., Holzmeister, P., Beater, S., Lalkens, B., Tinnefeld, P., Fluorescence enhancement at docking sites of DNA-directed self-assembled nanoantennas. *Science* 2012, *338*(6106), 506–510.
[17] Thacker, V.V., Herrmann, L.O., Sigle, D.O., Zhang, T., Liedl, T., Baumberg, J.J., Keyser, U.F., DNA origami based assembly of gold nanoparticle dimers for surface-enhanced Raman scattering. *Nature communications* 2014, *5*.
[18] Grzelczak, M., Vermant, J., Furst, E.M., Liz-Marzán, L.M., Directed self-assembly of nanoparticles. *ACS nano* 2010, *4*(7), 3591–3605.
[19] Zhao, Y., Thorkelsson, K., Mastroianni, A.J., Schilling, T., Luther, J.M., Rancatore, B.J., Matsunaga, K., Jinnai, H., Wu, Y., Poulsen, D., Small-molecule-directed nanoparticle assembly towards stimuli-responsive nanocomposites. *Nature materials* 2009, *8*(12), 979–985.
[20] Correa-Duarte, M.A., Liz-Marzán, L.M., Carbon nanotubes as templates for one-dimensional nanoparticle assemblies. *Journal of Materials Chemistry* 2006, *16*(1), 22–25.
[21] Correa-Duarte, M.A., Pérez-Juste, J., Sánchez-Iglesias, A., Giersig, M., Liz-Marzán, L.M., Aligning Au nanorods by using carbon nanotubes as templates. *Angewandte Chemie International Edition* 2005, *44*(28), 4375–4378.
[22] Correa-Duarte, M.A., Grzelczak, M., Salgueirino-Maceira, V., Giersig, M., Liz-Marzan, L.M., Farle, M., Sierazdki, K., Diaz, R., Alignment of carbon nanotubes under low magnetic fields through attachment of magnetic nanoparticles. *The Journal of Physical Chemistry B* 2005, *109* (41), 19060–19063.
[23] Rosi, N.L., Thaxton, C.S., Mirkin, C.A., Control of nanoparticle assembly by using DNA-Modified Diatom Templates. *Angewandte Chemie* 2004, *116*(41), 5616–5619.
[24] Hartgerink, J.D., Beniash, E., Stupp, S.I., Self-assembly and mineralization of peptide-amphiphile nanofibers. *Science* 2001, *294*(5547), 1684–1688.
[25] Kuzyk, A., Schreiber, R., Fan, Z., Pardatscher, G., Roller, E.-M., Högele, A., Simmel, F.C., Govorov, A.O., Liedl, T., DNA-based self-assembly of chiral plasmonic nanostructures with tailored optical response. *Nature* 2012, *483*(7389), 311–314.
[26] Rothemund, P.W., Folding DNA to create nanoscale shapes and patterns. *Nature* 2006, *440* (7082), 297–302.
[27] Geng, Y., Pearson, A.C., Gates, E.P., Uprety, B., Davis, R.C., Harb, J.N., Woolley, A.T., Electrically conductive gold-and copper-metallized DNA origami nanostructures. *Langmuir* 2013, *29*(10), 3482–3490.
[28] Sharma, J., Chhabra, R., Liu, Y., Ke, Y., Yan, H., DNA-templated self-assembly of two-dimensional and periodical gold nanoparticle arrays. *Angewandte Chemie International Edition* 2006, *45*(5), 730–735.
[29] Fan, Z., Zhang, H., Govorov, A.O., Optical properties of chiral plasmonic tetramers: Circular dichroism and multipole effects. *The Journal of Physical Chemistry C* 2013, *117*(28), 14770–14777.

EBSCOhost - printed on 2/14/2023 1:06 PM via . All use subject to https://www.ebsco.com/terms-of-use

[30] Zhang, C., Li, X., Tian, C., Yu, G., Li, Y., Jiang, W., Mao, C., DNA nanocages swallow gold nanoparticles (AuNPs) to form AuNP@ DNA cage core–shell structures. 2014.
[31] Tørring, T., Voigt, N.V., Nangreave, J., Yan, H., Gothelf, K.V., DNA origami: A quantum leap for self-assembly of complex structures. *Chemical Society Reviews* 2011, *40*(12), 5636–5646.
[32] Andersen, E.S., Dong, M., Nielsen, M.M., Jahn, K., Lind-Thomsen, A., Mamdouh, W., Gothelf, K.V., Besenbacher, F., Kjems, J., DNA origami design of dolphin-shaped structures with flexible tails. *ACS nano* 2008, *2*(6), 1213–1218.
[33] Mateu, M.G., Introduction: The structural basis of virus function. In *Structure and Physics of Viruses*, Springer: 2013, pp 3–51.
[34] Sun, J., DuFort, C., Daniel, M.-C., Murali, A., Chen, C., Gopinath, K., Stein, B., De, M., Rotello, V.M., Holzenburg, A., Core-controlled polymorphism in virus-like particles. *Proceedings of the National Academy of Sciences* 2007, *104*(4), 1354–1359.
[35] Minten, I.J., Ma, Y., Hempenius, M.A., Vancso, G.J., Nolte, R.J., Cornelissen, J.J., CCMV capsid formation induced by a functional negatively charged polymer. *Organic & biomolecular chemistry* 2009, *7*(22), 4685–4688.
[36] Brumfield, S., Willits, D., Tang, L., Johnson, J.E., Douglas, T., Young, M., Heterologous expression of the modified coat protein of Cowpea chlorotic mottle bromovirus results in the assembly of protein cages with altered architectures and function. *Journal of general virology* 2004, *85*(4), 1049–1053.
[37] Zhao, X., Fox, J.M., Olson, N.H., Baker, T.S., Young, M.J., In vitro assembly of cowpea chlorotic mottle virus from coat protein expressed in Escherichia coli and in vitro-transcribed viral cDNA. *Virology* 1995, *207*(2), 486–494.
[38] Wu, Y., Yang, H., Shin, H.-J., Viruses as self-assembled nanocontainers for encapsulation of functional cargoes. *Korean J. Chem. Eng* 2013, *30*(7), 1359–1367.
[39] Blum, A.S., Soto, C.M., Wilson, C.D., Cole, J.D., Kim, M., Gnade, B., Chatterji, A., Ochoa, W.F., Lin, T., Johnson, J.E., Cowpea mosaic virus as a scaffold for 3-D patterning of gold nanoparticles. *Nano letters* 2004, *4*(5), 867–870.
[40] Oh, D., Qi, J., Han, B., Zhang, G., Carney, T.J., Ohmura, J., Zhang, Y., Shao-Horn, Y., Belcher, A.M., M13 virus-directed synthesis of nanostructured metal oxides for lithium–oxygen batteries. *Nano letters* 2014, *14*(8), 4837–4845.
[41] Mandelkow, E., Holmes, K.C., Gallwitz, U., A new helical aggregate of tobacco mosaic virus protein. *Journal of molecular biology* 1976, *102*(2), 265–285.
[42] Fontana, J., Dressick, W.J., Phelps, J., Johnson, J.E., Rendell, R.W., Sampson, T., Ratna, B.R., Soto, C.M., Virus-templated plasmonic nanoclusters with icosahedral symmetry via directed self-assembly. *small* 2014, *10*(15), 3058–3063.
[43] Bawden, F., Pirie, N., Bernal, J., Fankuchen, I., Liquid crystalline substances from virus-infected plants. *Nature* 1936, *138*(3503), 1051–1052.
[44] Kegel, W.K., van der Schoot, P., Physical regulation of the self-assembly of tobacco mosaic virus coat protein. *Biophysical journal* 2006, *91*(4), 1501–1512.
[45] Sturtevant, J., Velicelebi, G., Jaenicke, R., Lauffer, M., Scanning calorimetric investigation of the polymerization of the coat protein of tobacco mosaic virus. *Biochemistry* 1981, *20*(13), 3792–3800.
[46] Kegel, W.K., van der Schoot, P., Competing hydrophobic and screened-Coulomb interactions in hepatitis B virus capsid assembly. *Biophysical journal* 2004, *86*(6), 3905–3913.
[47] Namba, K., Stubbs, G., Structure of tobacco mosaic virus at 3.6 A resolution: Implications for assembly. *Science* 1986, *231*, 1401–1407.
[48] Culver, J.N., Dawson, W.O., Plonk, K., Stubbs, G., Site-directed mutagenesis confirms the involvement of carboxylate groups in the disassembly of tobacco mosaic virus. *Virology* 1995, *206*(1), 724–730.

EBSCOhost - printed on 2/14/2023 1:06 PM via . All use subject to https://www.ebsco.com/terms-of-use

[49] Klug, A., The tobacco mosaic virus particle: Structure and assembly. *Philosophical Transactions of the Royal Society of London B: Biological Sciences* 1999, *354*(1383), 531–535.
[50] Lim, J.-S., Kim, S.-M., Lee, S.-Y., Stach, E.A., Culver, J.N., Harris, M.T., Quantitative study of Au (III) and Pd (II) ion biosorption on genetically engineered Tobacco mosaic virus. *Journal of colloid and interface science* 2010, *342*(2), 455–461.
[51] Górzny, M.Ł., Walton, A.S., Evans, S.D., Synthesis of high-surface-area platinum nanotubes using a viral template. *Advanced Functional Materials* 2010, *20*(8), 1295–1300.
[52] Balci, S., Bittner, A., Hahn, K., Scheu, C., Knez, M., Kadri, A., Wege, C., Jeske, H., Kern, K., Copper nanowires within the central channel of tobacco mosaic virus particles. *Electrochimica Acta* 2006, *51*(28), 6251–6257.
[53] Tsukamoto, R., Muraoka, M., Seki, M., Tabata, H., Yamashita, I., Synthesis of CoPt and FePt3 nanowires using the central channel of tobacco mosaic virus as a biotemplate. *Chemistry of materials* 2007, *19*(10), 2389–2391.
[54] Khan, A.A., Fox, E.K., Górzny, M.Ł., Nikulina, E., Brougham, D.F., Wege, C., Bittner, A.M., pH control of the electrostatic binding of gold and iron oxide nanoparticles to tobacco mosaic virus. *Langmuir* 2013, *29*(7), 2094–2098.
[55] Miller, R.A., Presley, A.D., Francis, M.B., Self-assembling light-harvesting systems from synthetically modified tobacco mosaic virus coat proteins. *Journal of the American Chemical Society* 2007, *129*(11), 3104–3109.
[56] Bruckman, M.A., Kaur, G., Lee, L.A., Xie, F., Sepulveda, J., Breitenkamp, R., Zhang, X., Joralemon, M., Russell, T.P., Emrick, T., Surface modification of tobacco mosaic virus with "click" chemistry. *ChemBioChem* 2008, *9*(4), 519–523.
[57] Bruckman, M.A., Hern, S., Jiang, K., Flask, C.A., Yu, X., Steinmetz, N.F., Tobacco mosaic virus rods and spheres as supramolecular high-relaxivity MRI contrast agents. *Journal of Materials Chemistry B* 2013, *1*(10), 1482–1490.
[58] Hu, J., Wang, P., Zhao, X., Lv, L., Yang, S., Song, B., Wang, Q., Charge-transfer interactions for the fabrication of multifunctional viral nanoparticles. *Chemical Communications* 2014, *50* (91), 14125–14128.
[59] Chen, L., Zhao, X., Lin, Y., Huang, Y., Wang, Q., A supramolecular strategy to assemble multifunctional viral nanoparticles. *Chemical Communications* 2013, *49*(83), 9678–9680.
[60] Holder, P.G., Finley, D.T., Stephanopoulos, N., Walton, R., Clark, D.S., Francis, M.B., Dramatic thermal stability of virus– polymer conjugates in hydrophobic solvents. *Langmuir* 2010, *26* (22), 17383–17388.
[61] Bruckman, M.A., Liu, J., Koley, G., Li, Y., Benicewicz, B., Niu, Z., Wang, Q., Tobacco mosaic virus based thin film sensor for detection of volatile organic compounds. *Journal of Materials Chemistry* 2010, *20*(27), 5715–5719.
[62] Niu, Z., Bruckman, M., Kotakadi, V.S., He, J., Emrick, T., Russell, T.P., Yang, L., Wang, Q., Study and characterization of tobacco mosaic virus head-to-tail assembly assisted by aniline polymerization. *Chemical communications* 2006, (28), 3019–3021.
[63] Bruckman, M.A., Soto, C.M., McDowell, H., Liu, J.L., Ratna, B.R., Korpany, K.V., Zahr, O.K., Blum, A.S., Role of hexahistidine in directed nanoassemblies of tobacco mosaic virus coat protein. *ACS nano* 2011, *5*(3), 1606–1616.
[64] Steinmetz, N.F., Findlay, K.C., Noel, T.R., Parker, R., Lomonossoff, G.P., Evans, D.J., Layer-by-layer assembly of viral nanoparticles and polyelectrolytes: The film architecture is different for spheres versus rods. *ChemBioChem* 2008, *9*(10), 1662–1670.
[65] Czapar, A.E., Zheng, Y.-R., Riddell, I.A., Shukla, S., Awuah, S.G., Lippard, S.J., Steinmetz, N.F., Tobacco mosaic virus delivery of phenanthriplatin for cancer therapy. *ACS nano* 2016, *10* (4), 4119.

EBSCOhost - printed on 2/14/2023 1:06 PM via . All use subject to https://www.ebsco.com/terms-of-use

[66] Finbloom, J.A., Han, K., Aanei, I.L., Hartman, E.C., Finley, D.T., Dedeo, M.T., Fishman, M., Downing, K.H., Francis, M.B., Stable disk assemblies of a tobacco mosaic virus mutant as nanoscale scaffolds for applications in drug delivery. *Bioconjugate Chemistry* 2016, *27*(10), 2480–2485.
[67] Tian, Y., Gao, S., Wu, M., Liu, X., Qiao, J., Zhou, Q., Jiang, S., Niu, Z., Tobacco mosaic virus-based 1D nanorod-drug carrier via the integrin-mediated endocytosis pathway. *ACS applied materials & interfaces* 2016, *8*(17), 10800–10807.
[68] Shukla, S., Serum albumin 'camouflage'of plant virus based nanoparticles prevents their antibody recognition and enhances pharmacokinetics. *Biomaterials* 2016, *89*, 89–97.
[69] Bhanushali, S., Ghosh, P., Ganesh, A., Cheng, W., 1D copper nanostructures: Progress, challenges and opportunities. *Small* 2015, *11*(11), 1232–1252.
[70] Royston, E., Ghosh, A., Kofinas, P., Harris, M.T., Culver, J.N., Self-assembly of virus-structured high surface area nanomaterials and their application as battery electrodes. *Langmuir* 2008, *24*(3), 906–912.
[71] Lee, S.-Y., Choi, J., Royston, E., Janes, D.B., Culver, J.N., Harris, M.T., Deposition of platinum clusters on surface-modified tobacco mosaic virus. *Journal of nanoscience and nanotechnology* 2006, *6*(4), 974–981.
[72] Yang, C., Meldon, J.H., Lee, B., Yi, H., Investigation on the catalytic reduction kinetics of hexavalent chromium by viral-templated palladium nanocatalysts. *Catalysis Today* 2014, *233*, 108–116.
[73] Kim, Y.-H., Jung, H., Yoon, T.-S., Jung, S., Yang, C., Yi, H., Lee, H.H., Electrical charging characteristics of palladium nanoparticles synthesized on tobacco mosaic virus nanotemplate for organic memory device. *ECS Journal of Solid State Science and Technology* 2016, *5*(9), Q226–Q230.
[74] Yang, C., Manocchi, A.K., Lee, B., Yi, H., Viral templated palladium nanocatalysts for dichromate reduction. *Applied Catalysis B: Environmental* 2010, *93*(3), 282–291.
[75] Chu, S., Gerasopoulos, K., Ghodssi, R., Tobacco mosaic virus-templated hierarchical Ni/NiO with high electrochemical charge storage performances. *Electrochimica Acta* 2016, *220*, 184–192.
[76] Chen, X., Guo, J., Gerasopoulos, K., Langrock, A., Brown, A., Ghodssi, R., Culver, J.N., Wang, C., 3D tin anodes prepared by electrodeposition on a virus scaffold. *Journal of Power Sources* 2012, *211*, 129–132.
[77] Chen, X., Gerasopoulos, K., Guo, J., Brown, A., Wang, C., Ghodssi, R., Culver, J.N., A patterned 3D silicon anode fabricated by electrodeposition on a virus-structured current collector. *Advanced Functional Materials* 2011, *21*(2), 380–387.
[78] Atanasova, P., Rothenstein, D., Schneider, J.J., Hoffmann, R.C., Dilfer, S., Eiben, S., Wege, C., Jeske, H., Bill, J., Virus-templated synthesis of ZnO nanostructures and formation of field-effect transistors. *Advanced Materials* 2011, *23*(42), 4918–4922.
[79] Fan, X., Naves, L., Siwak, N., Brown, A., Culver, J., Ghodssi, R., Integration of genetically modified virus-like-particles with an optical resonator for selective bio-detection. *Nanotechnology* 2015, *26* (20), 205501.
[80] Dujardin, E., Peet, C., Stubbs, G., Culver, J.N., Mann, S., Organization of metallic nanoparticles using tobacco mosaic virus templates. *Nano Letters* 2003, *3*(3), 413–417.
[81] Knez, M., Bittner, A.M., Boes, F., Wege, C., Jeske, H., Maiβ, E., Kern, K., Biotemplate synthesis of 3-nm nickel and cobalt nanowires. *Nano letters* 2003, *3*(8), 1079–1082.
[82] Knez, M., Kadri, A., Wege, C., Gösele, U., Jeske, H., Nielsch, K., Atomic layer deposition on biological macromolecules: Metal oxide coating of tobacco mosaic virus and ferritin. *Nano Letters* 2006, *6*(6), 1172–1177.

EBSCOhost - printed on 2/14/2023 1:06 PM via . All use subject to https://www.ebsco.com/terms-of-use

[83] Knez, M., Sumser, M., Bittner, A., Wege, C., Jeske, H., Kooi, S., Burghard, M., Kern, K., Electrochemical modification of individual nano-objects. *Journal of Electroanalytical Chemistry* 2002, *522*(1), 70–74.
[84] Knez, M., Sumser, M., Bittner, A.M., Wege, C., Jeske, H., Martin, T.P., Kern, K., Spatially selective nucleation of metal clusters on the tobacco mosaic virus. *Advanced Functional Materials* 2004, *14*(2), 116–124.
[85] Lee, S.-Y., Royston, E., Culver, J.N., Harris, M.T., Improved metal cluster deposition on a genetically engineered tobacco mosaic virus template. *Nanotechnology* 2005, *16* (7), S435.
[86] Kuncicky, D.M., Naik, R.R., Velev, O.D., Rapid deposition and long-range alignment of nanocoatings and arrays of electrically conductive wires from tobacco mosaic virus. *Small* 2006, *2*(12), 1462–1466.
[87] Yi, H., Nisar, S., Lee, S.-Y., Powers, M.A., Bentley, W.E., Payne, G.F., Ghodssi, R., Rubloff, G.W., Harris, M.T., Culver, J.N., Patterned assembly of genetically modified viral nanotemplates via nucleic acid hybridization. *Nano letters* 2005, *5*(10), 1931–1936.
[88] Tseng, R.J., Tsai, C., Ma, L., Ouyang, J., Ozkan, C.S., Yang, Y., Digital memory device based on tobacco mosaic virus conjugated with nanoparticles. *Nature nanotechnology* 2006, *1*(1), 72–77.
[89] Zahr, O.K., Blum, A.S., Solution phase gold nanorings on a viral protein template. *Nano letters* 2012, *12*(2), 629–633.
[90] Bayram, S.S., Zahr, O.K., Del Re, J., Blum, A.S., Nanoring formation via in situ photoreduction of silver on a virus scaffold. *Nanotechnology* 2016, *27* (48), 485603.
[91] Douglas, T., Young, M., Virus particles as templates for materials synthesis. *Advanced Materials* 1999, *11*(8), 679–681.
[92] Douglas, T., Young, M., Host–guest encapsulation of materials by assembled virus protein cages. *Nature* 1998, *393*(6681), 152–155.
[93] Liepold, L.O., Revis, J., Allen, M., Oltrogge, L., Young, M., Douglas, T., Structural transitions in Cowpea Chlorotic Mottle Virus (CCMV). *Physical biology* 2005, *2* (4), S166.
[94] Douglas, T., Strable, E., Willits, D., Aitouchen, A., Libera, M., Young, M., Protein engineering of a viral cage for constrained nanomaterials synthesis. *Advanced Materials* 2002, *14* (6), 415.
[95] Basu, G., Allen, M., Willits, D., Young, M., Douglas, T., Metal binding to cowpea chlorotic mottle virus using terbium (III) fluorescence. *JBIC Journal of Biological Inorganic Chemistry* 2003, *8*(7), 721–725.
[96] Allen, M., Bulte, J.W., Liepold, L., Basu, G., Zywicke, H.A., Frank, J.A., Young, M., Douglas, T., Paramagnetic viral nanoparticles as potential high-relaxivity magnetic resonance contrast agents. *Magnetic resonance in medicine* 2005, *54*(4), 807–812.
[97] Gillitzer, E., Willits, D., Young, M., Douglas, T., Chemical modification of a viral cage for multivalent presentation. *Chemical Communications* 2002, (20), 2390–2391.
[98] Klem, M.T., Willits, D., Young, M., Douglas, T., 2-D array formation of genetically engineered viral cages on Au surfaces and imaging by atomic force microscopy. *Journal of the American Chemical Society* 2003, *125*(36), 10806–10807.
[99] Suci, P.A., Klem, M.T., Douglas, T., Young, M., Influence of electrostatic interactions on the surface adsorption of a viral protein cage. *Langmuir* 2005, *21*(19), 8686–8693.
[100] Suci, P.A., Klem, M.T., Arce, F.T., Douglas, T., Young, M., Assembly of multilayer films incorporating a viral protein cage architecture. *Langmuir* 2006, *22*(21), 8891–8896.
[101] Cuillel, M., Berthet-Colominas, C., Krop, B., Tardieu, A., Vachette, P., Jacrot, B., Self-assembly of brome mosaic virus capsids: Kinetic study using neutron and X-ray solution scattering. *Journal of molecular biology* 1983, *164*(4), 645–650.
[102] Chen, C., Daniel, M.-C., Quinkert, Z.T., De, M., Stein, B., Bowman, V.D., Chipman, P.R., Rotello, V.M., Kao, C.C., Dragnea, B., Nanoparticle-templated assembly of viral protein cages. *Nano letters* 2006, *6*(4), 611–615.

EBSCOhost - printed on 2/14/2023 1:06 PM via . All use subject to https://www.ebsco.com/terms-of-use

[103] Chen, C., Kwak, E.-S., Stein, B., Kao, C.C., Dragnea, B., Packaging of gold particles in viral capsids. *Journal of nanoscience and nanotechnology* 2005, *5*(12), 2029–2033.
[104] Dixit, S.K., Goicochea, N.L., Daniel, M.-C., Murali, A., Bronstein, L., De, M., Stein, B., Rotello, V.M., Kao, C.C., Dragnea, B., Quantum dot encapsulation in viral capsids. *Nano Letters* 2006, *6*(9), 1993–1999.
[105] Dragnea, B., Chen, C., Kwak, E.-S., Stein, B., Kao, C.C., Gold nanoparticles as spectroscopic enhancers for in vitro studies on single viruses. *Journal of the American Chemical Society* 2003, *125*(21), 6374–6375.
[106] Loo, L., Guenther, R.H., Basnayake, V.R., Lommel, S.A., Franzen, S., Controlled encapsidation of gold nanoparticles by a viral protein shell. *Journal of the American Chemical Society* 2006, *128*(14), 4502–4503.
[107] Steinmetz, N.F., Lomonossoff, G.P., Evans, D.J., Cowpea mosaic virus for material fabrication: Addressable carboxylate groups on a programmable nanoscaffold. *Langmuir* 2006, *22*(8), 3488–3490.
[108] Meunier, S., Strable, E., Finn, M., Crosslinking of and coupling to viral capsid proteins by tyrosine oxidation. *Chemistry & biology* 2004, *11*(3), 319–326.
[109] Lin, T., Chen, Z., Usha, R., Stauffacher, C.V., Dai, J.-B., Schmidt, T., Johnson, J.E., The refined crystal structure of cowpea mosaic virus at 2.8 Å resolution. *Virology* 1999, *265*(1), 20–34.
[110] Wang, Q., Lin, T., Johnson, J.E., Finn, M., Natural supramolecular building blocks: Cysteine-added mutants of cowpea mosaic virus. *Chemistry & biology* 2002, *9*(7), 813–819.
[111] Steinmetz, N.F., Evans, D.J., Lomonossoff, G.P., Chemical introduction of reactive thiols into a viral nanoscaffold: A method that avoids virus aggregation. *ChemBioChem* 2007, *8* (10), 1131–1136.
[112] Wang, Q., Lin, T., Tang, L., Johnson, J.E., Finn, M., Icosahedral virus particles as addressable nanoscale building blocks. *Angewandte Chemie International Edition* 2002, *41*(3), 459–462.
[113] Wang, Q., Raja, K.S., Janda, K.D., Lin, T., Finn, M., Blue fluorescent antibodies as reporters of steric accessibility in virus conjugates. *Bioconjugate chemistry* 2003, *14*(1), 38–43.
[114] Wang, Q., Chan, T.R., Hilgraf, R., Fokin, V.V., Sharpless, K.B., Finn, M., Bioconjugation by copper (I)-catalyzed azide-alkyne [3+ 2] cycloaddition. *Journal of the American Chemical Society* 2003, *125*(11), 3192–3193.
[115] Gupta, S.S., Kuzelka, J., Singh, P., Lewis, W.G., Manchester, M., Finn, M., Accelerated bioorthogonal conjugation: A practical method for the ligation of diverse functional molecules to a polyvalent virus scaffold. *Bioconjugate chemistry* 2005, *16*(6), 1572–1579.
[116] Gupta, S.S., Raja, K.S., Kaltgrad, E., Strable, E., Finn, M., Virus–glycopolymer conjugates by copper (I) catalysis of atom transfer radical polymerization and azide–alkyne cycloaddition. *Chemical Communications* 2005, 34, 4315–4317.
[117] Steinmetz, N.F., Lomonossoff, G.P., Evans, D., Decoration of Cowpea mosaic virus with multiple, redox-active, organometallic complexes. *Small* 2006, *2*(4), 530–533.
[118] Kalsin, A.M., Fialkowski, M., Paszewski, M., Smoukov, S.K., Bishop, K.J., Grzybowski, B.A., Electrostatic self-assembly of binary nanoparticle crystals with a diamond-like lattice. *Science* 2006, *312*(5772), 420–424.
[119] Fialkowski, M., Bishop, K.J., Klajn, R., Smoukov, S.K., Campbell, C.J., Grzybowski, B.A., Principles and implementations of dissipative (dynamic) self-assembly. J. Phys. Chem B, 2006, *110*(6), 2482–2496.
[120] Hoeben, F.J., Jonkheijm, P., Meijer, E., Schenning, A.P., About supramolecular assemblies of π-conjugated systems. *Chemical Reviews* 2005, *105*(4), 1491–1546.
[121] van Herrikhuyzen, J., Janssen, R.A., Meijer, E., Meskers, S.C., Schenning, A.P., Fractal-like self-assembly of oligo (p-phenylene vinylene) capped gold nanoparticles. *Journal of the American Chemical Society* 2006, *128*(3), 686–687.

EBSCOhost - printed on 2/14/2023 1:06 PM via . All use subject to https://www.ebsco.com/terms-of-use

[122] Sidhaye, D.S., Kashyap, S., Sastry, M., Hotha, S., Prasad, B., Gold nanoparticle networks with photoresponsive interparticle spacings. *Langmuir* 2005, *21*(17), 7979–7984.
[123] Ahonen, P., Schiffrin, D.J., Paprotny, J., Kontturi, K., Optical switching of coupled plasmons of Ag-nanoparticles by photoisomerisation of an azobenzene ligand. *Physical Chemistry Chemical Physics* 2007, *9*(5), 651–658.
[124] Yamada, M., Shen, Z., Miyake, M., Self-assembly of discotic liquid crystalline molecule-modified gold nanoparticles: Control of 1D and hexagonal ordering induced by solvent polarity. *Chemical communications* 2006, (24), 2569–2571.
[125] Nie, Z., Fava, D., Kumacheva, E., Zou, S., Walker, G.C., Rubinstein, M., Self-assembly of metal–polymer analogues of amphiphilic triblock copolymers. *Nature materials* 2007, *6*(8), 609–614.
[126] Gast, A.P., Zukoski, C.F., Electrorheological fluids as colloidal suspensions. *Advances in Colloid and Interface Science* 1989, *30*, 153–202.
[127] Singh, J.P., Lele, P.P., Nettesheim, F., Wagner, N.J., Furst, E.M., One-and two-dimensional assembly of colloidal ellipsoids in ac electric fields. *Physical Review E* 2009, *79* (5), 050401.
[128] Lee, S.H., Liddell, C.M., Anisotropic magnetic colloids: A strategy to form complex structures using nonspherical building blocks. *Small* 2009, *5*(17), 1957–1962.
[129] Herlihy, K.P., Nunes, J., DeSimone, J.M., Electrically driven alignment and crystallization of unique anisotropic polymer particles. *Langmuir* 2008, *24*(16), 8421–8426.
[130] Smoukov, S.K., Gangwal, S., Marquez, M., Velev, O.D., Reconfigurable responsive structures assembled from magnetic Janus particles. *Soft Matter* 2009, *5*(6), 1285–1292.
[131] Gunes, D., Scirocco, R., Mewis, J., Vermant, J., Flow-induced orientation of non-spherical particles: Effect of aspect ratio and medium rheology. *Journal of Non-Newtonian Fluid Mechanics* 2008, *155*(1), 39–50.
[132] Fry, D., Langhorst, B., Wang, H., Becker, M., Bauer, B., Grulke, E., Hobbie, E., Rheo-optical studies of carbon nanotube suspensions. *The Journal of chemical physics* 2006, *124* (5), 054703.
[133] Kumnorkaew, P., Ee, Y.-K., Tansu, N., Gilchrist, J.F., Investigation of the deposition of microsphere monolayers for fabrication of microlens arrays. *Langmuir* 2008, *24*(21), 12150–12157.
[134] Kumnorkaew, P., Weldon, A.L., Gilchrist, J.F., Matching constituent fluxes for convective deposition of binary suspensions. *Langmuir* 2009, *26*(4), 2401–2405.
[135] Cui, Y., Björk, M.T., Liddle, J.A., Sönnichsen, C., Boussert, B., Alivisatos, A.P., Integration of colloidal nanocrystals into lithographically patterned devices. *Nano Letters* 2004, *4*(6), 1093–1098.
[136] Lin, Y., Böker, A., Skaff, H., Cookson, D., Dinsmore, A., Emrick, T., Russell, T.P., Nanoparticle assembly at fluid interfaces: Structure and dynamics. *Langmuir* 2005, *21*(1), 191–194.
[137] Böker, A., He, J., Emrick, T., Russell, T.P., Self-assembly of nanoparticles at interfaces. *Soft matter* 2007, *3*(10), 1231–1248.
[138] Lewandowski, E.P., Bernate, J.A., Tseng, A., Searson, P.C., Stebe, K.J., Oriented assembly of anisotropic particles by capillary interactions. *Soft Matter* 2009, *5*(4), 886–890.
[139] Madivala, B., Fransaer, J., Vermant, J., Self-assembly and rheology of ellipsoidal particles at interfaces. *Langmuir* 2009, *25*(5), 2718–2728.
[140] Ding, T., Song, K., Clays, K., Tung, C.H., Fabrication of 3D photonic crystals of ellipsoids: Convective self-assembly in magnetic field. *Advanced Materials* 2009, *21*(19), 1936–1940.
[141] Mittal, M., Furst, E.M., Electric field-directed convective assembly of ellipsoidal colloidal particles to create optically and mechanically anisotropic thin films. *Advanced Functional Materials* 2009, *19*(20), 3271–3278.

EBSCOhost - printed on 2/14/2023 1:06 PM via . All use subject to https://www.ebsco.com/terms-of-use

Cyril Aumaitre, Anthony Jolly, Jean-François Morin

13 Toward Well-Defined Carbon Nanotubes and Graphene Nanoribbons

Carbon nanomaterials, especially carbon nanotubes and graphene, have been among the most studied materials in the past fifteen years owing to their outstanding physcial properties. To obtain the desired properties, these nanomaterials need to be well-defined and as pure as possible, especially for electronic applications. In this chapter, we present the most promising strategies for the purification of single-walled carbon nanotubes(SWNTs), with an emphasis on the sorting of semiconducting SWNTs using conjugated polymers, and the synthesis of graphene nanoribbons.

Keywords: single-walled carbon nanotubes, graphene, graphene nanoribbons, carbon nanomaterials, electronics properties

13.1 Introduction

Carbon nanomaterials, especially carbon nanotubes and graphenic materials, have been revolutionizing the way scientists approach problems in many areas of fundamental and applied science. In fact, their unique electronic and mechanical properties make them highly promising candidates for existing and future generations of devices such as batteries, transistors, light-emitting diodes, sensors, solar cells, and so on. One of the most interesting and exploited features of these materials is that their shape, size, and topology have a tremendous impact on their properties. For example, armchair single-wall carbon nanotubes (SWNTs) are conducting, while the zigzag and chiral analogs are all semiconductors with bandgap depending on several parameters. Likewise, pristine graphene is a semimetal that can be transformed into a nonzero bandgap semiconductor after chemical modifications. This means that carbon nanomaterials can either replace traditional metals or semiconductors, depending on the target application.

Although spectacular advances have been made in the past five years regarding the integration of these materials in commercial devices, some issues need to be addressed at many levels. However, two challenges that draw most of the attention of the researchers in this field are particularly critical to bring these materials to the next step: (1) the preparation of well-defined materials with finite properties and (2) device integration. While the latter is more about engineering, the former

Cyril Aumaitre, Anthony Jolly, Jean-François Morin, Département de chimie and Centre de Recherche sur les Matériaux Avancés (CERMA) Université Laval, Quebec, Canada

https://doi.org/10.1515/9783110537734-013

EBSCOhost - printed on 2/14/2023 1:06 PM via . All use subject to https://www.ebsco.com/terms-of-use

belongs to chemists to improve. Since the most prevalent method to prepare carbon nanomaterials is the thermal treatment such as combustion and pyrolysis of simple carbon-rich source, the resulting materials are rarely found in pure form. In the case of SWNTs, a mixture of conducting and semiconducting forms is obtained. The SWNTs can also vary in diameter, length, and chirality. Unfortunately, no method allowing selective synthesis of one particular type of SWNTs has been developed yet. The best strategy known to date to obtain SWNTs with a specific diameter and chirality is to purify them from the as-prepared mixture using conjugated polymers that, in some cases, bind preferentially to semiconducting SWNTs. On the other hand, other carbon nanomaterials such as graphene nanoribbons (GNRs) can be prepared in pure form at the preparation stage since synthetic organic chemistry can be used to build the carbon network atom by atom, allowing a great level of precision in the final structures.

In this chapter, we review some of the most important aspects regarding the synthesis, purification, and applications of two highly praised carbon nanomaterials, namely carbon nanotubes and graphene nanoribbons. A particular emphasis has been put on the semiconducting form of these materials as it is, from author's opinion, the trickiest and most challenging to obtain and integrate in devices.

13.2 Single-Wall Carbon Nanotubes

13.2.1 SWNT Manufacturing and Purification Process

Since the first observation of carbon microtubule by Ijima and coworkers in 1991, the synthesis of SWNT has developed to industrial scale [1]. Various synthetic methods are employed, and each process brings different properties for the resulting SWNTs. Arc discharge [2] and laser ablation techniques [3] were developed in the 1990s, but they generally require high temperature (~4,000–6,000 K for generated plasma by arc discharge) and produce significant amounts of impurities. CoMoCAT® and HiPCo process were the most investigated process for mass production of SWNTs. The high-pressure carbon monoxide (HiPco) process was developed by the group of Smalley in 1999 [4]. This process produces carbon nanotubes from high-pressure carbon monoxide gas with iron carbon monoxide $Fe(CO)_5$ as a catalyst. The continuous gas-flow enables a gram- or kilogram-scale synthesis of nanotubes with high purity. The CoMoCAT® method is based on a specific catalyst (silica-supported Cobalt and Molybdenum mixture) developed in 2000 by Kitiyanan et al. [5]. This process uses metallic particles as nucleation center for the thermal decomposition of the carbon monoxide gas at high temperature (700–950 °C). Both methods produce less impurities and the nanotube structure (length, diameter, chirality polydispersity) can be controlled

EBSCOhost - printed on 2/14/2023 1:06 PM via . All use subject to https://www.ebsco.com/terms-of-use

according to the process parameters. Nowadays, SWNTs synthesized with these processes are commercially available in kilogram quantities.

Although large-scale production is mastered, the major problem remains the purity of the produced nanotubes. The commercial synthesis methods described above produce roughly 2:1 mixture of semiconducting and metallic SWNTs. These two types of nanotubes have very similar geometry, but totally different electronic properties. Generally, a few amounts of metallic SWNTs (m-SWNTs) can drastically reduce the performance of the semiconductor-based devices. Access to electronic grade SWNTs is still a huge challenge to develop flexible, stretchable, and printed electronics at low cost. Several methods have been developed to isolate pure semiconducting SWNTs (s-SWNTs) such as density gradient ultracentrifugation (DGU), agarose gel filtration, or size-exclusion chromatography. These methods are well described in the literature [6]. Despite getting electronically enriched SWNT samples, these methods suffer from major limitations such as low yield of enrichment and very low quantities at the end of the process (typically microgram). These drawbacks are in large part responsible for the current price of s-SWNTs (800–900 USD/mg) and strongly limit their integration in devices. Another alternative that has the potential to outmatch the current limitations is the utilization of conjugated polymers as dispersant for SWNTs. Since the pioneering work of Nicholas and coworkers in 2007, numerous examples of conjugated polymers for SWNTs dispersion have been reported with varying degree of success [7]. Some of these examples reach higher purity than 99.9% very easily via a simple sonication and centrifugation process [8]. Despite these few examples, further developments are required to integrate pure SWNTs in various devices such as field-effect transistors (FETs), organic solar cells, or batteries. Nowadays, it is still difficult to isolate one specific chirality and totally suppress the presence of metallic SWNT. Dilution is a major point for ink formulation and must be a critical point to enhance for printed electronics. The other major drawback is the lack of fundamental understanding of the dispersion selectivity mechanisms. Conjugated polymer extraction is a simple process with sonication and centrifugation steps that require few equipment (Figure 13.1). Whether it is the intrinsic properties of the polymer (monomer, molecular weight, electronics properties, etc.) or the dispersion parameters (solvents, temperature, time, etc.), no “design rules” were clearly identified; however, some trends have been recently reported.

The first and most common polymer class used for SWNT sorting is polyfluorene as demonstrated for the first time by Nish et al. in 2007 [7]. They showed that even a little variation in the alkyl chain length leads to very different chirality selectivity. They also prove that it can be a possible way to separate metallic nanotubes from the as-prepared mixture. Gomulya et al. synthesized polyfluorenes with various alkyl chain lengths (6–18 carbons) and found that long alkyl chains (≥10) tend to disperse large-diameter s-SWNTs to yield solutions with higher concentration [9]. However, the separation from the metallic species become less effective.

EBSCOhost - printed on 2/14/2023 1:06 PM via . All use subject to https://www.ebsco.com/terms-of-use

Figure 13.1: General procedure for SWNT dispersion with conjugated polymers and several examples. **Source**: Author's own representation.

Polythiophenes (PTs) are largely used in organic solar cells, especially the well-known poly(3-hexyl)thiophene (P3HT), which can achieve up to 7.4% power conversion efficiency in bulk heterojunction device configuration [10]. The ability of PT to disperse SWNTs was also extensively studied, and it was found that PTs form strong supramolecular complex with carbon nanotubes. Lee et al. have studied the dispersion properties of regioregular poly(3-alkylthiophene) [11]. They achieved selective dispersion of s-SWNT and observed the same trend as Gomulya [9]. They demonstrated that the supramolecular structure was formed as a "polymer shell" around the nanotube, thanks to the interdigitation of the side chains. The authors have prepared transistors with PT-dispersed SWNTs, which reached high mobility ($12\ cm^2\ V^{-1}\ s^{-1}$) and high I_{on}/I_{off} ratio values (10^6), indicating the complete removal of the metallic SWNTs. However, the strong affinity of PT with SWNT often results in poor selectively. Several examples of the poor selectivity of PTs with SWNTs of different sources (CoMoCAT and HiPCO) have been reported [12, 13].

Polycarbazole are structural analogues to polyfluorene but differ by the nature of the atom at the ninth position (N for carbazole and C for fluorene). The presence of a monosubstituted atom in the case of carbazole results in a lower steric hinderance and a different binding behavior for SWNTs. Lemasson et al. reported the comparison of SWNT dispersion with poly(*N*-decyl-2,7-carbazole) (Figure 13.1) and compared their results with polyfluorene [14]. Interestingly, this polymer exhibits selectivity with low chiral angle ($10^o < \Theta < 20^o$) contrary to polyfluorene that prefers large chiral angles ($>25^o$). This complementarity in selectivity is promising, but the authors mentioned that the dispersing efficiency is five times lower with polycarbazole than the polyfluorene. This was attributed to the single linear alkyl chain that limits the solubility compared to the two chains of the fluorene unit.

Large-diameter s-SWNTs are interesting for FET applications, and several examples of copolymers with fluorene and pyridine derivatives were described. Tange et al. used commercially available copolymers of 9,9-di-*n*-octylfluorene and

EBSCOhost - printed on 2/14/2023 1:06 PM via . All use subject to https://www.ebsco.com/terms-of-use

pyridine (PFO-Py, see Figure 13.1) to disperse large-diameter SWNTs (1.23–1.38 nm) [15]. Dispersion concentration remains a key factor to prepare commercial inks for printed electronics. Interestingly, Blackburn and coworkers have shown that concentrated inks can be made from PFO-Py dispersion, and they demonstrated that 33% of the starting material of the SWNTs was dispersed compared to 27% by density gradient ultracentrifugation separation (DGU) [16]. The authors estimated the concentration around 0.08 mg ml^{-1}, which is close to the concentration targeted for inkjet processes. Although conjugated polymers can disperse the carbon nanotubes well, they also have a negative impact on electrical properties of SWNT. One alternative to polymer wrapping is the utilization of selective and degradable polymers to isolate electronically enriched samples of pristine s-SWNTs. Joo et al. used PFO-Py to selectively disperse SWNT and make use of the chelation properties of the bipyridine unit to chelate Rhenium complex, causing a conformational change in the polymer backbone, forcing the polymer to uncoil (Figure 13.2) [17]. Some other polymer-removal mechanisms were used such as imine hydrolysis [18] or decomplexation of metal coordination polymers [19] using catalytic trifluoroacetic acid.

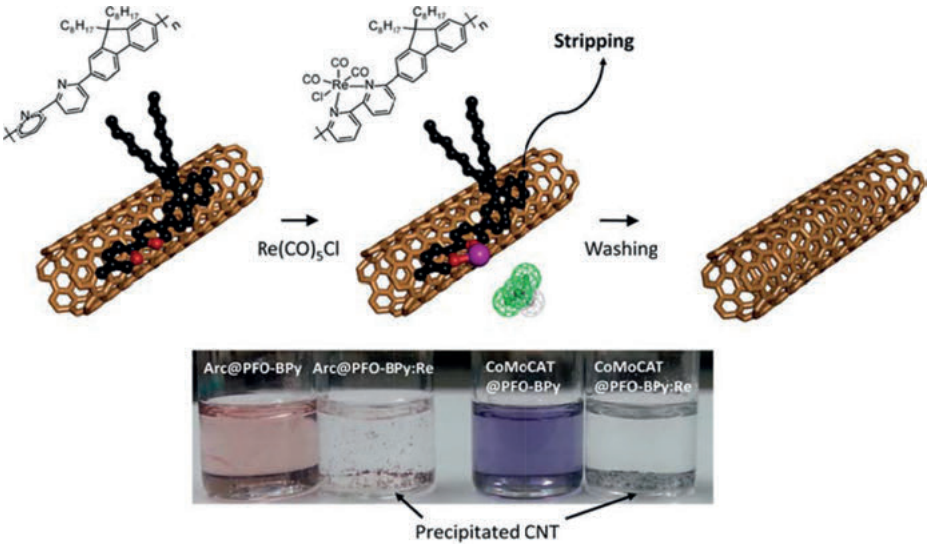

Figure 13.2: Schematic illustration of the process used to priduce pristine sc-SWNT by removing wrapped polymer from SWNT surface by complexation with Rhenium complex. Images of solutions of polymer-wrapped s-SWNTs before and after the reaction with $Re(CO)_5Cl$. Reprinted with permission from Ref. [17]. Copyright 2018, American Chemical Society.

Extraction of semiconducting SWNTs has attracted the utmost part of recent research because of their uses in electronic devices, leaving a large amount of the remaining materials. Although m-SWNTs must be avoided for some applications, they can be very useful in other applications such as transparent electrodes. Thus,

EBSCOhost - printed on 2/14/2023 1:06 PM via . All use subject to https://www.ebsco.com/terms-of-use

there is also a need to develop efficient strategy to selectively disperse them. Very few examples of selective dispersion of m-SWNTs with conjugated polymers were described and some hypothesis were made based on the experimental observations. For example, Adronov and coworkers postulate that decreasing the electron density in the polymer backbone raises the amount of dispersed m-SWNT [20]. By introducing a cationic charge in the polymer backbone (P2-Figure 13.2), they observed a large increase in the amount of dispersed m-SWNT. These results were corroborated by conductivity measurements and an increase by four orders of magnitude compared to the neutral polymer (from 3.1×10^{-4} S m^{-1} to 1.4 S m^{-1}) was observed, which confirms the presence of m-SWNTs.

13.2.2 SWNTs for Electronics and Optoelectronics

Organic Solar Cells

Organic photovoltaics are recognized as low-cost energy-producing devices, and extensive research is being conducted to increase the overall efficiency and to decrease the production cost of the devices. One way to achieve both the objectives is to use organic materials. Unlike inorganic semiconductors, organic materials can be solubilized in common organic solvents, which allows deposition of large substrates using industrial printable techniques like inkjet or roll-to-roll processes [21, 22]. These manufacturing methods are largely inspired from the paper industries and possess the advantage of being low cost and producing flexible devices at high speed at large scale.

In a bulk heterojunction solar cell (BHJSC) configuration, a p-type material is blended in a solution with an n-type material and deposited between a conductive substrate and a metallic electrode (Figure 13.3). Traditionally, π-conjugated polymers are used as p-type material and fullerene derivatives as n-type material. This configuration has led to power conversion efficiency exceeding by 10% through extensive efforts mainly devoted on the p-type polymer materials [23]. These kinds of devices are characterized by applying a sweep of potential and by measuring the output current in the dark and under calibrated illumination (P_{inc}= 100 mW cm^{-2}). Several parameters are extracted from the I–V curve like the open circuit voltage (V_{OC}), short-circuit current density (J_{SC}), fill factor (FF), and power conversion efficiency (PCE).

As shown in Figure 13.3, the photophysical processes occur at the interface between the donor and the acceptor materials. Under illumination, the donor material (p-type) absorbs a photon, leading to the creation of an electron-hole pair called exciton (step 1). Electrons from the highest occupied molecular orbital (HOMO) are promoted to the lowest unoccupied molecular orbital (LUMO) of the donor materials. Then, these excitons can travel about 10–20 nm in the polymer phase until they reach the interface of donor/acceptor. The nanoscale bulk heterojunction is particularly important to limit the exciton journey and facilitate their migration toward the

EBSCOhost - printed on 2/14/2023 1:06 PM via . All use subject to https://www.ebsco.com/terms-of-use

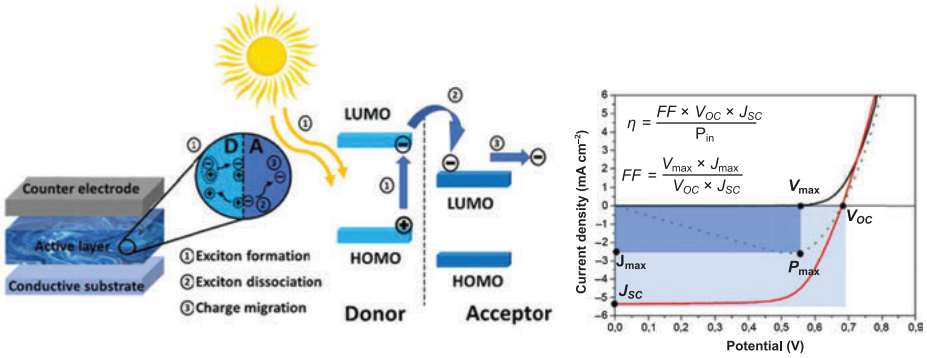

Figure 13.3: Illustration of the physical processes in bulk heterojunction solar cells and representation of the major parameters of devices on *I–V* curve.

interface without losses. The main step (step 2) concerns the transfer of the electron in the LUMO of the donor material to the LUMO of the acceptor material at the boundary. After this exciton separation, the charge carriers are free to migrate toward external circuit (step 3). It is noteworthy to mention that similar process occurs when light is absorbed directly by the n-type materials.

Fullerene-based molecules, especially [6,6]-phenyl C61 butyric acid methyl ester (PCBM) is widely used, however, electronic grade PCBM is very expensive (>$1,000/g) and rather unstable upon irradiation, which limits its potential for large-scale commercialization. Among the other n-type materials, nanostructured allotropic forms of carbon such as graphene and carbon nanotubes are rising as viable options. s-SWNTs exhibit an ambipolar character, and their energy levels can be tuned over a wide range by using different radii and chiralities. The high aspect ratio related to the high surface area (about 1,600 $m^2\ g^{-1}$) [24] makes these structures particularly suitable for OPV application. Inversely, the presence of the metallic SWNTs and several chiralities have a negative impact on the photovoltaic effect with an increase of recombination processes and a bad morphology at the nanoscale leading to poor efficiency [25]. The recent advances in polymer wrapping purification has given new hopes for SWNT integration in OPV devices with different roles.

The first example of SWNT-based OPV as fullerene alternative was described by Landi et al. with a poly-3-octylthiophene (P3OT):SWNT blend [25]. Devices containing 1% w/w SWNTs in P3OT have shown some low current densities but relatively high open-circuit voltages (≥ 1 V). This proof of concept has led to several attempts with different architectures, but the PCE remain inferior to 1% [26, 27]. The explanation of these low efficiencies was investigated by theoretical [28] and experimental [29] studies and the results show two main reasons. First, the presence of m-SWNT act like recombination centers that is unfavorable for the exciton separation and the photocurrent generation. Second, the presence of large-diameter m-SWNTs is

EBSCOhost - printed on 2/14/2023 1:06 PM via . All use subject to https://www.ebsco.com/terms-of-use

expected to significantly reduce the performance, and it has been suggested that only small-diameter SWNTs are relevant to improve the overall efficiency.

Despite conducting electrons, SWNTs are also investigated as hole-transporting materials due to their ambipolar characteristics. For example, Dabera et al. have used one layer of sc-SWNTs wrapped with P3HT as the hole-transporting layer and reached 7.6% PCE with PTB7:$PC_{70}BM$ active material [30]. They concluded that it can be a valuable alternative for expensive metallic counter electrode (ITO, gold, silver, etc.) in flexible devices. Numerous examples of SWNT-based counter electrodes have since been described in literature and demonstrate huge potential to replace electrode materials in solar cell devices [31, 32].

Energy Storage Technologies

The development of large-scale flexible electronic devices cannot be achieved without adequate power sources. We have seen previously that producing energy is still within our reach with solar cells, but energy demand is not necessary at the same time of energy production. Developing new energy storage devices is a cornerstone of the development of flexible electronic devices and research has been done to that extent. Generally, storage devices are composed of two electrodes (cathode and anode) separated by an ion-permeable membrane (separator) and an electrolyte connecting both electrodes (see Figure 13.4). Different types of devices can be manufactured and are generally classified by the Ragone plot (see Figure 13.4). This graphic represents power density versus energy density. Energy density is the capacity of a device to store or deliver energy over time. Power density is the quantity of power that a device can deliver. Electrochemical reactions in batteries permit accumulation of a large amount of charge carriers in a small volume, which bring a large energy density. However, the electrochemical reaction kinetics affect power density that limits the charge/discharge speed and the number of life cycles. In the opposite, electrostatic

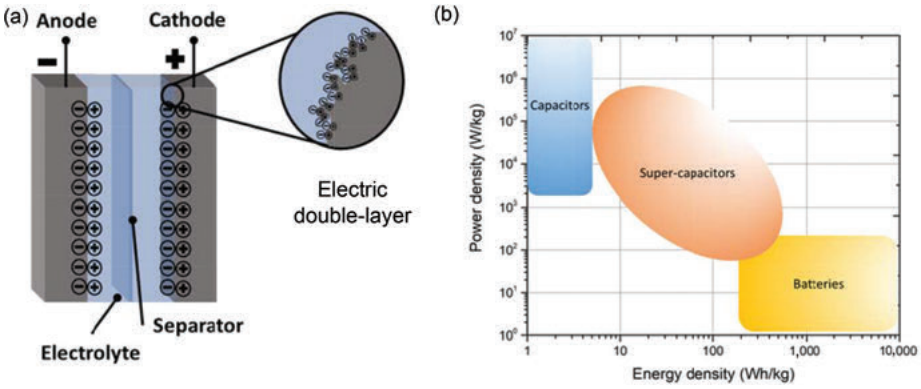

Figure 13.4: Illustration of a supercapacitor and Ragone plot illustrating classification of storage devices.

EBSCOhost - printed on 2/14/2023 1:06 PM via . All use subject to https://www.ebsco.com/terms-of-use

capacitors have a high-power density and a low-energy density, which limit the charge amount but increase the number and speed of the charge/discharge cycles. In the middle, supercapacitors use the advantages of both batteries and capacitors to propose devices with moderate-energy density and power density. This kind of devices bring new opportunities of applications, especially in the flexible optoelectronics because of the absence of electrochemical reactions and their compactness. The dominant mechanism of supercapacitor storage is the formation of an electrical double layer (EDL) of electrolyte ions on the surface of the conductive electrode (electric double-layer capacitors [EDLCs]). Due to the purely physical formation of the EDL without an electrochemical reaction, EDLCs are not limited by the electrochemical charge transfer kinetics of batteries, and thus can be fully charged/discharged in seconds over a million times. The number of charges will be limited by the specific area of the electrodes that impose a rational design of the electrode material.

At this time, more than 80% of actual supercapacitors are based on EDLCs using carbon as the electrode material: activated carbon (AC), graphene, or carbon nanotubes (CNTs). Among these materials, AC is the most used, due to its high availability, high surface area, and low cost. CNTs are also used due to their theoretical high intrinsic surface area and flexibility. However, strong van der Waals interactions between the individual nanotubes reduce the accessible surface area for the charge carriers and limit the energy density and their use in supercapacitors. In addition, the purification process remains expensive for mass production and limits their economic viability for high-capacity supercapacitors. Different authors have tried several conjugated polymers to wrap and disperse SWNTs and also to participate as an active material in charge storage. An et al. have used polypyrrole:SWNT composite electrodes in supercapacitors [33].

Nevertheless, the flexibility of carbon nanotubes is undeniably an asset for printed storage devices. For example, Chen et al. have fabricated SWNT thin-film electrodes on cloth fabric and flexible substrates by simply using SWNT inks and a commercial inkjet printer (see Figure 13.5) [34]. The as-fabricated printed SWNT supercapacitors exhibited enough capacitance and good stability after a large number of charge/discharge cycles, which revealed their potential for application in wearable energy storage devices.

13.2.3 Applications in Microelectronics

Field-effect Transistors

FETs are electronic switches used in most of our personal electronic devices as computer logics, displays, and so on. In most cases, FETs use high-purity silicon as semiconductor. In fact, the whole electronic industry is based on silicon, and a real paradigm shift or a great technological revolution is needed to move away from it. Nowadays, the demand shifts more and more toward flexible electronics, leading to

EBSCOhost - printed on 2/14/2023 1:06 PM via . All use subject to https://www.ebsco.com/terms-of-use

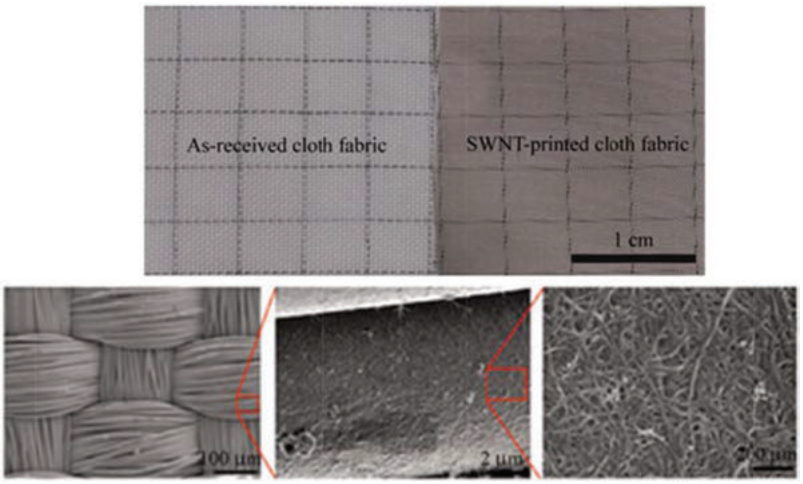

Figure 13.5: Optical photograph of cloth fabric before and after inkjet printing of SWNT films. SEM images of a cloth fabric with inkjet-printed SWNT films. Reprinted from Ref. [34].

new challenges. Silicon-based thin-film transistors (TFTs) are deposited on rigid substrate with expensive clean room process, which clearly limit their applications for low-cost flexible devices. Organic FETs (OFETs) can be manufactured using industrial printing processes (roll-to-roll or inkjet) at low temperature and high speed. The use of organic materials like conjugated polymers or carbon nanostructures with appropriate film forming and mechanical properties is a viable alternative to more rigid materials. The unique properties of CNTs make them strong candidates for their integration in OFETs. They show strong resilience and mechanical resistance, have an ambipolar behavior, and can reach high conductivity toward the nanotube length [35].

Generally, an OFET is composed of three electrodes: the gate, the source, and the drain. It is also composed of a dielectric layer and of a semiconducting layer as shown in Figure 13.6.

The working principle of an OFET begins by applying a constant potential between the source and the drain (V_{SD}) and by applying another potential to the gate (V_{GS}). When negative potential is applied to the gate, positive charge carriers are formed at the interface between the organic semiconductor and the dielectric layer. Credit goes to the constant potential V_{SD} between the source and the drain, these positive charge carriers can flow through the semiconducting channel forming a p-type OFET. In the opposite, the application of positive potential to the gate leads to negative charge carriers at the interface semiconductor/dielectric layer creating n-type OFET.

Generally, OFETs are characterized with an I–V curve (see Figure 13.6) and three values can be extracted from this experiment: the charge carrier mobility (electron mobility, μ_e for n-type and hole mobility, μ_h for p-type), the $I_{on/off}$ ratio, and the threshold voltage (V_T). The charge mobilities describe the speed at which the charges

EBSCOhost - printed on 2/14/2023 1:06 PM via . All use subject to https://www.ebsco.com/terms-of-use

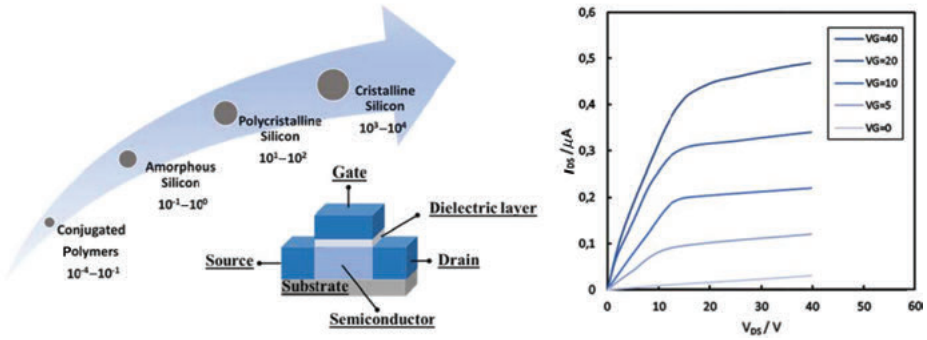

Figure 13.6: Illustration of common architecture of organic field effect transistor (top-gate) and typical *I–V* characteristics of OFET.

formed in the semiconducting layer travels from the source to the drain, the $I_{on/off}$ ratio refers to the ratio between current when the transistor is at the on-state and when it is at the off-state, the threshold voltage corresponds to the lowest voltage needed to switch the transistor state. Typical values of each characteristics are presented in Figure 13.6. High-performance OTFTs are characterized by high field-effect mobility (μ), high on/off ratio (I_{on}/I_{off}), and low-threshold voltage (V_T).

s-SWNTs have been identified as promising candidate for high-performance FET. Their intrinsic charge carrier mobility, owing to their unique ballistic transport property, is a major asset to overcome the commercial silicon-based FET. Nevertheless, it is difficult to use the full potential of the SWNT mainly because of the insufficient purity of the raw material as discussed above. The presence of m-SWNT and other carbon-based and metallic impurities result in charge-carrier leaks and short circuit. Hennrich et al. have dispersed SWNTs with polyfluorene and have fractioned the resulting suspension by size-exclusion chromatography (SEC) process [36]. This method has led to a purity of SWNT exceeding 99.7%, an impressive hole mobility of 297 $cm^2\ V^{-1}\ s^{-1}$ and on/off ratio as high as 10^8, which is better than usual amorphous silicon-based TFT (1 $cm^2\ V^{-1}\ s^{-1}$) utilized in standard electronic devices. Another major advantage of the s-SWNT is that they can be used in both n-type and p-type FETs. Bisri et al. used SWNT dispersion to make ambipolar FETs [37] They showed a hole mobility of 0.12 $cm^2\ V^{-1}\ s^{-1}$ and an electron mobility of 3.57 $cm^2\ V^{-1}\ s^{-1}$ with $I_{on/off}$ ratio up to 10^6. The high $I_{on/off}$ ratios demonstrate the absence of m-SWNT ($I_{on/off}$ =10^1–10^3 with m-SWNT and s-SWNT mixture) in the channel confirming a good separation during the polymer-wrapping process.

The actual trends with SWNT-based FETs turn to the flexible electronics (see Figure 13.7). The unique combination of high conductivity and strong mechanical resistance make the SWNTs a very good candidate for their integration in flexible OTFTs. For example, Miyata et al. have developed solution-processable TFTs with high mobility (167 $cm^2\ V^{-1}\ s^{-1}$), but improvements need to be made before printed large-area

EBSCOhost - printed on 2/14/2023 1:06 PM via . All use subject to https://www.ebsco.com/terms-of-use

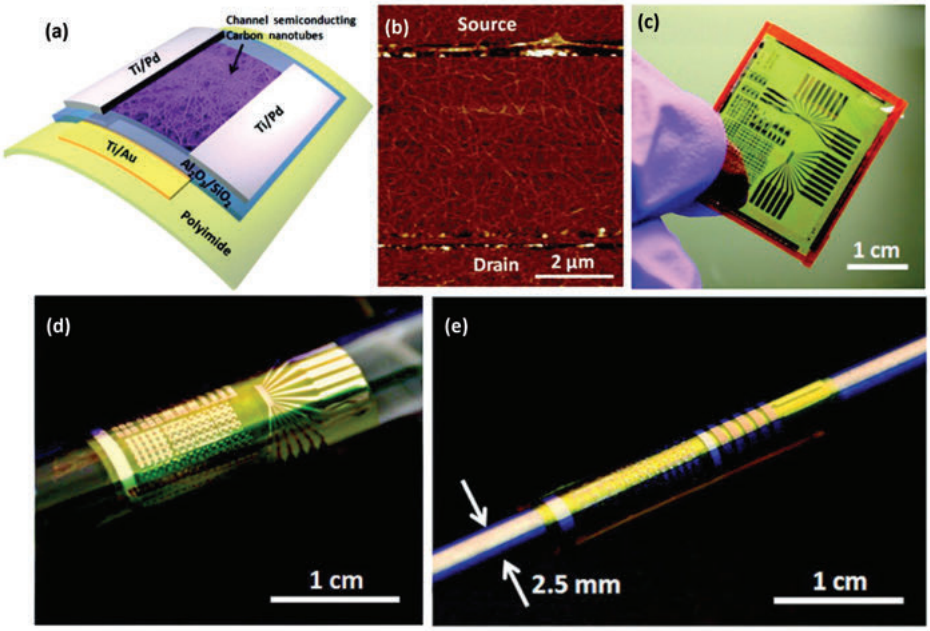

Figure 13.7: Flexible thin-film transistors and integrated circuits using semiconducting carbon nanotube networks. (a) Schematic diagram of a local-gated nanotube TFT on a flexible substrate. (b) AFM image showing the channel of the flexible nanotube TFT, which consists of random networks of semiconducting carbon nanotubes. (c) Photograph of a flexible nanotube circuit with a size of ~2.5 × 3 cm^2. (d, e) Photographs showing the extreme bendability of the flexible nanotube circuits, where the samples are being rolled onto a test tube with a diameter of 10 mm (d), and a metal rod with a diameter of 2.5 mm (e). Reprinted with permission from Ref. [39]. Copyright 2018 American Chemical Society.

electronics with inkjet or roll-to-roll process becomes a reality [38]. The main issues are the ink formulation starting from the raw SWNTs purification to the choice of all the additives and their influence on the performance and stability of the devices.

Sensors

As discussed for OFETs, even small modifications of CNTs environment result in variations in the performance and behavior of the device. It can be challenging, but it also offers a unique opportunity to use this property as a sensitive sensor. One of the first reports of gas sensors using a SWNT-based OFET was made by Kong et al. in 2000 [40]. Since then, numerous examples have been developed to use the electronic sensitivity of CNTs to detect a variety of analyte including gas, solvents, or biomolecules. For example, Khamis et al. have decorated SWNTs with different DNA sequences to discriminate different enantiomers and different molecules that differed in a single methyl group with a sensitivity of 1 ppm [41].

EBSCOhost - printed on 2/14/2023 1:06 PM via . All use subject to https://www.ebsco.com/terms-of-use

The unique properties of CNTs allow the design of different types of detectors by using the electrochemical, optical, or mechanical properties of SWNTs. In each case, the CNT can be decorated with polymers and biological sensing elements like protein or antibodies or fluorescent species. Each way brings specific response for different applications like gas detection, in vivo or in vitro analysis, and bioimaging.

Large surface area and good reversibility of SWNTs make them good candidates for electrochemical sensors. Zhu et al. have used a SWNT-based electrode to detect polycyclic aromatic hydrocarbons (PAH), which are environmental contaminants with high toxicity and bioaccumulative properties [42]. Generally, the analysis of these compounds is time-consuming and expensive. In this work, the authors synthesized perylenediimide molecules with β-cyclodextrin units as pendant chains. The perylene core bind with SWNT through π–π interactions and cyclodextrins serve as the recognition site for 9-anthracenecarboxylic acid (see Figure 13.8). Simple electrochemical measurements (differential pulse voltammetry) of this system showed a significant enhancement of the current response when a supramolecular complex is formed between the polyaromatic compound and the cyclodextrin site. This simple method decreases the detection limit to 0.65 nM and shows good reproducibility with real water samples.

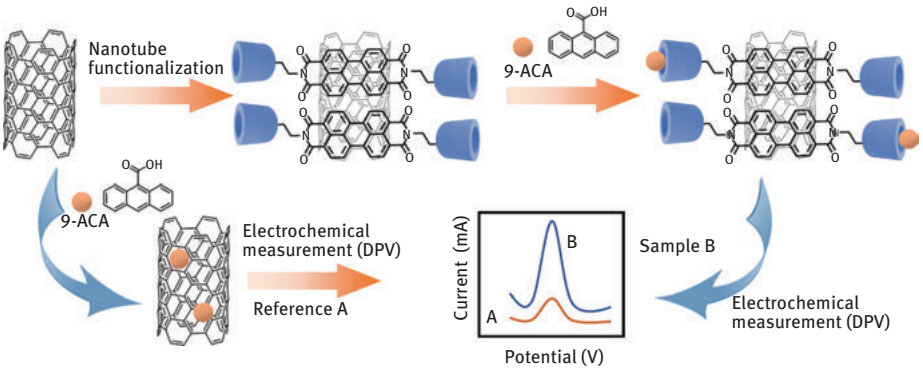

Figure 13.8: Illustration of the preparation and the effect of nanotube functionalization on electrochemical response as a sensor.

The near-infrared fluorescence properties (between 820 and 1600 nm) of SWNTs are particularly interesting for optical sensing with biological systems mainly by avoiding tissue absorption in this spectral window. Moreover, the emission spectra can be tuned depending on the SWNT chiral angle and suffer less from background fluorescence of the biological media. One remarkable example was described by Yum et al. by using dispersed (6,5) and (7,5) SWNTs modified with boronic acid derivatives for glucose detection [43]. The authors screened 30 boronic acid derivatives and studied the fluorescence response of the boronic acid-glucose complex in

EBSCOhost - printed on 2/14/2023 1:06 PM via . All use subject to https://www.ebsco.com/terms-of-use

aqueous media. They demonstrated that the fluorescence of the BA-SWNT complexes is quenched by the boronic acid receptor via an excited electron-transfer mechanism and can be selectively recovered upon binding of glucose to the boronic acid receptor on the nanotubes. This application opens the way for saccharide and glycoproteins sensing in various biological applications.

13.3 Graphene Nanoribbons

Graphene nanoribbons (GNRs) gained a lot of popularity lately as they exhibit high charge mobilities, both in the p-type and n-type regime. The main challenge remains the synthesis of well-defined GNRs in large scale. In the following section, we will discuss the latest development in this area using either the top–down or the bottom–up approach.

13.3.1 Top–Down Approach

Cutting or Etching of Graphene or Graphite Precursors

In 2007, fabrication of the first sub-50 nm nanoribbons from single sheets of graphene was proposed [44]. Graphene was patterned into narrow ribbons and an oxygen plasma was introduced to etch away the unprotected graphene to form nanoribbons with widths ranging from 10 to 100 nm and lengths of 1–2 μm. These nanoribbons were tested in FETs, but they showed high variability due to lack of control over the edge structure. Two years later, Bai et al. used a similar technique by employing chemically synthesized nanowires, obtained with controllable sizes down to 1–2 nm, as physical mask to protect the underlying graphene layer from oxygen plasma etch, as illustrated in Figure 13.9 [45].

The first solution-phase synthesis of graphene nanoribbons with width below 10 nm was reported by Li et al [46]. The GNRs were suspended in different solvents using noncovalent polymer functionalization and exhibited ultrasmooth edges. They dispersed commercial expandable graphite in a 1,2-dichloroethane (DCE) solution of poly(*m*-phenylenevinylene-co- 2,5-dioctoxy-p-phenylenevinylene) (PmPV) and sonicated to form a homogeneous suspension. Visualization using AFM showed numerous GNRs with various widths ranging from ~50 nm down to sub-10 nm. Topographic heights of the GNRs were mostly between 1 nm and 1.8 nm, which correspond to a single layer.

The same group designed a controlled hydrogen plasma reaction at 300 °C to etch selectively graphene and GNRs at the edges over the basal plane [47]. They obtained narrow GNRs (sub-5 nm). The hydrogen plasma reaction was performed several times giving single or few (≥2) layers. Meanwhile, Raman spectroscopy suggested selective etching at the graphene edges without introducing defects in the basal plane.

EBSCOhost - printed on 2/14/2023 1:06 PM via . All use subject to https://www.ebsco.com/terms-of-use

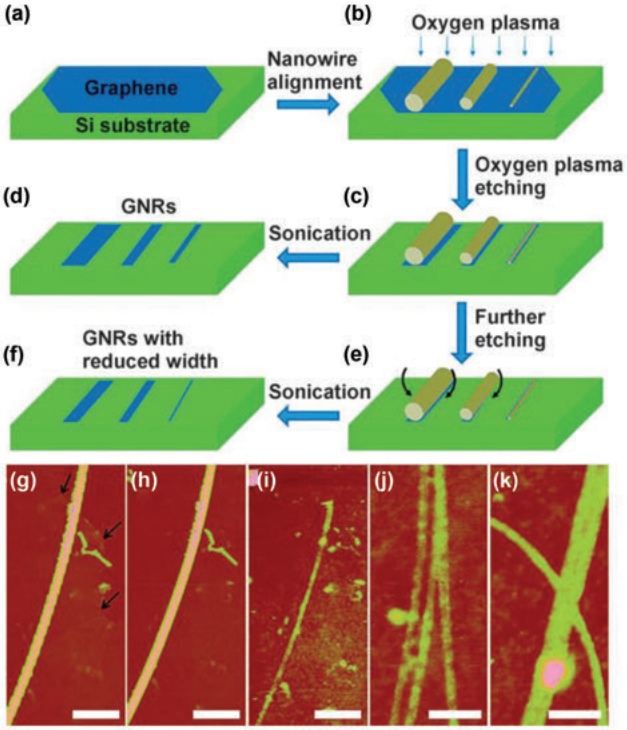

Figure 13.9: (a–f) Schematic fabrication process to obtain GNRs by oxygen plasma etch with a nanowire etch mask; (g, h) AFM images of a nanowire etch mask lying on top of a graphene flake before (g) and after (h) oxygen plasma etch (The arrows highlight the edge of the graphene sheet.); (i) AFM image of the resulting GNR after sonication removing the mask nanowire; (j, k) branched and crossed graphene nanostructures from merged and crossed nanowire masks. The scale bars in (g–i) are 300 nm, and those in (j, k) are 100 nm. Copyright © 2009, American Chemical Society.

They also found that hydrogen plasma at lower temperature (room temperature) or higher temperature (500 °C) could hydrogenate the basal plane or introduce defects in the basal plane.

Longitudinal Unzipping of CNTs

Another way to obtain GNRs is to use multi-walled carbon nanotubes (MWCNTs) of 40–80 nm as starting materials [48]. MWCNTs are treated in a oxidative solution of concentrated sulphuric acid and then potassium permanganate at room temperature. This chemical process enables the unwrapping of CNTs lengthwise forming GNRs up to 4 mm in length and 100–500 nm width. The resulting nanoribbons were highly soluble in water, ethanol, and other polar organic solvents. The proposed first step in the process is manganate ester formation by the oxidation of

EBSCOhost - printed on 2/14/2023 1:06 PM via . All use subject to https://www.ebsco.com/terms-of-use

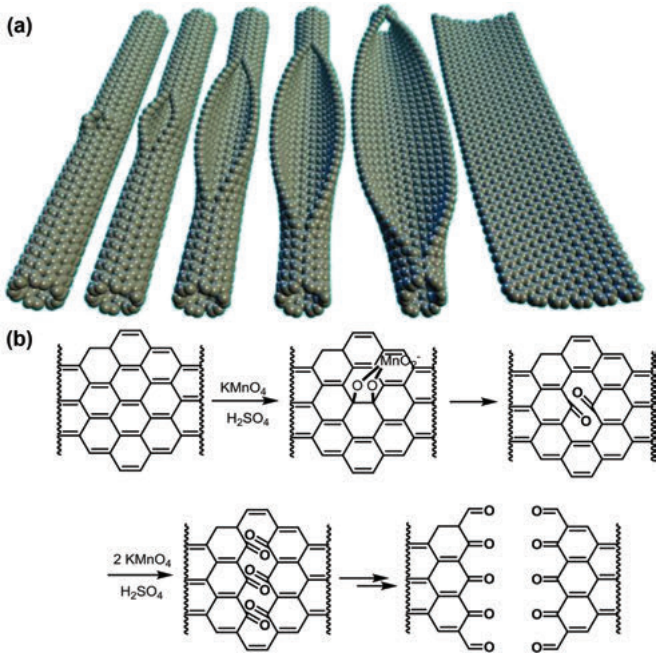

Figure 13.10: (a) Representation of the gradual unzipping of one wall of a carbon nanotube to form a nanoribbon. Oxygenated sites are not shown. Image by Dimitri V. Kosynkin. (b) The proposed chemical mechanism of nanotube unzipping. The manganate ester in 2 could also be protonated.

carbon–carbon double bond, and further oxidation is possible to afford the dione as shown in Figure 13.10.

To enhance the quality of the nanoribbons, a second acid such as H_3PO_4 or CF_3COOH could be used [49]. It was proposed that this acid inhibit the creation of vacancies in GNRs because of the protection of the formed diol groups. By controlling the temperature and the amount of $KMnO_4$ in the reaction, the degree of oxidation could be adjusted.

An alternative approach for unzipping CNTs to produce GNRs was proposed using an Ar plasma etching method [50]. MWCNTs were partly embedded in a poly (methyl methacrylate) (PMMA) layer as an etching mask. The PMMA–MWCNT film was peeled off in a KOH solution and then exposed to a 10-W Ar plasma for multiple times. The unprotected CNTs by the PMMA were etched faster and removed by the plasma. Single-, bi-, and multilayered GNRs were produced depending on the plasma treatment conditions. Finally, the PMMA film was removed using acetone vapor followed by a heat treatment to remove polymer residue. More detailed review on top–down synthesis of GNR can be found in the literature [51, 52].

These two techniques, graphene cutting and CNT unzipping, allow to obtain GNRs, but they mostly produce a panel of GNRs with different widths, single and

EBSCOhost - printed on 2/14/2023 1:06 PM via . All use subject to https://www.ebsco.com/terms-of-use

multilayers or even a limited atomic edge control. To overcome these limitations, the most common way to produce GNRs is to design precursors, polymerize and cyclize them in solution using organic synthetic tools. This so-called bottom–up allows synthesis of a wide variety of GNRs with well-defined width, edge configuration, and chemical functionalities.

13.3.2 Bottom–Up Synthesis

Over the past two decades, several synthetic methods have been developed for synthesizing graphene molecules with atomic precision. These methods are generally similar and they consist of two main steps: the synthesis of polyphenylene precursors, followed by multiple intramolecular aromatization reactions, the most popular being the oxidative cyclodehydrogenation, namely the Scholl reaction [53, 54]. Preparation of nanographenes and graphene nanoribbons with tailorable optoelectronic properties can be achieved using this versatile strategy.

Synthesis of Structurally Defined Nanographene Through Oxidative Cyclodehydrogenation

In 2008, Müllen group employed the Suzuki–Miyaura coupling reaction followed by cyclodehydrogenation (Scholl) reaction to obtain well-defined and straight $N = 9$ armchair GNRs **4** whose structure has been confirmed by scanning tunneling microscopy (STM) (Figure 13.11a) [55]. Bulky alkyl chains were attached on the edge of **1** and **2** to allow the preparation of stable dispersion in organic solvent. Nonetheless, only ~12 nm long GNRs were obtained due to high steric hindrance and high rigidity of the polymer backbone. To make longer GNRs, they synthesized a more flexible precursor

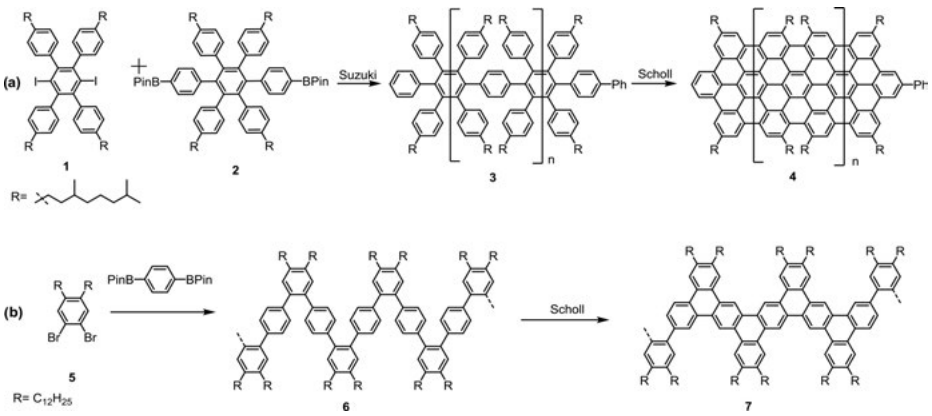

Figure 13.11: Suzuki strategy. Rigid bulky (a) and flexible (b) polymers synthesis.

EBSCOhost - printed on 2/14/2023 1:06 PM via . All use subject to https://www.ebsco.com/terms-of-use

5 giving an approximately 25 nm long polymer **7** (Figure 13.11b) [56]. Only by changing the design of the polymer they were able to increase by two the polymer length using the same synthetic strategy.

The same group has also synthesized GNR **11** through the A_2B_2-type Suzuki polymerization, starting from a 4,4-dibromobiphenyl-based precursor **8** and benzene-1,4-diboronic ester **9** [57]. (Figure 13.12a) The polyphenylene precursor **10** was obtained with a weight-average molecular weight (M_w) of 6,900 g.mol^{-1} and a PDI of 1.7 according to SEC analysis against a PS standard. They obtained an approximately 13 nm long polymer.

In 2013, Kim et al. investigated wider GNRs using naphthalene diboronic ester and anthracene diboronic ester as precursors [58]. Although they obtained wider GNRs, the cyclodehydrogenation did not go to completion as demonstrated by ^{1}H NMR.

Although easy to use, Suzuki coupling presents some drawbacks such as a low longitudinal extension of GNRs, a limitation of the molecular weight of precursors due to steric hindrance, the need of having two different monomers with the synthesis of boronic acid for one of them. The biphasic conditions might also affect the reaction efficiency. Yamamoto polymerization became an attractive alternative to overcome these limitations because it needs only a dihalogenated precursor, and it is also known to be efficient with bulky groups.

As an example [59], GNR **14** was synthesized though AA-type Yamamoto polymerization of a dichlorinated precursor **12** (Figure 13.12b). This reaction yielded to a longer polymer compared to those obtained using a A_2B_2-type Suzuki reaction with a M_w of 52,000 g.mol^{-1}, M_n of 44,000 g.mol^{-1}, and a PDI of 1.2 according to SEC analysis against a PS standard. It was also wider with a width of 1.54–1.98 nm.

A_2B_2-type Suzuki and AA-type Yamamoto allow the synthesis of atomically precise GNRs with length reaching 100 nm and more [60]. Nevertheless, these coupling reactions need expensive metal catalysts, which are not eco-friendly. In opposition, Diels–Alder reactions attract more and more scientists due to its easy use, and in the case of GNRs, M_w values higher than 100,000 g.mol^{-1} in many systems [60]. Another advantage of such reaction is the use of a very low amount of solvent or even to neatly perform the reaction such as the following example.

In 2014, Mullen group has reported an AB-type Diels–Alder polymerization to prepare **17** (Figure 13.12c) [61]. They obtained a 600 nm-long, 0.69–1.13 nm-wide GNR. Extremely high values of M_w and M_n of 640,000 and 340,000 g.mol^{-1}, respectively, were obtained.

Suzuki–Miyaura, Yamamoto, and Diels–Alder reactions are the most common strategies for the synthesis of GNRs, inspired by which, other precursor designs can be imagined and employed, such as N-doped GNRs, which shows high charge-carrier mobility (Figure 13.13) [62]. The amount of nitrogen doping in the polymer is controlled by the amount of pyrazine precursors used. The electron mobility increases as the number of nitrogen increases, leading to the formation of an n-type semiconductor.

EBSCOhost - printed on 2/14/2023 1:06 PM via . All use subject to https://www.ebsco.com/terms-of-use

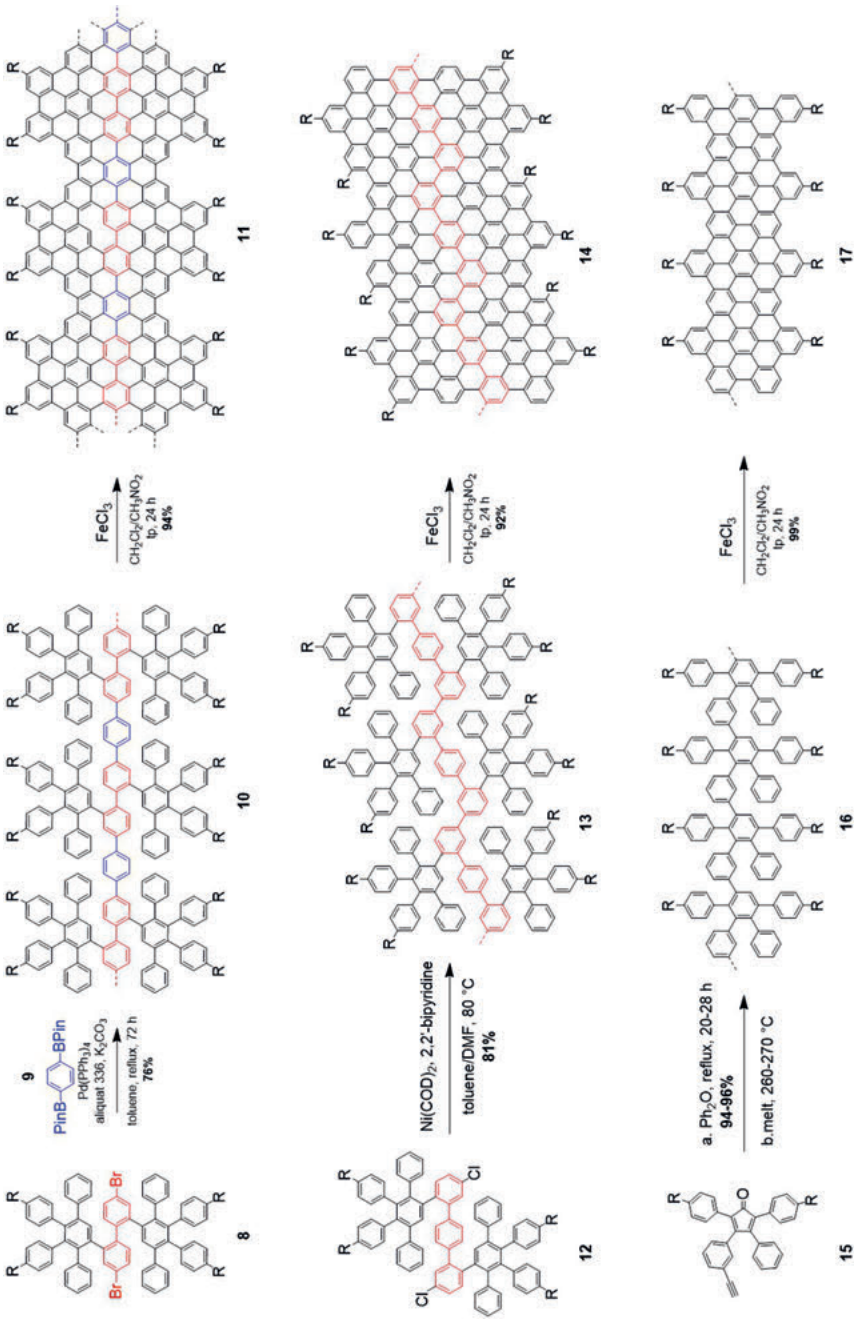

Figure 13.12: Suzuki (a), Yamamoto (b) and Diels–Alder (c) coupling followed by Scholl reaction.

EBSCOhost - printed on 2/14/2023 1:06 PM via . All use subject to https://www.ebsco.com/terms-of-use

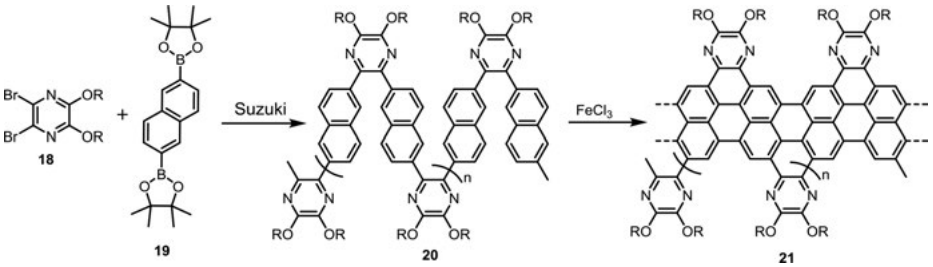

Figure 13.13: Design of *N*-doped GNR.

A sum up of these coupling reactions is done in Table 13.1, which shows the advantages and drawbacks of these reactions. Nevertheless, these synthetic methods have also been limited by several factors such as chlorination [63], incomplete graphitization [64], and unexpected structural rearrangements [65] during the Scholl reaction. In addition, small amount of $FeCl_3$ may remain and contaminate the polymer, which can lead to a decrease in the efficiency for applications. Furthermore, several substitutes to $FeCl_3$ were reported in the literature, including $MoCl_5$ [66], DDQ with $Sc(OTf)_3$ [67] DDQ with different protic or Lewis acid (CH_3SO_3H, $AlCl_3$,$BF_3{\cdot}OEt_2$) [68]. Less known but not least efficient techniques of cyclization were reported in the scientific literature.

Table 13.1: Summary of the Suzuki, Yamamoto, and Diels–Alder reactions for the synthesis of GNRs.

	M_w (g.mol^{-1})	M_n (g.mol^{-1})	PDI	Polymer width (nm)	Drawbacks/Advantages
Suzuki **11**	6,900	n.d.[a]	1.7	n.d.[a]	–Needs two precursors, low molecular weight, short polymers **+ Good yields, easy to perform, not water sensitive**
Yamamoto **14**	52,000	44,000	1.2	1.54–1.98	– Needs stoichiometric quantities of catalyst **+ One precursor, efficient with bulky groups**
Diels–Alder **17**	640,000	340,000	1.9	0.69–1.13	– Needs high temperature **+ Solvent-free, no metal catalyst, high molecular weight**

[a.] Not Determined

Other Cyclization Methods

$FeCl_3$ is the most employed reagent for the synthesis of PAH via oxidative cyclodehydrogenation. Nevertheless, it possesses some limitations such as the need of

EBSCOhost - printed on 2/14/2023 1:06 PM via . All use subject to https://www.ebsco.com/terms-of-use

large amount of reagent but also, as mentioned previously, the formation of chlorinated by-products and the complexation of $FeCl_3$ to form $HFeCl_3$.

In this part, we will discuss about photochemical dehydrohalogenation (CDH). This method of intramolecular cyclization was developed in the late 1960s and does not necessitate the use of an oxidant with the loss of H–X (X=Cl, Br, I) as the only by-products. Chlorine-containing derivatives led to high yields. It was suggested that the reaction proceeds through a $[4n+2]\pi$ electrocyclization followed by the elimination of HCl, whereas brominated and iodinated precursors cyclize through a radical mechanism, increasing the chances of the formation of by-products [69, 70] Another plausible mechanism was proposed involving the photolysis of the C–Cl bond to generate a phenyl radical intermediate [71].

Furthermore, CDH reactions possess several advantages: it is regioselective, so the edge control can be done very precisely during the synthesis of GNRs; it is a metal-free method; proper design of the monomer allows the chlorine atoms to be introduced where desired; mild conditions are used, thus enabling the introduction of different functional groups onto nanographenes.

Inspired by this eco-friendly and simple reaction, Morin's group designed various derivatives to investigate the usefulness of the photochemical cyclodehydrochlorination (CDHC) reaction. They synthesized different compounds to demonstrate that the reaction is regioselective, can undergo multiple cyclizations, and can work with electron-rich and electron-poor moieties. In all cases, the reaction proceeded very well with very high yield, up to 96% demonstrating the high efficiency of this method.

Using this CDHC reaction, they synthesized helically coiled **22** [72] and narrow thiophene-edged **23** and **24** [73] GNRs (Figure 13.14) using Suzuki cross-coupling reaction to obtain polymers and performing the CDHC to cyclize them. The CDHC was performed in decalin and under different wavelengths according to the light-absorption efficiency of the different precursors.

In 2016, Chalifoux and coworkers developed a new alkyne benzannulation reaction to prepare soluble GNRs (Figure 13.15) [74] Interestingly, this BrØnsted acid-catalyzed reaction is the only known method for the preparation of polyrylene, armchair-type GNR using a solution-phase synthesis. GNR **26** absorbs broadly in the visible region and exhibits a quite low bandgap of 1.03 eV. Using this reaction, the same group has reported the synthesis of long pyrene derivatives (peropyrenes and teropyrenes) [75] and chiral pyrene derivatives [76].

13.3.3 Surface-Assisted Synthesis

GNRs tend to aggregate and in-depth physical characterization remains a challenge. In 2007, surface-assisted method was introduced to obtain molecular network on surfaces locked by covalent interactions [77]. Covalent bonds were formed on the

EBSCOhost - printed on 2/14/2023 1:06 PM via . All use subject to https://www.ebsco.com/terms-of-use

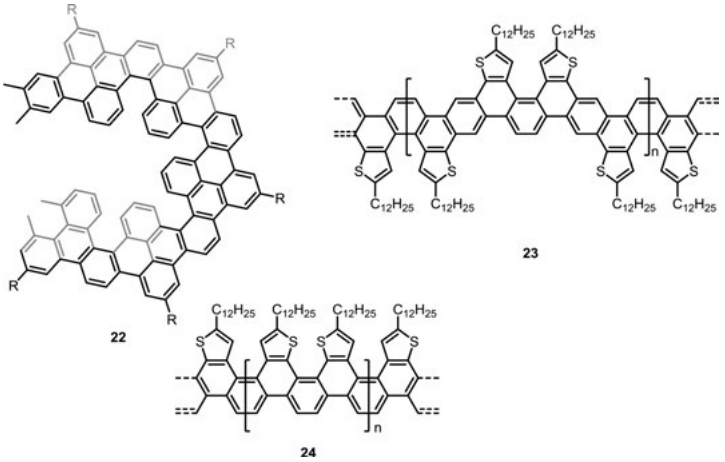

Figure 13.14: Synthesis of PAHs through the photochemical cyclodehydrochlorination (CDCH) reaction.
Source: Reference [72] and [73].

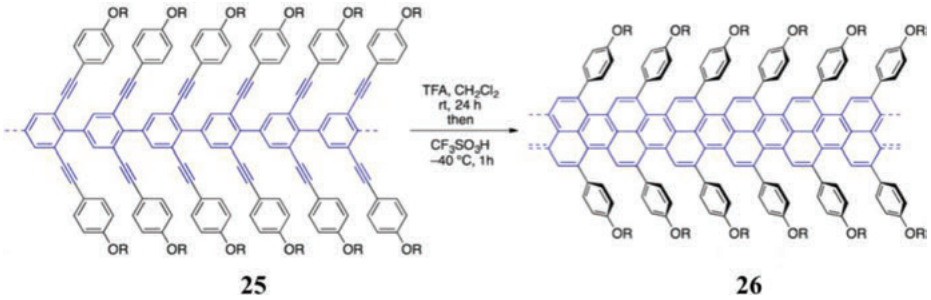

Figure 13.15: Synthesis of a soluble GNR using the alkyne benzannulation reaction.
Source: Modified with permission from ref [74].

surface of metal (gold or copper) with single crystals upon thermal activation of porphyrin building blocks. These nanostructures were precisely controlled and characterized with STM. The types of reactants, choice of metal surface, and initial conditions are critical parameters for the control of surface-assisted reactions.

In collaboration with the Fasel group, Müllen and coworkers used this method to produce GNRs with atomically precise structure and also some graphene nanoribbons heterojunctions and heterostructures [78, 79]. They obtained an armchair nanoribbon of width $N = 7$ starting from 10,10′-dibromo-9,9′-bianthryl precursor monomers (Figure 13.16). By heating the surface, monomers lose their halogens and yield to a surface-stabilized biradical form. During this activation, the monomer diffuse across the surface and produce a radical addition to form a linear polymer.

EBSCOhost - printed on 2/14/2023 1:06 PM via . All use subject to https://www.ebsco.com/terms-of-use

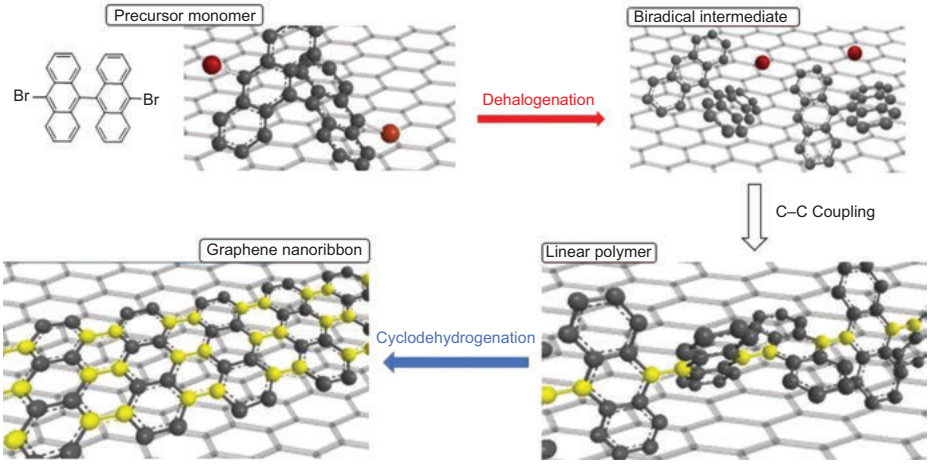

Figure 13.16: Key steps for surface-supported GNRs synthesis

Then a surface-assisted cyclodehydrogenation is performed by a second thermal activation leading to the fully conjugated and planar polymer.

This method has a lot of advantages but also some drawbacks, which limit this technique. As the reaction occur under vacuum, gases such as O_2 and CO_2 in air are not present and so do not affect the reaction. Furthermore, the absence of solvent allows a much larger range of reaction temperatures than for reactions in solution and insoluble substances are no longer restricted. Products can be visualized on surfaces by scanning probe microscopy (SPM). The SPM tip can operate directly on the substrate surface and measure the product's electronic properties.

In contrast, the surface substrate under low vapor conditions can produce some by-products (e.g., H_2 and H_2O) and because of strong interactions, molecules can be difficult or impossible to separate. Always because of strong interactions between the molecules and the metal substrate, the diffusion distance of molecules on surfaces is restricted. Additionally, the need for ultrahigh vacuum limits its potential industrialization.

Top–down (cutting or etching graphene) and bottom–up (polymerization followed by cyclization) synthesis are the most employed to obtain GNRs. Nonetheless, some nonconventional methods have been reported. As an example, GNRs can be obtained by micro-explosion in carbon nanotubes [80] MWCNTs are filled with potassium and then mixed vigorously with water. A micro-explosion generated by reaction between potassium and water splits MWCNTs in GNRs. Transmission electron microscopy (TEM) and scanning electron microscopy (SEM) showed that this method can produce GNRs. However, this method is not accurate as large MWCNTs (larger than 10 nm) were not split efficiently. Only GNRs with thickness less than

EBSCOhost - printed on 2/14/2023 1:06 PM via . All use subject to https://www.ebsco.com/terms-of-use

5 nm were observed to have smooth edges; the thicker the wall was, the smoother the edges were. Furthermore, several sizes of GNRs were also observed.

References

[1] Iijima, S., *Nature*, 1991, 354, 56–58.
[2] Iijima, S. and Ichihashi, T., *Nature*, 1993, 363, 603–605.
[3] Guo, T., Nikolaev, P., Thess, A., Colbert, D.T. and Smalley, R. E., *Chem. Phys. Lett.*, 1995, 243, 49–54.
[4] Nikolaev, P., Bronikowski, M. J., Bradley, R. K., Rohmund, F., Colbert, D.T., Smith, K.A. and Smalley, R.E., *Chem. Phys. Lett.*, 1999, 313, 91–97.
[5] Kitiyanan, B., Alvarez, W.E., Harwell, J.H. and Resasco, D.E., *Chem. Phys. Lett.*, 2000, 317, 497–503.
[6] Zhang, H., Wu, B., Hu, W. and Liu, Y., *Chem. Soc. Rev.*, 2011, 40, 1324–1336.
[7] Nish, A., Hwang, J.-Y., Doig, J. and Nicholas, R. J., *Nat. Nanotechnol.*, 2007, 2, 640–646.
[8] Brady, G. J., Joo, Y., Wu, M.-Y., Shea, M.J. , Gopalan, P. and Arnold, M.S., *ACS Nano*, 2014, 8, 11614–11621.
[9] Gomulya, W., Costanzo, G.D., de Carvalho, E.J.F., Bisri, S.Z., Derenskyi, V., Fritsch, M., Fröhlich, N., Allard, S., Gordiichuk, P., Herrmann, A., Marrink, S.J., dos Santos, M.C., Scherf U. and Loi, M.A., *Adv. Mater.*, 2013, 25, 2948–2956.
[10] Guo, X., Cui, C., Zhang, M., Huo, L., Huang, Y., Hou, J. and Li, Y., *Energy Environ. Sci.*, 2012, 5, 7943–7949.
[11] Lee, H.W., Yoon, Y., Park, S., Oh, J.H., Hong, S., Liyanage, L.S., Wang, H., Morishita, S., Patil, N., Park, Y.J., Park, J.J., Spakowitz, A., Galli, G. , Gygi, F. , Wong, P.H.-S., Tok, J.B.-H., Kim, J.M. and Bao, Z. , *Nat. Commun.*, 2011, 2, 541.
[12] Schuettfort, T., Snaith, H.J., Nish, A. and Nicholas, R.J., *Nanotechnology*, 2010, 21, 025201.
[13] Stranks, S.D., Weisspfennig, C., Parkinson, P., Johnston, M.B., Herz, L.M. and Nicholas, R.J., *Nano Lett.*, 2011, 11, 66–72.
[14] Lemasson, F.A., Strunk, T., Gerstel, P., Hennrich, F., Lebedkin, S., Barner-Kowollik, C., Wenzel, W., Kappes, M.M. and Mayor, M., *J. Am. Chem. Soc.*, 2011, 133, 652–655.
[15] Tange, M., Okazaki, T. and Iijima, S., *J. Am. Chem. Soc.*, 2011, 133, 11908–11911.
[16] Mistry, K.S., Larsen, B.A. and Blackburn, J.L., *ACS Nano*, 2013, 7, 2231–2239.
[17] Joo, Y., Brady, G.J., Shea, M.J., Oviedo, M.B., Kanimozhi, C., Schmitt, S.K., Wong, B.M., Arnold, M.S. and Gopalan, P., *ACS Nano*, 2015, 9, 10203–10213.
[18] Lei, T., Chen, X., Pitner, G., Wong, H.-S.P. and Bao, Z., *J. Am. Chem. Soc.*, 2016, 138, 802–805.
[19] Toshimitsu, F. and Nakashima, N., *Nat. Commun.*, 2014, 5, 5041.
[20] Fong, D., Bodnaryk, W.J., Rice, N.A., Saem, S., Moran-Mirabal, J.M. and Adronov, A., *Chem. – Eur. J.*, 2016, 22, 14560–14566.
[21] Kamyshny, A. and Magdassi, S., *Small*, 2014, 10, 3515–3535.
[22] Gu, X., Zhou, Y., Gu, K., Kurosawa, T., Guo, Y., Li, Y. , Lin, H., Schroeder, B.C., Yan, H., Molina-Lopez, F., Tassone, C. J., Wang, C., Mannsfeld, S.C.B., Yan, H., Zhao, D., Toney, M.F. and Bao, Z., *Adv. Energy Mater.*, 7, 1602742.
[23] Liu, Y., Zhao, J., Li, Z. , Mu, C., Ma, W., Hu, H., Jiang, K., Lin, H., Ade, H. and Yan, H., *Nat. Commun.*, 2014, 5, 5293.
[24] Cinke, M., Li, J., Chen, B., Cassell, A., Delzeit, L., Han, J. and Meyyappan, M., *Chem. Phys. Lett.*, 2002, 365, 69–74.

EBSCOhost - printed on 2/14/2023 1:06 PM via . All use subject to https://www.ebsco.com/terms-of-use

[25] Landi, B.J., Raffaelle, R.P., Castro, S.L. and Bailey, S.G., *Prog. Photovolt. Res. Appl*., 2005, 13, 165–172.
[26] Ren, S., Bernardi, M., Lunt, R.R., Bulovic, V., Grossman, J.C. and Gradečak, S., *Nano Lett*., 2011, 11, 5316–5321.
[27] Kazaoui, S., Minami, N., Nalini, B., Kim, Y. and Hara, K., *J. Appl. Phys*., 2005, 98, 084314.
[28] Kanai, Y. and Grossman, J.C., *Nano Lett*., 2008, 8, 908–912.
[29] Schuettfort, T., Nish, A. and Nicholas, R.J., *Nano Lett*., 2009, 9, 3871–3876.
[30] Dabera, G.D.M.R., Jayawardena, K.D.G.I., Prabhath, M.R.R., Yahya, I., Tan, Y.Y., Nismy, N.A., Shiozawa, H., Sauer, M., Ruiz-Soria, G., Ayala, P., Stolojan, V., Adikaari, A.A.D.T., Jarowski, P. D., Pichler, T. and Silva, S.R.P., *ACS Nano*, 2013, 7, 556–565.
[31] Rowell, M.W., Topinka, M.A., McGehee, M.D., Prall, H.-J., Dennler, G., Sariciftci, N.S., Hu, L. and Gruner, G., *Appl. Phys. Lett*., 2006, 88, 233506.
[32] Aitola, K., Sveinbjörnsson, K., Correa-Baena, J.-P., Kaskela, A., Abate, A., Tian, Y., Johansson, E.M.J., Grätzel, M., Kauppinen, E.I., Hagfeldt, A. and Boschloo, G., *Energy Environ. Sci*., 2016, 9, 461–466.
[33] An, K.H., Jeon, K.K., Heo, J.K., Lim, S.C., Bae, D.J. and Lee, Y.H., *J. Electrochem. Soc*., 2002, 149, A1058–A1062.
[34] Chen, P., Chen, H., Qiu, J. and Zhou, C., *Nano Res*., 2010, 3, 594–603.
[35] Kumar, S., Rani, R., Dilbaghi, N., Tankeshwar, K. and Kim, K.-H., *Chem. Soc. Rev*., 2017, 46, 158–196.
[36] Hennrich, F., Li, W., Fischer, R., Lebedkin, S., Krupke, R. and Kappes, M.M., *ACS Nano*, 2016, 10, 1888–1895.
[37] Bisri, S.Z., Gao, J., Derenskyi, V., Gomulya, W., Iezhokin, I., Gordiichuk, P., Herrmann, A. and Loi, M.A., *Adv. Mater*., 2012, 24, 6147–6152.
[38] Miyata, Y., Shiozawa, K., Asada, Y., Ohno, Y., Kitaura, R., Mizutani, T. and Shinohara, H., *Nano Res*., 2011, 4, 963–970.
[39] Wang, C., Chien, J.-C., Takei, K., Takahashi, T., Nah, J., Niknejad, A.M. and Javey, A., *Nano Lett*., 2012, 12, 1527–1533.
[40] Kong, J., Franklin, N.R., Zhou, C., Chapline, M.G., Peng, S., Cho, K. and Dai, H., *Science*, 2000, 287, 622–625.
[41] Khamis, S.M., Jones, R.A., Johnson, A.T.C., Preti, G., Kwak, J. and Gelperin, A., *AIP Adv*., 2012, 2, 022110.
[42] Zhu, G., Zhang, X., Gai, P., Zhang, X. and Chen, J., *Nanoscale*, 2012, 4, 5703–5709.
[43] Yum, K., Ahn, J.-H., McNicholas, T.P., Barone, P.W., Mu, B., Kim, J.-H., Jain, R.M. and Strano, M.S., *ACS Nano*, 2012, 6, 819–830.
[44] Han, M.Y., Özyilmaz, B., Zhang, Y. and Kim, P., *Phys. Rev. Lett*., 2007, 98, 206805.
[45] Bai, J., Duan, X. and Huang, Y., *Nano Lett*., 2009, 9, 2083–2087.
[46] Li, X., Wang, X., Zhang, L., Lee, S. and Dai, H., *Science*, 2008, 319, 1229–1232.
[47] Xie, L., Jiao, L. and Dai, H., *J. Am. Chem. Soc*., 2010, 132, 14751–14753.
[48] Kosynkin, D.V., Higginbotham, A.L., Sinitskii, A., Lomeda, J.R., Dimiev, A., Price, B.K. and Tour, J.M., *Nature*, 2009, 458, 872–876.
[49] Higginbotham, A.L., Kosynkin, D.V., Sinitskii, A., Sun, Z. and Tour, J.M., *ACS Nano*, 2010, 4, 2059–2069.
[50] Jiao, L., Zhang, L., Wang, X., Diankov, G. and Dai, H., *Nature*, 2009, 458, 877–880.
[51] James, D.K. and Tour, J.M., *Macromol. Chem. Phys*., 2012, 213, 1033–1050.
[52] Celis, A., Nair, M.N., Taleb-Ibrahimi, A., Conrad, E.H., Berger, C., de Heer, W.A. and Tejeda, A., *J. Phys. Appl. Phys*., 2016, 49, 143001.
[53] Scholl, R. and Seer, C., *Berichte Dtsch. Chem. Ges. B Ser*., 1922, 55, 109–117.
[54] Scholl, R. and Mansfeld, J., *Berichte Dtsch. Chem. Ges*., 1910, 43, 1734–1746.

EBSCOhost - printed on 2/14/2023 1:06 PM via . All use subject to https://www.ebsco.com/terms-of-use

[55] Yang, X., Dou, X., Rouhanipour, A., Zhi, L., Räder, H.J. and Müllen, K., *J. Am. Chem. Soc*., 2008, 130, 4216–4217.
[56] Dössel, L., Gherghel, L., Feng, X. & Müllen, K. Graphene Nanoribbons by Chemists: Nanometer-Sized, Soluble, and Defect-Free. *Angew. Chem. Int. Ed.* 2011, 50, 2540–2543.
[57] Schwab, M.G., Narita, A., Osella, S., Hu, Y., Maghsoumi, A., Mavrinsky, A., Pisula, W., Castiglioni, C., Tommasini, M., Beljonne, D., Feng, X. and Müllen, K., *Chem. – Asian J*., 2015, 10, 2134–2138.
[58] Kim, K.T., Jung, J.W. and Jo, W.H., *Carbon*, 2013, 63, 202–209.
[59] Schwab, M.G., Narita, A., Hernandez, Y., Balandina, T., Mali, K.S., De Feyter, S., Feng, X. and Müllen, K., *J. Am. Chem. Soc*., 2012, 134, 18169–18172.
[60] Vo, T.H., Shekhirev, M., Kunkel, D.A., Morton, M.D., Berglund, E., Kong, L., Wilson, P.M., Dowben, P.A., Enders, A. and Sinitskii, A., *Nat. Commun*., 2014, 5, 3189.
[61] Narita, A., Feng, X., Hernandez, Y., Jensen, S.A., Bonn, M., Yang, H., Verzhbitskiy, H., Casiraghi, C., Hansen, M.R., Koch, A.H.R., Fytas, G., Ivasenko, O., Li, B., Mali, K.S., Balandina, T., Mahesh S., Feyter, S.D. and Müllen, K., *Nat. Chem*., 2014, 6, 126–132.
[62] Vo, T.H., Shekhirev, M., Kunkel, D.A., Orange, F., Guinel, M.J.-F., Enders, A. and Sinitskii, A., *Chem. Commun*., 2014, 50, 4172–4174.
[63] Simpson, C.D., Brand, J.D., Berresheim, A.J., Przybilla, L., Räder, H.J. and Müllen, K., *Chem. – Eur. J*., 2002, 8, 1424–1429.
[64] Müller, M., Kübel, C., Morgenroth, F., Iyer, V.S. and Müllen, K., *Carbon*, 1998, 36, 827–831.
[65] Ormsby, J.L., Black, T.D., Hilton, C.L., Bharat and King, B.T., *Tetrahedron*, 2008, 64, 11370–11378.
[66] Waldvogel, S.R. and Trosien, S., *Chem. Commun*., 2012, 48, 9109–9119.
[67] Tsuda, A. and Osuka, A., *Science*, 2001, 293, 79–82.
[68] Zhai, L., Shukla, R. and Rathore, R., *Org. Lett*., 2009, 11, 3474–3477.
[69] Sato, T., Shimada, S. and Hata, K. , *Bull. Chem. Soc. Jpn*., 1971, 44, 2484–2490.
[70] Schnapperelle, I. and Bach, T., *Chem. – Eur. J*., 2014, 20, 9725–9732.
[71] Henderson, W.A., Lopresti, R. and Zweig, A., *J. Am. Chem. Soc*., 1969, 91, 6049–6057.
[72] Daigle, M., Miao, D., Lucotti, A., Tommasini, M. and Morin, J.-F., *Angew. Chem. Int. Ed*., 2017, 56, 6213–6217.
[73] Miao, D., Daigle, M., Lucotti, A., Boismenu-Lavoie, J., Tommasini, M. and Morin, J.-F., *Angew. Chem. Int. Ed*., 2018, 57, 3588–3592.
[74] Yang, W., Lucotti, A., Tommasini, M. and Chalifoux, W.A., *J. Am. Chem. Soc*., 2016, 138, 9137–9144.
[75] Yang, W., Kazemi, R.R., Karunathilake, N., Catalano V.J., Alpuche-Aviles, M.A. and Chalifoux, W.A., *Org. Chem. Front*., 2018, **5**, 2288–2295. DOI:10.1039/C8QO00389K.
[76] Yang, W., Longhi, G., Abbate, S., Lucotti, A., Tommasini, M., Villani, C., Catalano, V.J., Lykhin, A.O., Varganov, S.A. and Chalifoux, W.A., *J. Am. Chem. Soc*., 2017, 139, 13102–13109.
[77] Grill, L., Dyer, M., Lafferentz, L., Persson, M., Peters, M.V. and Hecht, S., *Nat. Nanotechnol*., 2007, 2, 687–691.
[78] Cai, J., Ruffieux, P., Jaafar, R., Bieri, M., Braun, T., Blankenburg, S., Muoth, M., Seitsonen, A. P., Saleh, M., Feng, X., Müllen, K. and Fasel, R., *Nature*, 2010, 466, 470–473.
[79] Cai, J., Pignedoli, C.A., Talirz, L., Ruffieux, P., Söde, H., Liang, L., Meunier, V., Berger, R., Li, R., Feng, X., Müllen, K. and Fasel, R., *Nat. Nanotechnol*., 2014, 9, 896–900.
[80] Fan, Y., Li, J., Liu, X. , Wang, L., Chen, X., Sun, S., Kawasaki, A. and Jiang, W., *Carbon*, 2011, 49, 1439–1445.

EBSCOhost - printed on 2/14/2023 1:06 PM via . All use subject to https://www.ebsco.com/terms-of-use

Danny Chhin, Md Sazzad Hossain, Steen B. Schougaard

14 Modeling of Lithium-Ion Batteries

Batteries are a complex system. The performances of a battery depend not only in the kinetics of the active material but also of mass transport limitations. Thus, the way the active material is processed into a composite electrode as well as the cell characteristic can impact overall cell performances significantly. As lithium-ion battery is poised to become a multi-billion-dollar industry that span over portable electronics, electric vehicles and storage of renewable energy, qualitative assessment of these limitations is key for future improvement. As such, simulation has become an invaluable tool in the field of lithium ion battery research. The following chapter introduces the Newman volume average approach for lithium-ion battery simulation. Notably this includes the description of fundamental processes occurring during lithium-ion battery operation, typical characterizations methods to obtain key simulation parameters and a complete simulation example.

Keywords: Li-ion battery, simulation, mass-transport, characterization

14.1 Introduction

The lithium-ion battery has been at the heart of the mobile revolution that has integrated well with our society over the past two decades. As energy storage devices, they offer good safety with catastrophic failure per produced unit in parts per billion (ppb) range, good cyclability with thousands of cycles before decaying to 80% of the initial capacity, low cost and most important, high-energy density [1]. The basis of high-energy density in Li-ion batteries is their unique insertion redox reactions, where the solid-state materials can retain their structural integrity during repeated insertion and release of Li^+/e^- couples [2, 3]. From Figure 14.1, it is clear that the potential energy available per charge is related to the chemical energy difference between Li^+ and e^- residing in the structure of the positive electrode versus the structure of the negative electrode. In a typical cell phone battery based on graphite anode [4, 5] and lithium cobalt oxide cathode [6], this translates into the following half-cell redox reactions:

Danny Chhin, Md Sazzad Hossain, Steen B. Schougaard, Université du Québec à Montréal, Montréal QC, Canada

https://doi.org/10.1515/9783110537734-014

EBSCOhost - printed on 2/14/2023 1:06 PM via . All use subject to https://www.ebsco.com/terms-of-use

$$\text{Negative electrode}: \quad Li^+ + e^- + \square C_6 \rightleftharpoons LiC_6 \tag{14.1}$$

$$\text{Positive electrode}: \quad Li^+ + e^- + \square CoO_2 \rightleftharpoons LiCoC_2 \tag{14.2}$$

$$\text{Total reaction}: \quad LiC_6 + \square CoO_2 \rightleftharpoons LiCoC_2 + \square C_6 \tag{14.3}$$

where $\square$ is a vacancy or space within the structure that can accommodate Li^+.

Our objective is to set up a numerical framework that allows us to analyze and predict Li-ion battery performance of batteries like the one in Figure 14.1. The first parameter to evaluate is the theoretical limit for how much energy can be stored per unit mass. To this end, we must evaluate (1) the maximum amount of work we can do per charge transferred from the negative to the positive electrode during discharge and (2) how much charge can be stored per unit mass.

The maximum amount of work that can be derived from a chemical reaction as in eq. (14.3) at fixed pressure and temperature is the Gibb's free energy ($\Delta_r G$). Similarly, the maximum amount of work that can be derived from moving an electronic charge between the two electrodes is equal to the electrostatic potential difference between the two, also known as the *voltageE* measured in volts (V = J/C). Thus, the relationship between electric potential energy and chemical energy becomes

$$-\Delta_r G = nFE \tag{14.4}$$

where F is the Faraday's constant, that is, the charge of one mole of electrons (96,845 C/mol). n is the number of electrons transferred, which in eq. (14.3) is one. $\Delta_r G$ can be calculated from the first principles, thermodynamic tables or other parameterized tables.

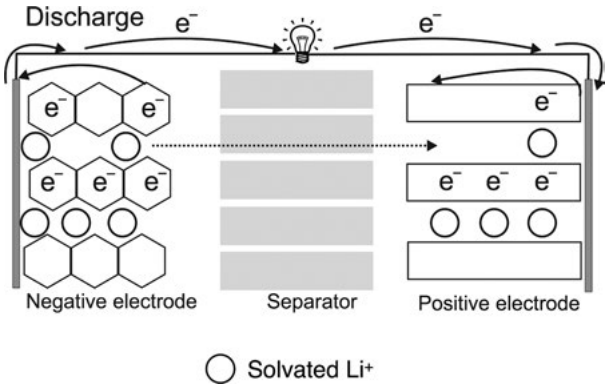

Figure 14.1: Scheme of discharge in a Li-ion battery for an insertion redox reaction within the structure of $LiCoO_2$ at the positive electrode and LiC_6 at the negative electrode.

The amount of charge that can be stored per unit mass of material, also known as the *capacity*, can be established by dividing the number of electrons that can be stored

EBSCOhost - printed on 2/14/2023 1:06 PM via . All use subject to https://www.ebsco.com/terms-of-use

per formula unit (n) with its molecular mass, and then again converting moles of electrons into charge using F. The common units are mAh/g or Ah/g, not C/g. Most important, the capacity is often reported selectively for one of the two electrode materials. However, to form a battery requires both the half-cells; and capacity based on the total reaction therefore becomes

$$\frac{1}{\mathbb{C}} = \frac{1}{\mathbb{C}_+} + \frac{1}{\mathbb{C}_-} \tag{14.5}$$

The theoretical energy density can now be calculated as the product of the voltage and capacity derived from eqs.(14.4) and (14.5), respectively. However, as we are interested in the energy storage performance of practical batteries, an analysis of the energy used to drive charge transport and chemical reaction is required. This in turn demands detailed knowledge of the operation processes of Li-battery as well as its physical structure, which is the subject of our discussion in the next sections.

Before continuing, a number of features related to our presentation should be underlined. Emphasis has been put on providing the most pedagogical introduction. As such, to simplify the formula toolbox, dilute solution theory is used throughout this text; concentrations rather than activities are therefore employed. Similarly, formulas are provided for the specific case of one-electron ($n = 1$) redox reaction, as these are the most common in lithium batteries. For a more complete treatment see Ref. [7]. Finally, to simplify the nomenclature, each variable is introduced with a minimal amount of dependencies in sub- and superscript as these should be clear from the text. As the presentation progresses, these are introduced only when absolutely necessary to avoid ambiguity.

14.1.1 Structure and Elemental Processes in Li-Ion Batteries

Batteries in practical applications do not use a single block or monolith of active material as electrodes. Rather, the active material is cast into a porous composite with a conductive additive and a polymer binder which adhere to a metallic current collector. To prevent short circuit, the two electrodes must be kept electrically separated. This is done by placing a porous glass or plastic membrane, known as the separator, between the two, thus forming a sandwich-type structure. The electrode and separator void is subsequently filled with electrolyte when the battery is assembled (Figure 14.2) The composite has the advantage compared to a monolith electrode in that it is more conducting for both electrons and ions, and it is more apt to accommodate the volume changes associated with Li^+ insertion and release [8].

Examining the operation principle of the composite electrode battery yields a series of subprocesses required to transfer Li^+ and e^- from an electroactive particle in

EBSCOhost - printed on 2/14/2023 1:06 PM via . All use subject to https://www.ebsco.com/terms-of-use

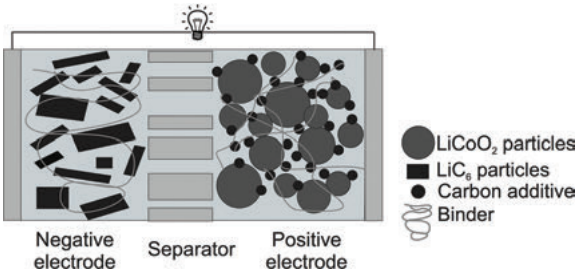

Figure 14.2: Scheme of a porous electrode Li-ion battery: Active material particles in the negative LiC_6 and the $LiCoO_2$ positive electrodes, binders, carbon additives, separators, current collectors (connected to the external circuit), and electrolyte filling the electrode as well as the separator voids.

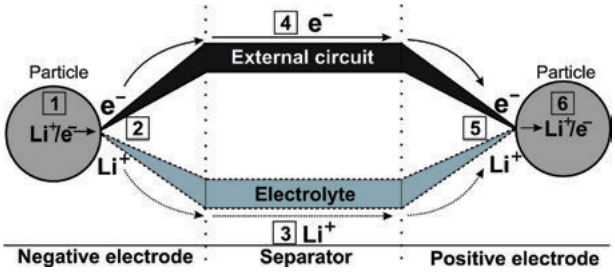

Figure 14.3: Scheme of Li-ion battery subprocesses during operation. (See text for labeling).

the negative electrode to a particle in the positive one during discharge (Figure 14.3). These include: (1) the transport of the Li^+/e^- pair from the bulk of the particle to the surface, (2) charge transfer at the particle surface, that is, redox reaction separating the Li^+ and e^- into different phases, (3) transport of Li^+ through the electrolyte that fills the porous electrode and separator, (4) transport of e^- through the solid part of the porous electrode and the external circuit, (5) charge transfer, that is, reassembly of the Li^+/e^- pair at the surface of the positive electrode particle, and (6) transport of the pair into the particle. Subprocesses (5) and (6) are the reverse of processes (2) and (1) and can be treated using the same formalism. The combined processes (1–6) form a full circuit; nevertheless, processes (1–2) and (5–6) must be treated at the particle or microscale, while the electron and ion transport can be treated at the macro level. This approach is consequently known as multiscale modeling.

Before any detailed analysis can be done, a formalism is required that allows the total energy from both chemical processes and electrostatics to be evaluated at any location and time within the battery. To this end, the theoretical construct of electrochemical potential has been developed.

EBSCOhost - printed on 2/14/2023 1:06 PM via . All use subject to https://www.ebsco.com/terms-of-use

14.1.2 The Electrochemical Potential

A convenient concept to evaluate the potential energy available to drive the charge transport and the redox processes within the battery as well as the devices inserted in the external circuit is the electrochemical potential ($\bar{\mu}$) [9] defined as follows:

$$\bar{\mu}_i(x) = \mu_i(x) + z_i F\phi(x) \tag{14.6}$$

where i is the chemical species, F is Faraday's constant, z is the charge, ϕ is the electrostatic potential, μ is the chemical potential, and $x$is the location. In short, the electrochemical potential is simply the sum of the potential free chemical energy of species i, also known as the chemical potential and the electrostatic energy because of its charge z_i. Examining the definition of $\bar{\mu}$ leads to the following observations:

$$\text{For neutral species } (z_i = 0): \bar{\mu}_i = \mu_i \tag{14.7}$$

$$\text{For electrons}: (z_i = -1): \bar{\mu}_e = \mu_e^{\ominus} - F\phi \tag{14.8}$$

where eq. (14.8) makes use of the fact that the concentration of electrons available in a metallic conductor is normally large and unaffected by the redox process taking place at the surface.

At equilibrium, the driving force for all mobile species (i) within a single phase must be zero, thus

$$\frac{\partial \bar{\mu}_i}{\partial x} = 0 \tag{14.9}$$

At a phase boundary, where a charge transfer reaction can take place, the free energy of the reactants must equal that of the products at equilibrium. Thus, the electrochemical potential can simply substitute the chemical one to account for the electrostatic energy, so that the familiar equilibrium conditions become

$$\sum_i \nu_i \bar{\mu}_i = 0 \tag{14.10}$$

where ν_i is the coefficient for species i in the reaction, signed negative for reactants and positive for products.

We can examine how this works in practice by deriving the voltage of a half-charged cell phone battery. In a standard electrochemical cell notation the battery becomes

$$\mathrm{Cu(s)|Li_{0.5}C_6|LiPF_6(sol)|Li_{0.5}CoO_2|Cu(s)}$$

The solvent (sol) is most often a mixture of organic carbonates like dimethyl carbonate (DMC) mixed with ethylene carbonate (EC). The voltage measured at open circuit is equal and opposite to the electrostatic potential that must be supplied if the circuit is closed and equilibrium is to be maintained, that is, there is no reaction

EBSCOhost - printed on 2/14/2023 1:06 PM via . All use subject to https://www.ebsco.com/terms-of-use

or charge movement. To avoid confusion, the Cu connectors will be labeled left and right, respectively in the following. We will now examine the equilibrium condition over each phase boundary from left to right:

Cu(s)|$Li_{0.5}C_6$

The only species that is present in both phases and is freely mobile over the interphase is electrons, thus

$$\bar{\mu}_e^{Cu,\,left} = \bar{\mu}_e^{Li_{0.5}C_6} \tag{14.11}$$

Since equilibrium is observed and the electrochemical potential is constant within the phase (eq. 14.9), the position variable can unambiguously be substituted for the phase label.

$Li_{0.5}C_6$ |$LiPF_6$(sol)

Across this interphase, there is the possibility of the charge transfer reaction

$$\delta\,\mathrm{Li}^+ + \delta\,\mathrm{e}^- + \mathrm{Li}_{0.5}\mathrm{C}_6 \rightleftharpoons \mathrm{Li}_{(0.5+\delta)}\mathrm{C}_6 \tag{14.12}$$

where δ is a small amount that does not affect the equilibrium significantly. This yields via eq. (14.10):

$$\bar{\mu}_{\mathrm{Li}_{(0.5+\delta)}C_6} - \delta\,\bar{\mu}_e^s - \delta\,\bar{\mu}_{\mathrm{Li}^+}^l - \bar{\mu}_{\mathrm{Li}_{0.5}C_6} = 0 \tag{14.13}$$

where phase labels l and s refer to the solid and liquid phase respectively. $Li_{0.5}C_6$ and $Li_{0.5+\delta}C_6$ are neutral and eq. (14.7) applies. Using the short-hand notation, Li for the Li^+ and e^- pair added to $Li_{0.5}C_6$ yields the following purely chemical potential:

$$\delta\,\mu_{\mathrm{Li}}^{\mathrm{Li}_{0.5}C_6} = \bar{\mu}_{\mathrm{Li}_{(0.5+\delta)}C_6} - \bar{\mu}_{\mathrm{Li}_{0.5}C_6} \tag{14.14}$$

so that eq. (14.13) combined with eq. (14.11) becomes

$$\bar{\mu}_e^{\mathrm{Cu,left}} = \mu_{\mathrm{Li}}^{\mathrm{Li}_{0.5}C_6} - \bar{\mu}_{\mathrm{Li}^+}^l \tag{14.15}$$

$LiPF_6$ (sol)|$Li_{0.5}CoO_2$

Again there is the possibility of a charge transfer reaction across the interphase, thus using the same approach as above yields:

$$\bar{\mu}_e^s = \mu_{\mathrm{Li}}^{\mathrm{Li}_{0.5}\mathrm{CoO}_2} - \bar{\mu}_{\mathrm{Li}^+}^l \tag{14.16}$$

$Li_{0.5}CoO_2$|Cu(s)

Similar to the first interphase, there is free movement of the electrons across the phase barrier, thus:

$$\bar{\mu}_e^{\mathrm{Li}_{0.5}\mathrm{CoO}_2} = \bar{\mu}_e^{\mathrm{Cu,\,right}} \tag{14.17}$$

EBSCOhost - printed on 2/14/2023 1:06 PM via . All use subject to https://www.ebsco.com/terms-of-use

Combining eqs. (14.17) and (14.16) yields:

$$\bar{\mu}_e^{\text{Cu,right}} = \mu_{\text{Li}}^{\text{Li}_{0.5}\text{CoO}_2} - \bar{\mu}_{\text{Li}^+}^{l} \tag{14.18}$$

which now can be combined with eq. (14.15) to yield:

$$\bar{\mu}_e^{\text{Cu,right}} - \bar{\mu}_e^{\text{Cu,left}} = \mu_{\text{Li}}^{\text{Li}_{0.5}\text{CoO}_2} - \mu_{\text{Li}}^{\text{Li}_{0.5}C_6} \tag{14.19}$$

Using the fact that the concentration of electrons is large in metals (eq. (14.8)) and that both connectors are made in the same material yields:

$$\phi_e^{\text{right}} - \phi_e^{\text{left}} = \frac{1}{F}\left(\mu_{\text{Li}}^{\text{Li}_{0.5}\text{CoO}_2} - \mu_{\text{Li}}^{\text{Li}_{0.5}C_6}\right) \tag{14.20}$$

where the left side of eq. (14.20) is the voltage difference between the two battery connectors. The right side of eq. (14.20) describes difference in potential energy of a Li^+/e^- pair residing in the positive electrode relative to the negative one. Consequently, eq. (14.20) is equivalent to eq. (14.4); however, it was obtained by keeping track of both chemical and electrostatic energy at every point within the electrochemical cell. This methodology will be central as we move from equilibrium to charging and discharging the battery.

14.2 Mass Transport Within Solid Particles

In heterogeneous electron transfer reactions, it is important to accurately describe the transport of reactants, like Li^+ ions, to the reaction surface. Since material is displaced, this is also known as mass transport. As detailed in Section 14.1.1, the active material in a lithium-ion battery such as LiCoO_2, and LiF etc so on typically has an intercalation structure that allows transport of Li^+ through the material during electrochemical processes [10]. During charging, Li^+ and vacancies exchange position in the particle to allow Li^+ ions to diffuse from the bulk of the active material particle to its surface or vice versa [11]. If the rate of mass transport (i.e., Li^+ and/or vacancies) through the active material to the particle surface is insufficiently high it may become the limiting step in the overall electrochemical process, thus limiting its performance.

14.2.1 Mass Transport by Diffusion

Diffusion in solids can be described by atoms "hoping" from one vacant site to another in the matrix of the crystal structure [11]. In the case of intercalation materials, although Li^+ and e^- travel in unison to preserve charge neutrality, they each have

EBSCOhost - printed on 2/14/2023 1:06 PM via . All use subject to https://www.ebsco.com/terms-of-use

their own transport mechanisms in the material. While Li^+ hops from site-to-site to diffuse, the movement of electrons typically requires a more intricate pathway. For example, in $LiCoO_2$, the electrons are transported by what chemists recognize as a cascade of redox reactions [3], that converts Co^{IV} ions into Co^{III} ions, while the Li^+ ions diffuse through vacancies in close proximity to the converted Co^{IV} ions as illustrated in Figure 14.4.

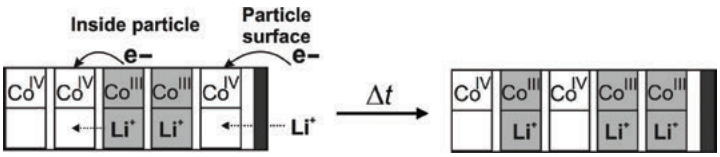

Figure 14.4: Scheme of diffusional transport in solid ($LiCoO_2$) via Li^+/e^+ pair exchange within the CoO_2 sites during discharge.

On a macroscopic scale, the net *flux* of the Li^+ and e^- pair, that is, number of "*Li*" particles traveling through an area per unit time, is driven by a chemical potential gradient since "*Li*" is neutral. This chemical potential gradient is generated by the surface reaction intake or release of Li^+ and e^- during charge/discharge process. Within an active material particle, diffusion may be used to describe the "Li" transport. As such it follows Fick's law [12], stated in one dimension as

$$\frac{\partial C^s(x,t)}{\partial t} = \frac{\partial}{\partial x}\left(D^s \frac{\partial C^s(x,t)}{\partial x}\right) \tag{14.21}$$

where C^s and D^s are the concentration and diffusion coefficient of "Li" in the solid (active material) system, respectively, while x defines the location in space, and t the time.

Typically, an active material particle can be assumed to have a spherical shape, which allows eq. (14.21) to be reformulated in spherical coordinates assuming isotropic diffusion [13]. As such, the "Li" gradient in a particle may be tracked along a single variable, its radius, r, which can greatly simplify calculations. In spherical coordinates, eq. (14.21) can be rewritten as follows:

$$\frac{\partial C^s(r,t)}{\partial t} = D^s\left(\frac{\partial^2 C^s(r,t)}{\partial r^2} + \frac{2}{r}\frac{\partial C^s(r,t)}{\partial r}\right) \tag{14.22}$$

where the second term on the right accounts for a convergent diffusion.

14.2.2 Diffusion Coefficient

The diffusion coefficient is a function of the crystal structure of the active material, the temperature and the local concentration of lithium species in the lattice [3, 10, 14]. For

EBSCOhost - printed on 2/14/2023 1:06 PM via . All use subject to https://www.ebsco.com/terms-of-use

example, in $LiCoO_2$, the diffusion coefficient remains mostly constant [15–17]. In other systems such as $LiFePO_4$ [18–20], $LiTi_5O_{12}$ [21], $Li_{4.4}Si$ [22], the insertion–disinsertion reaction is more complicated because of the phase changes [23]. However, a simple diffusion model may still be a good compromise between the calculational complexity and accuracy [24].

Typically, it is challenging to measure pure diffusion characteristics within a particle. Often, diffusion coefficients of an active material is measured using galvanostatic intermittent titration technique (GITT) [25] or electrochemical potential step methods [26]. However, great care must be taken when interpreting the results in these experiments, since both the ionic and electronic connection to the particles, that is, electrode effects, or charge transfer reaction at the particle surface of particles may dominate the response. As such, literature values are found to vary over several orders of magnitude [26]. Alternately, measurements in single crystals are possible in favorable cases [27]. Their usefulness is, however, often limited by accessibility to only a very restricted range of lithium-ion concentrations. Finally, the electrochemical potential step may be emulated by a chemical oxidation or reduction [24], which alleviates concerns about transport of electrons and ions to the particle surface.

14.3 Electron Transfer Kinetics

For the half-cell reaction to occur, Li^+ ions from the electrolyte, and electrons as well as Li^+ ions (or vacancies in a relative sense) from the particle bulk must be transported to the surface of the particle (Figure 14.3). However, once these components arrive, their rate of transformation is determined by the speed at which the electrons are taken up or released at the surface through electrochemistry. Again, examining the lithium cobalt oxide reaction:

$$Li^+ + e^- + \square CoO_2 \underset{k_b}{\overset{k_f}{\rightleftharpoons}} LiCoO_2 \tag{14.23}$$

we, in accordance with most presentations, consider the electron concentration as a constant in the following. This is justified by the fact that each $LiCoO_2$ particle is surrounded by a network of carbon additive in the electrode, which ultimately connects to the metallic current collector. This entire network thus presents a large pool of electrons. The current generated at the particle surface area (A), also known as the current density [28–32] is therefore

$$j_{ct} = \frac{i_{ct}}{A} = F(k_f\, C^l_{Li}\, C^{+s}_{\square} - k_b\, C^{+s}_{Li}) \tag{14.24}$$

where C refers to the concentrations in the immediate vicinity of the surface. Since we are dealing with several species in several different phases, the notation becomes

EBSCOhost - printed on 2/14/2023 1:06 PM via . All use subject to https://www.ebsco.com/terms-of-use

slightly complicated. Here the subscript on C, ϕ, and so on refers the species, while the superscript describes the phase or position. Hence, C^{l}_{Li} denotes the concentration of Li^{+} in the liquid electrolyte (l), whereas $C^{+s}_{\square}$ gives the concentration of vacant sites in the positive *solid* electrode $(+s)$. Moreover, to simplify the notations, the "+" sign Li^{+} is dropped in the remainder of the chapter.

Returning to eq. (14.24), the next step is to identify how k_f and k_b are dependent on the electrostatic potentials at the surface. Most important, in electron transfer reactions, there exist for any combination of concentrations a set of surface potentials that allow for equilibrium to be established, that is, the $j_{ct} = 0$ condition. Using the same methodology as in Section 14.1.2, where we examined the equilibrium condition explicitly, the surface potential *at equilibrium* (E_{eq}) for eq. (14.24) is

$$\phi^{s} - \phi^{l} = \frac{1}{F}\left(\mu^{+s}_{\mathrm{Li}} - \mu^{l}_{\mathrm{Li}} - \mu^{+s}_{2} - \mu^{+s}_{e}\right) = E_{\mathrm{eq}} \tag{14.25}$$

which is dependent on the concentration of the chemical species, temperature, and so on. When dealing with electron transfer reactions, a particularly convenient concept is overpotential (η), which is used to describe energy added or removed by the surface potential to drive the reaction away from equilibrium [9, 7]. Consequently,

$$\eta = \phi^{s} - \phi^{l} - E_{\mathrm{eq}} \tag{14.26}$$

has a significant effect on the rate constants. Let us now focus on this connection. We begin with the microscopic activated complex theory that describes most electron transfer reactions [33, 34], and the entailing Arrhenius behavior. We examine the *special* equilibrium case defined by the relation:

$$k^{eq}_{f}\, C^{l}_{\mathrm{Li}}\, C^{+s}_{\square} = k^{eq}_{b}\, C^{+s}_{\mathrm{Li}} \tag{14.27}$$

The relation signifies a second-order behavior in the forward direction (k^{eq}_{f}) while a first-order reaction in the backward direction (k^{eq}_{b}). Therefore, a single rate constant cannot be defined to express the equilibrium condition. As such, the rate constants for the forward and backward processes under equilibrium are given as

$$k^{eq}_{f} = \mathcal{A}_f \exp\left(\frac{-\Delta\overline{G^{\ddagger}_{\mathrm{eq}}}}{RT}\right) \text{ and } k^{eq}_{b} = \mathcal{A}_b \exp\left(\frac{-\Delta\overline{G^{\ddagger}_{\mathrm{eq}}}}{RT}\right) \tag{14.28}$$

respectively. Here, $\mathcal{A}_f$ and $\mathcal{A}_b$ are the preexponential factors of the Arrhenius equations, $\Delta\overline{G^{\ddagger}_{\mathrm{eq}}}$ is the free energy of the activated complex, where the overline serves as a reminder that it includes the electrostatic energy, RT is the ideal gas constant–temperature product.

Bringing the system out of equilibrium requires $\eta \neq 0$; however, only the free energy of the charged species in the reaction is affected by the electrostatic energies, that is, Li^{+} in the liquid electrolyte and e^{-} in the solid. It is therefore only the

EBSCOhost - printed on 2/14/2023 1:06 PM via . All use subject to https://www.ebsco.com/terms-of-use

free energy curve of the reactants that is shifted by η (Figure 14.5 blue line). This affects the activation energy, that is, the intercept of the free energy curves of the reactants and products (Figure 14.5) such that

$$k_f = k_f^{eq} \exp\left(\frac{-\alpha\eta F}{RT}\right) = A_f \exp\left(\frac{-(\Delta\overline{G_{eq}^{\ddagger}} + \alpha\eta F)}{RT}\right) \tag{14.29a}$$

$$k_b = k_b^{eq} \exp\left(\frac{(1-\alpha)\eta F}{RT}\right) = A_b \exp\left(\frac{-(\Delta\overline{G_{eq}^{\ddagger}} - (1-\alpha)\eta F)}{RT}\right) \tag{14.29b}$$

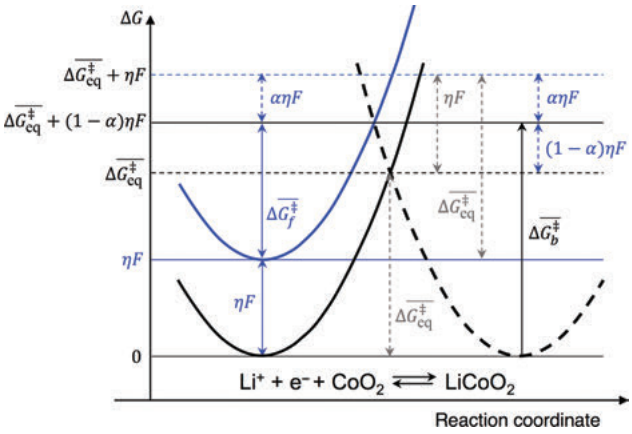

Figure 14.5: Schematic description of electron transfer reaction of $LiCoO_2$, showing free energy surfaces at equilibrium (solid and broken black profiles) and under applied bias η (blue solid and broken black profiles). *At equilibrium*, the free energy of the transition state is $\Delta\overline{G_{eq}^{\ddagger}}$ for both the forward and reverse reactions. *Under nonequilibrium*, the reactant free energy curve shifts up by the applied potential ηF (blue line). This affects the activation energy of the forward and backward reactions differently, that is, the intercept between the solid and broken lines moves. As a result, the required activation energy for the forward process ($\Delta\overline{G_f^{\ddagger}}$) reduces by $\alpha\eta F$, while the activation energy of the backward process ($\Delta\overline{G_b^{\ddagger}}$) is increased by an additional $(1-\alpha)\eta F$ compared to the initial free energy equilibrium $\Delta\overline{G_{eq}^{\ddagger}}$.

where α is the transfer coefficient, which is a measure of the symmetry of the energy barrier around the activated complex [9, 7]. Typically, $\alpha = 0.5$ is assumed in lithium-ion battery work [35]. Inserting eqs. (14.29a) and (14.29b) into eq. (14.24) yield the desired relation between the electrostatic potentials and the current density:

$$j_{ct} = F\left(k_f^{eq}\, C_{Li}^{l}\, C_{\square}^{+s} \exp\left(\frac{-\alpha\eta F}{RT}\right) - k_b^{eq}\, C_{Li}^{+s} \exp\left(\frac{(1-\alpha)\eta F}{RT}\right)\right) \tag{14.30}$$

EBSCOhost - printed on 2/14/2023 1:06 PM via . All use subject to https://www.ebsco.com/terms-of-use

Reliable measurement of k_f^{eq} and k_b^{eq} are difficult to obtain. Experimental methods include electrochemical impedance spectroscopy (EIS) [36, 37] and Tafel plots [38]. These techniques, however, yield directly what is known as exchange current density (j_0). j_0 is the theoretical current associated with the forward *or* the backward reaction at equilibrium. Most important, j_0 can be measured at concentrations different from the ones used in eq. (14.27). Equation (14.30) is therefore often in battery work is recast into:

$$j_{ct} = j_0 \left(\frac{C^l_{\mathrm{Li}}\, C^{+s}_{\square}}{C^{\star l}_{\mathrm{Li}}\, C^{\star +s}_{\square}} \exp\left(\frac{-\alpha\eta F}{RT}\right) - \frac{C^{+s}_{\mathrm{Li}}}{C^{\star +s}_{\mathrm{Li}}} \exp\left(\frac{(1-\alpha)\eta F}{RT}\right) \right) \tag{14.31}$$

where $C^\star$ refers to the surface concentrations at equilibrium where $\eta = 0$ and j_0 was measured, whereas C simply refers to the actual surface concentration for which j_{ct} is calculated. j_0 may also be calculated from the rate constants if these are know via

$$j_0 = F\, k_f^{0(1-\alpha)}\, k_b^{0(\alpha)}\, C^{\star l(1-\alpha)}_{\mathrm{Li}}\, C^{\star +s(1-\alpha)}_{\square}\, C^{\star +s(\alpha)}_{\mathrm{Li}} \tag{14.32}$$

Here, k_f^0 and k_b^0 are the standard rate constants for the reaction (14.23) in the absence of the surface potentials i.e. $\varphi\mathrm{s} - \varphi\mathrm{l} = 0$.

14.4 Solid-Phase Potential and Electron Transport

Up until now, we have looked at processes occurring at the particle scale, but electrons consumed or released from the particles will travel across the whole cell from one electrode to the other through the external circuit. Although it might be clear how electrons move in the external circuit, one might wonder how they behave in a mixed-phase medium like a porous electrode containing both liquid (electrolyte) and solid (graphite, $LiCoO_2$) phases. In this section, we discuss some salient features of electrochemical operations in porous electrodes.

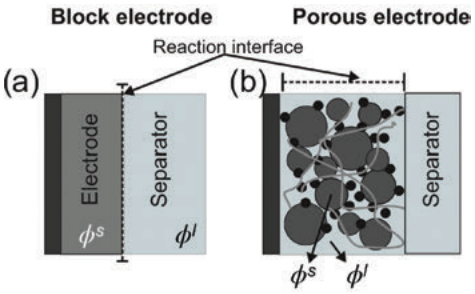

Figure 14.6: Scheme of (a) bloc electrode with a well-defined interface and (b) porous electrode with a network of interfaces between the solid active material and electrolyte.

EBSCOhost - printed on 2/14/2023 1:06 PM via . All use subject to https://www.ebsco.com/terms-of-use

The composite electrodes used in lithium-ion batteries lead to an electron transfer reaction interface that is distributed within the entire volume of the electrode. This means that the distance traversed by both e^- and Li^+ to arrive at the reacting particle varies significantly. As such, the energy lost to e^- and Li^+ transport is dependent on where the particle is located in the electrode [39]. Moreover, the microscopic inhomogeneity of the composite gives rise to a rather complicated potential distribution within the porous solid structure.

14.4.1 Solid-Phase Potential and Current Distribution

The driving force for electron transport is the free-energy differences between different locations within the electrode. Fortunately, we only need to examine the electrostatic potential in the solid (ϕ^s) when dealing with electrons, which can be derived from Ohm's law. Assuming constant electrical conductivity (σ^s), differentiating Ohm's law twice yields the current that is injected or removed by the charge transfer reaction (j_{ct}) discussed in Section 14.3.3. Since the variation in electrostatic potential (ϕ^s) is observed at the macroscale, the associated charge transfer current (j_{ct}) is averaged from all the particles contained within the *electrode volume element* of thickness *dx* and can be expressed as [39]:

$$-\sigma^s \frac{\partial^2}{\partial x^2}\phi^s = R_{sv}\, j_{ct} \tag{14.33}$$

where the right-hand side gives the average charge transfer current density values. The factor R_{sv} is employed here to convert the current density j_{ct} which is a function of the *particle* surface area into the current density generated within an *electrode* volume element of thickness *dx* at the macroscale (Figure 14.7). Therefore, R_{sv} serves as a link between the macro- and the particle scale, and can be calculated assuming spherical particle geometry via the formula:

$$R_{sv} = \frac{3}{r}\varepsilon_s \tag{14.34}$$

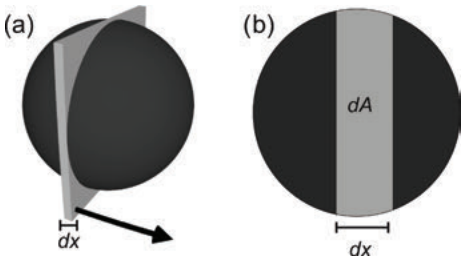

Figure 14.7: Scheme (a) is the volume of the active material probed by an electrode volume element of *dx* thickness and (b) is the corresponding particle surface area, where j_{ct} is generated.

EBSCOhost - printed on 2/14/2023 1:06 PM via . All use subject to https://www.ebsco.com/terms-of-use

where $3/r$ represents the surface area-to-volume ratio ($4\pi r^2/(4/3)\pi r^3$) of a sphere, and ε_s is the volume fraction of the active material within the (positive) electrode, as only a fraction of the electrode space is occupied by the active material.

The experimental measurement of electrode-scale conductivity of the solid phase (σ^s in eq. (14.33)) is quite challenging [40]. A typical technique is four-point probe measurements, which requires free-standing electrodes without the current collector that are difficult to fabricate. This is compounded by the volume change during repeated charge discharge, and swelling because of electrolyte uptake, as well as differences in the imposed pressures found in commercial batteries [41, 42]. Alternative techniques such as EIS measurement tend to measure both the electronic and ionic components of the conductivity [43, 44].

14.5 Liquid-Phase Potential and Ionic Transport

14.5.1 Diffusion Potential

The electronic transport was described previously using Ohm's law which is appropriate for electrons since their concentration is large and constant. This unfortunately is not the case for the ionic conductivity, which greatly complicates the transport modeling as we need to take concentration into account. Arguably, the simplest concentration gradient is two volumes with different concentrations, labeled α and β here, separated by a sharp phase barrier. Our standard battery cell from Section 14.1.2 then becomes:

$$\mathrm{Cu(s)|Li_{0.5}C_6|LiPF_6^{\alpha}|LiPF_6^{\beta}|Li_{0.5}CoO_2|Cu(s)}$$

Using the analysis technique from the same section,

$$\phi_{\text{right}} - \phi_{\text{left}} = \frac{1}{F}\left(\mu_{\text{Li}}^{\text{Li}_{0.5}\text{CoO}_2} - \mu_{\text{Li}}^{\text{Li}_{0.5}C_6}\right) + \frac{1}{F}\left(\bar{\mu}_{\text{LiPF}_6}^{\beta} - \bar{\mu}_{\text{LiPF}_6}^{\alpha}\right) \tag{14.35}$$

since the electrolyte electrochemical potential no longer cancels out. From the new electrochemical potential term, there is an electrostatic contribution $(\phi_{\text{LiPF}_6}^{\beta} - \phi_{\text{LiPF}_6}^{\alpha})$ called the diffusion potential, which entails a detailed analysis of the mass transport [45, 7].

14.5.2 Nernst–Planck Mass Transport Equation

In the electrolyte, the movement of ions is driven by the electrochemical potential. This follows from classical mechanics as, in general, a force exerted upon an object then its displacement will result in a potential energy change $(\partial E/\partial x \propto F)$ [46]. This

EBSCOhost - printed on 2/14/2023 1:06 PM via . All use subject to https://www.ebsco.com/terms-of-use

force, exerted by the electrochemical potential is opposed by the frictional force generated from collision with other species (solvent molecules or ions) in the environment. The size of this force is fv where v is the velocity and f is known as the frictional coefficient, dependent on the solvated ionic size and the viscosity. As the ions accelerate, they will reach what is known as the drift velocity, where the frictional force is equal and opposite to the electrochemical one ($F_{\bar{\mu}}$).

$$fv = -\mathcal{F}_{\bar{\mu}} \tag{14.36}$$

$$= \frac{\partial \bar{\mu}_i(x,t)}{\partial x} = RT\frac{\partial lnC_i^l(x,t)}{\partial x} + z_iF\frac{\partial \phi^l(x,t)}{\partial x} \tag{14.37}$$

In general, speed of charge carriers combined with their concentration yield current. As such eq. (14.36) can be reformulated in terms of the ionic current density ($j_{\text{ion},i}$) of species i, consisting of a diffusional and migrational term:

$$j_{\text{ion},i} = \underbrace{-z_iFD_i\frac{\partial C_i^l}{\partial x}}_{\text{Diffusion}} \underbrace{-z_i^2F^2\frac{D_i^l}{RT}C_i^l\frac{\partial \phi^l}{\partial x}}_{\text{Migration}} \tag{14.38}$$

where D_i is the diffusion coefficient of the ionic species i in the liquid phase. Typically, one may find the use of mobility u_i instead of D_i in the definition of the migration term, which can easily be correlated with the associated diffusion via the Einstein relation $u_i = z_iFD_i/RT$. While both representations converge into the same physical meaning, there appears to be distinct conventions for units adopted by various well-known authors in literature. For instance, Newman et al. employs normalized mobility via Faraday's constant F in transport expressions that corresponds to a unit cm^2mol/CVs, while Bard et al. maintain the absolute mobility (cm^2/Vs). To avoid any confusion in this regard, we chose herein to represent transport properties using the diffusion constant D_i, exclusively. Going back, the diffusion- and migration-based transport from all the charged species across an area gives rise to the total ionic current density in the form:

$$j_{\text{ion}} = \sum_{i=1}^{n} j_{\text{ion},i} = -z_iF\sum_i D_i^l\frac{\partial C_i^l}{\partial x} - F^2\frac{\partial \phi^l}{\partial x}\sum_i z_i^2\frac{D_i^l}{RT}C_i^l \tag{14.39}$$

Here, the fraction of the total migrational current carried by a single ionic species is known i as the transport number (t_i) and it is defined as follows:

$$t_i = \frac{|z_i^2|D_i^lC_i^l}{\sum_i |z_i^2|D_i^lC_i^l} = F^2\frac{|z_i^2|D_i^lC_i^l}{\kappa RT} \tag{14.40}$$

where κ is the ionic conductivity of the liquid phase.

EBSCOhost - printed on 2/14/2023 1:06 PM via . All use subject to https://www.ebsco.com/terms-of-use

14.5.3 Mass Transport for Binary Electrolyte within the Electrode

As eq. (14.39) gives the current of ionic species in the liquid electrolyte, we can move forward to establish how the spatial concentration of ionic charges evolve with time (dC^l/dt), mainly because of the electrochemical processes in the cell. While this can be calculated using the mass-transport equation in a straightforward manner, an appropriate expression must also capture the changes in ion (i.e., Li^+) concentration because of the redox processes at the solid–electrolyte interface that leads to insertion or release of Li^+. This requires the addition of charge transfer current in the mass-transport expression yielding:

$$\frac{\partial C_i^l}{\partial t} = \frac{1}{z_i F}\left(-\frac{\partial j_{\text{ion},i}}{\partial x} + R_{sv} j_{ct}\right) \tag{14.41}$$

which is derived by analyzing the ionic current moving over a distance δx between x and $x+\delta x$ through an area A while allowing for $\delta \to 0$, and adding the average current density (electronic) as an additional source term [46]. Let us now analyze the transport of the $Li^+PF_6^-$ electrolyte system based on this expression. First, we couple eq. (14.41) with our ionic current density formulation eq. (14.39) to obtain the evolution of Li^+ concentration (C_{Li}^l) in electrolyte over time:

$$\frac{\partial C_{Li}^l}{\partial t} = D_{Li}\frac{\partial^2 C_{Li}^l}{\partial x^2} + z_{Li}\frac{D_{Li}}{RT}F\frac{\partial}{\partial x}\left(C_{Li}^l\frac{\partial \phi^l}{\partial x}\right) + \frac{R_{sv} j_{ct}}{z_{Li}F} \tag{14.42}$$

This equation recalls that the source term in this equation for Li^+ stems from the Li^+ insertion and release during the redox process with solid particles. The counter ion PF_6^- however, does not participate in any interfacial redox processes (Figure 14.6). Hence, the expression for concentration changes for the PF_6^- groups can be written via the mass transport alone without any additional source term:

$$\frac{\partial C_{\text{PF}_6}^l}{\partial t} = D_{\text{PF}_6}\frac{\partial^2 C_{\text{PF}_6}^l}{\partial x^2} + z_{\text{PF}_6}\frac{D_{\text{PF}_6}}{RT}F\frac{\partial}{\partial x}\left(C_{\text{PF}_6}^l\frac{\partial \phi^l}{\partial x}\right) \tag{14.43}$$

In a binary lithium electrolyte like $LiPF_6$, the concentrations of Li^+ and PF_6^- remain equal at the macroscale to preserve electroneutrality. Therefore, we can generalize $C_{\text{Li}}^l = C_{\text{PF}_6}^l \equiv C^l$, and thus have the following condition:

$$\frac{\partial C_{\text{Li}}^l}{\partial t} = \frac{\partial C_{\text{PF}_6}^l}{\partial t} \equiv \frac{\partial C^l}{\partial t} \tag{14.44}$$

which allows us to extract a definition for the potential dependent term ($d\phi^l/dx$) by combining eqs. (14.42) and (14.43). That expression can be reinserted back into either one of these two equations to obtain the following:

EBSCOhost - printed on 2/14/2023 1:06 PM via . All use subject to https://www.ebsco.com/terms-of-use

$$\frac{\partial C^l}{\partial t} = \left(\frac{2D_{\mathrm{Li}}D_{\mathrm{PF_6}}}{D_{\mathrm{Li}} + D_{\mathrm{PF_6}}}\right)\frac{\partial^2 C^l}{\partial x^2} + \frac{j_{ct}\,R_{sv}}{F}\left(\frac{D_{\mathrm{PF_6}}}{D_{\mathrm{Li}} + D_{\mathrm{PF_6}}}\right) \tag{14.45}$$

considering $z_{\mathrm{Li}} = 1$ and $z_{\mathrm{PF_6}} = -1$. Here, we see that replacing the potential expression (not shown) in either Li^+ or $\mathrm{PF_6}^-$ yields a concentration equation without any migration term. This is a consequence of electroneutrality in a binary electrolyte system where both ions move together, which otherwise may generate a nontrivial potential difference. The fact that diffusion and migration are coupled together, leads us to an average coefficient of diffusion ($\bar{D}$), where mobilities of both ions are averaged via the transport number (t_{Li}). This means we can describe the mass transport of both ions conveniently using a single equation for binary electrolytes instead of describing each ionic species individually. Thus, we can reform eq. (14.45) to redefine the terms in parentheses to obtain [7] the following:

$$\varepsilon_l \frac{\partial C^l}{\partial t} = \frac{\partial}{\partial x}\left(\bar{D}\frac{\partial C^l}{\partial x}\right) + \frac{(1 - t_{Li})}{F} j_{ct}\,R_{sv} \tag{14.46}$$

where $\bar{D} = 2D_{\mathrm{Li}}D_{\mathrm{PF_6}}/(D_{\mathrm{Li}} + D_{\mathrm{PF_6}})$ is the average diffusion coefficient picked from eq. (14.45), while $t_{\mathrm{Li}} = D_{\mathrm{Li}}/(D_{\mathrm{Li}} + D_{\mathrm{PF_6}})$ in accordance with both eq. (14.40) and the argument preceding eq. (14.44). Here, the introduced term ε_l on the left represents the volume fraction occupied by the electrolyte as opposed to ε_s for the volume fraction occupied by the solid particles. The first term on the right in eq. (14.46) contributes to the concentration changes because of the mass transport in the liquid phase, while the second term represents the loss or gain of Li^+ through charge transfer reaction at the active material surface. The change in the form of the first term from eq. (14.45) stems from the possible variation of $\bar{D}$ as a function of C^l_{Li} in the electrolyte.

14.5.4 The Liquid-Phase Electrostatic Potential

With the concentration profile at hand, we can now include the diffusion potential (for a complete derivation, see Ref. [7]) in the description of current. Coupled with the ionic conductivity κ in the liquid, the diffusion potential gives the corresponding current averaged over volume. This can now be incorporated along with the migration of ions driven by liquid-phase electrostatic potential ϕ^l, to obtain the final current density [45, 7, 47]:

$$\underbrace{-\frac{RT(1 - 2t_{\mathrm{Li}})}{F}\kappa\frac{\partial}{\partial x}\left(\frac{\partial \ln C^l_{\mathrm{Li}}}{\partial x}\right)}_{\text{Diffusion}} + \underbrace{\frac{\partial}{\partial x}\left(\kappa\frac{\partial \phi^l}{\partial x}\right)}_{\text{Migration}} = R_{sv}\,j_{ct} \tag{14.47}$$

where t_{Li} is the transport number of Li^+ given by (14.38).

EBSCOhost - printed on 2/14/2023 1:06 PM via . All use subject to https://www.ebsco.com/terms-of-use

14.5.5 Tortuosity and Apparent Transport Properties

For a simple binary electrolyte such as $LiPF_6$ in a mixture of carbonate-based solvent, for example, propylene carbonate (PC), DMC, EC, and so on, mass transport is described via transport number t_{Li}, the diffusion coefficient $\bar{D}$, and the ionic conductivity κ [48, 49]. These properties can be obtained via the Hittorf method [48, 49], electrochemical polarization–relaxation methods [48, 49], EIS [50], pulsed-field gradient NMR technique [51, 52], and so on. In general, electrolyte concentration as well as temperature dependences complicate these measurements when concentrated electrolytes and environments relevant to practical battery operation are investigated.

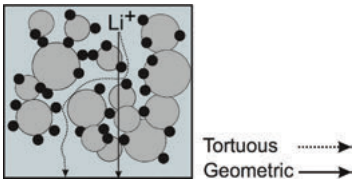

Figure 14.8: Scheme of tortuous path traveled by ions in active material as opposed to geometric distance.

Furthermore, the electrode microstructure affect the ionic transport as the ions (Li^+ and PF_6^-) must "go around" the solid phase of the composite structure (Figure 14.8). To capture this effect, the concept of *tortuosity* (τ) has been introduced, which is the ratio of the average travel distance of an ion relative to the shortest possible geometric path (Figure 14.8). The relationship often used to derive this parameter is the Bruggerman relation, which relates the electrode porosity and average particle size to tortuosity [53–55]. Therefore, all transport properties can be adjusted from their intrinsic values to reflect effective transport in a porous electrode such that

$$\tau = \frac{\gamma}{(\varepsilon_l)^{\beta}}, \quad \mathcal{D} = \frac{\bar{D}\varepsilon_l}{\tau}, \quad \text{and} \quad \bar{\kappa} = \frac{\kappa\varepsilon_l}{\tau} \tag{14.48}$$

where γ and β are adjustable parameters that can be determined by fitting into experimental data. Typically, in a Li-cell porous electrode $\gamma = 1$ and $\beta = 0.5$ is considered [56, 57]. This is followed by adjustment of both the average diffusion constant $\bar{D}$ and electrolyte conductivity κ by τ, which gives an *apparent* diffusion coefficient $\mathcal{D}$ and an apparent liquid conductivity $\bar{\kappa}$.

EBSCOhost - printed on 2/14/2023 1:06 PM via . All use subject to https://www.ebsco.com/terms-of-use

14.6 Assembling the Puzzle and a Practical Application

14.6.1 Numerical Method and Model Approximations

Thus far, a set of governing equations for the Li-ion cell has been defined, so that all the processes in Figure 14.3 can be described qualitatively. At this point, our attention can therefore be turned into solving these equations within a representative geometry. Unfortunately, the problem is too complex to find closed-form solutions; as such, numerical methods must be employed. These begin by dissecting the complex battery structure into smaller discrete elements. Within the discrete elements, the differential equations can be approximated in a polynomial representation. These are then solved as a set of algebraic equations in a matrix using a numerical solver such as COMSOL or MATLAB. For more information on numerical methods for solving partial differential equation, see [58, 59].

Examining Figure 14.3, suggests that each particle must be modeled individually, while taking into account the interaction with all other particles in the battery. At present, the computing power required to simulate an electrode of near-practical configuration with tens of thousands of particles is far beyond the capacity of a desktop computer. However, the computing resources needed for simulation can be significantly reduced by applying two-key approximations.

The first of these approximations is to perform simulation in only one dimension (1D) at the macroscale. The cell is thus approximated as a series of slices, arranged in parallel with the current collectors. This is justified on the basis that the major changes in potentials, as well as, in electronic and ionic currents are perpendicular to these planes. The second approximation is to use Newman's porous electrode volume averaging technique (Figure 14.9). This model ignores the direct microstructural details of a porous electrode; instead, the electrode is modeled as a theoretical homogeneous material with transport properties that are superposition of the solid- and liquid-phase fractions. As such, the electrostatic potential and the current transport can be effectively modeled. To account for the currents generated/consumed by the charge transfer reaction, it is required that the concentration profile at the particle scale is known. The model therefore becomes pseudo 2D, with the second variable being r [39, 60, 7]. In the next section, we will systematically implement this approach to simulate the discharge curve in a $LiCoO_2$/graphite full cell (Figure 14.1).

14.6.2 Practical Application: Discharge Curve of a Battery Cell

Discharge curves are a widely investigated performance-metric in the characterization of overall cell behavior. This is a galvanostatic technique, where the cell

EBSCOhost - printed on 2/14/2023 1:06 PM via . All use subject to https://www.ebsco.com/terms-of-use

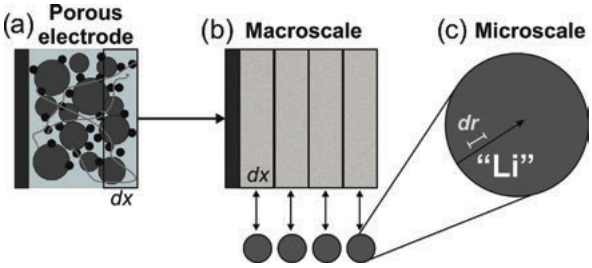

Figure 14.9: Schematic of Newman's volume average approach: a porous electrode (a) is broken into two parts. A 1D macroscale model consists of grids of width *dx* in series (b), where the solid and liquid phases of electrode are averaged together to form a homogeneous phase. This is then linked to a 2D microscale model to compute and analyze the transport events occurring at the particle scale (c). The changes at this scale are recorded in both radial and linear coordinates to represent the respective space inside a particle (c) and the position of that particle in the electrode (b).

voltage (V_{cell}) is measured as a function of time in response to an applied constant current density J_{cell}. This current is applied for a certain discharge time or until the cell potential reaches a set voltage limit. In this section, we simulate the underlying physical processes to implement this technique. While most of the required expressions have been presented already in the earlier sections, the associated boundary conditions and their correlation to physical behavior and limitations in the cell are discussed in this section.

To implement this technique, first we need to define the variables and place them within the cell geometry. The respective parameters and their connection between the macroscale and microscale regimes are outlined in Figure 14.10. Beginning from the macroscale, the battery is divided into three distinct areas: (1) the negative electrode, (2) the separator, and the (3) positive electrode, with thicknesses L_{neg}, L_{sep}, and L_{pos}, respectively (Figure 14.10). Therefore, the points $x = 0$ and $x = L_{\text{neg}} + L_{\text{sep}} + L_{\text{pos}} \equiv L$ define the system boundaries enclosed by the negative and positive current collectors.

Inside the domains, the solid- ($\phi^s(x,t)$) and liquid-phase ($\phi^l(x,t)$) electrostatic potentials, and the electrolyte concentration ($C^l(x,t)$) scalar values are defined via the differential equations defined in the previous sections. The challenge is now to identify the boundary conditions that will allow us to solve these equations, such that $V_{\text{cell}}(t) = \phi^s(L,t) - \phi^s(0,t)$ can be found. We begin with the macroscopic transport.

14.6.3 Solid-Phase Potential and Macroscopic Electron Transport

The solid-state electrostatic potential (ϕ^s) distribution within the solid regime is calculated from eq. (14.33). The boundary conditions employed to solve this expression

EBSCOhost - printed on 2/14/2023 1:06 PM via . All use subject to https://www.ebsco.com/terms-of-use

are established based on an analysis of the electronic current flowing through the two current collectors at $x = 0$ and at $x = L$. Under galvanostatic measurement, this corresponds to the imposed cell's current J_{cell} and then the boundary conditions can, using Ohm's law, be defined as

$$\sigma^s \frac{\partial \phi^s}{\partial x} = -J_{\text{cell}}, \quad at\ x = 0, \quad \text{and} \tag{14.49}$$

$$\sigma^s \frac{\partial \phi^s}{\partial x} = J_{\text{cell}}, \quad \text{at } x = L \tag{14.50}$$

At $x = L_{\text{neg}}$ and $x = L_{\text{neg}} + L_{\text{sep}}$ (Figure 14.10), the current is purely ionic, since the electrolyte in the separator does not conduct electrons. Therefore,

$$\sigma^s \frac{\partial \phi^s}{\partial x} = 0, \quad \text{at } x = L_{\text{neg}}, \text{ and at } x = L_{\text{neg}} + L_{\text{sep}} \tag{14.51}$$

for the negative and positive electrode interfaces with the separator, respectively. The initial potentials ϕ^s at the two electrodes are calculated from the equilibrium potential (E_{eq}) defined on the basis of the initial concentrations of Li^+ inside the two electrodes that is, $LiCoO_2$ and LiC_6 at $t = 0$. In the calculations discussed here, we assumed an initial 95% occupation of the concentration maximum ($\hat{C}^{-s}$) in the negative electrode (LiC_6), while 45% of the maximum possible occupation ($\hat{C}^{+s}$) on the positive side ($LiCoO_2$). To solve eq. (14.33) and find the ϕ^s using the boundary conditions in eqs. (14.49)–(14.51), requires the charge transfer current $j_{ct}(x)$, as defined in Section 14.3.3. Before continuing, we note that the solid-state conductivity σ^s is generally not the same for the two electrode materials.

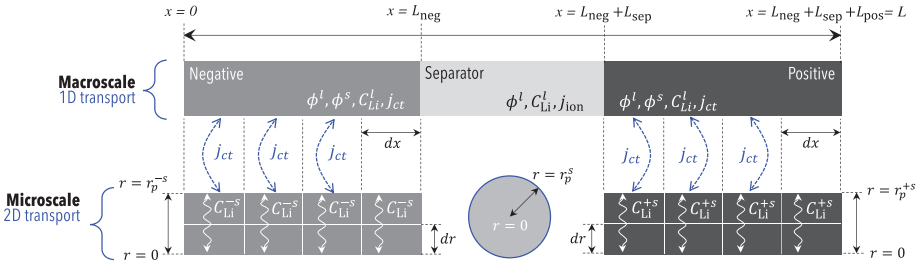

Figure 14.10: Schematic of Li-battery cell domains. Top: Macroscale properties (ϕ^l, ϕ^s, C^l_{Li} and j_{ct}) are modeled in a 1D domain consisting of intervals delimiting the negative electrode ($x = 0$, L_{neg}), the separator ($x = L_{\text{neg}}$, $L_{\text{neg}} + L_{\text{sep}}$) and the positive electrode ($x = L_{\text{neg}} + L_{\text{sep}}$, L). Bottom: Li^+ transport in the solid phase (via C^{-s}_{Li} and C^{+s}_{Li} etc.) is implemented in a 2D domain constructed with two rectangles, one for each electrode (gray and black), delimited by the average particle radii ($r = 0$ and $r = r^s_p$), and the respective electrode lengths for example, ($x = 0$, L_{neg}) and ($x = L_{\text{neg}} + L_{\text{sep}}$, L). The macro- (top) and microscale (bottom) domains are linked at the reaction interface ($r = r^s_p$) via the reaction current j_{ct}, where concentrations of Li^+ in the solid phases (C^{-s}_{Li} and C^{+s}_{Li}) are exchanged in the two submodels.

EBSCOhost - printed on 2/14/2023 1:06 PM via . All use subject to https://www.ebsco.com/terms-of-use

14.6.4 Kinetics of Charge Transfer and Current Density

From Section 14.3.3, we know that charge transfer current $j_{ct}(x)$ can be calculated for a given position x from eq. (14.30). This equation requires the evaluation of the concentration (C) terms under nonequilibrium conditions ($|\eta| > 0$) to find the updated charge transfer current j_{ct}. Therefore, we address the expressions to solve the concentration terms in eq. (14.30).

For the Li^+ transport in liquid phase that drives the charge transfer reaction at the solid–liquid interface, the governing equation is eq. (14.46). This was derived in Section 14.5.5 from macroscale mass transport in electrolyte, and is coupled to the solid-state transport that is, of $C_{\square}^{+s}$ and C_{Li}^{+s} at the particle scale. Before we discuss the required conditions to solve these expressions, we turn our attention momentarily to the overpotential $\eta = \phi^s - \phi^l - E_{\mathrm{eq}}$ as defined in eq. (14.26). The components of this relation are strongly related to the transport characteristics in eq. (14.30).

Here, E_{eq} is given for the predefined initial equilibrium, as discussed in Section 14.3.3. This initial state E_{eq} can be defined on the basis of the thermodynamics of a given domain, for example, concentrations of charged species at time $t = 0$ under zero bias. More complex measures of E_{eq} at different $C_{\square}^{+s}$ concentrations, that is, the *state of charge (SOC)* are often used. The effect using other equilibrium conditions is however rarely rigorously implemented into the exchange current (j_0), instead the same Nernst equation approximation as was used in Section 14.3 is implemented. In the next section, we put specific focus on liquid- and solid-phase parameters that drive the ultimate battery operation in a cell.

Liquid-Phase Potential and Mass Transport

Within the battery, the liquid phase, that is, the electrolyte, permeates both the electrodes and the separator (Figure 14.6). As such, the defining electrostatic potential distribution (ϕ^l) across all three domains (Figure 14.10) must be considered using eq. (14.47). To solve eq. (14.47), we first look at the two boundaries (Figure 14.10) at $x = 0$ (negative current collector) and at $x = L$ (positive current collector). Since ions cannot permeate the current collector the boundary condition becomes

$$\bar{\kappa}\frac{\partial \phi^l}{\partial x} = 0, \quad \text{at } x = 0 \text{ and } x = L \tag{14.52}$$

Interestingly, the *absolute* value of the liquid-phase potential ϕ^l is not important, as only its derivative enters the transport eq. (14.47), and therefore does not affect the target $V_{\mathrm{cell}}(t)$. Hence, for the computation we set a reference potential arbitrarily to "0" at the negative current collector ($x = 0$) such that at all times

$$\phi^l(0, t) = 0 \tag{14.53}$$

EBSCOhost - printed on 2/14/2023 1:06 PM via . All use subject to https://www.ebsco.com/terms-of-use

Under zero bias condition ($|\eta| = 0$), we assume that $\phi^l(x, 0) = 0$, such that E_{eq} is determined from ϕ^s as discussed previously. With these boundary definitions, eq. (14.47) is solved directly in the numerical solver, for example, COMSOL.

In the code/solver, eqs. (14.46) and (14.47) must be solved iteratively to obtain the concentration C^l_{Li} and potential ϕ^l in a self-consistent manner. To elaborate, while eq. (14.47) allows us to calculate ϕ^l, its distribution in the macroscopic cell space depends on the Li^+ concentration in the electrolyte (C^l_{Li}). Therefore, it needs to be coupled with Li^+ mass transport across the cell via eq. (14.46) that captures the evolution of C^l_{Li} under nonequilibrium conditions ($|\eta| > 0$). The initial conditions for this implementation may conveniently be chosen as follows:

$$C^l_{Li}(x, 0) = C_{LiPF_6} \tag{14.54}$$

Typically, the electrolyte ($LiPF_6$) concentration in organic carbonate based solvents is 1 M. Given that the simulation begins with the battery in a state of equilibrium, the initial concentration C^l_{Li} can be rendered uniform across the electrolyte between $x = 0$ and $x = L$. Just as above, the current would be zero at these two boundaries, since the liquid phase does not permeate the current collectors. This allows us to define

$$\mathcal{D}\frac{\partial C^l_{Li}}{\partial x} = 0, \quad \text{at } x = 0, \text{ and at } x = L \tag{14.55}$$

With the liquid-phase characteristics defined, we move on to the transport inside the particle where Li^+ and e^- combine along with a vacant site in the CoO_2 matrix to complete the reaction (14.23). This obviously requires capturing diffusional transport of Li^+. Here we remind the reader that the characteristics are dealt with at the particle scale.

Mass Transport Inside Solid Particles

For the analysis of mass transfer in individual particles, a 2D domain is required, where linear coordinate (x) indicates the position of a given particle in the cell, and radial coordinate (r) describes the position of species, that is, "Li" inside that particle (Figure 14.10). Thus, the concentration profile of "Li" *inside* a particle at the negative (C^{-s}_{Li}) and the positive (C^{+s}_{Li}) electrodes can be calculated using eq. (14.22) as a function of r, assuming no direct diffusional communication between the particles along the x axis.

The boundary conditions for the radial form of eq. (14.22) are derived from the fact that the flux of Li^+ at the particle surface ($r = r^s_p$) is given by the charge transfer current density $j_{ct}(x, t)$, and that the diffusion is radial, that is, symmetric in all directions from the particle center, such that there can be no concentration gradient at $r = 0$. In the adopted formulation, the radius of solid particles is averaged in such

EBSCOhost - printed on 2/14/2023 1:06 PM via . All use subject to https://www.ebsco.com/terms-of-use

a way that all the particles from the negative electrode have the same radius r_p^{-s}, while the positive electrode particles have radius r_p^{+s}. For the negative electrode ($x = 0$ and $x = L_{neg}$) the boundary conditions are therefore

$$-D^{-s}\frac{\partial C_{Li}^{-s}}{\partial r} = \frac{j_{ct}(x,t)}{F}, \quad \text{at } r = r_p^{-s} \text{ and} \tag{14.56}$$

$$-D^{-s}\frac{\partial C_{Li}^{-s}}{\partial r} = 0 \quad \text{at } r = 0. \tag{14.57}$$

Similarly, for the positive electrode region ($x = L_{neg} + L_{sep}$ and $x = L$),

$$-D^{+s}\frac{\partial C_{Li}^{+s}}{\partial r} = \frac{j_{ct}(x,t)}{F}, \quad \text{at } r = r_p^{+s} \text{ and} \tag{14.58}$$

$$-D^{+s}\frac{\partial C_{Li}^{+s}}{\partial r} = 0 \quad \text{at } r = 0. \tag{14.59}$$

Recalling the initial equilibrium state of the battery in eq. (14.55), we enforce the same initial condition that there is no concentration gradient of C_{Li}^{+s} within the particle. As mentioned already, for the solid-phase potential, the initial "Li" occupation is limited to 95% of the maximum concentration ($\hat{C}^{-s}$) in the negative (LiC_6) electrode, while it is set to 45% of the maximum concentration ($\hat{C}^{+s}$) on the positive side ($LiCoO_2$). The maximum concentration of "Li" in the solid ($\hat{C}_{Li}^{+s}$) is given by the following equation:

$$\hat{C}_{Li}^{+s} \equiv C_{Li}^{+s}(r, t = 0) = \frac{\rho}{nM} \tag{14.60}$$

where M is the molar mass of the active material, n is the number of Li^+ that can be released or taken up from one formula unit, and ρ is the material density. Most important, eq. (14.19) does not require solving for the vacancy concentration $C_{\square}^{+s}$ since the condition

$$\hat{C}_{Li}^{+s}(r,t) = C_{Li}^{+s}(r,t) + C_{\square}^{+s}(r,t) \tag{14.61}$$

must be conserved at all times.

14.6.5 Running the Simulation

With all the parameters, boundary conditions and initial states defined and formulated, the model can now be implemented in a numerical solver to simulate and analyze battery operation and performances. The process begins with a selected cell current that remains constant throughout the calculation. This current drives Li^+ across the phases and domains, which in turn causes changes

EBSCOhost - printed on 2/14/2023 1:06 PM via . All use subject to https://www.ebsco.com/terms-of-use

in potential values in solid and liquid. In the simulation, time is divided into small steps, where the state *before* the time step serves to calculate the projected set of concentration and potential values *after* the time step. These updated values can then be utilized to repeat the process over the next time step. The size of the time step is chosen in such a way that the simulation time is practical, while the model remains numerically stable. The numerical stability also depends on the required spatial resolution. For instance, a coarse resolution will generally allow for larger time steps.

During the simulation, the performance parameter recorded is the cell potential,

$$V_{\text{cell}}(t) = \phi^s(L, t) - \phi^s(0, t) \tag{14.62}$$

where $L = (L_{\text{neg}} + L_{\text{sep}} + L_{\text{pos}})$ is the width of the cell. This relation captures the difference in solid-phase potential between the points $x = 0$ and L. The simulation can be chosen to continue until a preset discharge time is reached. Most often it is preferable to set a potential as the breaking point for the simulation. In the example below, the breaking point is $V_{\text{cell}}(t) = 3\ V$. The cell potential is recorded as a function of time (or concentration), which is easily convertible to *capacity* in mAh, using the imposed current J_{cell}.

14.6.6 Results and Analysis

On the basis of the method discussed earlier, the discharge curves in Figure 14.11 are recorded, which show the cell potential as a function of capacity at two different applied current densities (J_{cell}). Under higher current rate ($-30\ \text{mA/cm}^2$), both capacity and cell potential diminishes at a significantly higher rate compared to those under the lower applied current ($-3\ \text{mA/cm}^2$). This clearly predicts a greater energy loss under high discharge current, which is well in accordance with experimental observations. Moreover, the final capacity under the high-current case

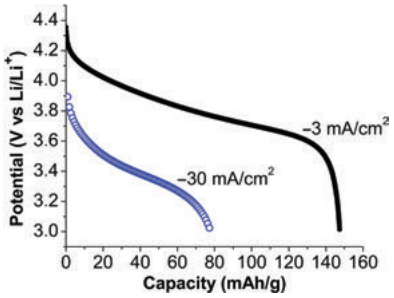

Figure 14.11: Discharge curves for $LiCoO_2/LiC_6$ cell with two different applied current densities J_{cell}.

EBSCOhost - printed on 2/14/2023 1:06 PM via . All use subject to https://www.ebsco.com/terms-of-use

(~78 mAh/g) seems to be only half of that (~148 mAh/g) for the low-current case. The calculated lower cell potential at the beginning of the process under high current (3.9 V vs. 4.3 V for the low current rate) stems directly from Ohm's law, demanding more potential to drive the higher current under constant resistance. This overconsumption of energy for transport leads to a lower output voltage (V_{cell}), since the chemical energy available to drive all processes in the battery is fixed by thermodynamics (see Section 14.1.1). To comprehend and optimize these variations, it is important to analyze the coupled electrochemical and mass transport events taking place at particular phases in different parts of the system.

Li^+ Concentration in Liquid Across the Cell

Beginning with the analysis of Li^+ concentration and its evolution in time under the two applied current rates in the electrolyte phase ($C^l_{Li}(x,t)$) across the entire cell (Figure 14.12). The constant initial concentration represents the 1 M $LiPF_6$ introduced into the system at $t=0$, which dissociates into 1 M of Li^+ and 1 M of PF_6^- ions. Hence, one can establish $C^l_{Li}(x,0)=1$. It is important to keep in mind that this quantity does not represent the Li^+ residing inside the solid phases, that is, graphite and $LiCoO_2$. However, as soon as the current is applied, the resident Li^+ in the solid gets directly involved. Further investigation with the high current shows the -30 mA/cm^2 driving Li^+ from the negative to the positive electrode, revealing that the rate of Li^+ transport in the liquid is not strong enough to support the high cell current. The sluggish transit problem is compounded by the simultaneous electrochemical release of Li^+ from the layers of graphite ($x \le L_{neg}$) into the electrolyte phase (eq. (14.23)). When coupled, these two factors inevitably raise the local concentration of Li^+ at the negative electrode well beyond the original 1 M, such that $C^l_{Li}(x<L_{neg},t) \ge 1$ M. This is shown by the blue profile in Figure 14.12 on the negative side.

This mechanism continues along the cell into the positive electrode ($x \ge L_{neg}+L_{sep}$) as well. The difference here is that the initially unoccupied sites in the positive

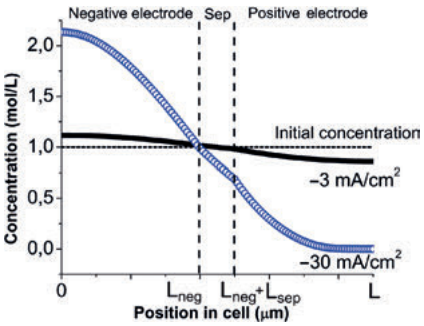

Figure 14.12: Concentration distribution of Li^+ in the electrolyte phase across the cell at time $t \gg 0$ for two different input current densities. The calculations are performed with a 25 μm separator sandwiched between two 100 μm electrodes.

EBSCOhost - printed on 2/14/2023 1:06 PM via . All use subject to https://www.ebsco.com/terms-of-use

electrode *take up* Li^+ during discharge. Just as before, the Li^+ transport in the electrolyte is insufficient to compensate the loss in C_{Li}^l at the positive side, which entails a significant concentration variation over the positive region of the cell (Figure 14.12). Combining the concentration profiles in the two electrodes inevitably gives rise to a steep concentration gradient under the high cell current scenario.

In the low current (-3 mA/cm^2) example, the challenges related to the large concentration gradient, like poor conductivity because of increased viscosity or lack of charge carriers, are greatly reduced. This is because the intrinsic rate of Li^+ diffusion inside the solid match the flow of Li^+ in an electrolyte from the negative to the positive side. Hence, the concentration buildup at the solid–liquid interface is much less likely. Under low cell current therefore, simultaneous release(negative electrode) and uptake (positive electrode) of Li^+ by the solid at the two electrodes are less consequential compared to the high-current case.

At this stage, an important investigation is how the spatial variation of Li^+ in the electrodes lead to the predicted variation in the capacity and voltage of the battery (Figure 14.11). Typically, this can be analyzed from the viewpoints of three major transport characteristics. The first one, as apparent from the earlier discussion, is the lack of uniformity in Li^+ concentration at the liquid phase within the electrodes. The second one is the electronic conductivity through the porous solid network inside the electrode to/from the current collector. This can often be an issue if an electrode lacks quality, for example, poor distribution of carbon particles in establishing conductive network. While of great practical interest, this subject is beyond the scope of this chapter. The third issue, the Li^+ distribution within the active particle at different applied current will be addressed in the next section as it plays an important role in the observed cell response of Figure 14.11 and in general.

Li^+ Concentration Inside an Active Material

As discussed in the previous sections, the liquid-phase Li^+ transport is strongly correlated to its intercalation/deintercalation inside the active material. Considering Li^+ moving into a particle, it is clear that the rate of "Li" diffusion inside the solid following the charge transfer reaction (14.23) is a crucial determinant of the final capacity of a battery (Figure 14.11).

To capture this effect, a $LiCoO_2$ particle located at a zone neighboring the separator/positive electrode interface will be analyzed. This particle is marked with the box *A* in Figure 14.13(a). The particles in this zone intuitively experience the maximum flux of Li^+ through the surrounding liquid phase. Under different current rates, that is, -30 and -3 mA/cm^2, calculations predict a significant variation in the buildup of "Li" inside a particle. This is shown in Figure 14.13(b). Under high cell current, "Li" accumulates to its maximum capacity only at the surface region, as its diffusion toward the center of the particle is not fast enough in relation to the "Li" arriving at the surface through the charge transfer process. This difference in

EBSCOhost - printed on 2/14/2023 1:06 PM via . All use subject to https://www.ebsco.com/terms-of-use

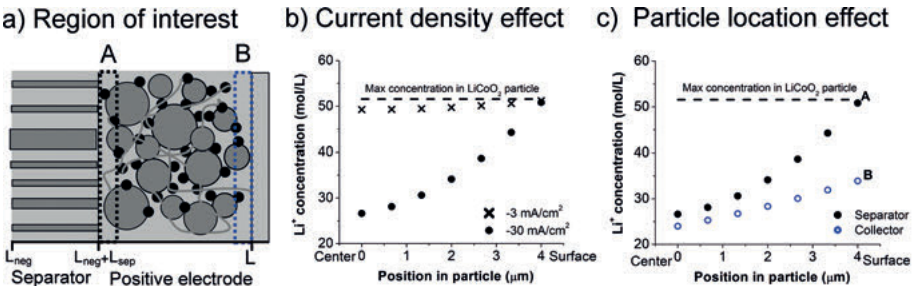

Figure 14.13: Comparison of "Li" concentration evolution inside a $LiCoO_2$ particle at a specific time. Two zones A and B in the positive electrode are marked (a). The occupation characteristics inside a particle at zone A is presented as a function of current density (b). The effectiveness of Li^+ occupation as a function of particle position inside the positive side (at the two extremes – A and B) is shown in (c). The latter is investigated only in the high current limit (-30 mA/cm^2).

rate generates a high C_{Li}^{+s} gradient in the particle and results in poor particle utilization by means of the *leftover* unoccupied sites $C_{\square}^{+s}$. This can be correlated back to the poor capacity predicted in Figure 14.11 for high cell current. The situation much improve under the low current rate (-3 mA/cm^2) scenario, where "Li" diffusion rate inside the particle is close to the rate of "Li" arrival at the surface. This produces a rather uniform "Li" occupation in the particle with near maximum utilization of its capacity (Figure 14.13(b)).

The discussion thus far has given important insights into the role played by the coupled dynamics of "Li" in the positive electrode particle. This analysis is further complicated by the location of the particle within the electrode as can be seen from the comparative study of "Li" occupation inside $LiCoO_2$ particles at the two extreme ends of the positive electrode. These two zones at $x = L_{\mathrm{neg}} + L_{\mathrm{sep}}$ and at $x = L$ are marked with boxes *A* and *B* in Figure 14.13, respectively. Focusing on the "Li" occupation trend at high cell current (-30 mA/cm^2) exclusively (Figure 14.13(c)), the first observation is that for both regions the incoming "Li" is predominantly localized in the surface region. The concentration decays consistently inward ending up with a trivial occupation density at the particle center. Second, the surface concentration is maximized for particles neighboring the separator, whereas particles near the current collector experience around ~50% occupation of the available sites near the surface (marked with "Max concentration" in the figure). This clearly establishes the presence of a negative concentration gradient of "Li" in the liquid phase at $|\eta| > 0$ during discharge within the positive electrode from separator toward current collector, caused by sluggish "Li" diffusion through the liquid. These predictions and analyzes provide a strong justification for the application of porous and thinner electrodes in battery systems for high power, keeping in mind the possible loss of energy density because of an increase in the mass fraction of inactive components (current collector, separator, cell casing, *etc.*).

EBSCOhost - printed on 2/14/2023 1:06 PM via . All use subject to https://www.ebsco.com/terms-of-use

While $LiCoO_2/LiC_6$ cell was used as a case study of galvanostatic discharge here, the same numerical framework may be applied to battery systems in general. These can include positive electrode materials such as $LiFePO_4$ [61, 62, 20], $Ni_{1/3}Mn_{1/3}Co_{1/3}O_2$ [63] and so on. Moreover, the governing equations and the boundary conditions of the model can be adapted to allow simulation of electrochemical methods such as cyclic voltammetry [64] and EIS [65, 43]. The numerical framework discussed here, however, incorporates electrochemical processes only. Therefore, effects such as temperature [66, 67], particle size distribution [68, 69], concentrated electrolyte theory [7, 70, 71] and capacity fading from seconds [72, 73, 67], and so on are beyond the scope of this chapter. These may, however, be integrated into the framework by including the appropriate governing equations. The capacity of the final form, whether the present one or an extended framework depends on the interest and needs of the user.

14.7 Conclusion

Despite the inherent complexity in modeling multiple electrochemical and physicochemical processes, numerical simulations can accurately depict Li-ion battery performances under the appropriate framework. Hence, it is used in the battery industry, to analyze the limiting factors in cell design like electrode thickness, active material mass loading, electrode porosity, and so on. By doing so, a great number of battery configurations can be tested in a short period of time to optimize battery performances in accordance to their intended applications such as portable electronics or electric vehicles [70, 74, 75]. In addition, simulations can be used to investigate parameters that are difficult to determine experimentally, such as the *in operando* electrolyte concentration gradient [76, 77, 71]. Similarly, effects that occur over long timescale like battery decay over thousands of cycles, that is, multiple years can be simulated within a few weeks [72, 78]. With continual improvement in Li-ion battery characterization along with availability in computing power, the accuracy and the range of effects that can be numerically simulated is bound to increase. Hence, numerical simulation will become a critical skill and tool in the field of Li-ion battery research, as we move to incorporate these devices in more widespread applications, like storage of renewable energy, electric vehicles, and energy recovery.

Appendix

– The parameters used to conduct the simulation in Section 14.13.

EBSCOhost - printed on 2/14/2023 1:06 PM via . All use subject to https://www.ebsco.com/terms-of-use

EBSCOhost - printed on 2/14/2023 1:06 PM via . All use subject to https://www.ebsco.com/terms-of-use

Table 14.1: Computational parameters for simulation.

Parameter	Negative	Positive	Separator	Description
$L[\mu m]$	100	100	25	Cell design parameters obtained from electrode measurements
ε_l	0.485	0.385	0.41	
ε_s	0.386	0.461	0.41	
$k_f^0 \times k_b^0$	1.89×10^{-6}	9.81×10^{-7}	–	Rate constant for electrochemistry
α	0.5	0.5	–	Symmetry parameter
$r_p[\mu m]$	2	4	–	Particle radius
$D^s[m^2/s]$	3.9×10^{-14}	1×10^{-14}	–	Diffusion constant in solid
$\hat{C}^s[mol/cm^3]$	0.0305	0.0515	–	Maximum concentration
$\sigma[S/cm]$	5.7	12.1	–	Electronic conductivity
$K(C_{Li}^l)[mS/cm]$	$1.297(C_{Li}^l)^3 - 25.1(C_{Li}^l)^{1.5} + 33.29C_{Li}^l$			Ionic conductivity
$\bar{K}(C_{Li}^l)[mS/cm]$	$K \times (\in_l)^{1.5}$	$K \times (\in_l)^{1.5}$	$K \times (\in_l)^{1.5}$	Apparent ionic conductivity
t_{Li}	0.36			Li transport number
$\bar{D}(C_{Li}^l)[m^2/s]$	$6.5 \times 10^{-10} e^{-0.7C_{Li}^l}$			Average diffusion constant
$D(C_{Li}^l)[m^2/s]$	$\bar{D}(C_{Li}^l) \times (\in l)^{1.5}$	$\bar{D}(C_{Li}^l) \times (\in l)^{1.5}$	$\bar{D}(C_{Li}^l) \times (\in l)^{1.5}$	Apparent diffusion constant

– The equilibrium potential for the negative electrode LiC_6

$$E_{\text{eq}} = 0.722 + 0.1387\,\theta^{-s} + 0.029(\theta^{-s})^{0.5} \frac{0.0172}{\theta^{-s}} + 0.2808e^{(0.9-15\,\theta^{-s})} - 0.7984e^{(0.4465\,\theta^{-s}-0.4108)}$$

where $\theta^{-s} \equiv C^{-s}/\hat{C}^{-s}$ defines the parameter for the negative (LiC_6) electrode.

– The positive electrode ($LiCoO_2$) equilibrium potential

$$E_{\text{eq}} = (-4.656 + 88.67\,(\theta^{+s})^2 - 401.119\,(\theta^{+s})^4 + 342.909(\theta^{+s})^6 - 462.471(\theta^{+s})^8 + 433.434(\theta^{+s})^{10}) \div (-1 + 18.99(\theta^{+s})^2 - 79.532(\theta^{+s})^4 + 37.31(\theta^{+s})^6 - 73.083(\theta^{+s})^8 + 95.96(\theta^{+s})^{10})$$

where $\theta^{+s} \equiv C^{+s}/\hat{C}^{+s}$.

List of Symbols

α	Transfer coefficient
$\bar{\kappa}$	Apparent liquid conductivity, S/cm
β	Fitting parameter in tortuosity
$\Delta\overline{G^{\ddagger}_{eq}}$	Free energy of activated complex, J/mol
$\Delta_r G$	Gibb's free energy, J/mol
ε_l	Volume fraction of electrolyte inside the electrode
ε_s	Volume fraction of active-material inside the electrode
η	Overpotential, V
γ	Fitting parameter in tortuosity
κ	Ionic conductivity in liquid, S/cm
$\mathbb{C}$	Total interface capacity from redox reaction, Ah/g
$\mathbb{C}_+$	Capacity at positive electrode, Ah/g
$\mathbb{C}_-$	Capacity at negative electrode, Ah/g
$\mathcal{A}$	Pre-exponential factor in Arrhenius equation
$\mathcal{D}$	Apparent diffusion constant, cm^2/s
R_{sv}	Geometric averaging factor for current density, 1/cm
μ	Chemical potential, J/mol
ν	Coefficient of reaction
$\bar{\mu}$	Electrochemical potential, J/mol
$\bar{D}$	Apparent diffusion coefficient, cm^2/s
ϕ	Electrostatic potential, V
ϕ^l	Electrostatic potential in liquid, V
ϕ^s	Electrostatic potential in solid, V
ρ	Material density, g/cm^3

EBSCOhost - printed on 2/14/2023 1:06 PM via . All use subject to https://www.ebsco.com/terms-of-use

σ^s	Electronic conductivity in solid, S/cm
$\square$	Vacancy in solid
τ	Tortuosity
$\hat{C}$	Maximum of concentration, mol/cm^3
C	Concentration (general), mol/cm^3
$C^\star$	Equilibrium concentration, mol/cm^3
D	Diffusion coefficient (general), cm^2/s
D^{+s}	Diffusion coefficient in positive electrode, cm^2/s
D_{Li}	Li^+ diffusion coefficient in liquid phase, cm^2/s
$D_{\mathrm{PF_6}}$	PF_6^- diffusion coefficient in liquid phase, cm^2/s
E	Voltage, V
E_{eq}	Equilibrium potential, V
F	Faraday's constant, C/mol
$\mathcal{F}$	Friction force, J/mol-cm,
f	Friction coefficient, Js/mol$-$cm^2
i_{ct}	Current due to charge transfer, A
j_0	Exchange (charge transfer) current density, A/cm^2
J_{cell}	Applied cell current density, A/cm^2
j_{ct}	Current density due to charge transfer, A/cm^2
j_{ion}	Mass transport (ionic) current density, A/cm^2
k_b	Backward reaction rate, cm/s
k_b^{eq}	Backward equilibrium rate constant, cm/s
k_f^0	Forward standard reaction rate, cm^4/s – mol
k_b^0	Backward standard reaction rate, cm/s
k_f	Forward reaction rate, cm^4/s – mol
k_f^{eq}	Forward equilibrium rate constant, cm^4/s – mol
L	Thickness of entire cell, μm
L_{neg}	Thickness of negative electrode, μm
L_{pos}	Thickness of positive electrode, μm
L_{sep}	Thickness of separator, μm
M	Molar mass, g/mol
n	Number of transferred electron
R	Ideal gas constant, J/mol – K
r_p^{+s}	Particle ($LiCoO_2$) radius in positive electrode, μm
r_p^{-s}	Particle (C_6) radius in negative electrode, μm
T	Temperature, K
t	Time, s
t_{Li}	Lithium transference number
v	Velocity, cm/s
V_{cell}	Potential difference between two electrodes, V
z	Number of charge

EBSCOhost - printed on 2/14/2023 1:06 PM via . All use subject to https://www.ebsco.com/terms-of-use

References

[1] Blomgren, G. E. *J. Electrochem. Soc. 164*, 1 (2017), A5019–A5025.
[2] Whittingham, M. S. *J. Electrochem. Soc. 123*, 3 (1976), 315–320.
[3] Armand, M. B. Intercalation Electrodes. In *Materials for Advanced Batteries*, NATO Conference Series. Springer, Boston, MA, 1980, pp. 145–161.
[4] Fong, R., Sacken, U. v., and Dahn, J. R. *J. Electrochem. Soc. 137*, 7 (1990), 2009–2013.
[5] Yazami, R., and Touzain, P. *J. Power Sources 9*, 3 (1983), 365–371.
[6] Mizushima, K., Jones, P. C., Wiseman, P. J., and Goodenough, J. B. *Mater. Res. Bull. 15*, 6 (1980), 783–789.
[7] Newman, J. S., and Thomas-Alyea, K. E. *Electrochemical Systems*. Wiley- Interscience, 2012.
[8] Bruce, P., Scrosati, B., and Tarascon, J.-M. *Angew. Chem. Int. Ed. 47*, 16 (2008), 2930–2946.
[9] Bard, A. J., and Faulkner, L. R. *Electrochemical methods: Fundamentals and applications*, 2nd ed ed. Wiley, New York, 2001.
[10] Massé, R. C., Liu, C., Li, Y., Mai, L., and Cao, G. *Natl. Sci. Rev. 4*, 1 (2017), 26–53.
[11] Mehrer, H. *Diffusion in solids: fundamentals, methods, materials, diffusion-controlled processes*, vol. 155. Springer Science & Business Media, 2007.
[12] Fick, A. *J. Membr. Sci. 100*, 1 (1995), 33–38.
[13] Crank, J. *The mathematics of diffusion*, 2d ed ed. Clarendon Press, Oxford, [Eng, 1975.
[14] Van der Ven, A., Bhattacharya, J., and Belak, A. A. *Acc. Chem. Res. 46*, 5 (2013), 1216–1225.
[15] Nakamura, K., Ohno, H., Okamura, K., Michihiro, Y., Nakabayashi, I., and Kanashiro, T. *Solid State Ionics 135*, 1 (2000), 143–147.
[16] Levi, M. D., Salitra, G., Markovsky, B., Teller, H., Aurbach, D., Heider, U., and Heider, L. *J. Electrochem. Soc. 146*, 4 (1999), 1279–1289.
[17] Xia, H., Lu, L., and Ceder, G. *J. Power Sources 159*, 2 (2006), 1422–1427.
[18] Churikov, A. V., Ivanishchev, A. V., Ivanishcheva, I. A., Sycheva, V. O., Khasanova, N. R., and Antipov, E. V. *Electrochim. Acta 55*, 8 (2010), 2939–2950.
[19] Prosini, P. P., Lisi, M., Zane, D., and Pasquali, M. *Solid State Ionics 148*, 1 (2002), 45–51.
[20] Srinivasan, V., and Newman, J. *J. Electrochem. Soc. 151*, 10 (2004), A1517–A1529.
[21] Verde, M. G., Baggetto, L., Balke, N., Veith, G. M., Seo, J. K., Wang, Z., and Meng, Y. S. *ACS Nano 10*, 4 (2016), 4312–4321.
[22] R. Szczech, J., and Jin, S.*Energy Environ. Sci. 4*, 1 (2011), 56–72.
[23] Zeng, Y., and Bazant, M. Z. *SIAM J. Appl. Math. 74*, 4 (2014), 980–1004.
[24] Lepage, D., Sobh, F., Kuss, C., Liang, G., and Schougaard, S. *J. Power Sources 256* (2014), 61–65.
[25] Wen, C. J., Boukamp, B. A., Huggins, R. A., and Weppner, W. *J. Electrochem. Soc. 126*, 12 (1979), 2258–2266.
[26] Tang, K., Yu, X., Sun, J., Li, H., and Huang, X. *Electrochim. Acta 56*, 13 (2011), 4869–4875.
[27] Amin, R., Balaya, P., and Maier, J. *Electrochem. Solid-State Lett. 10*, 1 (2007), A13–A16.
[28] Eyring, H.,Lin, S., and Lin, S. *Basic chemical kinetics*. Wiley-Interscience Publication, 1980.
[29] Johnston, H. *Gas phase reaction rate theory*. Modern concepts in chemistry. Ronald Press Co., 1966.
[30] Gardiner, W. *Rates and Mechanisms of Chemical Reactions*. Physical chemistry monograph series. W.A. Benjamin, 1972.
[31] Thirsk, H., and Harrison, J. *A guide to the study of electrode kinetics*. Academic Press, 1972.
[32] Erdey-Grúz, T. *Kinetics of electrode processes*. Wiley-Interscience, 1972.
[33] Laidler, K. J., and King, M. C. *J. Phys. Chem. 87*, 15 (1983), 2657–2664.
[34] Glasstone, S., Eyring, H., and Laidler, K. *The Theory of Rate Processes*. International chemical series. McGraw-Hill, 1941.

EBSCOhost - printed on 2/14/2023 1:06 PM via . All use subject to https://www.ebsco.com/terms-of-use

[35] Bazant, M., Chu, K., and Bayly, B. *SIAM J. Appl. Math. 65*, 5 (2005), 1463–1484.
[36] Zhao, J., Wang, L., He, X., Wan, C., and Jiang, C. *Int. J. Electrochem. Sci. 5* (2010), 11.
[37] Swiderska-Mocek, A., and Lewandowski, A. *J. Solid State Electrochem. 21*, 5 (2017), 1365–1372.
[38] Fang, Y.-H., and Liu, Z.-P. *ACS Catal. 4*, 12 (2014), 4364–4376.
[39] Newman, J. S., and Tobias, C. W. *J. Electrochem. Soc. 109*, 12 (1962), 1183–1191.
[40] Peterson, S. W. *The Effect of Microstructure On Transport Properties of Porous Electrodes*. Brigham Young University, 2015.
[41] Lanterman, B. J., Riet, A. A., Gates, N. S., Flygare, J. D., Cutler, A. D., Vogel, J. E., Wheeler, D. R., and Mazzeo, B. A. *J. Electrochem. Soc. 162*, 10 (2015), A2145–A2151.
[42] Thorat, I. V., Joshi, T., Zaghib, K., Harb, J. N., and Wheeler, D. R. *J. Electrochem. Soc. 158*, 11 (2011), A1185–A1193.
[43] Meyers, J. P., Doyle, M., Darling, R. M., and Newman, J. *J. Electrochem. Soc. 147*, 8 (2000), 2930–2940.
[44] Ogihara, N., Itou, Y., Sasaki, T., and Takeuchi, Y. *J. Phys. Chem. C 119*, 9 (2015), 4612–4619.
[45] Smyrl, W. H., and Newman, J. *J. Phys. Chem. 72*, 13 (1968), 4660–4671.
[46] Atkins, P. W., and De Paula, J. *Elements of physical chemistry*, 5th ed ed. Oxford University Press, Oxford; New York, 2009.
[47] Chen, Y., Huo, W., Lin, M., and Zhao, L. *PLOS ONE 13*, 1 (2018), 1–16.
[48] Valøen, L. O., and Reimers, J. N. *J. Electrochem. Soc. 152*, 5 (2005), A882–A891.
[49] Nyman, A., Behm, M., and Lindbergh, G. *Electrochim. Acta 53*, 22 (2008), 6356–6365.
[50] Zugmann, S., Fleischmann, M., Amereller, M., Gschwind, R. M., Wiemhöfer, H. D., and Gores, H. J. *Electrochim. Acta 56*, 11 (2011), 3926–3933.
[51] Klett, M., Giesecke, M., Nyman, A., Hallberg, F., Lindström, R. W., Lindbergh, G., and Furó, I. *J. Am. Chem. Soc. 134*, 36 (2012), 14654–14657.
[52] Krachkovskiy, S. A., Bazak, J. D., Fraser, S., Halalay, I. C., and Goward, G. R. *J. Electrochem. Soc. 164*, 4 (2017), A912–A916.
[53] Matyka, M., Khalili, A., and Koza, Z. *Phys. Rev. E 78*, 2 (2008).
[54] Chung, D.-W., Ebner, M., Ely, D. R., Wood, V., and Edwin Garca, R. *Modell. Simul. Mater. Sci. Eng. 21*, 7 (2013), 074009.
[55] Tjaden, B., Cooper, S. J., Brett, D. J., Kramer, D., and Shearing, P. R. *Curr. Opin. Chem. Eng. 12* (2016), 44–51.
[56] Zacharias, N. A., Nevers, D. R., Skelton, C., Knackstedt, K., Stephenson, D. E., and Wheeler, D. R. *J. Electrochem. Soc. 160*, 2 (2013), A306–A311.
[57] Thorat, I. V., Stephenson, D. E., Zacharias, N. A., Zaghib, K., Harb, J. N., and Wheeler, D. R. *J. Power Sources 188*, 2 (2009), 592–600.
[58] Versteeg, H. K., and Malalasekera, W. *An introduction to computational fluid dynamics: the finite volume method*, 2nd ed ed. Pearson Education Ltd., 2007.
[59] Ames, W. F. *Numerical Methods for Partial Differential Equations*. Academic Press, 2014.
[60] Fuller, T. F., Doyle, M., and Newman, J. *J. Electrochem. Soc. 141*, 1 (1994), 1–10.
[61] Smith, R. B. *Nonequilibrium thermodynamics of porous electrodes for lithium-ion batteries*. PhD Thesis, Massachusetts Institute of Technology, 2017.
[62] Li, X., Xiao, M., Choe, S.-Y., and Joe, W. T. *Electrochim. Acta 155* (2015), 447–457.
[63] Wu, S.-L., Zhang, W., Song, X., Shukla, A. K., Liu, G., Battaglia, V., and Srinivasan, V. *J. Electrochem. Soc. 159*, 4 (2012), A438–A444.
[64] Mei, B.-A., Li, B., Lin, J., and Pilon, L. *J. Electrochem. Soc. 164*, 13 (2017), A3237–A3252.
[65] Huang, R. W. J. M., Chung, F., and Kelder, E. M. *J. Electrochem. Soc. 153*, 8 (2006), A1459.
[66] Cai, L., and White, R. E. *J. Power Sources 196*, 14 (2011), 5985–5989.
[67] Kupper, C., and Bessler, W. G. *J. Electrochem. Soc. 164*, 2 (2017), A304–A320.

EBSCOhost - printed on 2/14/2023 1:06 PM via . All use subject to https://www.ebsco.com/terms-of-use

[68] Albertus, P., Christensen, J., and Newman, J. *J. Electrochem. Soc. 156*, 7 (2009), A606–A618.
[69] Thomas-Alyea, K. E. *ECS Trans. 16*, 13 (2008), 155–165.
[70] Doyle, M., Newman, J., Gozdz, A. S., Schmutz, C. N., and Tarascon, J.-M. *J. Electrochem. Soc. 143*, 6 (1996), 1890–1903.
[71] Farkhondeh, M., Safari, M., Pritzker, M., Fowler, M., Han, T., Wang, J., and Delacourt, C. *J. Electrochem. Soc. 161*, 3 (2014), A201–A212.
[72] Ramadass, P., Haran, B., White, R., and Popov, B. N. *J. Power Sources 123*, 2 (2003), 230–240.
[73] Zhu, M., Park, J., and Sastry, A. M. *J. Electrochem. Soc. 159*, 4 (2012), A492–A498.
[74] Ramadesigan, V., Methekar, R. N., Latinwo, F., Braatz, R. D., and Subramanian, V. R. *J. Electrochem. Soc. 157*, 12 (2010), A1328.
[75] Danner, T., Singh, M., Hein, S., Kaiser, J., Hahn, H., and Latz, A. *J. Power Sources 334*, Supplement C (2016), 191–201.
[76] Masoudi, R., Uchida, T., and McPhee, J. *J. Power Sources 291* (2015), 215–224.
[77] Nyman, A., Zavalis, T. G., Elger, R., Behm, M., and Lindbergh, G. *J. Electrochem. Soc. 157*, 11 (2010), A1236–A1246.
[78] Delacourt, C., and Safari, M. *J. Electrochem. Soc. 159*, 8 (2012), A1283–A1291.

EBSCOhost - printed on 2/14/2023 1:06 PM via . All use subject to https://www.ebsco.com/terms-of-use

EBSCOhost - printed on 2/14/2023 1:06 PM via . All use subject to https://www.ebsco.com/terms-of-use

Index

https://doi.org/10.1515/9783110537734-015

EBSCOhost - printed on 2/14/2023 1:06 PM via . All use subject to https://www.ebsco.com/terms-of-use

EBSCOhost - printed on 2/14/2023 1:06 PM via . All use subject to https://www.ebsco.com/terms-of-use

EBSCOhost - printed on 2/14/2023 1:06 PM via . All use subject to https://www.ebsco.com/terms-of-use

EBSCOhost - printed on 2/14/2023 1:06 PM via . All use subject to https://www.ebsco.com/terms-of-use